# SEDIMENT DYNAMICS OF MACROTIDAL SAND BARS, BAY OF FUNDY

# SEDIMENT DYNAMICS OF MACROTIDAL SAND BARS, BAY OF FUNDY

By

ROBERT WALKER DALRYMPLE, B.Sc.

A Thesis

Submitted to the School of Graduate Studies

in Partial Fulfilment of the Requirements

for the Degree

Doctor of Philosophy

McMaster University

February, 1977

DOCTOR OF PHILOSOPHY (1977)
(Geology)

McMaster University
Hamilton, Ontario

TITLE: Sediment Dynamics of Macrotidal Sand Bars, Bay of Fundy

AUTHOR: Robert Walker Dalrymple, B.Sc. (University of Western Ontario)

SUPERVISOR: Professor G.V. Middleton

NUMBER OF PAGES: xxviii, 635

## ABSTRACT

The Minas Basin and Cobequid Bay, Nova Scotia, possess the highest tides in the world: maximum measured range = 16.3 m; mean range = 11.9 m. Numerous large sand bars, with exposed lengths ranging from 1 to 10 km, and widths from 0.2 to 4.25 km, are developed in the area. The total relief reaches 15 m in Cobequid Bay, but only the upper 6 to 7 m is exposed at low tide. The bars are generally asymmetric with the gentler side facing the shoreline, which is commonly bordered by a gravel-veneered, wave-cut platform. The sedimentation dynamics of five major bars has been studied in detail.

Reversing tidal currents are the dominant process operating on the sand bars; wave action is limited by the small fetches. The flood tide is of shorter duration than the ebb throughout the area, because the turn of the tide at low water is delayed up to 1.5 hours by bottom friction and the ebb hydraulic gradient. The delay increases toward the head of Cobequid Bay.

Time-averaged mean current speeds range from 0.2 to 0.9 m/s, and shear velocities from 1.0 to 5.0 cm/s, with the higher values generally occurring in the channels. Because the bars lie at a slight angle to the flow, their upstream sides experience stronger currents than the

downstream sides as the currents flow over the bars. These zones alternate position with every flow reversal, producing an inequality between the ebb and flood currents at most locations. This process, and not helical flow, is responsible for the origin of the bars.

Fluorescent tracer experiments reveal that residual sediment transport occurs almost everywhere. Residual unit discharges range from 0.38 to 1793 kg/tidal cycle, and average approximately 350 kg/cycle. (Particle transport speeds average only 1 to 2 m/cycle.) On individual bars, sediment moves in opposite directions on either side of the crestline, with upslope components on both sides. Within Cobequid Bay, ebb-dominated transport is largely confined to the axis of the bay, whereas flood transport occurs along either shore. A sediment circulation system analogous to that of ebb-tidal deltas is produced, with clockwise sediment circulation in the northern half of the bay, and counter-clockwise transport in the southern half. The swatchways break these large circulation cells into smaller units.

Sediment dispersal from a point source is fundamentally similar to that occurring in unidirectional flow because of the residual transport. The tracer distributions are skewed in the direction of residual transport, but become more symmetrical as time passes. The longitudinal dispersion is positively correlated with the centroid

migration speed and flow strength, and averages 3.5 times the lateral dispersion.

Two distinct types of large-scale bedforms are recognized: megaripples (dunes) and sand waves; the sand waves are subdivided into rippled and megarippled varieties, depending on the superimposed features. Megaripples are more irregular in appearance than sand waves, and possess scour pits which sand waves lack. Sand waves are generally larger but flatter than megaripples, and rarely possess an avalanche face, so that the internal stratification is composite and produced by the superimposed bedforms. Rippled sand waves form where peak mean speeds are less than 0.8 m/s. Both megarippled sand waves and megaripples exist in faster flows; megaripples where mean grain sizes are finer than 1.7 phi (0.31 mm), and megarippled sand waves in coarser sediment.

On average, the sediments are medium sands with moderately well sorted, nearly symmetrical and leptokurtic size distributions. The coarsest sizes and poorest sortings occur near areas of gravel lag, and the channels tend to be coarser than bar crests. The finest sands are found in the ebb-dominated parts of Cobequid Bay.

There are three fundamental, overlapping-normal size populations: the traction (C), intermittent suspension (A), and continuous suspension (B) populations. The average mean

size and sorting of each are: C: -0.18 phi and 1.15 phi-units; A: 1.70 phi and 0.44 phi-units; and B: 2.56 phi and 0.93 phi-units. The fine-grained character of the sediment in the ebb-dominated part of Cobequid Bay is retained during transport (inherited) because the flow energy increases along the transport path. Elsewhere, both A and C populations (and the total sample) tend to be finer where the currents are weaker.

Tracer experiments show that the transport and dispersion rates are almost independent of grain size within the traction population, whereas the rates increase rapidly as the size decreases for sizes travelling in intermittent suspension. The transition in behaviour occurs at the grain size whose fall velocity is equivalent to the average maximum shear velocity of the currents. The "break" between the C and A populations, as determined by the point of equal overlap, bears a similar, statistically significant relationship to the shear velocity. The point of intersection of straight-line segments gives less satisfactory results.

ACKNOWLEDGEMENTS

Numerous people deserve thanks for assistance, guidance, and encouragement given during the five and a half years devoted to this thesis. Foremost among these is Dr. G.V. Middleton, the research supervisor, whose suggestions and criticisms have substantially improved the thesis, and contributed to the education of the author. The remaining members of the supervisory committee, Drs. McCann, Walker, and Woo are acknowledged for their interest and guidance throughout the research, and for reading portions of a preliminary draft of the thesis. Dr. P.D.M. Macdonald of the Applied Mathematics Department, McMaster University, deserves special thanks for his continued interest and assistance with the statistical aspects of the tracer analysis, and the size-population dissection, despite often naive badgering by the author.

Cheerful and conscientious assistance in the field was provided by Ray Featherstone, Tak-Chi (Mike) Yu, Jim Moffat, and Mike Festeryga, in spite of the often long, tedious hours and hazardous conditions. Aubrey Scott, Adrien LaBlanc, Guy Macalony, Logan Lewis, and Bill Miller are thanked for ably providing the essential boat services,

and for their tolerance of the seemingly odd nature of the work. The kindnesses and hospitality of many other local inhabitants of the Cobequid Bay-Minas Basin area will always be fondly remembered.

In addition, several people have been of invaluable assistance during the laboratory analyses and final preparation of the thesis. The author particularly thanks Tak-Chi (Mike) Yu, Brenda O'Connor, and Rick Cheel, who carried out the arduous task of analysing the tracer samples, and Maureen Dickson who performed most of the sediment size analyses. The photographic reproduction of the figures and appendices would not have been possible without the help of Jack Whorwood. Pat Young and Helen Elliott typed the final manuscript, sometimes acting as proof-readers and handwriting experts in the process.

Many fellow graduate students also deserve acknowledgement. John Knight and Joe Lambiase have contributed directly to the thesis with the exchange of needed computer programs and critical discussion. The author has also benefitted from stimulating conversations with Doug Cant, Richard Hyde, and Peter McCabe. Ko Griep, Mike Marchand, Nick Massey, Dick Page, and others have contributed indirectly by helping to make the time spent at McMaster pass more quickly and enjoyably.

Special thanks are given to Chris Fuss who performed

the singular task of typing much of the first draft from the author's scrambled handwriting. Her sympathy and encouragement throughout the writing helped keep the author sane.

Financial assistance for much of the field work has come from the Department of Energy, Mines, and Resources, and the National Research Council of Canada through grants to Dr. G.V. Middleton. The research was conducted while the author was the recipient of a National Research Council of Canada 1967 Science Scholarship and a Gulf Oil Canada Limited Graduate Fellowship.

TABLE OF CONTENTS

CHAPTER 6 (Continued)

## LIST OF FIGURES

## LIST OF TABLES

## SYMBOL NOTATION AND ABBREVIATIONS

All mathematical symbols and abbreviations used in this thesis are listed below in alphabetical order, with a brief statement of the usage or meaning of each item. Wherever possible, an attempt has been made to retain the notation used in the various source references, and as a result, a number of symbols have multiple definitions here. For this reason, the section(s) in which those symbols or abbreviations which appear infrequently are found have been included for cross reference. If a particular symbol or usage recurs in more than two sections, however, no section listing has been given. For further comment on the meaning of any particular item, the appropriate section of the text should be consulted.

The metric system of units has been used exclusively in this thesis, with the exception that time is expressed in hours or tidal cycles where such usage is appropriate. The dimensions of each symbol or abbreviation are also listed below in general form, with L = length, M = mass, and T = time.

| Symbol | Where Used | Meaning | Dimensions |
|---|---|---|---|
| a | 6.2.2 | reference level in flow | L |
| a | 6.3.5 | cross-product term in moment function | various |
| A | 3.1.2 | area of current vane | $L^2$ |
| A | 6.2.2; 6.2.4 | dimensionless parameter | - |
| $A_E$ | 6.2.2 | dimensionless thickness of bedload layer | - |
| $A_s$ | 6.3.5 | area of grid square | $L^2$ |
| $A_1$ | 6.2.3 | dimensionless proportionality factor | - |
| b(*) | 6.3.5 | binomial distribution | - |
| B | 3.1.3 | constant in logarithmic velocity distribution | - |
| B | 6.2.2 | dimensionless parameter | - |
| C | 3.1.3 | Chezy resistance factor | $L^{1/2}T^{-1}$ |
| C | 5.1.2 | bedform crest sample | - |
| C | 6.2.4 | dimensionless parameter | - |
| C | 6.3 | dimensionless tracer concentration | - |
| $C_D$ | 3.1.2 | drag coefficient | - |
| $C_y$ | 6.2.2 | suspended sediment concentration at height y in flow | - |
| $C_1$ | 4.2.2; 6.4.3 | constant of integration of bedload discharge calculation, from bedform migration | $MT^{-1}$ |
| $d, d_{35}$ | | grain diameter, at indicated percentile (finer) | L or $-\log_2 L$ |
| D | 6.3.4 | displacement of tracer centroid | L |

| Symbol | Where Used | Meaning | Dimensions |
|---|---|---|---|
| $D_{gr}$ | 6.2.4 | dimensionless grain size | - |
| E | 5.1.2 | sample from ebb stoss side | - |
| E | 6.2.4 | transport efficiency | - |
| $E_f$ | 6.2.3 | effective flow energy | $ML^3T^{-3}$ |
| ES | 5.1.2 | sample from ebb stoss side | - |
| $E_\ell$ | 6.3.4 | elongation ratio | - |
| E( ) | 6.3.5 | expected value | - |
| f | 3.1.3; 6.2.3 | Darcy-Weisbach friction factor | - |
| $f_1$( ) | 6.2.4 | function of | - |
| F | 5.1.2 | sample from flat, rippled surface | - |
| $F_{gr}$ | 6.2.4 | particle mobility number | - |
| Fr | 3.1.3 | Froude number | - |
| FS | 5.1.2 | sample from flood stoss side | - |
| g | | acceleration of gravity | $LT^{-2}$ |
| $G_{gr}$ | 6.2.4 | dimensionless transport rate | - |
| h | | water depth | L |
| H | | bedform height | L |
| HFI | 4.2.1 | horizontal form index | - |
| i | 6.3.3 | integer | - |
| $I_1, I_2$ | 6.2.2 | integrals in Einstein transport function for suspended load | - |
| j | 6.2.2 | integer | - |
| k | 6.3.5 | integer | - |
| $k_s$ | 3.1.3; 3.2.2 | equivalent sand roughness | L |

| Symbol | Where Used | Meaning | Dimensions |
|---|---|---|---|
| K | 6.3.5 | arbitrary constant | - |
| l | 3.1.3 | Prandtl's mixing length | L |
| L | | bedform length | L |
| L | 5.1.2 | sample from base of bedform lee side | - |
| m | 6.2.4 | exponent in Ackers-White transport function | - |
| m | 6.3.5 | integer | - |
| M | 3.1.2 | mass of current vane | M |
| n | | integer | - |
| n | 6.2.4 | transition exponent | - |
| N | 6.3.3 | number of tracer grains counted | - |
| p | 6.3.3 | proportion of material in size range of tracer | - |
| $p_c$ | 6.3.5 | proportion of injected tracer in proper size range | - |
| $p_i$ | 5.3.2 | cumulative percent at size fraction i | - |
| $p_j$ | 6.2.2 | fraction of bed material with size $d_j$ | - |
| $p_T$ | 6.3.4 | proportion of mobile layer in proper size range | - |
| $p_\delta$ | 6.3.4; 6.3.5 | proportion of mobile layer reworked | - |
| p( ) | 6.3.5 | Poisson distribution | - |
| P | 6.2.2 | probability of a grain moving | - |
| $P_c$ | 5.3.2 | proportion of size population in sample | - |
| q | 3.1.3; 3.2.2 | unit discharge of fluid | $L^2T^{-1}$ |

| Symbol | Where Used | Meaning | Dimensions |
|---|---|---|---|
| $q_b$, $q_{sb}$ | | unit mass discharge of bedload | $ML^{-1}T^{-1}$ |
| $q_{ni}$ | 5.3.2 | cumulative percent in population n, out of 100% | - |
| $q_s$ | | total unit mass discharge of sediment | $ML^{-1}T^{-1}$ |
| $q_{ss}$ | 6.2.2 | unit mass discharge of suspended load | $ML^{-1}T^{-1}$ |
| r | | correlation coefficient | - |
| r | 6.3 | integer giving order of moment in x-direction | - |
| R | 6.3.5 | numerator of moment function | various |
| Re | 3.1.3 | Reynolds number | - |
| $R_E$ | 6.3.5 | recovery efficiency | - |
| s | 6.2.4 | ratio of sediment and fluid specific gravities | - |
| s | 6.3 | integer giving order of moment in y-direction | - |
| S | | slope of energy grade line | - |
| S | 6.3.5 | denominator of moment function | various |
| SI | 4.2.1 | sinuosity index | - |
| t | | time | T |
| T | 5.1.2 | sample from bedform trough | - |
| T | | time | T |
| Tr | 3.2 | tidal coefficient | - |
| u | 3.1.3 | current speed at one height above bed | $LT^{-1}$ |
| $u_{100}$ | 3.1.3 | current speed one metre above bed | $LT^{-1}$ |

| Symbol | Where Used | Meaning | Dimensions |
|---|---|---|---|
| $u_*$ | | shear velocity | $LT^{-1}$ |
| U | | current speed | $LT^{-1}$ |
| $v_{11}$ | 6.3.5 | variance of R | various |
| $v_{12}$ | 6.3.5 | covariance of R and S | various |
| $v_{22}$ | 6.3.5 | variance of S | various |
| V | 6.3.5 | coefficient of variation | - |
| $V_b$ | | bedform migration speed | $LT^{-1}$ |
| $V_c$ | 6.3.4 | speed of centroid movement | $LT^{-1}$ |
| w | 5.3.1 | particle settling velocity | $LT^{-1}$ |
| w | 6.3.3 | average weight of a tracer grain | M |
| W | 5.1.3 | cumulative weight percent | - |
| W | 6.3.3 | weight of sediment scanned in concentration determination | M |
| $W_f$ | 6.2.3 | rate of work done | $ML^3T^{-3}$ |
| x | | distance parallel to transport direction | L |
| x | 6.2.2 | correction factor in velocity distribution | - |
| X | 6.2.2 | characteristic grain size | L |
| X | 6.2.4 | mass flux per unit of flow | $ML^{-3}$ |
| y | | distance transverse to transport direction | L |
| y | 3.1.3 | height above bed | L |
| Y | 6.2.2 | correction factor for lift coefficient | - |

| Symbol | Where Used | Meaning | Dimensions |
|---|---|---|---|
| $z$ | 6.2.2 | Rouse exponent | - |
| $z$ | 6.3.5 | abscissa of standard normal curve | - |
| $z_o$ | 3.1.3 | height at which velocity goes to zero | L |
| $\alpha$ | 6.2.4 | dimensionless constant | - |
| $\alpha$ | 6.3.5; 6.4 | probability level | - |
| $\alpha_1, \alpha_2, \alpha_3$ | 6.2.3 | proportionality factors | - |
| $\beta$ | 6.2.3 | dimensionless shear stress | - |
| $\beta$ | 6.3.4 | skewness | - |
| $\gamma$ | | specific weight of fluid | $ML^{-2}T^{-2}$ |
| $\gamma_s$ | | specific weight of sediment | $ML^{-2}T^{-2}$ |
| $\delta$ | 3.1.3 | thickness of laminar sublayer | L |
| $\delta_b$ | 6.3.4; 6.3.5 | effective thickness of mobile layer | L |
| $\Delta$ | 6.2.2 | apparent bed roughness | L |
| $\Delta$ | 6.3 | increment of a quantity | - |
| $\zeta$ | 4.2.2; 6.3.4 | one minus the sediment porosity | - |
| $\eta_o$ | 6.2.2 | dimensionless parameter | - |
| $\Theta$ | 3.1.2 | angle of current vane cable | degrees |
| $\Theta$ | 6.2.3 | dimensionless shear stress | - |
| $\kappa$ | 3.1.3 | von Kármán constant | - |
| $\lambda$ | 6.3.5 | parameter of Poisson distribution | - |
| $\mu$ | | dynamic viscosity | $ML^{-1}T^{-1}$ |

| Symbol | Where Used | Meaning | Dimensions |
|---|---|---|---|
| $\mu$ | 5.1.3; 6.3.4 | moments about the mean | various |
| $\mu'$ | 5.1.3; 6.3.4 | moments about the origin | various |
| $\nu$ | 6.2 | kinematic viscosity | $L^2T^{-1}$ |
| $\xi$ | 6.2.2 | hiding factor | - |
| $\xi_*$ | 6.3.5 | known tracer concentration | - |
| $\rho$ | | density of fluid | $ML^{-3}$ |
| $\rho_s$ | | density of sediment | $ML^{-3}$ |
| $\sigma$ | 6.3.4 | standard deviation | L |
| $\tau$ | | shear stress | $ML^{-1}T^{-2}$ |
| $\phi$ | | $-\log_2$ of grain diameter in millimetres | - |
| $\Phi$ | 6.2.2 | intensity of bedload transport | - |
| $\Psi$ | 6.2.2 | flow intensity parameter | - |
| $\omega$ | 3.1.3; 6.4.3 | stream power per unit area of bed | $MT^{-3}$ |
| $\Omega$ | 6.3.4 | direction of centroid movement | degrees |

Superscripts

| | | | |
|---|---|---|---|
| $'$ | 3.1.3 | turbulent component of velocity | - |
| $'$ | 6.2 | value related to grain roughness | - |
| $''$ | 6.2 | value related to form roughness | - |
| $\hat{}$ | 5.3.2; 6.3.5 | estimated value | - |
| $-$ | | mean value or time average | - |

| Symbol | Where Used | Meaning | Dimensions |
|---|---|---|---|
| Subscripts | | | |
| cg | 6.2.4 | pertaining to coarse grain sizes | - |
| cr | | critical value for initiation of motion | - |
| E | | pertaining to the ebb phase of the tide | - |
| fg | 6.2.4 | pertaining to fine grain sizes | - |
| F | | pertaining to the flood phase of the tide | - |
| o | | quantity evaluated at the datum or origin | - |
| 1,2 | 3.1.3 | levels within the flow | - |

# CHAPTER 1

# INTRODUCTION

## 1.1 The Study Area

The area under investigation in this thesis is located in the Minas Basin and Cobequid Bay, Nova Scotia, Canada, the eastern arm at the head of the Bay of Fundy (Figures 1.1, 1.2 and 1.3), and situated at approximately $45^{o}$ 20' N latitude, and between $63^{o}$ 30' W and $64^{o}$ 10' W longitude. This area is renowned for its high tidal range, which is reputed to be the largest in the world (McWhirter and McWhirter, 1972 - Guinness Book of Records). The largest tidal range that has been measured is 16.3 metres (Dawson, 1917) at Burntcoat Head, on the south side of Cobequid Bay (Figure 1.2). This clearly qualifies the Minas Basin and Cobequid Bay as a macrotidal environment as defined by Davies (1964) and Hayes (1975), where macrotidal refers to tidal ranges in excess of four metres.

At low tide, an extensive intertidal zone is exposed, surrounding the Minas Basin, and in Cobequid Bay. The area of the intertidal zone is estimated to be in the range of 200 - 300 $km^2$. Much of the intertidal foreshore is a wave-cut platform, covered with a thin layer of gravel and mud. Mud is extensive, however, in a few sheltered areas only. The

most distinctive features of the shallow subtidal and intertidal areas are large, linear sand bars that are widely developed around the margin of the Minas Basin, and in Cobequid Bay (Figures 1.2 and 1.3). The largest complex lies in the west-central part of Cobequid Bay, extending the entire width of the bay (Figure 1.3). Another major area of bars is located in the Avon River estuary in the southwest corner of the Minas Basin (Figure 1.2). Along the north shore of the Minas Basin, sand bars are developed at Five Islands and at the tip of Economy Point. Several additional examples are present along the south shore, west of Walton (Figure 1.2). All of these sand bars have lengths in the range of 1 - 10 km and widths of 0.2 - 4.25 km, with relief of up to 20 metres between the crests and the adjacent channel bottoms. These bars are the object of the research described in this thesis.

During the course of the field work, conducted during the summers of 1971 to 1974, four separate localities were investigated in detail. These major areas are: Selmah Bar (Figure 1.2, area D, and Figure 1.3), located in the southeast corner of Cobequid Bay; Diamond Bar (Figure 1.2, area B, and Figure 1.3), in the north-central part of Cobequid Bay; Centre and East Bars (Figure 1.2, area C), at the tip of Economy Point; and Big Bar, Figure 1.2, area A), situated north of the islands at Five Islands. These areas provide the bulk of the quantitative data that are the basis of this thesis. In addition, six smaller bars were studied in less detail: Spencer Point Bar,

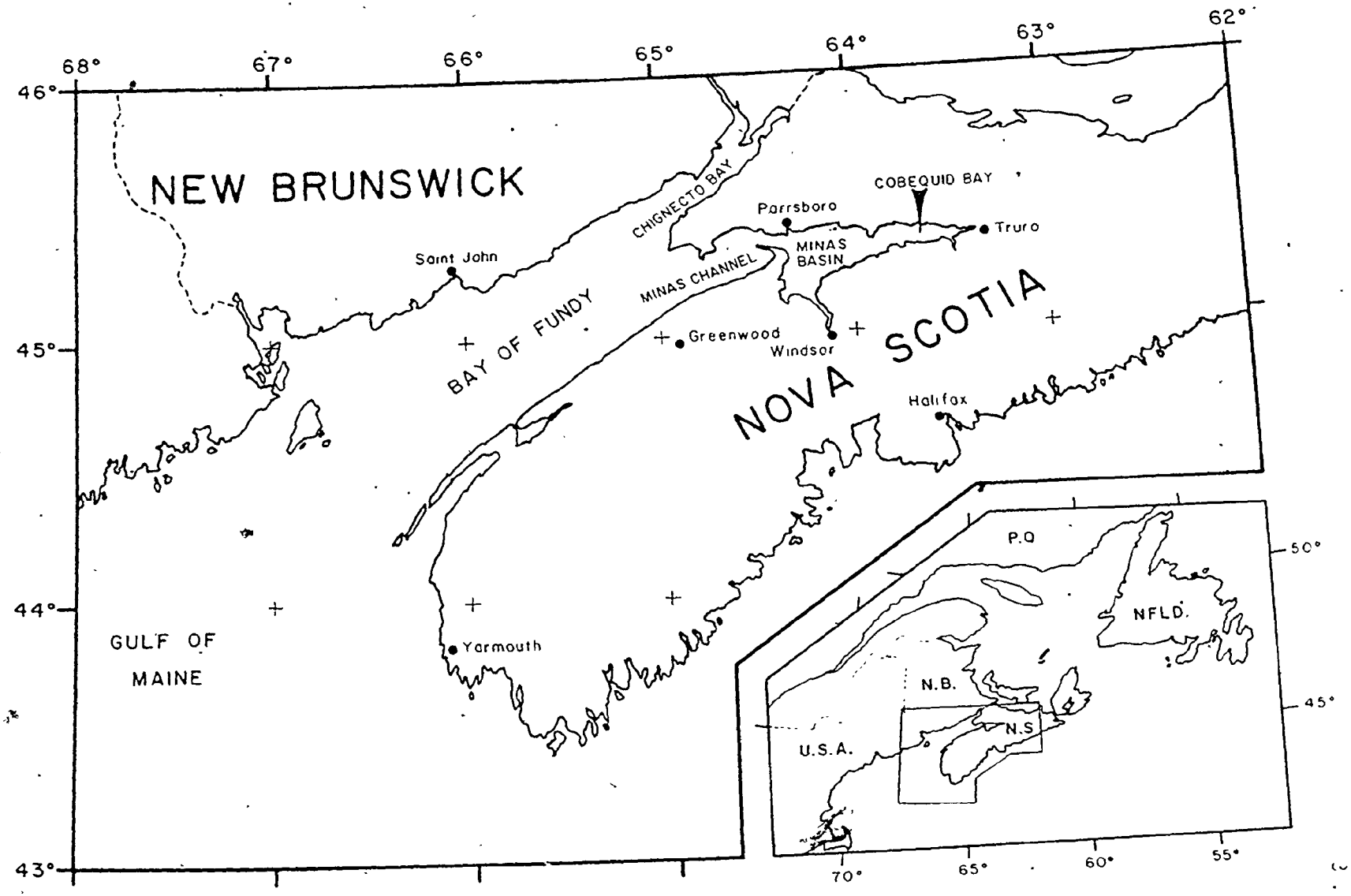


FIGURE 1.1 : Location of the study area. Major cities, towns, and subdivisions of the Bay of Fundy are shown.

FIGURE 1.2 : Intertidal zone in the Minas Basin and Cobequid Bay (stippled). The four major localities studied are indicated by the rectangles: A - Big Bar; B - Diamond Bar; C - Centre and East Bars; D - Selmah Bar. Sources for the intertidal-zone limits: Cobequid Bay and the north shore as far west as Big Bar - air photos taken June 5, 1973; Avon River and approaches - J. J. Lambiase, personal communication, 1976; the remainder from Canadian Hydrographic Chart 4010, 1971.

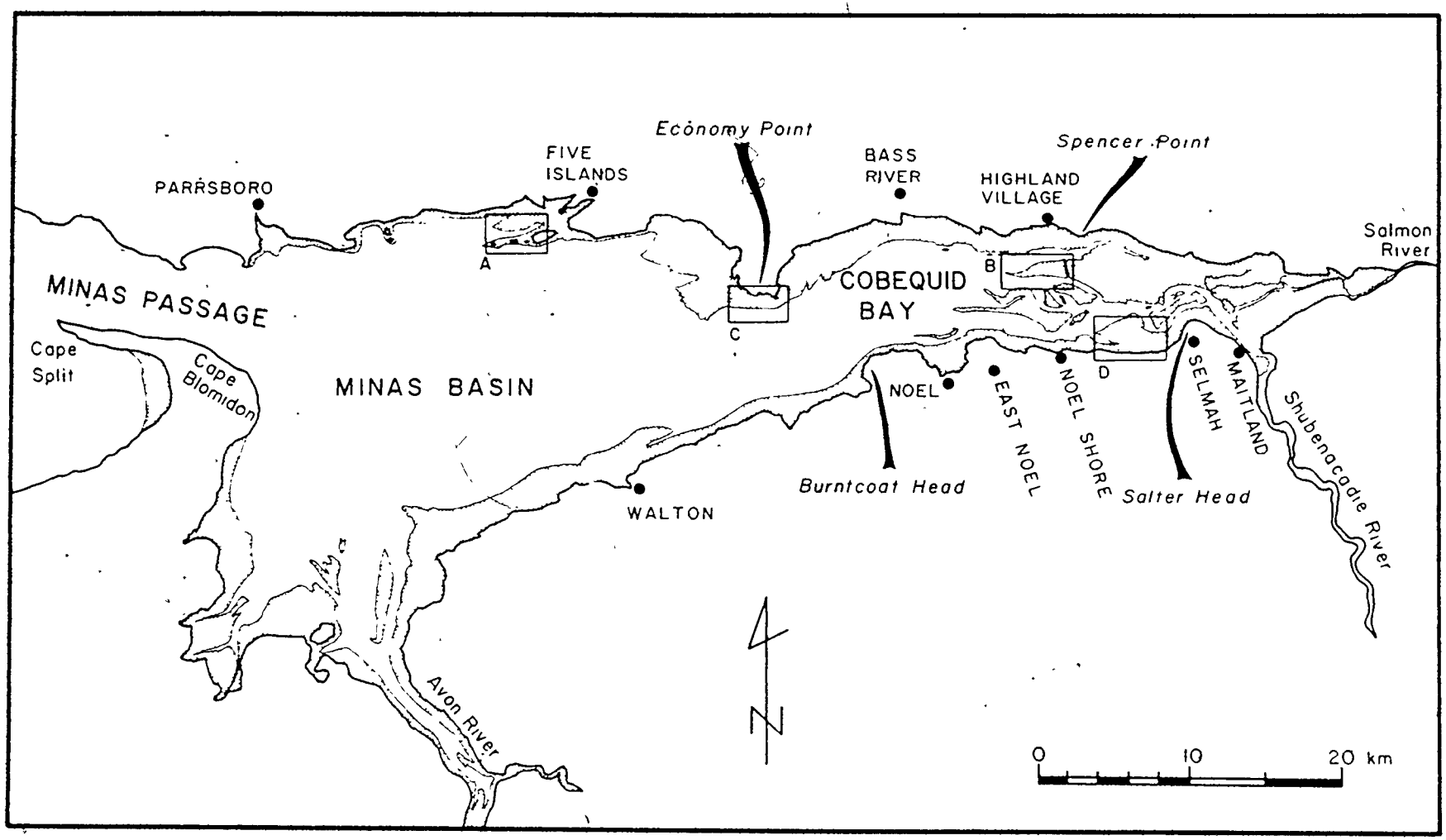
PARRSBORO
FIVE ISLANDS
Economy Point
BASS RIVER
HIGHLAND VILLAGE
Spencer Point
Salmon River
A
B
C
D
MINAS PASSAGE
COBEQUID BAY
Cape Split
Cape Blomidon
MINAS BASIN
NOEL
EAST NOEL
NOEL SHORE
SELMAH
MAITLAND
Shubenacadie River
Burntcoat Head
Salter Head
WALTON
Avon River
0
10
20 km

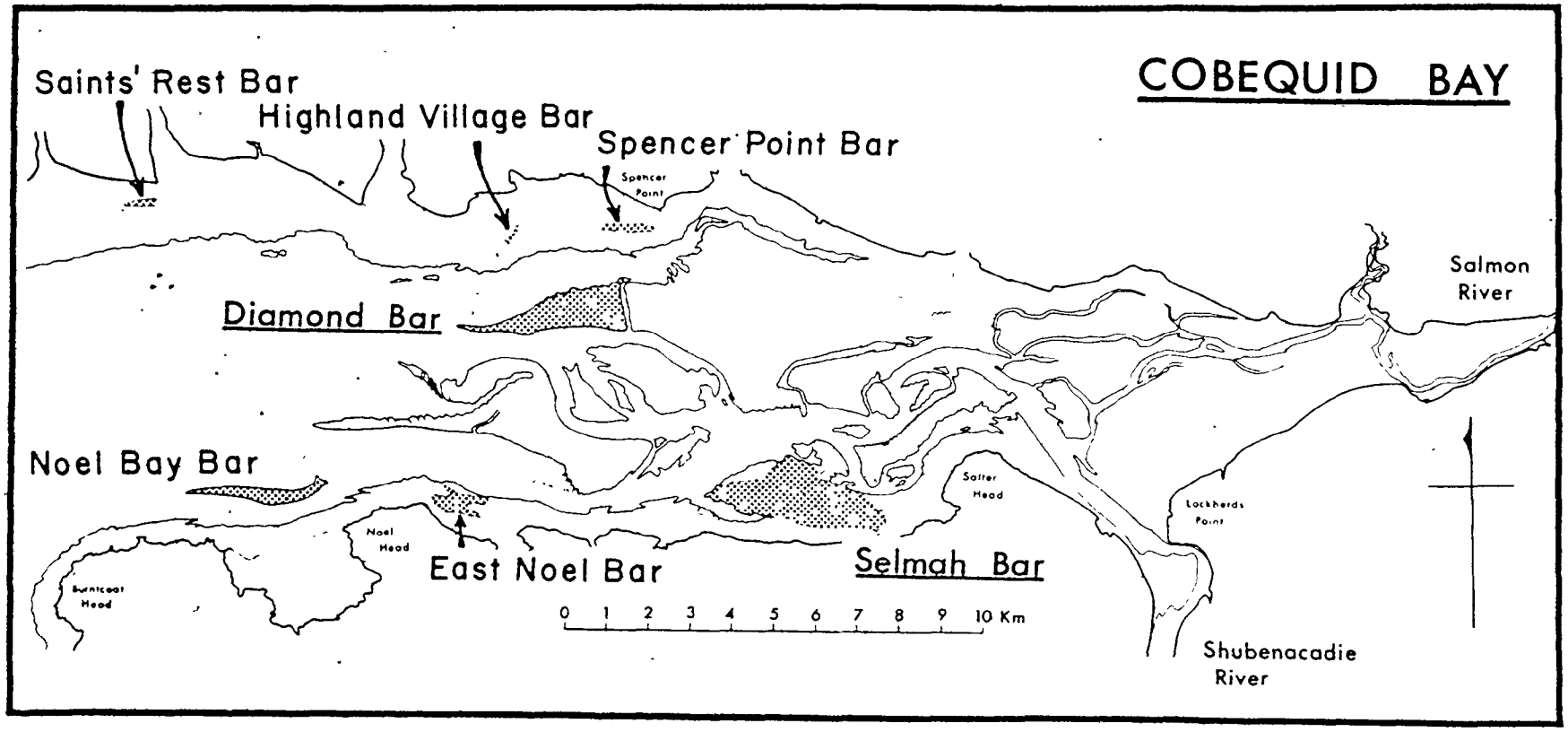


FIGURE 1.3 : Location of the studied bars in Cobequid Bay (stippled). Outline of the intertidal zone from air photos taken June 5, 1973.

Highland Village Bar, and Saints' Rest Bar (Figure 1.3), all situated on the intertidal foreshore along the north side of Cobequid Bay; East Noel Bar (Figure 1.3), on the intertidal foreshore on the south side of Cobequid Bay; Noel Bay Bar (Figure 1.3), located across the mouth of Noel Bay; and Pinnacle Flats, extending between Long and Pinnacle Islands at Five Islands (Figure 1.2, area A, and Figure 2.10). These areas provide further qualitative and quantitative data to support the observations from the main study bars.

## 1.2 Nature of the Research

The research reported here can be broadly described as an investigation of sedimentation dynamics on the intertidal sand bars mentioned above. This involves the description of the processes and responses that occur in the study area. At all stages, every attempt is made to relate the responses to the processes in the most quantitative manner possible, for it is only in this way that the intuitive and qualitative conclusions presented in previous literature can be tested, and the level of their universality be raised.

The first task is the description of the study area. What processes are operative? What are their relative importances, and what time variabilities are there? In the present situation, the answers to these questions involve primarily tidal currents. Also, what is the character of the sediment that is subjected to the action of the tidal currents? In this investigation, attention is given primarily to the sediment grain size.

Next, how do the sediments respond to the applied processes? What form does the response take, and how does it change with variations in tidal current strength and direction? The most obvious response is the generation of a suite of bedforms of various sizes and shapes, and the production of internal stratification. Questions related to this aspect of the sediment response are presently under investigation by Knight (1971, 1972, 1973), but comparative, and supporting observations will be given.

Another aspect of sediment response is size sorting, and the modification of grain-size distributions. What is the nature of these distributions, and of the component size populations? Do the individual components have physical significance in terms of transport mechanisms as suggested by Visher (1969, 1972), and if so, what are the controls operating to produce them? What can the analysis of size distributions tell us about processes?

The most fundamental sediment response that is associated with both the generation of bedforms and size sorting, is movement, or sediment transport. Questions to be considered include: What is the nature of sediment transport and dispersion in a tidal environment? Does sediment move back and forth, with no net movement, or are there preferred directions of residual transport? If the answer to this last question is yes, as has been suggested by a number of workers, what are the rates and patterns of net transport on intertidal sand bars? Does the

sand move around and around on one sand bar as suggested by Houbolt (1968) for sand ridges in the North Sea, and by Klein (1970) for Big Bar at Five Islands? How does the form of the bar reflect, and in turn influence, the transport? What are the hydraulic controls on sediment movement? The answers to these questions have applicability not only to the study area itself, but also to other macrotidal environments, and in general to all tidal sediments.

Many of the process-response relationships to be investigated in the context of a macrotidal environment also have a wider significance on a second, more general level that is not restricted to a single environmental setting. Of particular importance at this level are such topics as: bedform types and their relationships to controlling variables; response of bedforms to time-varying conditions; sediment transport behaviour, especially as a function of grain size; and the nature and significance of grain size distributions. The confident extension of results obtained in a tidal situation to a more general level requires, in most cases, a clear evaluation of the effects of reversing tidal currents, as compared to unidirectional flow conditions.

The above paragraphs provide a general statement of the scope and nature of the research. Not only are problems specific to the Minas Basin and Cobequid Bay being attacked, but an attempt is being made to provide additional data and shed further light on some fundamental areas of concern in sedimentology.

## 1.3 Previous Work

At this point in the thesis it is impossible to summarize all of the available literature that is pertinent to every aspect of the research. Rather, specialized references will be discussed as required, during the presentation and analysis of the results. It is the intention here to place this work in its proper context in relation to previous work on linear, tidal sand bodies.

Because of the fact that the study area has the largest tides in the world, it is valid to question the use of the Minas Basin-Cobequid Bay area as a model for other areas. Unfortunately, it is difficult to assess the degree to which the area is unique due to the lack of detailed investigations in other localities. However, it has been suggested by Hayes (1975), in an extension of the work of Davies (1964), that wherever the tidal range exceeds a value of about four metres (= macrotidal), the general forms of sediment accumulation are similar, the characteristic feature being large, linear sand bodies, disposed parallel to the tidal currents. The study area is consistent with this. It is also significant to note that nearly one-third of the world's shorelines are macrotidal according to the above definition.

Although the literature on tidal sediments is very large, as is evidenced by the massive bibliography given by Reineck (1972), there have been few studies of the linear sand bodies that characterize macrotidal sedimentation. Most of

the papers on tidal sediments deal with the facies in mesotidal areas ( 2 - 4 m tidal range). Even in areas with macrotidal ranges, the studies have concentrated largely on the marginal, primarily fine-grained intertidal foreshores, because the sand bars are often not easily accessible, and may not even be exposed at low tide. The larger tidal range in the Bay of Fundy has the advantage of exposing these bars, allowing direct observation. In addition, most of the studies conducted in the well-known tidal flat areas have been concerned primarily with general facies descriptions and the establishment of stratigraphic facies models. As a result, there have been few systematic and detailed studies of process-response relationships on a quantitative level, as will be presented here. Examples of the more general studies are: Reineck (1963), and Reineck and Singh (1967) along the German North Sea coast; Evans (1965) in The Wash, England; Phlipponneau (1956) and Bajard (1966) from the Baie due Mont Saint-Michel, France; and Thompson (1968) on the Colorado River delta.

The linear sand bodies of supposed tidal current origin described in the literature may be grouped into two classes by location: the first in somewhat restricted, estuarine or nearshore conditions; and the second on open, tide-swept shelves. Examples of the first class include the German bight of the North Sea (Reineck, 1963); the Gironde River estuary (Allen, 1972); the Tay River estuary, Scotland (Green, 1975); the Ord River estuary, Australia (Wright, Coleman and Thom,

1975); Vineyard Sound, Cape Cod (Smith, 1969); Chesapeake Bay entrance (Ludwick, 1972, 1974, 1975b); and the present study area, described by Swift and McMullen (1968) and Klein (1968, 1970). The second class of large, linear sand bodies are present on many parts of the world's continental shelves, and have been called "tidal current ridges" by Off (1963, p.324). These features measure 7.5 - 30 metres in height, 8 - 65 km in length, and have a spacing between 1.5 and 10 km. The best studied occurrence is in the North Sea and adjoining parts of the continental shelf to the west (Bouysse et al, 1976; Caston, 1972; Caston and Stride, 1970; Houbolt, 1968). Other examples from George's Bank in the Gulf of Maine have been described by Jordon (1962) and Stewart and Jordon (1965). At present it is not clear whether the two types are truly identical, because of a lack of detailed quantitative information from the shelf type, which is rarely exposed. Off (1963) groups both types together in his discussion, and there is a tendency among workers to consider them similar. If such is the case, then the Minas Basin-Cobequid Bay area might prove to be a valuable model.

Of the studies on linear, tidally-produced sand bodies listed above, most present qualitative, observational descriptions. Only the papers by Green (1975), Klein (1970), Ludwick (1975b) and Smith (1969) contain any significant amount of quantitative information on the tidal currents, bedforms, or sediment transport patterns and rates.

Green (1975) occupied three stations in a channel of the Tay River estuary, and monitored tidal currents while observing the bedforms and their behaviour. He was able to show a general correlation between the bed observations and the hydraulic variables.

The study of Klein (1970) was concerned primarily with the description of sediment grain size, bedform features, and internal sedimentary structures, but a number of point current measurements plus a few stands of longer duration were obtained. These data, when combined with some fluorescent tracer dispersal observations, suggested that the net sediment transport pattern forms a closed elliptical cell on Big Bar at Five Islands, with opposite directions of transport on either side of the crest. In a subsequent paper (Klein and Whaley, 1975), an attempt was made to differentiate the hydraulic controls governing the migration of dunes and a larger bedform type called sand waves.

Ludwick (1975b) used an extensive set of tidal current data to delineate areas of inferred erosion or deposition in the entrance to Chesapeake Bay, and to show the existence of mutually evasive ebb and flood paths that correspond to a series of alternate-facing ebb and flood parabolic shoals. Net sediment transport was again found to be oppositely directed on either side of the shoal crests. In an earlier paper, Ludwick (1972) provided some quantitative data on the migration of sand waves in the same area.

Smith (1969), working in Vineyard Sound, Cape Cod, obtained a number of current velocity profiles over a sand ridge and found that a net counterclockwise circulation of water and sediment existed around the ridge. It was also discovered that even large bedforms with heights up to 2 metres could be reversed during each half tidal cycle.

From this brief review of the more quantitative papers dealing with linear sand bodies, it is obvious that our present knowledge of sediment dynamics in areas with large tidal ranges is limited.

The study reported in this thesis is one of three currently being conducted into various aspects of the sand dynamics in Minas Basin and Cobequid Bay by students at McMaster University, Hamilton, under the supervision of Dr. G. V. Middleton. Some preliminary and general descriptive results have been published: Dalrymple (1973a, 1973b, 1974, 1976); Dalrymple, Knight and Middleton (1975); Knight (1971, 1972, 1973); Knight and Dalrymple (1975, 1976); Middleton, Knight and Dalrymple (1976); Middleton, Knight, Dalrymple and Lambiase (1975); and Lambiase (1976). Of these, Dalrymple, Knight and Middleton (1975) give the most comprehensive statement of the summer conditions, while Knight and Dalrymple (1976) treat winter conditions at some length.

Previous work dealing with the sand bars in the area is limited. Swift and McMullen (1968) made some of the first observations and suggested that the bar surfaces are dominated

by flood currents, while the channels are ebb dominated. Klein (1968, 1970), Klein and Whaley (1972) and Balazs and Klein (1972) report on an extensive series of studies, centred at Five Islands and Economy Point. Some of the observations have been mentioned earlier. Particular attention was paid to the delineation of facies zonations on the sand bars.

Works of a more general nature on the sediments include Pelletier and McMullen (1972), who described the general distribution of sediment types in the Bay of Fundy and Minas Basin. They, along with Swift and McMullen (1968) suggested that Coriolis forces produce a counter-clockwise residual transport of sediment in Minas Basin and Cobequid Bay. The muds support an extremely abundant fauna that has been investigated by Craig (1976), Craig and Risk (1975), Moffat (1975), Risk et al (1976), Szczuczko (1975) and Tunnicliff (1975). Finally, C. Amos (1975) is presently conducting an investigation into the overall sediment budget of the Minas Basin-Cobequid Bay system, to determine sediment sources, and areas of net deposition.

The whole Bay of Fundy system is under study with regard to the potential generation of electricity from the tides, and one particular site under active consideration is located at Economy Point. Feasibility studies conducted by the Atlantic Tidal Power Engineering and Management Committee (1969) (hereafter abbreviated to ATPEMC for simplicity) have compiled a wide variety of useful background data.

The above survey of the literature sets the context within which this study lies. Present knowledge of tidally-produced, linear sand bars is generally of limited scope, and lacking in quantitative detail. There has been much speculation and many questions have been raised that remain to be answered. This study is intended to provide some of the much needed quantitative information concerning sedimentation dynamics in this poorly known environment, particularly with regard to the sediment grain size and its transport. The remainder of the thesis is organized in the following manner: Chapter 2 - Setting: background information on the physical and environmental factors affecting the study area, along with a general description of modern sediment facies; Chapter 3 - Tidal Currents: presentation of pertinent hydraulic theory and of the time and areal variability of the tidal currents; Chapter 4 - Bedforms: description of the bedforms developed on the sand bars and their behaviour in the reversing tidal currents; Chapter 5 - Grain Size: presentation of the areal trends of the commonly used descriptive parameters, decomposition of the size distributions into the component populations, and analysis of the hydraulic controls; Chapter 6 - Sediment Transport: study of the dispersion and residual transport of sediment by tidal currents, through the use of fluorescent tracers, with an investigation of the influence of grain size on dispersion and transport rates; and finally Chapter 7 - Summary and Conclusions.

# CHAPTER 2

## PHYSICAL AND ENVIRONMENTAL SETTING

### 2.1 Physical Factors

#### 2.1.1 Introduction

The Bay of Fundy lies between the provinces of New Brunswick and Nova Scotia (Figure 1.1) and extends northeastward from the Gulf of Maine. The main body of the bay is almost rectangular, with an average width of 56 km and a length of 190 km from the mouth to Cape Chignecto. At this point it splits into two arms: one turns northward as Chignecto Bay, with Shepody Bay and the Cumberland Basin at its head; the other is directed eastward, and consists of the Minas Channel, Minas Passage and Minas Basin. The Minas Basin, and Cobequid Bay at its inner end, constitutes the study area.

Minas Basin and Cobequid Bay (Figure 1.2 and 2.1) form a roughly triangular body of water with a length of 62 km and a maximum width of 26 km at the west end. Within Cobequid Bay, east of Economy Point, the width is relatively constant at 8 km. The length of Cobequid Bay is 30 km. The Minas Basin and Cobequid Bay are separated from the Minas Channel by the arcuate Cape Blomidon-Cape Split peninsula. The narrow Minas Passage (4.8 km wide) is the only connection between the Minas Basin and the outer parts of the Bay of Fundy.

FIGURE 2.1 : Topography and bathymetry of the Minas Basin, Cobequid Bay, and surrounding area. Contours after Canadian Hydrographic Chart 4010, 1971. Datum for bathymetry is lowest low water. All contours in metres.

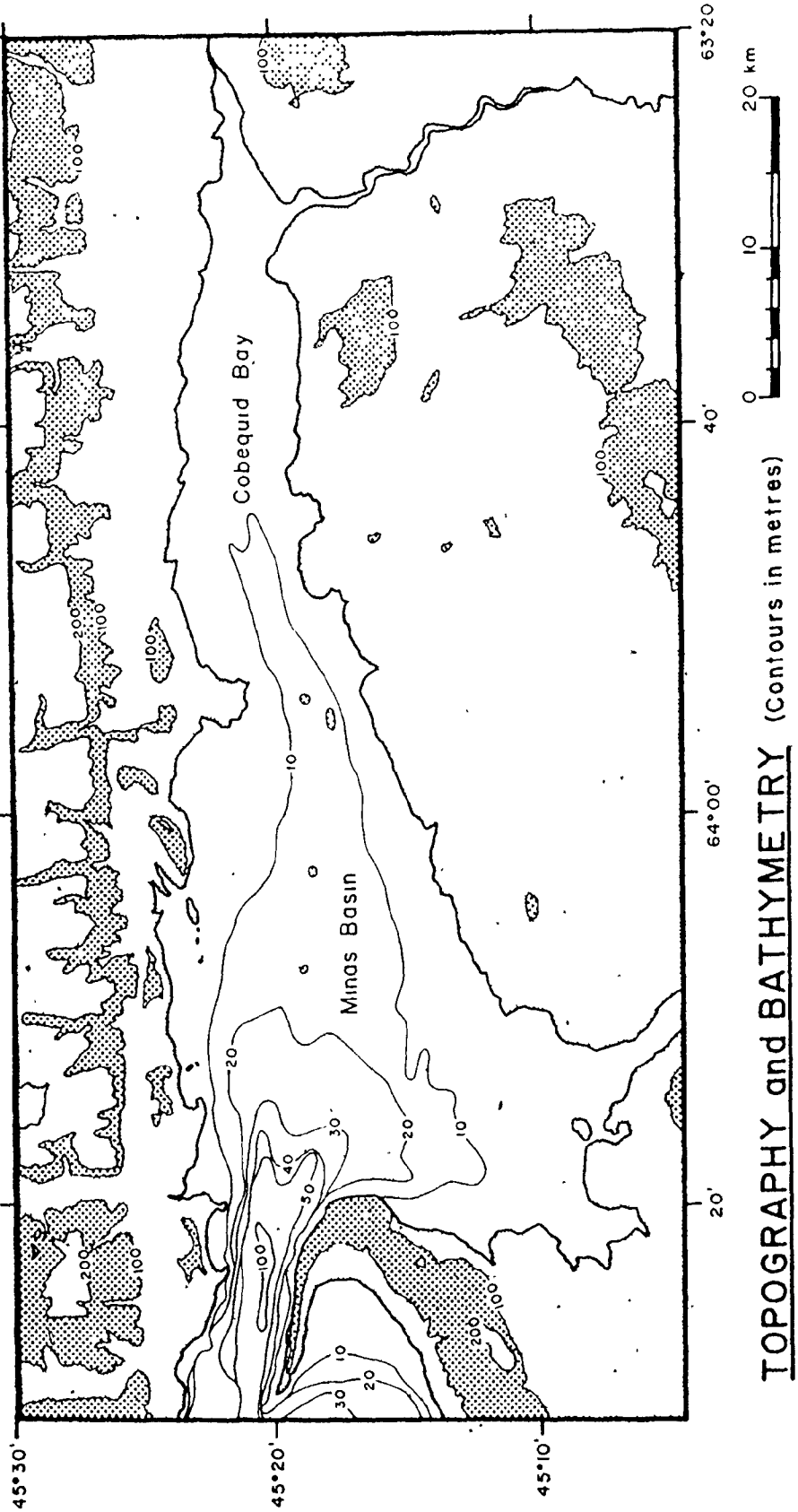


TOPOGRAPHY and BATHYMETRY (Contours in metres)

### 2.1.2 Regional Geology and History

The geology of the region surrounding the Minas Basin is complex (Figure 2.2). The oldest rocks in the area are Ordovician sandy and shaly flysh of the Meguma Group (Harris and Schenk, 1975). These rocks are tightly folded and well indurated, but are poorly exposed. Outcrop areas are restricted to the southern border of the area (Figure 2.2).

The next youngest sequence of rocks forms the Cobequid Mountains that lie to the north of the Minas Basin. This sequence, of presumed Silurian to early Devonian age (Figure 2.2) is composed of immature sediments with a major volcanic component (Stevenson, 1958; Weeks, 1948).

Multicoloured shales, argillites and sandstones, plus tuffs, breccias, and minor basic volcanics are present. Many of the rocks are severely sheared, and highly chloritized. This sedimentary sequence has been intruded by late Devonian granites and syenites, during the Acadian orogeny. Red orthoclase phenocrysts are a common and diagnostic characteristic. The southern edge of the Cobequid Mountains is formed by the Glooscap Fault (Schenk, 1975), a long-lived structure with unknown displacement and tectonic significance.

Carboniferous sediments underlie large parts of the area (Figure 2.2), on both sides of the Minas Basin. Rocks of Mississippian age have been divided into two groups, both believed to be deposited in fault-bounded grabens, as time

FIGURE 2.2: Geology of the Minas Basin - Cobequid Bay area. (From the Geological Map of the Province of Nova Scotia, 1965.)

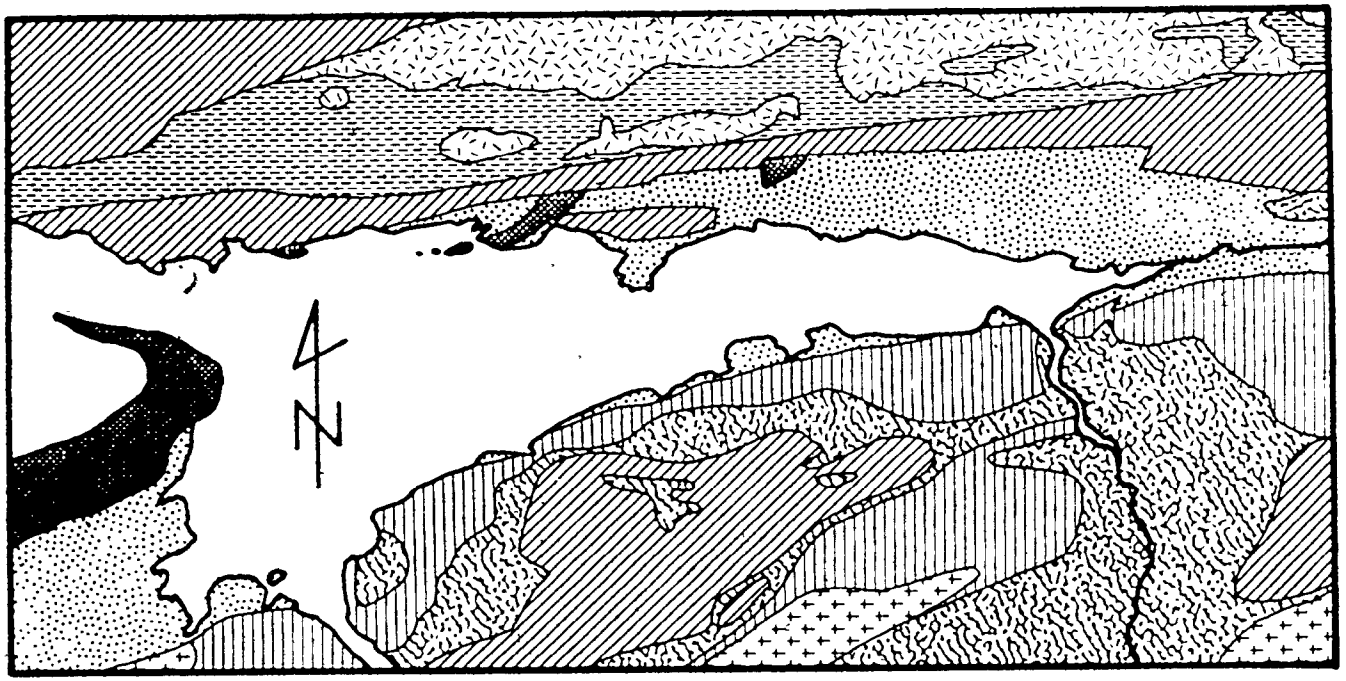

# GEOLOGY AROUND THE MINAS BASIN

0 10 20 30 40 km

Ordovician - Meguma Group
shale, siltstone, sandstone

Silurian & Devonian - Cobequid
Complex - volcanics, shale

Devonian - granite

Mississippian - Horton Group
sandstone, conglomerate, shale

Mississippian - Windsor Group
gypsum, shale, sandstone

Pennsylvanian - sandstone
conglomerate, coal

Triassic - Annapolis Group
sandstone, conglomerate, siltstone

Triassic - basalt

equivalents (Schenk, 1969). The Horton Group, composed of arkosic sandstones, conglomerates and shale, is thought to be a marginal alluvial fan facies. The Windsor Group is made up of finer-grained clastics, plus evaporites, including gypsum, anhydrite, salt, and minor limestone, that occupied the central parts of the grabens. Pennsylvanian sediments were deposited in a similar tectonic setting, but lack the evaporite component. The predominent rock types are conglomerate, sandstone, and shale, with minor coal and limestone. All Carboniferous rocks are folded and well indurated. Outcrops near the Glooscap Fault are strongly sheared.

Most of the shoreline and area immediately adjacent to the Minas Basin and Cobequid Bay (Figure 2.2) is composed of Triassic conglomerate, sandstone and siltstones of the Wolfville and Blomidon Formations (Jensen, 1975; Klein, 1962). These were deposited as alluvial fan and lacustrine facies in a half graben, bounded on the north by the reactivated Glooscap Fault. Klein (1962) determined that the sandstones are composed predominantly of quartz, but with a significant proportion of rock fragments and feldspar in some areas. All Triassic sediments are red in colour, and very friable. The Triassic sequence is capped by the North Mountain Basalt composed of basalt and dolerite flows, which forms Cape Blomidon and Cape Split (Figure 2.2). The McKay Head Basalt (Klein, 1962) lies within the sedimentary sequence, and outcrops in several places on the Minas Basin north shore (Figure 2.2),

including the islands at Five Islands. Zeolites and amethyst are common in both basalt units.

During the Pleistocene, Nova Scotia was covered by continental ice sheets at least twice (Prest, 1970), with ice-flow directions for the last advance toward the south-southeast. Silty till, with abundant pebbles and cobbles, was deposited over most of the area, but is generally less than 10 metres thick. A local source is evident for much of the till, but more distantly derived material is present as well. During deglaciation, ice remained longest in the Cobequid Mountains and large amounts of sandy and gravelly outwash are present along the north shore. On the south side, outwash is uncommon.

Sea level movements from deglaciation to the present are complicated, due to the offsetting factors of sea-level rise and isostatic rebound. At some time between 13,000 and 11,500 years B.P., immediately following deglaciation, the sea invaded the Minas Basin, and much of the outwash along the north shore was deposited as marine deltas (Swift and Borns, 1967). Rebound then overtook sea-level rise and the sea withdrew (Grant, 1971). As rebound slowed, 5,000 - 6,000 years ago, the sea again invaded the area.

Grant (1970) has presented data indicating that the Bay of Fundy area has experienced submergence during the last 4,000 years, at a rate that is about 24 cm/100 years greater than eustatic sea-level rise. Isostatic depression due to the loading of water on the continental shelf can account for a

part of this, but the remainder is apparently due to the increase in tidal range over this period. Grant (1970) suggests that the water depth over Georges Bank was insufficient to allow significant forcing of the Gulf of Maine-Bay of Fundy tides by the Atlantic Ocean until approximately 4,000 years ago. Since then, as water depths increased, the tidal range has grown to its present size. Support for the idea of smaller tides immediately following deglaciation has been given by Wightman (1975, 1976). Study of a raised beach on Cape Chignecto revealed a tidal range of only 3.4 metres at the time of formation, 13,000 to 11,500 years B.P., compared to the present-day value of 12.6 metres. This estimate is based on "The vertical distance between the berm and tidal terrace facies...." (Wightman, 1975, p.881).

Pleistocene deposits are believed to underlie most of the modern sediments in the Minas Basin and Cobequid Bay (ATPEMC, 1969; R. J. Knight, 1975, personal communication). Pre-Wisconsin stream channels that are deeply incised into bedrock are filled with Pleistocene material. Most of the subtidal bedrock outcrops in the Minas Basin are thought to be Triassic, although Carboniferous sediments are exposed in places. Much more work is required to outline adequately the distribution of pre-Holocene deposits in the Minas Basin and Cobequid Bay.

### 2.1.3 Topography and Bathymetry

The topography is strongly controlled by the geology. The highest points in the area are located in the Cobequid Mountains, where elevations over 300 metres can be found within 11 km of the Minas Basin shore. South of the Cobequids and the Glooscap Fault, the land drops rapidly to the Triassic lowlands, which rarely exceed 60 metres in elevation. The shores of the Minas Basin are almost everywhere bordered by cliffs that reach up to 30 metres in height, cut into Triassic sediments. On Cape Blomidon, the North Mountain Basalt forms a cuesta approximately 190 metres high.

The surface underlain by Carboniferous sediments on the south shore rises much more gradually than do the Cobequid Mountains, and generally does not exceed 180 metres in elevation within 10 km of the shore.

The whole area has been smoothed and rounded by glaciation and can be described as rolling. The southern edge of the Cobequid Mountains is the most rugged part, and here streams have cut deep canyons, and descend to the lowlands through a series of waterfalls and rapids. Stream gradients are on the order of 30 metres per kilometre in this section of their course, but flatten to about 3 m/km on the Triassic lowlands. Streams on the south shore also have low gradients of approximately 3 m/km or less, and are smaller.

In addition to these small streams, three large rivers empty into the Minas Basin: the Salmon and Shubenacadie Rivers enter at the east end of Cobequid Bay; and the Avon River and its tributaries discharge into the southwest corner of the Minas Basin. All three of these rivers are tidal for many kilometres upstream. On the Shubenacadie, tidal influence is noticable over 40 km above Maitland (Figure 1.2).

The bathymetry of the Minas Basin (Figure 2.1) is apparently simple, except in Cobequid Bay where tidal currents have moulded the bottom into an elongate complex of sand bars and channels, large parts of which are exposed at low tide (Figure 1.3). The remainder of the Minas Basin is also relatively shallow, with water depths in the range of 15 to 20 metres below lowest low water (Canadian Hydrographic Service Chart D7-4010). Depths increase rapidly as the Minas Passage is approached. Here, with tidal currents up to 5.5 m/s, concentrated flow has scoured to depths of almost 120 metres. Another smaller scour is present south of Economy Point. Pleistocene deposits, combined with the present hydraulic regime, have acted to smooth out most irregularities.

## 2.2 Environmental Factors

### 2.2.1 The Climate

The climate of the study area is temperate continental, due to the passage of cyclonic storms that originate in the midcontinent. The close proximity to the Bay of Fundy and the

Atlantic Ocean moderates temperatures and increases the precipitation. Knight and Dalrymple (1976) have summarized the climatic data for the Minas Basin using meteorological observations from Halifax International Airport, Greenwood Airforce Base, Parrsboro, and Truro (Figure 1.1), the nearest weather stations, for the years 1968 to 1972 (Canadian Department of Transport, Monthly Record, Meteorological Observations in Canada). Monthly averages of temperature and precipitation are given in Figures 2.3A and 2.3B respectively.

January is the coldest month, with a mean temperature of $-6^{\circ}C$, while July is the warmest at $20^{\circ}C$. Four months, December to March, have mean temperatures below freezing, and will be considered as the "winter" months. The average winter temperature is $-5.2^{\circ}C$, and the average summer temperature is $12^{\circ}C$.

Precipitation is evenly distributed throughout the year (Figure 2.3B), but with a slight maximum in November and December. The mean annual precipitation is 118 cm, and snowfall averages 260 cm a year.

Prevailing winds are from the west throughout the year (Figure 2.3C), but with a more southerly component in the summer. Again using data for the period 1968 to 1972, mean wind speed is greatest during the winter, and least in midsummer (July, August and September) (Figure 2.3D). Over the five-year period analyzed, calm conditions existed 8.2% of the time, 1.5 - 20 km/hr winds 61.2% of the time, and winds

FIGURE 2.3 : Climatic data for the study area. Based on data from the Monthly Record, Canadian Department of Transport, for Halifax International Airport, Greenwood Airforce base, Truro airport, and Parrsboro.

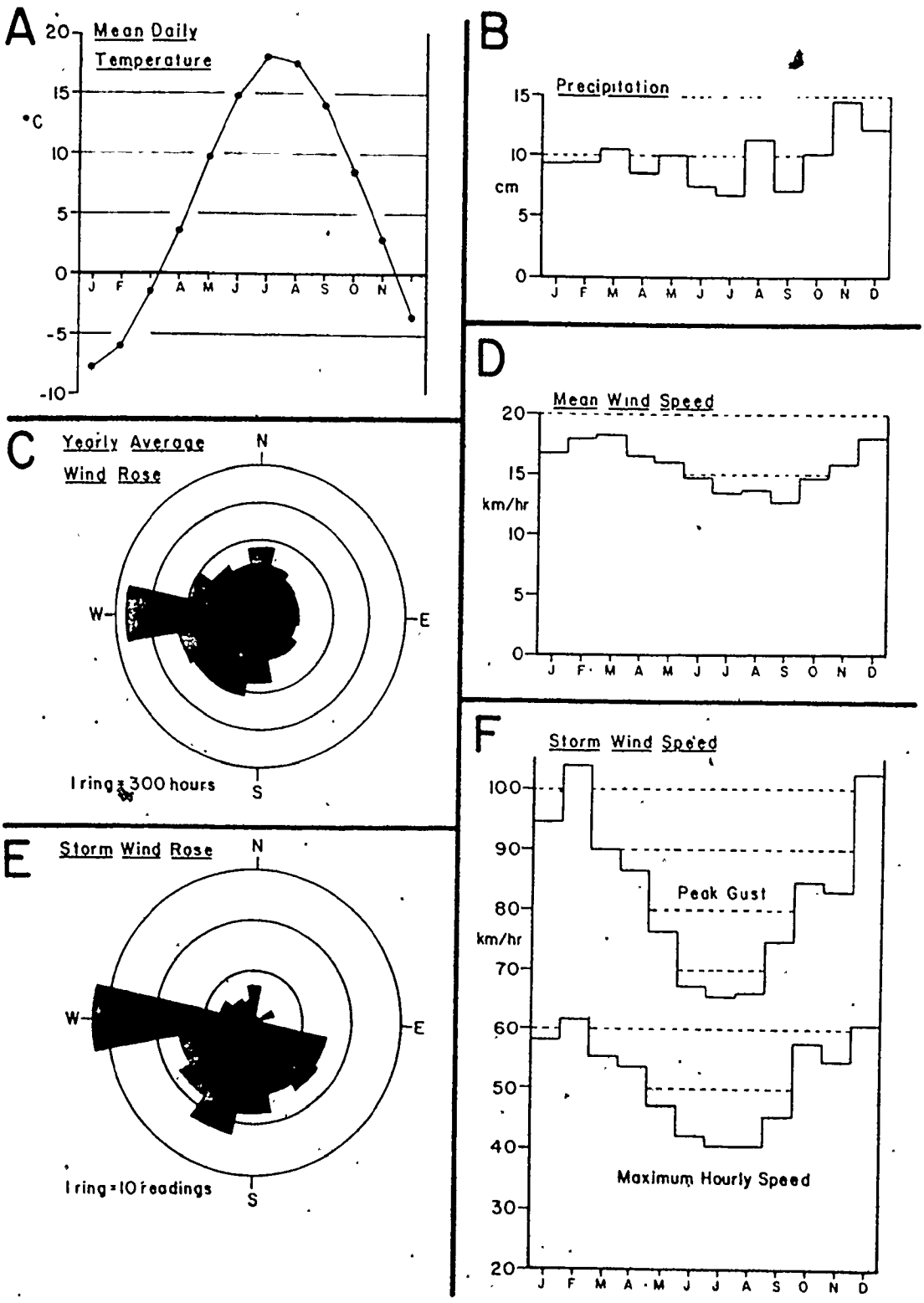
A
Mean Daily Temperature
°C
20
15
10
5
0
-5
-10
J F M A M J J A S O N D
B
Precipitation
cm
15
10
5
0
J F M A M J J A S O N D
C
Yearly Average Wind Rose
N
W
E
S
1 ring = 300 hours
D
Mean Wind Speed
km/hr
20
15
10
5
0
J F M A M J J A S O N D
E
Storm Wind Rose
N
W
E
S
1 ring = 10 readings
F
Storm Wind Speed
km/hr
100
90
80
70
60
50
40
30
20
Peak Gust
Maximum Hourly Speed
J F M A M J J A S O N D

from 20 - 60 km/hr 30.6% of the time. Gales with wind speeds over 60 km/hr were recorded only 14 times from all three stations combined, or less than 0.1% of the time. In order to obtain a better knowledge of storm winds, the maximum hourly reading and the strongest gust during each month were averaged over the five-year period (Figure 2.3F). The variation of storm wind intensity shows the same monthly trend as do the mean wind speeds. The normal field season from May to September experiences much weaker winds than does the remainder of the year, when storms are more common. The wind direction for the maximum hourly speeds is plotted in Figure 2.3E, and shows a similar distribution to the total of all winds (Figure 2.3C). Storm winds blow most commonly from the west, parallel to the long axis of the Minas Basin and Cobequid Bay, or from the south-southwest.

### 2.2:2 Waves

Waves are a potentially important dynamic agent in any nearshore environment. Unfortunately, a lack of data from the Minas Basin precludes a quantitative assessment of the importance of waves in this area. A number of predictions combined with qualitative observations give some idea of the wave climate.

The Cape Blomidon-Cape Split peninsula is effective in isolating the Minas Basin from waves generated in the main Bay of Fundy. Wave refraction studies by ATPEMC (1969) show

that it is "....very unlikely that waves having a period longer than approximately 12 sec. or less than approximately seven seconds would refract around Cape Split and enter Minas Basin." (p.A4-12). In general, therefore, only waves generated within the Minas Basin will be present. ATPEMC (1969) predict that the one percent, deep-water wave height will reach 9 metres once every twenty years (p.A4-16) at Economy Point. This condition requires wind speeds of 135 km/hr, blowing from 275.5°. For a 32 km/hr wind, the corresponding wave height is only 1.4 metres. Refraction studies (ATPEMC, 1969) show that wave energy is concentrated at the tip of Economy Point, the location of Centre and East Bars (Figure 1.2) and on Cape Tenny, directly across the basin on the south shore. This convergence of wave orthogonals onto these promontories indicates that very little of the wave energy will reach the bars in Cobequid Bay.

Qualitative observations during the field season, when wind speeds are at their least, indicate that waves rarely exceed one metre in height, with estimated wavelengths on the order of 10 to 20 metres. Heights up to 2 metres have been observed during storms. The wave fields tend to be extremely complex, with two sets of wave crests at an angle to each other. The waves are usually larger at the tip of Economy Point than at either Five Islands or in Cobequid Bay. Wave action is also concentrated on bar crests, due to refraction.

In order to obtain a more complete picture of normal conditions, wave forecasts have been made for three locations: one on Big Bar, another on Centre Bar, and a third on Diamond Bar (Figure 2.4), for a number of different wind speed-duration combinations (Table 2.1). The wind speeds chosen for the analysis correspond to: 20 km/hr - the approximate mean wind speed; 40 km/hr - summer storm winds; 60 km/hr - winter storm winds; and 120 km/hr - the exceptional storm. Wind directions corresponding to the two maxima in Figure 2.3E (202.5$^{o}$ and 270$^{o}$) were used in the forecasts (Figure 2.4). The effective fetches at high tide in both directions were determined for all three locations by the method given by Coastal Engineering Research Centre (1973, p.3-30). The significant deep-water wave parameters were obtained from Figure 3-15 of the same source. The assumption of deep water conditions seems justified at high tide, when water depths over most of the fetches are in the range of 20 to 40 metres. The calculated wave heights and periods are larger than would be the case for intermediate or shallow water conditions. The results are listed in Table 2.1.

The results obtained show surprising agreement with the qualitative observations reported above. Average wind speeds generate waves less than half a metre in height, while summer storms produce waves of approximately one metre. Waves 1.5 to 2 metres high can be expected during winter storms, and exceptional storms could produce waves with a

FIGURE 2.4 : Locations and wind directions used in wave predictions. See also Table 2.1.

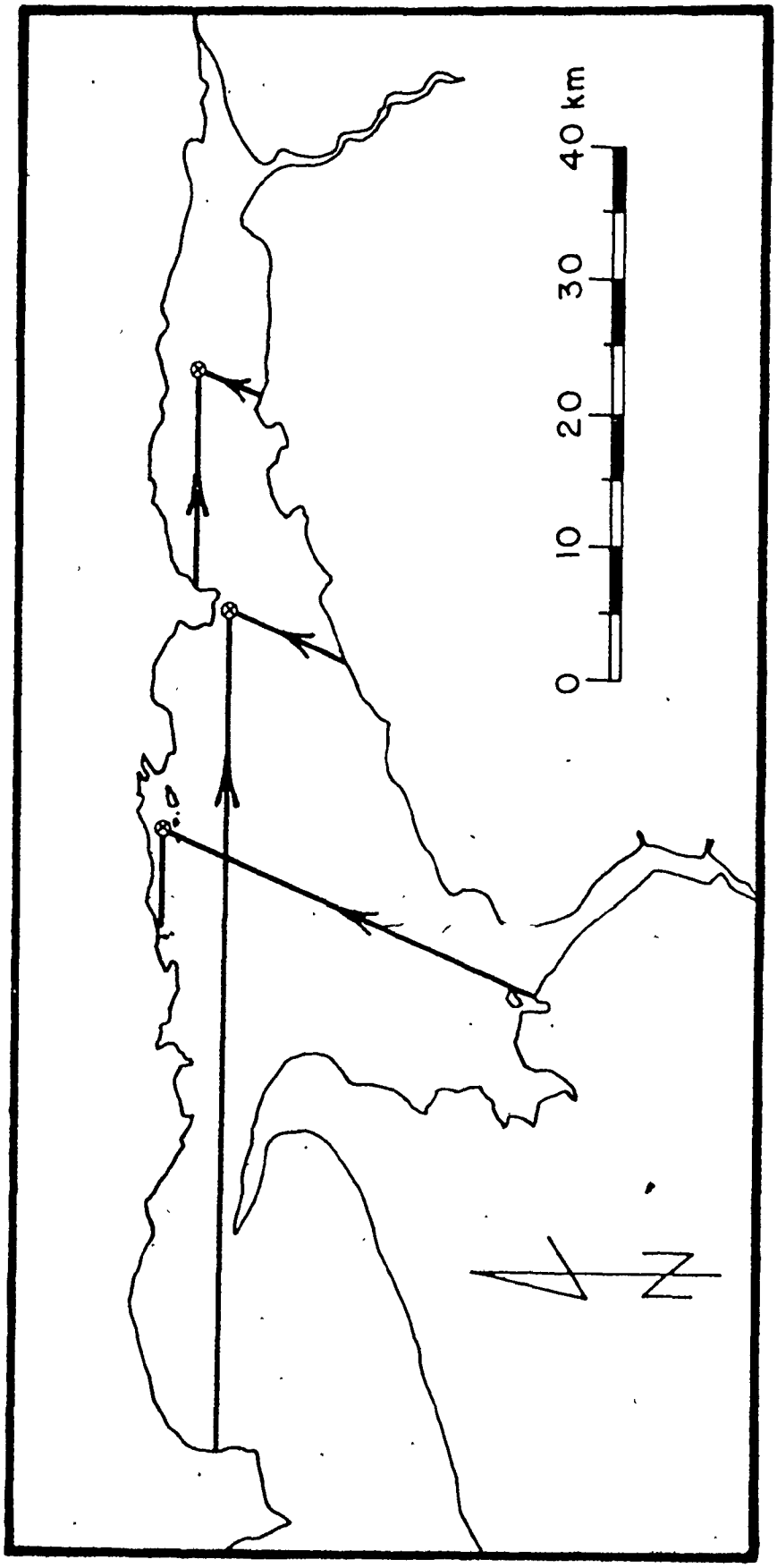
0
10
20
30
40 km
N

TABLE 2.1 : Predicted deep water waves for Minas Basin and Cobequid Bay. See text for details, and Figure 2.4 for locations and wind directions. Wave characteristics for starred entries are limited by wind duration; all others limited by fetch.

| Location | Wind Direction | Effective Fetch (km) | Wind Speed (km/hr) | Wind Duration: 2 Hours Sign. Height (m) | 2 Hours Sign. Period (s) | 5 Hours Sign. Height (m) | 5 Hours Sign. Period (s) |
|---|---|---|---|---|---|---|---|
| Big Bar | 270° | 10.4 | 20.0 | 0.30 * | 2.2 | 0.34 | 2.3 |
| | | | 40.0 | 0.76 | 3.3 | 0.76 | 3.3 |
| | | | 60.0 | 1.49 | 4.7 | 1.49 | 4.7 |
| | | | 120.0 | 2.72 | 6.0 | 2.72 | 6.0 |
| | 202.5° | 10.2 | 20.0 | 0.30 * | 2.2 | 0.34 | 2.3 |
| | | | 40.0 | 0.76 | 3.3 | 0.76 | 3.3 |
| | | | 60.0 | 1.49 | 4.7 | 1.49 | 4.7 |
| | | | 120.0 | 2.72 | 6.0 | 2.72 | 6.0 |
| Centre Bar | 270° | 21.2 | 20.0 | 0.30 * | 2.2 | 0.40 | 2.5 |
| | | | 40.0 | 0.88 * | 3.6 | 0.97 | 3.9 |
| | | | 60.0 | 1.55 * | 4.8 | 1.58 | 4.9 |
| | | | 120.0 | 3.62 | 7.1 | 3.62 | 7.1 |
| | 202.5° | 12.9 | 20.0 | 0.30 * | 2.2 | 0.37 | 2.3 |
| | | | 40.0 | 0.82 | 3.5 | 0.82 | 3.5 |
| | | | 60.0 | 1.31 | 4.4 | 1.31 | 4.4 |
| | | | 120.0 | 2.98 | 6.4 | 2.98 | 6.4 |
| Diamond Bar | 270° | 19.2 | 20.0 | 0.30 * | 2.2 | 0.40 | 2.5 |
| | | | 40.0 | 0.85 * | 3.6 | 0.91 | 3.7 |
| | | | 60.0 | 1.46 | 4.7 | 1.46 | 4.7 |
| | | | 120.0 | 3.28 | 6.8 | 3.28 | 6.8 |
| | 202.5° | 5.2 | 20.0 | 0.27 | 2.1 | 0.27 | 2.1 |
| | | | 40.0 | 0.70 | 3.2 | 0.70 | 3.2 |
| | | | 60.0 | 1.13 | 3.9 | 1.13 | 3.9 |
| | | | 120.0 | 2.44 | 5.7 | 2.44 | 5.7 |

significant height of nearly four metres at Economy Point, but only about three metres at either Big Bar or Diamond Bar. The predicted wave heights are limited by the effective fetch in almost all cases studied, except for the combination of the shortest duration, weakest winds, and longest fetch (starred entries in Table 2.1). In only one case does the effective fetch exceed 20 km, despite the fact that the maximum over water distances from the selected locations can be in excess of 60 kilometres. Because of the short fetches, the waves would be steep, and their action destructive, rather than constructive.

Both the observations and the predictions indicate that wave heights are usually small in all of the study area. Furthermore, the extreme tidal range disperses the effect of waves over a large vertical distance. The rapid rate of water level change does not allow wave activity to be concentrated at any one level for very long, except at the high tide mark, where significant cliff erosion and longshore transport occurs. The net result of these factors is that waves can be disregarded as a dynamic agent on the sand bars, in comparison to tidal currents.

### 2.2.3 Tides and Tidal Currents

The unique aspect of the dynamic environment in the Minas Basin and Cobequid Bay is the large tidal range. The tides in the area are dominated by the lunar semi-diurnal ($M_2$)

component, with a period of 12.42 hours. The diurnal component is small, with a maximum diurnal inequality of approximately 0.8 metres at Burntcoat Head. Predicted values of the mean and large tidal ranges at Burntcoat Head and Five Islands are:

| Location | Mean Range | Large Range |
|---|---|---|
| Burntcoat Head | 11.9 m | 16.1 m |
| Five Islands | 11.6 m | 15.8 m |

(From: Canadian Hydrographic Service, 1975, Canadian Tide and Current Tables, Vol. 1.)

Due to the small difference between the two locations, the values for Burntcoat Head will be used throughout the thesis. Dawson (1917) has reported the largest directly measured tidal range of 16.3 metres. He estimates the mean spring ranges at lunar apogee and perigee to be 12.3 m and 15.4 m, respectively. Tidal ranges at neap tide average approximately 10 metres.

The cause of the large tides is usually ascribed to resonant amplification within the Bay of Fundy. A number of numerical studies (Harleman, 1966; Rao, 1968; Redfield, 1950; Yuen, 1969) have shown, however, that the natural period of the Bay of Fundy, including its branches, is considerably less than the period of the semi-diurnal tide. Recent studies by Duff (1970) and Garrett (1972, 1974) indicate that the tides may, in fact, be due to resonance conditions, if the system is taken to include both the Bay of Fundy and the Gulf

of Maine, from Cape Cod to the southern end of Nova Scotia, out to the edge of the continental shelf.

The amount of water entering and leaving the Minas Basin every half tidal cycle has been variously estimated as $2.94 \times 10^9$ $m^3$ (ATPEMC, 1969) or $8.81 \times 10^9$ $m^3$ (Godin, 1968). The tidal currents associated with this mass transport of water reach 5.5 m/sec in the Minas Passage (Cameron, 1961). In the open portions of the Minas Basin, tidal currents are much slower, however. Current speeds have been reported in a number of studies (C. Amos, 1975, personal communication; ATPEMC, 1969; Godin, 1968). At no location have peak speeds been measured in excess of 2.0 m/sec. Maximum speeds for both ebb and flood currents range from 0.7 to 1.8 m/sec. The currents seem to be strongest in the northern half of the Minas Basin, in a line between the Minas Passage and the channel south of Economy Point, while they are somewhat weaker in the southwest corner of the Minas Basin. In virtually all cases, current flow is unidirectional from the surface to the bed. The currents are strongly rectilinear. The strength of the flow increases at spring tides, relative to neap tides.

A numerical study of residual currents in the Minas Passage and its approaches by Tee (1974) shows the existance of a clockwise eddy in the western Minas Basin, produced by the inertial effect of the flood jet entering the Basin from Minas Passage. Unfortunately, the model is not sufficiently

detailed to provide useful information in Cobequid Bay; however, a weak clockwise eddy is suggested at the tip of Economy Point. Within Cobequid Bay, Pelletier and McMullen (1972) and Swift and McMullen (1968) have suggested that Coriolis force should produce a counterclockwise circulation of water and a corresponding pattern of sediment transport. No data is available to support this.

Investigations of currents over the tidal sand bodies in the Minas Basin and Cobequid Bay indicate that currents are locally extremely variable in strength and direction, although they attain speeds comparable to the values cited above. Dalrymple et al (1975) and Knight and Dalrymple (1976) state that near-bottom maximum current speeds in Cobequid Bay vary between 0.5 and 1.5 m/sec, depending on location. Local bathymetry is given as the primary controlling variable for these differences. Klein (1970) and Klein and Whaley (1972) report similar values from the sand bars at Five Islands and Economy Point. The subject of tidal currents over the sand bars will be considered at length in Chapter 3.

These tidal currents are believed to be the dominant sediment transport agent on the sand bars, and to be responsible for most of the features seen. It is clear from a comparison of normal wave heights (approximately 0.5 m or less) with the speed of tidal currents (0.5 - 1.5 m/sec) that tidal currents are far more important, except possibly during extreme conditions.

### 2.2.4 The Water

As mentioned earlier in this chapter, three major rivers empty into the Minas Basin, in addition to many smaller streams. Extensive data on the river discharges are not available, except for the Salmon River (ATPEMC, 1969; J. E. Peters, 1974, personal communication to R. J. Knight). These data show that the mean annual water discharge has varied from 8.8 $m^3$/sec to 13.9 $m^3$/sec during the period 1968 - 1972. Maximum discharges occur during March and April, and exceed 55 $m^3$/sec. Minimum discharges are during mid-winter and mid-summer.

The suspended sediment concentration in the Salmon River varies widely, between 2 mg/l and 140 mg/l, with a mean annual concentration in the range of 6 - 15 mg/l. Annual sediment discharges average approximately 22 x $10^3$ kg/day. The nature and amount of bed load transport is unknown. Comparable values are not known for the Shubenacadie and Avon Rivers, and their tributaries, but are probably comparable. The smaller streams are nearly dry during the summer, but can become raging torrents after storms. Because of their steep gradients, these small streams probably transport sand and gravel during floods, as evidenced by the sandy-gravel deltas at their mouths.

River discharges, although small, are sufficient to lower the salinity to between 26 and 31 parts per thousand. In the main body of the Minas Basin, C. Amos (1975, personal

communication) reports salinities averaging 30 °/oo. Data obtained by ATPEMC (1969, Table A3-10) show that salinities decrease as one moves eastwards into Cobequid Bay. South of Economy Point, salinities are about 29 °/oo, while 8 km to the east, they are 28 °/oo. At any given point, clear cyclical trends are evident, with lowest salinities at low tide, and highest at high water, reflecting the westward migration of the salinity gradient during the ebb tide and the return eastward on the flood. No salinity stratification is evident in the Minas Basin or Cobequid Bay.

Suspended sediment concentrations in the Minas Basin and particularly Cobequid Bay, are high. Measurements of ATPEMC (1969, Table A3-10) vary from 0.0 mg/l to a maximum near-bottom value of 1157 mg/l. Most of the measurements fall in the range of 50 - 200 mg/l; values that are significantly higher than the average concentrations in the rivers. Qualitative observations indicate that the suspended sediment concentration is lower in the Minas Basin than in Cobequid Bay. This suggests the presence of a turbidity maximum in the upper reaches of Cobequid Bay, analogous to those found in estuaries with lower tidal ranges. Cyclic variations in suspended sediment concentrations throughout the tidal cycle reflect the east-west movement of this turbidity maximum on every tidal cycle. Because of extreme variability in the suspended sediment distributions, no statement can be made regarding vertical concentration gradients.

Data on water temperatures are more extensive than are measurements of either salinity or suspended sediment. Measurements have been taken by the author over Diamond Bar, and at the tip of Economy Point, from late June to the end of August, 1974. Figures 2.5A and 2.5B present a summary of the data. Water temperatures over Diamond Bar (standardized to three hours after high water) increase from 15°C to nearly 20°C during the 49-day period. The apparent periodicity of the increase during July appears to be related to the weather conditions. Water temperatures also increased at Economy Point over the course of the summer at the same rate as at Diamond Bar, but the temperatures were consistently about 1.4°C cooler. Data from ATPEMC (1969) and C. Amos (1975, personal communication) indicate that the east-west temperature gradient continues into the Minas Basin. Water temperatures also vary over the tidal cycle as shown in Figure 2.5B. The water is always cooler at high tide than at low tide, when warmer water from further up the bay has moved westward. Temperature stratification is very weak, with the difference from the surface to the bottom averaging 0.2°C. The water temperature is usually constant throughout the entire flow depth, with the exception of the surface metre, which is heated by the air. The few temperature measurements available from the winter indicate that the water is only slightly above the freezing point of salt water (-2°C) in the upper reaches of Cobequid Bay.

FIGURE 2.5 : Water temperature variations (1974). A: Temperature change over the summer, standardized to a time 3 hours after high water. B: Temperature variations over the tidal cycle at Diamond Bar.

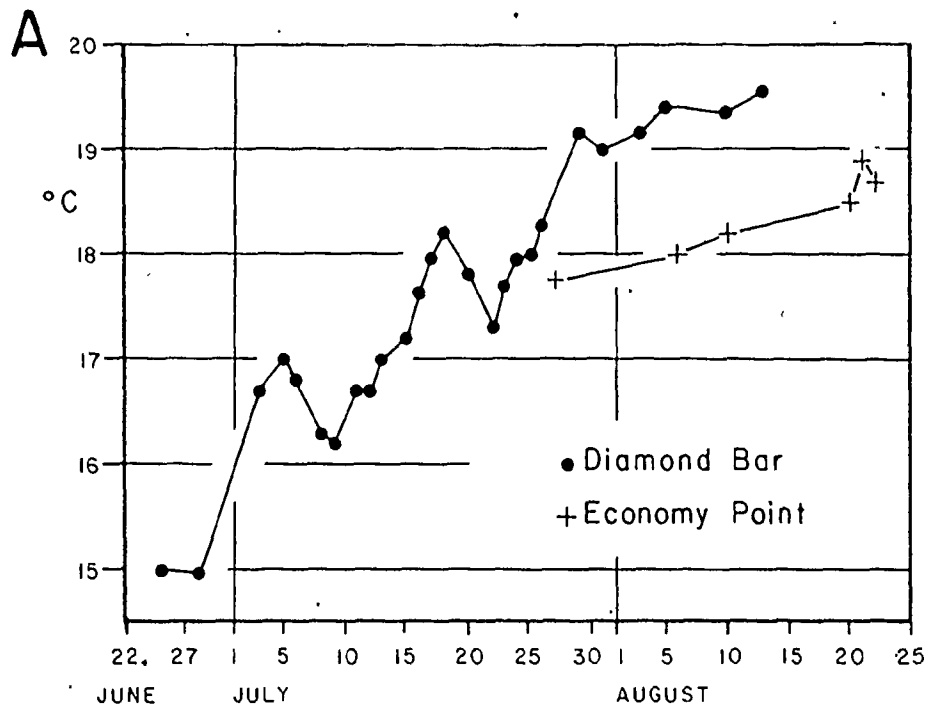
A
20
19
°C
18
17
16
15
● Diamond Bar
+ Economy Point
22 27 1 5 10 15 20 25 30 1 5 10 15 20 25
JUNE
JULY
AUGUST

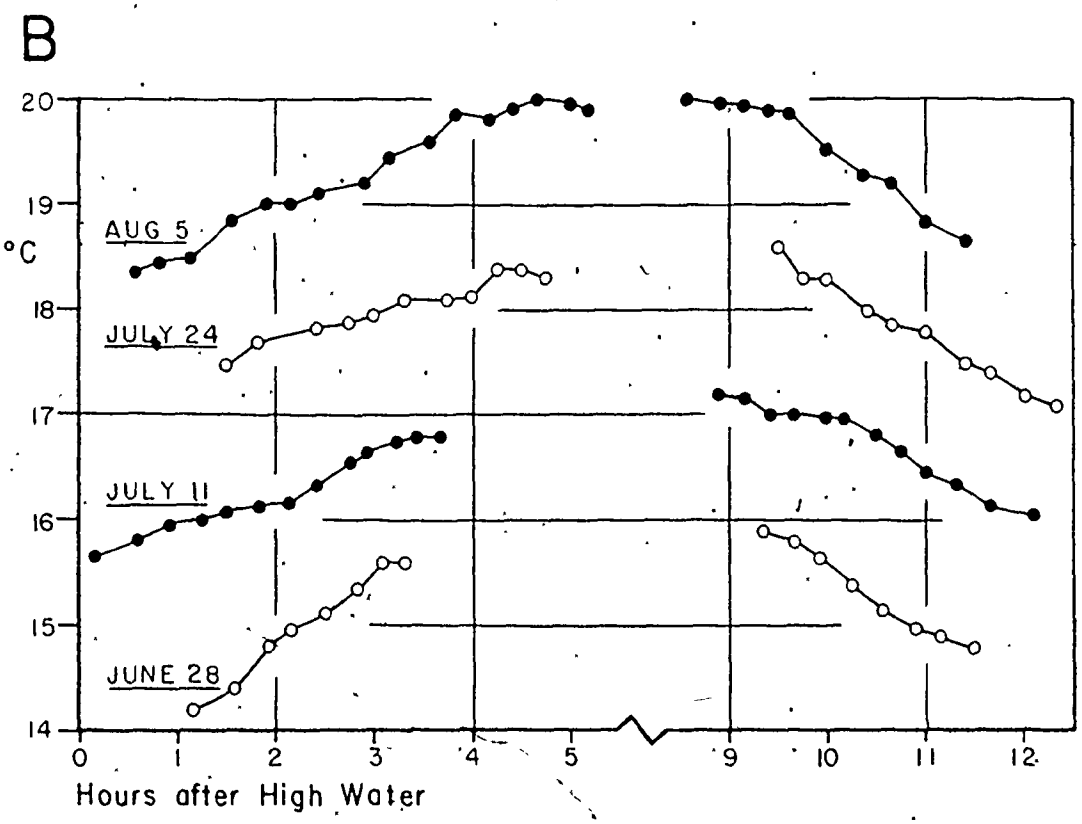
B
20
19
°C
18
17
16
15
14
AUG 5
JULY 24
JULY 11
JUNE 28
0 1 2 3 4 5 9 10 11 12
Hours after High Water

Cameron and Pritchard (1963, p.306) have defined an estuary as: ".... a semi-enclosed body of water which has a free connexion with the open sea and within which sea water is measurably diluted with fresh water derived from land drainage." The salinity measurements given above indicate, therefore, that the Minas Basin and Cobequid Bay can be considered as an estuary. All vertical profiles of tidal currents, salinity, temperature, and suspended sediment from the area show that the water is completely mixed, however. It is estimated that the tidal prism of Cobequid Bay alone is on the order of 1,000 times the daily fluvial input. The longitudinal increase toward the head of the bay in suspended sediment concentration and temperature, and the decrease in salinity are the only gradients detected.

### 2.2.5 Ice

During the winter months of December through March, when average air temperatures are below the freezing point of sea water, ice is a visually impressive feature of the study area. Ice begins to form in December. It continues to grow until the end of February, and persists until the end of March, or into early April. Three major forms of ice occurrence can be distinguished in mid-winter: 1) an ice foot; 2) drift ice; and 3) an ice crust, covering the surface of the intertidal zone sediments.

1) The ice foot (Figure 2.6A) forms a shorefast rampart along the high water level. The seaward edge of the ice foot is a near-vertical wall with a height varying from 1.5 metres to 9 metres, depending on whether the shoreface is gently sloping or steep, respectively. The width of the ice foot varies from 5 to 30 metres, usually in inverse relation to the height. The upper surface of the ice foot builds up to approximately the spring tide, high water level. The upper surface is a jumbled mass of drift ice blocks that have floated on during high tides.

2) Drift ice is the most impressive aspect of the winter conditions in the Minas Basin and Cobequid Bay. During February, up to 90% of the water surface can be covered (ATPEMC, 1969) by a loose mass of ice blocks and cakes of variable size (Figure 2.6B). The actions of the tidal currents and winds keep the individual blocks in constant motion (Hind, 1875, p.195) and prevent the formation of a continuous ice sheet, except in local cases when onshore winds pack the ice against the shore for several days at a time (Knight and Dalrymple, 1976). Drift ice commonly becomes stranded on the intertidal surfaces during emergence, particularly on the foreshore and on the crestal portions of the sand bars. The blocks usually float away on the next flood tide, carrying sediment attached to their bases. Occasionally, however, a block may become so solidly frozen to the surface that it remains rooted in place for several tidal cycles before breaking loose. Drift ice is

FIGURE 2.6 : Winter ice morphology. A - Ice foot (arrow), developed along the shoreline south of Selmah Bar; B - Drift ice on crest of Selmah Bar. Note scoured hole. Figure in front of large ice block for scale; C - Close-up of ice crust. Scale in centimetres and decimetres; D - East end of Selmah Bar showing extensive development of an ice crust.

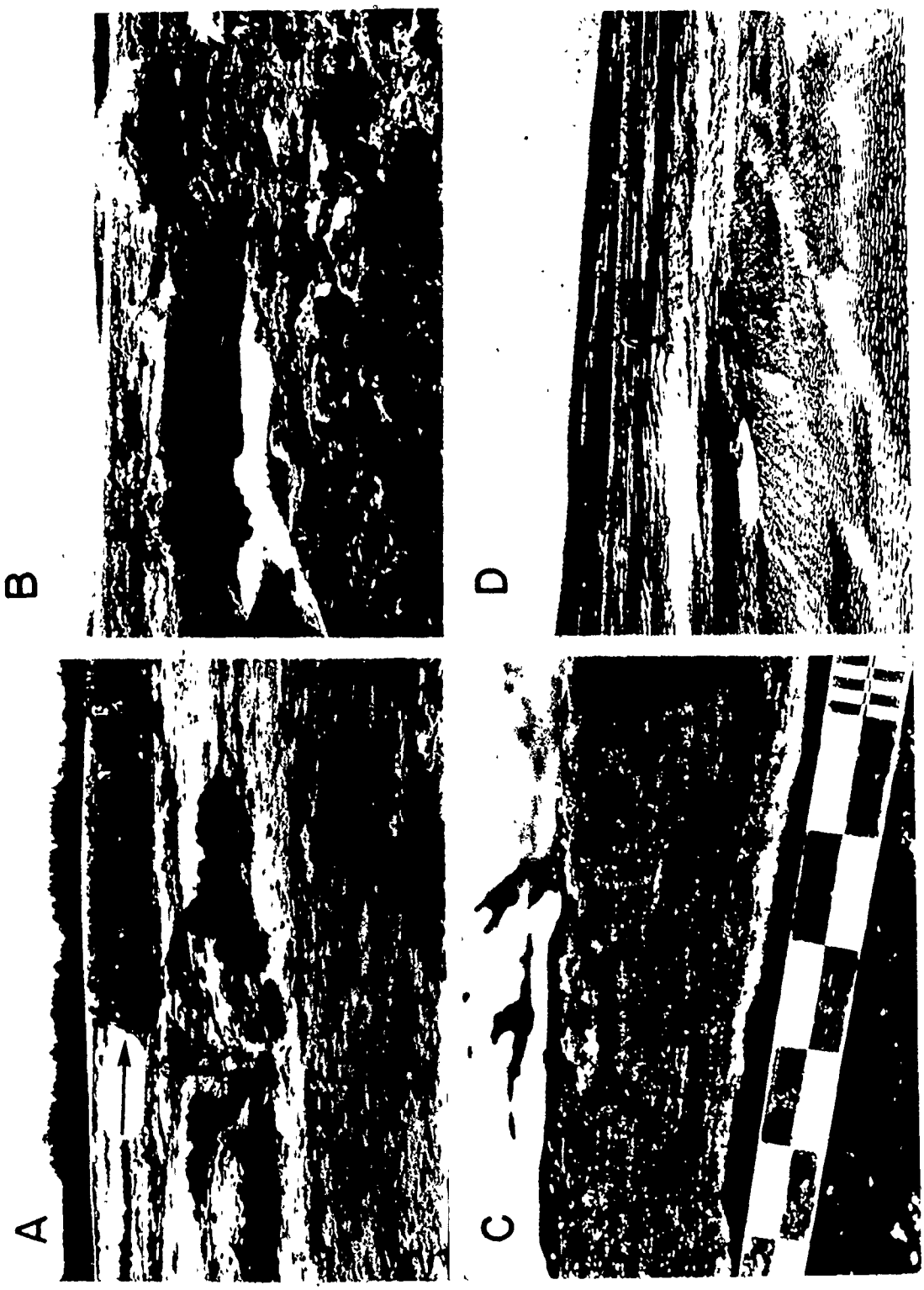
A
B
C
D

also commonly scattered over the surfaces of the marshes by high spring tides. Abundant drift ice during the winter may act to damp the waves generated by storms, thereby lessening their importance.

3) The ice crust was first described by Knight and Dalrymple (1976). It consists of alternate ice and sediment layers (Figure 2.6C) that are laterally continuous and that parallel the upper surface of the crust. When well-developed, this crust varies in thickness from 5 cm on the mudflats, to a maximum of 50 cm on parts of intertidal sand bars. The crust is very extensive (Figure 2.6D), covering many hundreds of square metres without interruption. It does not extend below the average low tide level into the subtidal zone, however, because of insufficient exposure time to freezing air temperatures at low tide. It is believed that the crust accretes upward by the freezing of snow, slush ice, and ebb runoff onto the surface. Downward freezing of pore water in the sediment also occurs, but vertical build-up appears to be most important, because of the lack of preserved sedimentary structures in the crust, and the low sediment content, which is reflected in the ability of small pieces of crust to float. Observations made by J. J. Lambiase (1976, personal communication) in the Avon River estuary following an unseasonably warm period in late February, 1976, indicate that the frozen crust may not be a permanent winter phenomenon.

The presence of the ice crust is significant in several ways, the most important of which is the almost complete immobilization of sand on the surface of the bars. Some of the potentially preservable results of ice action on the sand bars will be considered in Chapter 4; however, virtually all visible evidence of winter ice is quickly obliterated after breakup. Knight and Dalrymple (1976) conclude that tidal currents dominate sedimentation in the Minas Basin and Cobequid Bay year-round, both in terms of energy expended, and as preserved in the geological record.

## 2.3 Holocene Sediments

### 2.3.1 Facies Distribution and Descriptions

The distribution of recent sediment facies within the Minas Basin and Cobequid Bay shows a high degree of ordering on a large scale, although there is considerable local variability. As one moves progressively eastward from the Minas Basin through Cobequid Bay and into the estuaries of the Salmon and Shubenacadie Rivers, the sediments and their distribution reflect a decrease in wave energy, and also in tidal current strength over the central and innermost parts of Cobequid Bay.

In the Minas Basin and the outer part of Cobequid Bay, where wave action is strongest, cliffs are developed along the majority of the shoreline (Figure 2.7B) and extensive wave-cut platforms with widths of up to 2 kilometres underlie the intertidal foreshore (Figure 1.2). The modern sediment veneer

FIGURE 2.7 : Exposed-foreshore facies. A - Sequence of facies developed on the foreshore south of Selmah Bar. A gravel beach is present in the foreground, passing abruptly into the mud veneer, with harrow-marked, lag gravel in the middle distance; B - Sandy beach at the foot of cliff cut into Triassic sandstone; C - Gravel beach with pebble ridges (McManus, 1973), northwest of Highland Village Bar; D - Harrow-marked lag gravel, south of Selmah Bar.

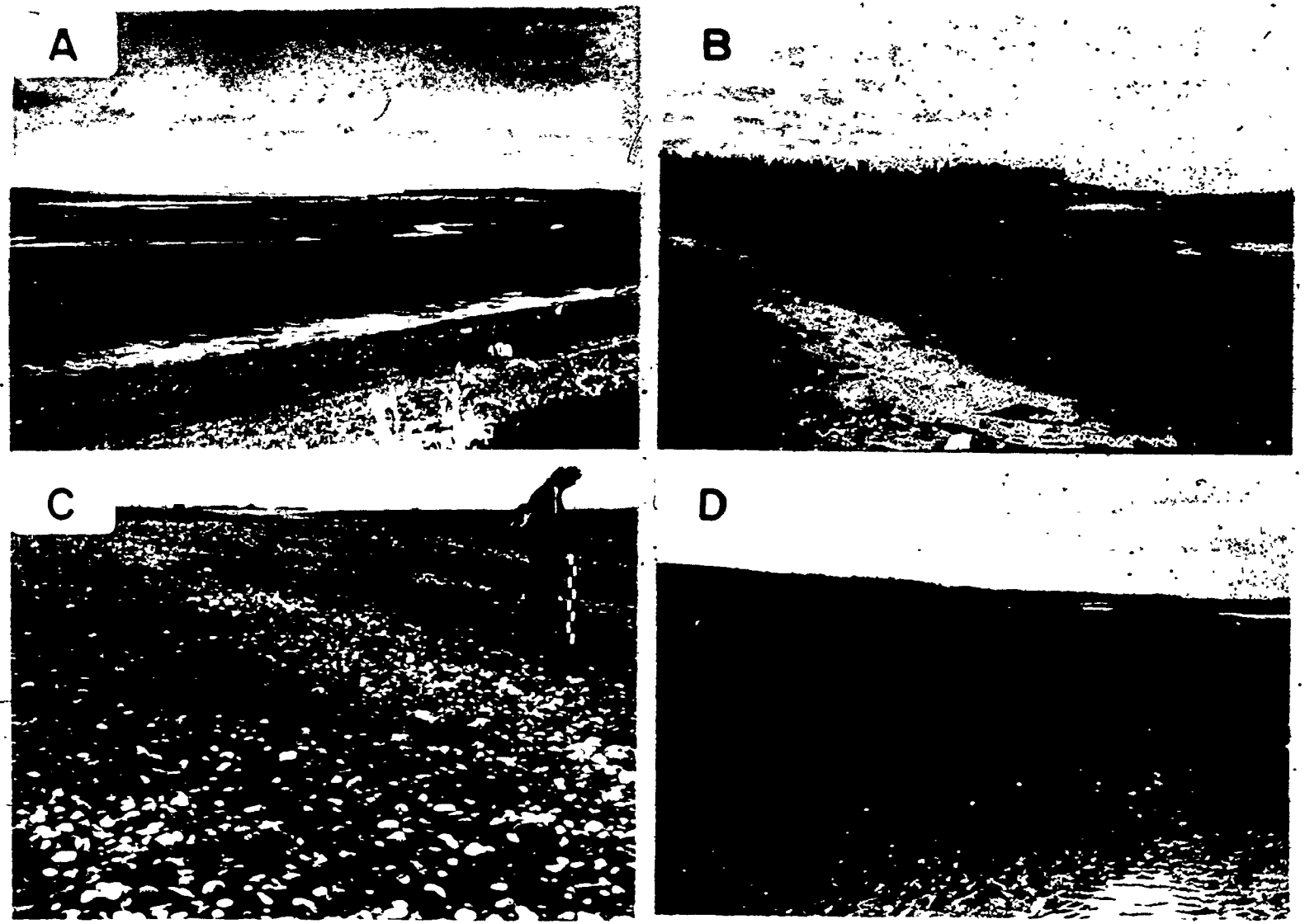
A
B
C
D

on these rocky foreshores is thin and is composed primarily of a gravel lag, with a thin mud cover in the upper part of the foreshore (Figure 2.7A). On the lower part of the foreshore, isolated sand bodies of various sizes can be found in places. Extensive areas of mud accumulation are rare, and are restricted to protected embayments such as Noel Bay (Figure 1.3) and to the small estuaries at the mouths of the minor streams along the north and south shores.

As one moves eastward into the inner part of Cobequid Bay, the width of the wave-cut platform decreases, and the amount of mud increases, presumably due to a decrease in wave action, resulting from refraction and attenuation by the sand bars that occupy the offshore part of Cobequid Bay. Mudflats and salt marshes are most extensive in the estuaries of the Salmon and Shubenacadie Rivers (Figure 1.2).

The subtidal portions of the Minas Basin and outermost Cobequid Bay are floored with gravel and sandy-gravel (C. Amos, 1976, personal communication; Pelletier and McMullen, 1972). Unfortunately, little is known about the distribution of these sediments or the extent to which their characteristics are determined by the present hydraulic regime. Bedrock outcrops also occur. Within Cobequid Bay, and extending eastwards into the mouths of the rivers at its head, a large, partly intertidal sand body is developed (Figures 1.2 and 1.3), with a length of over 25 kilometres and a width of 10 kilometres. Its thickness reaches nearly 20 metres (R. J. Knight, 1975,

personal communication) under the crests of the large sand bars that have been produced by the tidal currents. This major sand accumulation can be subdivided into outer, middle and inner sections on the basis of bar morphology and predominant bedform type.

The outer, western portion of the sand body extends approximately from Noel to Spencer Point (Figures 1.2 and 1.3). In this region, where the wave activity and tidal current speeds are believed to be greatest, all of the sand bars are distinctly elongated, and have from 10 to 20 metres of relief above the adjacent channel bottoms (R. J. Knight, 1975, personal communication). The water depth over the crests of the bars at high tide is generally more than 8 metres. Megaripples, which are analogous to dunes, are the most common bedform type, and have wavelengths of 1 to 12 metres, and heights from 10 to 70 centimetres.

The middle part of the Cobequid Bay sand body, from Spencer Point to Salter Head (Figures 1.2 and 1.3) is characterized by bars that are broader and more irregular in outline than those in the outer part (Figure 1.3). The relief of these bars is less also, ranging from 2 to approximately 12 metres, and bar crests are covered by no more than 5 metres of water at high tide. Although megaripples are developed in this section, the most prominent bedform type is a larger feature termed a sand wave after Boothroyd (1969) and Klein (1970). They have wavelengths from 5 to over 40 metres, and

heights of 20 to 150 centimetres. Sand waves are believed to require lower current speeds for their existence than do mega-ripples (Boothroyd, 1969; Costello, 1974; Knight, 1972).

The innermost subdivision, lying to the east of Salter Head (Figure 1.2 and 1.3) consists of a number of low relief, irregular sand bars and flats that are separated by a braided system of shallow channels. This region has been called the Braided Inner Sand Bars by Swift and McMullen (1968) and is analogous to the sandy tidal flats of Reineck (1972). Ripples of both wave and current origin are widely developed (Figure 2.8F); larger bedforms are not present, presumably due to the weakness of the tidal currents over these flats. In comparison to the medium and coarse sand of the outer and middle subdivisions, the sediment in this area is predominantly fine sand, which grades landward into extensive mudflats and salt marsh.

From this outline of the sediment types and their distributions, it is possible to see that there is a general eastward decrease in wave activity and tidal current strength, at least within Cobequid Bay. A similar pattern of sediment types might well be expected in other wide, funnel-shaped embayments with large tidal ranges. Progradation of the facies zonation just described should produce a fining-upward sequence that begins at the base with a gravel lag that is overlain by cross-bedded medium sand and then by rippled fine sand. The entire sequence would be capped by mud.

At this point, each of the major components of the modern sediment distribution will be considered: i) the exposed intertidal foreshores; ii) the protected mud flats and salt marshes; and iii) the intertidal sand bars. The descriptions are taken primarily from Dalrymple et al (1975) and Knight and Dalrymple (1976). Klein (1963, 1967, 1970) and Swift and McMullen (1968) also provide brief descriptions of some of the recent sediment facies.

i) Exposed Intertidal Foreshores: The vertical cliffs that form much of the shoreline are cut primarily into easily erodable Triassic sandstones, and Pleistocene till and outwash (Figure 2.7B). Wave erosion of these cliffs at a rate of up to 2 metres per year (Churchill, 1924; Klein, 1968) is believed to be the most important present-day source of sediment in the area. Where the cliffs are entirely composed of Triassic sandstone or Pleistocene outwash sand, the beach is also sand (Figure 2.7B); but because coarser Pleistocene material (till or outwash gravel) is present at the top of most cliffs, the beaches are generally composed of pebble to boulder size material (Figure 2.7C) Most of the sand and finer sediment is carried away by wave and tidal current activity. Beach cusps and pebble ridges (Figure 2.7C) similar to those described by McManus (1973) are present in places. The prevailing winds and waves produce a longshore transport from west to east, and gravel spits are developed across the mouths

of most small estuaries (Figure 2.10). Klein (1967) reports that these spits can advance at the rate of 1.25 metres per year.

At the foot of the beach, in all but the most exposed rocky headland positions, there is an abrupt transition from beach gravels and sands to mud (Figure 2.7B). The mud is present throughout the upper one-third to one-half of the intertidal foreshore zone as a veneer overlying lag gravel (or bedrock) that is an extension of the beach. This mud veneer is usually 10 to 30 centimetres thick, but can be up to 60 or 70 cm thick in more sheltered areas. Shallow runoff channels, with a straight or meandering pattern, traverse the mud and expose underlying material in many places. The muds support a large invertebrate fauna (Craig, 1976) which thoroughly bioturbates most of the sediment. However, crude horizontal lamination as well as flaser and lenticular bedding is preserved in some places. Moving down the foreshore, the mud veneer thins and becomes more sandy. Current and wave ripples are more abundant here than higher on the foreshore, and bioturbation is less.

On the lower half of the foreshore, the gravel lag reappears from beneath the mud veneer. Sandy harrow marks plus wave and current ripples are common on its surface (Figure 2.7D), and current scours are present around the ice-rafted boulders that dot the foreshore. Locally, accumulations of sand form small, isolated bars that rest on the lag gravel.

Examples of these that have been investigated in this study are: East Noel Bar (Figure 1.3); Saints' Rest Bar (Figure 1.3); Highland Village Bar (Figure 1.3 and 2.14); and Spencer Point Bar (Figures 1.3 and 2.14). Larger sand bars that are equivalent in size to those in Cobequid Bay are present in places along the seaward edge of the Minas Basin foreshore, but are separated from the foreshore in all cases by a channel that usually becomes emergent at low tide. These bars can occur singly, such as Big Bar at Five Islands (Figure 2.10), or as a series of two or three bars arranged end-to-end parallel to the shoreline. Examples are the Walton and Rainy Cove Bars on the south shore of the Minas Basin (Swift and McMullen, 1968), and the Economy Point complex on the north shore (Figure 2.16).

The facies sequence described here and illustrated in Figure 2.7A is developed in most areas that are exposed to wave activity. The regular pattern can be disrupted, however, by bedrock outcrops, as in the vicinity of Economy Point (Figure 2.16), or by low deltaic fans of sandy gravel that have been constructed at the mouths of the small steep-gradient streams, particularly along the north shore. The tops of these deltas are traversed by a network of shallow, braided distributaries at low tide, that shift across the surface rapidly and distribute the coarse material supplied by the streams.

ii) Mud Flats and Salt Marshes: In areas that are protected from strong wave and tidal current action, fine-grained sediments can accumulate. The topographically highest facies in such settings is the supratidal marsh, which is flooded only during high spring tides. The major vegetation here consists of fox grass (Spartina juncea) and black grass (Juncas gerardii) (Goldthwaite, 1924), which trap and bind the silt and clay that settle out of suspension during submergence. Isolated patches of ice-rafted gravel (Figure 2.8A) are scattered near the deeply incised gullies that drain the marshes. Around the margins of the Minas Basin and Cobequid Bay, the salt marshes are almost everywhere terminated abruptly at their seaward edge by an erosional scarp, 0.25 to 2.5 metres high (Figure 2.8B). In places, gravel beaches are being driven landward as washover fans over salt marsh deposits, which outcrop on the beach face (Figure 2.8C). Active progradation of the salt marsh is rare and restricted to a few localities in the innermost Cobequid Bay and estuaries of the Salmon and Subenacadie Rivers. Continued wave erosion at the high tide level since the stabilization of sea level is the most likely cause for the restriction of salt marsh extent.

Seaward of the salt marsh, muddy tidal flats analogous to those described by Reineck (1967) are developed. An abundant fauna is present in the muds (Craig, 1976) and bioturbation is extensive, but tidal bedding and lenticular bedding (Reineck and Wunderlich, 1968) are preserved in places. In

FIGURE 2.8 : Sheltered-embayment features. A - Ice-rafted gravel beside tidal gully in salt marsh, west of Highland Village; B - Eroding outer edge of salt marsh, Highland Village; C - Gravel beach advancing over salt marsh, Highland Village; D - Tidal gullies in mudflat between Selmah Bar and Salter Head; E - Drift-ice gouging and deformation of mudflats, near Walton; F - Rippled surface of bar in the innermost part of Cobequid Bay, at Lockherds Point.

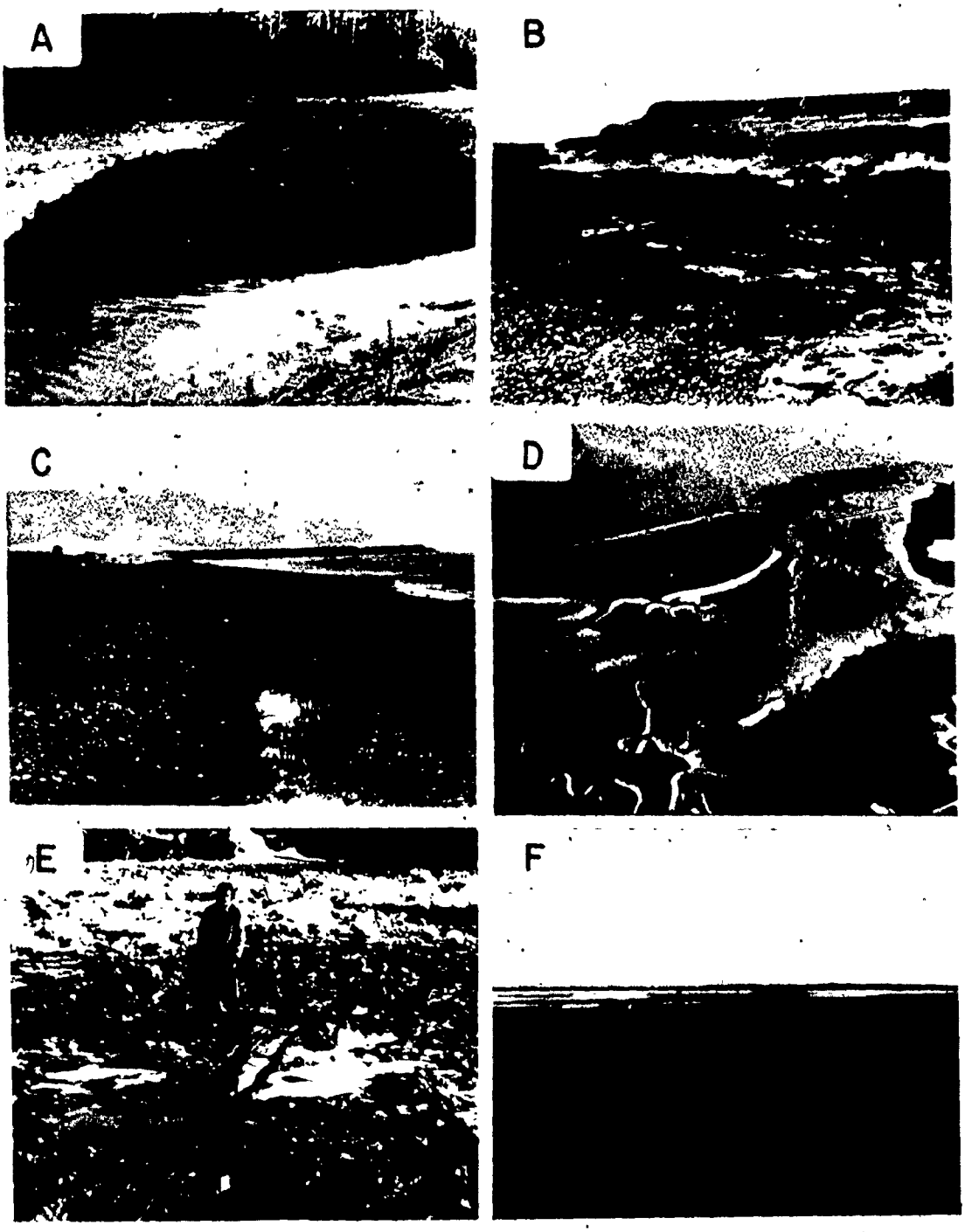
A
B
C
D
E
F

addition, soft sediment deformation and abrupt lateral discontinuities in bedding can be expected due to drift ice grounding (Figure 2.8E) and to the rip-up of sections of frozen crust during the winter, as described by Knight and Dalrymple (1976). Ice-rafted sand and gravel are common in some areas. The mudflats are dissected by a network of dendritic, meandering gullies (Figure 2.8D). The floor of these gullies is usually sandy, with minor numbers of terrigenous clasts and mud pebbles. Lateral migration of the gullies produces "longitudinal cross-bedding" (Reineck, 1967).

In most cases, the seaward extent of the mudflats is limited by an increase in exposure to waves and tidal currents. The classic intertidal-zone sequence of mudflats passing gradationally seaward through mixed flats into sandy tidal flats as described by Reineck is developed only in the estuaries of the Salmon and Shubenacadie Rivers. In the exposed portions of the Minas Basin and Cobequid Bay, ~~ha~~rrow-marked, lag gravel is generally encountered seaward of mudflats. Lateral variations in the degree of exposure can result in transitions from the exposed foreshore sequence to more normal mudflats with salt marsh in the sheltered areas. Examples of this occur northeast of Big Bar (Figure 2.10) and at the east end of Selmah Bar (Figure 2.11).

iii) Intertidal Sand Bars: The intertidal sand bars are the most characteristic component of the recent facies assemblage in the study area, and are widely developed both

in Cobequid Bay and around the margins of the Minas Basin as mentioned above. Similar sand bars also occur in, and at the mouth of, the Avon River and are under study by Lambiase (1976).

Individual bars vary considerably in size and shape, but all major ones are elongated in an east-west direction, roughly parallel to the shorelines and to the tidal currents. At spring low tide, the exposed portions of the bars range from 1 to 10 km in length, while bar widths are 0.2 to 4.25 km (Figure 1.3). The relief of the bar crests above the immediately adjacent channel bottoms is most commonly 10 to 15 metres, but ranges from two to nearly 20 metres as described above. At most, only the upper 6 to 7 metres of this are exposed at low tide, with the highest part of almost every bar near its eastern end, a feature that mirrors the overall trend of higher crestal elevations in the inner part of Cobequid Bay. Although underlying Pleistocene material or Triassic bedrock is exposed in some of the channels, seismic reflection studies do not show the existance of a core of older material beneath any of the bars in Cobequid Bay (R. J. Knight, 1975, personal communication; Swift and McMullen, 1968).

The surfaces of all the bars are covered with an array of lower flow regime bedforms: ripples, megaripples, and sand waves, as described above. Ripples, although forming the sole bedform phase in only restricted areas where there are low current speeds, are widespread at low tide and mantle most

intertidal surfaces, including previously formed megaripples and sand waves. They are believed to form during the last few minutes of the waning ebb tide, just prior to emergence.

Upper flow regime conditions are not common, and are restricted to localized areas where ebb runoff is channelized, or where sheet flow occurs during emergence.

In addition to the primary bedforms just described, a number of emergence and late-stage ebb modification features are present. The visible influence of waves is minor, and is confined to destructive rounding of current-generated bedforms on exposed portions of the bars, plus the formation of small-scale liquifaction features. All bedform features will be discussed more extensively in Chapter 4.

The predominant grain size of the sands on most bars is medium sand. Sediment with a mean size in either the coarse or fine sand grade is not common. In general, it appears that the coarsest sizes lie closest to the shorelines. The sediment tends to become finer away from the foreshores, and eastward at the head of Cobequid Bay where it merges with the estuaries of the Salmon and Shubenacadie Rivers. On virtually all sand bars, the sand on the crest is finer than the material in the channels on either side. Grain size is considered in more detail in Chapter 5.

### 2.3.2 Sand Bar Settings

The above description of the recent facies and their distribution in the study area is intended to establish in a general way, the setting of the sand bars that are under investigation. Each of the bars studied will now be considered individually, beginning with the four major areas: i) Big Bar; ii) Selmah Bar; iii) Diamond Bar; and iv) Economy Point. These will be followed by a brief description of the six additional areas where supporting observations were obtained: v) Noel Bay Bar; vi) East Noel Bar; vii) Spencer Point Bar; viii) Highland Village Bar; ix) Saints' Rest Bar; and x) Pinnacle Flats.

i) Big Bar lies between the shore and the islands at Five Islands (Figure 1.2, area A and Figure 2.10), on the north shore of the Minas Basin. The sediments and bedforms have been described by Klein (1970). Topographically, Big Bar is the simplest of the bars studied, and is roughly oval in plan, with an arm branching northeastward from its west end. The maximum exposed length of the bar, based on air photos taken June 5, 1973, at spring low tide, is 3.4 km, while the width of the main body of the bar is 0.7 km. In cross-section, the bar is asymmetric with the crest lying close to the southern edge of the bar. No major depressions cross the bar and disrupt the continuity of the crest. The dip of the steep southern side of the bar averages $4^{\circ}$, with maximum values of $6^{\circ}$ locally. The gentle side dips northward

at 1 - 2°. A topographic map prepared by Klein (1970, Figure 9A) shows more than 6 metres of relief above the low tide level in the channel to the south of the bar. The islands situated one kilometre south of the bar crest shelter Big Bar from much of the wave activity.

The sediment on the bar is predominantly medium sand, but with some coarse sand along the north side, and fine sand on the steep south side. Ripples alone are present on this steep side. The lower part of the gentle side is covered with megaripples, while the crestal portion displays small (rippled) sand waves. Larger sand waves are present on the northwest arm, and at the western tip of the bar. The channels on both the north and south sides of the bar are floored with harrow-marked lag gravel (Figure 2.10). North of the gravel, one encounters a mud and sandy-mud veneer. More extensive mudflats are present in the small estuaries to the northeast of the bar.

Study of old air photos from 1947 to 1963 by Klein (1970) show that the sedimentary facies and morphology of Big Bar have remained unchanged since 1947. Klein (1970) attributes this stability to the existence of an equilibrium counter-clockwise sediment circulation cell, centred on the bar.

ii) Selmah Bar is located on the south shore of Cobequid Bay, immediately to the west of Salter Head (Figures 1.2, area D, and 2.11). Previous descriptions of Selmah Bar appear in papers by Dalrymple (1973a, b), Dalrymple et al (1975), Knight (1972) and Knight and Dalrymple (1975, 1976).

# LEGEND

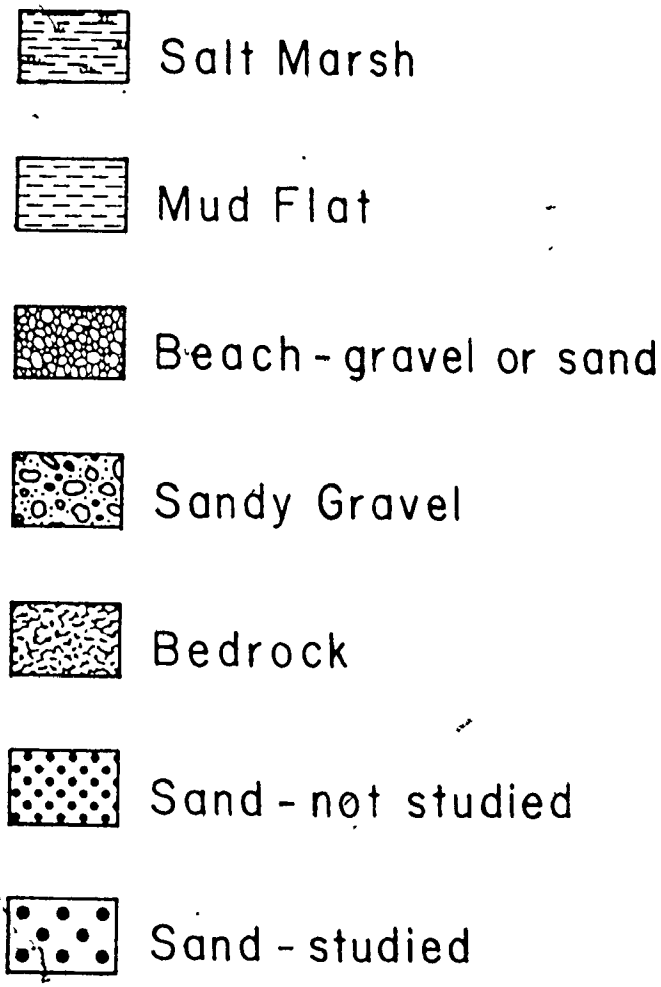


FIGURE 2.9 : Legend of sediment types used in Figures 2.10, 2.11, 2.14 and 2.16.

FIGURE 2.10 : Facies setting of Big Bar and Pinnacle Flats. See Figure 2.9 for legend. Information from air photos taken June 5, 1973.

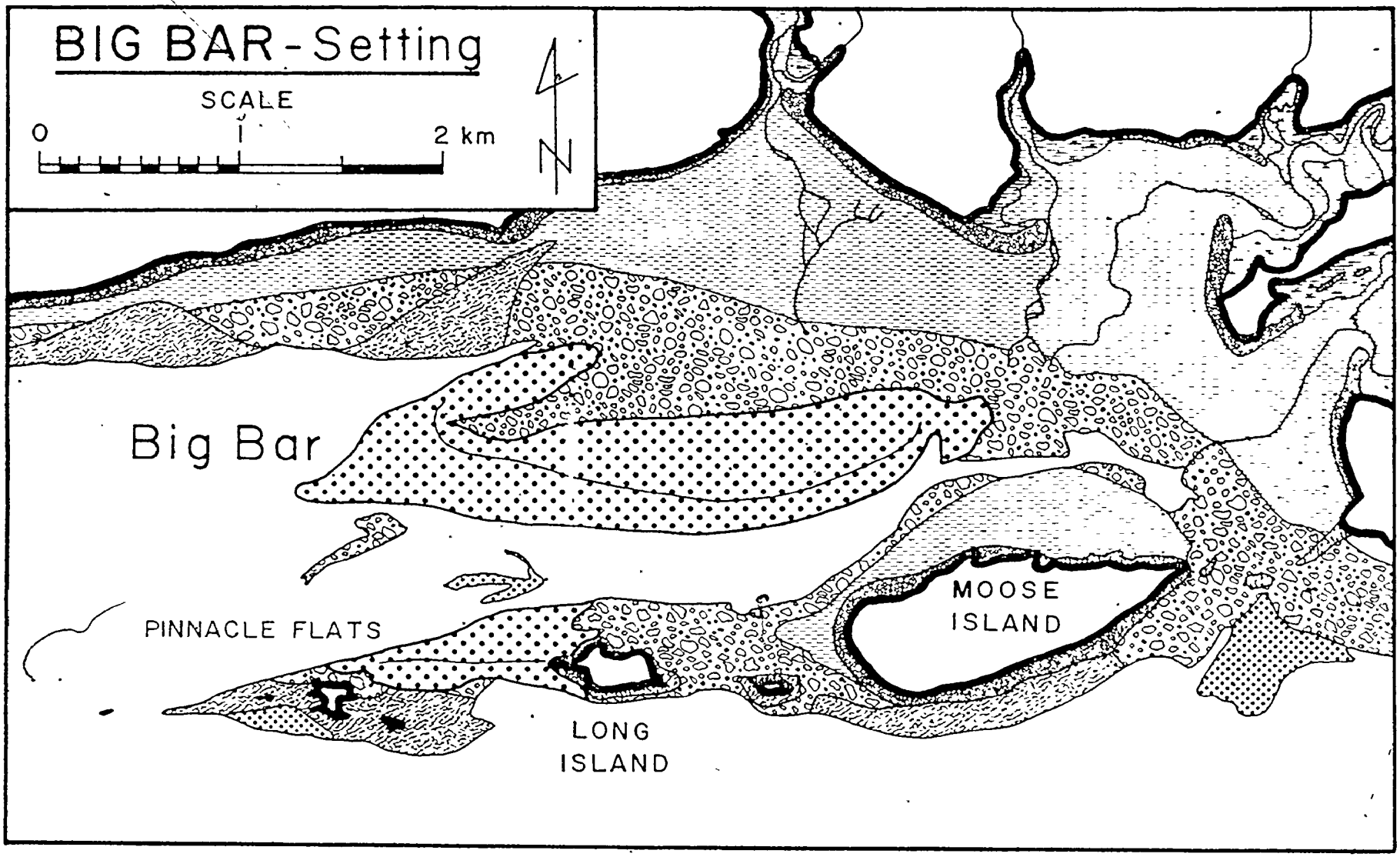
BIG BAR - Setting
SCALE
0
1
2 km
N
Big Bar
PINNACLE FLATS
MOOSE
ISLAND
LONG
ISLAND

FIGURE 2.11 : Facies setting of Selmah Bar. See Figure 2.9 for legend. Information from air photos taken June 5, 1973.

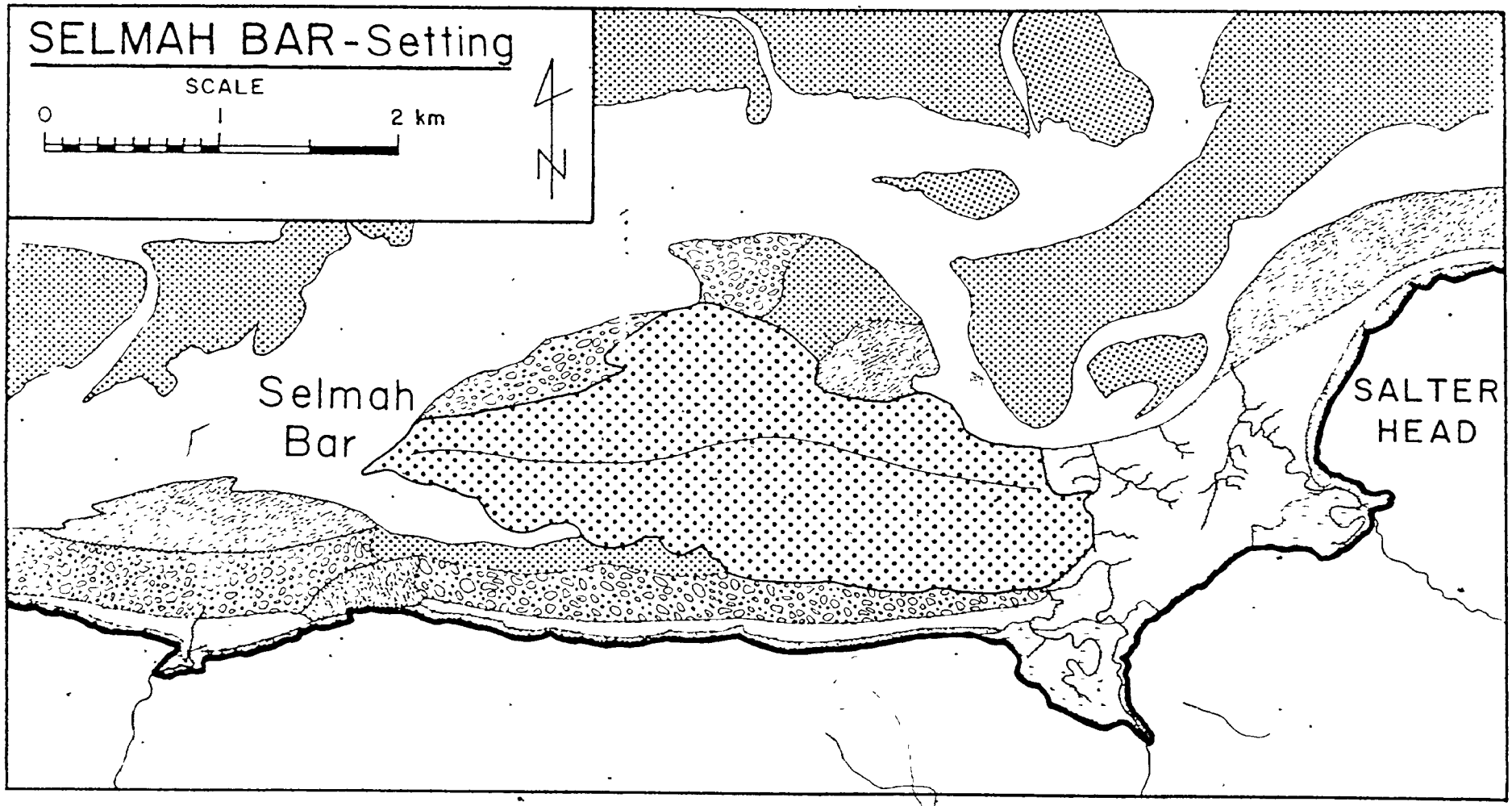
SELMAH BAR-Setting
SCALE
0
1
2 km
N
Selmah
Bar
SALTER
HEAD

FIGURE 2.12 : Topography of Selmah Bar. Constructed from a plane table survey conducted in June, 1971. Datum is approximately mean low water.

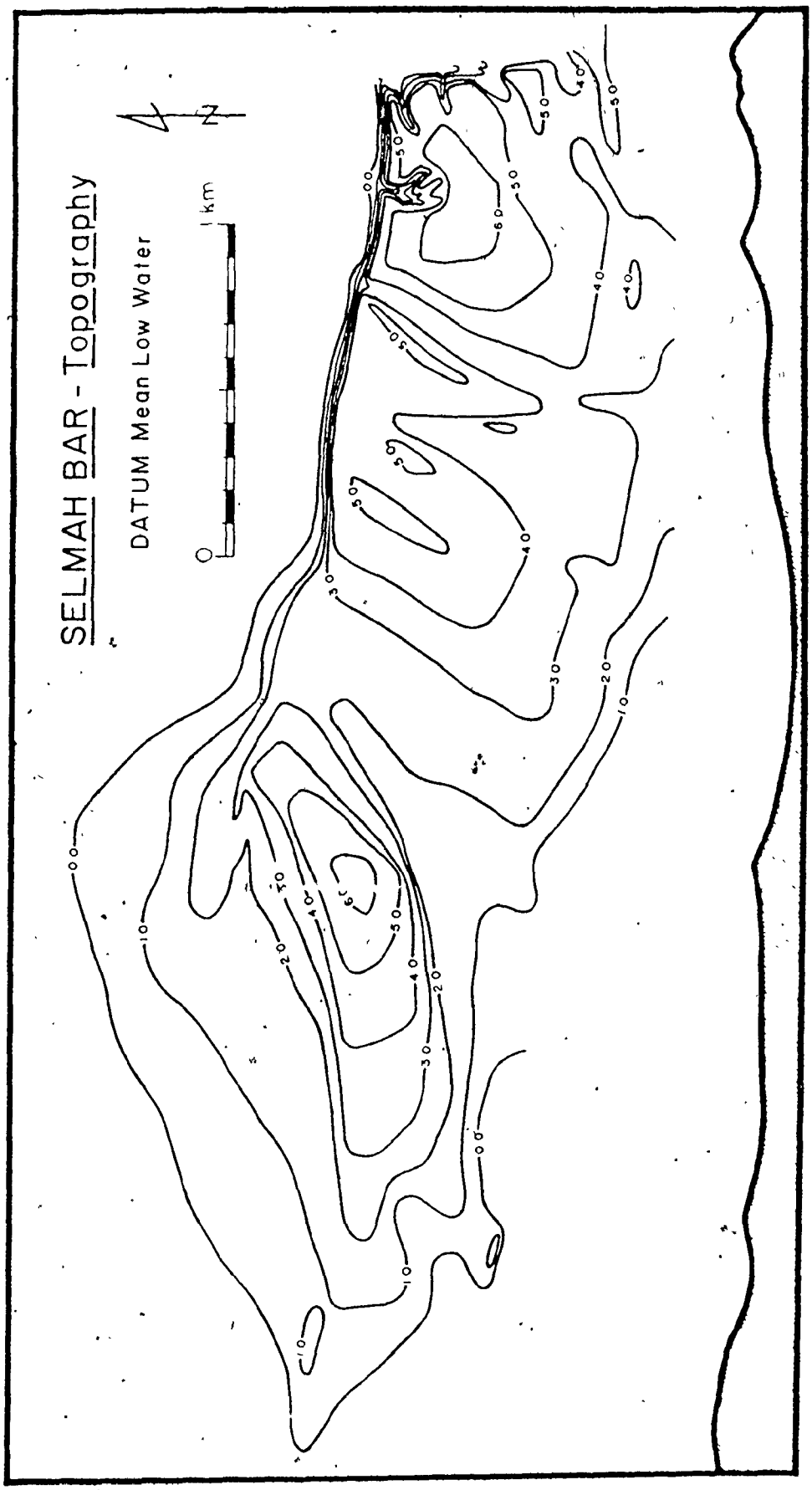
SELMAH BAR - Topography
DATUM Mean Low Water
N
0
1 km

This bar is one of the largest studied, with an exposed length of 4.2 km at spring low tide, and a maximum width of 1.6 km. It is separated from the foreshore by a channel that shoals eastwards. Selmah Bar is topographically much more complex than Big Bar, as is evident from Figure 2.12, a topographic map constructed from 1971 survey data. In the middle of the bar, a major swatchway ("a short transverse channel across an elongated sandbank", Robinson, 1960, p.186) cuts the bar in two. At its eastern end, the crest is located along the northern edge. Slopes to the north are steep, reaching $8^{o}$, while the south side dips at $0.5 - 1.5^{o}$. Several minor swatchways and gullies dissect this part of the bar. In the western half of the bar, the crest swings closer to the southern side. The highest parts of both halves of the bar are in excess of 6 metres above mean low tide, and lie at the eastern end of each section.

Selmah Bar is unique among the major bars studied because it passes eastward into mudflats (Figure 2.11). In part, the transition is gradual, but along much of its length, there is an abrupt change from sand to mud across a tidal gully. Along the south shore, an exposed-foreshore sequence of facies is developed. Rock outcrops of Triassic sandstone off Salter Head and at the western tip of the bar break the regularity of the facies pattern. Triassic bedrock or bedrock with a gravel veneer is also exposed on the northern edge of the bar, between the bar and a major channel which carries

much of the tidal discharge from the estuaries at the head of the bay.

The sediment on Selmah Bar is coarse sand along the very southern edge, but this grades quickly northward into medium sand. Fine sand is present at the east end, and on the eastern half of the steep northern edge.

Ripples alone are extensively developed in fine sand that is transitional to the mudflats. An extensive field of sand waves is present between the crest of the bar and the southern channel, to the east of the major swatchway, while the western half of the bar is covered with well-developed megaripples.

Selmah Bar has existed in the same location and in a recognizable form since at least 1860, which is the date of the first available chart. Along the northern edge of the bar and the adjoining mudflats, however, an orderly sequence of changes can be seen since 1938, when the first air photos were taken. The changes between 1960 and 1975 are shown in Figure 2.13. Between 1938 and 1972, there is obvious erosion in the area mentioned, that is the result of the progressive southward migration of the channel, in a manner analogous to a river meander. The erosional character of this portion of the bar was clearly evident on the ground. In 1975, however, the previous trend was reversed, and the bar margin was displaced northward by the deposition of more than a metre of fine, rippled sand in the location previously occupied by

FIGURE 2.13 : Historical development of Selmah Bar, 1963 - 1975. Outline of intertidal zone in 1963 and 1972 taken from vertical air photos. 1975 outlines reconstructed from oblique air photos.

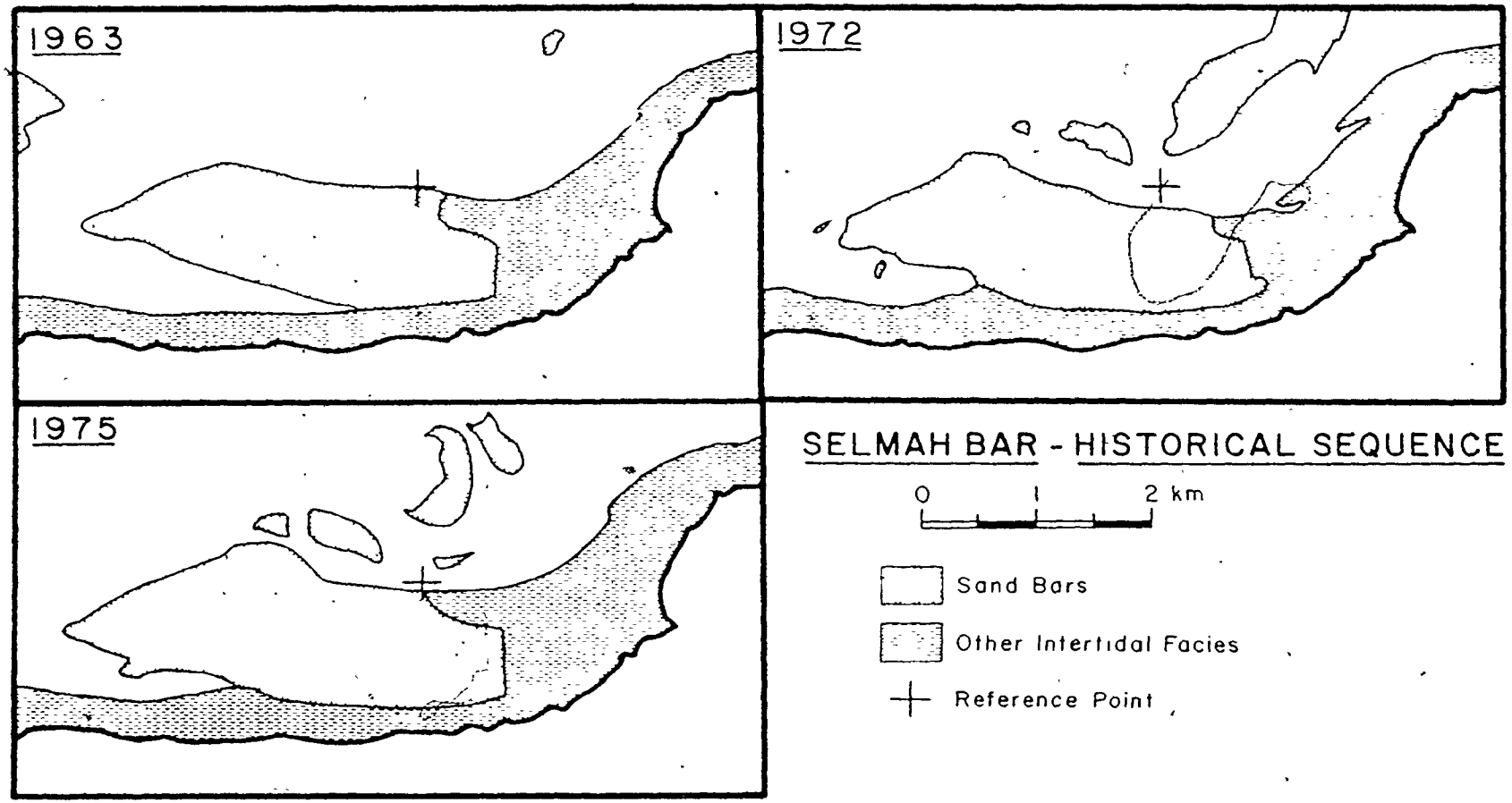
1963
1972
1975
SELMAH BAR - HISTORICAL SEQUENCE
0
1
2 km
Sand Bars
Other Intertidal Facies
Reference Point

the channel. This sudden change appears to be due to the abandonment of the curved 1972 channel in favour of a straighter course.

iii) Diamond Bar is located in the north-central portion of Cobequid Bay (Figure 1.2, area B and Figure 2.14) and is separated from the north shore by a deep channel that is more than a kilometre wide at spring low tide. The influences of shore irregularities are minimal, therefore, and it is believed that Diamond Bar is representative of other bars in the central part of Cobequid Bay. Diamond Bar is roughly triangular in plan, and has an exposed length of about 4 km and a width at its eastern end of 1.3 km. The bathymetry in the vicinity of Diamond Bar is shown in Figure 2.15 with respect to a datum 12.0 metres above the Canadian Hydrographic Service mean low water datum. The topographically highest part of the bar is located at its eastern end and is 6.5 metres above spring low water. Like Selmah Bar, Diamond Bar is divided into an eastern and western part by a swatchway. At its eastern end, the bar crest lies closer to the southern edge of the bar, so that most of the exposed bar surface dips northward at less than $1^{\circ}$. At the low water level, the slope steepens to between 3 and $4^{\circ}$. The exposed south side of the bar dips at about $4^{\circ}$ also. The bar is more symmetrical along its western half, but the crest is still displaced toward the south side. At its eastern end, Diamond Bar is separated from Great Village Bar by a major swatchway. A comparison of

FIGURE 2.14 : Facies setting of Diamond, Highland Village, and Spencer Point Bars. See Figure 2.9 for legend. Information from air photos taken June 5, 1973.

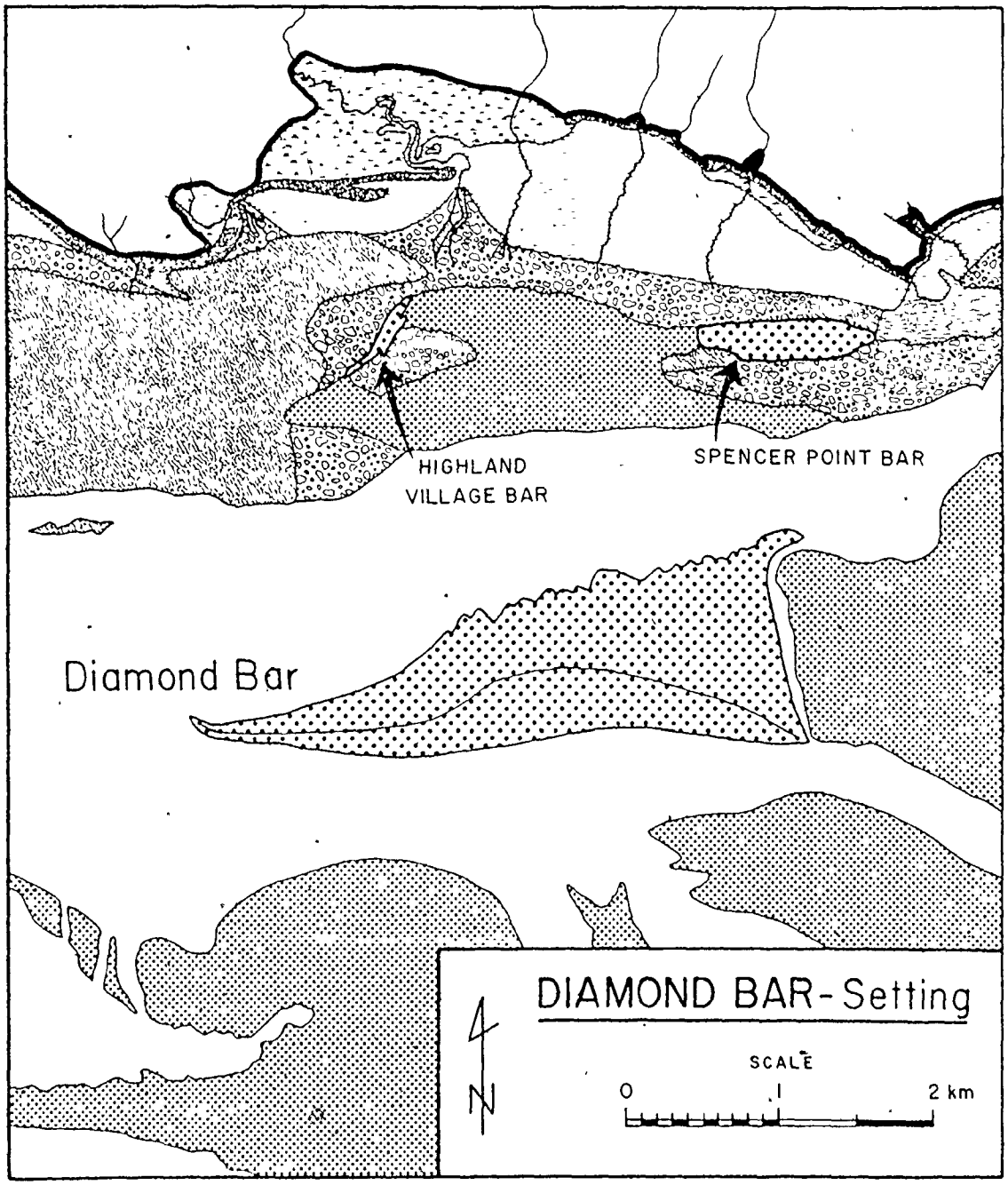
HIGHLAND
VILLAGE BAR
SPENCER POINT BAR
Diamond Bar
DIAMOND BAR - Setting
N
SCALE
0
1
2 km

FIGURE 2.15 : Bathymetry of Diamond Bar. Constructed from depth-sounder records obtained in July, 1974. All depths standardized to a high tide level 12.0 metres above mean low water.

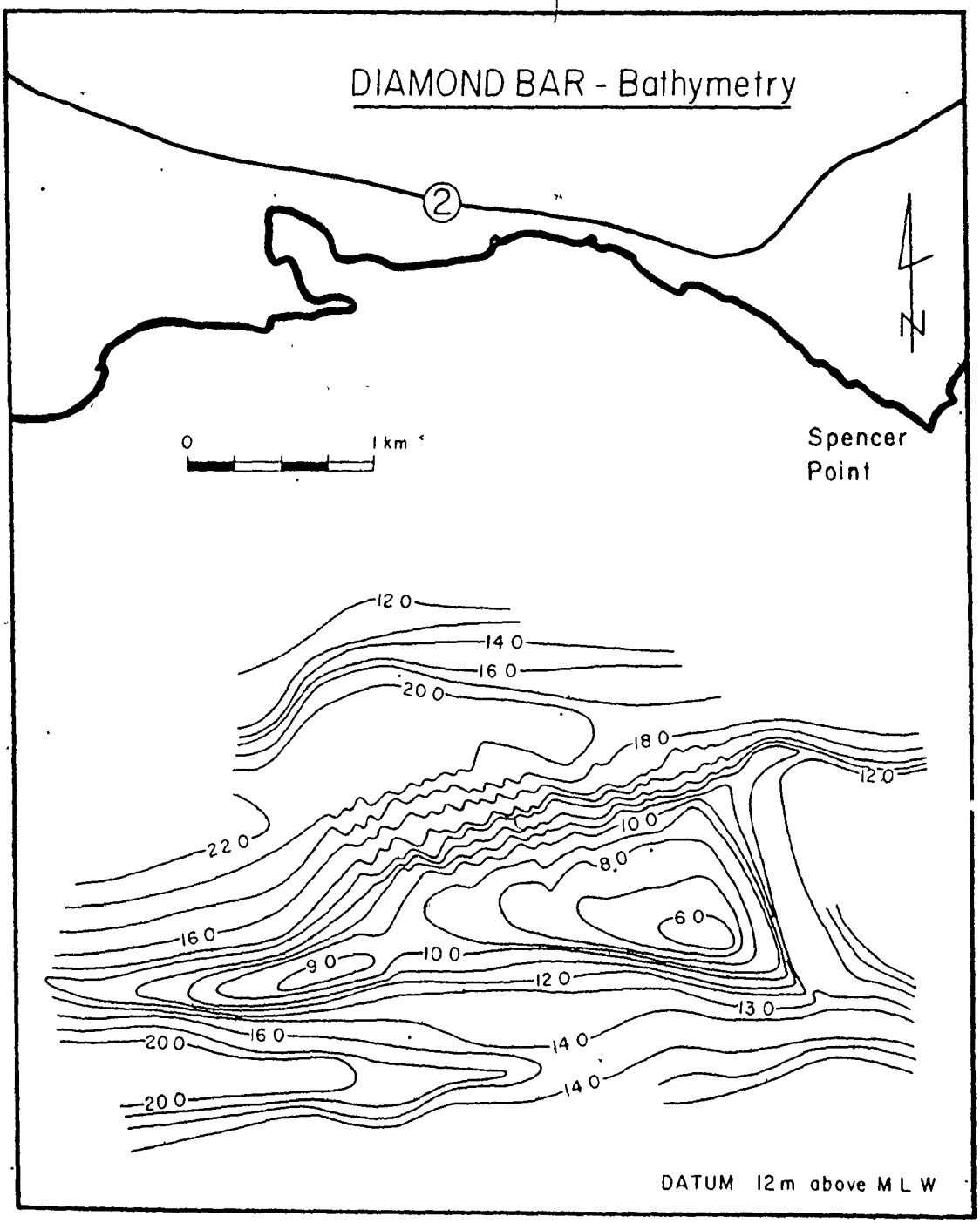
DIAMOND BAR - Bathymetry
2
N
0
1 km
Spencer
Point
12 0
14 0
16 0
20 0
18 0
12 0
22 0
10 0
8.0
6 0
16 0
9 0
10 0
12 0
13 0
20 0
16 0
14 0
20 0
14 0
DATUM 12 m above M L W

the bar outline of Figure 2.14 with the bathymetry in Figure 2.15 suggests the presence of a water surface slope to the west at low tide on the order of 1 metre in 4 km, or $0.014^{o}$.

The mean size of the sediment on Diamond Bar is predominantly medium sand. Fine sand is present on the crest of the bar at its eastern and western ends, while coarse and very coarse sand is present in the northern channel, and along the northern edge of the bar.

Megaripples are developed on all parts of the bar. In addition, large sand waves are present on the north side of the crestline, and extend into the bottom of the north channel. They are clearly visible on Figure 2.15, where individual bedform crests can be traced for over half a kilometre.

Bars in the centre of Cobequid Bay are much less stable than those adjacent to the shore, and experience much more profound and rapid changes. Diamond Bar, for example, is only recognizable for the first time in 1971 air photos. Prior to that, one single large bar (called "Betsy Bob" Bar by Swift and McMullen, 1968) occupied the centre of the bay, and the channel along its northern margin restricted the westward extension of Great Village Bar, that has subsequently become Diamond Bar.

iv) Economy Point: Three major sand bars, lying end to end are present south and west of the tip of Economy Point (Figures 1.2, area C, and 2.16). The two eastern bars, named

FIGURE 2.16 : Facies setting of the Economy Point complex. See Figure 2.9 for legend. Information from air photos taken June 5, 1973.

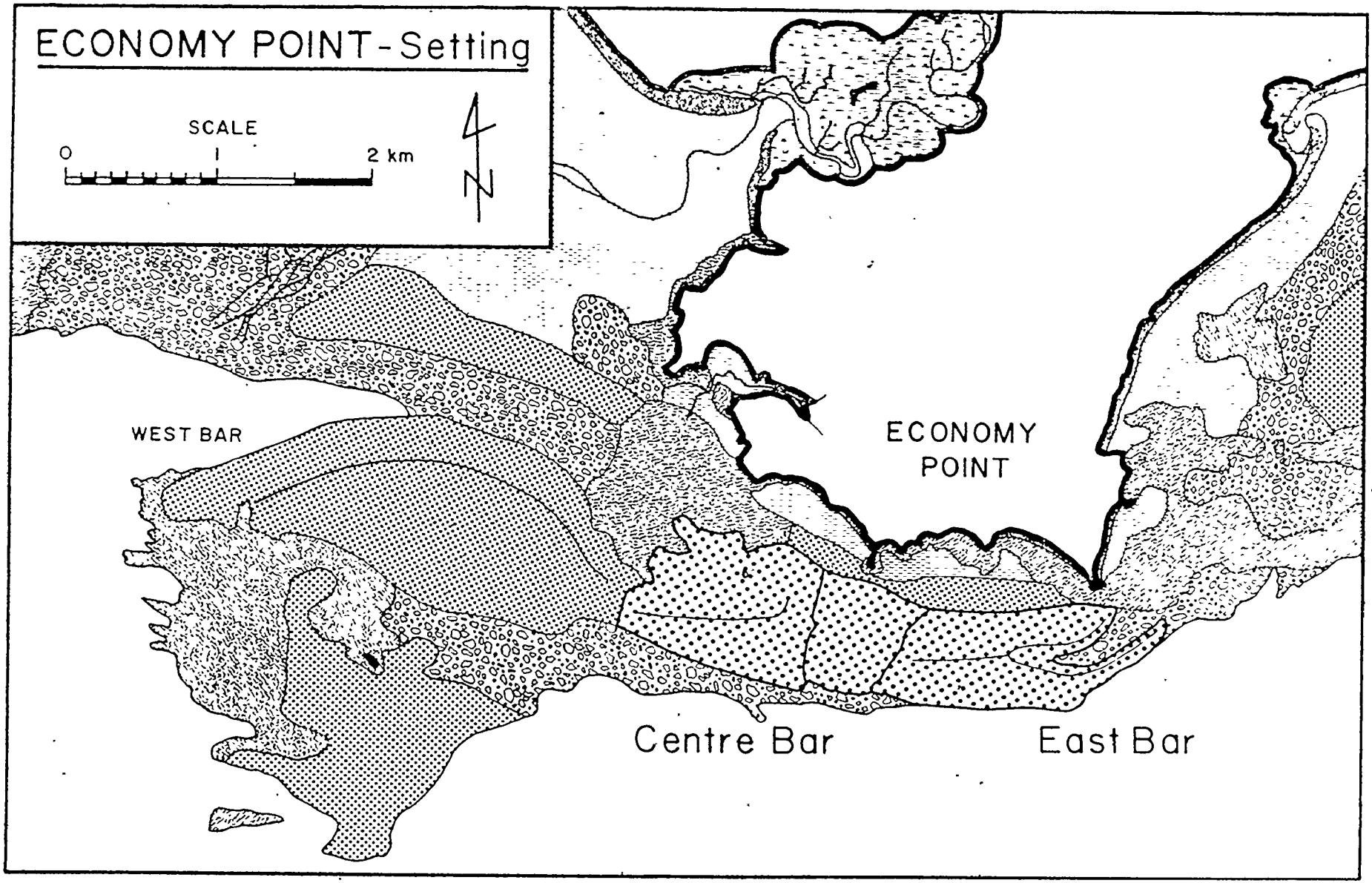
ECONOMY POINT-Setting
SCALE
0
1
2 km
N
WEST BAR
ECONOMY
POINT
Centre Bar
East Bar

FIGURE 2.17 : Bathymetry of Centre and East Bars at Economy Point. Constructed from depth-sounder records obtained in July and August, 1974. All depths standardized to a high tide level 12.0 metres above mean low water.

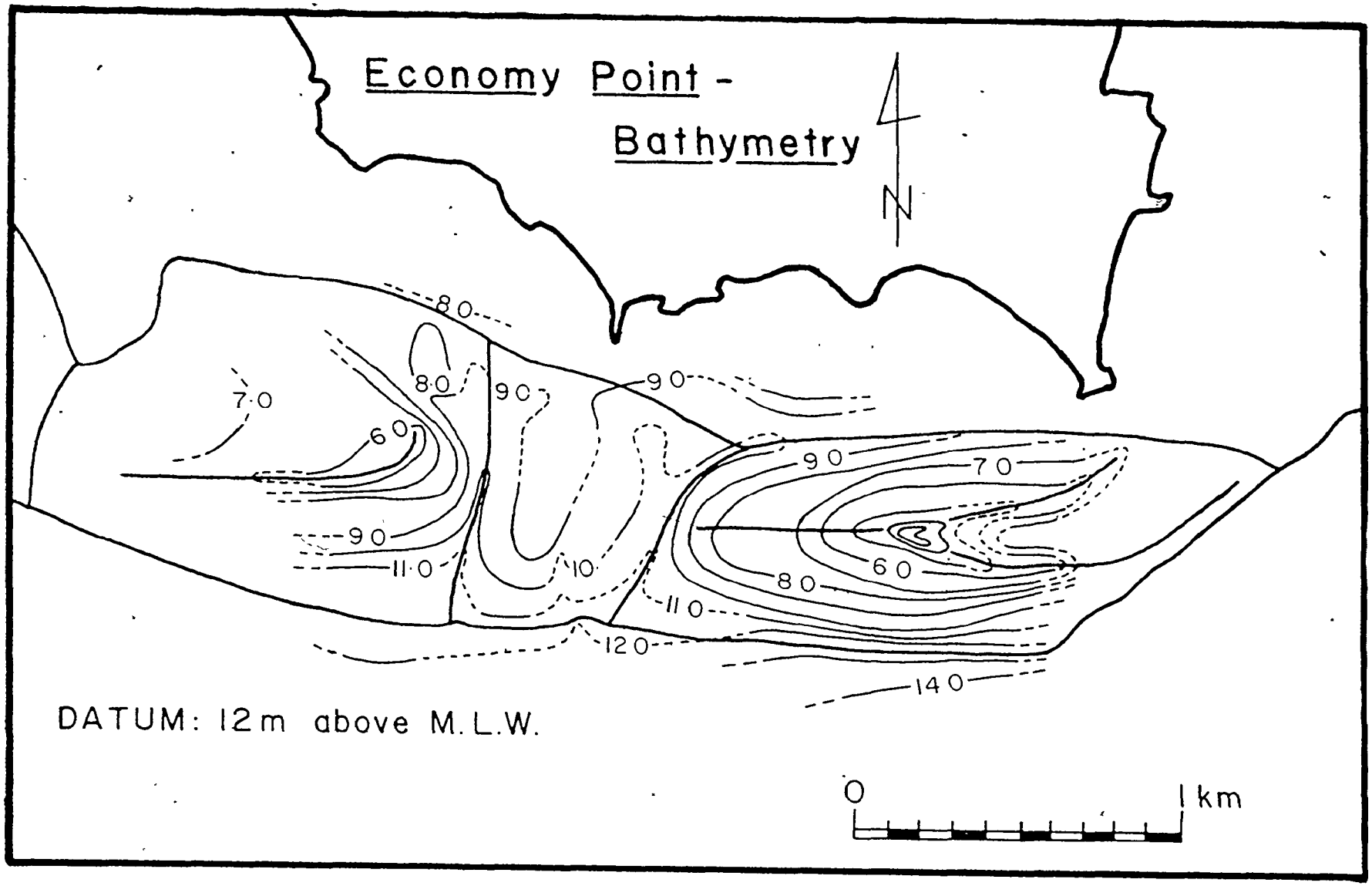
Economy Point -
Bathymetry
N
80
70
80
90
90
90
70
60
90
110
10
60
80
110
120
140
DATUM: 12m above M.L.W.
0
1 km

Centre and East Bars by Klein (1970) who studied the complex, plus the unnamed section between them have been investigated. These bars occupy an exposed position and are subjected to the strongest wave action of the areas studied, as discussed in Section 2.2.2. Bathymetrically, Centre and East Bars are unique among the bars studied (Figure 2.17). The crestline of Centre Bar runs from west to east, and then at its eastern end, curves abruptly northward. The crestline of East Bar also runs east-west, offset slightly to the south of the Centre Bar crest. Near the eastern end of the bar, the crest bifurcates, giving rise to a tuning-fork-like shape that encloses a blind ebb channel. Both Centre and East Bars are separated from the shore by east-west channels that are exposed at low tide, and the bars are divided from each other by north-south extensions of the shoreward channels. On East Bar, the highest point is at the crestline triple junction, and is covered by only 3 metres of water at neap tide. On Centre Bar, the highest area is located where the crest runs north-south. Here, the water depth is just over 5 metres at neap tide.

The Economy Point bars possess the coarsest sediment of the main bars studied, with approximately equal amounts of medium and coarse sand present. Unlike the other bars, the coarsest sediment tends to lie seaward of finer sand.

Centre Bar is completely covered with megaripples, but with three or four large sand waves present on the north side of the crest. Small sand waves are present on the section

between Centre and East Bars, while large sand waves cover East Bar. Both of these areas have ripples superimposed on most of the sand waves, except at spring tides when mega-ripples appear.

Triassic bedrock outcrops are common in all intertidal areas surrounding the Economy Point bars (Figure 2.16). A gravel lag over bedrock is present south of Centre Bar, while most of the sediments shoreward of the bars are sandy and derived directly from the Triassic sandstones. The embayment west of Economy Point is the only location of extensive mud deposition in the area.

Despite their exposed position at the tip of Economy Point, the sand bars have changed remarkably little since the first air photos were taken in 1938. Klein (1970) has analyzed these photos and indicated that only two small-scale changes have occurred: firstly, the cutting of the channel that now separates West and Centre Bars, and an increase in the height of Centre Bar; and secondly, the progressive westward extension of the blind ebb channel into the east end of East Bar.

This concludes the introduction of the four areas that have provided the bulk of the data included in this thesis. The remaining six small, isolated bars were not the subject of the intensive study given the above four areas and as a result, these bars will be used only to support observations from the primary study areas. For this reason, the setting of each will be presented in a cursory manner only.

v) Noel Bay Bar is located across the mouth of Noel Bay (Figure 1.3), but is separated from the shore by a deep channel. Its exposed length on the 1973 air photos is 3.2 km, and its maximum width is 0.35 km. The crestline of the bar lies closer to the south side, such that most of the exposed top of the bar slopes gently northward. The exposed relief of the bar at spring low water is approximately 6 metres. Most of the sand on the bar is medium sand and megaripples plus small rippled sand waves are developed. On the adjacent foreshore, Triassic bedrock is exposed off both headlands, and across much of the mouth of Noel Bay. A shoal has been present in the approximate location of Noel Bay Bar since before 1860, the date of the first accurate survey of the Minas Basin and Cobequid Bay.

vi) East Noel Bar is a patch of sand resting on the southern foreshore of Cobequid Bay in the embayment on the east side of Noel Head (Figure 1.3). The length of this sand patch is 1.3 km and its width is 0.5 km. The thickness of the sand forming East Noel Bar is less than 2 metres. Triassic bedrock outcrops both to the east and west of the bar, but is overlain by a lag gravel on the north side of the bar. Along its southern side and to the southeast, the medium sand of the bar grades through fine sand into mudflats. The surface of the bar is covered with megaripples, except in the areas transitional to the mudflats where ripples are developed. Two large, poorly-defined sand waves are present at the western end of the bar.

vii) Spencer Point Bar lies on the intertidal foreshore on the north side of Cobequid Bay, southwest of Spencer Point (Figures 1.3 and 2.14). This bar is part of a larger area of fine sand on the foreshore north of Diamond Bar. The portion studied is 1.15 km long by 0.25 km wide and rises no more than 2 metres above its surroundings. Large sand waves are well developed on much of the bar's surface, with megaripples present on the remaining part. The sediment forming the bar is coarse and medium sand. Harrow-marked lag gravel is exposed both north and south of the bar, overlying Triassic bedrock that outcrops at Spencer Point and at the west end of the bar. A large area of mud is present in the somewhat sheltered embayment west of Spencer Point and north of the bar.

viii) Highland Village Bar is also located on the foreshore north of Diamond Bar (Figures 1.3 and 2.14), 2 km west of Spencer Point Bar. Its dimensions are 600 m by 100 m and it is elongated in a northeast-southwest direction. This is the only area studied that is not elongate parallel to the tidal flow, but has its long dimension at an angle of 50 - 55$^{o}$ to the currents. This is due to the fact that the entire bar is composed of only two sand waves, with heights of 1.25 metres. The sediment making up these sand waves is medium to coarse sand. Highland Village Bar rests on a surface of lag gravel which itself is only a thin veneer over Triassic sandstone. Extensive outcrops of bedrock are present a short distance west of the bar.

ix) Saints' Rest Bar is located high on the intertidal foreshore, just west of the mouth of Bass River (Figure 1.3). At its eastern end, the bar almost connects with the foot of the high tide gravel beach. This bar is only 600 metres long by 125 metres wide, and has a height of only about 1.5 metres above the surrounding harrow-marked lag gravel. Saints' Rest Bar is composed primarily of medium sand and shows a well-defined sequence of bedforms along its length. Sand waves are present over most of the bar surface, but megaripples are developed at its eastern end, and ripples at the western end.

x) Pinnacle Flats has a unique location, stretched between Long and Pinnacle Islands, just south of Big Bar at Five Islands (Figure 1.2, area A, Figure 2.10). Klein (1970) studied Pinnacle Flats in considerable detail. This bar is 1.3 km long and 0.5 km wide at its eastern end. Klein's (1970, Figure 9B) topographic map of Pinnacle Flats shows that the crest rises up to 6 metres above the low tide datum used by Klein. The bar is asymmetrical, with the crest lying closer to the southern edge of the bar. Medium sand is the most common sediment size on the bar, and sand waves of various dimensions are developed over much of the surface. Triassic basalt and sandstone outcrop in the island cliffs and in the intertidal zone surrounding Pinnacle Flats. A gravel lag is present over some of the bedrock platforms and in the channel north of the bar.

From the preceeding descriptions, it is clear that each bar is different from every other bar, despite having certain similarities. Some of these common features are: an elevated topographic expression; an elongation roughly parallel to the tidal current flow directions; crestlines that are not perfectly straight, but show bends or bifurcations; an asymmetry either to the north or south; medium sand as the predominant grain size, but with finer material usually at a topographically higher elevation; and tidal-current bedforms on their surfaces. The most obvious differences between bars relate to the three-dimensional shape of the bar, including the exact form of the crestline in plan view and the attitude of the side slopes. More subtle differences are also evident in the distribution of bedforms, grain size, and tidal currents that ultimately control the bedforms, grain size and sediment transport over the bars. The remaining chapters will concentrate on these more subtle differences. Before proceeding with this, however, one final aspect of the setting must be investigated; that is, the nature of the sediment itself.

### 2.3.3 The Sand

Klein (1971) suggested that an intertidal environment such as that in the Minas Basin and Cobequid Bay might be a good place in which to produce supermature quartz arenites. This was based on the assumption that all intertidal sand bars

exhibit a closed sediment transport pattern in which the sediment can travel long distances while remaining in a restricted geographic area. The grains were believed to move an average of 100 metres every tidal cycle so that long time spans are not required. Balazs and Klein (1972) followed up this idea by an investigation of the mineralogy and roundness of sand from Pinnacle Flats (Figure 2.10). It is questionable, however, whether their samples are truly representative of all intertidal sands because of the unique setting of Pinnacle Flats and the close proximity of Triassic basalt in the islands. In order to gain a somewhat more comprehensive picture of the mineralogy and roundness, eight samples have been analyzed, two from each of the four major bars, with one from each side of the crestline. The sample locations are shown on Figure 2.18. There is no intention of being either completely comprehensive, or rigorous in this investigation, as it is only of marginal relevance to the stated objectives of the thesis.

The mineralogy of the sands was determined by point-counting thin sections of unsieved sand, mounted in epoxy resin, using 300 points per slide. The sections were stained with sodium cobaltinitrite to aid in the identification of potassium feldspars (Friedman, 1971). Roundness values were estimated for the same grains using the silhouettes of the images shown by Powers (1953) as a guide. The mineralogical results are summarized in Figure 2.19, and are listed in Table 2.2, along with the roundness values which are given using Folk's (1955) rho scale.

FIGURE 2.18 : Location of samples used in the mineralogical study. A - Big Bar; B - Diamond Bar; C - Economy Point; D - Selmah Bar.

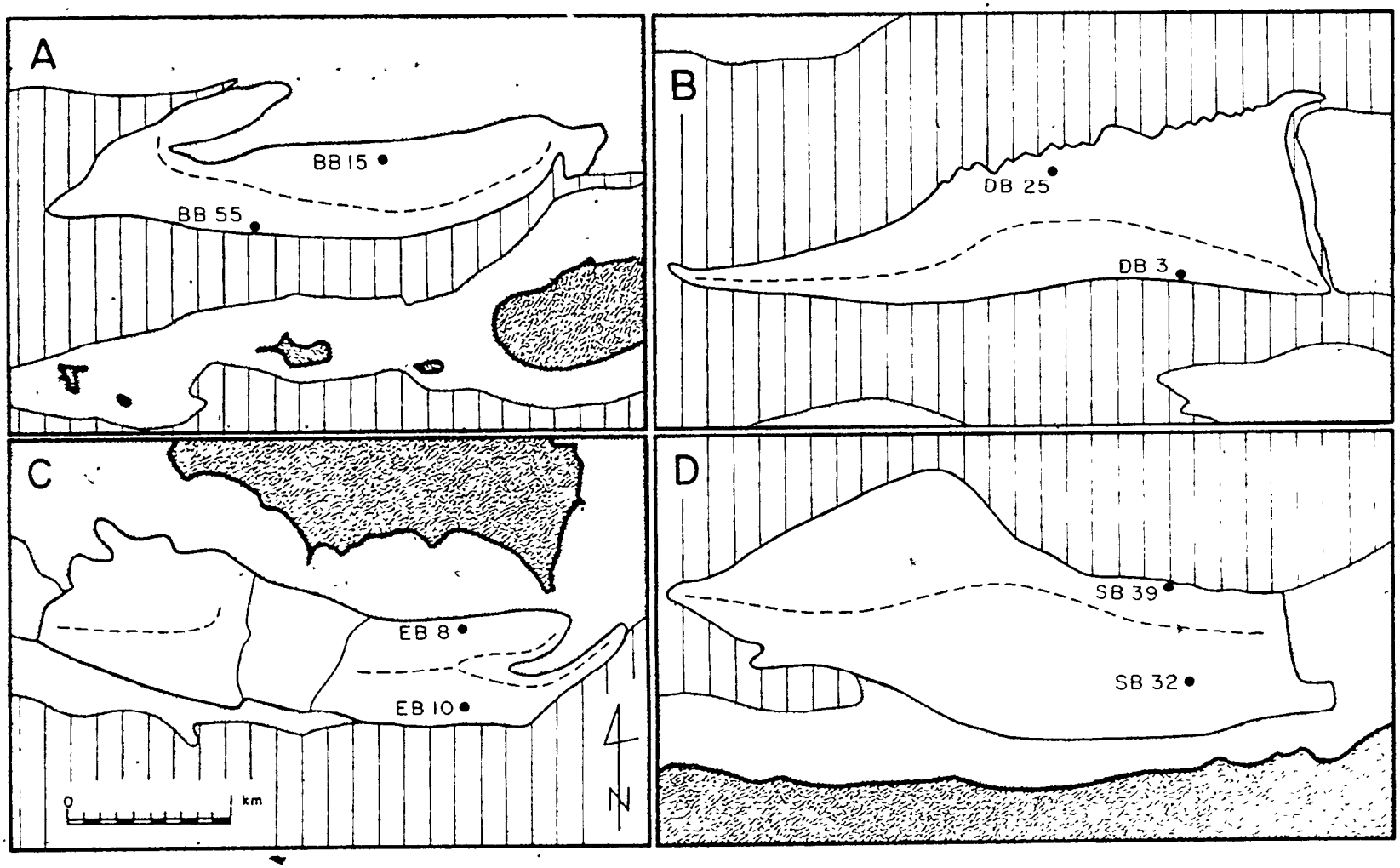
A
BB 15
BB 55
B
DB 25
DB 3
C
EB 8
EB 10
0
km
N
D
SB 39
SB 32
Land
Water
Studied Bar
(with crestline)
Other Intertidal Areas

FIGURE 2.19 : Mineralogical classification of Minas Basin and Cobequid Bay sands. See also Table 2.2. Included is the average composition determined by Balazs and Klein (1972) for Pinnacle Flats (Figure 2.10). Classification scheme from Pettijohn, Potter and Siever (1972).

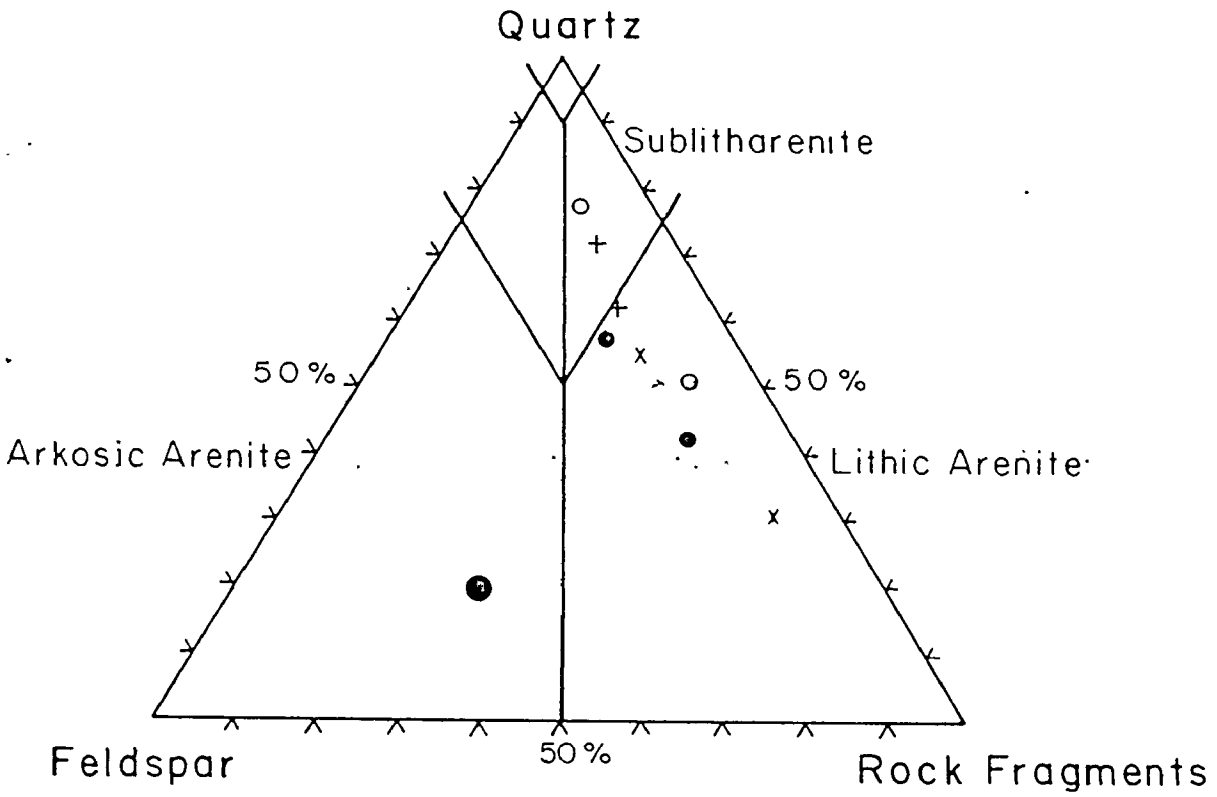


- ● BIG BAR
- o DIAMOND BAR
- X ECONOMY POINT
- \+ SELMAH BAR
- ● Balazs & Klein (1972)

TABLE 2.2 : Mineralogy and roundness of intertidal sands in the Minas Basin and Cobequid Bay. All values in percent unless otherwise indicated.

| Mineral Species | Balazs & Klein (1972) | Big Bar | | Economy Point | | Diamond Bar | | Selmah Bar | | Mean (excluding Balazs & Klein |
|---|---|---|---|---|---|---|---|---|---|---|
| | | BB 15 | BB 55 | EB 10 | EB 8 | DB 25 | DB 3 | SB 32 | SB 39 | |
| Mean Grain Size (Ø) | | 1.25 | 2.71 | 0.95 | 1.3 | 1.14 | 2.40 | 1.29 | 2.03 | |
| QUARTZ | | | | | | | | | | |
| - total | 19.41 | 42.0 | 56.3 | 30.1 | 53.7 | 50.3 | 73.7 | 61.1 | 69.7 | 54.6 |
| - nonund. | 5.48 | 10.7 | 17.7 | 5.0 | 12.7 | 16.3 | 18.0 | 14.9 | 20.3 | 14.4 |
| - und. | 13.09 | 21.0 | 29.6 | 18.5 | 28.0 | 25.3 | 37.7 | 31.7 | 32.7 | 28.1 |
| - polycryst. | 0.84 | 10.3 | 9.0 | 6.6 | 13.0 | 8.7 | 18.0 | 14.6 | 16.7 | 12.1 |
| FELDSPAR | | | | | | | | | | |
| - total | 49.6 | 13.0 | 15.3 | 8.0 | 12.3 | 9.3 | 9.3 | 12.4 | 9.7 | 11.2 |
| - orthoclase | 40.51 | 6.3 | 5.7 | 4.0 | 5.0 | 7.3 | 3.0 | 3.5 | 5.0 | 5.0 |
| - plagioclase | 9.12 | 6.7 | 9.6 | 4.0 | 7.3 | 1.7 | 6.3 | 8.9 | 4.7 | 6.2 |
| ROCK FRAGMENTS | | | | | | | | | | |
| - total | 28.32 | 42.0 | 25.7 | 58.4 | 31.7 | 39.0 | 12.0 | 25.5 | 17.3 | 31.5 |
| - sedimentary | 3.72 | 27.0 | 18.7 | 32.3 | 21.7 | 25.4 | 4.3 | 9.2 | 7.0 | 18.2 |
| - plutonic | 10.46 | 8.3 | 4.7 | 22.1 | 6.7 | 10.0 | 4.0 | 10.0 | 7.3 | 9.1 |
| - volcanic | 11.24 | 5.7 | 2.3 | 2.7 | 2.3 | 2.3 | 2.7 | 5.7 | 2.7 | 3.3 |
| - others | 2.90 | 1.0 | 1.0 | 1.3 | 1.0 | 1.3 | 1.0 | 0.6 | 0.3 | 0.9 |
| ACCESSORIES | | | | | | | | | | |
| - total | 2.29 | 3.4 | 2.7 | 2.6 | 2.3 | 1.3 | 4.9 | 1.0 | 3.3 | 2.7 |
| RATIOS | | | | | | | | | | |
| - nonund/und. | 0.42 | 0.51 | 0.60 | 0.27 | 0.45 | 0.64 | 0.48 | 0.47 | 0.62 | 0.51 |
| - ortho./plag. | 4.44 | 0.94 | 0.59 | 1.00 | 0.68 | 4.53 | 0.47 | 0.39 | 1.07 | 0.81 |
| MEAN QUARTZ | | | | | | | | | | |
| - roundness (rho) | 4.2 | 2.93 | 1.91 | 3.38 | 2.84 | 2.83 | 2.73 | 2.88 | 2.84 | 2.79 |
| - roundness sorting (rho-units) | | 1.07 | 1.15 | 1.20 | 1.06 | 1.26 | 1.01 | 0.93 | 0.90 | 1.07 |

Combining the data from all 8 samples, quartz is the most abundant component, with an average of 55%. Rock fragments constitute an appreciable proportion of the sediment, however, (31.5%) while feldspars account for only slightly more than 10%. Of the total feldspar, plagioclase is twice as abundant as orthoclase. It is evident, however, that a high degree of variability exists in the mineralogy of the intertidal sands, a portion of which is due to grain size differences between samples. As one might expect, the finer sands contain fewer rock fragments, but more quartz than do coarser sands on the same bar. Total feldspar content shows no clear trend with grain size, but orthoclase is slightly more abundant, relative to plagioclase in the coarser sands. Differences between individual sand bars cannot be recognized with the available data. There is the suggestion, however, that the bars in Cobequid Bay (Diamond and Selmah Bars) have more quartz (63.7%), but less rock fragments (23.5%) and feldspar (10.2%) on average, than do the isolated bars along the Minas Basin shoreline (Big Bar and Economy Point ) - 45.5% quartz; 39.5% rock fragments; and 11.2% feldspar. Despite the variations, six of the samples plot in the lithic arenite field of Pettijohn, Potter and Siever's (1972) sandstone classification (Figure 2.19), while the other two, which are the finest samples from Cobequid Bay, are sublitharenites.

When the composition of the Pinnacle Flats sands as reported by Balazs and Klein (1972, Table 2) is compared with the results obtained by this author (Table 2.2, Figure 2.19),

major differences are evident. The quartz content given by Balazs and Klein is more than 30% lower than in the samples analyzed here, including those from Big Bar, while orthoclase feldspar is 30% more abundant. The percentage of rock fragments is approximately equal in both suites. The average Pinnacle Flats sand has an arkosic arenite composition (Figure 2.19). At this point, the reason for the large difference cannot be given, and more work is necessary.

The mineralogy of these intertidal sands reflects the source area as described in Section 2.1.2 above. In the eight samples analyzed, recognizable Triassic sandstone fragments averaged 10%, with a maximum of 19.8% at Economy Point, indicating that the Triassic is a particularly important component of the source. The mineralogical immaturity of the sands suggests either that the model proposed by Klein (1971) for the generation of quartz arenites is less effectual than believed and has not been operating for a sufficient length of time, or/and that the immature material is being continuously replenished.

Analysis of the roundness data also proves interesting (Table 2.2). On average, the quartz grains studied are subangular, with a mean roundness of 2.8 rho, and only 47% of the grains fall in the subrounded, rounded and well-rounded classes combined. These results have been corroborated independently using samples from Economy Point (Cant, 1976, personal communication) and Selmah Bar (Wehrfritz, 1973,

personal communication). As with the mineralogy, no differences in roundness are detectable between bars, except that mean roundness values appear to be more uniform in Cobequid Bay than for the isolated bars in the Minas Basin. Mean roundness does not correlate with grain size variations in either area. Roundness sorting as defined by Folk (1955) averages approximately one rho unit (one roundness class). It is interesting that the sample with the best rounding contains the highest percentage of Triassic rock fragments.

Balazs and Klein (1972) report that quartz from Pinnacle Flats has a mean roundness of approximately 4.2 rho, and that 86% of the quartz grains have roundness values greater than three rho. These values are quite different to those obtained here. Some limited data are also presented by Balazs and Klein (1972) to indicate that the sand on the sand bars are more than three rho units better rounded than the source sand. This is almost twice as much improvement in rounding as is implied by the present data. It has been found in a number of studies (Cant, 1976, personal communication; Folk, 1955) that operator variance is large in roundness studies, with a standard deviation due to operator variance of approximately 0.35 rho units. It is therefore possible, but unlikely, that the difference between 2.8 and 4.2 rho is due to operator bias.

The significance of these differences cannot be assessed at this time, but Pinnacle Flats certainly appears unique in terms of both roundness and mineralogy, among all

of the sand bars investigated to date. The poorer roundness in other areas again suggests that the effectiveness of Klein's (1971) model is less than indicated by the data of Balazs and Klein (1972).

Preliminary examination of quartz grain surface textures using scanning electron microscopy does indicate, however, that some modification of grain shape is occuring in the intertidal zone. Brisbin (1974, personal communication) found that intertidal grains possess a different suite of surface textures than do Pleistocene outwash sands. In addition, Wehrfritz (1973, personal communication) determined that rounder intertidal grains show fewer glacial features and more non-oriented V-shapes than more angular grains. Triassic source sands have not yet been investigated.

Unfortunately, the mineralogical, roundness, and surface texture data raise more questions than they answer. The Klein (1971) model for the formation of supermature quartz arenites requires further testing before its status can be evaluated finally.

## 2.4 Summary

This chapter has provided the background necessary for the more detailed studies to follow, by describing the physical and environmental framework within which the bars are located.

The region surrounding the study area is rolling to hilly, and the shoreline in most places is bordered by cliffs of easily eroded Triassic sandstone, and Pleistocene till and

outwash. Wave erosion of these cliffs is believed to be the major source of sediment at the present time. The mineralogy of the intertidal sands reflects the composition and proximity of the source by the large number of sandstone and plutonic rock fragments, and by the subangular average roundness of the grains.

Although the long axis of the Minas Basin and Cobequid Bay is parallel to the direction of the prevailing winds, wave action is relatively unimportant, except at the high water level, due to the limited effective fetch and the large extent of the intertidal zone. The large semidiurnal tide for which the area is famous has a mean range of 11.9 metres, but tides up to 16.3 metres have been measured. The currents associated with the tidal water-level changes attain near-bottom speeds of 0.5 to 1.5 m/s and are the most important process operating on the sand bars. Ice that is present during the four winter months, although an impressive sight, has only minor effects compared to the everyday action of the tidal currents.

The response of the recent sediments to the processes operative is highly organized and reflects the amount of energy expended. Wide, wave-cut platforms with only a thin, gravelly sediment cover are present along most of the Minas Basin and outer Cobequid Bay shorelines. Mud and fine sand are most extensive in the estuaries of the Salmon and Shubenacadie Rivers at the head of Cobequid Bay, where wave

and tidal current strengths are least. The large, 10 by 25 km, sand body situated in Cobequid Bay and the mouths of the rivers also shows an eastward decrease in tidal current strength, primarily by the sequence of predominant bedforms developed on the sand bars: large megaripples at the western, outer end; sand waves with small megaripples in the central portion; and ripples only at the innermost, eastern end.

The individual, major sand bars are large, with exposed lengths and widths of 1 - 10 km and 0.2 - 4.25 km respectively. The relief averages 10 to 15 metres, of which 6 to 10 metres is exposed at low tide. The four major areas studied come from a variety of settings. Diamond Bar is located in the outer, high energy portion of Cobequid Bay, some distance from the shoreline, while Selmah Bar is situated further east in the lee of Salter Head, and shows a transition to mudflats at its eastern end. The sand bars at the tip of Economy Point are expected to experience the strongest wave influence of any of the studied areas because of their exposed position. In contrast, Big Bar occupies a very sheltered position north of the islands at Five Islands. This variety should provide a representative sampling of the possible conditions that exist in the Minas Basin and Cobequid Bay.

# CHAPTER 3

# TIDAL CURRENT HYDRAULICS

## 3.1 Data Collection and Analysis

### 3.1.1 Introduction

Knowledge of the tidal currents and tidal-current hydraulics is essential in any attempt to understand present-day sedimentation in the Minas Basin and Cobequid Bay. As a result, considerable effort has been directed towards obtaining current measurements from as many of the studied areas as possible, with as complete areal and time coverage as resources and weather allowed. During the summers of 1971, 1973 and 1974, a total of 34 stations were occupied (Figure 3.1), and 1,275 vertical profiles of current velocity were measured. The distribution of the data is as follows: 9 stations with 428 profiles from Big Bar (1973); 14 stations and 622 profiles on Diamond Bar (1974); 6 stations with 153 profiles at Economy Point (1974); and only 5 sites and 72 profiles from Selmah Bar (1971). Some additional data for Selmah Bar is given by Dalrymple et al (1975). Many of the stations were occupied at least twice, in an effort to ascertain the variation in current speed with tidal range, and the currents were measured over as much of the tidal cycle as possible during

each visit to a site. All of the primary velocity data are presented in Appendix 1.

Before proceeding into a discussion of the tidal speeds and flow patterns over the bars presented in the second part of this chapter, it is necessary first to describe the current measuring devices used, and the procedure used to cross-correlate the results, followed by a digression into some hydrodynamic theory regarding the nature of flow in open-channel boundary layers. This is intended to introduce the various hydraulic parameters that have been calculated from the current profile data, and that appear in Appendix 2.

### 3.1.2 The Current Meters

In the course of the investigations, three different measuring devices were employed, one in each of the three summers when current data were obtained: 1971 - a Kelvin-Hughes remote reading current meter; 1973 - a Pritchard-Burt current vane; and 1974 - an Endeco Type 110 remote reading current meter.

The current data available from Selmah Bar were measured with a Kelvin-Hughes remote reading current meter which was loaned to the author for a brief period by R. J. Knight. This meter allowed the direct, ship-board monitoring of current speed and direction. The data are believed to be reliable, with the possible exception of the speed values for Buoy 5, which may be a little high due to calibration difficulties on that day.

FIGURE 3.1 : Location of the current metering stations. A - Big Bar; B - Diamond Bar; C - Economy Point; D - Selmah Bar.

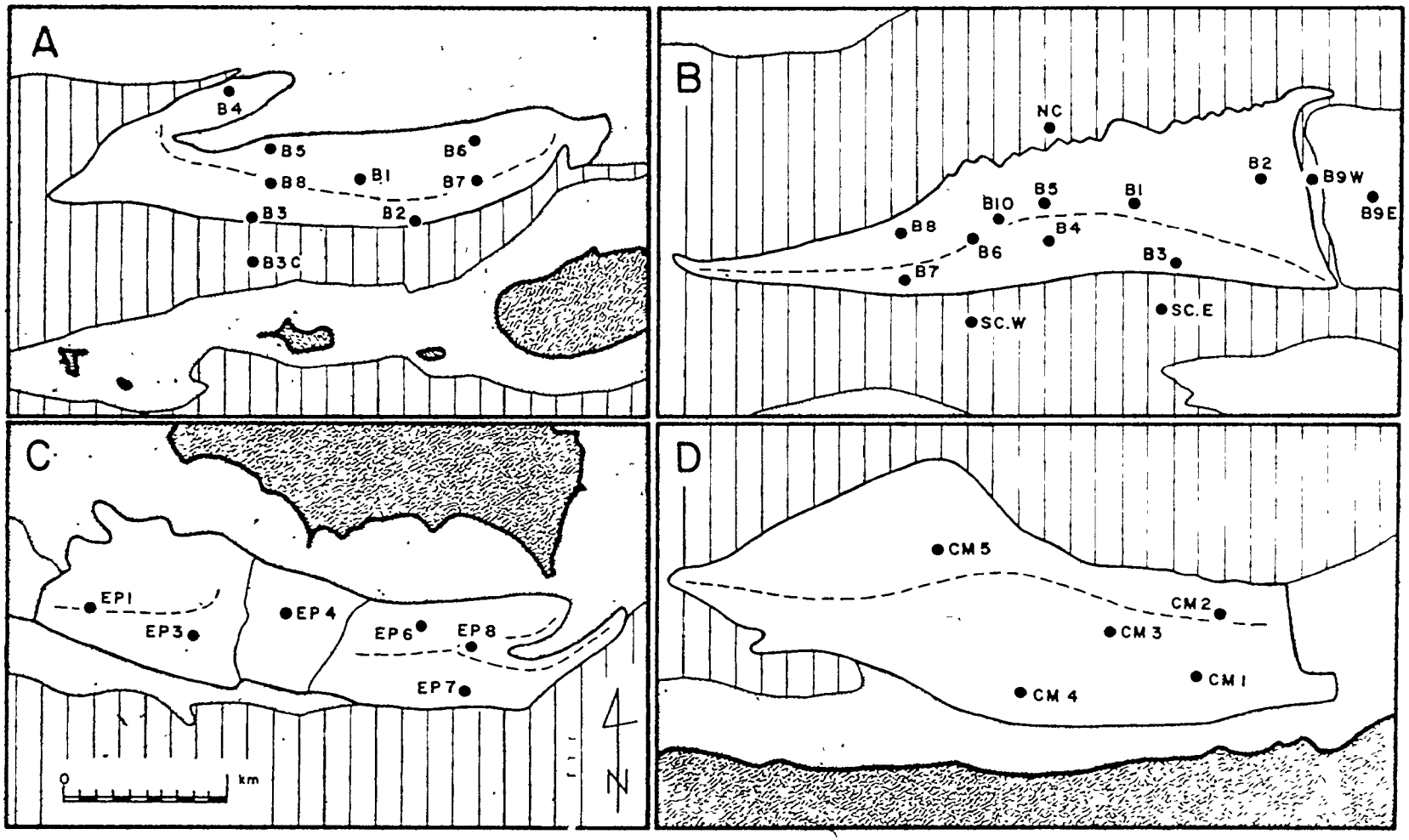
A
B4
B5
B6
B8
B1
B7
B3
B2
B3C
B
NC
B2
B9W
B9E
B10
B5
B1
B8
B4
B6
B3
B7
SC.W
SC.E
C
EP1
EP3
EP4
EP6
EP8
EP7
0
km
N
D
CM5
CM2
CM3
CM1
CM4
Land
Water
Studied Bar
(with crestline)
Other Intertidal Areas

The majority of the current measurements reported in Appendix 1, specifically those made on Diamond Bar and at Economy Point, were obtained with the use of an Endeco Type 110 Remote Reading current meter, manufactured by Environmental Devices Corporation, Marion, Massachusetts. This meter allowed the direct read-out on deck of current speed and direction, plus the water depth over the meter, and the water temperature. The meter was calibrated before leaving the factory, so that current speeds could be determined with an accuracy of ± 0.08 m/s (± 0.15 knots) and direction to within ± 7.2°. This meter has been used as a standard in the calibration of the remaining device used.

Because a meter such as the Endeco was not available during the summer of 1973 when Big Bar was under investigation, a biplane drag (Pritchard and Burt, 1951) had to be used to measure the current speed. (Current direction was estimated from the alignment of the boat.) This vane (Figure 3.2A) consisted of two plywood sheets in the form of a cross, with a height of 0.45 m (1.5 feet) and a total width for each plane of 0.62 m (2.0 feet). Three individually removable 6.8 kg (15 lb.) weights were attached beneath the vane, while the vane itself was suspended in the current on a 5 mm thick steel cable. The flow of the water exerts a force on the vane which causes the cable to be deflected from the vertical by an amount proportional to the current speed. Pritchard and Burt (1951, p.183) derive a simple relationship relating the

FIGURE 3.2 : Calibration of the current vane. A - Schematic diagram of vane;
B - Calibration curve for 6.8 kg (15 lb.) weight;
C - Calibration curve for 13.6 kg (30 lb.) weight;
D - Calibration curve for 20.6 kg (45 lb.) weight.
Theoretical curves after Pritchard and Burt (1951).

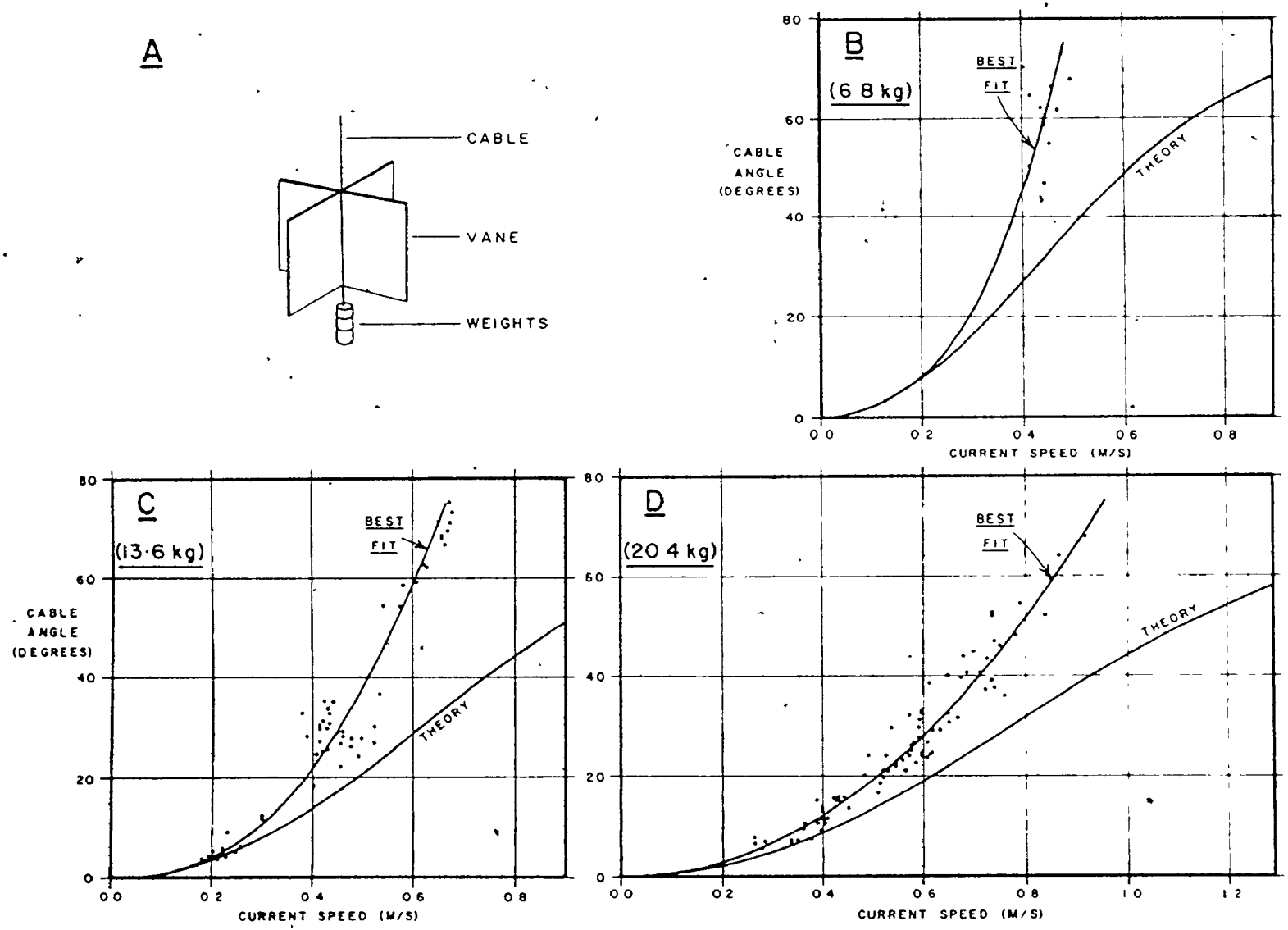
A
CABLE
VANE
WEIGHTS
B
(6 8 kg)
BEST FIT
THEORY
CABLE ANGLE (DEGREES)
CURRENT SPEED (M/S)
C
(13·6 kg)
BEST FIT
THEORY
CABLE ANGLE (DEGREES)
CURRENT SPEED (M/S)
D
(20 4 kg)
BEST FIT
THEORY
CURRENT SPEED (M/S)

current speed (u) and the cable angle (Θ) by assuming a vectorial balance between the force exerted by the flow and the gravitational restoring force:

$$u = \frac{2\,Mg}{C_D\,A\rho} \tan \Theta \qquad (3.1)$$

where M = the mass of the vane and weights; g = the gravitational acceleration; $C_D$ = a drag coefficient; A = projected area of the vane; and ρ = the density of the fluid. This relationship was found to be of limited use, however, because it neglects the tension in the cable which causes the vane to tip so that its axis does not remain vertical. Once this occurs, a lift force is initiated which results in the cable being deflected further from the vertical than anticipated acording to (3.1) for a given current speed (Figure 3.2). The ultimate result is that the vane planes along the surface of the water above a certain current speed. Unfortunately, the introduction of the lift force makes a theoretical calibration of the vane extremely complicated. An attempt was made to obtain a calibration using a force field analysis, but success was limited by inadequate knowledge of lift and drag coefficients for a configuration such as the vane. The calibration was achieved, therefore, by taking simultaneous measurements of current speed with the vane and the Endeco current meter (Figure 3.2). Sufficient data were obtained with 13.6 kg and 20.4 kg weights to allow a least-squares

regression of cable angle on current speed. These best-fit lines are included in Figures 3.2C and 3.2D, and have the following equations (with the current speed in m/s):

$$\text{- for 13.6 kg - cable angle} = 204.8\ (\text{speed})^{2.44} \qquad (3.2)$$

$$\text{- for 20.4 kg - cable angle} = 82.71\ (\text{speed})^{2.08} \qquad (3.3)$$

Both regression lines have correlation coefficients of 0.95. Also presented on the figures are the appropriate theoretical calibration curves determined from equation (3.1). Unfortunately, technical difficulties did not allow the collection of sufficient calibration data for the 6.8 kg weight, and the appropriate relationship had to be selected somewhat arbitrarily (Figure 3.2B) as:

$$\text{cable angle} = 540.0\ (\text{speed})^{2.7} \qquad (3.4)$$

The above three equations have been used to convert all of the cable angle measurements into current speeds, which are listed in Appendix 1.

### 3.1.3 Hydrodynamic Theory

The nature of turbulent flow and the way in which a rough bed influences the flow is extremely complex. As a result, the simplifying assumption is usually made in theoretical considerations that the flow is steady (no change through time at any location), uniform (no variation from place to place in the horizontal), and two-dimensional. However, even

a brief inspection of tidal currents indicates that these conditions are not fulfilled in the present situation. Therefore, in order to apply the theory that is presented below, it is necessary to make the assumption that the rate of change is sufficiently small that one can consider the flow to be steady for brief periods of time, and uniform over a restricted area. This assumption is implicit in all previous field investigations of tidal hydraulics.

The movement of any fluid can either be laminar, in which the flow paths are regular, and viscous forces predominate, or turbulent, with irregular eddies and the predominance of inertial forces. The relative importance of these two forces is expressed by the Reynolds number (Re)

$$Re = \frac{\rho \bar{U} h}{\mu} \qquad (3.5)$$

which can be considered as proportional to the ratio of inertial to viscous forces. In equation (3.5), $\mu$ is the dynamic viscosity, $\bar{U}$ is the mean velocity over the total flow depth h, and $\rho$ is the fluid density as defined previously. Large Reynolds numbers imply turbulent conditions and, as will be seen, all of the currents present in the study area are sufficiently fast and deep to be turbulent.

The nature of a turbulent flow can be characterized by considering that the instantaneous foreward speed (u) at any level y above the bed is the sum of the time-averaged velocity at that level ($\bar{u}$) and a randomly fluctuating turbulent component ($u'$):

$$u = \bar{u} + u' \qquad (3.6)$$

(Note that small $\bar{u}$ and large $\bar{U}$ are not in general the same.) The intensity of the turbulence, as measured by the root mean square of the fluctuations ($\sqrt{\overline{u'^2}}$) as a fraction of u, is greatest a short distance above the bed (Bowden and Howe, 1963; McQuivey and Richardson, 1969; Raichlen, 1967), but goes to zero in the vicinity of the bed.

The presence of a non-moving boundary at the base of the flow produces a resistance that is transmitted upwards throughout the current, and causes an internal shearing stress. The total shear stress ($\tau$) at any given level y is sufficient to balance the down-slope component of mass of the fluid above that level:

$$\tau = \gamma S(h-y) \qquad (3.7a)$$

where $\gamma$ is the specific weight of the fluid, and S is the slope angle, which is considered to be small so that (sin S) can be replaced by S. From this relation it is evident that the total shear stress increases linearly with depth from the surface, and reaches a maximum at the bed ($\tau_o$):

$$\tau_o = \gamma Sh. \qquad (3.7b)$$

In turbulent flow, the shear stress is generated in two ways. The most important mechanism by far is the bulk momentum flux associated with the turbulent velocity fluctuations (Schlichting, 1968, p.527 - 528). An additional

component of the shear stress results from the dynamic viscosity ($\mu$) of the fluid. In most natural flows, the Reynolds number is so high, however, that viscous shear can generally be ignored, and the total shear considered equal to the turbulent shear (Yalin, 1972, p.23). Only in a region very close to the bed where the turbulence decreases in intensity does the viscosity dominate, resulting in what is known as the laminar sublayer (Schlichting, 1968, p.531). The thickness of this sublayer ($\delta$) is an inverse function of a Reynolds number (Yalin, 1972, p.25 - 26), formed using the grain size of the sediment (d) and the shear stress: ($Re_\delta = d\sqrt{\tau_o \rho}/\mu$). Therefore, as the speed of the flow and the shear stress on the bed increases, the thickness of the laminar sublayer shrinks until it is totally submerged in the voids between the sand grains on the bed. Flows such as this, which includes most natural currents, are termed hydraulically rough, because the roughness elements on the bed protrude into the turbulent portion of the flow and have a direct influence on the shape of the time-averaged velocity distribution.

The theoretical derivation of the form of the velocity distribution in a turbulent flow is based on the assumption stated above that the turbulent shear stress is equal to the total shear stress. From this point, the approaches taken by various workers diverge. The most commonly accepted derivation is that of Prandtl who made two important additional assumptions: firstly, that the intensity of the

turbulence as measured by Prandtl's mixing length (l) increases linearly with distance from the bed ($l = \kappa y$; $\kappa$ = the von Kármán constant); and secondly, that the shear stress is constant and equal to the shear stress at the bed ($\tau_o$) as defined in equation (3.7b). (Because of this last assumption, Prandtl's equation for the velocity distribution is commonly referred to as the Law of the Wall.) Both of these assumptions are intended to apply only to a narrow region close to the boundary. From them, Prandtl derived the widely used logarithmic velocity profile equation:

$$\frac{\bar{u}}{u_*} = \frac{1}{\kappa} \ln(y) + B \qquad (3.8)$$

in which $\bar{u}$ is the time-averaged velocity at the level y, $u_*$ is the shear velocity, defined as:

$$u_* = \sqrt{\frac{\tau_o}{\rho}} \qquad (3.9)$$

and B is a constant of integration. The reader is referred to Schlichting (1968, p.554 - 557) for the complete derivation of equation (3.8).

The value of the constant B in (3.8) is dependent on conditions at the base of the flow, and can theoretically be evaluated by setting the turbulent velocity equal to zero at the junction of the turbulent and laminar sublayers. In hydraulically rough flow, this occurs somewhere below the top of the roughness elements, and B is best determined by experimentation. In a classic series of experiments using

sand grains as the roughness, Nikuradse (see Keulegan, 1938, p.713; or Yalin, 1972, p.28) found that the velocity distributions could be closely approximated by the following form of Prandtl's Law of the Wall:

$$\frac{\bar{u}}{u_*} = \frac{1}{\kappa} \ln (y/k_s) + 8.5 \qquad (3.10)$$

where $k_s$ is the grain size of the sand used. Subsequent work has shown that the value of the constant in equation (3.10) is only applicable for a roughness composed of sand grains, with $k_s$ defined as above. If the geometry of the roughness elements is changed, then a new value of the constant must be determined. Therefore, to simplify the problem, the value of 8.5 is frequently accepted as universally constant for open channel flow, regardless of the roughness configuration, and $k_s$ is defined as the size of the sand grains that would produce the same effect on the flow as the real roughness does. For this reason, $k_s$ is called the equivalent sand roughness.

Equations (3.8) and (3.10) have been used extensively in the study of river and tidal currents (Charnock, 1959; Dyer, 1970, 1972; Nece and Smith, 1970; Smith, 1969; Sternberg, 1968, 1970). From these studies and flume experiments, it has been found that the Law of the Wall is an acceptable approximation to the velocity distribution throughout the entire flow depth, despite the theoretical restrictions imposed by the assumptions made by Prandtl. Ludwick (1974) has argued, however, that the logarithmic distribution of

equation (3.8) should not be used, except in the vicinity of the bed. Instead, he advocates the use of an empirical velocity-defect law based on the von Kármán similarity principle (Schlichting, 1968, p.551 - 554) that gives a parabolic velocity distribution. In the present study, the logarithmic velocity distribution has been retained, despite the arguments of Ludwick (1974), in accordance with normal practice (Yalin, 1972, p.30 - 33).

Now that Prandtl's Law of the Wall has been adopted for use in this study, all of the hydraulic parameters necessary for the characterization of the flows can be determined, once an appropriate value is selected for $\kappa$. $\kappa$ is commonly assumed to be a universal constant with a value of 0.4; however, it is also known that the presence of suspended coarse sediment (sand) in the water decreases the value of $\kappa$ (Vanoni, 1953). Without accurate measurements of the amount and type of suspended sediment present though, it is not possible to determine the proper value of $\kappa$. As a result, the usually accepted value of 0.4 is used throughout the calculations.

From this point on, the derivation of the various hydraulic variables depends on the ability to fit the theoretical velocity distribution to the measured profiles, which can be done simply by the use of linear regression. If equation (3.8) is rewritten in a velocity defect form, and rearranged, a more usable equation is obtained:

$$\frac{\bar{u}_1 - \bar{u}_2}{\log(y_1/y_2)} = \frac{2.3\ u_*}{\kappa} \qquad (3.11)$$

In this version of the Law of the Wall, the expression on the left is simply the slope of the straight line relationship that should be found when the velocity is plotted against the log of the height above the bed. When measured velocity profiles are plotted in this fashion, however, (Figures 3.4 and 3.5) there is some scatter about the best-fit regression line. This scatter results from the fact that each data point represents an instantaneous velocity (u), and not a time-averaged value ($\bar{u}$). Turbulent fluctuations can, therefore, be expected to cause any individual reading to deviate from the time-averaged profile and, in fact, the amount of scatter about the regression line should be a measure of the intensity of the turbulence. In Appendix 2, which contains all of the derived hydraulic parameters, the value of TURB (column 7) is the standard deviation about the regression line.

Once the equation of the velocity profile has been determined, all of the parameters listed in Appendix 2 can be calculated using the theory above, plus a few additional relationships. The shear velocity ($u_*$) is derived directly from (3.11) by setting the slope of the regression line equal to $2.3u_*/\kappa$. From $u_*$, the bed shear stress ($\tau_o$) is determined from equation (3.9). The energy slope (S) can then also be

obtained from the definition of $\tau_o$ in (3.7b). From the equation of the regression line itself, the mean velocity of the flow ($\bar{U}$) can be determined either from the relationship

$$\bar{u} = \bar{U}, \quad \text{at } y = 0.368\ h \qquad (3.12)$$

which is derived by integrating the Law of the Wall, or by averaging the velocities at 0.2h and 0.8h in accordance with standard engineering field practice. The latter method has been used in this study. For reference with other studies, the velocity one metre above the bed ($u_{100}$) is also given in Appendix 2. From the mean velocity, the Reynolds number of the flow is obtained from (3.5), and the discharge per unit width (the unit discharge) can be calculated ($q = \bar{U}\ h$). The equivalent sand roughness $k_s$ can be derived from equation (3.10) by applying the relationship given in (3.12). Another measure of the roughness height is provided by determining, from the regression equation, the height above the bed ($z_o$) at which the velocity goes to zero (Briggs and Middleton, 1965, p.8).

Three other parameters that have not yet been defined are included in Appendix 2. They are the stream power ($\omega$), the Darcy-Weisbach friction factor (f), and the Froude number (Fr).

The stream power is defined simply as the product of the mean velocity and the bed shear stress:

$$\omega = \bar{U}\ \tau_o \qquad (3.13)$$

and can be considered as the rate at which the flow does work on a unit area of the bed. As such, the stream power is an important measure of the sediment transport capacity of a current.

The Darcy-Weisbach friction factor was originally defined to express the frictional resistance experienced by flows in pipes (Streeter, 1971, p.283 - 289). The equation defining f can be adapted for open-channel flows as shown by Briggs and Middleton (1965, p.12), giving the following equation from which f can be evaluated:

$$\tau_o = f\rho\,\bar{U}^2/8 \qquad (3.14)$$

Another common resistance factor that is not listed in Appendix 2 is the Chézy C; however, it can be determined directly from f:

$$C = \sqrt{8g/f} \quad . \qquad (3.15)$$

Note that C varies inversely to f.

Finally, the Froude number can be determined from the equation

$$Fr = \bar{U} / \sqrt{gh} \quad . \qquad (3.16)$$

Like the Reynolds number, it is a dimensionless number, that is proportional to a ratio of forces acting on the flow; in this case, the ratio of inertia to the gravitational body force, which is important in determining the behaviour of waves on the surface. For values of the Froude number less than one, surface waves can propagate upstream, and the flow

is considered tranquil; for Froude numbers greater than one, waves cannot move upstream, and the flow is rapid. The Froude number is important in the study of bedforms, because the transition from the lower to upper flow regime is defined by a critical Froude number (Kennedy, 1963).

This completes the introduction the the hydraulic principles that are necessary for a basic understanding of tidal current flow, and for the calculation of the various parameters used in this study. Specific aspects of the relation between the hydraulics and various sedimentological responses will be presented as needed in subsequent chapters. The remainder of this chapter will concentrate on the description of the tidal currents themselves, and their variations in time and space.

## 3.2 Tidal Current Description

### 3.2.1 Turbulence, Profile Shape, and Reliability of the Data

Inspection of the Reynolds numbers tabulated for each profile in Appendix 2 shows that nearly all are in the range of $10^6$ to $10^7$, indicating that the tidal currents should be fully turbulent as stated in the previous section. This point is of importance because the presence of turbulence has a profound effect on the reliability of the calculated hydraulic parameters.

Because of the turbulence, instantaneous velocity measurements would not be expected to fall on the time-averaged velocity distribution, but to be scattered randomly about it (Figures 3.3 and 3.4). The amount of scatter should be determined in part by the intensity of the turbulence, and also by the extent to which the measurement process averaged out the fluctuations. This scatter, expressed as the standard deviation about the regressed logarithmic velocity distribution, is listed in Appendix 2 under the heading TURB. Study of these values indicates that the deviations from the regression line are in the range of 2 to 8 cm/s for all areas. The size of the fluctuations does tend to be less in profiles measured with the current vane over Big Bar, however, which could be due either to real differences in the intensity of the turbulence, or more probably to the slower response capability of the current vane as compared to either the Endeco or Kelvin-Hughes current meters.

An independent measure of the scale of the macro-turbulence was obtained by suspending the Endeco current meter at a fixed depth and taking instantaneous readings of flow speed every five seconds over a 15 to 20 minute period. Only two such sequences of measurements were obtained, both at Buoy 2 on Diamond Bar, during the middle of the morning ebb tide of July 29, 1974. At this site, large megaripples are exposed at low tide. After the removal of any linear trend from the data, the standard deviations were found to be

8.0 cm/s for measurements 0.75 metres above the bed, and 5.7 cm/s, 0.5 metres below the surface. Expressed as a percentage of the time-averaged mean current speed for each sequence, these values become 11.0% and 4.7% respectively. The marked decrease in the intensity of the turbulence away from the bed is in agreement with the results of many workers (Bowden and Howe, 1963; McQuivey and Richardson, 1969, Raichlen, 1967; Raudkivi, 1967) and is due to the fact that turbulence is generated at the bed by the roughness elements (the bedforms) and is dissipated upwards in the flow. The similarity between these values of the turbulence intensity and the standard deviations about the regression lines indicates that the latter is at least a minimum estimate of the scale of the macro-turbulence in most cases.

A comparison between observed current data and the theoretical velocity distributions, as represented by the regression lines (Figures 3.3 and 3.4), indicates that the deviations are usually randomly distributed about the regression line, as would be expected of turbulent fluctuations about a logarithmic profile. The periodicity shown by the deviations in some profiles, such as those at hours 3.33, 8.92 and 10.00 (reference is to hours after high water in all cases) in Figure 3.4, with a vertical dimension of 1 - 2 metres, may be a reflection of macro-turbulence. Some of the profiles, however, suggest the presence of systematic divergence from the logarithmic distribution. Two types are present in

FIGURE 3.3 : Current profiles from Big Bar, Buoy 5 (6/8/73). Included for each profile are the values and standard deviations (in brackets) of the mean speed and shear velocity, plus the turbulence intensity.

| | | | | | | | | | |
|---|---|---|---|---|---|---|---|---|---|
| 0 428 (0 006) | 0 521 (0 018) | 0·610 (0 019) | 0·437 (0 023) | = $\overline{U}$ = | 0·313 (0 Q08) | 0·356 (0 005) | 0 330 (0 006) | 0 181 (0 006) | (M/S) |
| 0 030 (0·003) | 0 055 (0·009) | 0 050 (0·011) | 0 029 (0·018) | = $U_*$ = | 0 022 (0 008) | 0 014 (0 003) | 0 009 (0·003) | 0 007 (0 003) | (M/S) |
| 0 023 | 0·061 | 0·058 | 0·045 | = TURB = | 0·014 | 0·013 | 0 019 | 0 024 | (M/S) |

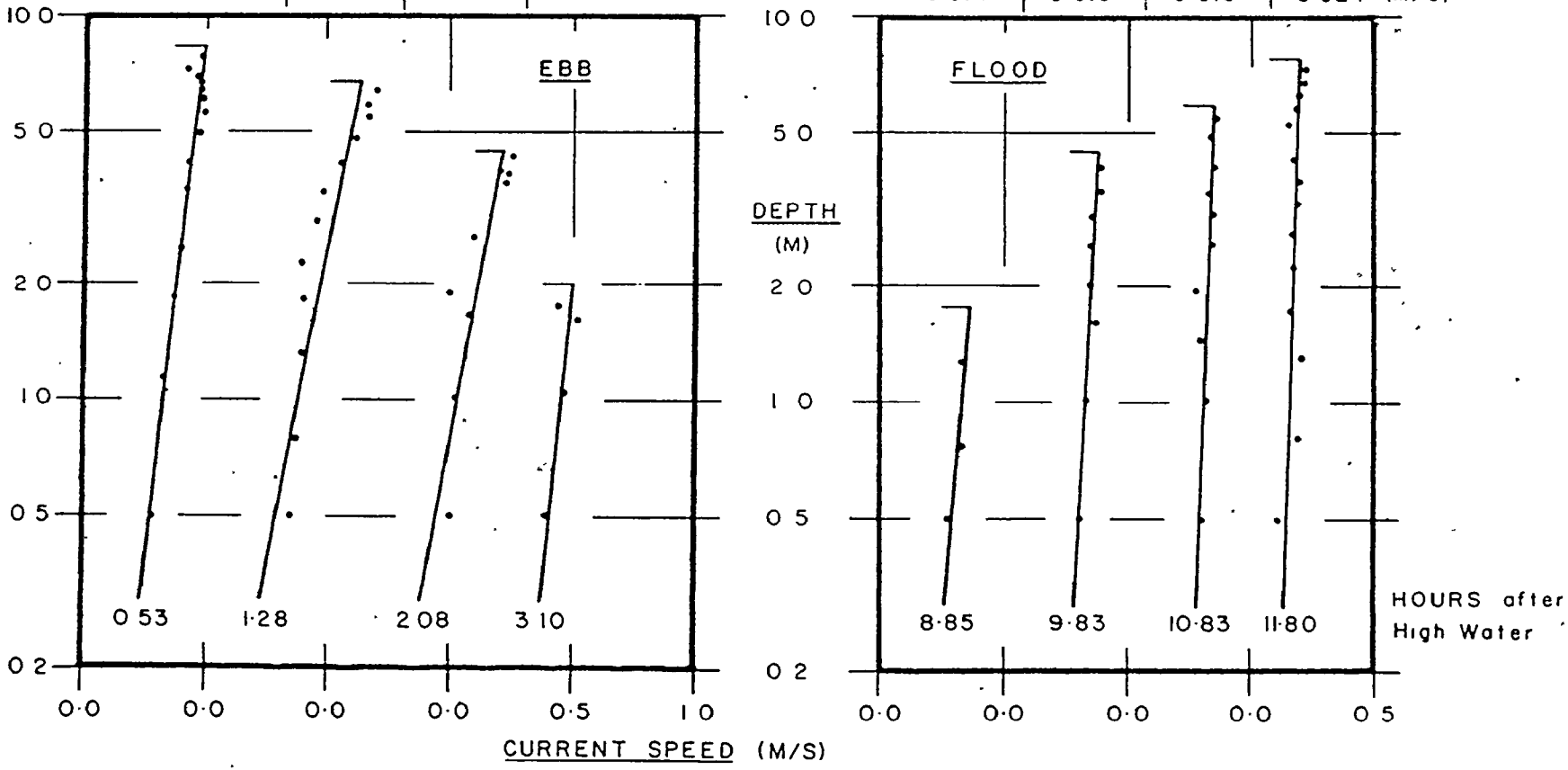

FIGURE 3.4 : Current profiles from the North Channel, Diamond Bar. Included for each profile are the values and standard deviations (in brackets) of the mean speed and shear velocity, plus turbulence intensity. All values have units of metres per second.

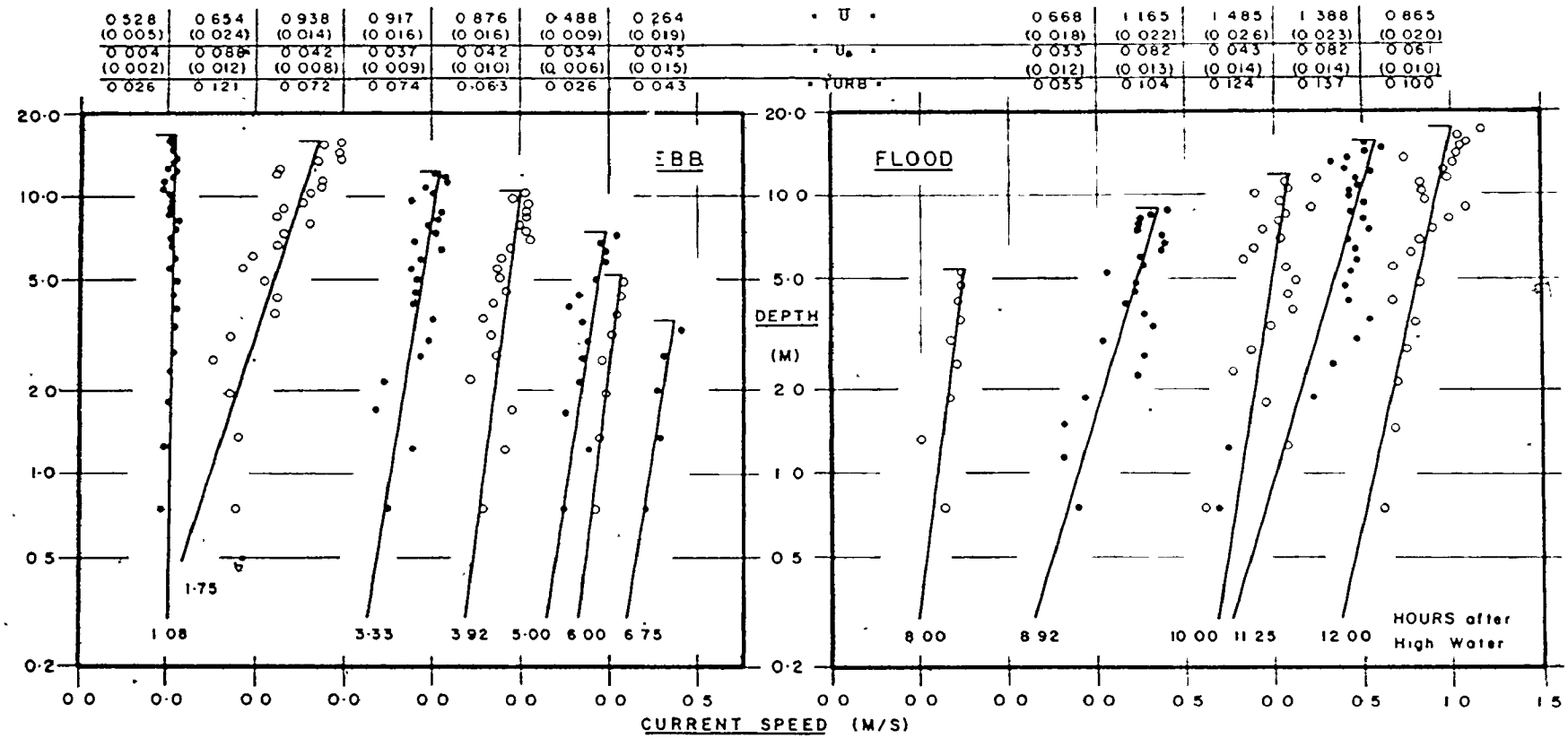
0 528 (0 005) | 0 654 (0 024) | 0 938 (0 014) | 0 917 (0 016) | 0 876 (0 016) | 0 488 (0 009) | 0 264 (0 019) | • Ū •
0 004 (0 002) | 0 088 (0 012) | 0 042 (0 008) | 0 037 (0 009) | 0 042 (0 010) | 0 034 (0 006) | 0 045 (0 015) | • U* •
0 026 | 0 121 | 0 072 | 0 074 | 0 063 | 0 026 | 0 043 | • TURB •
0 668 (0 018) | 1 165 (0 022) | 1 485 (0 026) | 1 388 (0 023) | 0 865 (0 020)
0 033 (0 012) | 0 082 (0 013) | 0 043 (0 014) | 0 082 (0 014) | 0 061 (0 010)
0 055 | 0 104 | 0 124 | 0 137 | 0 100
EBB
FLOOD
20·0
10·0
5·0
2·0
1·0
0·5
0·2
DEPTH (M)
1·75
1 08
3·33
3 92
5·00
6 00
6 75
8 00
8 92
10 00
11 25
12 00
HOURS after High Water
0·0
0·5
1·0
1·5
CURRENT SPEED (M/S)

the figures: the first, with examples at hour 1.28 in Figure 3.3 and hour 1.75 in Figure 3.4, shows higher than expected speeds near the bed and at the surface, and lower speeds at intermediate depths; and the second, illustrated by the profile at hour 11.25 in Figure 3.4, shows the opposite pattern of deviation. The nature and significance of these deviations is under investigation by R. J. Knight (personal communication, 1975).

In spite of the turbulence and possible systematic deviations, the majority of the profiles are closely approximated by a logarithmic velocity distribution. Inspection of the correlation coefficients, which provide a measure of how well the measured profiles conform to the logarithmic model, shows that more than two-thirds of the fitted distributions are significant at more than the 0.95 level, while 85% are significant at more than the 0.75 level. In Appendix 2, non-significant profiles are indicated by a dot if the level of significance is between 0.95 and 0.75, and by two dots if it is less than 0.75. Only 7.4% of the calculated regression lines have a negative slope; that is, the predicted current speed is higher near the bed than at the water surface.

It was noted that, in general, the largest proportion of profiles with negative slopes or non-significant correlation coefficients occurred in shallow water depths near low tide when very few data points are available to define the velocity distribution. It is at this time also when the flow is most

affected by large bedforms that are often present and by the macro-turbulence that they generate. In addition, correlation coefficients tend to be lower at times when waves are present.

The presence of a large amount of scatter in the data will have obvious effects on the reliability of the calculated hydraulic parameters, particularly those derived from the slope of the regression line, namely $u_*$, $\tau_o$, $\omega$, S, f, $k_s$ and $z_o$. As the scatter increases and the correlation coefficient goes to zero, the slope of the regression line also goes to zero, independently of the true values of the parameters listed above. This is evident, for example, from a scrutiny of the values calculated for the flood portion of the tidal cycle at Buoy EP 7 (10/8/74) on East Bar at Economy Point (Figure 3.9): the low values of $u_*$ at hours 10.33, 11.25, and 12.00 are all associated with correlation coefficients of less than 0.05, which indicates that the logarithmic velocity distribution is inappropriate for these profiles. The adjacent higher values of $u_*$ from significant profiles indicate that the low values are not, in fact, a true representation of the flow conditions, but are the result of the large amount of scatter, and should be ignored. By comparison, calculated values of the mean current speed for the same non-significant profiles do not appear to be affected by the scatter, and fall on the trend of decreasing speed as high tide is approached that is shown by the other mean velocities (Figure 3.9).

The reliability of the mean current speed and shear velocity can also be expressed in terms of standard deviations using formulae for the variance of the mean and slope of the regression line that are available in any statistical text. The calculated standard deviations are listed on Figures 3.3 and 3.4 for the profiles shown, and two standard deviation error bars are given for the values plotted in Figures 3.5 through 3.9. Although the standard deviations of both the mean speed and the shear velocity are approximately equal, that of the shear velocity is one to two orders of magnitude larger than that of the mean current speed, when they are expressed as a percentage of the value in question (= the coefficient of variation). It is obvious, therefore, that the values of shear velocity are much less reliable than those of mean current speed, and that trends in the mean current speed can be identified with much greater certainty than can variations in shear velocity, as evidenced by Figures 3.5 to 3.9.

These errors are also passed on to the other parameters derived from the mean speed and shear velocity, so that the further removed one becomes from the original data, the larger is the potential error. As a result, field determinations of parameters such as the stream power, energy slope, Darcy-Weisbach friction factor, and the equivalent sand roughness, must be treated with caution.

When considering the time variations of the various parameters in the next section, the possibility must also be kept in mind that there may be longer-term fluctuations about an average trend than those represented by the turbulence described above. Such larger-scale variations would be a result of macro-turbulence that had a period of several minutes, and a vertical dimension comparable to the flow depth.

### 3.2.2 Variations over a Tidal Cycle

Tidal currents are characterized by their time variability in response to many astronomically determined periodicities, the most important of which in the study area is the 12.42 hour semi-diurnal tidal cycle. The associated variations in i) water depth; ii) current direction; iii) current speed; and iv) shear velocity are shown in Figures 3.5 to 3.9 for representative stations at Big Bar, Diamond Bar, and the Economy Point bars. For the location of all current monitoring stations, see Figure 3.1. These examples could be replaced by any number of other cases without affecting the validity of the observations and conclusions presented here. No examples from Selmah Bar have been used in this section because R. J. Knight is in the process of analyzing that data in detail, and any discussion of it here would be redundant.

(i) Water Depth: The most striking feature of the plot of water depth versus time is the rapid rate of change of the water level, as would be expected from the high tidal range

in the area. At all five stations, the rate of rise or fall for the entire flood or ebb phase of the tidal cycle averages in excess of 2 m/hour, and reaches nearly 5 m/hour during the early portion of the flood at Buoy 3 on Diamond Bar (Figure 3.6). Obviously, these rates will change with variations in the tidal range. (On Figures 3.5 to 3.9, and elsewhere in this thesis, the tidal range is expressed by the dimensionless "tidal coefficient" (Tr) which is the ratio of the predicted tidal range for Burntcoat Head on a given day to the range of the large tide in the area, given as 16.1 metres in section 2.2.3.)

Two other important features can be seen in these plots: firstly, that the rate of water level rise on the flooding tide is greater than the rate of fall of the ebb; and secondly, that the duration of the flood is shorter than that of the ebb. Both of these characteristics are a manifestation of the distortion and resulting asymmetry of the tidal wave in the Minas Basin and Cobequid Bay. A similar shortening of the flood tide and lengthening of the ebb is noted in other shallow estuaries (see, for example, Wright, Coleman and Thom, 1973), and is explained by the fact that water depths under the crest of the tidal wave are significantly greater than those under the trough, so that the crest propagates more quickly than the trough, and tends to overtake it (Maxwell, 1966; Wright, Coleman and Thom, 1973).

Because the tide in the area is basically a standing wave, high water is nearly synchronous throughout the Minas Basin and Cobequid Bay, and generally occurs no more than 15 minutes after the predicted time at Burntcoat Head. Some of the data from Selmah Bar, collected at spring tide, shows that high tide can be delayed by up to approximately 30 minutes at the east end of Cobequid Bay. Although observations of the time of low tide are not abundant, there is an indication that the turn of the tide becomes progressively later as one moves eastward. At Big Bar and Economy Point in the Minas Basin, the turn occurs approximately 15 to 30 minutes after the time expected for a symmetrical tidal wave. In the channel north of Diamond Bar, in the central part of Cobequid Bay, the turn is delayed by 1.25 hours, and at Selmah Bar, the turn at low tide is 1.5 hours or more late. These values reflect an increasing asymmetry of the tidal wave as it travels up the Minas Basin and Cobequid Bay, similar to the behaviour documented by Wright, Coleman and Thom (1973) for the macrotidal Ord River in Australia.

The data presented above are consistent with those given by Swift and McMullen (1968) which show that the duration of the ebb in the channels is approximately one hour longer than the flood in the central part of Cobequid Bay. Swift and McMullen (1968) also indicate the existence of a low-water channelized phase in Cobequid Bay. In the major channels, the water depth can remain essentially constant for a period

of up to one and one-half hours at low tide, or possibly longer as one goes eastward. The flow during this time is controlled by the ebb discharge and the channel characteristics, and is independent of the tide in the outer part of the bay.

(ii) Current Direction: One crucial aspect of tidal current flow is the approximately 180° reversal in the flow direction between the ebb and flood portions of the tidal cycle, as shown by the sequential vectors of surface currents in Figure 3.5, and bottom currents (0.75 metres above the bed) in Figures 3.6 to 3.9. Inspection of these diagrams shows that the tidal currents in the study area are rectilinear, and not rotary in the sense used for ocean tides. Sequential variations in direction are evident in most areas, particularly during the one or two hour period just before emergence and after submergence, but these are due to the influence of the bar topography. Near high tide, when the water depth is greatest, the flow is almost independent of the bar topography; however, as the crest of the bar becomes emergent, the flow is diverted more and more, until it is directed down the slope away from the bar crest. The reverse pattern occurs on the incoming flood tide.

The directional variation at Buoy 3 on Diamond Bar (Figure 3.6) is an exception to the general pattern described above, and shows the opposite sense of rotation relative to the topography. This may be due to the location of Buoy 3 on the outside of a bend in the channel.

It has traditionally been assumed (Houbolt, 1968; Off, 1963) that elongate tidal sand bodies form in response to helical flow, in which there is a convergence of bottom currents toward the bar crest, and a divergence of surface currents away from the crest. This causes the scouring of sediment from the channels and deposition on the bar, thereby maintaining the bar as a positive topographic entity. In order to ascertain the importance of helical flow in the present study area, all profiles from the sides of Diamond Bar in more than 3.5 metres of water were analyzed to see if there were directional differences between the surface and bottom currents consistent with the presence of such secondary flows. Out of 216 profiles, only 97 or 45% show the proper directional swing from the top to the bottom, and these show no preferred time of occurrence in the tidal cycle. Because more than half of the profiles display a directional variation that is opposite to that expected of a helical flow pattern, the implication is that helical flow is not of particular significance in the study area.

Plots of the vector means of bottom currents for each of the study bars in part A of Figures 3.13 and 3.15 to 3.17 also suggest that secondary currents are not a consistent phenomena, because these vector means are oriented downslope on one side of the crest during both the ebb and flood phases of the tide. If helical flow were present, the bottom currents should be directed up the slope on both sides of the bar crest

at the same time. The conclusion must be that some mechanism other than helical flow is primarily responsible for the formation and maintenance of the sand bars.

(iii) Current Speed: The variation of current speed over a tidal cycle is complex, and differs from location to location, depending on the influence of a number of factors, but certain generalities can be observed.

Beginning at high water when the flow momentarily ceases, the current speed increases steadily at a rate that appears to be determined by the distance of the station from the Minas Passage. A comparison of Figure 3.5 with Figures 3.6 and 3.7 indicates that stations further east experience a less rapid increase in current speed than stations to the west. Within the first one to two hours, the current achieves a speed that is then maintained at an almost constant value for a period often exceeding two hours. Buoy 3, Diamond Bar (Figure 3.6) is a good example. In the latter stages of the ebb, most stations on the lower parts of the bars experience a sudden increase in current speed, often following a period of declining speeds (Figures 3.5 and 3.7). This feature can generally be related to the exposure of the crest of the bar, and the consequent confinement of the flow to a smaller cross-sectional area. This channelization of the flow commonly results in the highest current speeds of the ebb occurring closer to low tide than to high tide.

The ebb tide at Economy Point (Figures 3.8 and 3.9) is clearly different from the pattern described above, particularly with respect to the sudden drop in speed at approximately 1.25 hours after high water. This is coincident with the emergence of extensive bedrock ledges to the east of Economy Point (Figure 2.16), which must deflect the ebb currents to the south of the sand bar complex.

Following the very brief still-stand associated with the turn of the tide in the channels, or immediately after submergence, there is a very rapid increase in current speed to values that at many stations are the highest during the flood. Throughout the middle of the flood tide, the speed of the flow again tends to remain essentially constant as it did during the ebb, until approximately 1.5 - 2 hours before high water when the speed begins to decrease at an almost linear rate toward zero at the next high tide.

The slow increase in current speed at the beginning of the flood at Buoy 3, Diamond Bar (Figure 3.6) is an exception to the general pattern given above. It may be that this behaviour is due to the hypsometry of the area being flooded through this channel. The bathymetric map of Diamond Bar (Figure 2.15) and air photos reveal that this channel has steep lower margins along much of its length, but opens into a broad, flat area to the south-east of Diamond Bar. As long as the rising tide is confined to the steep-sided portion of the channel, the flood currents will be low because a small

volume of water is needed to raise the water surface by a given amount. Once the tide spills out onto the broad flat area at the head of the channel, however, the flow through the channel and the speed will increase because the volume of water now required to raise the water surface the same amount has increased markedly. Additional data are required to confirm this hypothesis.

Further examination of Figures 3.5 to 3.9 shows that the ebb and flood currents differ with regard to the maximum speed attained, and/or the duration of the peak speeds. Differences such as these between the ebb and flood have been termed a time-velocity asymmetry by Klein (1970), and result in the dominance of one phase of the tide at the site. A clear distinction must be made between the definition of time-velocity asymmetry used here after Klein (1970), pertaining to velocity differences between the flood and ebb, and that used by Postma (1967), referring to the pattern of velocity variations within a single ebb or flood tide. For reasons of convenience, the definition of Klein (1970) will be retained in this thesis.

Because the time-velocity asymmetry is a function of both the absolute values of the currents and their duration, the time-averaged mean current speed for the ebb and flood can be used to describe the nature of the asymmetry. (The time-averaged current speed is obtained by integrating the area under the plot of speed versus time for one phase of the

tidal cycle, and dividing by the flow duration.) The values calculated in this manner are shown in Figures 3.5 to 3.9 by the horizontal lines and the adjacent numerical values. Turning to the examples, we find that Big Bar, Buoy 5 (Figure 3.5) and Diamond Bar, Buoy 3 (Figure 3.6) have higher current speeds during the ebb than during the flood, despite the fact that the ebb is of longer duration than the flood. Time-averaged flood speeds are greater at the other three stations, although the difference between the flood and ebb is not great at either station on Economy Point. It is of interest to note that the maximum current speeds in general show the same asymmetry as the time-averaged values, although there are exceptions as illustrated by Buoys EP 3 and EP 7 (Figures 3.8 and 3.9) at Economy Point.

As a consequence of the above asymmetries in the time-averaged current speed, one finds corresponding differences in the unit discharges past any given station during the ebb and flood. These discharges are given under the plot of mean current speed versus time for each example, and one can see that the difference is appreciable in every case. Buoy EP 7 (Figure 3.9) is the closest to showing an equality between the ebb and flood discharges, but the difference still amounts to 12% of the larger (flood) discharge. The greatest asymmetry occurs at Buoy 5 on Diamond Bar (Figure 3.7), where the ebb discharge is 31% less than the flood discharge.

It must be stressed that the asymmetries between the ebb and flood portions of the tidal cycles given in the examples are not simply the result of different tidal ranges for each half of the tidal cycle. Comparison of the tidal coefficients with the asymmetries shown indicates that in three of the five examples, the tidal range is actually less for that part of the tidal cycle with the greater discharge and time-averaged current speed. This indicates that there are real differences between the flood and ebb that are independent of the tidal range and are, therefore, the result of some other external factor. Further discussion of this is deferred until Section 3.2.5, after the presentation of the areal distributions of the currents. Time-velocity asymmetries have been noted by other authors (Boothroyd and Hubbard, 1975; Klein, 1970; Ludwick, 1974; Smith, 1969; Swift and McMullen, 1968), so that the results reported here are not unique.

(iv) Shear Velocity: Due to the large possible error associated with every individual shear velocity, it is difficult to define with any certainty the time variation of shear velocity at any station. In Figures 3.5 through 3.9, smooth curves have been drawn arbitrarily to show the major features of the variations. The curves, though not fitted by any objective criterion, do fall within two standard deviations of each point, with the exception of a few values derived from profiles with non-significant correlation coefficients.

Inspection of the time-variation patterns shows that the shear velocity follows that same general trend as the mean current speed. A closer look reveals that for the ebb portion of the tidal cycle, three of the five examples show some evidence of a bimodal distribution in time of high shear velocities, one peak early in the ebb, often during the second hour, and the other 0.5 - 1.5 hours before emergence. This is shown most clearly at Diamond Bar, Buoy 5 (Figure 3.7). By contrast, the time distribution of flood shear velocities is unimodal, with the peak coinciding approximately with the maximum flood current speeds, early in the flood tide.

These distributions of $u_*$ can be explained in more actualistic terms by a consideration of the fact that:

$$u_* = \sqrt{g\ h\ S} \qquad (3.17)$$

which is obtained by the combination of equations (3.7b) and (3.9) and the elimination of $\tau_o$. Inspection of the water depths and calculated energy slopes in Appendix 2 shows that both vary within a single ebb or flood tide: the depth changes during the measurement period by approximately an order of magnitude, from 1 to 10 metres, while the slope varies by two orders of magnitude in many instances. In addition, a comparison of water depth and $u_*$ in Figures 3.5 to 3.9 shows that $u_*$ commonly varies inversely to the depth, which implies that the energy slope, and by extension, the water surface slope (assuming that the non-uniformity of the flow is not too

great), is the primary factor controlling the distribution of $u_*$ through time in the tidal environment.

Examination of the calculated slopes indicates that there is a recurring pattern of variation that mimics the changes in $u_*$. Beginning at high tide, the slope increases gradually from zero with the onset of the ebb, and attains inclinations generally in the range of 1 to 10 x $10^{-5}$. These values may be maintained during the middle part of the ebb, or more commonly, there is a decrease in the slope at this time. Late in the ebb as the depths lessen and the relative roughness increases, the calculated slopes increase again, at the same time as the flood becomes more channelized between the bar crests. On the flood, the initial innundation is usually accompanied by steep slopes that are generally among the highest of the entire flood tide. After this, the calculated energy slopes decrease irregularly to zero at high tide.

Asymmetries in shear velocities between the ebb and flood can be identified in the same manner as in the case of mean current speeds. The time averages shown in Figures 3.5 to 3.9 have been calculated using the original data values, rather than the interpolated smooth curve. Certain points obtained from profiles with near-zero correlation coefficients were eliminated from the calculations. Comparing the ebb and flood time averages, one can see that Diamond Bar, Buoy 5 (Figure 3.7) and Economy Point, Buoy EP 3 (Figure 3.8)

FIGURE 3.5 : Hydraulic data for Big Bar, Buoy 5 (6/8/73). E and S give times of emergence and submergence of the bar crest. Thin vertical lines are two standard deviation error bars. Horizontal lines and associated numbers are the time averages. Current indicators show the direction toward which the current flowed. Tr = tidal coefficient. q = unit discharge.

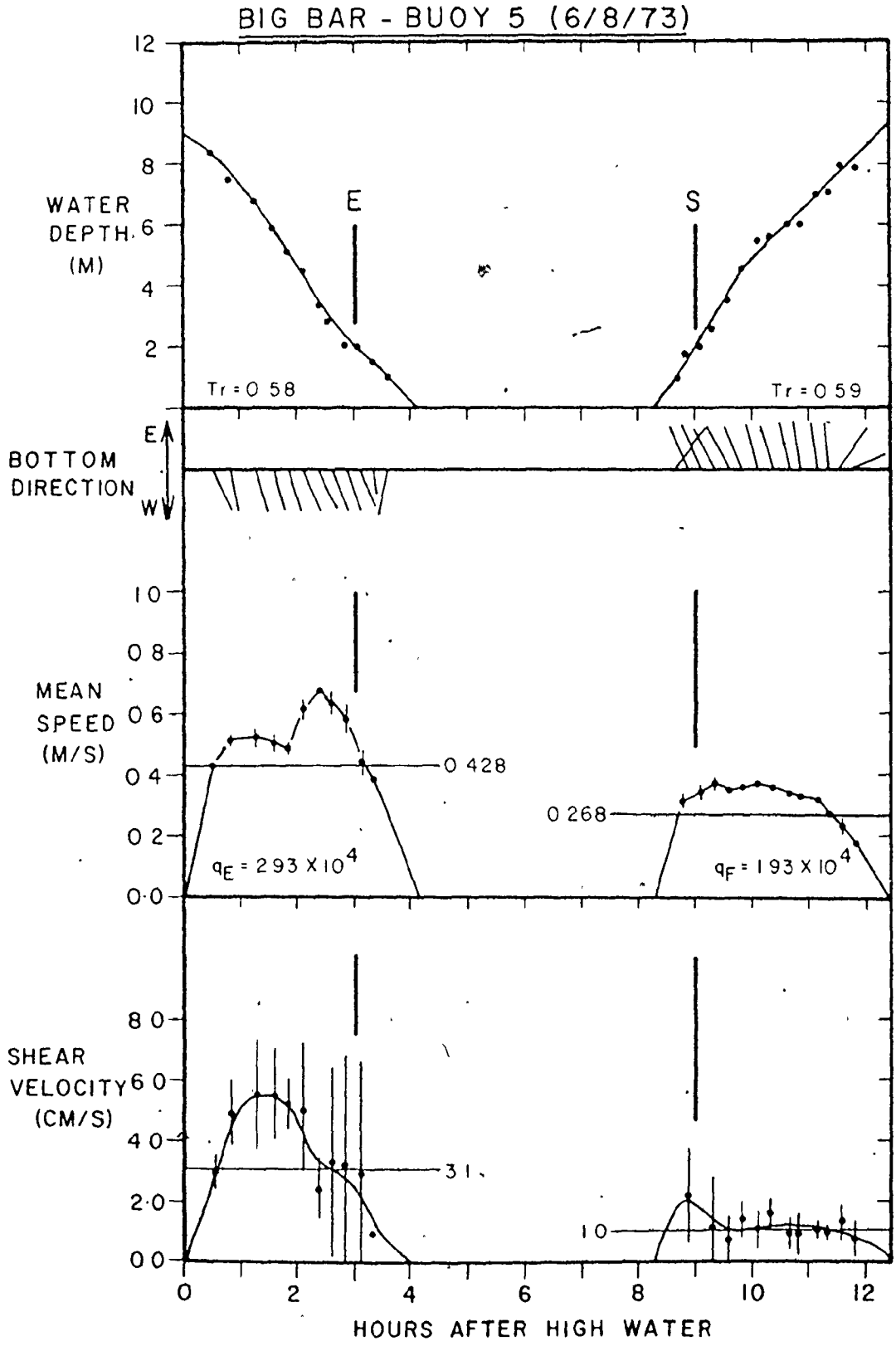
BIG BAR - BUOY 5 (6/8/73)
WATER DEPTH (M)
12
10
8
6
4
2
E
S
Tr = 0 58
Tr = 0 59
BOTTOM DIRECTION
E
W
MEAN SPEED (M/S)
1 0
0 8
0 6
0 4
0 2
0·0
0 428
0 268
$q_E = 2.93 \times 10^4$
$q_F = 1.93 \times 10^4$
SHEAR VELOCITY (CM/S)
8 0
6 0
4 0
2·0
0 0
3 1
1 0
0
2
4
6
8
10
12
HOURS AFTER HIGH WATER

FIGURE 3.6 : Hydraulic data for Diamond Bar, Buoy 3 (6/7/74). See Figure 3.5 for further explanation.

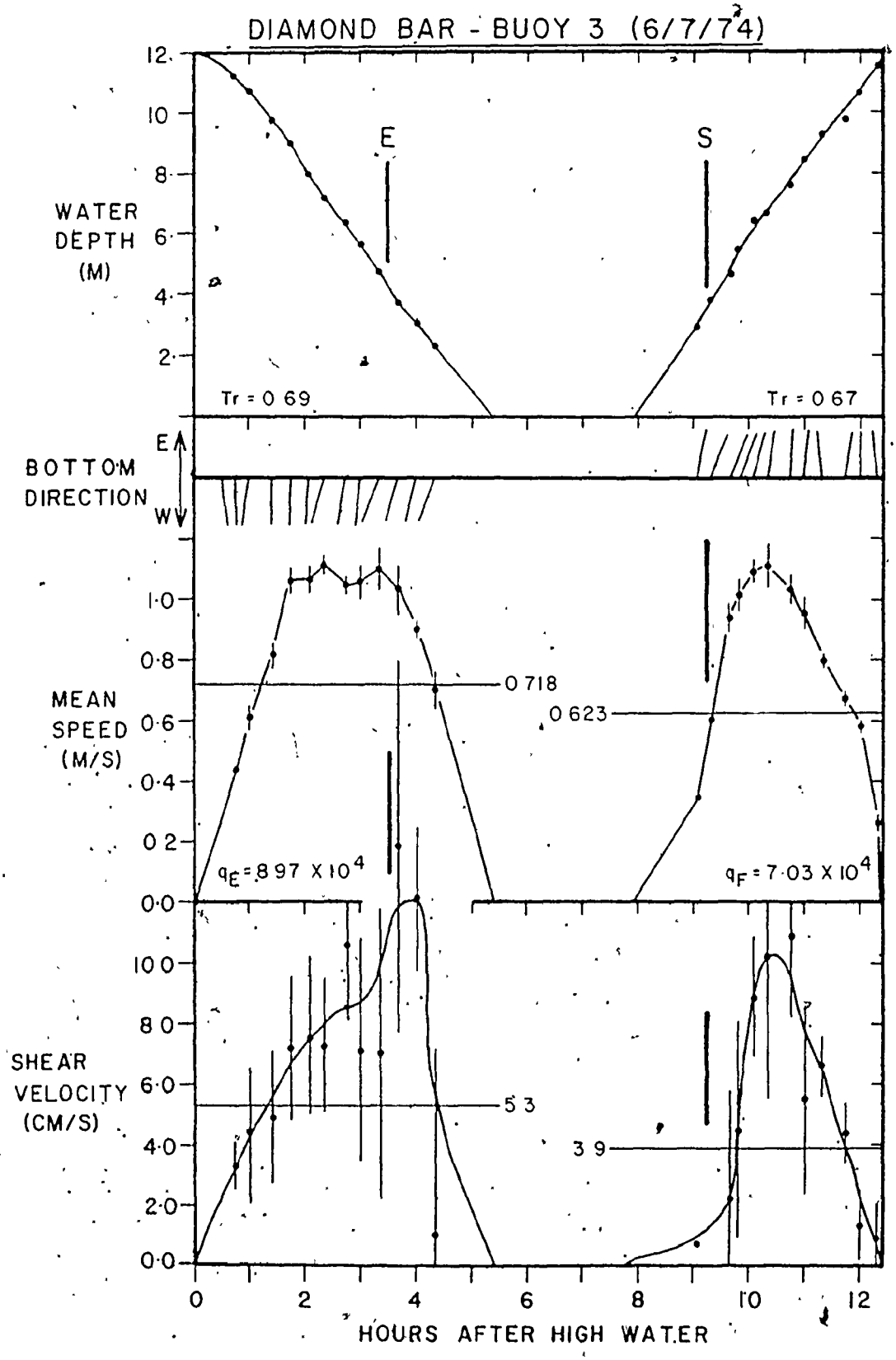
DIAMOND BAR - BUOY 3 (6/7/74)
WATER DEPTH (M)
E
S
Tr = 0 69
Tr = 0 67
BOTTOM DIRECTION
E
W
MEAN SPEED (M/S)
0 718
0 623
$q_E = 8.97 \times 10^4$
$q_F = 7.03 \times 10^4$
SHEAR VELOCITY (CM/S)
5 3
3 9
HOURS AFTER HIGH WATER

FIGURE 3.7 : Hydraulic data for Diamond Bar, Buoy 5 (9/7/74). See Figure 3.5 for further explanation.

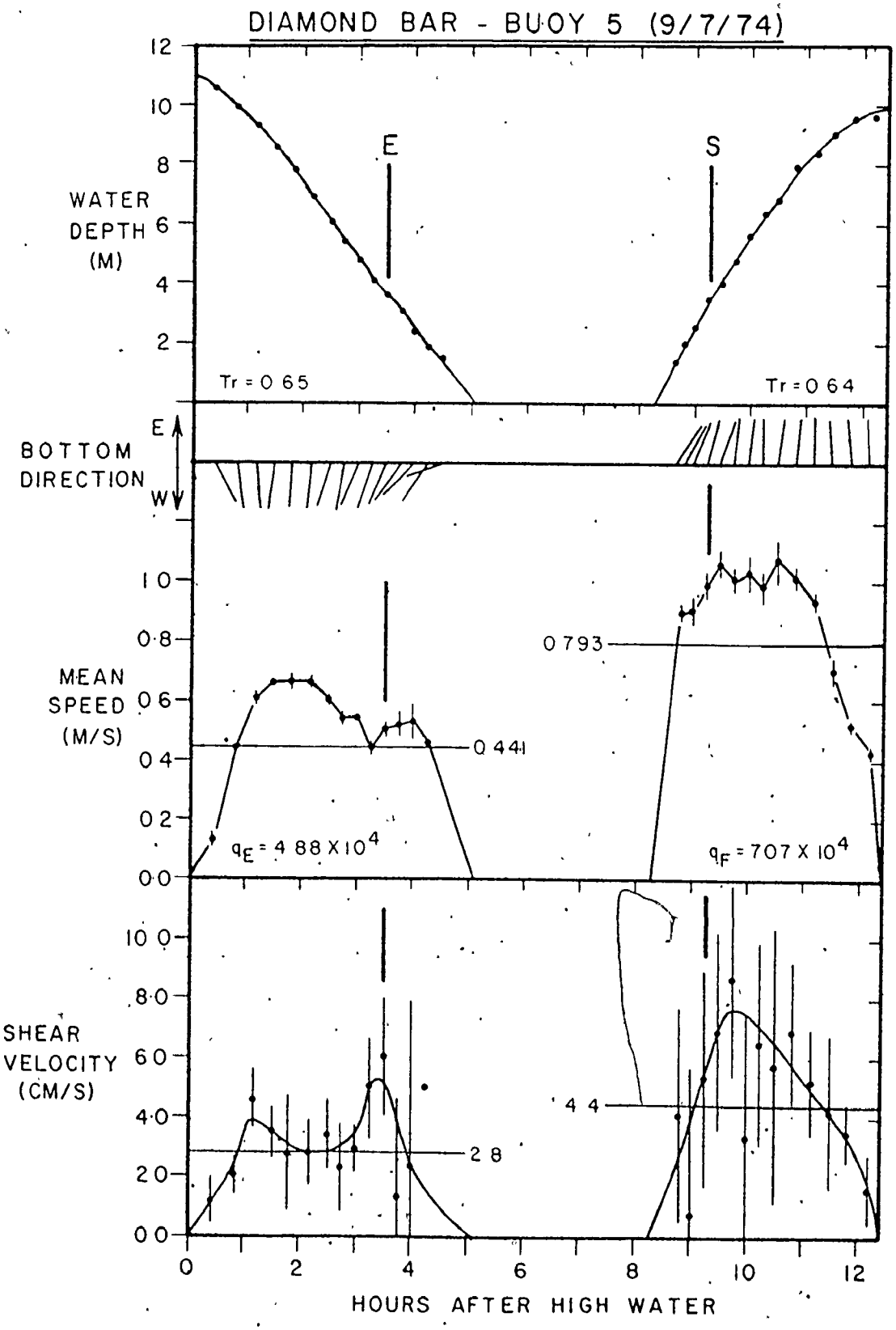
DIAMOND BAR - BUOY 5 (9/7/74)
WATER DEPTH (M)
12
10
8
6
4
2
E
S
Tr = 0 65
Tr = 0 64
BOTTOM DIRECTION
E
W
MEAN SPEED (M/S)
1 0
0·8
0 6
0 4
0 2
0 0
0 441
0 793
$q_E = 4\ 88 \times 10^4$
$q_F = 707 \times 10^4$
SHEAR VELOCITY (CM/S)
10 0
8·0
6 0
4·0
2 0
0 0
2 8
4 4
0
2
4
6
8
10
12
HOURS AFTER HIGH WATER

FIGURE 3.8 : Hydraulic data for Economy Point, Buoy EP 3 (21/8/74). See Figure 3.5 for further explanation. First E and second S refer to rock ledges east of Economy Point, while the others refer to the crest of Centre Bar.

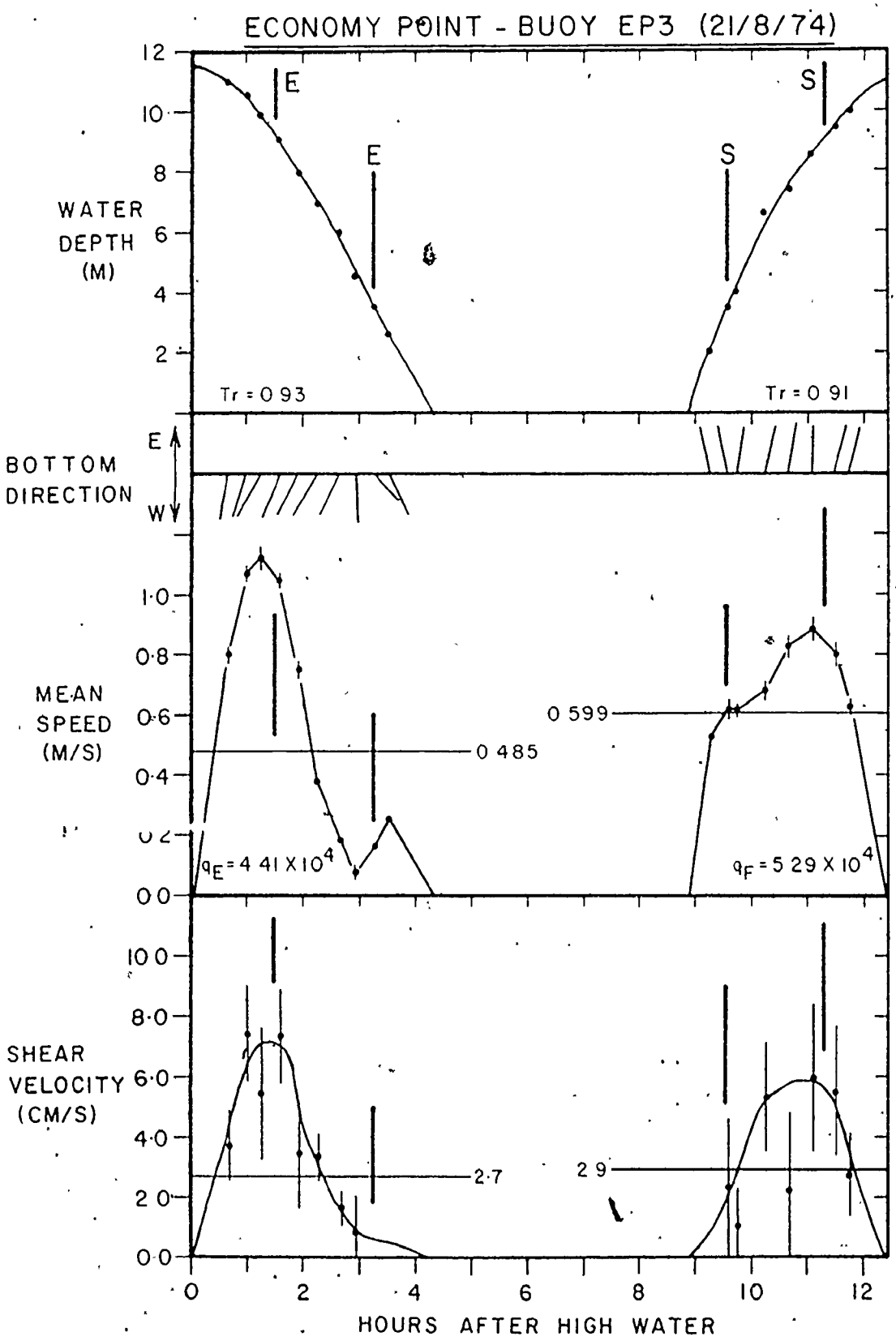
ECONOMY POINT - BUOY EP3 (21/8/74)
WATER DEPTH (M)
12
10
8
6
4
2
E
E
S
S
Tr = 0 93
Tr = 0 91
BOTTOM DIRECTION
E
W
MEAN SPEED (M/S)
1·0
0·8
0·6
0·4
0 485
0 599
$q_E = 4\ 41 \times 10^{-4}$
$q_F = 5\ 29 \times 10^{-4}$
SHEAR VELOCITY (CM/S)
10 0
8·0
6·0
4·0
2 0
0 0
2·7
2 9
0
2
4
6
8
10
12
HOURS AFTER HIGH WATER

FIGURE 3.9 : Hydraulic data for Economy Point, Buoy EP 7 ( 10/8/74). See Figures 3.5 and 3.8 for further explanation. Second E and first S refer to crest of East Bar.

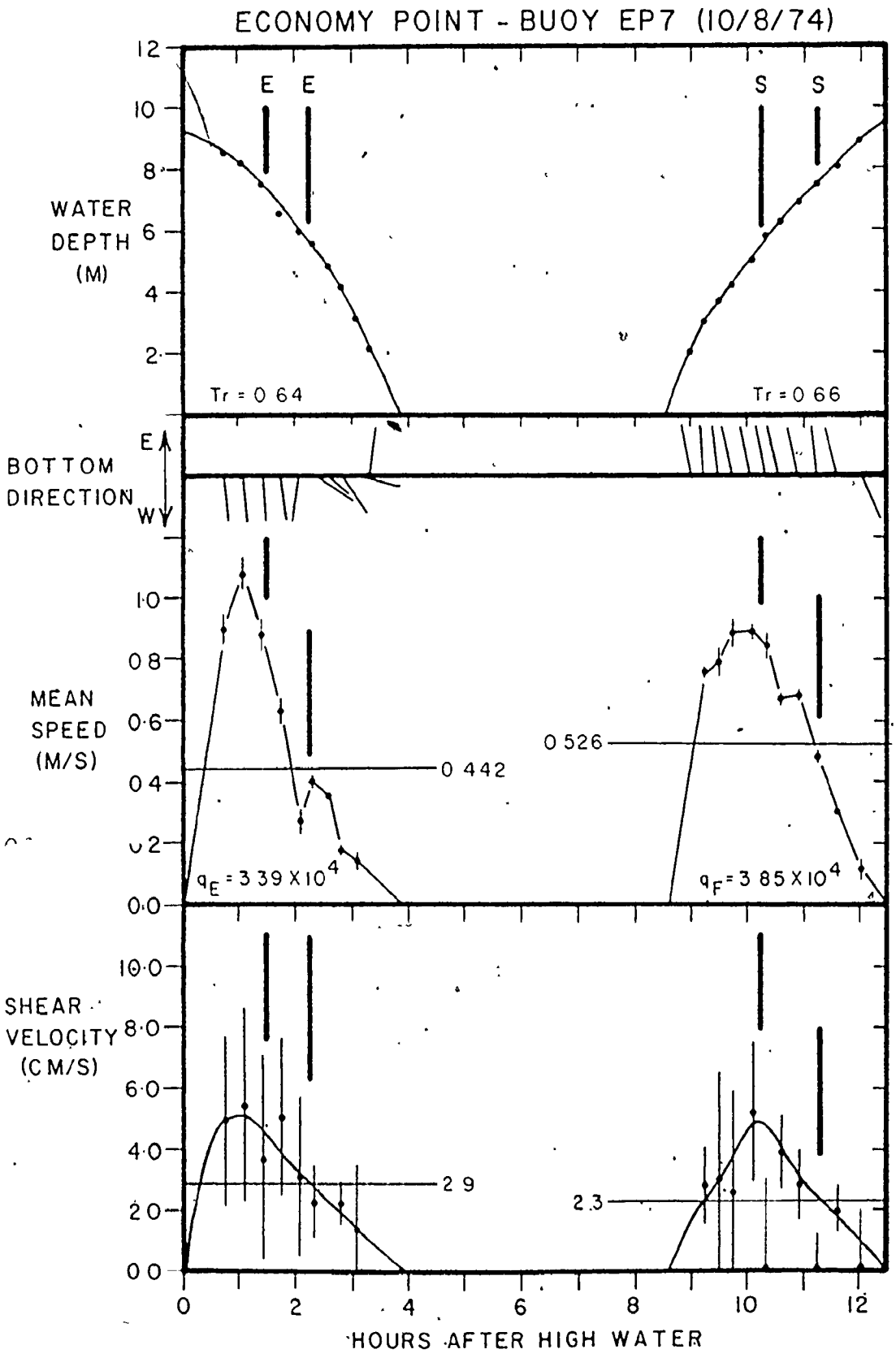
ECONOMY POINT - BUOY EP7 (10/8/74)
WATER DEPTH (M)
E E
S S
Tr = 0 64
Tr = 0 66
BOTTOM DIRECTION
E
W
MEAN SPEED (M/S)
0 442
0 526
$q_E = 3\,39 \times 10^4$
$q_F = 3\,85 \times 10^4$
SHEAR VELOCITY (CM/S)
2 9
2 3
HOURS AFTER HIGH WATER

experience higher shear velocities during the flood than during the ebb, while the remaining three stations show the opposite (ebb) asymmetry. In all cases, except Economy Point, Buoy EP 7 (Figure 3.9), these asymmetries have the same sense as those derived from the time-averaged mean current speeds.

One further feature of the tidal currents that will be considered briefly here is the time variability of the equivalent sand roughness ($k_s$). Figure 3.10 shows the values of $k_s$ for two of the stations discussed previously: Big Bar, Buoy 5 (Figure 3.5) and Diamond Bar, Buoy 5 (Figure 3.7). At both stations, for both the ebb and flood, the data appear to suggest the presence of two peaks in the distribution of $k_s$, one early and the other late in each half of the tidal cycle. The confidence that can be placed in this apparent pattern is limited by the error that is associated with the values, which in turn is related to the errors present in the mean current speeds and shear velocities, from which $k_s$ is derived as described in Section 3.1.3.

The behaviour of the bedforms (to be discussed more fully in Section 4.2.2) appears to be related, at least in part, to the observed pattern of $k_s$ values. When the tide has just turned, either at the start of the ebb or flood, it encounters bedforms which were produced by flow in the opposite direction. These bedforms are now out of equilibrium, and may be responsible for the initial peak of $k_s$ values early in the flood and ebb. During the middle portion of the ebb

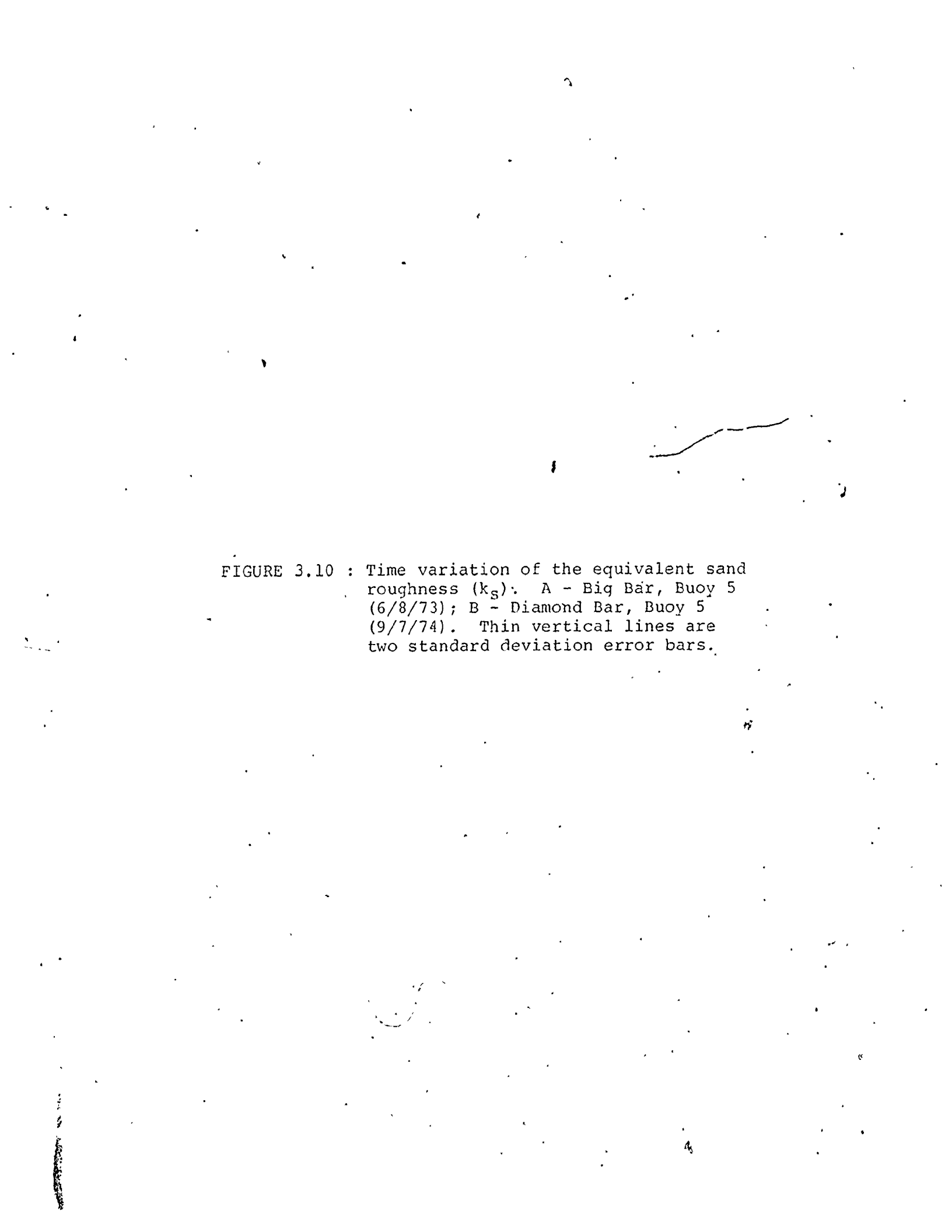

FIGURE 3.10 : Time variation of the equivalent sand roughness ($k_s$). A - Big Bar, Buoy 5 (6/8/73); B - Diamond Bar, Buoy 5 (9/7/74). Thin vertical lines are two standard deviation error bars.

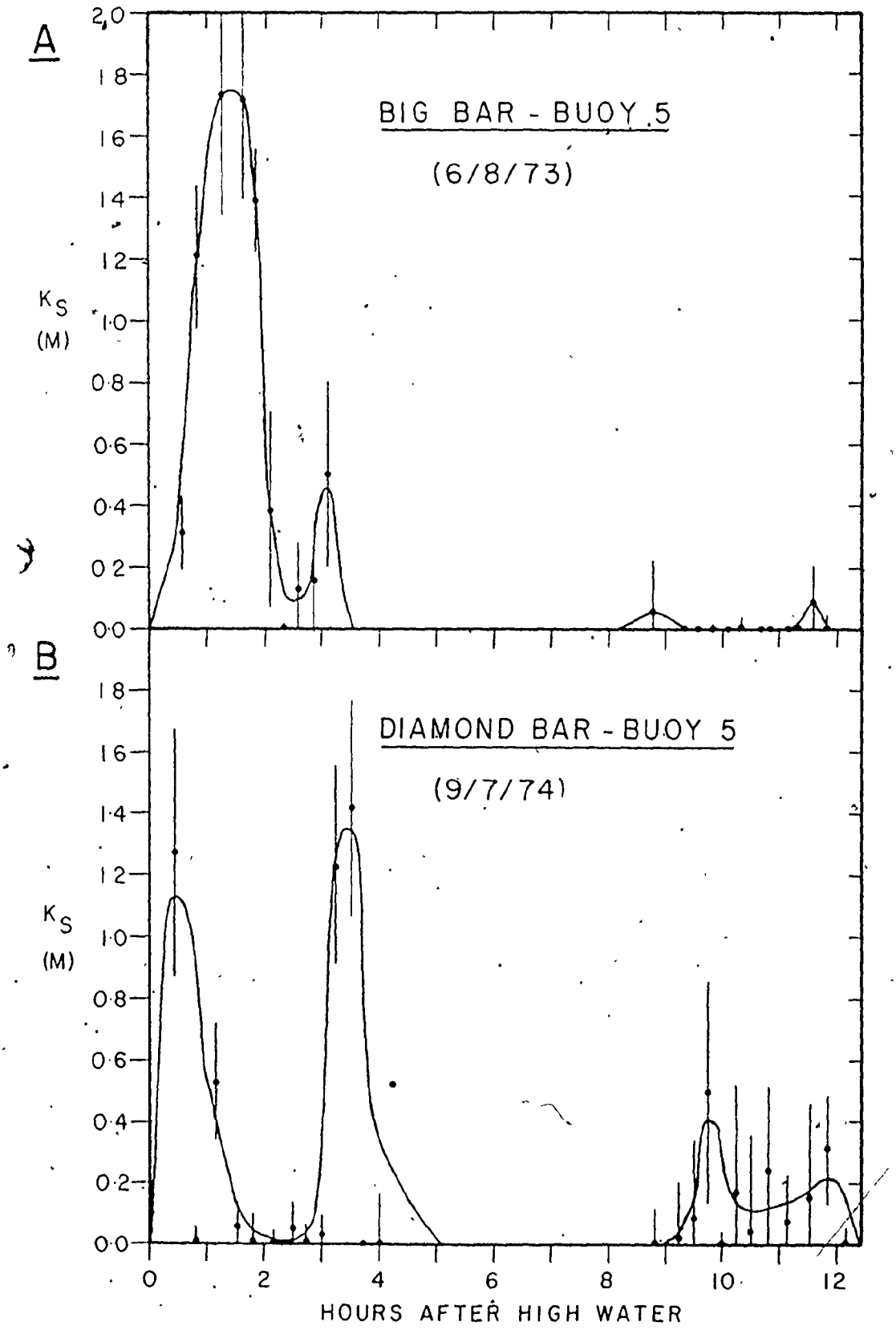
A
BIG BAR - BUOY 5
(6/8/73)
$K_S$ (M)
2.0
1.8
1.6
1.4
1.2
1.0
0.8
0.6
0.4
0.2
0.0
B
DIAMOND BAR - BUOY 5
(9/7/74)
$K_S$ (M)
1.8
1.6
1.4
1.2
1.0
0.8
0.6
0.4
0.2
0.0
0
2
4
6
8
10
12
HOURS AFTER HIGH WATER

and flood, when the current velocities are high, the bedforms should gradually reverse and tend toward equilibrium with the flow. It is at this time when the values of $k_s$ drop considerably. High $k_s$ values are again experienced late in each phase of the tide, when the water depth is either shallow (low tide), or deep (just before high tide). The falling current speeds at these times reduce the ability of the bedforms to adjust to changed conditions, and the bedforms may again be expected to depart progressively from any near-equilibrium state that may have been achieved earlier, as the conditions continue to change. It appears in general, therefore, that the times when the bedforms are most likely to be out of equilibrium are the times when the calculated $k_s$ values are at a maximum.

One particular feature of note which this simplistic argument cannot explain is the significantly higher values of $k_s$ experienced on the ebb as compared to the flood at both buoys. Ludwick (1975a) has noted a similar phenomenon in the entrance of Chesapeake Bay, and ascribes it to stronger ebb than flood currents. Such an explanation does not hold universally, because the currents at Buoy 5 on Diamond Bar (Figure 3.7) are flood-dominated. Much more work is obviously necessary before the complex interrelationships of the hydraulic variables are completely understood in the tidal environment.

### 3.2.3 Effect of Tidal Range

The difference in tidal range between neap and spring tide, which can reach 6.5 metres or about 40% of the large range, produces a large increase in the discharge at spring tide, and can also be expected to produce an increase in the time-averaged current speed and shear velocity. Other workers have previously noted such relationships for both the mean speeds (Ludwick, 1974) and the maximum speeds (Allen et al, 1969). Plots of the time-averaged speed and shear velocity against the tidal coefficient for Big Bar (Figure 3.11) and Diamond Bar (Figure 3.12) data, show that both parameters do increase at the majority of stations as the tidal range increases, despite a disturbing number of cases in which the opposite trend is seen. Much of this scatter is believed to result primarily from errors associated with the determination of the time-averaged quantities, rather than being a true reflection of the tidal current flow behaviour. Each possible source of error will be considered briefly because the time averages form an important part of subsequent analyses.

The first source of potential error which affects all of the time averages arises from the error that is associated with each individual mean current speed or shear velocity. This error results primarily from the effect of turbulence as discussed in Section 3.2.1, and the greater the possible error associated with each value, the greater will be the potential error in the time average. This problem becomes particularly

FIGURE 3.11 : Variation of time-averaged hydraulic parameters with the tidal coefficient on Big Bar. A - mean speed; B - shear velocity.

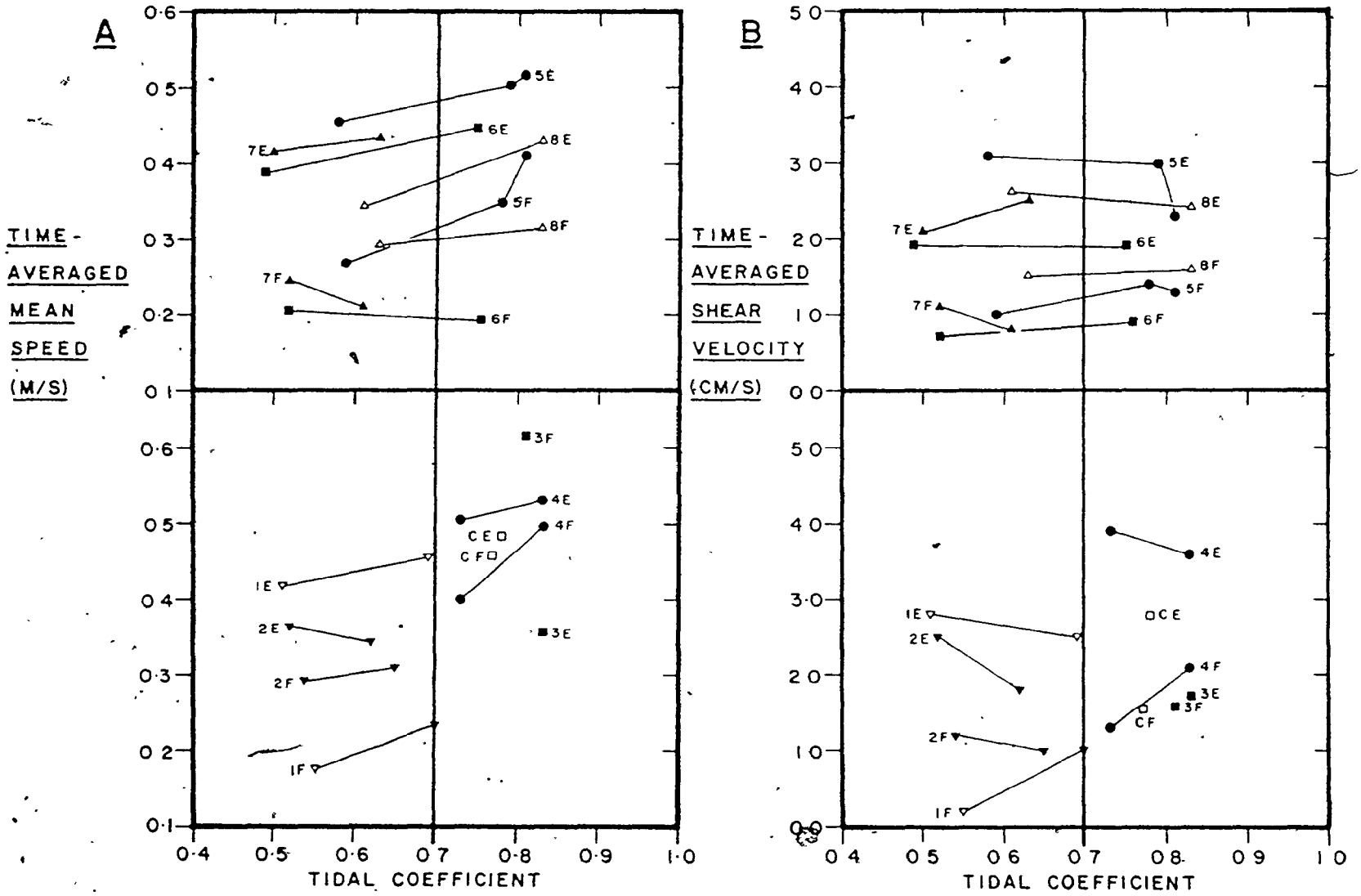
A
TIME-AVERAGED MEAN SPEED (M/S)
0·6
0·5
0·4
0·3
0·2
0·1
5E
6E
7E
8E
5F
8F
7F
6F
3F
4E
CE
CF
4F
1E
2E
3E
2F
1F
0·4
0·5
0·6
0·7
0·8
0·9
1·0
TIDAL COEFFICIENT
B
TIME-AVERAGED SHEAR VELOCITY (CM/S)
5·0
4·0
3·0
2·0
1·0
0·0
5E
8E
7E
6E
8F
5F
7F
6F
4E
1E
CE
2E
4F
3E
3F
CF
2F
1F
0·4
0·5
0·6
0·7
0·8
0·9
1·0
TIDAL COEFFICIENT

FIGURE 3.12 : Variation of time-averaged hydraulic parameters with the tidal coefficient on Diamond Bar. A - mean speed; B - shear velocity.

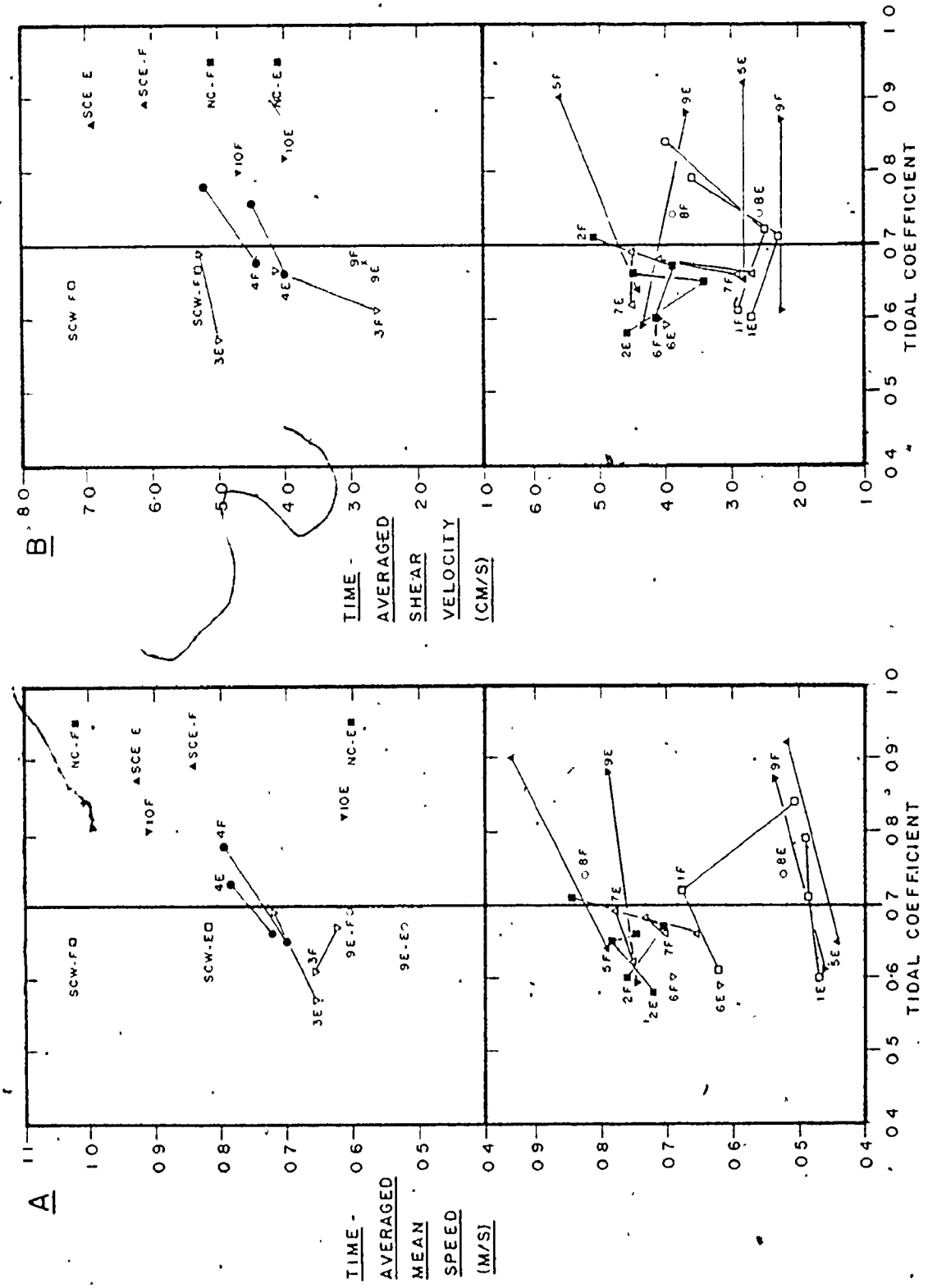
A
B
TIME - AVERAGED MEAN SPEED (M/S)
TIME - AVERAGED SHEAR VELOCITY (CM/S)
TIDAL COEFFICIENT
SCW-F
SCW-E
SCE-F
SCE-E
NC-F
NC-E

important when profiles are not significantly linear, and near-zero shear velocities are calculated which are not in all likelihood a true expression of the flow conditions. An example of this is provided by the time-averaged flood shear velocity for Buoy EP 7 (Figure 3.9). If the near-zero shear velocities from the non-significant profiles at hours 10.33, 11.25 and 12.00 had been included, then the calculated time average would have been lower than it probably is in fact.

The second source of error is relevant only to data from Big Bar and results from the fact that the current vane planes at high current speeds. Therefore, the time averages do not include the extremely important peak values of mean speed and shear velocity, and are, therefore, less than the true value by an unknown amount. Problems of this type fortunately affect only a few single ebb and flood portions of tidal cycles, particularly those with high tidal ranges. Inclusion of these values produce some of the unexpected negative slopes in Figure 3.11.

The third reason for potentially erroneous time-average values is also due to the incompleteness of the measurements, in this case because various factors often did not permit the monitoring of currents over the entire ebb or flood portion of a tidal cycle. In most cases, the period(s) for which data are missing is either near high or low water, and can be estimated with reasonable accuracy by a linear extrapolation to zero flow, as has been done in Figures 3.5

to 3.9. If the length of time for which measurements are not available is longer than about an hour, however, there could be considerable discrepancy between the actual and extrapolated values, and the calculated time averages could be in error.

In certain cases, it is possible to obtain a time average that by itself is reliable, but is not strictly comparable with other values obtained at the same buoy location. If there are steep local gradients in the hydraulic parameters, due to a steep topographic slope, such as at Buoys 2 and 3 on Big Bar (Figure 3.1) or Buoys 3 and 7 on Diamond Bar, or for other reasons, then slightly different mooring locations on successive visits to the site can produce time averages that reflect the lateral gradient, rather than the variation due to tidal range. This is believed to be the explanation for the lack of a consistent trend in the values from Buov 2 on Diamond Bar in Figure 3.12.

All factors considered, it may be surprising that so many of the buoy locations show the expected increase in current speed and shear velocity with increased tidal range. A careful scrutiny of every individual time-average calculation indicates that most, but not all, of the points that do not fit with expectation are subject to one or more of the above sources of error. On the other hand, most of the points that agree with expectation appear to be free of obvious error. Therefore, the expected increase in current speed and shear velocity with tidal range has been accepted as being demonstrated.

By comparing the vertical spacing between sets of points for the ebb and flood at each buoy location, the form and degree of asymmetry can be seen immediately. There is no case in which the sense of the asymmetry changes with an increase or decrease in the tidal range. However, there does appear to be a tendancy for the value of the flood time averages to increase at a faster rate than corresponding values for the ebb. Unfortunately, the quality of the data is such that it is not possible to draw any detailed conclusions from Figures 3.11 and 3.12 regarding the influence of tidal range on the hydraulics. One obvious feature that may be of significance is the steeper average slope of the trends indicated for Diamond Bar as compared to Big Bar, which may simply reflect the above-mentioned inadequacy of the current vane, or be due to some other unknown factor(s).

The next step in the analysis of the tidal currents is the determination of any areal variations in the parameters discussed above that may exist over the bars being studied. In order to do this, however, the values for each buoy location should be standardized to a common tidal coefficient, in order to remove the effect of the tidal range. Ludwick (1974) accomplished this by multiplying each individual value by the ratio of the mean tidal range to the range on the day when the measurements were conducted. This approach presupposes that the parameters under consideration go to zero at zero tidal range. Such is not the case, however, with any

of the data in Figures 3.11 or 3.12. Extrapolation of the trends shown to a tidal coefficient of 0.0 yields positive intercept values for both the time-averaged mean current speed and shear velocity. Because of this, Ludwick's method cannot be applied. In its place, a graphical technique has been used to standardize the values to a tidal coefficient of 0.70, corresponding to a tidal range of 11.3 metres, which is slightly less than the mean tide. The appropriate values of the time-averaged mean current speed and shear velocity were estimated either by interpolation between reliable data points, or by extrapolation from single values, using an average value for the slope of the trends indicated on the figures for each bar. If inspection of the original data showed the presence of an obvious error in a particular time-average value, then that time average was ignored in favour of more reliable data, or, if necessary, it was adjusted to compensate for the error as much as possible. Although this procedure is not as rigorous as that advocated by Ludwick (1974), it does have the advantage that obvious errors are not carried blindly into subsequent stages of the analysis. This does not mean that it has been possible to remove all uncertainty from the values, and they must be considered as only a best approximation to the conditions as they actually exist.

The slower than expected rate of increase of current speed and shear velocity with the tidal coefficient that was noted above is also evident in data presented by Allen et al (1969) from the Gironde estuary, France. These data indicate that the rate of increase decreases as the tidal range goes up. This phenomenon may be due to the hypsometry of the estuary. If the middle part of the intertidal zone is gently sloping, and the upper part more steeply sloping, then less water will be required to raise the water surface by a given amount at higher tidal ranges than at lower ranges, when only the gently sloping portion is being covered. The bedrock cliffs that border much of Cobequid Bay, and the small scarps at the edges of the salt marshes are believed to produce the required shape of the hypsometric curve in the study area.

### 3.2.4 Areal Variations

In this section, the areal variations of certain summary hydraulic parameters will be presented for the study bars, as a means of describing the flow patterns and conditions experienced in each area. The parameters selected are: the vector mean of bottom current directions (measured 0.75 metres above the bed) weighted by the current speed one metre from the bottom, except on Big Bar, where the directions refer to surface currents; the standardized, time-averaged mean current speed; the standardized, time-averaged shear velocity; and the standardized total energy expended on the bed, which

is the integration of the stream power over each half of the tidal cycle. The total energy has been standardized in the same manner as discussed above for the time-averaged mean current speed and shear velocity. For simplicity, the terms standardized time-average, and vector mean will be omitted, except where necessary for clarity.

Of prime importance in these discussions is the areal distribution of flood and ebb time-velocity asymmetries, because of the implications that these have with regard to net sediment transport patterns. The presence of time-velocity asymmetries implies that the transport capacity of the flood and ebb currents are not equal and that residual transport must occur in the direction of the stronger current. In the preceeding sections, the stronger current has been defined for descriptive purposes on the basis of the time-average of either mean current speed or shear velocity. However, neither of these can be considered as a direct representation of the sediment transport capacity of the currents, for various reasons. Although the relationship between flow parameters and sediment transport is extremely complex (see Section 6.2), it has been known for many years that the sediment discharge increases in proportion to a power of the current speed. The exponent is most commonly given the value three, but values up to seven have been proposed for deep flows (Colby, 1964). Based on such a relationship, the maximum mean current speeds might be more informative with regard to sediment transport

than the time averages. The one single parameter listed in Appendix 2 that is most directly related, therefore, to the movement of sediment is the stream power (defined by equation (3.13) above), because it is proportional to the velocity cubed, and expresses the energy available for the transport of sediment (Bagnold, 1966). It is for this reason that the stream power, integrated over each phase of the tide, has been included in the subsequent discussion.

(i) Big Bar: Figure 3.13 shows the distribution of the selected parameters over Big Bar. It should be noted before continuing that some of the values used in constructing the contoured distributions are lower than they should be due to the planing of the current vane as discussed above. The large-scale features of the patterns are not altered, however, with the possible exception of the channel station south of Buoy 3.

Considering first the ebb currents, we can see from Figure 3.13A that the flow is directed towards the west-southwest at all stations, resulting in a strong upslope component at Buoys 1, 5 and 6 on the north side of the crestline, and a downslope flow on the south side. This pattern of current flow results in the presence of a sheltered area with low current speeds along the south-central and southwestern edge of the bar (Figure 3.13B), in the lee of the crest. The north side of the bar experiences stronger currents, as does the channel between the bar and the islands. The fastest

FIGURE 3.13 : Areal variation of hydraulic parameters on Big Bar. A - vector means of surface currents; B - time-averaged mean speed (m/s); C - time-averaged shear velocity (cm/s); D - total stream power ($kg/s^2$). Flood dominated areas stippled. All values standardized to a tidal coefficient of 0.70.

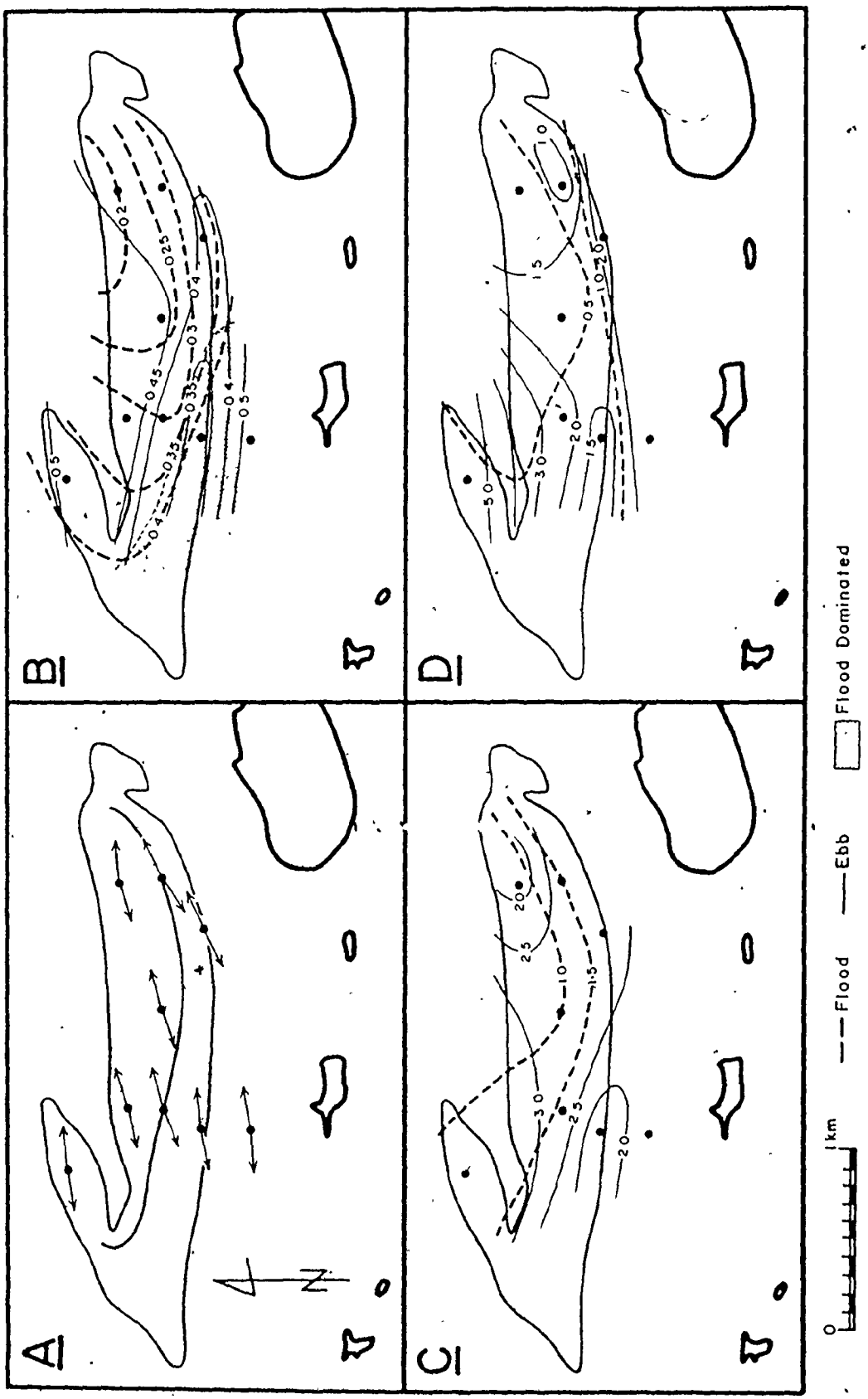
A
B
C
D
N
0
1 km
Flood
Ebb
Flood Dominated

ebb flow in this channel might be deflected towards its southern side and away from the bar, because of the curvature of the channel, thereby enhancing the area of low ebb current speeds along the southwestern side of the bar.

The patterns of shear velocity and total energy (Figures 3.13C and 3.13D) are almost identical, as might be expected because the shear velocity squared appears in the definition of the stream power by way of the shear stress ($\tau_o$). These distributions are also similar in most respects to that of mean ebb current speeds, with the highest values on the northwestern portion of the bar, and in the southern channel. The low values at Buoy 3 again reflect its location in the lee of the crest. Low values of both the shear velocity and total energy are also present at the eastern end of the bar, and may be due to the sheltering of that area by the northward bend of the crestline at its eastern end. The low total energy at Buoy 7 is due to its high topographic position and resulting short period of submergence.

A reversed pattern of current speeds and flow directions is present during the flood tide (Figures 3.13A and 3.13B). Flood currents, which enter the study area from the west-southwest, are strongest at the west end of the bar, although the positioning of the contours cannot be considered exact in this area, and along the southern side. The bar crest is clearly responsible for shielding the northeastern portion of the bar and creating a pocket of very low flood current speeds

there. Accompanying this is a deflection of the flood currents in a clockwise direction, such that they are not directed in a completely opposing direction to those of the ebb at Buoys 1, 6 and 7.

The distribution of flood shear velocities (Figure 3.13C - heavy broken lines) shows a great similarity to that of the corresponding mean current speeds, as does the total energy (Figure 3.13D). The highest values are found along the southern side of the bar, with lower values on the north side of the crest at the east end. This again emphasizes the extent to which the bar crest protects this area from the flood currents.

It is also of interest to consider the sum of the available energies for the ebb and flood tides (Figure 3.14), because this gives a simple overview of the gross features of the flow over the bar. In Figure 3.14A, there is an obvious band of low values originating at the northeast corner of the bar, and extending diagonally over the crest in a west-southwest direction through Buoys 1 and 3. High values of the combined total energy are found in the southern channel, but the highest values are present on the northwestern arm. This pattern may, in part, result from the effects of the shore configuration and the presence of the islands, but it appears to be influenced most directly by the configuration of the channels on either side of the bar.

FIGURE 3.14 : Areal variation of total combined stream power ($kg/s^2 \times 10^3$). A - Big Bar; B - Diamond Bar; C - Economy Point; D - Selmah Bar.

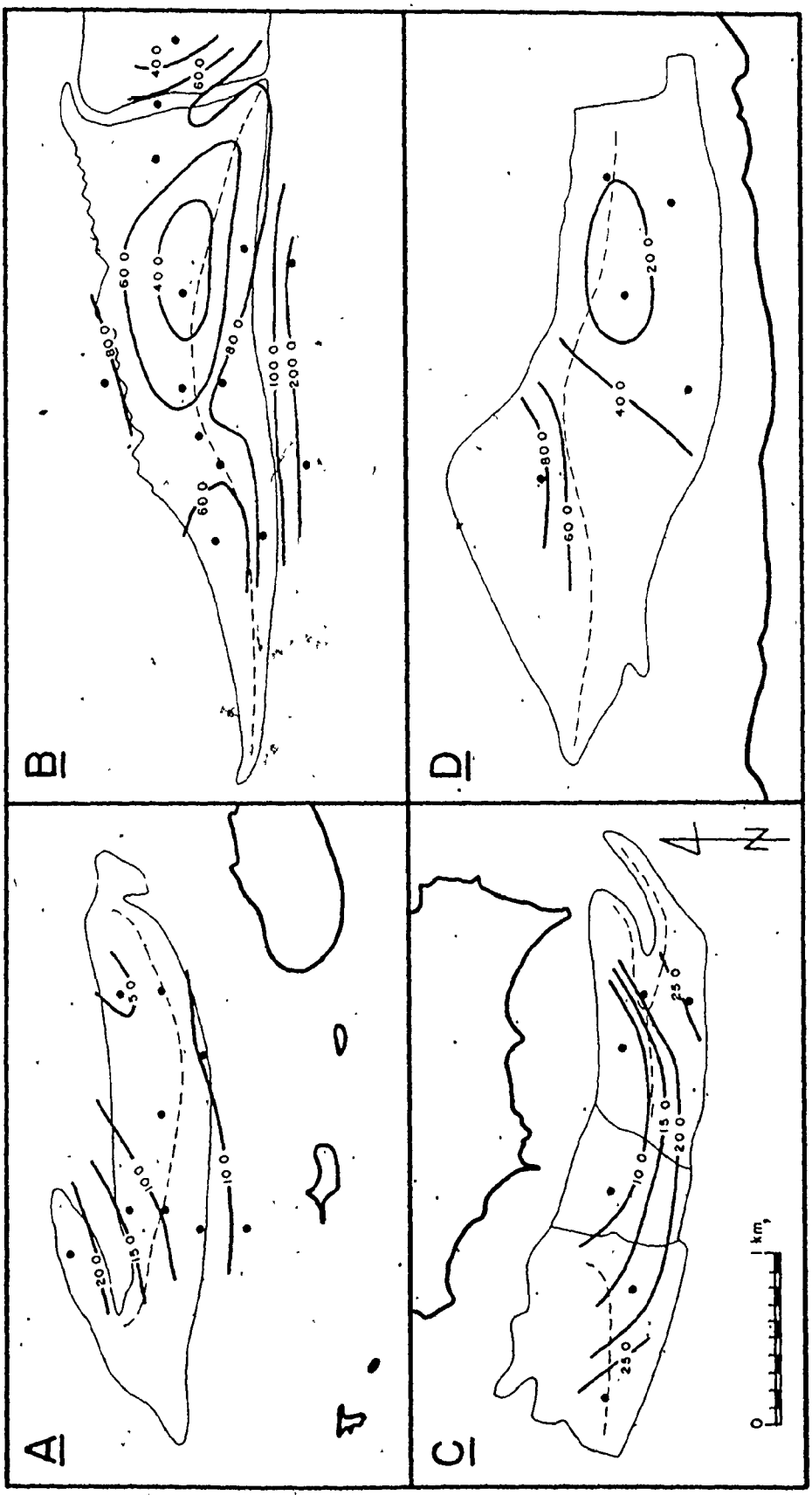
A
B
C
D
N
km

The presence of time-velocity asymmetries can be easily determined by comparing values given by the superimposed contour patterns for the various parameters at any point. Doing this, one finds that both the shear velocities and total energy (Figures 3.13C and 3.13D) are ebb dominant over the entire surface of the bar, indicating ebb-dominated sediment transport (solid arrows, Figure 3.18A). Only with the mean current speed (Figure 3.13B) can an area with higher flood speeds be delineated (stippled region) over the southwest part of the bar. Due to the uncertainty of the flood speeds at the channel station, it is not known if this region is also flood-dominated or not. If the ebb speeds are indeed higher than the flood, then the area of flood dominance is restricted to a narrow strip along the edge of the bar.

Klein (1970, Table 9) also presents some current data from Big Bar that are of interest here. Unfortunately, much of his data is composed of spot determinations of bottom speeds only, obtained at various times during the tidal cycle, so that calculation of other hydraulic parameters is impossible, and comparison with data obtained in this study is difficult. It appears, however, that many of Klein's recorded current speeds are higher than those reported in Appendix 1 of this thesis. Because Klein used a Pritchard-Burt current vane that was calibrated theoretically, it is possible that the higher values result from the failure to consider the effect of lift forces on the vane, as described in Section 3.1.2. This

problem aside, there is a general agreement between the distributions of current speeds measured in both studies, and between the areas of flood and ebb dominance outlined by them, with the notable exception of the eastern end of the steep south side of the bar. Klein (1970) contends that the entire length of the steep side is flood dominated, while the present data indicate that at most, only the western half is flood dominated. Even this is not supported by the shear velocities and total energy. Additional sedimentological evidence must be used to clear up the conflict.

(ii) Diamond Bar: Ebb current flow over Diamond Bar (Figure 3.15A) is directed slightly north of west, parallel to the crestline at the very eastern-most end of the bar, possibly as a result of the orientation of the major channel to the southeast of the bar (Figure 2.14). This produces an upslope component to the flow on the south side of the crest and a downslope component on the north side, particularly in the vicinity of the two swatchways, where there is a strong component of flow across the bar crest. In the northern channel, the flow is directed towards the south-southwest. The fastest ebb currents (Figure 3.15B) are present south of the bar crest, as well as at the eastern end, where a part of the flow breaks across the trend of the bar in the major swatchway. A smaller northward deflection of the contours is evident in the vicinity of the minor swatchway, where additional flow diagonally across the bar is concentrated. The

FIGURE 3.15 : Areal variation of hydraulic parameters on Diamond Bar. Subdivisions same as in Figure 3.13, except in A, where the vector means are of bottom currents. Ebb-dominated area stippled.

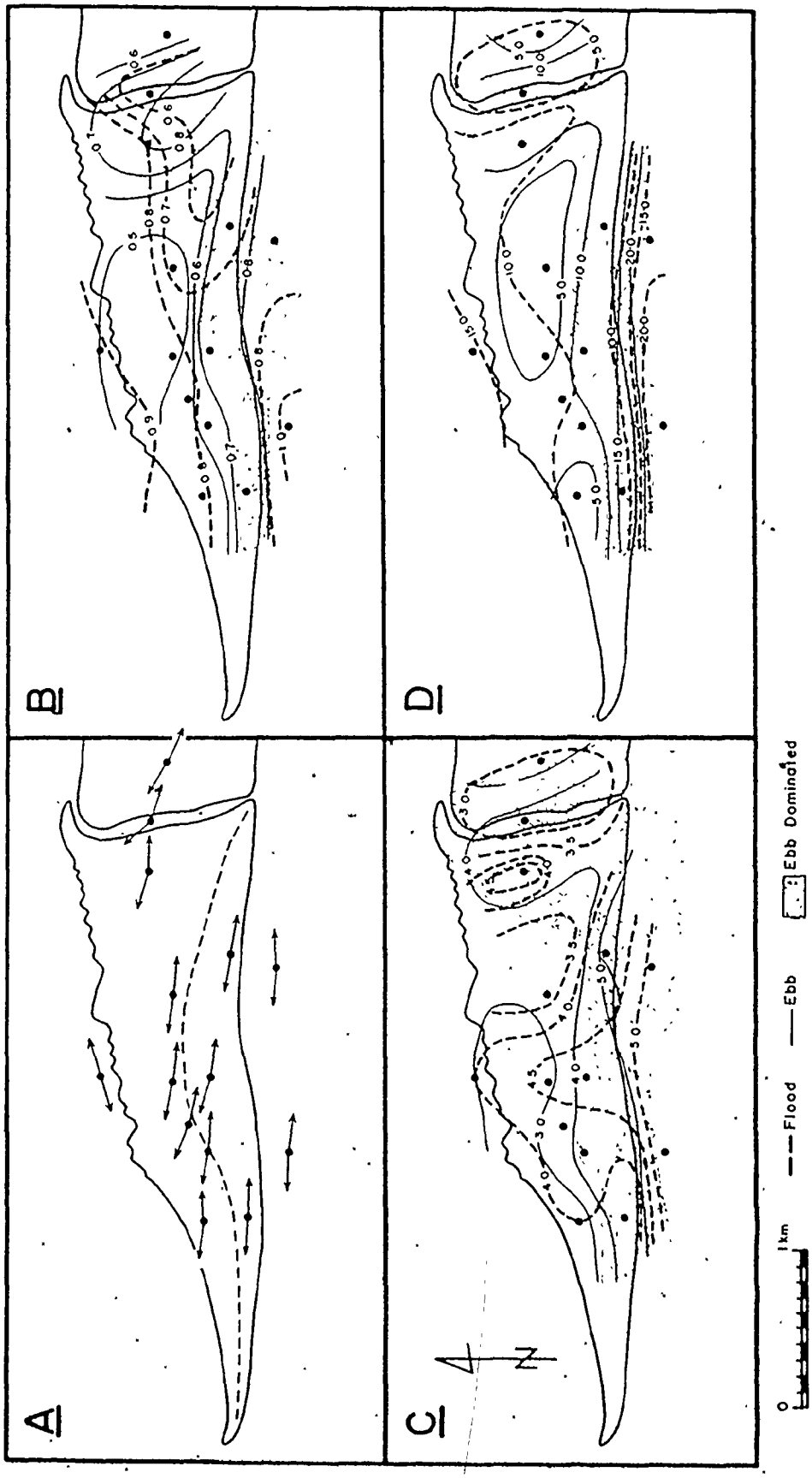
A
B
C
D
N
0
1 km
Flood
Ebb
Ebb Dominated

weakest currents are found in a pocket on the north-central surface of the bar, and in an area flanking the east side of the major swatchway. Both of these areas lie in sheltered positions, in the lee of a bar crest. Flow in the northern channel, although faster than that on the adjacent surface of the bar, is slower than that in the southern channel.

The distribution of ebb shear velocities (Figure 3.15C) is identical in all essential features to the pattern of mean ebb current speeds (Figure 3.15B). The values are highest in the southern channel and on the western side of the major swatchway, and lowest over the northwestern surface of the bar. A similar pattern is also displayed by the total energy (Figure 3.15D). This figure clearly shows a band of lower values, lying on the sheltered northern side of the bar crest-line, that is disrupted in two places by higher values produced by cross-bar flow concentrated in the swatchways.

Flood tidal currents (Figure 3.15A) are directed almost $180^{o}$ away from those of the ebb at all stations, except in the main swatchway, where there is not such a strong cross-bar flow as on the ebb. As a result, the flow is directed roughly parallel to the east-west segments of the crest so that flow across the crest is again concentrated in both swatchways. The higher parts of the bar now shield the southern side and eastern end, which experience the lowest flood current speeds (Figure 3.15B), while the more exposed northern and western portions have faster currents. The highest current speeds are still found in the southern and northern channels.

Flood shear velocities (Figure 3.15C) show a pattern that is considerably more complex than the distribution of flood current speeds (Figure 3.15B). In general, the highest flood shear velocities are present in the southern channel, with lower values on the northern side of the bar crest. The regularity of the trend is disrupted by two north-south oriented bands of higher values separated by areas with low shear velocities. The high values west of the major swatchway are probably due to the constriction of the flow depth as the currents pass over the topographically higher area there. The increase in depth as they enter the major swatchway is the likely cause of the sharp eastward decrease in the values. The other area of higher shear velocities in the central portion of the bar may also be due to the presence of the minor swatchway, and to the decrease in depth experienced by the currents as they flow toward the bar crest.

The total energy for the flood tide (Figure 3.15D) also follows the same general pattern, with the highest values in the channels, and lower values along the south side of the bar and at the eastern end, the two areas that are sheltered by higher parts of the bar.

The most striking feature of the combined ebb and flood energy (Figure 3.14B) is the large elliptical area of low values centred to the north of the crest at Buoy 1. Portions of similar lows are present at the west end of the bar, and east of the major swatchway, on Great Village Bar. Diagonal

bands of higher total energy, centred over the swatchways, separate the areas of low values, and connect the higher values in the north and south channels. This pattern basically reflects the longer duration and concentration of flow in the lower, channelized areas.

The stippled areas in Figures 3.15B, 3.15C and 3.15D delineate those regions with higher ebb than flood values of the various parameters. A remarkable consistancy is evident between the three figures. Virtually all of the north side of the bar is strongly dominated by the flood currents. A strong ebb asymmetry is shown, however, along the entire southern side of the bar and on the western side of the major swatchway, areas which are directly exposed to the westward flowing ebb currents, and sheltered from the flood tide. At the western end of the bar, this ebb-dominated region is a narrow band only, bordered on the south by an area that is flood-dominated in the centre of the channel. This may be due to the lateral segregation of strong ebb and flood currents because of the arcuate shape of the channel. Passing eastwards, the ebb-dominated area expands southward to include all of the flood of the southern channel.

The only substantial differences between the three patterns involve the extent of the slight northward bulge of ebb dominance in the vicinity of the minor swatchway, where Buoys 4 and 6 show differing asymmetries, depending on the parameter used. Differences in the shape of the northward

extension of ebb dominance in the major swatchway cannot be considered significant, due to the extrapolation of the contours in that area. It is evident, however, that one should expect an easterly transport of sediment on the northern side of the bar, and an opposite westerly movement on the south side (Figure 3.18B). The ebb-dominated transport will have a more northerly component on the west side of both swatchways (Figure 3.18B).

(iii) Economy Point: The Economy Point complex of sand bars is topographically the most complex of the four areas studied, and, unfortunately, insufficient reliable data are available for the area to represent adequately the current variability that is to be expected. The exposed location of these bars and the common occurrence of waves resulted in a large number of non-significant velocity profiles. Therefore, the location of the contours could be shifted appreciably with the acquisition of additional data.

On the ebb tide (Figure 3.16B) the mean current speed generally decreases toward the headland. The region of low current speeds near the shore is most extensive in the low-lying area between Centre and East Bars, and faster currents extend in an arcuate belt around this central area, with the highest ebb current speeds occurring over the southeast corner of East Bar, and the southwest part of Centre Bar. The flow directions (Figure 3.16A) appear to follow the contours of current speed, with northwesterly currents on Centre Bar and

FIGURE 3.16 : Areal variation of hydraulic parameters at Economy Point. Subdivisions same as in Figure 3.15. Flood shear velocities (part C) are lower to the south of the contour line. (Ebb-dominated area stippled.)

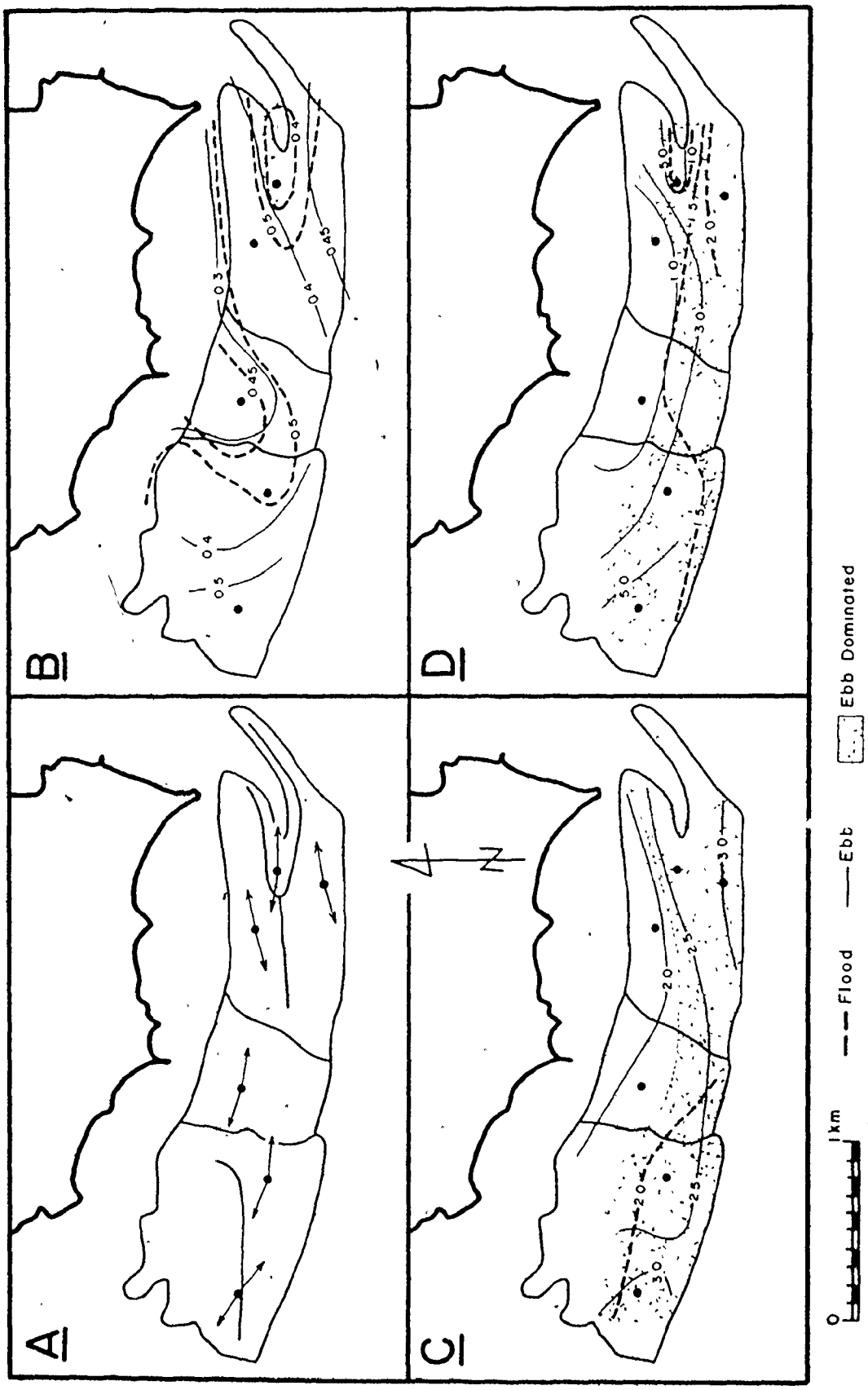
A
B
C
D
N
0
1 km
Flood
Ebb
Ebb Dominated

southwesterly flow on East Bar, except in the blind channel at its eastern end where the currents are confined between the two branches of the crest. The rather stagnant character of the flow at Buoy EP 4 between Centre and East Bars is further reflected in the pattern of directional change over the ebb tide. At the beginning of the ebb, the flow is toward the northwest, but after approximately one hour, there is a reversal and it is directed to the east for a short time. The currents then swing gradually in a clockwise direction ending with the final flow directed towards the southwest. It appears, therefore, that a weak eddy may exist in this location during the ebb.

The distributions of ebb shear velocities and total energy (Figures 3.16C and 3.16D, respectively) must be considered as provisional due to the necessity of including many non-significant profiles in the calculations. Both parameters do, however, show a trend that is roughly similar to that of the mean current speeds, with the lowest values located closest to the headland, surrounded by higher values on the outer edges of the complex.

On the flood tide (Figure 3.16B), the area between East and Centre Bars is again the site of weak current activity, but this appears to be due to its sheltered position east of the north-south portion of the crest on Centre Bar. A similar sheltered area is present in the blind channel on East Bar. Faster currents flow on both sides of these two

protected pockets, but like the ebb, the speeds are highest on the southern side of the complex, and at the western end of Centre Bar, where the flow that is concentrated in the channel to the north of West Bar (Figure 2.16) is funnelled onto Centre Bar.

The values of flood shear velocity (Figure 3.16C) are quite uniform and do not show prominent areal variations. However, the lowest values are found along the south side of Centre Bar, and in the blind channel on East Bar. The total flood energy (Figure 3.16D) also shows low and rather uniform values over much of the area. Only Buoy EP 7 on the southeast corner of the complex has an appreciably higher value.

The combined energy for both the ebb and flood (Figure 3.14C) clearly displays the increase in current strength outward away from Economy Point. This pattern must be responsible in part for the presence of sand bars in this otherwise exposed area. The buoy locations are not sufficiently closely spaced to allow the influence of bar topography to be discerned.

The extent of areas with an ebb dominance is shown in Figures 3.16B to 3.16D by the stipple. Based on the mean current speeds, almost the entire surface of the Economy Point sand bars studied experiences faster flood than ebb currents. Two small areas with an ebb dominance do exist, one in the blind channel on East Bar, and the other on the crest of Centre Bar. Unfortunately, the exact extent of this latter area

cannot be determined due to the lack of control. From the shear velocity and total energy contours (Figures 3.16C and 3.16D, respectively), the ebb-dominated area is considerably more extensive than that defined by the mean current speeds. Not only does it include the two small areas outlined in Figure 3.16B, but it also extends along the entire south side of the studied bars. The area of flood asymmetry is restricted to a small region on the shoreward side of East Bar and the adjacent part of the low area between it and Centre Bar.

The current speed data of Klein (1970, Table 9), although suffering from the same deficiencies as those for Big Bar, do provide some further information regarding the areas of flood and ebb dominance. It appears from these data that much of the area studied by this author is flood-dominated, including the entire west end of East Bar and the low area between East and Centre Bars, in agreement with the results for mean current speed shown in Figure 3.16B here. As well, all of the area north of the crest on Centre Bar is shown as flood-dominated by Klein (1970). On East Bar, one station whose position coincides with the blind channel is ebb-dominated. Figure 11 of Klein (1970) depicts this ebb area as encompassing the entire southeast corner of East Bar, however. The whole crestline of Centre Bar is also shown to be ebb-dominated in Klein's figure, a contention supported by the data for Buoy EP 1.

As might be expected, Klein's (1970) current speed data are in better agreement with Figure 3.16B than with either of Figures 3.16C or 3.16D. Because of the low density of the control and the general unreliability of the shear velocity and energy data, it is not possible to reconcile conclusively the differences between the various patterns of dominance shown. Delineation of the paths of residual sediment transport must await the presentation of additional sedimentological evidence in latter parts of the thesis.

(iv) Selmah Bar: Because of the small amount of data from Selmah Bar, it is not possible to position the contours of the various parameters (Figure 3.17) with any certainty, due to the anticipation of significant topographic controls on their distribution. Some further idea of the distribution of current speed over the bar can be obtained from Figure 4 of Dalrymple et al (1975), in which the contours of maximum bottom currents are shown for the flood and ebb. The patterns displayed there, plus knowledge of the influence of topography gained from the other areas has been used as a rough guide in contouring the data in Figures 3.14D and 3.17. The distributions must, nevertheless, be regarded as provisional.

During the ebb, the flow is directed southwestward across the crest of the bar at its eastern end (Figure 3.17A) and then continues to the west in the channel next to the shore. The crest is responsible for sheltering the south side of the bar, where the lowest current speeds are recorded

FIGURE 3.17 : Areal variation of hydraulic parameters on Selmah Bar. Subdivisions same as in Figure 3.15. Ebb-dominated area stippled in part B after Dalrymple et al (1975, Figure 4).

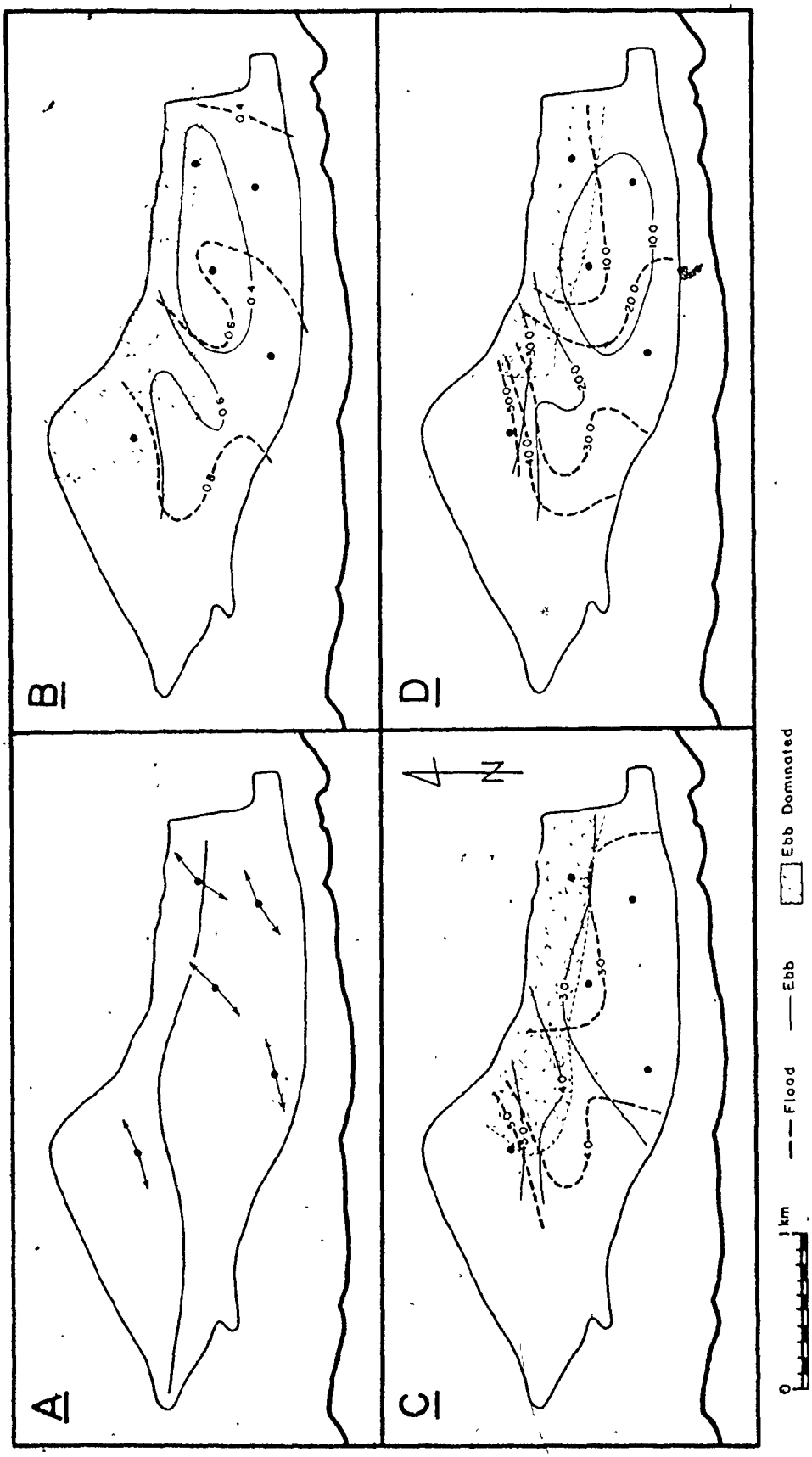
A
B
C
D
N
0
1 km
Flood
Ebb
Ebb Dominated

(Figure 3.17B), particularly at the east end. Faster currents are directed through the major swatchway, but the highest speeds are found over the northwest section of the bar.

The shielding influence of the crest is also evident in the distributions of ebb shear velocity (Figure 3.17C) and total energy (Figure 3.17D). For both of these parameters, the lowest values are recorded south of the crest, at its east end. High values are present on the northwest part of the bar, and are shown extending southward a short distance along the west side of the swatchway, by analogy with Diamond Bar.

On the flood, the pattern of current flow is reversed (Figure 3.17A), flowing in from the west, and turning northeastward to flow obliquely across the bar crest. Current speeds (Figure 3.17B) show a regular eastward decrease, because the southern channel is essentially dead-ended to the east, where it passes into the mudflats (Figure 2.11). The northward bulge of the 0.6 m/s contour at Buoy CM 3 results from the location of that station in one of the minor swatchways (Figure 2.12). As on the ebb, the highest current speeds are found in the northwest section, despite the fact that the flood speeds recorded for Buoy CM 5 are believed to be somewhat too high, because of calibration difficulties with the current meter.

The distributions of flood shear velocities and total energy (Figures 3.17C and 3.17D, respectively) show similar

trends to that of the current speed. Both parameters show an eastward decrease along the south side of the bar, toward the head of the channel. The lowest values are located on the crest of the bar, to the east of the swatchway. The highest values of both are again present north of the crest at the west end.

The total energy available over the tidal cycle (Figure 3.14D) shows that those areas east of the swatchway experience much weaker currents than the western half of the bar, because of the dead-end nature of this channel, and its sheltered location on the ebb tide.

A comparison of the ebb and flood contours for shear velocity (Figure 3.17C) and total energy (Figure 3.17D) allows an area of ebb dominance to be delineated (stippled) along the eastern half of the north side, extending westward almost to Buoy CM 5. All of the south side and western tip of the bar have flood asymmetric currents. The true boundaries of this area cannot be determined precisely, because of the lack of control and the uncertainty of the contour positioning from which the boundary is derived. No similar area of ebb dominance is shown by the current speeds, which indicate that all of the bar experiences higher flood than ebb currents. The map of maximum bottom speeds presented by Dalrymple et al (1975, Figure 4) does, however, show an area of ebb dominance along the northeast side of the bar. This region has been shown on Figure 3.17B for reference. It extends further to

the west than suggested in either of Figures 3.17C or 3.17D, but this may be due to the calibration problems experienced during the flood at Buoy CM 5. All evidence indicates, however, that the area south of the bar crest, and much of the western end of the bar, should have flood-residual sediment transport (Figure 3.18D).

### 3.2.5 Discussion

It can be seen from all of the data presented above that time-velocity asymmetries, or a dominance of one half of the tidal cycle over the other, is a common characteristic of the tidal currents. At any given location, the asymmetry displayed is generally consistent, regardless of the parameter taken as the measure of current strength, and one can be fairly certain that there will be a residual transport of sediment in the direction of the strongest currents. The transport patterns suggested by the current data are shown in Figure 3.18. In a number of locations, however, notably at Economy Point, the various parameters show differing asymmetries, which indicates that there is no overwhelming dominance and makes the determination of residual transport patterns less certain.

From the available data, it appears that, in general, areas with opposing asymmetries are situated on opposite sides of a bar crest, so that opposite sides experience transport in directions approximately $180^{\circ}$ apart. Diamond Bar (Figure 3.18B) is a particularly good example, as is the east end of

FIGURE 3.18 : Residual sediment transport directions deduced from hydraulic data. Solid arrows - based on consistent time-velocity asymmetries; broken arrows - predicted from a consideration of tidal-current inertia. A - Big Bar; B - Diamond Bar; C - Economy Point; D - Selmah Bar.

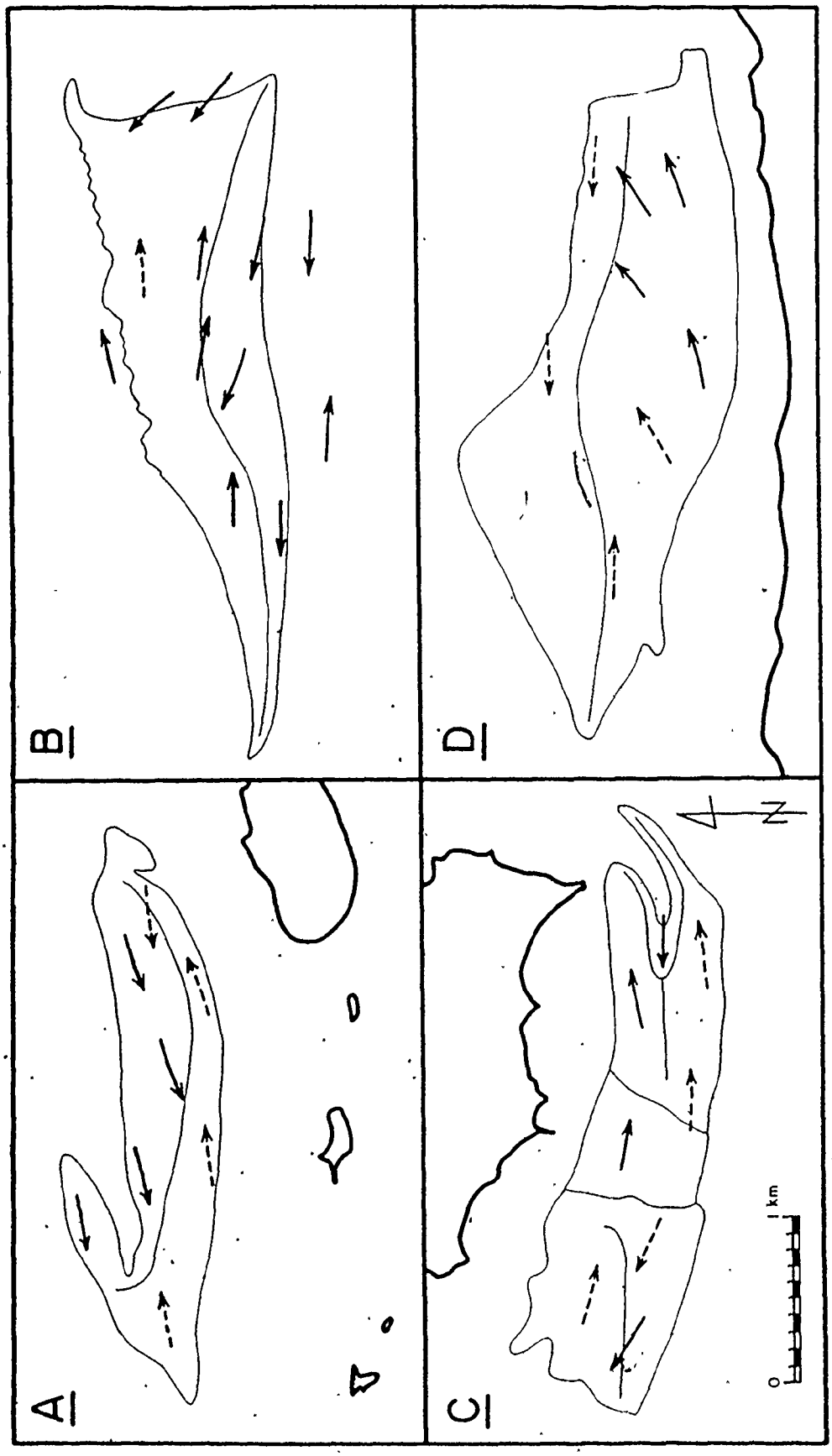
A
B
C
D
N
1 km
0

Selmah Bar (Figure 3.18A), and possibly on East Bar (Figure 3.18C), although the situation there is much more complicated because of the topography and scarcity of reliable data.

At this point, however, no explanation has been offered for the existance of time-velocity asymmetries, and for their areal distributions on the various bars. A consideration of the contributing factors and of their implications is the subject of this discussion.

If the floor of the area were entirely featureless, one would expect a flood dominance in all areas because of the distortion of the tidal wave that occurs in shallow water. This distortion shortens the flood, and lengthens the ebb, which, in turn, leads to higher flood current speeds in order that continuity be maintained (neglecting river input, as it is insignificant in comparison to the tidal prism - Section 2.2.4). One possible consequence of this factor is the massive accumulation of sand in the head of Cobequid Bay, but it is not capable by itself of explaining the observed patterns of dominance.

When a system of straight, linear bars and channels, oriented parallel to the flow is introduced, the pattern of asymmetries becomes more complex. The asymmetry of the tidal wave is capable of producing a flood dominance on the bar tops, because the flow is unaffected by the topography in large measure at this time. On the ebb tide, however, the flow is channelized between the bars for a considerable period, because

of the long duration of the ebb. This confinement of the ebb produces higher speeds than would otherwise be expected, and the result is an ebb dominance of the channel floors. The resulting pattern of residual transport should display a clear separation of ebb and flood areas, based solely on elevation.

Examples of flow systems such as this have been reported from several estuaries (G. P. Allen, 1972; DaBoll, 1969; Wright, Coleman and Thom, 1973). Swift and McMullen (1968) have also suggested that it applies in Cobequid Bay, so that bar surfaces are flood-dominated, and channels are ebb-dominated. This factor is, indeed, of some importance in the study area, but the patterns of dominance shown above are much more complicated than allowed by this explanation because parts of channels are flood-dominated, and some bars experience ebb asymmetric currents.

The observed distributions of time-velocity asymmetries can be explained if the tidal currents are no longer considered to flow parallel to the topographic contours. Examination of the bottom currents over Diamond Bar, for example, during both the flood and ebb, shows that (Figure 3.15A) such is the case, although the angular difference between the contours and the flow may be small. In this situation, the inertia of the currents becomes very significant, as they flow over and around the bars. On the upstream side of the bar, inertia brings faster flowing water closer to the bed, while on the

downstream side the opposite effect occurs. This produces higher shear stresses on the upstream side, and lower values on the downstream portion of the bar. Furthermore, as the currents encounter the upstream slope, the bottom currents are deflected to the left, relative to the surface currents, thereby bringing about a convergence of the streamlines and faster current speeds in this area. On the other side of the bar, gravity causes the bottom currents to turn to the right, down the bar slope, resulting in a divergence of the flowlines and weaker currents. Examination of bottom and surface current directions from velocity profiles measured on Diamond Bar shows that 55% of them have the proper directional change. The result of these two factors, combined with the reversal in flow direction, is the production of areas of ebb and flood dominance on opposite sides of the bar, because the side that is sheltered during one half of the tidal cycle is exposed to the brunt of the currents during the other part of the cycle.

The influence of inertia, as just described, appears to be the primary factor responsible for the observed patterns of flood and ebb dominance, and almost all of the consistent time-velocity asymmetries shown in the previous section (3.2.4) are explainable in these terms. Because the influence of tidal current inertia is so important, this concept may be of value in predicting the patterns of residual transport in those areas where the current data did not give a conclusive

picture (broken arrows, Figure 3.18). One can therefore suggest that: the west end of Big Bar and much of the south side in the vicinity of Buoy 3 should be flood-dominated (Figure 3.18A); the area immediately south and east of the crest of Centre Bar near Buoy EP 3, should be ebb-dominated, while the region northwest of the crest should be flood-dominated (Figure 3.18C), as indicated by Klein's data; and the surface of East Bar surrounding the blind channel, including the vicinity of Buoy EP 7 should be flood-dominated (Figure 3.18C). Additional sedimentological data, including tracer results (Chapter 6), are available to support these predictions, but a detailed consideration of the evidence will be deferred until later in the thesis.

Various workers have also noted the relationship between the topography and currents described here (Klein, 1970; Ludwick, 1974; Postma, 1967; Robinson, 1960). Inertial effects, therefore, appear to be a common characteristic of sedimentation in tidal environments, and have important implications with regard to the formation and maintenance of a bar topography. Because the flow of the dominant phase of the tide has an upslope component on both sides of a bar crest, there will be a net convergence of sediment at the bar crest, and by extension, a net divergence in the channels, in many instances. In this way, the topography can be maintained without recourse to helical flow, which was shown previously in this chapter not to be important in the study

area. The extent to which oblique flow and inertial residuals, rather than helical flow, is applicable to other areas and to the open shelf variety of tidal sand ridges in particular, cannot be ascertained at this time, and further work is required.

3.3 Summary

Over the course of the 1971, 1973 and 1974 field seasons, a total of 1,275 vertical velocity profiles were collected (Appendix 1) from 34 stations: 9 on Big Bar, 14 on Diamond Bar, 6 at Economy Point, and 5 on Selmah Bar. Analysis of the profiles shows that more than two-thirds of them conform closely to a logarithmic velocity distribution (fitted by regression), in agreement with the findings of other field studies. As a result, Prandtl's Law of the Wall and associated theory for open-channel, boundary-layer flow can be used to calculate a suite of hydraulic variables (Appendix 2). Turbulent velocity fluctuations with a magnitude in the range of 2 to 8 cm/s produce a scattering of the readings about the fitted distributions and make the calculated parameters inexact estimates of the true values. This is particularly the case with the shear velocity which is derived from the slope of the regression line.

Tides in the study area are the result of a standing wave, as indicated by the nearly synchronous time of high tide and the correspondence of zero velocity with high and low water.

The tidal wave is deformed, however, so that the ebb is of longer duration than the flood, by an amount ranging from 15 to 30 minutes in the Minas Basin, and up to 1.5 hours or more at Selmah Bar.

The current directions near high water, when the bar topography is deeply submerged, are largely unaffected by the bar and channel configurations, and flow oblique to the bar crestline is common on both the flood and ebb. As the bar crests emerge, the flow is confined to the channels and a directional shift occurs, ending with a strong component of flow laterally away from the bar crest during the final minutes of the ebb. Evidence of helical flow is lacking, because more than half of the 216 profiles examined do not exhibit the directional variation between bottom and surface currents expected of helical flow.

The distributions of current speed and shear velocity over a tidal cycle are complex and vary from place to place. During the ebb tide, two periods of high values are commonly seen, one within the first two hours after high water, and the other roughly coincident with the emergence of the bar crest, which channelizes the flow. In other areas, only a single, long period of essentially constant current speed is observed. At Economy Point, the exposure of bedrock ledges to the east of the headland produces a sudden drop in current speed and shear velocity, presumably by deflecting the currents to the south around the sand bars. On the flood at most locations,

there is only a single peak in the distributions of these parameters, which generally occurs in the first half of the tide. Both current speed and shear velocity increase as the tidal range increases.

Despite the need to maintain continuity, the current strengths of the flood and ebb are unequal at almost all stations, producing a dominant direction of water and sediment discharge. These time-velocity asymmetries between the flood and ebb are believed to result primarily from the influence of the bathymetry. Inertial effects produce strong current flow on the upstream side of bars oriented obliquely to the flow, and weak currents on the downstream side. Current reversals lead, therefore, to opposing directions of dominance on opposite sides of bar crests, and also on either side of channel axes that are curved, or are oblique to the main flow. Other factors contributing to the generation of time-velocity asymmetries are the asymmetry of the tidal wave, and the concentration of a large part of the ebb in the channels.

On Big Bar, the fastest currents, highest shear velocities, and total energies are all located over the north-west corner of the bar and in the southern channel. These two areas are separated by a band of weaker flow that stretches in a southwesterly direction across the bar. All areas north of the bar crest are ebb-dominated and it is predicted that the west end and much of the south side should be flood-dominated, although the current data do not provide conclusive evidence of this.

All parameters studied show that Diamond Bar is flood-dominated over all of its north side, and ebb-dominated along the southern edge and at the east end on the west side of the major swatchway. On both the flood and ebb, the fastest currents are located in the channels and the swatchways, but the flows are particularly strong in the southern channel. Lower energy conditions prevail over the topographically higher areas, and alternate their position between the north and south sides of the crest as the flow reverses from ebb to flood.

The currents at Economy Point display an increase in strength radially outward from the headland during both the flood and ebb, with the highest values of most quantities present on the southeast corner of East Bar, and on the southwest corner of Centre Bar. Lack of control, plus much unreliable data resulting from the large amount of scatter in the profile readings, does not allow the clear delineation of ebb and flood-dominated areas. The blind ebb channel on East Bar and the crestal area of Centre Bar are apparently ebb-dominated, whereas the region between East and Centre Bars, and the north side of East Bar are flood-dominated, according to the data. It is predicted that all of East Bar, excluding the blind channel, and the northwestern part of Centre Bar experience flood-asymmetric residual transport, and that the southeast corner of Centre Bar is ebb-dominated.

On Selmah Bar, the currents for both the ebb and flood are strongest west of the major swatchway, and particularly to the north of the crest. Along the south side of the bar, there is a general eastward decrease in current activity, because this channel terminates at the east end of the bar. This fact, combined with the shielding afforded by the bar crest, results in a flood dominance for the entire south side of the bar. Flood currents are also stronger over much of the western end of the bar as well. An area of ebb dominance is indicated for the eastern half of the northern side.

Despite the local variations just described, it is evident that Diamond Bar experiences the most energetic conditions of any of the bars studied. Only the west end of Selmah Bar has comparable currents. In contrast, Big Bar and Economy Point are the sites of weak current activity, with total energies in the order of one-tenth to one-half of those present on Diamond Bar. As a result, a wide range of dynamic conditions are available for study in the four areas.

# CHAPTER 4

# BEDFORMS

## 4.1 Introduction

The surfaces of the sand bars display a wide variety of bedforms that are an obvious response of the sediment to the tidal currents, and to other processes operating in the environment. These surface features can be subdivided into three main groups based on the processes responsible for their formation: i) primary tidal-current bedforms, produced by the flow over the complete tidal cycle; ii) low-tide modification features, attributable to changing water levels, emergence, or wave activity at low tide; and iii) winter features, that result from exposure of the sand bar surfaces to subfreezing air temperatures.

Although the study of these bed features is not the primary focus of this study, an investigation of them is important not only for a complete description of the environment, but also as an essential prerequisite to an understanding of the transport behaviour of the sediment. In this regard, the primary bedforms are of greatest significance, and most of this chapter will be devoted to a description of their external and internal form. An attempt is made to determine

the hydraulic and grain-size relationships governing their occurrence, and various aspects of their response to the tidal currents are presented. In addition, the other modification and winter features are described, with particular reference to their preservation potential.

Before proceeding with the descriptions, a brief word on the techniques used is appropriate. On all of the four major bars studied, and on many of the other smaller ones, observations and measurements of bedform morphology have been conducted on a regular grid, in order to provide a comprehensive and representative picture of the bedform types present. The terminology used in the descriptions corresponds closely with that of J. R. L. Allen (1968a) with the exception that the term length is used in place of chord for the brink-to-brink spacing of bedforms. At various locations, the internal stratification produced by the bedforms has been investigated by trenching, and through the use of large epoxy relief peels that were made using the method described by Barr, Dinkelman and Sandusky (1970). Bedform migration and scour were monitored at representative sites using metal rods and washers, following the example of Clifton (1969).

## 4.2 Primary Bedforms

### 4.2.1 Description and Distribution

The majority of the bed features observed on the bar surfaces during the summer are asymmetrical, current-generated

bedforms that correspond, in part, to the lower flow regime bedforms described from flume experiments by Simons and Richardson (1961) and Simons, Richardson and Nordin (1965a). Unlike these authors, who distinguish only two types of lower flow regime bedforms, three major types are recognized here: i) current ripples; ii) sand waves; and iii) megaripples, of which the last two are areally most abundant. Upper flow regime features are not common as a primary bed configuration, except in a few channel locations at low tide.

Asymmetrical ripples, defined as having heights of less than 4 cm and lengths less than 60 cm (J. R. L. Allen, 1968a), are present on virtually all parts of every bar. In most cases, they are not believed to be the primary bedform, but are produced during the final few minutes of the ebb tide, while current speeds are low, just before emergence. Because of this, ripples will also be discussed in the section dealing with low-tide modification features. In two restricted areas (Figure 4.3), one on the south side of Big Bar, and the other at the extreme eastern end of Selmah Bar, ripples exist as the only bed feature, as evidenced by the internal stratification (Figure 4.16E) and by the lack of deep scouring. The ripples exhibit a wide variety of three-dimensional shapes, and are commonly modified by wave activity during emergence. The sediment in both areas of ripple occurrence is fine sand.

Large-scale bedforms are produced by the tidal currents on all of the remaining bar surfaces. In this study, the distinction is made between two types, megaripples (van Straaten, 1953, p.1) and sand waves (Boothroyd and Hubbard, 1972; Klein, 1970), on the basis of morphological differences similar to those employed by Boothroyd and Hubbard (1972) to separate dunes from sand waves, and by Costello (1974) to distinguish between dunes and "bars".

In the traditional view of bedforms, as expressed by J. R. L. Allen (1968a), Allen and Collinson (1974) and Simons and Richardson (1961) among others, all large-scale bedforms with dimensions greater than those of ripples are considered to be a single bedform type, with a common mechanism of formation. A number of workers studying the modern tidal sediments (Boothroyd and Hubbard, 1972; Dalrymple et al, 1975; Klein, 1970; McCave, 1971; Reineck, 1963), however, distinguish at least two types of large-scale bedform, based most commonly on a length criterion. A recent flume study by Costello (1974; see also Southard, 1975) is the first to provide experimental evidence for the existence of a second large-scale bedform in addition to dunes. The observations presented below appear to support this contention, but much more work is necessary before the true significance of sand waves is established conclusively.

The external morphological appearance of the bedforms, although somewhat subjective, provided the initial grounds on which megaripples and sand waves were distinguished in this study. As will be shown, however, these morphological differences are associated with other features that suggest that a real (genetic) distinction has been made.

Megaripples (Figure 4.1) are characterized by a more irregular appearance than sand waves. Megaripples are commonly sinuous in plan view, but straight, catenery, and lunate varieties can be found. Large megaripples generally show remarkable lateral continuity of their crestlines (Figure 4.1E), in comparison to dunes from other environments, but smaller examples are more commonly less continuous and more three-dimensional (Figure 4.1A). The elevation of the crest- and troughlines is also irregular (Figure 4.1C), primarily due to the presence of scour pits in the troughs, separated by weakly developed spurs. In vertical profile, megaripples appear steeper than sand waves, and have a lee face that is at or near the angle of repose of the sediment, unless modified by emergence features or wave activity. The summit point is located either at the brinkpoint, or more commonly a short distance behind, so that a crestal shoulder is developed.

Individual sand waves (Figure 4.2) appear to show a much greater regularity than do megaripples. In plan view, sand waves are straight to sinuous (Figures 4.2A and 4.2C,

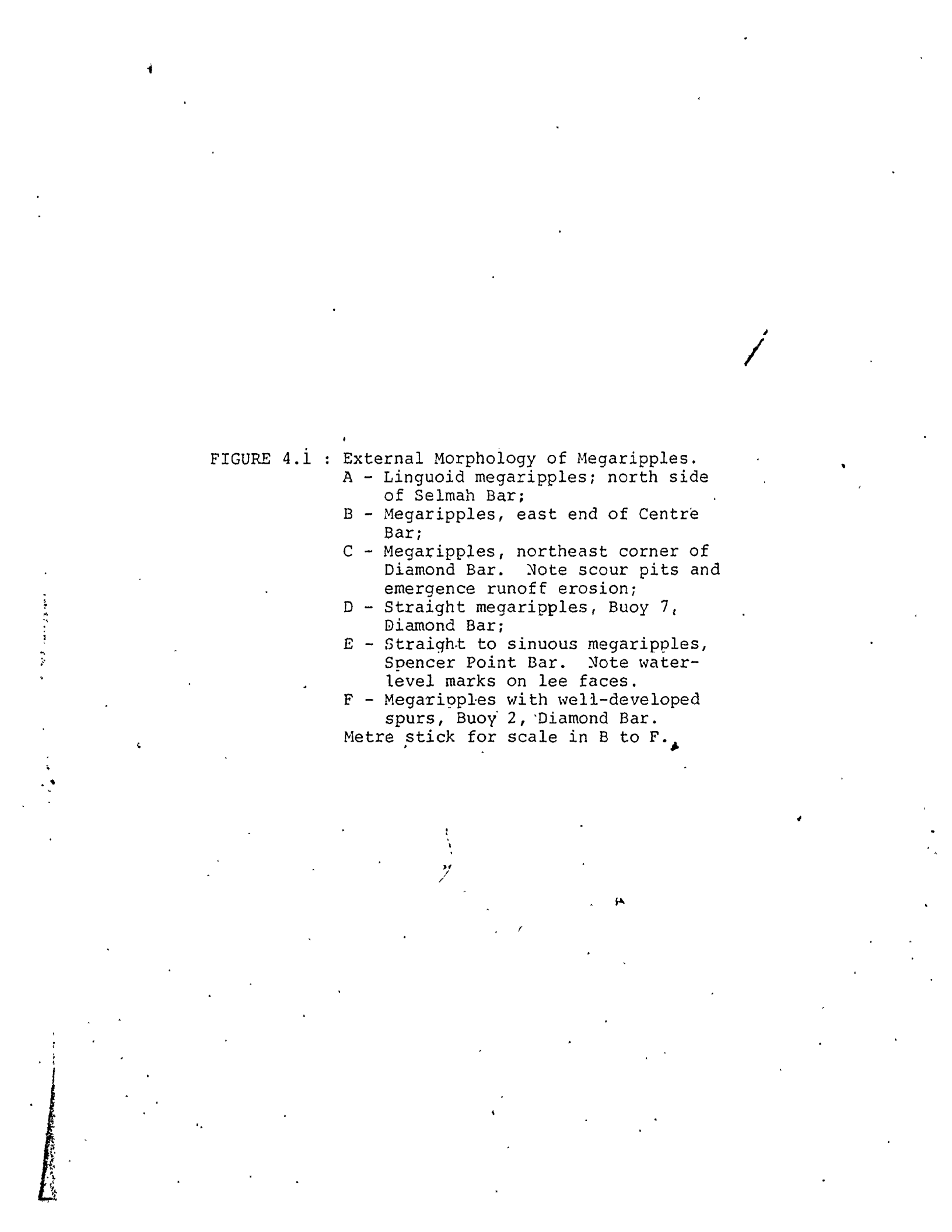

FIGURE 4.1 : External Morphology of Megaripples.
A - Linguoid megaripples; north side of Selmah Bar;
B - Megaripples, east end of Centre Bar;
C - Megaripples, northeast corner of Diamond Bar. Note scour pits and emergence runoff erosion;
D - Straight megaripples, Buoy 7, Diamond Bar;
E - Straight to sinuous megaripples, Spencer Point Bar. Note water-level marks on lee faces.
F - Megaripples with well-developed spurs, Buoy 2, Diamond Bar.
Metre stick for scale in B to F.

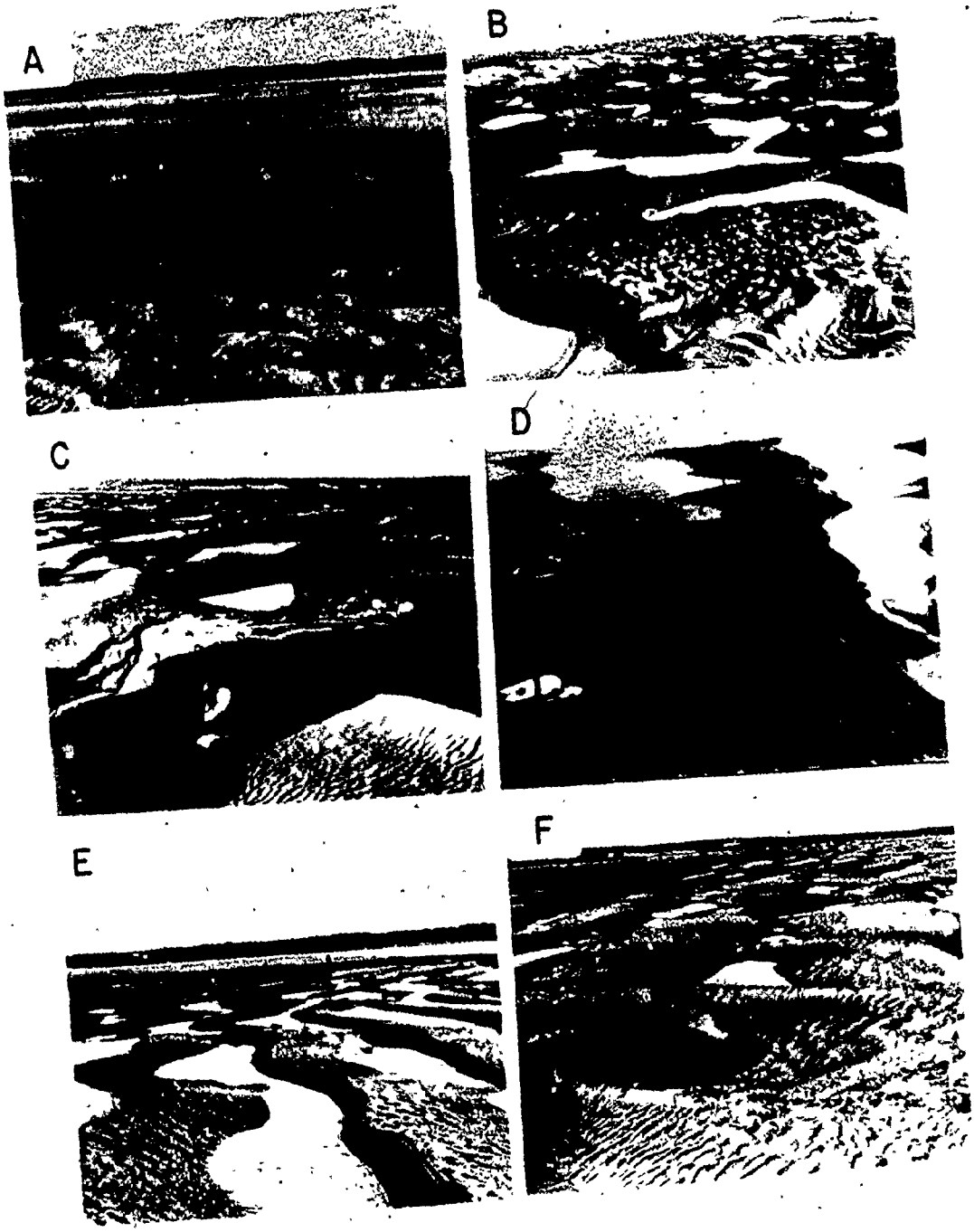
A
B
C
D
E
F

FIGURE 4.2 : External Morphology of Sand Waves.
A - Megarippled sand waves, Spencer Point Bar. Megaripples show wave modification. Figure for scale.
B - Megarippled sand wave, East Bar, at spring tide.
C - Rippled sand wave, Buoy EP 4, Economy Point. Note absence of scour pits.
D - Same location as B, at neap tide.
E - Rippled sand wave, crest of Big Bar. Note toesets and absence of scour pits.
Metre stick for scale in C to E.

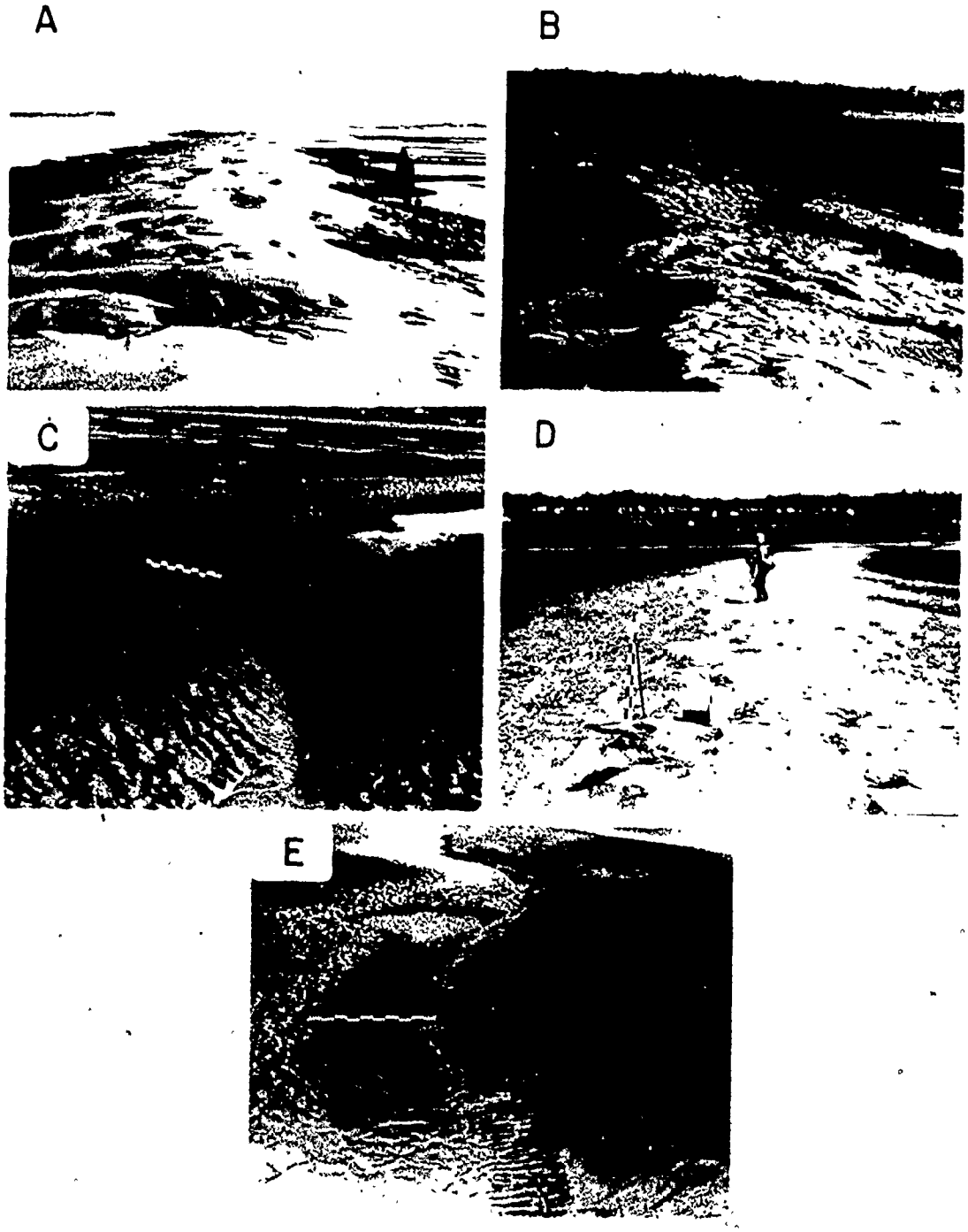
A
B
C
D
E

respectively), or more rarely exhibit a catenary shape. The crestlines show good lateral continuity in most cases. Crest- and troughlines are very uniform in elevation, due to a complete absence of scour pits (Figures 4.2C and 4.2E). Most sand waves are larger than megaripples, but some are of equivalent size. In all cases, sand waves appear less steep than megaripples. Although some small sand waves have slip faces (Figure 4.2E), most of the larger examples have lee faces that are much less than the angle of repose (Figures 4.2A and 4.2D), with inclinations of about $20^{\circ}$ being most common. A few sand waves have rounded, symmetrical profiles, with slopes of less than $10^{\circ}$.

A part of the greater apparent regularity of sand waves, particularly in plan view, may be an illusion produced by the larger size of sand waves. Measurements of the sinuosity index (SI = ratio of the span to the crestline length) and the horizontal form-index (HFI = ratio of the span to the length) (J. R. L. Allen, 1968a, p.63) have been made on some large megaripples and sand waves on Selmah Bar, using vertical air photos taken in 1972. Both parameters show considerable overlap between the bedform types, and the differences in the mean values are small. The data indicate, however, that the measured megaripples (SI = 0.98) are straighter than the sand waves (SI = 0.94), whereas the sand waves (HFI = 10.06) are more continuous than the megaripples (HFI = 9.30). The measurements for megaripples are biased against the smaller,

more three-dimensional forms, because they could not be seen on the air photos used. As a result, further field measurements are necessary to clarify the possible differences in plan shape between megaripples and sand waves.

Using the above criteria, there is generally little problem in distinguishing between megaripples and sand waves. There are, however, features that are transitional between megaripples and small sand waves, and an arbitrary assignment must be made in these instances. In general, the larger sand waves are more clearly distinct from megaripples than are smaller examples, because these large features commonly have small to intermediate size megaripples developed on them (Figures 4.2A and 4.2B). Smaller sand waves generally do not have well-developed megaripples superimposed on them, but instead are covered by ripples (Figures 4.2C and 4.2E) and/or very small dunes that are transitional in size with ripples. In the sequence of bedforms outlined by Costello (1974), in which "bars" (sand waves) are supposedly transitional between ripples and dunes (megaripples), the superposition of megaripples on sand waves presents a problem and Costello (1974) suggests that the megaripples are a metastable phase. For this reason, it seems appropriate to distinguish between those sand waves bearing obvious megaripples, called megarippled sand waves, and those with ripple-scale bedforms, rippled sand waves, in the subsequent discussions.

The areal distribution of these various bedform types are outlined in Figure 4.3, and can also be seen in the air photos reproduced in Figure 4.4. Examination of these figures shows that rippled sand waves, megarippled sand waves and megaripples all occupy distinct areas, as determined from observations made on a gridded network, which suggests that the distinctions are indeed real. If the distributions had been more irregular, then the validity of the distinctions could have been questioned. In the figures, lateral transitions between all three types of large-scale bedform can be found: rippled to megarippled sand waves; rippled sand waves to megaripples; and megarippled sand waves to megaripples.

On Big Bar (Figure 4.3A), a simple progression is seen from rippled sand waves on the bar crest, through megaripples to megarippled sand waves on the northwestern arm of the bar. Although the boundary between the rippled sand waves and megaripples is not obvious on the air photo (Figure 4.4A), it can be seen in other, oblique air photos. The megarippled sand waves are clearly visible in Figure 4.4A.

Diamond Bar (Figures 4.3B and 4.4B) shows an even simpler pattern than Big Bar. Megaripples cover most of the bar surface, and all of the southern channel. Very large megarippled sand waves, which reach maximum lengths and heights of 350 metres and 3.5 metres respectively, are present on the north-central part of the bar, and extend into the subtidal portion of the channel, as is evident in the bathymetric map

FIGURE 4.3 : Areal Distribution of Bedform Types.
A - Big Bar; B - Diamond Bar; C - Economy Point;
D - Selmah Bar. M = megaripples; MSW = megarippled sand wave; RSW = rippled sand wave; R-F = rippled or flat bed; R = ripples. Dots indicate current metre stations.

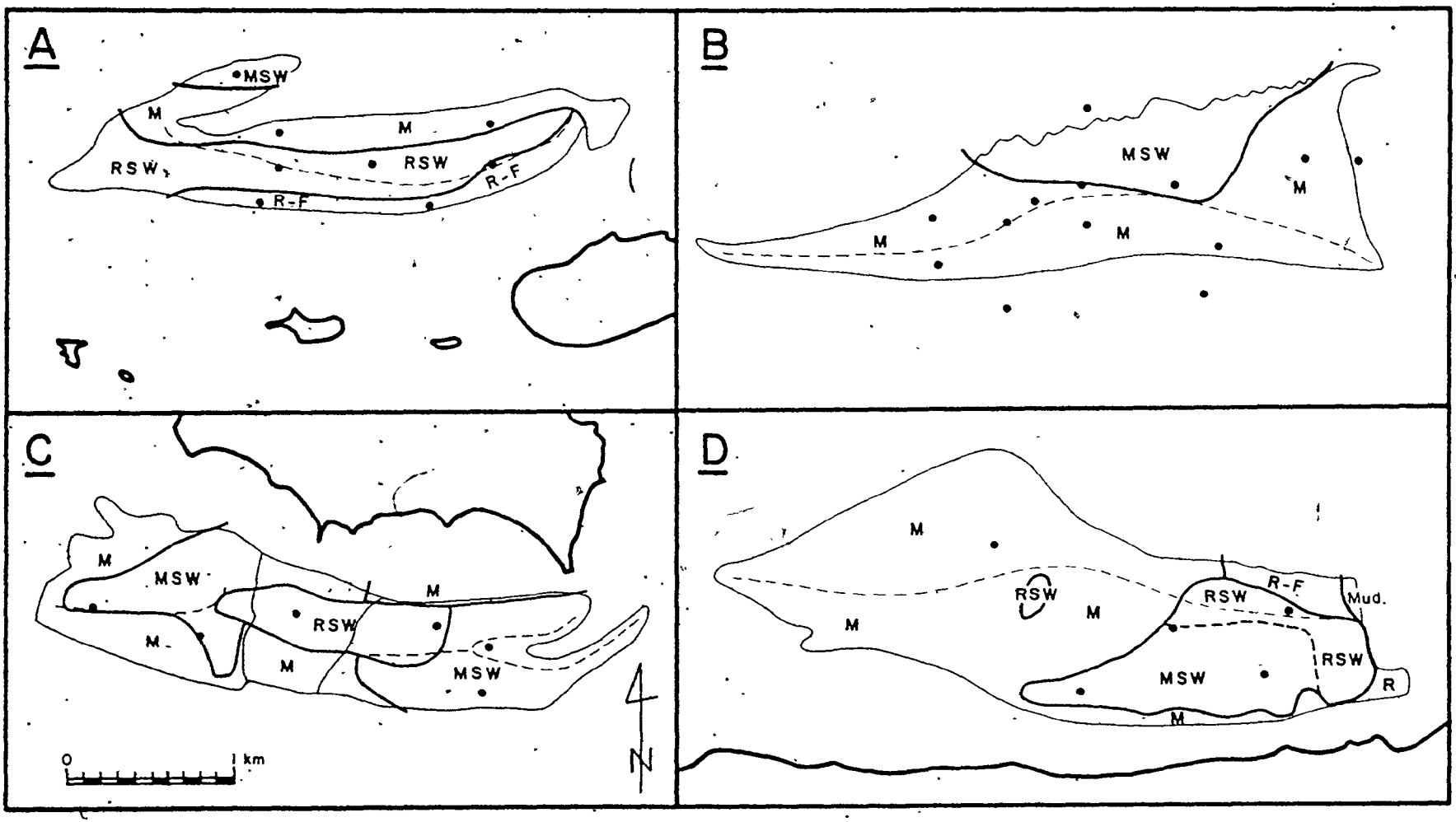
A
MSW
M
M
RSW
RSW
R-F
R-F
B
MSW
M
M
M
C
M
MSW
M
RSW
M
M
M
MSW
0
km
N
D
M
RSW
R-F
RSW
Mud.
M
M
RSW
MSW
R
M

FIGURE 4.4 : Vertical Air Photos of the Study Bars.

A - Big Bar; B - Diamond Bar;

C - Economy Point; D - Selmah Bar.

Flown June 5, 1973 at spring low tide.

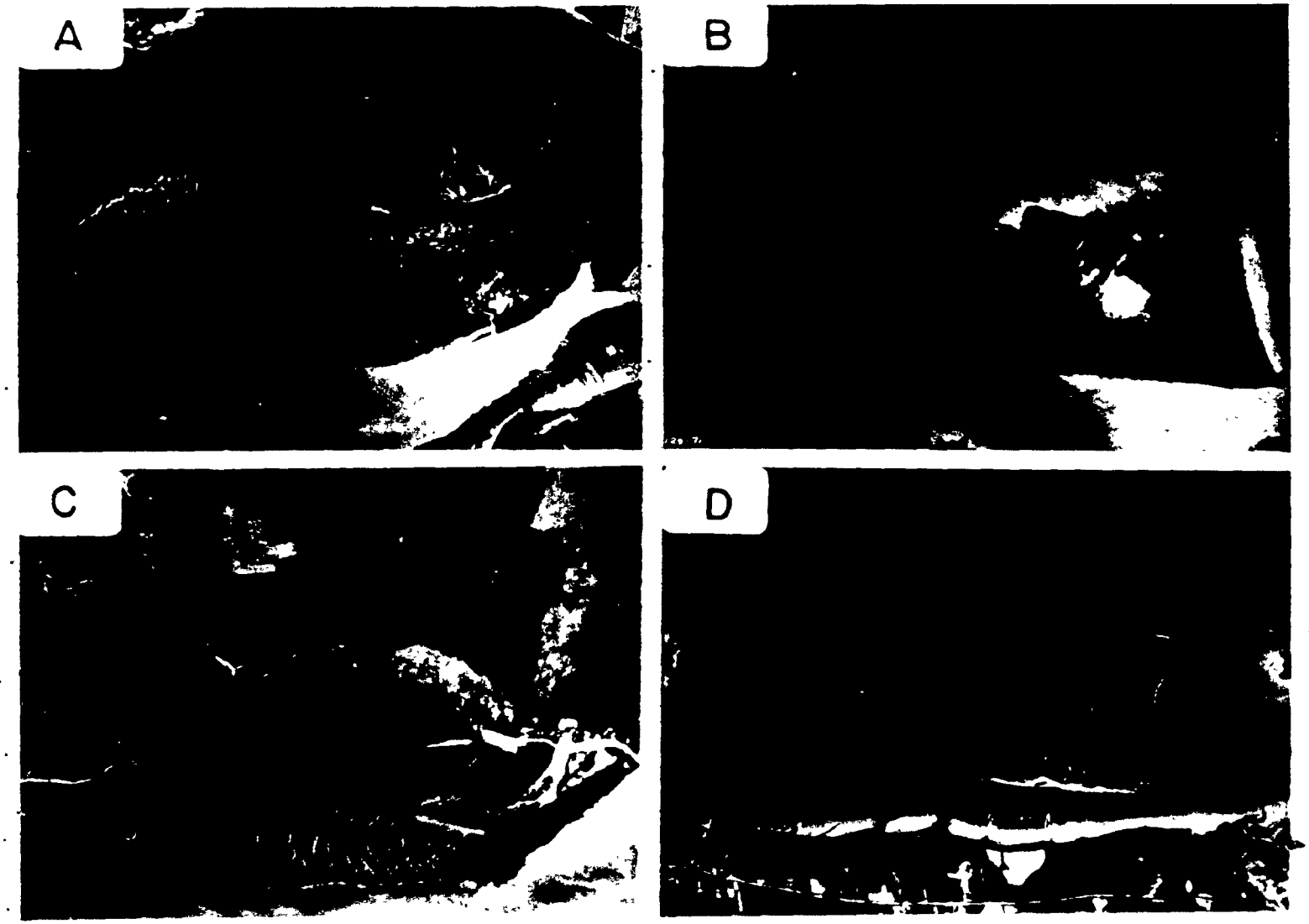
A
B
C
D

of Diamond Bar (Figure 2.15). These features are also notable for their very straight crests, and their skewed orientation with respect to both ebb and flood current directions (Figure 3.15A). This is a common characteristic of large sand waves in other areas as well.

Economy Point (Figures 4.3C and 4.4C) shows the most complex distribution of bedform types present on any of the bars. Sand waves are developed in most areas, and megaripples are present on most of them. Rippled sand waves are present in the central part of the complex, but then only at low to intermediate tidal ranges, because megaripples appear in most of these areas at high spring tides. Megaripples by themselves are extensively developed only on parts of Centre Bar. The sand waves on East Bar are somewhat unusual in several respects, although they do show the basic characteristics described above. In plan view (Figure 4.4C), the arcuate pattern of crestlines that wrap around the nose of the blind ebb channel, combined with the oblique superposition of smaller-scale, sand-wave-like features is not seen elsewhere. Also, the lack of a consistent direction of asymmetry and the presence of symmetrical forms is in contrast to the regular pattern of asymmetry observed in other areas.

On Selmah Bar, a large field of sand waves is developed on the southeast portion of the bar surface. Most of these are megarippled, but areas near the bar crest and at the eastern end possess only the rippled type. Another area of

rippled sand waves is present immediately to the west of the major swatchway, surrounded by megaripples that cover all of the western half of the bar.

To this point, the distinction between megaripples and sand waves has been entirely descriptive and qualitative. Most authors, however, including Dalrymple et al (1975) and Knight and Dalrymple (1976), give specific size criteria for the separation between megaripples and sand waves. Figure 4.5 shows the frequency distributions of length and height for the various bedform types on each of the major study bars, plus the total distribution for all areas investigated by the author. Table 4.1 summarizes the means and standard deviations of these distributions. It should be noted that the length and height distributions of sand waves are biased towards smaller values due to the difficulty of measuring some of the very large features encountered. In particular, this accounts for the absence of sand wave values in the distributions for Diamond Bar.

In Table 4.1, it is evident that sand waves have average lengths and heights that are larger than those of megaripples. In addition, the standard deviations of the sand wave distributions for lengths and height are several times greater than the corresponding values for megaripples. All of these results, with the exception of the larger height of sand waves as compared to megaripples, is in complete accord with the observations of Costello (1974, Figures 3.9

FIGURE 4.5 : Frequency Distributions of Bedform Lengths (A) and Heights (B). Number of megaripples (Nm) and sand waves (Nsw) contributing to each distribution shown. Range of lengths and heights given only for sand waves (S.W.) on Diamond Bar.

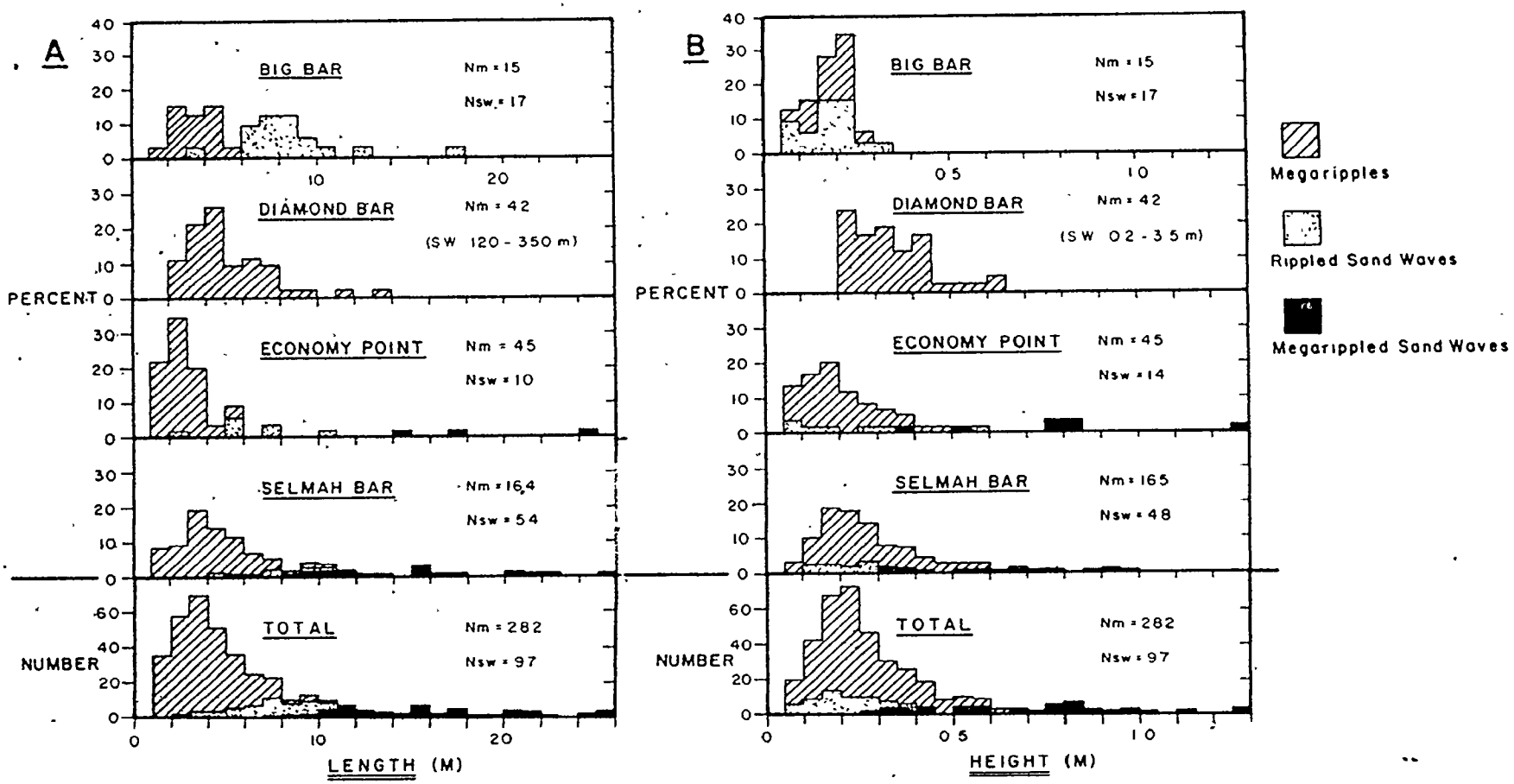
A
BIG BAR
Nm = 15
Nsw = 17
DIAMOND BAR
Nm = 42
(SW 120 - 350 m)
ECONOMY POINT
Nm = 45
Nsw = 10
SELMAH BAR
Nm = 16.4
Nsw = 54
TOTAL
Nm = 282
Nsw = 97
PERCENT
NUMBER
LENGTH (M)
B
BIG BAR
Nm = 15
Nsw = 17
DIAMOND BAR
Nm = 42
(SW 0.2 - 3.5 m)
ECONOMY POINT
Nm = 45
Nsw = 14
SELMAH BAR
Nm = 16.5
Nsw = 48
TOTAL
Nm = 282
Nsw = 97
PERCENT
NUMBER
HEIGHT (M)
Megaripples
Rippled Sand Waves
Megarippled Sand Waves

TABLE 4.1 : Summary of large-scale bedform size characteristics. The frequency distributions for all areas are given in Figure 4.5.

| Bar | | Megaripples | | Sand Waves | |
|---|---|---|---|---|---|
| | | Length (m) | Height (m) | Length (m) | Height (m) |
| Big Bar | mean | 3.64 | 0.177 | 8.60 | 0.185 |
| | (st.dev.) | (1.04) | (0.058) | (3.00) | (0.074) |
| Diamond Bar | mean | 5.36 | 0.346 | | |
| | (st.dev.) | (2.37) | (0.110) | | |
| Economy Point | mean | 2.70 | 0.191 | 10.20 | 0.515 |
| | (st.dev.) | (1.07) | (0.089) | (6.81) | (0.386) |
| Selmah Bar | mean | 4.43 | 0.277 | 13.34 | 0.407 |
| | (st.dev.) | (2.07) | (0.145) | (6.31) | (0.253) |
| Grand Total | mean | 4.18 | 0.264 | 12.80 | 0.436 |
| | (st.dev.) | (2.08) | (0.136) | (7.58) | (0.318) |

and 3.10) for his bars and dunes. The large heights of intertidal sand waves may be a result of the reversing flow.

Further inspection of Table 4.1 and Figure 4.5 shows that the average size of both megaripples and sand waves varies from area to area. The megaripples and sand waves on Diamond Bar are the largest in terms of both length and height, while Big Bar possesses the smallest sand waves. Megaripple heights are least on Big Bar, but megaripple lengths are smallest on Economy Point.

On the basis of the histograms (Figure 4.5), it is difficult to detect any natural and universal division in either length or height between sand waves and megaripples. In the combined distributions, an almost complete overlap of lengths and heights can be seen; however, a better separation of megaripples and sand waves is possible on the basis of length than can be obtained using height. This overlap is also evident in each individual area, with the exception of the lengths on Big Bar, where a clear distinction can be made at a value of 6 metres. (It is notable that this is the same figure cited by Boothroyd and Hubbard (1972) to separate their dunes and sand waves.) The overlap indicates that no single size parameter can be used to classify the bedforms from a number of areas.

A bivariate plot of height versus length (Figure 4.6) for megaripples and sand waves does, however, permit a nearly perfect separation of the two forms using the relationship

$$\text{Height} = 0.072 \ \text{Length} - 0.210 \qquad (4.1)$$

where height and length are both expressed in metres. This relationship misclassifies only 13 out of 379 cases, or 3.4% of the observations. This result might have been partially expected, because steepness was mentioned above as a distinguishing criterion. In most cases, megaripples have ratios of length to height of less than 30, and in three-quarters of the examples, the steepness is less than 20. By contrast, only exceptional sand waves have steepness values of 20 or less, and nearly solitary features with length to height ratios as high as 150 have been observed.

In Figure 4.6, the distinction has also been made between rippled and megarippled sand waves. As mentioned above, rippled sand waves are generally smaller than those bearing megaripples. Although there is overlap in the sizes of the two varieties of sand wave, a reasonable separation can be achieved using a height of 0.3 metres as the dividing line.

The internal stratification of megaripples (Figure 4.7) and sand waves (Figure 4.8) reflects the external morphology of these bedforms.

Because megaripples possess a simple avalanche face, a single set of cross-bedding, generally with a tangential base resting on an erosion surface, is the structure most commonly seen within them (Figure 4.7A and 4.7B). The sinuous

FIGURE 4.6 : Plot of bedform length versus height. Data from all studied areas included. Thin diagonal lines give steepness ratios (length/height). Heavy diagonal line is best dividing line between megaripples and sand waves: only 13 of 379 points misclassified.

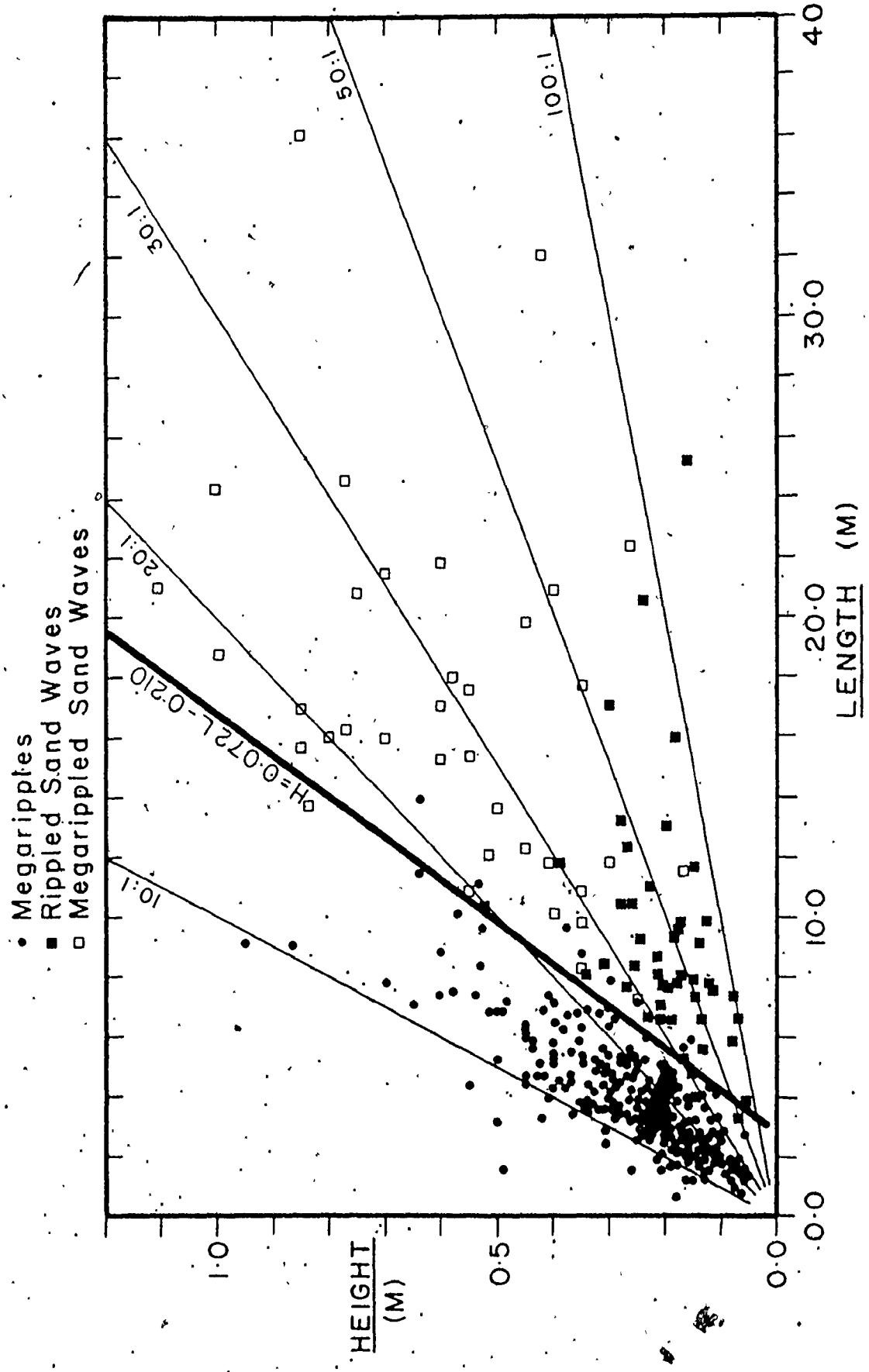
• Megaripples
■ Rippled Sand Waves
□ Megarippled Sand Waves
H=0·072L-0·210
1:10
20:1
30:1
50:1
100:1
HEIGHT (M)
LENGTH (M)
0·0
0·5
1·0
10·0
20·0
30·0
40·0

FIGURE 4.7 : Internal stratification of megaripples.
A - Peel perpendicular to megaripple crest, Buoy 2, Diamond Bar. Ripple cross-lamination at surface.
B - Peel perpendicular to megaripple crest, Buoy 3, Diamond Bar. Note tangential base. Ripple cross-lamination at surface.
C - Peel parallel to megaripple crest, Buoy 3, Diamond Bar. End-on view of scour fill. Flow out of page.
D - Peel perpendicular to megaripple crest, Buoy 5, Big Bar. Note low-angle, down-current-dipping laminae formed beneath crestal shoulder.
Scale divisions are 5 cm. throughout.
Ebb flow to the left in A, B and D.

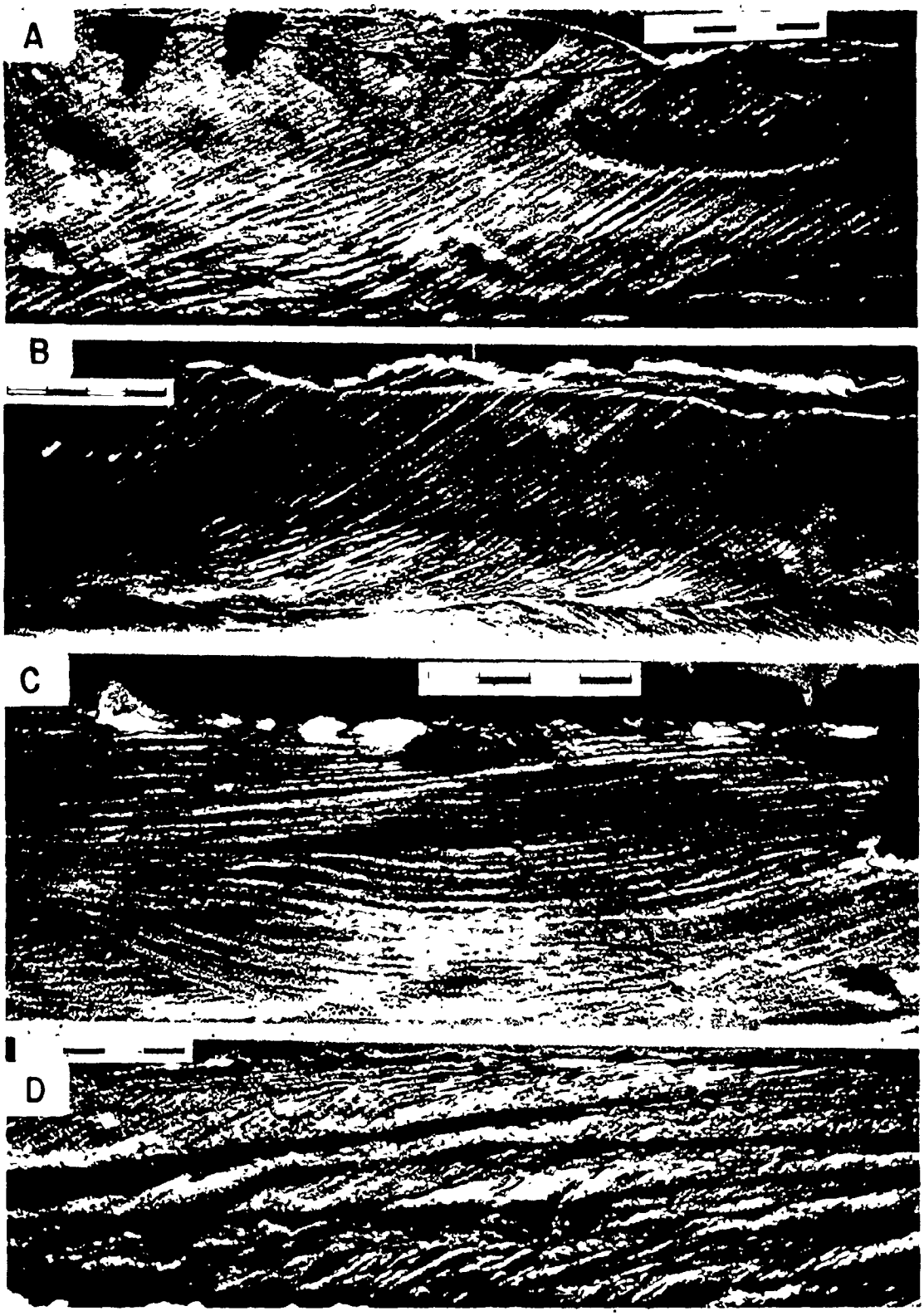
A
B
C
D

FIGURE 4.8 : Internal stratification of sand waves.
A - Peel perpendicular to sand wave crest covered with small megaripples, Buoy EP 6, Economy Point. Note composite internal stratification.
B - Peel perpendicular to crest of megarippled sand wave, Saints' Rest Bar. Note composite internal stratification.
C - Peel perpendicular to rippled sand wave with a slip face, Buoy 8, Big Bar. Reactivation surfaces dip to the west at 15° to 20°.
D - Peel perpendicular to sand wave, near Buoy 2, Big Bar. Toesets well developed. "Strings" are impregnated Paraonis burrows.
Scale divisions are 5 cm throughout.
Ebb flow to the left in all peels.

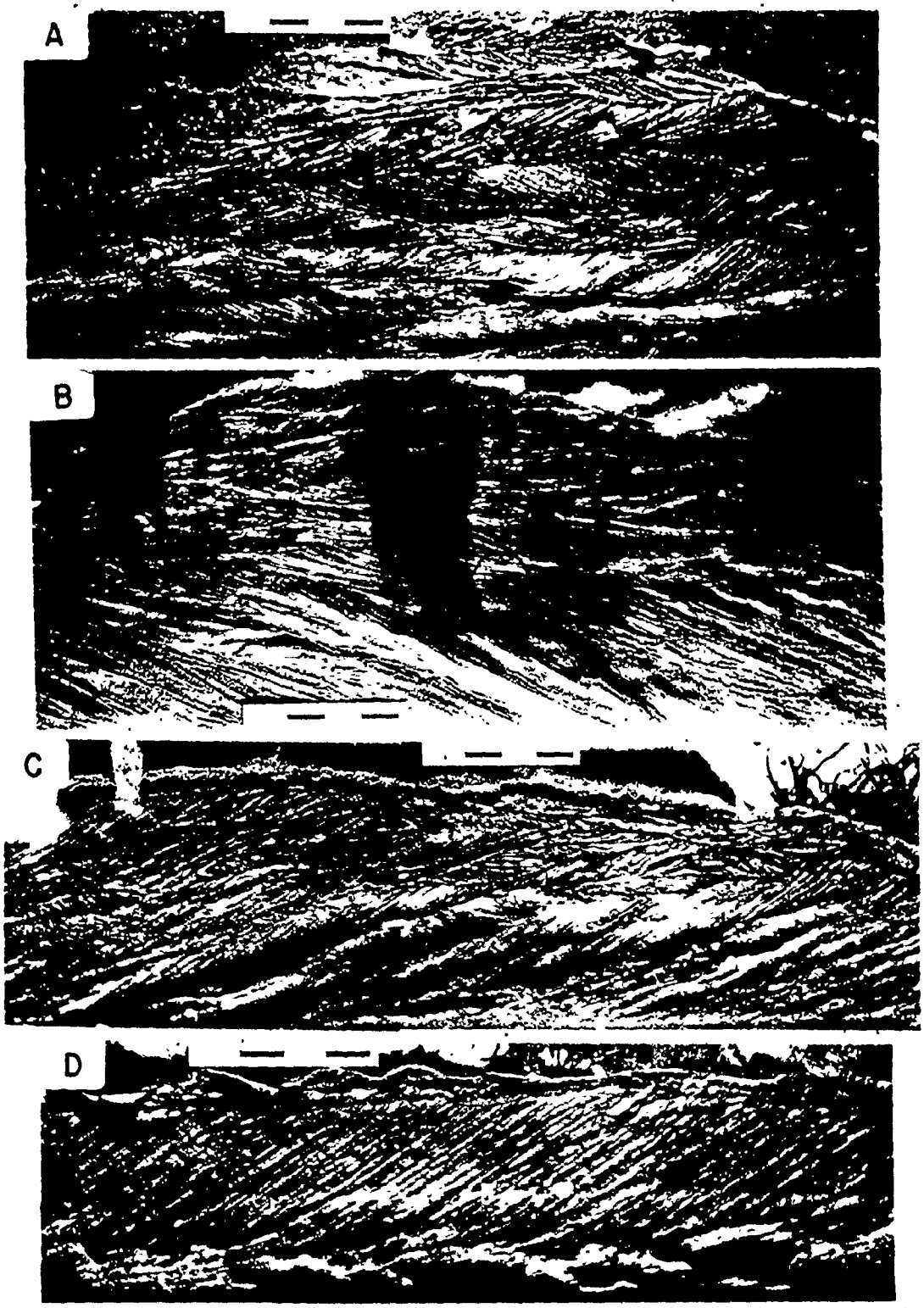
A
B
C
D

to lunate shape of the megaripples is more likely to result in broad, open, trough cross-bedding (Figure 4.7C) than in planar-tabular sets. It has also been noted that low-angle cross-stratification, with dips of less than $6^{o}$ down-flow is produced during the migration of megaripples that have a distinct crestal shoulder (Figure 4.7D). Reactivation surfaces, to be discussed more fully in the next section, commonly disrupt the lateral continuity of the cross-bedding.

The lack of a slip face on most sand waves, plus the migration of the superimposed ripples and megaripples over the sand wave form, results in internal stratification which is generally of a composite nature (Figures 4.8A and 4.8B). The individual sets are produced by the superimposed bedforms, and therefore have thicknesses that are less than the height of the sand wave. As a result, it would be difficult to establish the presence of the sand wave form from the preserved stratification, unless the outline of the sand wave profile were recognizable in some fashion, possibly because of the presence of reactivation surfaces. In this case, internal structures resembling the down-current dipping cross-stratification of Banks (1973) might be produced, similar to that shown in Figure 4.8C. Bipolar, herring-bone, cross-stratification is not uncommon in sand waves. Some small, rippled sand waves, such as those at the crest of Big Bar (Figure 4.3A) do have lee faces at close to the angle of

repose, and single cross-bed sets, with closely spaced reactivation surfaces, are produced (Figure 4.8D). In the example shown, well-developed bottomset beds are present (see also Figure 4.2E).

### 4.2.2 The Dynamic Behaviour of Bedforms

In the above descriptions of the external morphology and internal structures of the primary current bedforms, only the most basic features are presented, and the responses of the bedforms to speed and directional unsteadiness in the flow are not considered. In this section, a number of aspects of bedform behaviour will be discussed, including asymmetry reversals, bedform life spans, and net migration rates and directions.

The primary morphological change in the bedforms brought about by the $180^{\circ}$ swing in current direction, that occurs twice in every tidal cycle, is a reversal in bedform asymmetry; a reversal in morphology that reflects the reversal in sediment transport direction. Suppose, as is shown in Figure 4.9A, that a flood-asymmetric megaripple exists at high tide. With the commencement of the ebb, the brink of the flood bedform is eroded and the sediment is deposited on the flood stoss side in the form of a small cap of ebb-oriented cross-strata (Figure 4.9B). As erosion of the flood lee side and of the flood stratification continues, the ebb cap grows in size, until the point is reached when the entire flood profile has been either eroded or buried, and the

FIGURE 4.9 : Schematic Bedform Reversal.
A - Flood megaripple at high tide.
B - Initial erosion of flood brink and formation of small ebb cap early in the ebb tide.
C - External form completely reversed but flood core remains. Note overly steep lower portion of stoss side.
D - Flood core no longer present, and reversal is complete.
E - Partially reversed flood megaripple containing several reactivation surfaces.

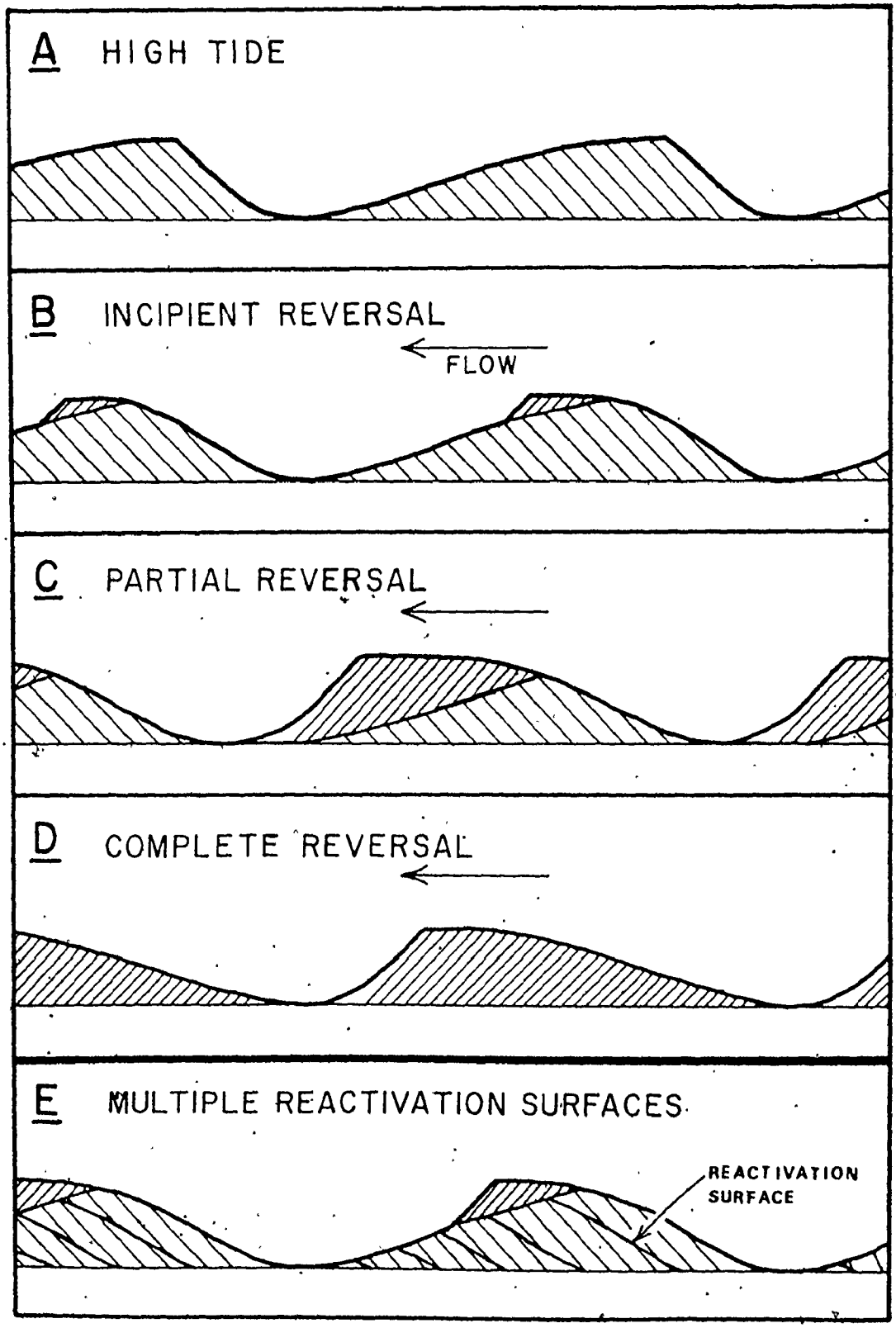
A HIGH TIDE
B INCIPIENT REVERSAL
FLOW
C PARTIAL REVERSAL
D COMPLETE REVERSAL
E MULTIPLE REACTIVATION SURFACES
REACTIVATION SURFACE

FIGURE 4.10 : External form and internal stratification of incompletely reversed megaripples.
A - Incipient reversal of flood megaripple, Saints' Rest Bar.
B - Partial reversal of flood megaripple with base of ebb stoss visible beneath metre stick.
C - Peel perpendicular to megaripple crest shown in A. Six reactivation surfaces can be seen.
D - Peel perpendicular to ebb megaripple crest, near Buoy 3, Diamond Bar.
Scale divisions 5 cm in C and D.
Ebb flow to the right in A and B, to the left in C and D.


A
B
C
D

external form is completely ebb-oriented (Figure 4.9C). A remnant of the original flood bedform may still be present in the core of the new ebb feature. Continued migration of the ebb bedform will eventually cause the total erosion of all pre-existing stratification (Figure 4.9D). When the currents again reverse at the beginning of the subsequent flood tide, the above sequence of changes in the bedform profile will recur. If the asymmetry reversal produced by the ebb tide only proceeds as far as the stage shown in Figure 4.9C, however, and a core of flood cross-bedding remains, then the new set of flood cross-bedding deposited by the re-established flood megaripple will be separated from the earlier set by a low-angle surface, as described by Boersma (1969). This has been called a reactivation surface (Collinson, 1970), and represents the erosional stoss side of the intervening ebb bedform (Figure 4.9E).

A complete spectrum of external and internal features illustrating the entire reversal sequence described above can be found at low tide. If the reversal stops at stage B of Figure 4.9, then a distinctive external morphology is produced (Figure 4.10A), in which the previous flood stoss side can be seen extending from beneath the ebb slip face. In addition, the stoss of the ebb form will be unusually steep, with dips of from $7^{\circ}$ to $20^{\circ}$. This feature can often be used, even when the reversal has progressed almost as far as stage C of Figure 4.9, as an indication of the presence of a remnant

flood core (Figure 4.10B), because bedforms without such cores most commonly have stoss sides which dip at $2^{o}$ to $5^{o}$. The internal stratification of these incompletely-reversed bedforms almost always shows one or more reactivation surfaces like those in Figure 4.9E. These reactivation surfaces, because they are buried ebb stosses, are generally planar or gently convex up, and dip most commonly at $7^{o}$ to $15^{o}$. The horizontal spacing between them is equivalent to the net migration of the bedform during a single tidal cycle, and the dip direction of the cross-stratification preserved indicates the dominant phase of the tidal cycle. Both ebb- (Figures 4.10C and 4.10D) and flood-produced (Figure 4.8C) reactivation surfaces can be found, depending on which half of the tidal cycle is dominant in a given area. If, however, either the flood or the ebb is capable of causing the bedform to migrate more than the length of the feature next down stream, then no reactivation surfaces will be preserved, assuming that no net accretion occurs. Examples of this are common in many areas of megaripple occurrence. The external morphology of such megaripples has already been shown in Figure 4.1, and examples of the internal stratification, consisting of a single unbroken cross-bed set are given in Figures 4.7A and 4.7B.

Most of the effects of the reversing flow described above are best developed, or are seen only in megaripples, either where they occur by themselves, or where they are

superimposed on sand waves. No sand waves are known to the author that show a complete asymmetry reversal with each half of the tidal cycle, regardless of their size. While most megaripples are ebb-oriented at low tide, due to a complete or nearly complete reversal, flood sand waves are common, bearing smaller ebb-oriented features. This low sensitivity of sand waves to the reversing flow directions is due to three factors: i) the larger average size of sand waves as compared to megaripples (Table 4.1), which means that a greater volume of sediment must be moved in order to produce an equivalent change in morphology or position of a sand wave; ii) the occurrence of sand waves in areas with lower current speeds than those characterizing areas of megaripples, as will be seen in the next section; and iii) the common occurrence of sand waves in areas where there is a strong time-velocity asymmetry.

This insensitivity to change, or inertia, of the larger bedforms is most evident in the identifiable life span of the various bedforms. If a bedform responds slowly to the flow, or more specifically, if the volume of the bedform is large relative to the sediment transport rate, then that bedform will change slowly, and will retain a recognizable form for many tidal cycles. On the other hand, if the sediment transport rate is large relative to the size of the bedform, then it may either be modified sufficiently in plan shape, or migrate far enough to lose its identity within a single tidal cycle.

Because megarippled sand waves are the largest bedforms present (Figure 4.6), they remain recognizable for the greatest length of time, and field observations show that they retain their identity for at least 3 to 4 months. Only one instance of the destruction of a large sand wave has been observed by the author. This occurred during August, 1974, when a megarippled sand wave with a height of 0.75 metres on the exposed, south side of East Bar was obliterated by 1 - 1.5 metre high waves. Study of air photos of Selmah and East Bars taken in 1972 and 1973 shows that individual large sand waves cannot, in general, be recognized with certainty after a one-year period. This is not to say that the same individuals do not still exist, but that they are sufficiently changed to make identification difficult. On Diamond Bar (Figure 4.4B), the very large sand waves that extend into the subtidal can, however, be correlated with little problem between air photos and depth-sounder records spanning the period July, 1972 to July, 1974.

In comparison to the long-term stability of large sand waves, megaripples and smaller, rippled sand waves have a much shorter recognizable life span. On the north side of Big Bar, where the mean current speeds rarely exceed 0.7 m/s, individual rippled sand waves or megaripples can be recognized on a day-to-day basis, but they do change at a sufficiently high rate that specific forms can be identified only with difficulty after periods as short as 6 to 10 tidal cycles.

New megaripples have been observed to form on the lower half of the stoss side of mature individuals where the length is larger than average. The new feature migrates forward rapidly and grows in height and length in a manner similar to that described by J. R. L. Allen (1973, Figure 3e and p.198). This often occurs at the expense of the bedform next downstream, which is commonly overtaken by the new one. On other bars where the current speeds are higher, the bedform assemblage appears to be completely changed within as little as two tidal cycles, and it is impossible to correlate bedforms from one visit to the next. It is in these areas where reactivation surfaces are never observed.

Because there exists a time-velocity asymmetry in most areas as described in Section 3.2.4, the distances migrated during each half of a tidal cycle will not as a rule be equal, due to different sediment transport capacities of the ebb and flood. This difference will take the form of a net migration of the bedforms in the direction of the residual sediment transport. As a result, information regarding the pattern of residual sediment transport can be obtained easily by observing the direction and rate of net migration of the bedforms. Unfortunately, this method cannot be used in those areas where either half of the tidal cycle is capable of reworking the entire bedform. In these areas, no remnant stratification or external form remains to permit the direction of net migration to be determined, unless the ebb

is clearly subordinate to the flood, and it is often not possible to identify the same bedform on subsequent visits. Because of this, most net migration measurements have been conducted in sand wave areas where migration rates are low.

It has been known for many years that the rate of migration of bedforms is proportional to the bedload transport rate, which is that portion of the total discharge which remains in almost continuous contact with the bed. If it is assumed that the bedforms have triangular shapes in cross-section, then the mass discharge of bedload per unit width of bed ($q_b$) is given by (after Simons, Richardson and Nordin, 1965b, equation 8, p.1):

$$q_b = \rho_s \zeta V_b (H/2) + C_1 \qquad (4.2)$$

where $V_b$ is the bedform speed, H is the bedform height, $\rho_s$ is the sediment density, $\zeta$ equals one minus the sediment porosity, and averages 55% for freshly deposited sand (Pryor, 1971), and $C_1$ is a constant of integration which can be interpreted as that portion of the total bedload that does not contribute to the migration of the bedforms, $C_1$ is assumed to have the value zero for lower flow regime conditions.

Simons, Richardson and Nordin (1965b) have found that this simple relationship yields estimates of the bedload transport for ripples and dunes under flume conditions that are in good agreement with known values. In applying equation (4.2) to the observed net migration rates of intertidal

bedforms, less reliable results are to be expected. Firstly, many of the large sand waves for which measurements are available do not have triangular shapes, and secondly, a part of the bedload may not contribute to the migration of the large sand waves that lack a slip face ($C_1 \neq 0$) because ripples and megaripples can migrate down their lee faces. Nevertheless, the results obtained should provide an informative lower limit on the rates of residual sediment transport occurring on the study bars. In the next paragraphs, the patterns and rates of computed residual sediment transport based on the migration studies will be summarized for each of the study bars, in order to complete the description of bedform behaviour in the tidal environment. A more comprehensive and detailed discussion of residual sediment transport is reserved for Chapter 6.

The longest and most complete set of migration data available comes from Big Bar, where bedform height and migration rate were monitored at Buoys 1, 5 and 6 (Figure 3.4) over a 34-day (66 tidal cycle) period spanning two neap-spring cycles (Figure 4.11). Buoys 1 and 6 are located in rippled sand waves, and Buoy 5 in megaripples (Figure 4.3), but because the results are similar at all three sites, they have been combined, and the averages only are shown in Figure 4.11.

All of the monitored bedforms moved in a westerly direction, in agreement with the ebb dominance shown by the tidal currents (Figure 3.13). The average net migration rate

FIGURE 4.11 : Variation of bedform characteristics and bedload discharge over two neap-spring cycles on Big Bar. Values are the averages of five stakes at each of Buoys 1, 5 and 6.

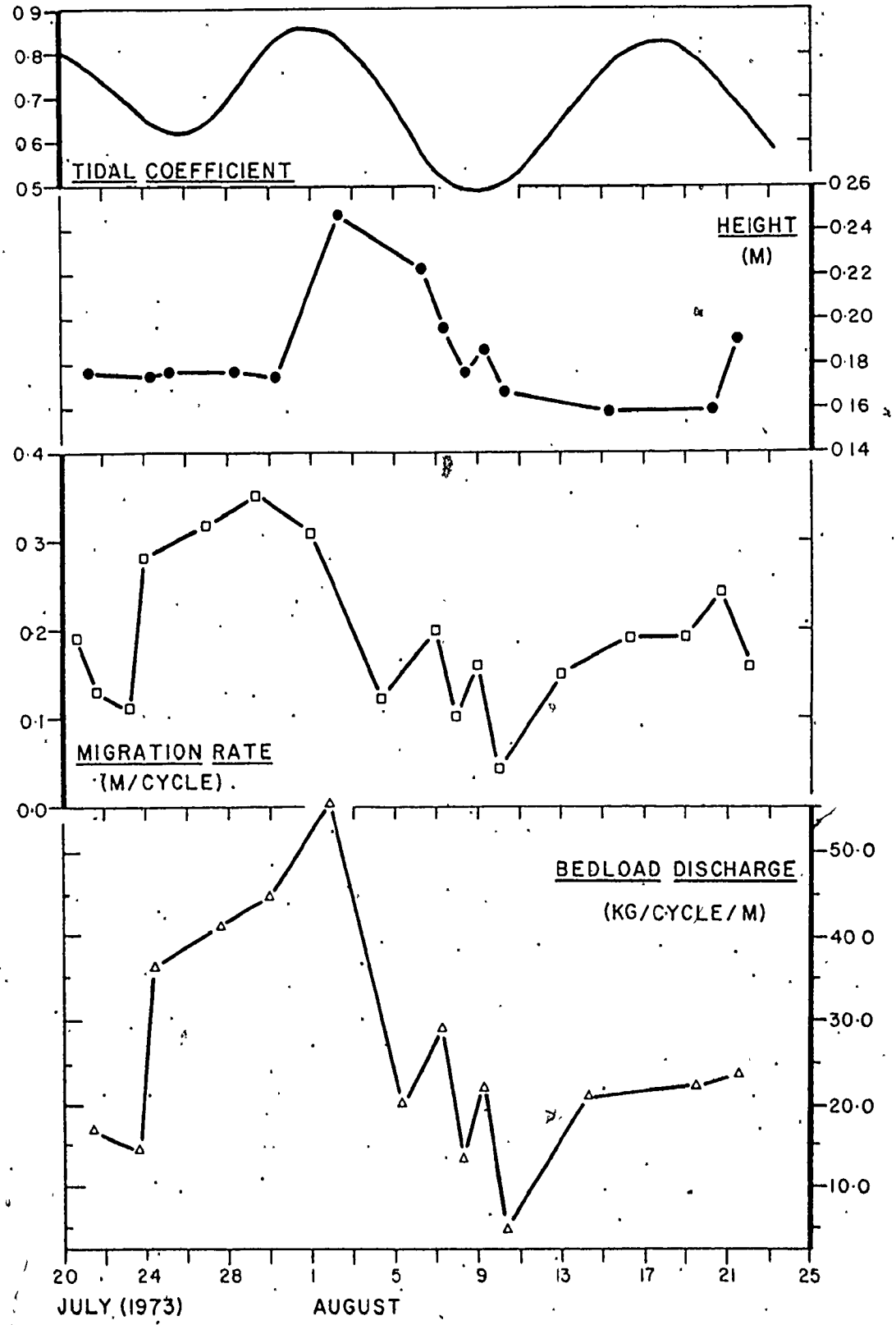
TIDAL COEFFICIENT
0·9
0·8
0·7
0·6
0·5
HEIGHT
(M)
0·26
0·24
0·22
0·20
0·18
0·16
0·14
MIGRATION RATE
(M/CYCLE).
0·4
0·3
0·2
0·1
0·0
BEDLOAD DISCHARGE
(KG/CYCLE/M)
50·0
40·0
30·0
20·0
10·0
20
24
28
1
5
9
13
17
21
25
JULY (1973)
AUGUST

and height for the entire period were 0.19 metres/tidal cycle and 0.18 metres respectively, which yield an average net bedload discharge of just under 25.0 kilograms/tidal cycle/metre width of bed. (Hereafter, these units will be abbreviated to kg/cycle for convenience, and per unit width understood unless specifically stated otherwise.) There were, however, large variations in the calculated discharge during the period (Figure 4.11), ranging from a high of 55.9 kg/cycle at the time of the highest tidal ranges, to a low of 4.8 kg/cycle during the smallest tides.

This increase in the residual unit bedload discharge with the tidal range, and therefore with the current speeds (see Figure 3.11) is explainable by the fact that the residual transport depends not only on the magnitude of the time-velocity asymmetry, but also of the absolute values of the ebb and flood velocities, because the sediment transport ($q_s$) is supposedly a function of a power of the current speed:

$$q_s \alpha \left| U_E^n - U_F^n \right| \qquad (4.3)$$

where U is a representative velocity, E and F stand for ebb and flood respectively, and n is an exponent in the range of 3 to 7. This means that for a constant difference in the measured velocities, the residual transport is greatest at spring tides when both ebb and flood current speeds are greater. Although there is a basic agreement between the variations in bedload discharge and the tidal coefficient

(Figure 4.11), there are discrepancies, particularly during the first neap and last spring tide periods which cannot be explained. A simple comparison between the residual sediment discharge estimated from bedform migration and current data, using either the time-averaged mean velocities or the maximum mean velocities in equation (4.3) (with n = 3), showed positive but statistically non-significant correlations at the 90% significance level. Much of the scatter is produced by data for Buoy 1 which shows migration rates that are less than would be expected from the velocities. This site does have the finest grain size of the three, and it could be that less of the bedload contributes to the bedform migration here than at the other stations. Another possible explanation for this is that the use of these single velocity values does not provide an accurate representation of the sediment transport capacity of the entire tidal cycle. A more detailed treatment of this problem will be given in Chapter 6.

Additional migration studies have been conducted on the large, ebb-oriented sand waves on the northwestern arm of Big Bar (Figure 4.3A). The average height of the monitored forms was 0.61 metres and the migration rate was 0.07 metres/tidal cycle, giving a residual ebb discharge of bedload of 31.0 kg/cycle, which is very similar to the results presented above for the rippled sand waves and megaripples on the main body of the bar.

On Diamond Bar, virtually the entire surface is covered by megaripples which are sufficiently mobile to preclude the determination of migration rates with any certainty. In a few instances, tentative correlations between individual bedforms on subsequent visits can be made at stations along the south side and at the extreme eastern end of the bar. In these cases, net migration rates between 1 and 2 metres/tidal cycle in the ebb direction are obtained, in agreement with the dominance of ebb currents in these areas (Figure 3.15). The associated bedform heights average 0.4 metres, giving an estimated net bedload discharge of 292.0 to 583.0 kg/cycle, which is an order of magnitude larger than the highest values obtained on Big Bar. These values must be regarded with considerable caution, however, due to the uncertainty of the migration rates.

At Buoy 1 (Figure 3.1), in the area of the flood sand waves, a more reliable average migration rate of 0.35 metres/tidal cycle was determined for a sand wave with a height of approximately 0.4 metres. This represents a residual bedload discharge of 102.0 kg/cycle to the east, which may be low because of the superimposed megaripples as described above. This transport rate is still considerably higher than any of the values calculated for Big Bar.

At Economy Point, the migration of sand waves has been monitored at Buoys EP 4, 6 and 7 (Figure 3.1) over a neap-spring cycle with interesting results (Figure 4.12).

FIGURE 4.12 : Migration rate variations with tidal range at Buoys EP 4, EP 6, and EP 7, Economy Point. Values are the averages of three or four stakes at each site.

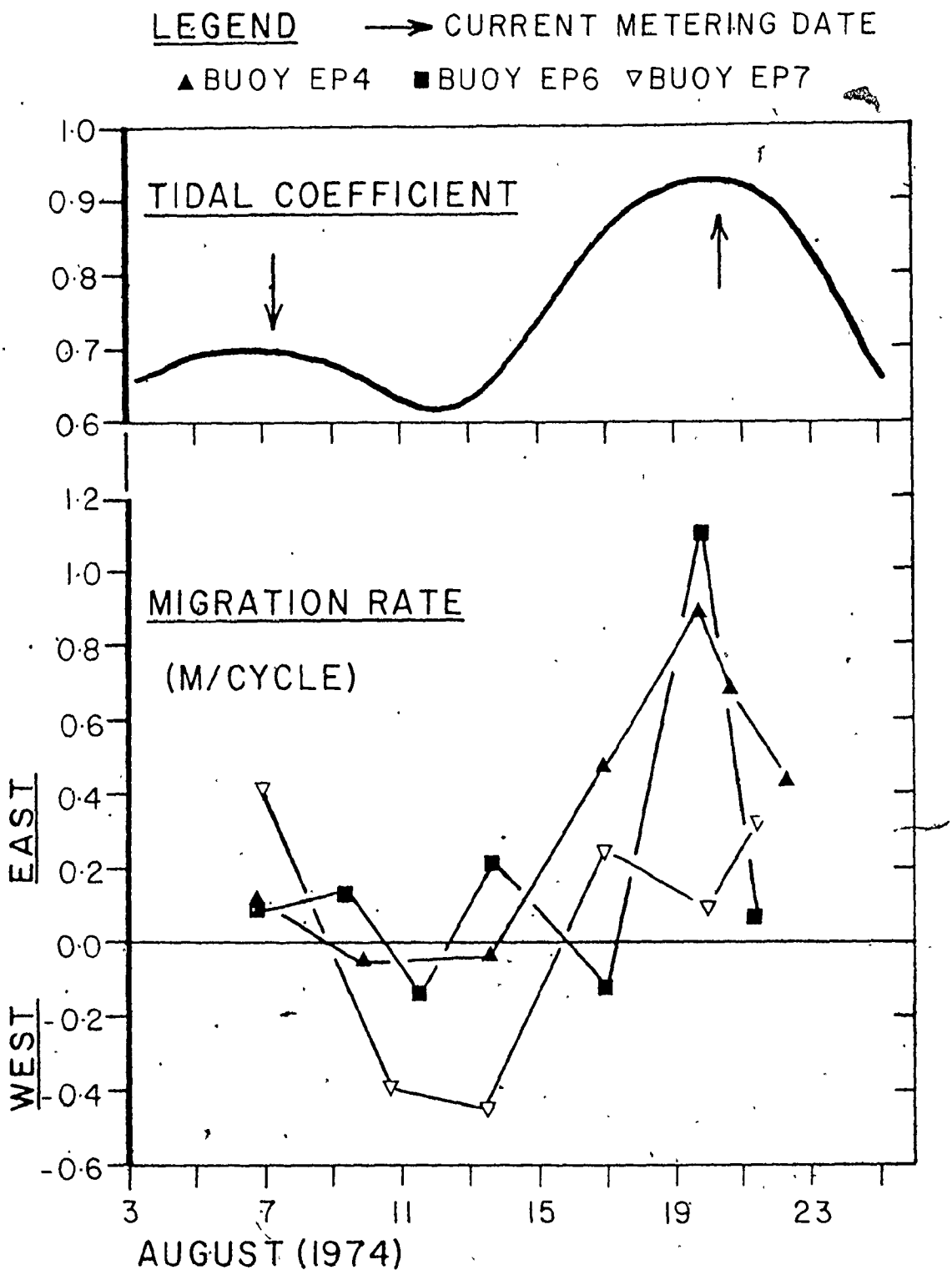
LEGEND
CURRENT METERING DATE
BUOY EP4
BUOY EP6
BUOY EP7
TIDAL COEFFICIENT
1·0
0·9
0·8
0·7
0·6
MIGRATION RATE
(M/CYCLE)
1·2
1·0
0·8
0·6
0·4
0·2
0·0
-0·2
-0·4
-0·6
EAST
WEST
3
7
11
15
19
23
AUGUST (1974)

During the neap tides, there is almost negligible migration at either Buoy EP 4 or EP 6, but with the onset of spring tides, the migration rates increase dramatically, in the flood direction at both stations. Unfortunately, no sequential measurements of bedform height are available, but the use of estimated heights at neap and spring tides suggests that the residual bedload transport changes from 20.4 kg/cycle in the ebb direction to 195.0 kg/cycle in the flood direction at Buoy EP 4, and from approximately 14.6 to 200.0 kg/cycle both in the flood direction at Buoy EP 6, a 14-fold increase. (At Buoy EP 6 there is an accompanying transition from predominantly ripples at neap tide to megaripples at large spring tides on the backs of the sand waves.) Current data obtained a short distance from the stakes at Buoy EP 6 on the 7th and 20th of August, 1974 (tidal coefficients of 0.69 and 0.90 respectively) (Figure 4.12) show that the time-averaged mean velocities increased from 0.529 m/s to 0.698 m/s for the flood, and from 0.323 m/s to 0.340 m/s for the ebb. Using these values in equation (4.3) with n = 3 suggests that the residual transport should increase by approximately 2.5 times. Even if n = 5 is used in equation (4.3), the calculated increase is only 4.25 times, which is still considerably less than the increase indicated by the migration rates.

At Buoy EP 7, there is a clear reversal in the direction of residual migration from westward at neap tides to eastward during spring tides. Residual discharges at neap

tide are approximately 233.0 kg/cycle, and at spring tide 175.0 kg/cycle, but the record is not sufficiently long to indicate the long-term direction of net transport.

No migration rate data is available from locations on Centre Bar, because the megaripples being monitored changed too quickly for their progress to be followed. To the north and west of the crest, however, the abundance of incompletely reversed flood megaripples at low tide indicates that this area is flood-dominated, as suggested in Section 3.2.5 above. All bedforms on the opposite side of the crestline are ebb asymmetric and contain no remnant flood cross-stratification which is consistant with, but does not prove, the suggested ebb dominance in this region.

Finally, turning to Selmah Bar, measurements conducted at six locations in the southeast part of the bar where there are large sand waves (Figure 4.3D) show that they migrate eastward at an average rate of 0.24 metres/tidal cycle, in accord with the flood dominance indicated for this area in Figure 3.17. At most stakes, no obvious correlation can be seen between the bedform migration rate and the tidal coefficient, and none of the bedforms show a reversal in the direction of migration, similar to that seen at Economy Point (Figure 4.12). The residual transport rate averaged over the three-week monitoring period for each location ranges from a high of 217.0 kg/cycle at the west end of the sand wave field, to a low of 34.2 kg/cycle at the very eastern end. The other

remaining values also generally conform to this pattern of eastward decreasing residual sediment discharges. Most of the decrease appears to occur in the western third of the sand wave field. This areal variation in the residual transport values is in broad agreement with the current data (Figure 3.17), which show an eastward decrease in both ebb and flood current speeds, without a compensating increase in the time-velocity asymmetry. Unless sediment is lost over the crest of the bar, or moved back westward by ebb runoff in the channel along the southern side of the bar, the implication must be that there is a general accretion at the east end of the bar.

The only other location on Selmah Bar where the bedform migration rate could be measured is in the small patch of rippled sand waves lying immediately to the west of the major swatchway (Figure 4.3D). These ebb-oriented bedforms, with a height of 0.21 metres, migrate at an average rate of 0.3 metres/tidal cycle in a southwesterly direction, giving an ebb-dominated residual transport of 45.9 kg/cycle.

On most other parts of the bar, the megaripples are completely reversed with each tide, and no direction of net migration can be determined. On the flat, westward sloping portion of the bar crest, west of the major swatchway, however, some incompletely reversed flood megaripples can be seen, indicating that the flood dominance shown by the current data (Figure 3.17) for this area is reflected in the residual sediment transport.

The results presented here show that the simple observation of the external morphology and internal structures of the bedforms, combined with measurements of their migration, can in many areas provide a valuable and easily determined guide to the patterns of residual transport on the sand bars, without recourse to expensive and time-consuming current measurements. As mentioned above, these data will be discussed further in Chapter 6, during the consideration of sediment transport rates as determined from fluorescent tracer experiments and hydraulic transport equations. It is interesting at this point, however, to briefly compare the magnitude of the calculated residual bedload discharges with similarly calculated values for ripples and dunes in unidirectional flume flows. In Cobequid Bay and Minas Basin, the residual discharges range from 4.8 kg/cycle on Big Bar, to a potential high of 583.0 kg/cycle in an area of dunes on Diamond Bar. A typical calculated transport rate would be on the order of 130.0 kg/cycle. When the data of Simons, Richardson and Nordin (1965b, Figures 2 and 3) are converted into similar units, it is found that the bedload transport rates for a dune bed are rarely less than 1300 kg/12.4 hours and extend up to nearly 130,000 kg/12.4 hours. Also, the transport rates for ripples are generally higher than 130.0 kg/12.4 hours, the typical residual discharge for the study area. Therefore, the residual bedload transport in a tidal situation is approximately one to two orders of magnitude less than that which

would accompany the observed bed configuration in a unidirectional flow situation. It is possible, however, that the total bedload transport (the sum of ebb and flood discharges) is comparable to the unidirectional values.

### 4.2.3 Controls on Bedform Distribution

It has been recognized for many years that the type of bedform produced depends in some fashion on a number of factors relating to the nature of the generating flow and the sediment. Attempts to quantify the relationships between the various bed configurations and the supposed controlling factors have occupied the attention of many sedimentologists and engineers, but no complete solution has yet been found. Although this subject is not of central importance to this thesis, a brief discussion of the available data is presented here.

The most common means of establishing the conditions governing the development of bedforms is to select the parameters believed most important and to plot the fields of bedform occurrence in either two- or three-dimensional phase diagrams, depending on the number of parameters selected for consideration. Of the many that have been published, the three-dimensional representation recently proposed by Southard (1971, 1975), using axes of mean current speed, water depth, and mean sediment size is selected for use here. The choice is based partially on the simplicity of these diagrams, but

also on the fact that sand waves have been included as a separate field. In addition, this representation has been used previously for the presentation of data from another tidal environment (Boothroyd and Hubbard, 1972; Southard, 1975). The use of the mean current speed rather than the shear velocity (Vanoni, 1974, Figure 7) or the stream power (J. R. L. Allen, 1968a, Figure 6.9) as the measure of flow strength is preferred in the present case because the greater uncertainty associated with the field measurement of these latter parameters might obscure the existing relationships controlling the occurrence of the various bedforms. For comparative purposes, the relationship proposed by Vanoni (1974, Figure 7) is presented at the end of this section.

In an environment such as the Minas Basin and Cobequid Bay where the current speed, water depth and flow direction change significantly on a short time scale, it becomes difficult to select the proper speed and depth combination, or even the proper half of the tidal cycle that is responsible for the observed bedforms. In areas where the bedforms retain either external or internal evidence of a pre-existing flood bedform at low tide, the flood tide values have been used in constructing the phase diagrams. Elsewhere, the ebb tide is considered as being most important, because it has moulded the observed features. Within the selected half of the tidal cycle, the problem still remains as to what velocity and depth have the greatest influence in determining the bed

configuration. Because the sediment discharge is a power function of the current speed, it can be considered that the maximum current speeds are most influential in generating the observed bedforms. Based on this premise, the maximum mean current speed and the water depth in which it occurred have been used in the phase diagrams, with the qualification that the selected speed must have an associated depth of more than approximately 2.5 metres. Flows shallower than this are known to cause modification of earlier bedforms and should be excluded from this discussion. In such cases, the next highest current speed in the appropriate depth range has been used. Data from all four study areas have been included, and if any single station was occupied more than once, then a separate data point has been plotted for each visit.

Figure 4.13A is a plot of the maximum mean velocity and the associated water depth for those stations with a mean grain size of medium sand (1 - 2 phi; 0.5 - 0.25 mm). It can be seen that an excellent separation is achieved between rippled sand waves which occur at the lowest velocities, megarippled sand waves at intermediate velocities, and mega-ripples which are the stable bedform at the highest current speeds encountered. Only one point out of 29 falls outside of its proper field, based on the phase boundaries that have been drawn arbitrarily to provide the best separation. These boundaries (solid lines) do, however, show a remarkable agreement with the position of those extrapolated from

FIGURE 4.13 : Depth-current speed-grain size phase diagrams of bedform types.
A - Peak mean speed versus the associated water depth.
B - Mean grain size versus peak mean speed. Thin bars on data points are two standard deviation error limits for the mean speed. Thin dashed phase boundaries in A are extrapolations from Southard (1975, Figure 2-10).

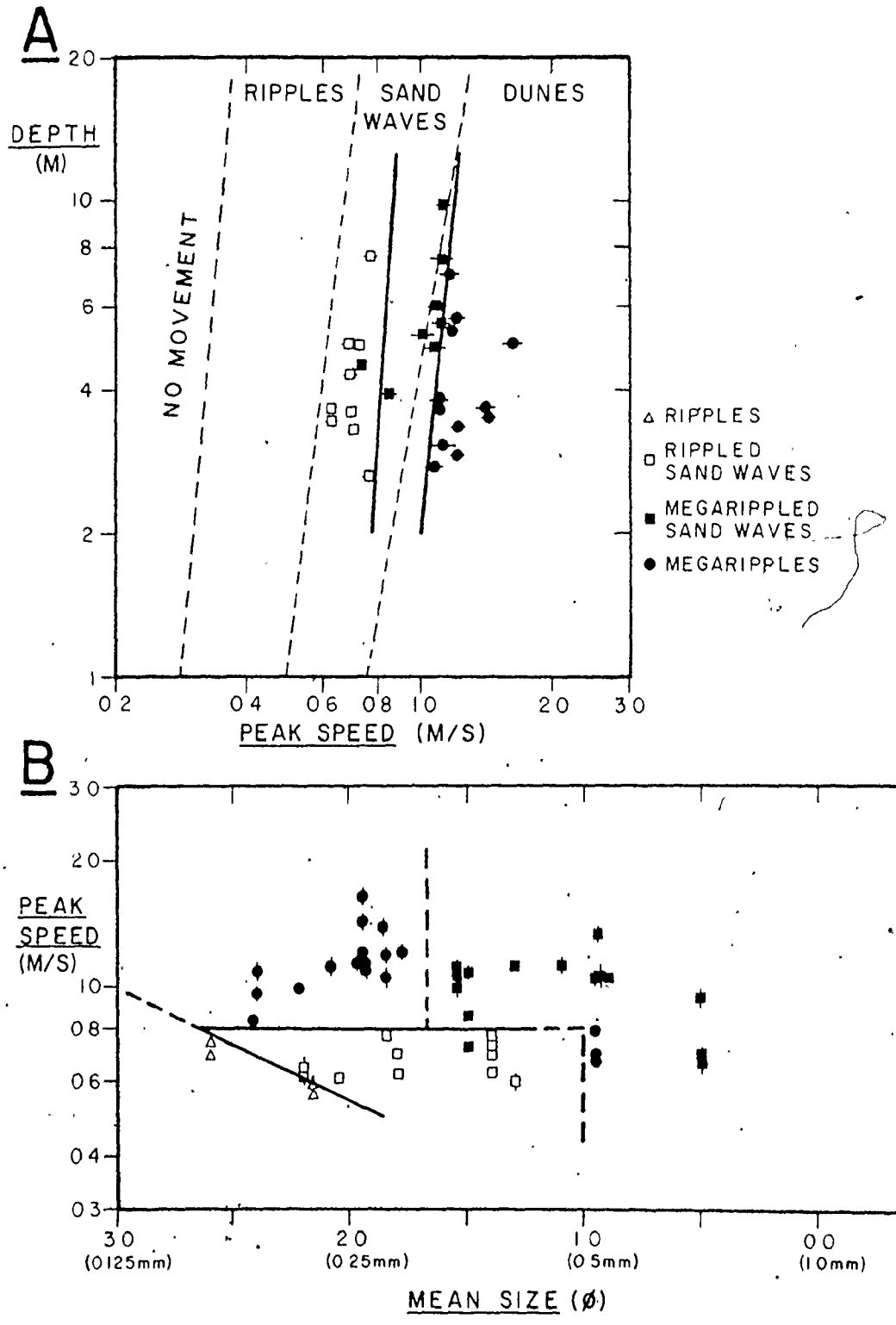
A
RIPPLES
SAND WAVES
DUNES
NO MOVEMENT
DEPTH (M)
20
10
8
6
4
2
1
0 2
0 4
0 6
0 8
1 0
2 0
3 0
PEAK SPEED (M/S)
RIPPLES
RIPPLED SAND WAVES
MEGARIPPLED SAND WAVES
MEGARIPPLES
B
PEAK SPEED (M/S)
3 0
2 0
1 0
0 8
0 6
0 4
0 3
3 0 (0125mm)
2 0 (0 25mm)
1 0 (0 5mm)
0 0 (1 0mm)
MEAN SIZE (ø)

Southard (1975, Figure 2-10) (broken lines) based on the data of Boothroyd and Hubbard (1972). It is interesting to note that the division between rippled and megarippled sand waves falls approximately in the middle of Southard's (1975) sand wave field. Depth obviously has little control on the type of bedform produced by a given velocity.

In order to consider the effects of grain size, the maximum mean speed is plotted against the mean grain size in Figure 4.13B. Because of the virtual independence of the phase boundaries on depth, all of the available data have been used. Again, a good separation can be seen between the various bedform types, although there are several discordant points. The most notable feature of Figure 4.13B is the nature of the apparent boundary between megarippled sand waves and megaripples. No evidence is available here to indicate that a transition from megarippled sand waves to megaripples is possible by increasing the current speed, as is suggested in Figure 4.13A. Rather, the division appears to be based on grain size alone, with megarippled sand waves present only in sand coarser than 1.7 phi (0.31 mm). This termination of the megarippled sand wave field allows the direct transition between rippled sand waves and megaripples, a phenomenon seen areally in several places (Figure 4.3). All occurrences of rippled sand waves are in sands finer than approximately 1.0 phi (0.50 mm), giving them a very restricted field. In the study area, ripples occur alone only in fine

sands, and the data presented show that they have a stability field which cuts across that of the rippled sand waves, and possibly also that of megaripples.

In Figure 4.13B, three megaripple points (all for Buoy 5 on Big Bar - Figure 3.1) plot well away from the megaripple field, and would fall in the rippled sand wave field if it were extended to a slightly coarser grain size. Two possibilities for this discrepancy are: i) that the subjective criteria used to distinguish between sand waves and megaripples does not coincide exactly with the hydraulic differences and that some or all of the megaripples on Big Bar have been misclassified; or ii) that the phase relationships are more complicated than are suggested in Figure 4.13B, and a separate area of megaripple stability does exist at the coarse-grained end of the rippled sand wave field. However, no conclusive explanation can be given at this time, and further work is necessary.

The discussion presented above makes the implicit assumption that the bedform assemblages are in equilibrium with the maximum mean current speeds; however, as shown in Section 3.2.2, there are large velocity changes over a tidal cycle, and the flow conditions can pass through several stability fields during each half tidal cycle. It has been suggested by Allen and Collinson (1974) that the superposition of megaripples on larger asymmetric features is due to time variations in depth and velocity, with the two scales of

bedform in equilibrium at different times. Although it is not possible to resolve the problem here, the good separation of the various assemblages into discrete fields in the depth-velocity-size diagrams (Figure 4.13) indicates that the associations may occur together in at least near-equilibrium. The suggestion of Costello (1974) that the megaripples superimposed on the sand waves are metastable features is not contrary to any of the available data.

The nature of the time variability of the flow can be seen more clearly when sequential mean velocity-depth pairs for a tidal cycle are plotted on the depth-velocity face of the bedform phase diagram (Figure 4.13A). Four examples from Diamond Bar are shown in Figure 4.14, two each from stations in megarippled sand waves, and megaripples. The two solid boundaries are those derived from the present data, and the broken ones are the Southard (1975) extrapolations. These plots give a crude estimate of the bedform type that should be stable at any time during the tidal cycle.

Looking first at the plots for megarippled sand waves (Figure 4.14A and 4.14D), it can be seen that at both buoy locations, there is a pronounced time-velocity asymmetry, with significantly lower velocities on the ebb. In both cases, the ebb currents are not capable of totally reworking the flood megaripples superimposed on the sand waves. The time history of the flood depth-velocity pairs at Buoy 5 (Figure 4.14D) is particularly interesting because of the extreme

FIGURE 4.14 : Time sequence of mean speed and water depth over a tidal cycle. Broken bedform phase boundaries extrapolations from Southard (1975, Figure 2-10); solid boundaries from Figure 4.13A. Open circles - flood tide; solid circles - ebb tide.

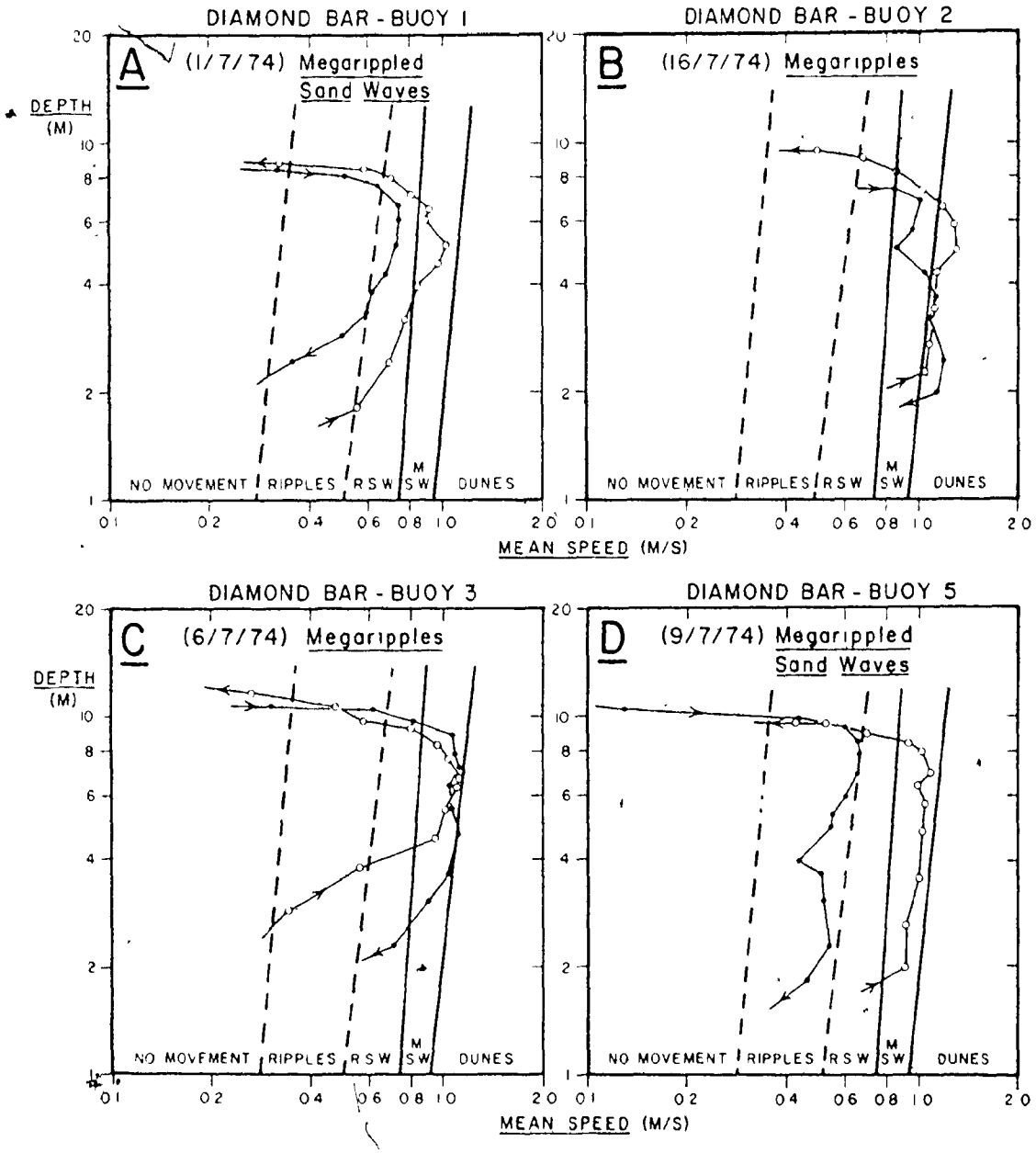
DIAMOND BAR - BUOY 1
A
(1/7/74) Megarippled Sand Waves
DIAMOND BAR - BUOY 2
B
(16/7/74) Megaripples
DIAMOND BAR - BUOY 3
C
(6/7/74) Megaripples
DIAMOND BAR - BUOY 5
D
(9/7/74) Megarippled Sand Waves
DEPTH (M)
NO MOVEMENT
RIPPLES
RSW
MSW
DUNES
MEAN SPEED (M/S)

constancy shown with respect to the bedform phase boundaries. This behaviour also suggests that the sand waves and superimposed megaripples must be a near-equilibrium configuration.

Turning next to the plots from megarippled areas, one sees that the peak velocities attained are slightly higher than in the megarippled sand wave areas, but more significantly, the peak velocities for the ebb and flood are nearly equal. It has previously been stated (Boothroyd and Hubbard, 1972; Southard, 1975) that sand waves are generally found in areas where there is a strong time-velocity asymmetry, while megaripples do not show any trend in this regard. Both of these points are supported by the data in Figure 4.14; however, the existence of symmetrical sand waves, and of continuous sand waves with one end ebb asymmetric and the other flood-oriented on Saints' Rest Bar and Spencer Point Bar, indicates that a strong time-velocity asymmetry is not a prerequisite for sand wave formation. It is possible that sand waves can exist under a wider range of velocity conditions if a strong dominance exists than otherwise, but there is insufficient data to judge whether this is, indeed, the case or not at this time.

Vanoni (1974) has proposed that the shear velocity is the most appropriate hydraulic variable for separating lower flow regime bedforms, and presents a relationship which effectively differentiates ripples and dunes. Sand waves are not recognized by Vanoni (1974). Vanoni's relationship,

together with the Shields criterion for the initiation of motion have been plotted in Figure 4.15, with axes of mean grain size and shear velocity. The shear velocity assigned to each data point is an average maximum value, determined by averaging the three maximum values from the dominant half of the tidal cycle.

Inspection of Figure 4.15 reveals that there is considerably more overlap between the various bedform types than was evident in Figure 4.13B, and it is impossible with the available data to draw the appropriate phase boundaries with any certainty. It is notable, however, that megarippled sand waves and megaripples overlap considerably in terms of shear velocity, such that the division between them is again a function primarily of grain size, as in Figure 4.13B. It is also interesting to note that all megaripple points and all but one of the megarippled sand wave points fall above the ripple-dune boundary suggested by Vanoni (1974), whereas all four ripple points lie below the line. Rippled sand wave values are almost equally divided between the ripple and dune fields. It is clear that much more work is necessary before the conditions governing the formation of tidal bedforms and sand waves in particular, are completely understood.

## 4.3 Low-tide Modification Features

As used here, the term modification feature refers to any change in the geometry of a primary bedform or to any

FIGURE 4.15 : Shear velocity-grain size phase diagram of bedform types. Average maximum shear velocity versus the mean grain size. Ripple-dune boundary after Vanoni (1974).

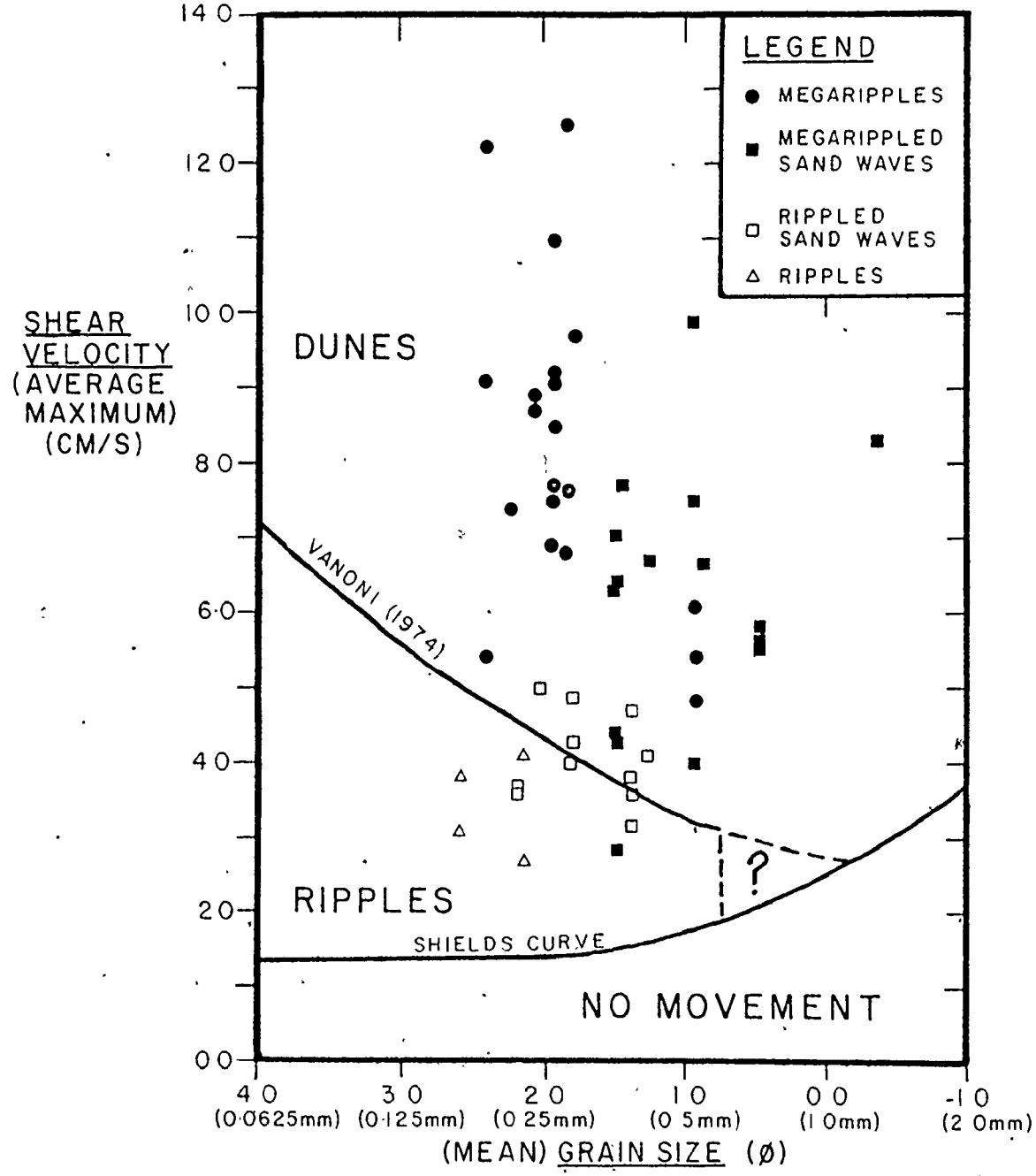
LEGEND
MEGARIPPLES
MEGARIPPLED SAND WAVES
RIPPLED SAND WAVES
RIPPLES
DUNES
VANONI (1974)
?
RIPPLES
SHIELDS CURVE
NO MOVEMENT
SHEAR VELOCITY (AVERAGE MAXIMUM) (CM/S)
140
120
100
80
60
40
20
00
40 (0·0625mm)
30 (0·125mm)
20 (0·25mm)
10 (0·5mm)
00 (1·0mm)
-10 (2·0mm)
(MEAN) GRAIN SIZE (ø)

bedform or other surface marking that occurs as the result of current velocity and water depth changes related to emergence or near emergence. Some of the features described below from the surface of the bars can also form in the shallow subtidal, and as such are not diagnostic of the intertidal zone, but only reflect the unsteady flow conditions. Three processes act at low tide to modify the surface morphology generated by the preceedqng tidal currents: tidal current flow while the location is still shallowly submerged; channelized ebb runoff; and wave activity. The products of each will be considered in turn.

Two modified megaripple forms are produced as the result of changes in the speed and direction of the tidal currents in the last one-half to one hour before emergence. These features are planed-off megaripples (Boothroyd, 1969; Knight, 1971) and swept-catenary megaripples (J. R. L. Allen, 1968a).

In certain areas, primarily on slight topographic highs, locally steep water-surface slopes are generated for a short period just prior to emergence. These flows with high Froude numbers cause the erosion of the crest of the bedforms and the formation of flat crestal platforms (Figure 4.16A). Parallel lamination that is gently inclined down flow is produced in some cases. The resulting reduction in bedform height caused by the planing-off is responsible for most of the megaripple data points in Figure 4.6 that fall in the sand wave field.

Changes in current direction, generally associated with the gradual emergence of the bar as described in Section 3.2.2, is responsible in certain areas for the production of spurs oriented obliquely to the megaripple crestline. This swept catenary megaripple pattern (Figure 4.1F) is best developed on the northeast corner of Diamond Bar, near Buoy 2 (Figure 3.1). Here, during the first three hours of the ebb tide, the currents flow perpendicular to the observed megaripple crests. At approximately one hour before emergence, the current shifts gradually in a clockwise direction by 25° to 40°, and the oblique spurs are then formed, parallel to these currents.

Current ripples, produced during the final few minutes of the ebb as the current speed passes through the ripple stability field, are widely developed on most parts of the bars (see Figures 4.1 and 4.2), and are the most common modification feature. These ripples have a linguoid shape, but sinuous and straight crested varieties are also observed. Occasionally, rhomboid ripples can be seen as well. A regular sequence of ripple sizes is seen on the stoss sides of some megaripples and sand waves, with smaller ripples in the trough and lower stoss side, and larger ones which may be transitional with dunes on the crestal portion of the underlying feature (Figure 4.2D). This is presumably due to the constriction of the ebb flow over the crest of the primary bedform, causing an increased current speed and shear stress in this area.

The superimposed ripples are generally oriented at an angle to the larger bedforms, and almost always indicate a down-slope component to the flow that produced them. This is due to the fact that they form during the last minutes of the ebb tide, when the currents are being deflected away from the bar crest by the emergence of the bar.

In the final stages of emergence, the remaining water is confined to the troughs of the large-scale bedforms and flows down the slope, at right angles to the direction of the peak tidal currents. At this time, straight ripples are commonly formed on the slip faces of the megaripples (Figure 4.16C). Ladder-back ripples (Figure 4.16B) are also produced in the megaripple and sand wave troughs by the modification of slightly earlier ripples. The resulting directional variance of ripples is much greater than that of the larger bedforms, as has been documented by Klein (1970). It is obvious that ripple and megaripple cross-stratification reflect different aspects of the flow system, and failure to recognize this in an ancient example will obscure the true flow patterns.

Continued drainage and flow along the bedform troughs can cause the erosion of spurs and the undermining of megaripple slip faces (Figure 4.1C). Upper flow regime conditions commonly occur in the miniature braided streams that occupy these runoff channels, and numerous small deltas (Figure 4.1C) are constructed laterally into the pre-existing scour pits.

FIGURE 4.16 : Low-tide modification features.
A - Planed-off megaripples, near Buoy 6, Diamond Bar. Figure for scale.
B - Ladder-back ripples, near Buoy 1, Big Bar.
C - Ripples on megaripple slip face, near Buoy 1, Big Bar. Metre stick for scale in B and C.
D - Wave-smoothed megarippled sand wave, Buoy EP 7, Economy Point. Figure for scale.
E - Peel taken parallel to dip on steep south side of Big Bar at Buoy 2. Note parallel lamination in upper part of peel. Scale divisions are 5 cm.

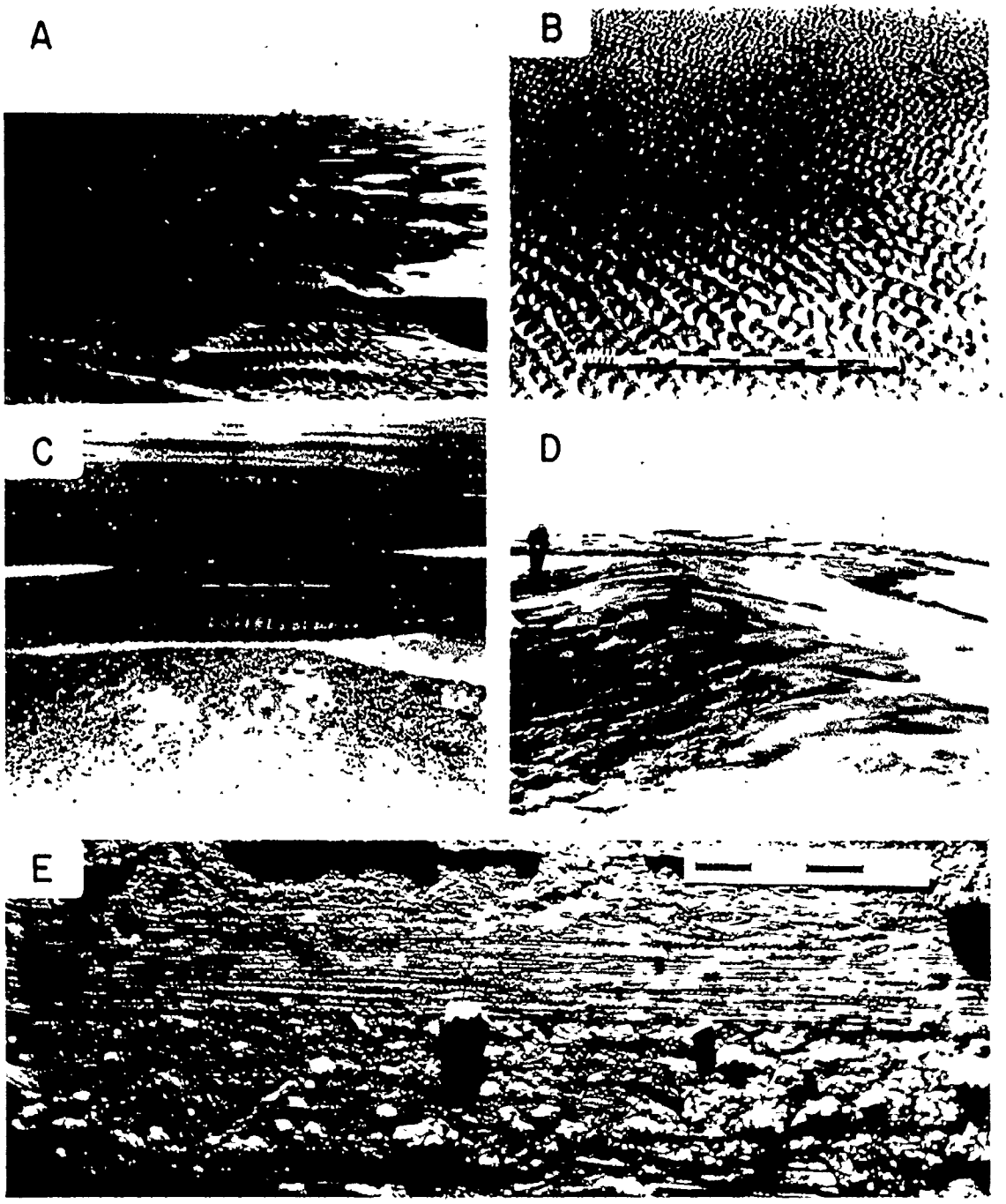
A
B
C
D
E

Rill marks of various types (see Reineck and Singh, 1975, p.58-62) are produced by the seepage of pore water out of the sand, particularly along the base of megaripple and sand wave lee faces, and by flow down the smooth, steep sides of Big and Selmah Bars.

In Section 2.2.2, the point was made the wave activity is of secondary importance to tidal currents with respect to the sedimentation dynamics of the sand bars. The main role of waves is to modify pre-existing tidally-produced features.

Water-level marks (Häntschel, 1938; Klein, 1970) are small, horizontal steps eroded into the lee faces of megaripples and sand waves (Figure 4.1E) by water waves on the surface of pools standing in the troughs and scour pits. If preserved, they clearly indicate emergence.

Wave ripples are produced in shallow areas during the falling tide, and are about the same size as the current ripples that may also be present in the vicinity. Wave ripples are most commonly found on the smooth, steep sides of bars, such as on Big and Selmah Bars, but they are often present on other exposed parts of bars as well.

Because of the steepness of most waves, the most usual expression of their presence is a destructive rounding of current bedform crests. On the smallest scale, current ripples can be decapitated producing flat-topped or rounded ripples, that may have pointed troughs. The rounding and smoothing of megaripples and sand waves (Figures 4.1A and

4.16D) is a regular occurrence in exposed areas, but the modification is limited by the rapid change in water level and the resulting short time that any location spends within the zone of strong wave action. On steep bar slopes, however, waves can act for a much longer time, and even megaripples can be completely obliterated at times of strong wave action, leaving a beach-like surface that may contain a few remnant and partially-filled scour pits. (The most spectacular instance of bedform destruction, in which a 0.75 metre high sand wave was obliterated has already been mentioned.) Longshore transport of sediment might be of some importance in areas such as this, and swash marks are common. A peel taken from the steep, south side of Big Bar (Figure 4.16E) shows a 10 cm thick set of parallel lamination, inclined at the same angle as the present bar surface ($4^{o}$ S) that may have been formed by wave action.

An interesting liquefaction structure (Figure 4.17) that is believed to be produced by wave action, has also been observed on exposed and topographically high parts of Diamond and Selmah Bars, where mean sand sizes are finer than 1.95 phi (0.26 mm). The author is not aware of any other reported examples from modern sediments, therefore, these features will be discussed in some detail.

These liquefaction features are small slumps that are generally situated on the stoss (or eastern) side of an ebb megaripple. They have a distinctive external morphology that

FIGURE 4.17 : Liquefaction slump structures.
A - Liquefaction slump showing vertical slump scar, near Buoy 3, Diamond Bar.
B - Liquefaction slump modified by waves, near Buoy 3, Diamond Bar. Metre stick for scale in A and B.
C - Peel perpendicular to megaripple crest through liquefaction slump, Buoy 3, Diamond Bar.
D - Peel through liquefaction slump, perpendicular to megaripple crest, near Buoy 2, Diamond Bar. Note load structures at top of peel with a 15 to 20 cm spacing. Scale divisions are 5 cm in C and D.
Ebb flow to the left in C and D.

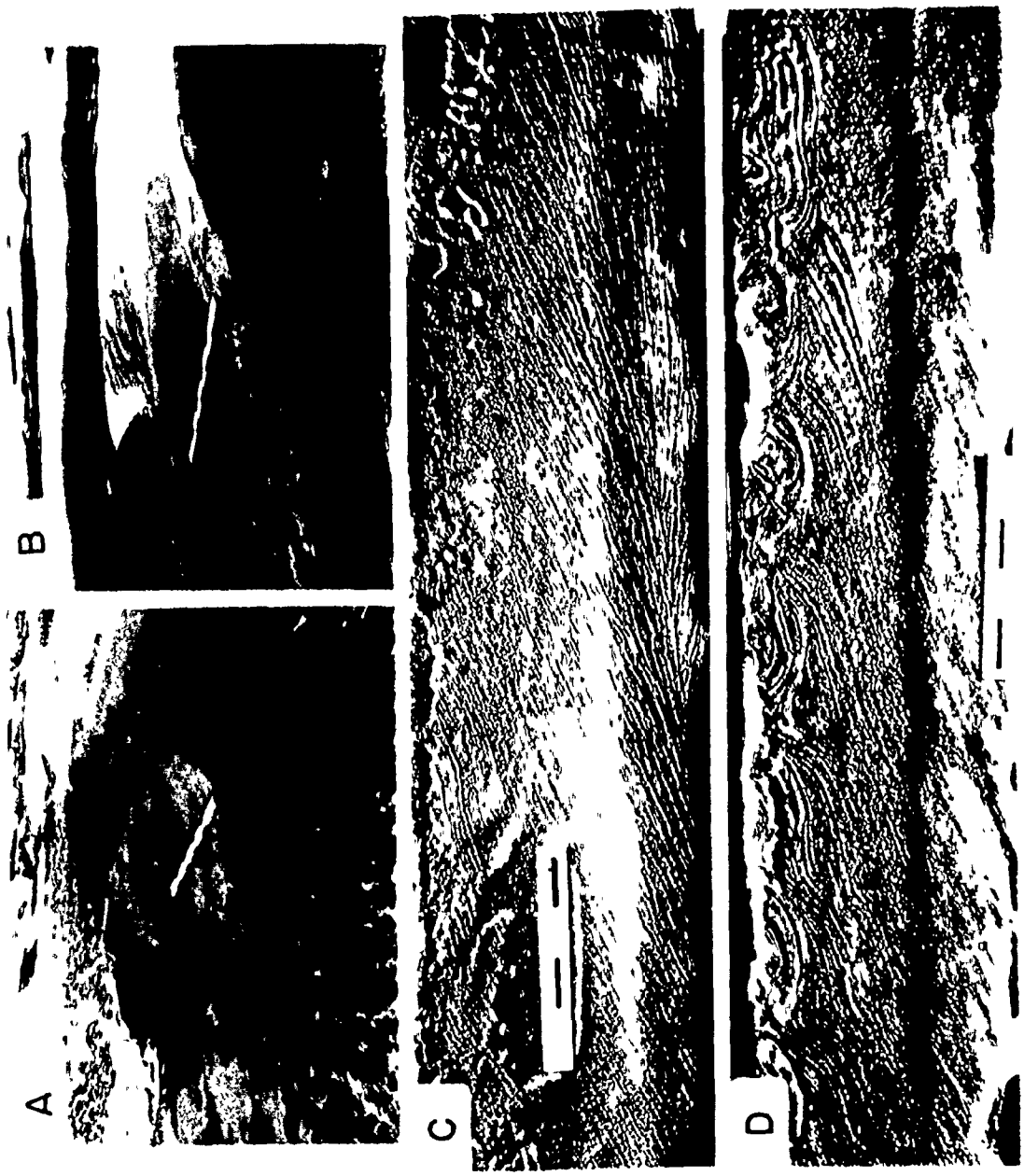
A
B
C
D

consists of a level platform, ranging in size from 0.75 x 0.75 metres to 1.5 x 2.0 metres in size, bounded on the side adjacent to the bedform crest by an abrupt upward step with a height of 5 to 25 cm that is the slump scar, and on the trough side by a sharp drop that is the nose of the slump. In fresh examples, the platform is perfectly smooth, and the slump scar is a vertical cliff (Figure 4.17A). Most examples, however, show some wave modification such that the slump scar is rounded (Figure 4.17B) and wave or current ripples are developed on the surface of the platform. It appears that these features have been formed by the processes of liquefaction, gravitational slumping and flowage.

Examination of the internal structures shows that the avalanche foresets deposited during megaripple migration have been deformed in a coherent manner. In the upper left of Figure 4.17C, above the scale, obvious deformation of the laminae has taken place in the vicinity of the slump scarp, which is not included in the peel. The depth to which the deformation has penetrated increases to the right, toward the nose of the slump, and extends to a depth of approximately 15 cm. To the right of the scale, a slight decrease in the dip of the laminae can be seen at the base of the deformed zone, with more steeply inclined beds above, suggesting that the upper part of the slump has rotated counterclockwise. A similar general pattern is seen in Figure 4.17D, but is accompanied by much greater deformation near the surface, in

the form of load structures. Careful examination of the load balls reveals that small-scale cross-lamination is present in some of the cores, suggesting that these load structures resulted from the foundering of current ripples. The 15 - 20 cm spacing is consistent with this interpretation.

Several pieces of circumstantial evidence indicate that wave activity is responsible for these liquefaction features: i) the features occur only in those areas where the strongest wave activity on the bar has been observed; ii) the slumps are almost non-existant on days when the water surface is dead calm, but become abundant when waves of even 10 - 30 cm height are present during emergence; iii) the fresh appearance of most examples, and the lack of examples showing a spectrum of tidal current obliteration suggests that they form late in the tidal cycle, after the generation of current ripples on the megaripple, and possibly just prior to emergence; iv) no other triggering mechanism such as earthquakes, as invoked by Allen and Banks (1972), Schwarz (1975) and Wunderlich (1970) is acceptable for the almost daily occurrence of these liquefaction features; and v) the wake of the research boat has been observed to produce similar, but much larger features. It is known that the fine sand in the areas of slump occurrence is commonly close to the point of liquefaction when water saturated, because the weight of a person walking on the crest of a partially submerged megaripple can cause slumping and the production of identical

features up to one metre away. The conclusion drawn, therefore, is that the shock of waves breaking on the saturated fine sand is sufficient to trigger the liquefaction, slumping and resulting deformation of the cross-bedding.

Wunderlich (1967) (see also Reineck and Singh, 1975, p.78) has observed convolute bedding that appears similar to that of Figure 4.17D on the exposed, steep margins of tidal flats bordering the German Bight. He contends that the deformation results from liquefaction due solely to dewatering of fine sand during emergence. Active lateral flow of pore water would encourage liquefaction by supporting a portion of the grain weight, but the scarcity of slumps on calm days indicates that this process by itself is not the primary triggering mechanism. Wunderlich (1967) does state that winds had been strong for a period prior to the discovery of the convolute bedding, which would favour the explanation presented here.

Two miscellaneous features remain to be cosidered briefly before ending this section: mud drapes, and bubbled sand.

Mud drapes are observed in the troughs of megaripples and sand waves in all four areas, but are most common on Diamond and Selmah Bars where the turbidity of the water is greatest (Section 2.2.4). On Diamond Bar, mud pebbles eroded out by runoff channels can be found with minimum dimensions of one centimetre, showing that large-scale flasers with

thicknesses of at least one centimetre are present. Such flasers associated with cross-bed sets with thicknesses of 5 - 15 cm have been exposed on occasion in trenches.

Fine sand containing the moulds of trapped air bubbles a few millimetres in diameter is common along the upper part of the steep side of Big Bar and Selmah Bar. These bubbles are believed to form when the sediment is rapidly inundated by the flooding tide (Emery, 1945). The bubbled layer never extends beyond a depth of approximately 5 - 10 cm, in part because the bubble moulds are easily collapsed by the weight of the overlying sediment. As a result, this structure has a poor preservation potential. However, it may have some influence in the destruction of previously-formed stratification.

In general, the preservation potential of many of the modification features described here is low, because of their small size, exposed position, and the vigour of the tidal currents. The features that are believed to have the best chance of preservation because of their position below the mean bed elevation are: swash-zone parallel stratification on the exposed, steep sides of the bars; ripples generated by runoff in larger bedform troughs; cross-bedding formed by deltas building laterally into megaripple scour pits; and the large-scale flasers. The fate of the wave-triggered slumps is uncertain because they generally occupy the crestal portions of megaripples and, therefore, are likely to be

eroded. The recognition of any of the above modification features in an ancient deposit can be extremely useful, because they provide valuable evidence that water level changes and current speed variability were factors influencing the deposition of the sediments in question.

## 4.4 Winter Conditions

In Section 2.2.5, the three forms of ice accumulation that exist in the Minas Basin and Cobequid Bay during the winter were described. The presence of drift ice and the ice crust on the sand bars (Figures 2.6B and 2.6D) produces a number of features which stand some chance of preservation (Knight and Dalrymple, 1976). The observations reported here come entirely from Selmah Bar, which is the only one of the four study areas that has been visited by the author in the winter.

The formation of the ice crust effectively immobilizes most of the sediment on the intertidal portions of the sand bar, and prevents the generation of the various primary current bedforms and modification features described above: The sand waves and megaripples existing at the time when the crust is initiated become rounded (Figure 4.18A) and are reduced in height, or even obliterated. This is believed to result from the combined action of tidal current scour, and redistribution of unfrozen sediment, the buildup of the ice crust, and the dragging of drift ice over the crest of the

bedforms. The surface of the sand bar during the winter, therefore, is smooth and gently undulating, with subdued relief. In the subtidal zone, bedform generation and sediment transportation continue unchanged from the summer. Water temperatures during the winter (approximately $0^{o}C$) are, however, much lower than in summer when they average about $20^{o}C$. This causes a change in the viscosity from 0.001072 to 0.001866 kg/ms, or a 1.75 times increase, which should be reflected in the sediment discharges. No visible effects of this have been observed, but it may be of importance, combined with the immobility of the bar sediments, in initiating intermediate to large-scale morphological changes.

On the bar, the continuity of the ice crust is broken at places where there is standing or running water, such as in bedform troughs and scour pits (Figure 4.18B). In other locations, grounded drift ice that has become frozen to the bottom removes portions of the crust when it breaks free. All of these spots where unfrozen sediment is exposed are subjected to tidal current scour and portions of the adjacent crust are undermined and broken off. At low tide, ebb-oriented wedges of sediment can be seen building into these scoured depressions (Figure 4.18C). Similar cross-bedded sets that were presumably deposited by the flood currents have been completely removed. The ebb sets, however, stand a somewhat better chance of preservation, because their upper surface becomes frozen during low tide exposure. As a result,

FIGURE 4.18 : Winter features. A - Rounded and subdued rippled sand wave, near Buoy 1 on Selmah Bar.
B - Scoured depression on the crest of Selmah Bar.
C - Ebb-oriented sediment wedges, top and lower right of photo. From Selmah Bar. Metre stick for scale.
D - Runoff channel with erosive margins, north side of Selmah Bar. Shovel near head of gulley (arrow) is 80 cm long. Drift ice stranded on bar in background.
E - Ice-rafted boulder of bedrock on steep, rippled side of Big Bar. Scour is flood-oriented.

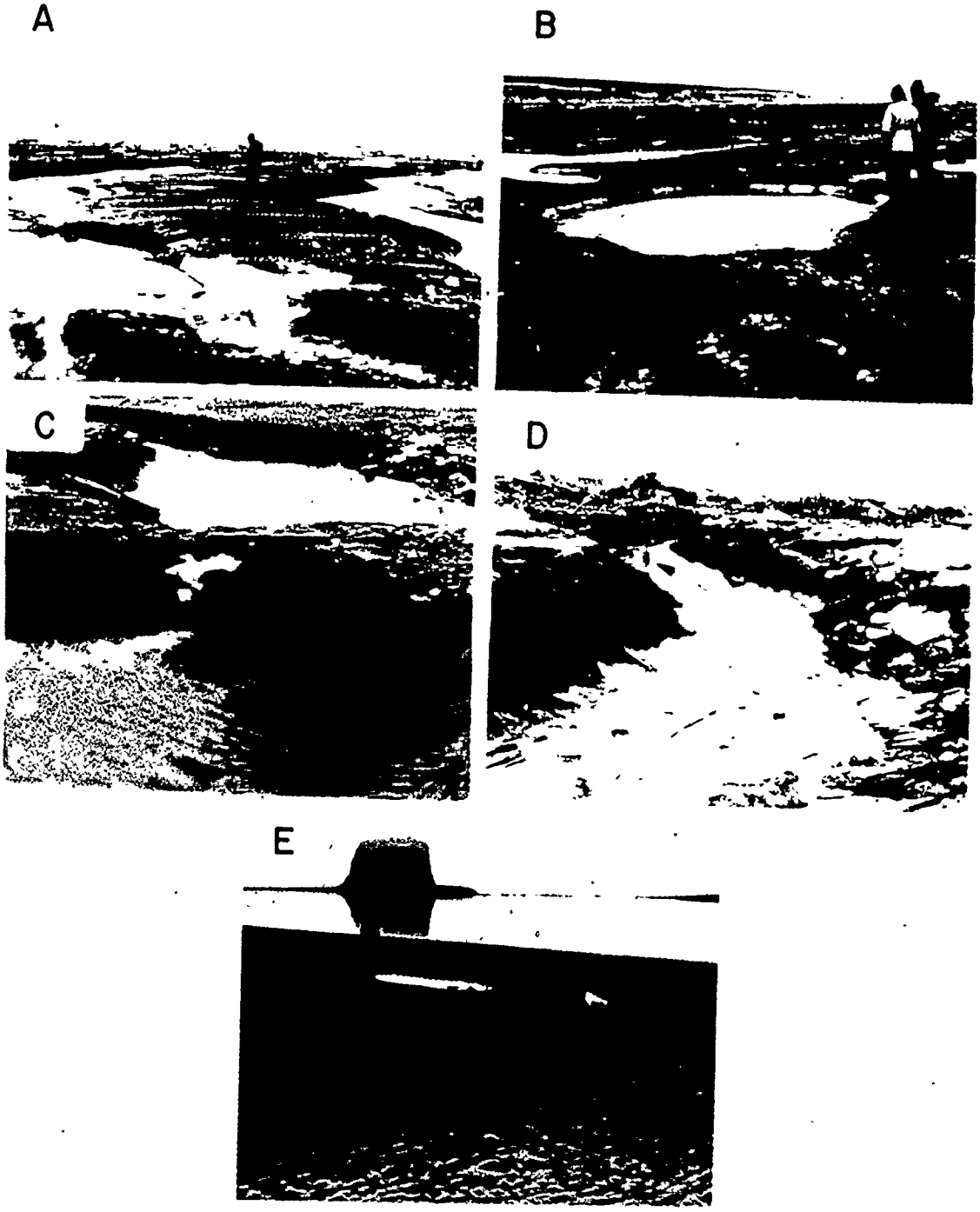
A
B
C
D
E

large-scale, tabular or trough, ebb cross-bedding might be preserved even in areas where the remainder of the sets are flood-oriented.

The presence of the ice crust on the sand bars effectively halts any residual transport of sediment that the tidal currents are capable of producing at all times of the year. In contrast, the lateral flow of water and sediment away from the bar crest in bedform troughs and larger ebb-runoff channels during emergence is enhanced by the ice crust because the downward percolation of water into the sand is inhibited, and as a result, lateral drainage is concentrated more than during the summer. This causes the lateral runoff channels to be more deeply incised during the winter and to have more erosive margins (Figure 4.18D).

Drift ice is important for the transport of exotic material onto the sand bars. In the summer, roughly circular patches of pebbles and cobbles are commonly seen (Figure 4.18E) and isolated boulders of Triassic sandstone and pieces of salt marsh sediment, with maximum diameters up to 1.5 meters, can also be found. These materials are apparently deposited from drift ice as it melts, and stand a good chance of preservation because the tidal currents are not competent to move such large objects.

In general, the features produced by the winter conditions are of a more erosional nature than are those generated during the summer. Over the majority of the sand bar, however,

winter is a time of inactivity, relative to the summer, because of the ice crust. With the breakup, and the freeing of the sediment, tidal currents quickly re-establish the suite of bedforms described in Sections 4.2.1 and 4.3 above, and obliterate any surface evidence of the winter features. The coarse ice-rafted debris is the only surficial evidence of ice action, and tidal-current cross-bedding is expected to dominate the preserved stratigraphic record.

## 4.5 Summary

The tidal currents in the Minas Basin and Cobequid Bay are sufficiently strong to produce a diverse suite of lower flow regime bedforms on the study bars, in which two large-scale morphological types are distinguished: megaripples (dunes) and sand waves.

Megaripples are, in general, characterized by their three-dimensional appearance, with irregular trough- and crestlines, scour pits, and lack of crestal continuity, although more regular examples can be found. Sand waves appear more two-dimensional by comparison and have regular trough- and crestlines, and lack scour pits. Two varieties of sand waves are recognized, rippled and megarippled, depending on the predominant superimposed bedforms. Megaripples with a mean length of 4.18 metres and a mean height of 0.26 metres, are smaller and steeper on average than sand waves (mean length 12.80 metres; mean height 0.44 metres), although there

is considerable overlap in both dimensions. Megarippled sand waves are also larger than rippled varieties. On a bivariate plot of length and height, sand waves and megaripples are almost completely separated by the equation (H = 0.072 L - 0.21), with height (H) and length (L) expressed in metres.

Because megaripples possess an angle of repose lee face, the internal stratification is a single set of cross-bedding which may be broken by reactivation surfaces produced by the reversal of the megaripple form during each half of the tidal cycle. Most sand waves by contrast do not have a slip face, and the internal structure is composite, and produced by the superimposed megaripples and ripples.

Megaripples and the two sand wave types are formed under differing maximum mean velocity, water depth, and mean grain size conditions. The bedform sequence from rippled sand waves to megarippled sand waves to megaripples represents a general increase in current speed, but grain size is also of importance for no megarippled sand waves occur in sands finer than 1.7 phi (0.31 mm), and no rippled sand waves in sands coarser than about 1 phi (0.50 mm).

The presence of time-velocity asymmetry imparts a preferred asymmetry to sand waves in a given area and produces a net migration of the bedforms in the direction of the dominant currents. Measurement of this movement is difficult with megaripples, due to their high mobility and rapid shape changes. Sand waves, which have life spans approaching

several years, can be monitored with results that suggest that there are residual transport rates in the range of 4.8 to 240.0 kg/tidal cycle/unit width of bed; values which are 10 to 100 times less than the discharges for ripples or dunes in flume experiments.

The surfaces of the bars show a number of modifications due to water depth changes and current variations during the low tide period. Locally steepened water surface slopes cause the planing-off of the primary bedforms, and in some channels upper flow regime conditions persist for 1 - 1.5 hours. Directional changes prior to emergence produce swept-catenary megaripples. Virtually all areas are mantled with current ripples generated by the last minutes of the ebb tide, which generally flows laterally away from the bar. At very shallow depths, the flow is channelized in bedform troughs and produces ripples on megaripple slip faces, and builds small deltas into scour depressions. Mud flasers up to 1 cm thick are deposited in stagnant pools at this time. Wave action in shallow water is generally destructive, rounding and even obliterating already formed ripples, megaripples and sand waves. Swash-zone parallel lamination is produced on exposed, steep bar surfaces where large current bedforms are not present. Wave shock appears to be the agent responsible for triggering the liquefaction and slumping of fine sand on the backs of megaripples in exposed areas. The preservation potential of most modification features is low, but not zero.

Winter is a time of inactivity on the bars, due to the presence of the ice crust which immobilizes the sediment, and bedforms are reduced in height or obliterated. In places where the crust has not formed or is removed, deep scouring occurs, either by tidal currents or by lateral runoff which is channelized to a greater extent than in the summer. The fill of the scours is suggested to be primarily ebb cross-stratification, because it is protected from erosion by a thin, frozen surface layer that forms during exposure. Drift ice transports exotic coarse material to the bars, where tidal currents are incapable of transporting it. In the subtidal channels, tidal current sedimentation continues, and sediment transport should be enhanced by the 1.75-fold increase in viscosity resulting from the near-freezing water temperatures. In the spring, evidence of the winter features is rapidly destroyed, and normal summer sedimentation, which is believed to dominate the stratigraphic record, resumes.

# CHAPTER 5

# SEDIMENT GRAIN SIZE

## 5.1 Introduction

### 5.1.1 General

Grain size is an important property of any clastic sediment, and a complete understanding of the sedimentary dynamics of any modern environment cannot be achieved unless the grain-size characteristics are studied in some detail. In most of the studies of recent tidal deposits, the sediment grain size has been treated superficially, and little attempt has been made to explain either the size-frequency distributions or the areal variations of grain size in terms of the physical or environmental factors influencing the sedimentation. In this chapter, grain-size data from the studied sand bars will be analyzed in detail, specifically so that the sedimentary dynamics of these bars can be more fully understood. During the course of the investigations, however, a number of fundamental problems in the interpretation of grain-size data arise which must be considered at some length, thereby making the discussions of more general interest as well.

In the first part of the chapter, a general description of the grain-size characteristics of the sands will be given using primarily summary statistics, calculated by the method of moments. Included in this section are: the nature of the size segregations over the various types of bedforms; and the areal patterns of grain-size variation on the sand bars, together with a discussion of the extent to which the local hydraulics control the distributions of mean size that are observed.

In the second part of the chapter, the nature of the size-frequency distributions will be considered in more detail than is allowed using only summary statistics. The component size populations present in the observed size-frequency distributions will be determined through the use of a graphical dissection technique which is based on the assumption that the populations are overlapping log-normal distributions. Most of the remaining discussion is then concerned with the significance of these populations. An analysis of the data using a technique such as this provides a clearer understanding of sand bar dynamics than is possible with moment statistics.

### 5.1.2 Sample Collection

A total of 296 samples have been analyzed in the course of this investigation. The majority of these (263) come from the four major study bars, but some samples have been included from each of the other areas.

Because the areal variations in the sediment size characteristics are of central importance in this study, most of the samples collected have come from the crest of the bedform present at the sampling site, in order to eliminate the influence of local size segregation over the bedform profiles. The number of crest samples analyzed from each bar is as follows: Big Bar - 18; Diamond Bar - 41; Economy Point - 30; Selmah Bar - 114; Noel Bay Bar - 5; East Noel Bar - 4; Pinnacle Flats - 11; Spencer Point Bar - 4; Highland Village Bar - 2; and Saints' Rest Bar - 3. Only those from the four major study areas will be discussed specifically; their distribution on the bars is shown in Figure 5.1. On several of the bars, additional samples were analyzed to ascertain the nature of the size variations between different portions of the bedform. Out of a total of 77 such samples, 13 are from Big Bar, 20 from Economy Point, 28 from Selmah Bar, and 10 from Pinnacle Flats.

The size data from all of these samples, in the form of cumulative weight percentages, plus the mean, sorting, skewness and kurtosis (calculated by the moment method) are listed in Appendix 3. In this Appendix, the sample numbers are followed by a letter to designate the position on the bedform from which they came: C - crest; L - base of the lee side; ES and FS - ebb and remnant flood stoss sides, respectively, where both are present; E - stoss side, where only one stoss is developed; T - trough bottom; and F - flat,

FIGURE 5.1 : Sediment sample locations. A - Big Bar; B - Diamond Bar; C - Economy Point; D - Selmah Bar. Grain-size data for all samples listed in Appendix 3. If more than a single sample has been collected at one location, only the first sample number of the sequence has been listed.

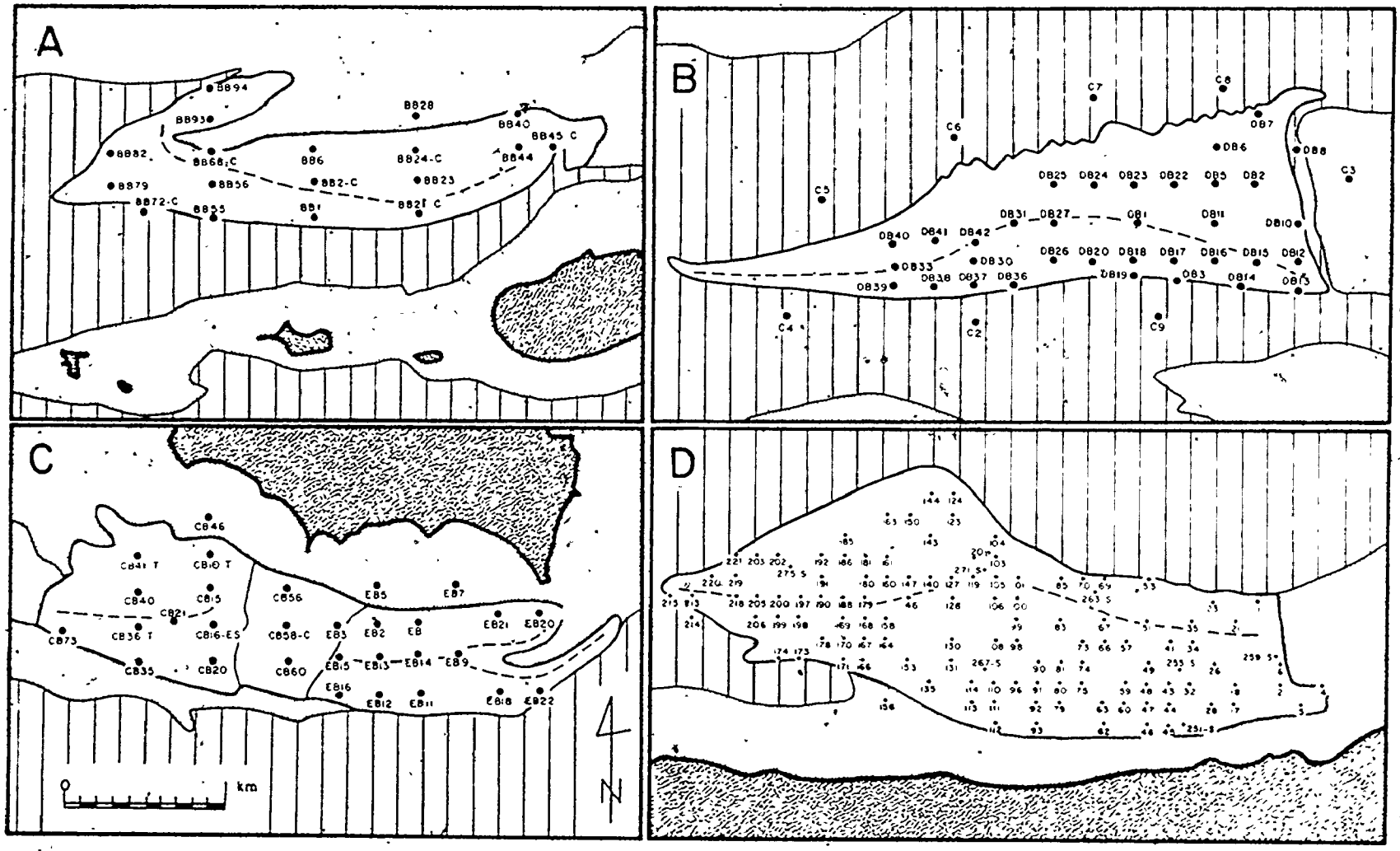
A
B
C
D
km
N
Land
Water
Studied Bar
(with crestline)
Other Intertidal Areas

rippled or wave-washed surfaces. At all other locations, where only a single crest sample was collected, the sample number is given alone.

All samples, regardless of location, were obtained with a small trowel, and come from the surface one to two centimetres of the bedform. The only exceptions to this are 8 samples, labelled C2 to C9 in Appendix 3, that were collected with a van Veen grab sampler, from the channels surrounding Diamond Bar.

### 5.1.3 Analytical and Computational Methods

Throughout this thesis, all grain sizes are expressed in terms of the dimensionless phi scale (Krumbein, 1934) ($\phi$), which is related to the grain diameter (d) in millimetres by the relationship (McManus, 1963):

$$\phi = - \log_2 (d/d_o) \qquad (5.1)$$

where $d_o$ is the standard diameter of 1 mm. The phi scale is the logarithmic equivalent of the Udden-Wentworth grade scale (Udden, 1898; Wentworth, 1922), and the verbal divisions of that scale have been retained here. For convenience, the corresponding millimetre values are given in parentheses whenever specific phi values are quoted.

All of the size analyses made in the course of this study were obtained by the sieve method, using a complete series of sieves with an interval of one-quarter phi unit, from -3.50 phi to 4.0 phi (11.31 - 0.0625 mm). All of the

sieving was carried out on a Ro-Tap machine with a shaking time of ten minutes. The analysis of two splits of several samples at different times showed that the precision of the technique was good, particularly for the mean and standard deviation, for which the average difference between the values calculated from the two splits was 0.02 phi units and 0.01 phi units respectively. These results compare favourably with similar studies by Folk (1955) and Rogers (1965) using graphical statistics. Skewness and kurtosis values were not nearly so reproducible, however, with average differences of 0.36 and 1.93 respectively.

Before sieving, all samples were washed with distilled water on a 4.0 phi (0.0625 mm) sieve to remove the soluble salts, plus the silt and clay fraction, in order to improve the accuracy of the results. The weight of the silt and clay fraction was initially determined by filtering the wash water. However, the very small proportion of fines present in most samples (less than 0.5%) did not warrant the additional work required by this procedure. As a result, its use was discontinued, unless visual inspection suggested that unusual amounts of silt and clay were present. It was found from these trials that the weight of fines retained on the filter paper was approximately equal to 30% of the weight lost by the sample during washing. The weight of fines calculated in this manner, combined with any pan fraction (less than 4.0 phi) recorded during sieving has been used as an estimate of the proportion of silt and clay present in the samples.

In this thesis, moment methods have been used to calculate the summary statistics of mean size, standard deviation, skewness and kurtosis, for the size distributions. The computational technique used in the calculations is that of Seward-Thompson and Hails (1973), who advocate the use of a linear interpolation between data points during the integration of the cumulative curve to obtain the moments about the origin ($\phi = 0.0$):

$$\mu_n' = \frac{1}{100} \int_0^{100} \phi^n \, dW \qquad (5.2)$$

(Seward-Thompson and Hails, 1973, Equation 1) where W is the percent cumulative weight. No class interval correction is necessary using this method. From the moments about the origin ($\mu_n'$), the moments ($\mu_n$) about the mean size can be calculated by the following formulae:

$$\begin{aligned} \mu_2 &= \mu_2' - \mu_1'^2 \\ \mu_3 &= \mu_3' - 3\mu_1'\mu_2' + 2\mu_1'^3 \\ \mu_4 &= \mu_4' - 4\mu_1'\mu_3' + 6\mu_1'^2\mu_2 - 3\mu_1'^4 \end{aligned} \qquad (5.3)$$

From the above:

$$\begin{aligned} \text{Mean size } (\phi) &= \mu_1' \\ \text{Standard deviation } (\phi\text{-units}) &= \sqrt{\mu_2} \\ \text{Skewness} &= \mu_3/(\mu_2)^{1.5} \\ \text{Kurtosis} &= \mu_4/\mu_2^2 \end{aligned} \qquad (5.4)$$

Equations (5.3) and (5.4) can be found in most statistics or sedimentology texts. For a normal distribution, the values of skewness and kurtosis are 0.0 and 3.0 respectively, so that departures from these values are an indication of a non-log-normal grain-size distribution. The summary statistics calculated from (5.4) are listed for all of the analyzed samples in Appendix 3. In the calculations, the pan fraction has arbitrarily been assigned a size of 5.0 phi (0.031 mm). Also, if either the pan fraction or the -3.5 phi (11.31 mm) fraction contained more than 5% of the total sample, then the moments have not been calculated, because the size distribution is too open-ended as indicated by Jones (1970).

During the discussion of the results, the verbal classification of sorting values (standard deviations) proposed by Friedman (1962) will be used. The limits of these verbal classes in terms of phi-units are: very well sorted, <0.35; well sorted, 0.35 - 0.50; moderately well sorted, 0.50 - 0.80; moderately sorted, 0.80 - 1.40; poorly sorted, 1.40 - 2.00; very poorly sorted, 2.00 - 2.60; and extremely poorly sorted, >2.60 phi-units.

No similar verbal subdivision of skewness is available; therefore, skewness values in excess of -1.0 or +1.0 will be informally designated as very negatively or very positively skewed, respectively, and values in the range of +0.50 to -0.50 will be considered as near-symmetrical.

Samples with a kurtosis of less than 3.0 are platykurtic, while those with a kurtosis greater than 3.0 are leptokurtic. Kurtosis values above 10.0 are informally termed very leptokurtic. A mnemonic attributed to Student, and quoted by Yule and Kendal (1950, p.164), may be of interest at this point: "Platykurtic curves, like the platypus, are squat with short tails. LeptoKurtic curves are high with long tails like the kangaroo--noted for "lepping"!".

## 5.2 Basic Description

### 5.2.1 General Characteristics

Using the statistics calculated for all 296 samples, the characteristics of the average sample from the intertidal sand bars can be obtained (Table 5.1 - Grand Means). This average sample is medium sand (mean size = 1.50 $\phi$ = 0.35 mm) and moderately well sorted (standard deviation = 0.63 $\phi$-units). It is slightly negatively skewed (average skewness = -0.19) and is leptokurtic (kurtosis = 8.92). As indicated by the large standard deviations associated with each of the grand mean values, however, and as shown more graphically by the large spread of the histograms of the various statistics in Figure 5.2, there is a great deal of variability from place to place in the characteristics of the sediments.

A large proportion of this variability is introduced in the coarse tail of the distributions. The 296 samples contain an average of 3.3% granules and pebbles (coarser than

TABLE 5.1 : Summary of grain-size characteristics. Means and standard deviations (in brackets) of grain-size parameters for each major bar studied. Bedform crest samples only used.

| Bar | Mean Size (ø) | Sorting (ø-units) | Skewness | Kurtosis | % Granules & Pebbles | % Silt & Clay |
|---|---|---|---|---|---|---|
| Big Bar | 1.60 ø (0.71) | 0.91 (0.43) | -0.57 (0.57) | 5.54 (2.28) | 5.00% (9.29) | 0.45% (0.15) |
| Economy Point | 1.23 ø (0.51) | 0.79 (0.27) | -0.91 (0.69) | 7.45 (3.73) | 3.69% (4.37) | 0.23% (0.15) |
| Diamond Bar | 1.70 ø (0.66) | 0.57 (0.27) | -0.11 (1.08) | 9.64 (4.69) | 0.76% (1.79) | 0.31% (0.15) |
| Selmah Bar | 1.65 ø (0.34) | 0.43 (0.11) | 0.12 (1.19) | 10.68 (4.84) | 0.31% (0.87) | 0.17% (0.31) |
| Grand Means | 1.50 ø (0.62) | 0.63 (0.36) | -0.19 (1.08) | 8.92 (5.07) | 3.34% (8.03) | 0.25% (0.24) |

FIGURE 5.2 : Frequency distributions of grain-size summary statistics.
A - Mean size (phi);
B - Sorting (phi-units);
C - Skewness;
D - Kurtosis;
E - Modal sizes (phi). Roman numerals indicate modes in the distribution. Heavy vertical lines are verbal class boundaries (see Section 5.1.3).

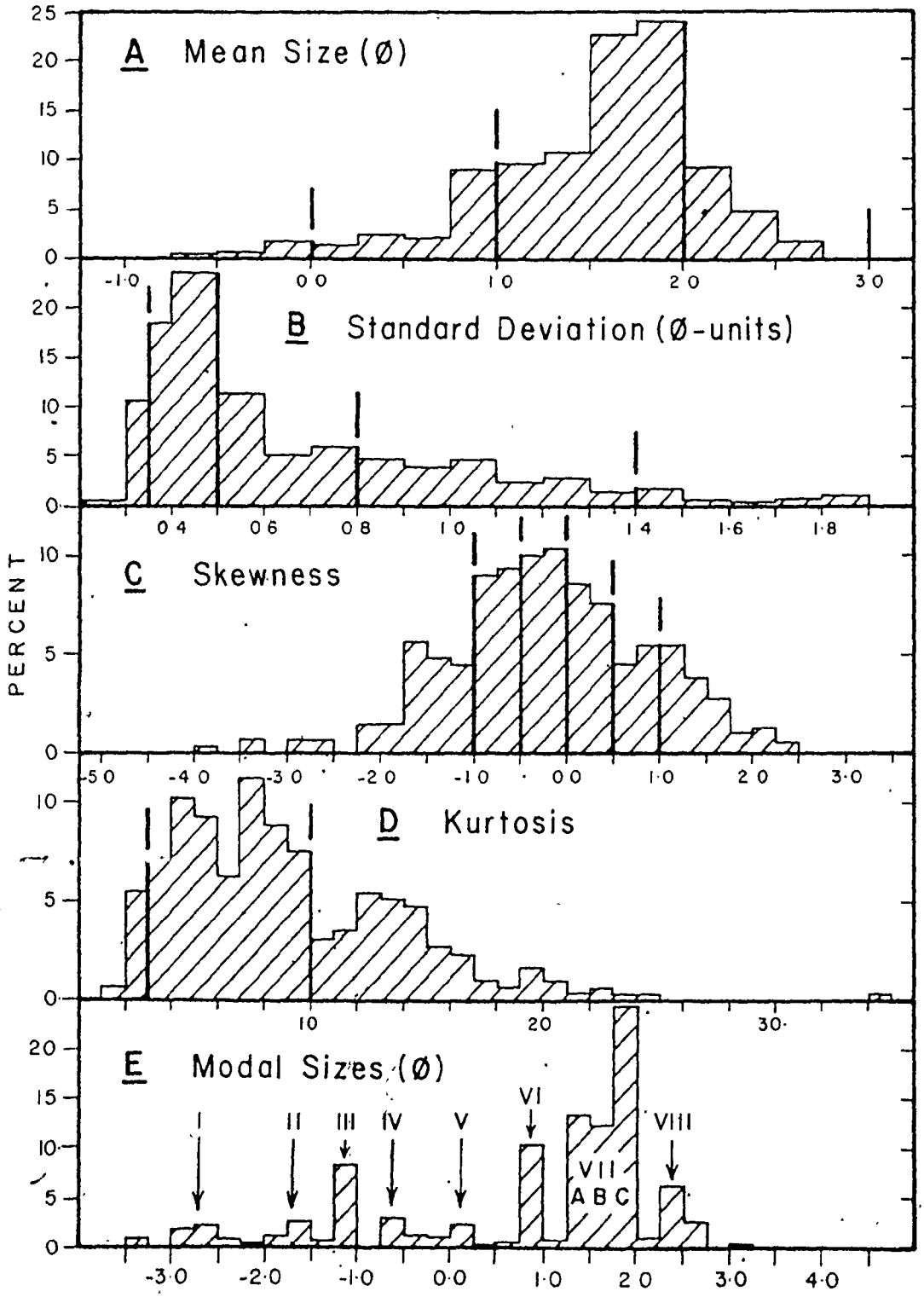
A Mean Size (Ø)
B Standard Deviation (Ø-units)
C Skewness
D Kurtosis
E Modal Sizes (Ø)
PERCENT
I
II
III
IV
V
VI
VII
A B C
VIII

-1.0 phi or 2.0 mm), with a standard deviation of 8.0% and a range from zero to a maximum of over 64%. In contrast, the silt plus clay fraction is very small (average = 0.25%), and present in a relatively constant amount (standard deviation = 0.24%). This difference in the size of the two tails is responsible for the negative average skewness of the samples.

Looking at the distributions of the four summary statistics (Figure 5.2) in more detail, it can be seen that over two-thirds (66.8%) of the samples have mean sizes in the medium sand grade, while 15.8% are fine sand, 14.7% are coarse sand, and only 2.7% are very coarse sand. Notable by their absence are sands with a mean size in the very fine sand grade. The distribution of sorting values (standard deviations) has its mode in the well sorted class which contains 42.1% of the samples, but there are also significant numbers of samples in the moderately well, and moderately sorted divisions (22.3% and 19.9% respectively). 11.0% of the total are very well sorted, but only one sample is poorly sorted. The calculated skewness values cover a wide range of values, from -3.76 to +2.35. The largest proportion of the samples (36.6%) have near symmetrical skewnesses between -0.5 and +0.5. The distribution of values is skewed towards negative values, however, with 20.0% of the samples highly negatively skewed, compared to 15.2% that are highly positively skewed. This is due to the presence of the coarse tail as mentioned above. Kurtosis values also show a very wide distribution. It is notable that

only 6.1% of the samples have a kurtosis of less than 3.0 (platykurtic), while 36.8% are strongly leptokurtic (kurtosis greater than 10.0), which indicates that the sorting in the central (modal) portion of the distributions is very good, relative to the tails.

A wide variety of cumulative curve shapes (plotted with a probability scale) are associated with the above summary statistics, and although a thorough investigation into the significance of these shapes is deferred until Section 5.3, some general results are warranted at this time. Inspection of all 296 cumulative curves indicates that most of them can be closely approximated by a series of straight-line segments as suggested by Sindowski (1957) and Visher (1969), despite the fact that many of the segments are, in fact, gentle curves. Out of the continuum of curve shapes, four basic types can be identified, depending on the presence or absence of various segments. A representative example of each type is given in Figure 5.3, but it must be pointed out that continuous gradations occur between all end members.

Type A curves (e.g., BB56, Figure 5.3) are the most common, amounting to 43.6% of the total, and are composed of three straight-line segments. The central segment is the steepest of the three and corresponds to the saltation population of Visher (1969) or the intermittent suspension population of Middleton (1976). The coarse- and fine-tail segments are called the traction and suspension populations, respectively, by Visher (1969).

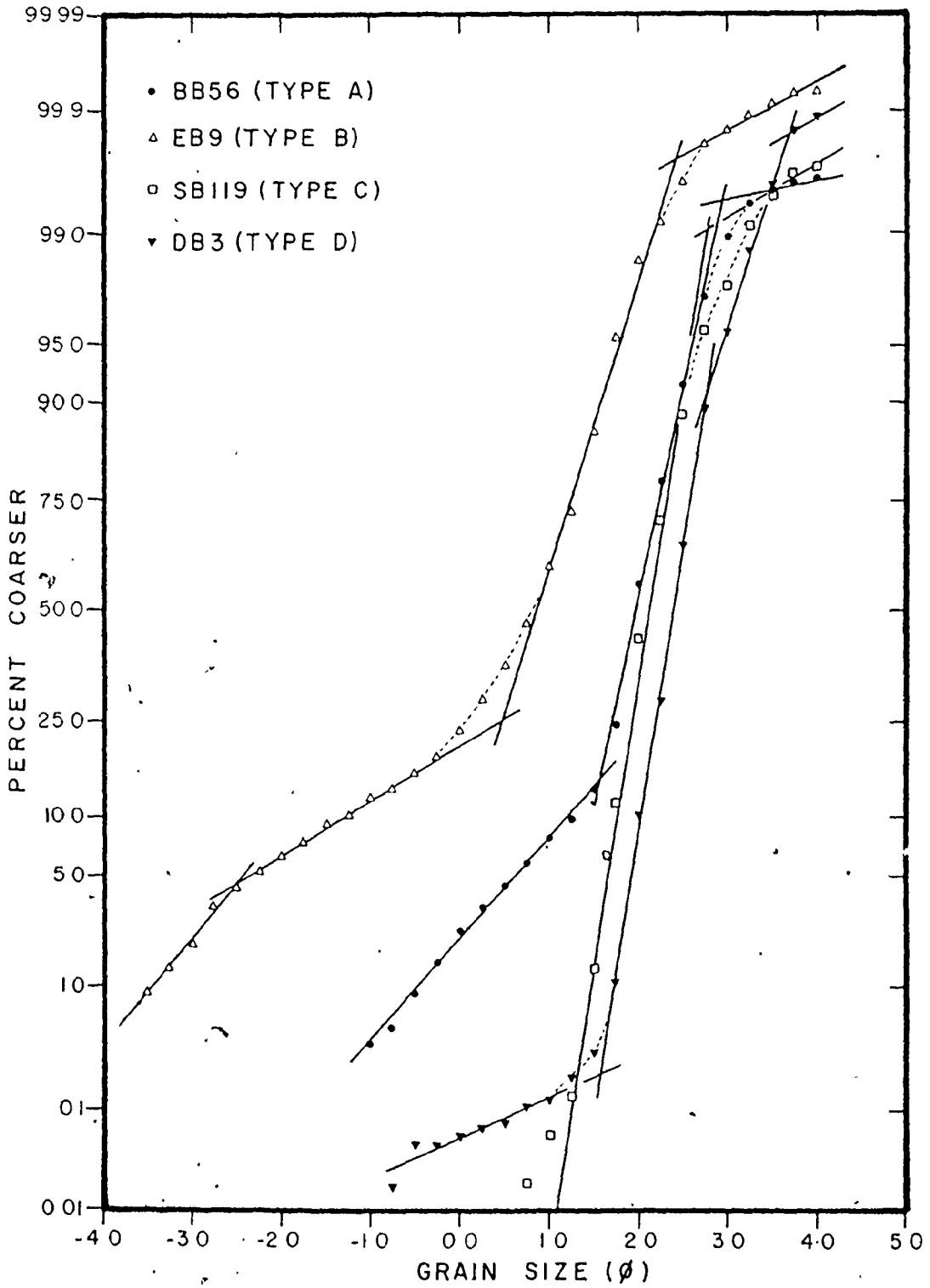
• BB56 (TYPE A)
△ EB9 (TYPE B)
□ SB119 (TYPE C)
▼ DB3 (TYPE D)
PERCENT COARSER
99 99
99 9
99 0
95 0
90 0
75 0
50 0
25 0
10 0
5 0
1 0
0 1
0 01
-4 0
-3 0
-2 0
-1 0
0 0
1 0
2 0
3 0
4 0
5 0
GRAIN SIZE (ø)

Type B curves (e.g., EB9, Figure 5.3) possess the same three segments shown by Type A, but in addition, there is a fourth (steeper) segment attached to the coarse end of the traction population. 24.4% of the curves have this form.

In contrast to the above, curves of Type C (e.g., SB119, Figure 5.3) possess no traction population and are composed almost entirely of the steep, intermittent suspension population. Pure Type C curves are relatively rare, because most samples show at least a small deflection at the coarse tail, so that assignment to either Type A or Type C becomes arbitrary. Only 8.0% of the samples have been classified as Type C.

All of the above cumulative curve types have the common feature of possessing only a single intermittent suspension population. Type D curves (e.g., DB3, Figure 5.3) on the other hand, are characterized by having two (and in some cases, three) steep, intermittent suspension segments and are, therefore, similar to the beach foreshore samples shown by Visher (1969, Figure 7). Curves of this type may or may not have a coarse tail, and as a result, samples which otherwise would be classified as Type A, B or C are included in the Type D designation: the example shown in Figure 5.3 (SB119) is a Type A curve, except for the second steep population at the fine tail. 24.0% of the curves are Type D, with by far the largest number coming from Selmah Bar.

In arriving at the above classification, neither the nature of the breaks between the straight-line segments, nor the position of the breaks in terms of either grain size or cumulative percent has been considered. There is, therefore, considerable room for variation within each group with regard to the sharpness of the breaks, the steepness of the various line segments, and the proportion of the total represented by each segment. As indicated by the thin, dashed lines in Figure 5.3, most of the breaks are rounded to some degree, and the examples shown in Figure 5.3 are also representative of the range of line slopes and proportions of the various populations. The suspension population rarely exceeds 1% of the sample, but is present in almost all samples (94.5%), and as a result, no separate group has been erected for samples lacking it. Material coarser than the intermittent suspension population(s) commonly comprises 10%, and can reach up to 70% of the sample. The proportions of the traction and suspension populations are in agreement with the differing abundances and standard deviations of the granule-pebble and silt-clay fractions reported in Table 5.1. As mentioned previously, the significance of the various curve shapes will be investigated further in Section 5.3.

It is of interest to note that 28.6% of all samples contain more than a single mode, and that some samples possess up to 8 discrete modes. (In this discussion, the modes are defined simply on the basis of local maxima in the histograms

of weight percent, and the modal sizes are taken as the sieve intervals containing the maxima. Only classes containing more than 1% of the sample have been considered.) Many of the modes are found to recur, not only in a few samples from a single bar, but also in samples from widely separated bars. As a result, the frequency distribution of modal sizes (Figure 5.2E) itself shows eight clearly defined modes which have been designated by Roman numerals I through VIII, from coarsest to finest, for easy identification. The large, broad peak labelled VII is further subdivided into A, B and C parts at 0.25 phi-unit intervals. Calibration measurements made on the sieves give no indication that these modes are due to defective sieves.

Modes I to V usually fall in the coarse tail of the size distributions (traction population) and are only rarely present as the dominant or maximum mode in the sample. The largest mode in 79% of all the samples falls in the medium sand grade (mode VII), while the fine sand mode (mode VIII) is dominant in 10.5% of the samples, and mode VI in 7.1%.

With the exception of Selmah Bar, the average samples for each bar (Figure 5.4), determined by averaging the weight percents for each size class, also contain more than one mode. The modes present in the average samples are: on Big Bar - numbers I, III, VI, VIIC, and VIII; on Diamond Bar - numbers I, II, III, and VIIC; at Economy Point - numbers III and VIIB; and on Selmah Bar - number VIIC only. The finest mode in each

FIGURE 5.4 : Average cumulative curves for the major study bars. Vertical axis is probability scale.

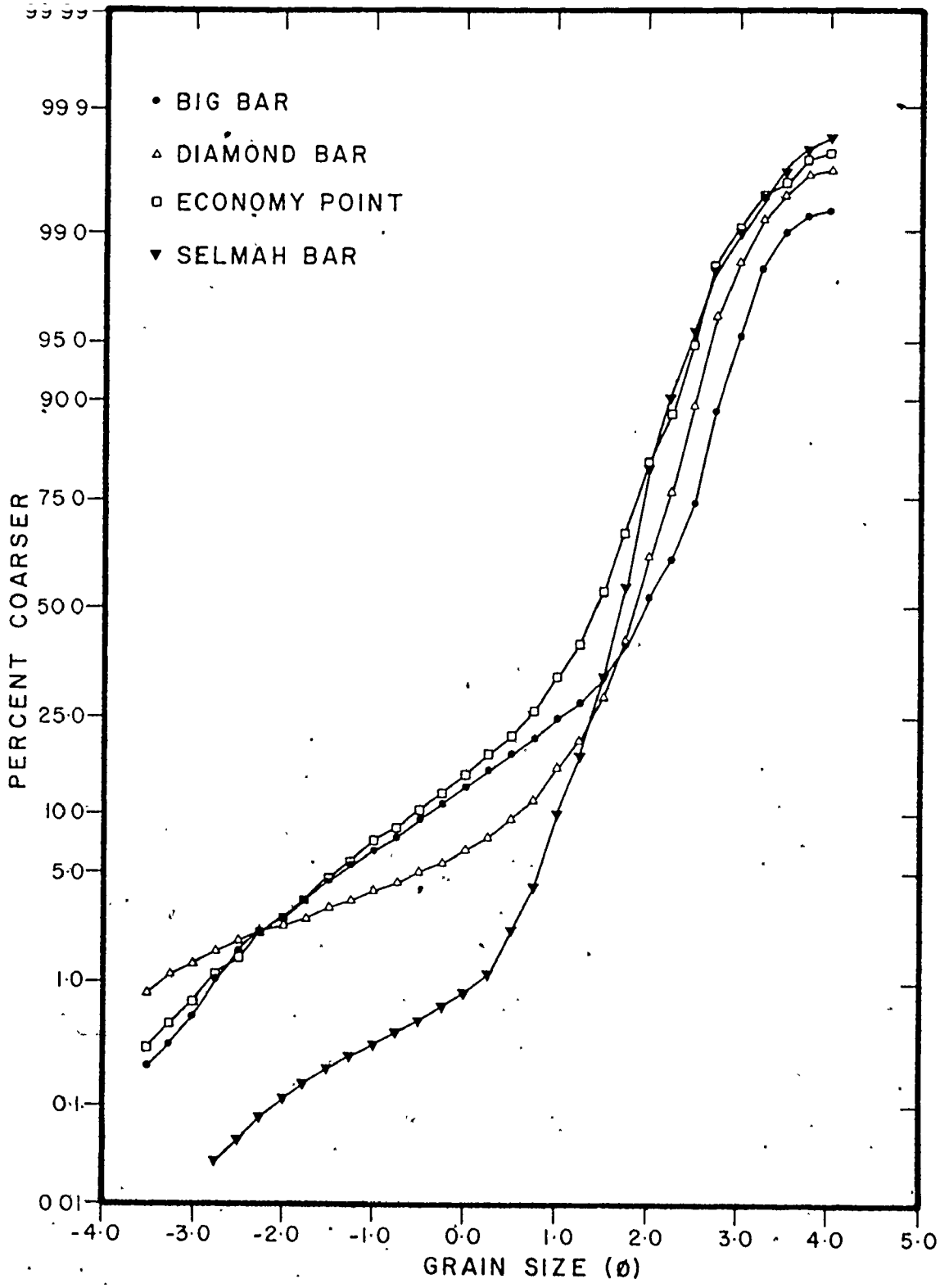
• BIG BAR
△ DIAMOND BAR
□ ECONOMY POINT
▼ SELMAH BAR
PERCENT COARSER
99 99
99 9
99 0
95 0
90 0
75 0
50 0
25·0
10 0
5·0
1·0
0·1
0 01
-4·0
-3·0
-2·0
-1·0
0·0
1·0
2·0
3·0
4·0
5·0
GRAIN SIZE (ø)

case is clearly the dominant one, with the exception of Big Bar, where two subequal modes (VIIC and VIII) are present. These plot as two intermittent suspension populations in the cumulative curves (Figure 5.4). The average samples for the other bars show only a single, steep, intermittent suspension population as would be expected from the single predominant mode. All of the average samples have a well-developed traction population plus a small suspension population (Figure 5.4).

Further differences between the grain-size composition of each bar are revealed by the averages of the summary statistics for each bar (Table 5.1), calculated using bedform crest samples only. The sediment at Economy Point is clearly the coarsest of all the bars, and is also the most negatively skewed. The sands on Big Bar, which are the second coarsest on average, have the poorest sorting and lowest kurtosis values, and also contain a larger percentage of both the granule-pebble and silt-clay fractions than does the sediment from any of the other bars. In marked contrast to this, Selmah Bar sands, which have the second finest average mean size, have the best sorting, highest kurtosis, and the lowest percentage of both the <-1.0 phi (>2.0 mm) and >4.0 phi (<0.063 mm) fractions.

Further inspection of these data show that a marked difference exists between those bars that are part of the Cobequid Bay complex (Diamond and Selmah Bars) and those that

are isolated along the Minas Basin foreshore (Big Bar and the Economy Point complex). The sands from Cobequid Bay have an average mean size that is finer; they are markedly better sorted, have much more nearly symmetrical size-frequency distributions and have higher kurtosis values than the sediment on Big Bar or at Economy Point. These differences in the characteristics between the two areas can be explained in part by comparing the abundances of material coarser than -1.0 phi (2.0 mm): 0.76% and 0.31% on Diamond and Selmah Bars respectively, versus 5.00% and 3.69% on Big Bar and at Economy Point. The differences may reflect the much more intimate association that Big Bar and the Economy Point complex have with coarse-grained, gravel lag areas. There is also the implication that the sand in Cobequid Bay has undergone much more extensive reworking and sorting than that on the isolated bars along the shore of the Minas Basin; Diamond and Selmah Bars, which have the highest energy levels of the four bars (Figure 3.14), also have the finest sand and the smallest coarse tails. These relationships are the opposite of what would be expected on the basis of competency considerations, suggesting that some factor other than local hydraulics is responsible for the overall characteristics of the sands. This topic will be investigated further in Sections 5.2.4 and 5.3.

It is of interest to compare briefly the characteristics given above for this macrotidal environment with those cited by Friedman (1967) for beach and river sands. Friedman found that beach sands contain a smaller percentage of silt and clay (generally less than 0.2%), have better sorting (most commonly less than 0.6 - 0.7 phi-units), and are more negatively skewed than river sands. In addition, the range of each of these parameters is less for beaches than for rivers. On the basis of the above characteristics, the present suite of intertidal sands possess features common to both beach and river sands. The good sorting and negative average skewness are reminiscent of beach sediments, but the large numbers of moderately well and moderately sorted samples, and of positively skewed sands are more typical of rivers. Furthermore, the average content of silt and clay (0.25%) present in the intertidal sands is borderline between beach and river values as shown by Friedman's (1967) Figures 7, 8 and 12. The large coarse tail present in many intertidal samples is also more characteristic of rivers. It appears, therefore, that the vigorous action of the tidal currents is capable of producing better sorting, and of more effectively removing the fine tail than is river flow, but that the results are not as good as those achieved by swash action.

A comparison of the cumulative curve shapes presented above with those considered to be environmentally sensitive by Visher (1969) is also informative. It was mentioned above

that some of the Type D curves with their two saltation (or intermittent suspension) populations are similar to those obtained from the beach foreshore environment (Visher's Figure 7). There is no field evidence to suggest, however, that swash and backwash are responsible for these populations. Furthermore, the Type A curves are very similar to those given by Visher (1969, Figure 9) as characteristic of the offshore wave zone, where currents are presumably of limited importance relative to waves, in marked contrast to the true situation in the Minas Basin and Cobequid Bay. Using Visher's (1969) criteria, the fluvial environment would be ruled out for almost all samples because the traction population is too abundant, and, more importantly, because the saltation population is too well sorted. Visher (1969, p.1093 and Table 1) does indicate, however, that a considerable traction population together with a well sorted saltation population, such as is found in curve Types A and B, may be characteristic of tidal action. Further work is necessary before the true worth of Visher's approach can be evaluated.

### 5.2.2 Relationships between Parameters

In the above discussion of the average size characteristics for each bar (Table 5.1), certain relationships between the four summary statistics are evident; namely that poorer sorting, more negative skewness, and lower kurtosis values are all associated with coarser mean grain sizes, and with larger percentages of material coarser than -1.0 phi

(2.0 mm). Similar relationships have been described by numerous other workers. Folk and Ward (1957) and Thomas et al, (1972, 1973), have observed that sinusoidal relationships exist between pairs of parameters when a sufficiently wide range of mean sizes is available for study. Analysis of the statistics for the individual samples from each bar shows that comparable patterns exist, bearing in mind the much more limited range of mean sizes present here.

Figure 5.5 gives the plots of sorting versus mean size for each of the bars, together with the best fit linear regression lines. All of the correlation coefficients shown are significant at the 99% level. Despite the scatter, it can be seen that the relationships are essentially linear, with the exception of that for Selmah Bar, so that the sorting is best for fine sands and worsens as the mean size becomes coarser. On Selmah Bar, however, the best sorting is found in the medium sand grade. There is an indication that the trend of the values for Diamond Bar is also sinusoidal (broken line), with the suggestion of a maximum at 0.0 phi (1.0 mm) and a minimum in the range of 2.0 to 2.5 phi (0.25 - 0.18 mm).

Figure 5.6 shows the plots of skewness against mean size, and it is immediately evident that the relationships between these two parameters are not linear. On Big Bar, Diamond Bar, and at Economy Point (Figures 5.6A, 5.6B and 5.6C respectively), the patterns are concave up, with the most

FIGURE 5.5 : Plot of sorting versus mean size.
A - Big Bar; B - Diamond Bar;
C - Economy Point; D - Selmah Bar;
E - Summary of the trend lines.
R = correlation coefficient for best-fit linear regression.
Thin lines give verbal class boundaries (see Section 5.1.3).

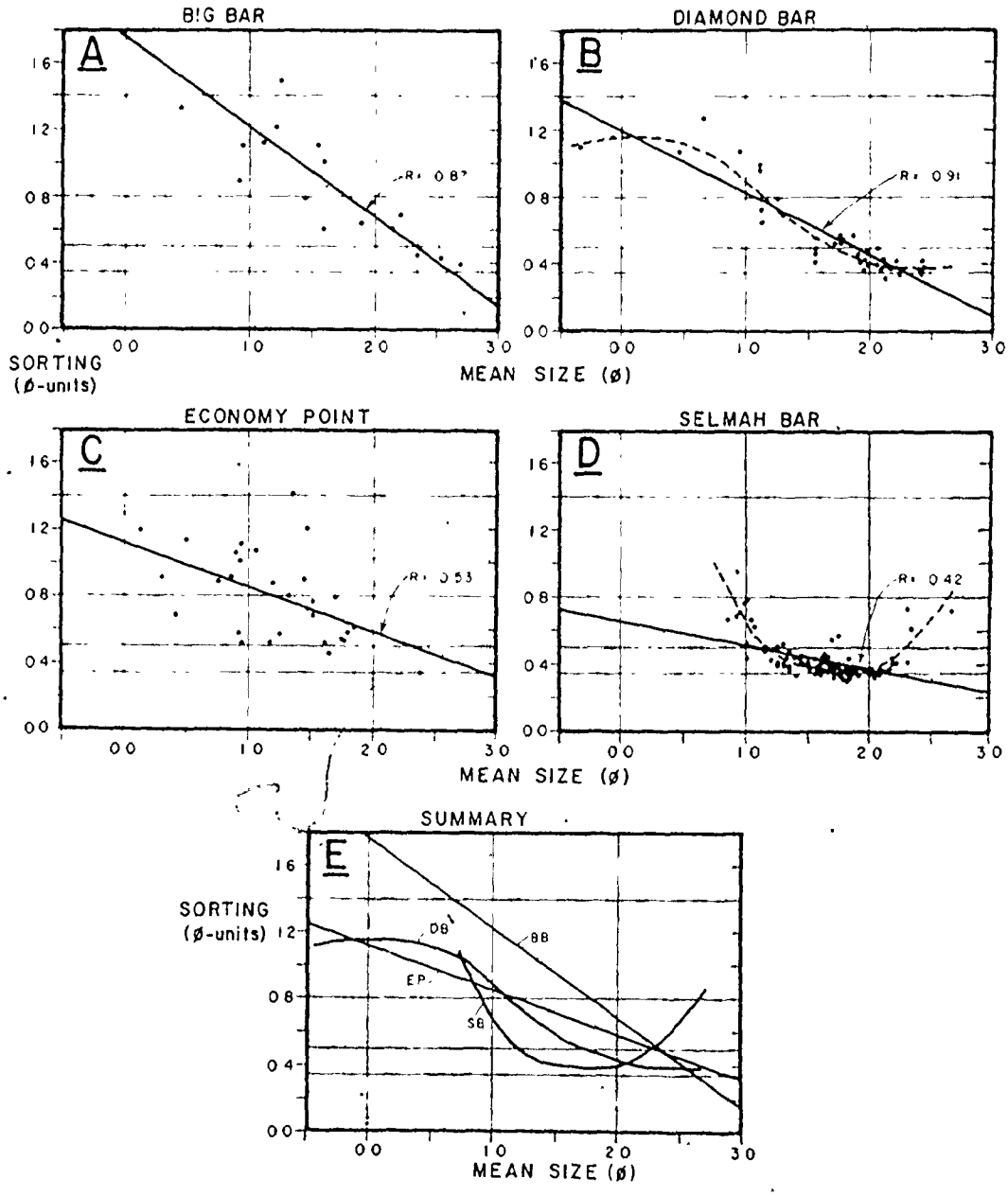
BIG BAR
A
DIAMOND BAR
B
ECONOMY POINT
C
SELMAH BAR
D
SUMMARY
E
SORTING
(ø-units)
MEAN SIZE (ø)
DB
BB
EP
SB

FIGURE 5.6 : Plot of skewness versus mean size. Divisions same as Figure 5.5. Thin lines are verbal class boundaries (see Section 5.1.3). Data points falling outside the figures indicated by arrows.

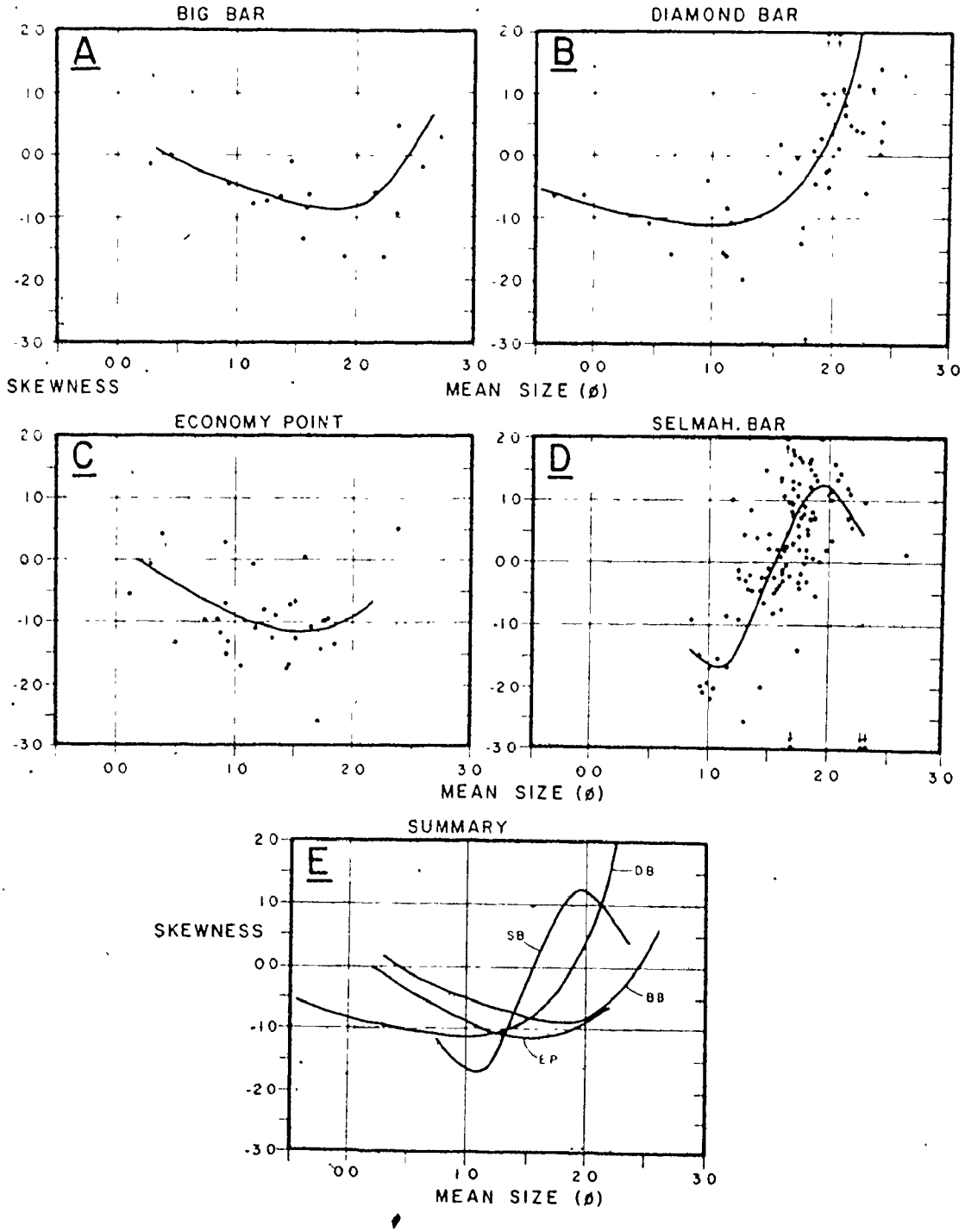
BIG BAR
A
DIAMOND BAR
B
SKEWNESS
MEAN SIZE (ø)
ECONOMY POINT
C
SELMAH. BAR
D
MEAN SIZE (ø)
SUMMARY
E
SKEWNESS
DB
SB
BB
EP
MEAN SIZE (ø)

negative skewness values occurring in sands with mean sizes between 1.0 and 2.0 phi (0.5 - 0.25 mm). More nearly symmetrical, or even positively skewed distributions are found in coarse and fine sands. As was the case for sorting, Selmah Bar (Figure 5.6D) shows a considerably different trend that appears to have a minimum at approximately 1.1 phi (0.47 mm) and a maximum at 1.9 phi (0.27 mm).

The relationship between kurtosis and mean size for each bar is shown in Figure 5.7. These plots are characterized by a large amount of scatter which makes the indicated trends of doubtful value. A large part of this scatter may be due to the lack of reproducibility of kurtosis values noted in Section 5.1.3 above. One feature common to all bars is that the highest measured kurtosis occurs for mean sizes between 1.5 and 2.0 phi (0.35 - 0.25 mm). On Diamond Bar and at Economy Point (Figures 5.7B and 5.7C respectively), this also coincides with the peak in the suggested trend. The lowest kurtosis values in these two areas, and on Big Bar, are found in the coarsest sands. On Selmah Bar, no pattern can be detected.

Folk and Ward (1957) and Thomas et al (1972, 1973) explain the trends that they observe as being the result of mixing two or three discrete populations or modes in variable proportions. A similar explanation appears possible here as well, and can be expressed in terms of the populations indicated by the cumulative curves shown in Figures 5.3 and 5.4.

FIGURE 5.7 : Plot of kurtosis versus mean size. Divisions same as Figure 5.5. Thin lines are verbal class boundaries (see Section 5.1.3). Data points falling outside the figures indicated by arrows. No trend is evident in the Selmah Bar data.

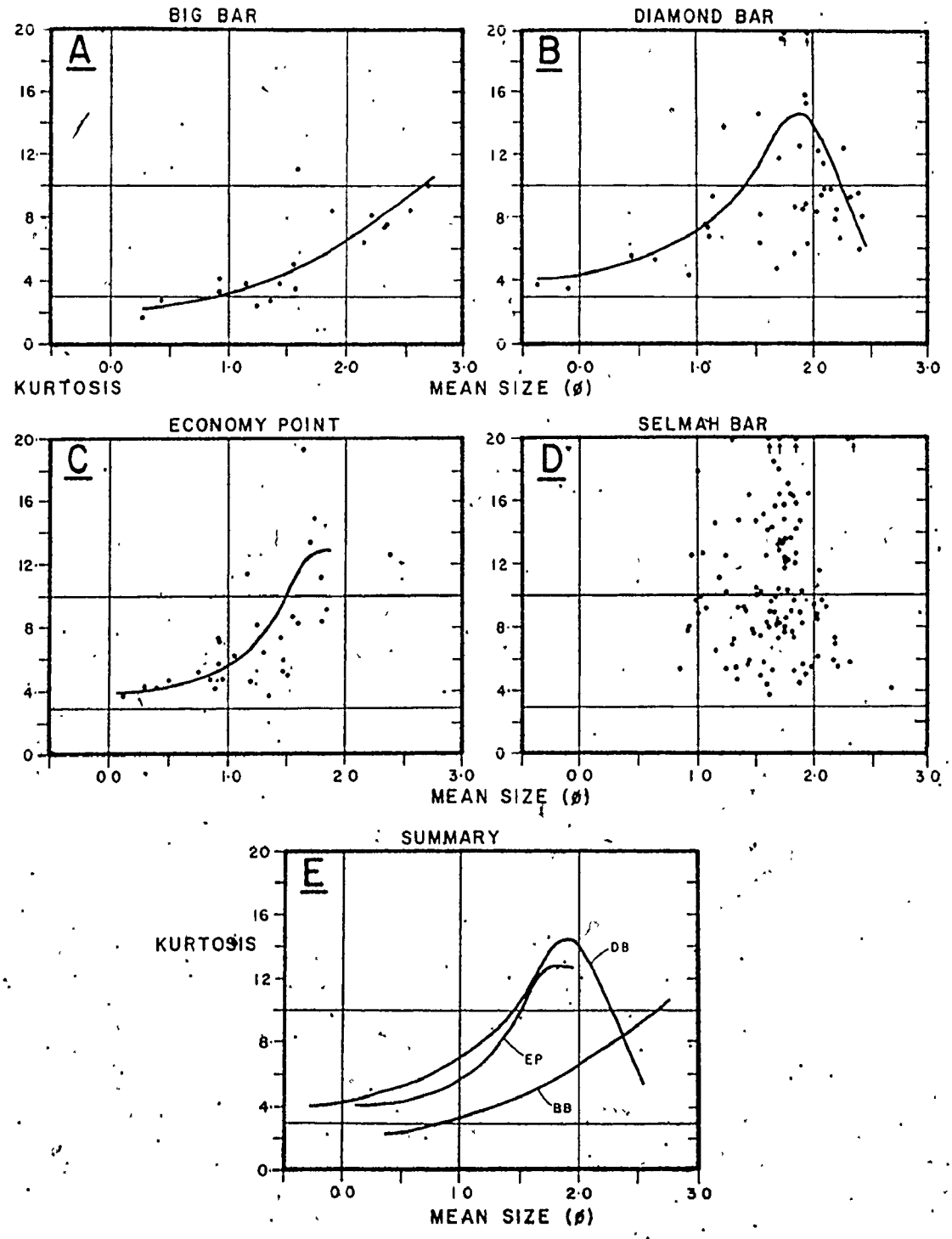
BIG BAR
A
DIAMOND BAR
B
KURTOSIS
MEAN SIZE (ø)
ECONOMY POINT
C
SELMAH BAR
D
MEAN SIZE (ø)
SUMMARY
E
KURTOSIS
DB
EP
BB
MEAN SIZE (ø)

The basic populations involved are the traction population, the suspension population, and the intermittent suspension population. The addition of a small suspension fraction and a somewhat larger traction population to a dominant intermittent suspension population results in a sorting that is poorer than that of the intermittent suspension population alone, and produces a negatively skewed and leptokurtic distribution. This is the usual situation in the study area, because the intermittent suspension population only rarely occurs alone. This explains why mean sizes only slightly coarser than the predominant modal size have negative skewness (Figure 5.6E). A progressive increase in the proportion of the traction population causes the following changes as the mean size becomes coarser: the sorting continues to worsen on all bars (Figure 5.5E), due to the poor sorting of the traction population; the skewness becomes more negative at first while the traction population is subordinate to the intermittent suspension population, but then returns to near zero values as the two attain subequal proportions (Figure 5.6E); and the kurtosis values decrease continuously (Figure 5.7E). Analogous changes in the statistics are to be expected from the addition of material finer than the dominant intermittent suspension population: as the mean size becomes finer, the sorting should worsen, the skewness values become positive as seen for Big Bar, Diamond Bar and Selmah Bar; and the kurtosis decreases as is the case for Diamond Bar and Economy Point.

Although the above model does explain the gross features of the trends shown in Figures 5.5, 5.6 and 5.7, the lack of the predicted worsening in the sorting in the fine sand sizes for Big Bar, Diamond Bar and Economy Point warrants some further comment. As indicated in the previous section, the percentage of silt and clay (suspension population) present in the samples does not vary greatly. Instead, the fine and very fine sand added to the predominant medium-sand mode to produce mean sizes in the fine sand grade occurs as a second, well-sorted, intermittent suspension population (Type D cumulative curves). As a result, the sorting remains good in the fine sands. The increase in the sorting values in this range shown on Selmah Bar is not an exception to this explanation. In this case, the fine sands, which are located in areas adjacent to the mudflats (Figure 5.11), contain mud pellets that cause the observed trends in sorting (Figure 5.5D) and skewness (Figure 5.6D).

The trends shown by the Big Bar samples, although agreeing in general form with that predicted above, are displaced from those of the other bars: upwards in the case of sorting, and to the right for both skewness and kurtosis. This is believed to result from the fact that the dominant mode on Big Bar is finer than on any of the other bars (Table 5.2), while the traction population is as coarse as elsewhere, and is almost as abundant as at Economy Point (Table 5.1 and Figure 5.4).

Both Diamond and Selmah Bars differ from the other two areas in the large number of samples having positive skewness and the resulting length and steepness of the positively-sloping limb of their skewness trends (Figures 5.6B and 5.6D). In the previous section, the low average skewness for these bars was interpreted as due to the small size of the coarse tail, which suggests, therefore, that the coarse, traction population is effectively excluded from sands having mean sizes finer than approximately 1.5 phi (0.35 mm). On Big Bar and at Economy Point, in contrast, these finer sands are negatively skewed, indicating that the coarse tail is still present.

Because of the large amount of scatter present in most of the plots in Figures 5.5, 5.6 and 5.7, it is evident that the explanations given above will not necessarily apply to any specific sample, but rather are a statement of the "average" characteristics of the sands. For this reason, reliance on an analysis of this type does not permit all of the available information to be extracted from the data. Only the detailed examination of individual size-frequency distributions, using some type of dissection technique, as is done in Section 5.3.3, allows the true nature of the populations to be determined.

### 5.2.3 Size Segregation over Bedforms

Before considering the areal variations in grain size over the bars, as shown by the samples coming from the crests of bedforms, the size variations over the bedforms should be investigated. As was mentioned earlier, 77 samples collected for this purpose have been analyzed, and the data are given in Appendix 3. These samples come from 20 different locations, on Big Bar, Selmah Bar, Economy Point and Pinnacle Flats, and represent a variety of average grain sizes, and bedform types. The data are not sufficiently extensive, however, to permit a discussion of the hydraulic factors controlling the size segregations observed.

Inspection of the data indicates that two different patterns of size variation over bedforms can be identified, depending, apparently, on whether the bedform does or does not possess an avalanche face. Two representative examples of each pattern are given in Table 5.2, together with the averages of the differences between crest and trough samples for each bedform type.

The first pattern of size segregation is shown by a megaripple from Centre Bar and a rippled sand wave from the crest of Big Bar (Table 5.2). The consistent feature of this pattern is the concentration of coarse material in the trough, and on the lower half of the stoss side and slip face. If a large amount of coarse material is present, then the segregation of the coarse fraction can be very striking, as in the

TABLE 5.2 : Grain-size segregation over bedforms. Average differences obtained by subtracting the trough value from the crest value for all sites with a similar segregation pattern and averaging.

| Bedform Type (sample members) | Sample Position | Mean Size (ø) | Sorting (ø-units) | Skewness | Kurtosis | % coarser than -1.0 ø |
|---|---|---|---|---|---|---|
| A. Bedforms with slip faces: | | | | | | |
| Megaripple (CB16 - CB19) | crest | 1.80 | 0.58 | -0.93 | 8.37 | 0.41 |
| | slip face | 1.98 | 0.59 | -1.63 | 15.39 | 0.37 |
| | stoss side | 1.62 | 0.89 | -1.39 | 6.04 | 1.91 |
| | trough | 1.84 | 0.91 | -1.71 | 7.52 | 2.19 |
| Rippled sand wave (BB2 - BB5) | crest | 1.57 | 1.01 | -0.78 | 3.47 | 1.58 |
| | slip face | 1.74 | 0.96 | -0.76 | 3.34 | 0.63 |
| | stoss side | 1.63 | 1.05 | -0.64 | 2.90 | 0.99 |
| | trough | 1.03 | 1.88 | -0.68 | 2.13 | 23.05 |
| Average Difference | | +0.41 | -0.49 | | | -11.98 |
| B. Bedforms without slip faces: | | | | | | |
| Rippled sand wave (SB255 - SB258) | crest | 1.41 | 0.45 | -0.86 | 8.29 | 0.19 |
| | lee side | 1.40 | 0.41 | -0.08 | 6.84 | 0.07 |
| | stoss side | 1.61 | 0.49 | 0.11 | 7.63 | 0.07 |
| | trough | 1.72 | 0.55 | 0.50 | 7.63 | 0.13 |
| Rippled sand wave (BB21 - BB22) | crest | 2.16 | 0.61 | -0.93 | 6.35 | 0.07 |
| | trough | 2.65 | 0.35 | 0.28 | 12.40 | 0.01 |
| Average Difference | | -0.34 | 0.00 | | | -0.29 |

case of the rippled sand wave from Big Bar, and the crest of the bedform has a finer mean size than the trough. If the coarse fraction is less abundant, then the mean size may not show any difference between the crest and trough. Furthermore, the surface of the stoss side is almost always coarser than the lee side, in terms of mean size and percentage of material coarser than -1.0 phi (2.0 mm), presumably due to the formation of a lag deposit on the surface during the erosion of the stoss side. The stoss side and trough samples also exhibit poorer sorting than those from the crest or slip face. Many workers, including J. R. L. Allen (1965) and Basumallick (1966) have noted the tendency for coarse material to be concentrated at the base of the slip face. This feature is usually explained as resulting from the action of dispersive pressure (Bagnold, 1954) during avalanching.

In some places where the mean sand size is fine sand, toesets are developed, which have mean grain sizes that are generally finer than those in the slip face. Settling of material from suspension in the separation eddy is believed to be responsible for this (Jopling, 1965). The fine mean size of the trough sample from the first example in Table 5.2 may reflect the presence of such settled material, although no obvious toesets were noted when the samples were collected.

The second pattern of grain-size variation over bedforms is illustrated by an example from a large, flood-asymmetric, rippled sand wave on Selmah Bar, and by a low, symmetrical

rippled sand wave on the crest of Big Bar (Table 5.2). In both cases, there is no avalanche face. From these examples, it can be seen that the crests of such bedforms are composed of coarser material than the trough, and there is little difference in the amount of coarse material in either position. Visual observations indicate that megarippled sand waves also conform to this pattern, and Wells and Ludwick (1974) present data which show a similar trend for sand waves in the entrance to Chesapeake Bay.

The reason(s) for the concentration of the coarser material on the crest of these bedforms are not known, but three possibilities, which need not work independently, can be suggested: i) without the presence of avalanching, the settling of material from suspension should be the predominant process sorting the sediment in the lee of these bedforms, producing a decrease in grain size downstream of the crest in the trough, as described by Jopling (1965) and J. R. L. Allen (1968b); ii) higher current speeds and average shear stresses over the crests might result in coarse material being left behind on the crests as a lag; iii) the concentration of wave activity on the crestal areas could also produce coarse mean sizes there by winnowing out the fine material.

Further work is necessary to substantiate the validity of the distinctions made here regarding the patterns of size segregation with respect to bedform morphology. The causes of the observed size variations are not fully understood, especially for the large sand waves that lack an avalanche face.

### 5.2.4 Areal Trends

In this section, the geographic distribution of the various summary statistics will be described for each of the major study areas (Figures 5.8 to 5.11). It should be remembered throughout that all samples under discussion were collected from the crest of the bedforms present at the sampling sites. In Appendix 3, the numbers of these samples appear either without any designating letter (i.e., BB1) or followed by the letter C (= crest) (i.e., BB2-C).

(i) Big Bar: On Big Bar, the mean size (Figure 5.8A) decreases regularly from north to south, with the finest sands present along the southern edge. The coarse sand along the northern side is obviously a reflection of the proximity to the harrow-marked gravel lag (Figure 2.10). Somewhat coarser sand is also present in the southern channel as shown by the sample at the west end of the bar.

In Figure 5.8B, the sorting can be seen to improve in a southerly direction across the bar, from poorly sorted on the northern side to well sorted along the southwest edge. A comparison of this distribution with that of mean sizes (Figure 5.8A) reveals the correlation between the two that was shown in Figure 5.5A.

Skewness values (Figure 5.8C), by contrast, show a significantly different pattern of areal variation. Only two samples from the southwest corner of the bar have positive skewness, while all the remainder are negative, indicating that

FIGURE 5.8 : Areal variation of grain-size characteristics on Big Bar.
A - Mean size (phi); B - Sorting (phi-units); C - Skewness;
D - Kurtosis.
Contours correspond to verbal class boundaries.

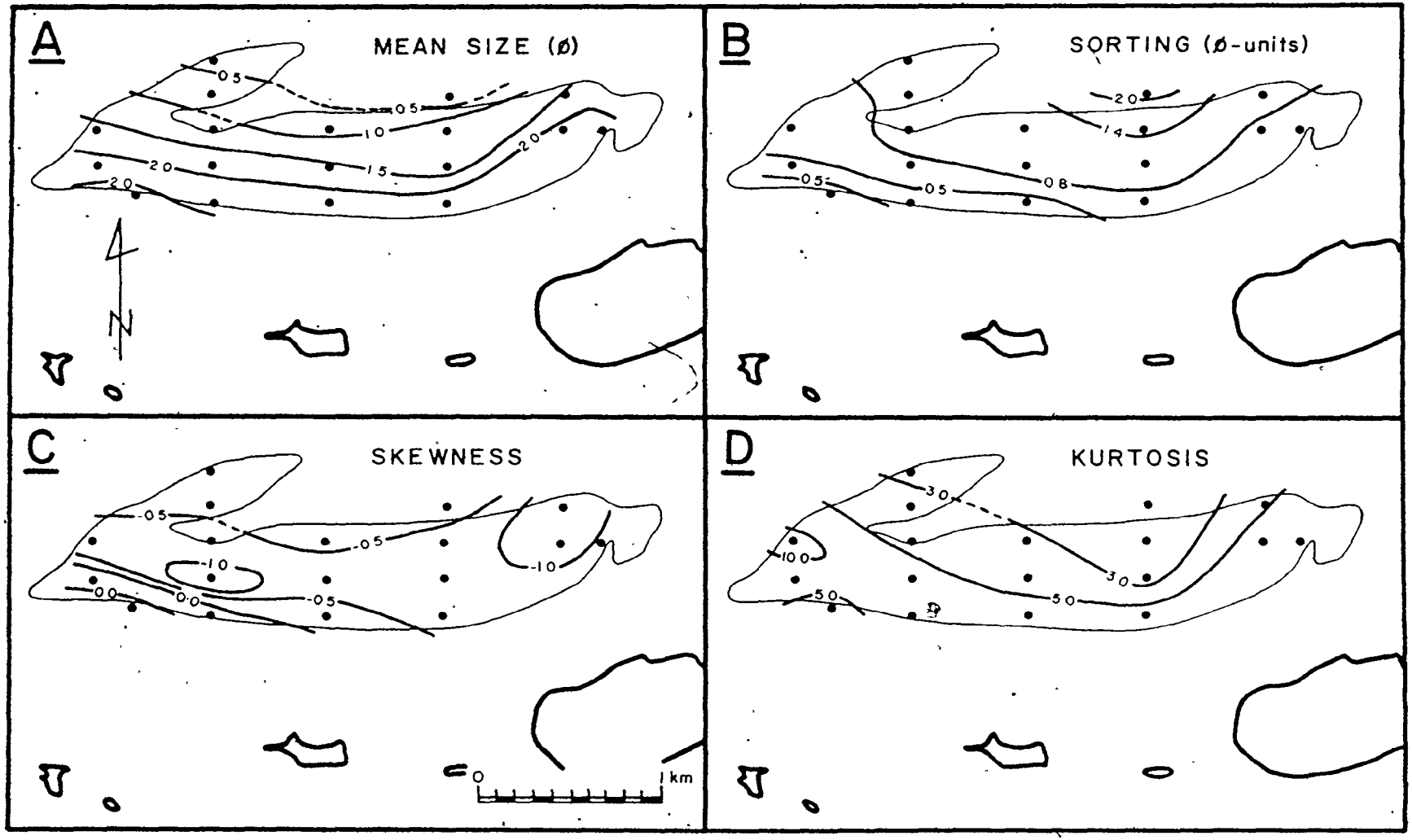
A
MEAN SIZE (ø)
0.5
0.5
1.0
2.0
1.5
2.0
2.0
N
B
SORTING (ø-units)
2.0
1.4
0.5
0.5
0.8
C
SKEWNESS
-0.5
-0.5
-1.0
-1.0
0.0
0.0
-0.5
0
1 km
D
KURTOSIS
3.0
10.0
3.0
5.0
5.0

a coarse tail is present over most of the bar. The most negatively skewed samples are located in a band that straddles the crest of the bar where the mean size is medium sand. This area is flanked to the north and south by less negative skewness values in coarser and finer sands.

Kurtosis (Figure 5.8D), like sorting, has a distribution that is broadly similar to that of mean grain size. The lowest values (all less than 5.0 and some less than 3.0) are found to the north of the crestline. Higher values (generally in the range of 5.0 to 10.0) are present in the area south and west of the crest.

The summary statistics, calculated from the data supplied by G. deV. Klein, display areal variations that are in general agreement with those shown in Figure 5.8. It is not possible with these data to tell if there has been any subtle change in the grain size characteristics of the Big Bar sands between 1966-67 and 1973 because of the fact that Klein's data is based on sieving at a half-phi interval, and because the control on sample location is poor, particularly with respect to positioning on the bedforms. If any changes have occurred in the 7 - 8-year period between samplings, then they are below the limit of detection, which cannot be determined with the available data.

(ii) Diamond Bar: On Diamond Bar, the finest mean grain sizes (finer than 2.0 phi - 0.25 mm) (Figure 5.9A) occur as a continuous band, extending along the southern edge of the

FIGURE 5.9 : Areal variation of grain-size characteristics on Diamond Bar. Divisions same as in Figure 5.8. Contours correspond to verbal class boundaries.

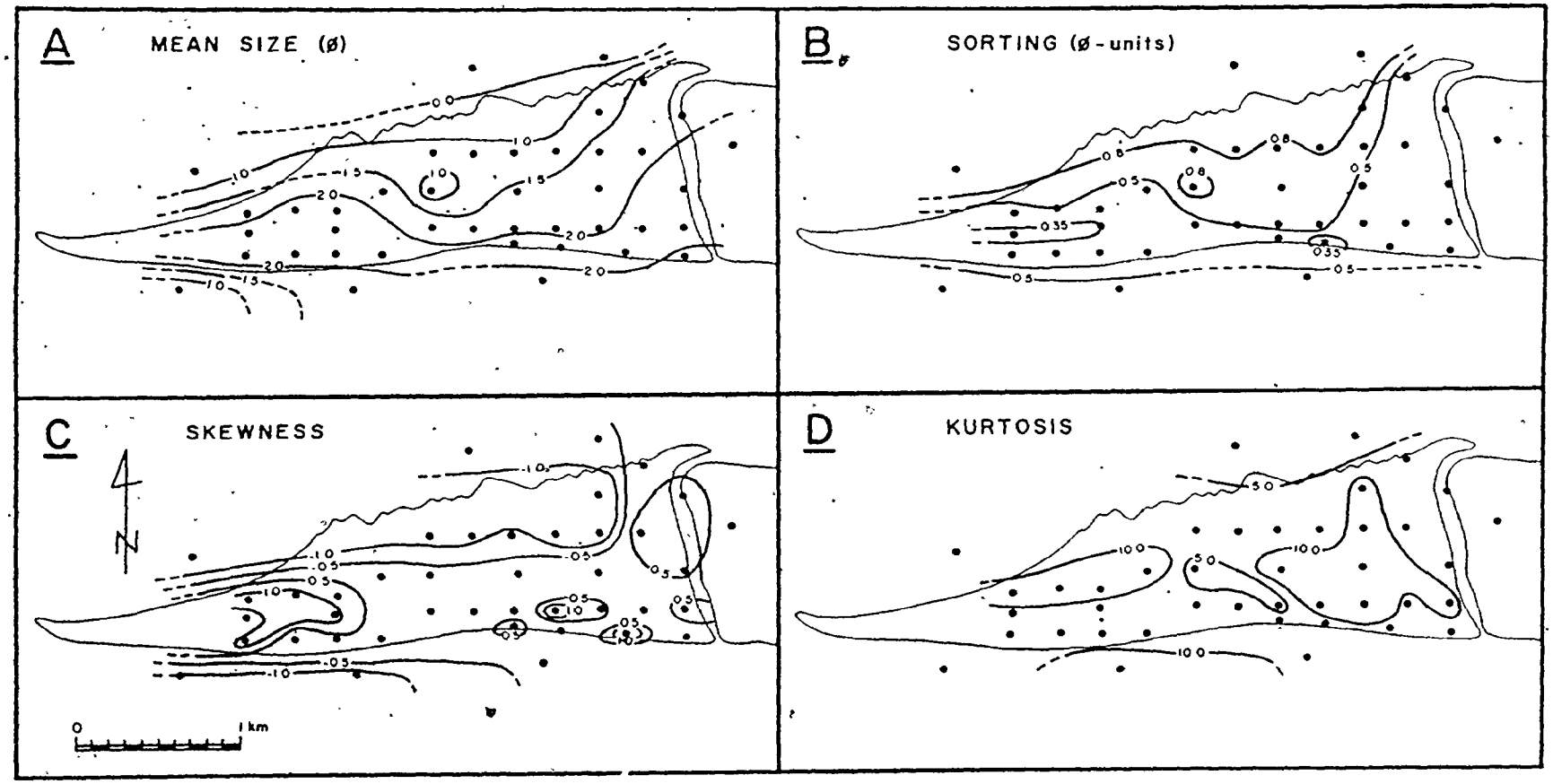
A
MEAN SIZE (ø)
B
SORTING (ø-units)
C
SKEWNESS
N
0
1 km
D
KURTOSIS

bar. Although this band lies primarily south of the crestline, there are two prominent northward extensions across the crest, on the west side of each swatchway. Much coarser mean sizes occur across the minor swatchway on its eastern side (Figure 5.9A). Also, the grain size increases to the north and south of the band of fine sand, but the size increase is not nearly so great in the southern channel as in the northern one, where coarse and very coarse sand is found.

A very similar contour pattern is shown in Figure 5.9B for the values of the standard deviation. As on Big Bar, the best sorting occurs in the finer sands, so that the smallest standard deviations are present on the south side of the crest, but again showing northward extensions west of each swatchway. More poorly sorted sands occur both to the north and south, but particularly in the northern channel.

Skewness values (Figure 5.9C) are more irregularly distributed than any of the other parameters, especially on the southeast corner of the bar where strongly negative and strongly positive skewnesses alternate. In general, however, the more negatively skewed sands are located in the two channels, while near symmetrical or positively skewed sands are concentrated along the crest, with a marked area of strong positive skewness at the west end of the bar.

The kurtosis values (Figure 5.9D) are in excess of 10.0 in two areas on the bar, one centred on the eastern half of the bar between the two swatchways, and the other on the north

side of the crestline, in the minor swatchway and immediately west of it. Kurtosis values less than 5.0 occur between these two areas of high values, and in the northern channel, but none of the samples analyzed has a kurtosis of less than 3.0.

(iii) Economy Point: The distribution of mean size (Figure 5.10A) at Economy Point reveals that, in general, the finest sizes are found closest to the shore, a pattern that is the reverse of those displayed on the other three study bars. The coarser sizes on the outer edge of the complex do, however, lie adjacent to extensive intertidal and subtidal areas of lag gravel (Figure 2.16). The northward extension of the 1.0 and 1.5 phi (0.50 and 0.35 mm, respectively) contours at the east end of Centre Bar in Figure 5.10A is coincident with a north-south strip of gravel that lies just east of the drainage channel.

The areal variation of sorting (Figure 5.10B) does not show as close a relationship with grain size as it does on the other bars. Although the best sorting is present in the two areas with the finest mean sizes, on the northwest corner of East Bar and at the west end of Centre Bar, the more poorly sorted sands (moderately sorted) are not confined to the coarser grained, outer edge of the complex, but are present at both the east and west ends of the area studied, and along much of the sandy foreshore.

FIGURE 5.10 : Areal variation of grain-size characteristics at Economy Point. Divisions same as in Figure 5.8. Contours correspond to verbal class boundaries.

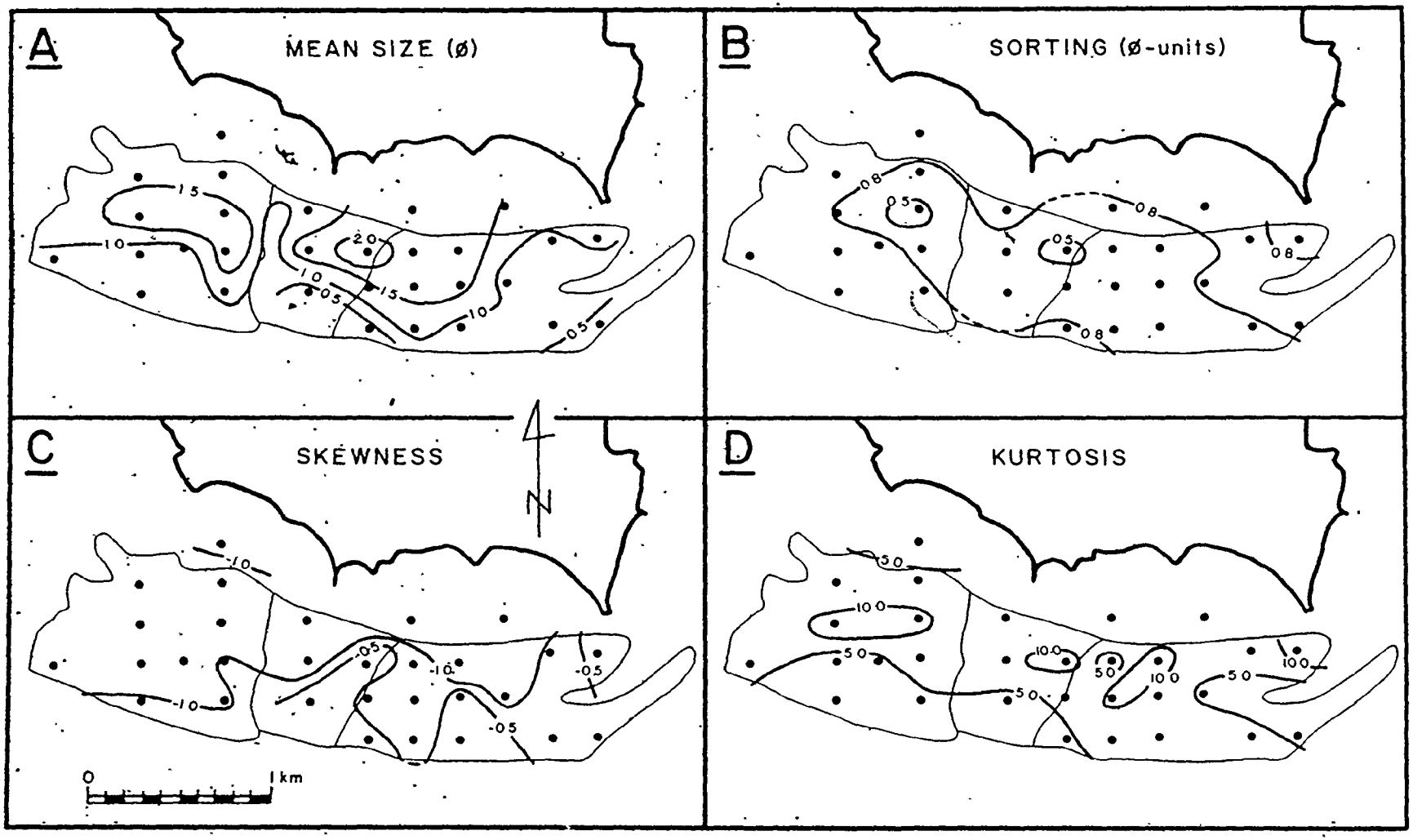
A
MEAN SIZE (ø)
1.5
1.0
2.0
1.0
0.5
1.5
1.0
0.5
B
SORTING (ø-units)
0.8
0.5
0.8
0.5
0.8
0.8
C
SKEWNESS
N
-1.0
-0.5
-1.0
-0.5
-1.0
-0.5
0
1 km
D
KURTOSIS
3.0
10.0
5.0
10.0
5.0
10.0
5.0
5.0
10.0

All but four of the samples analyzed have negative skewness values, and nearly half are strongly negatively skewed. These strongly negatively skewed samples cover virtually all of East Bar (Figure 5.10C) and extend in a band along the south side of the remainder of the area. The four positive skewness values all come from the south-central part of the complex: on East Bar, and the low area at its western end.

A plot of the kurtosis values (Figure 5.10D) does not reveal any distinct pattern of variation. There are four isolated areas of values in excess of 10.0 lying in a row, just north of the crestlines of the bars. One large region of low values (<5.0) occurs along the southern edge, while other smaller areas are present on the foreshore north of Centre Bar, and on East Bar.

As was the case on Big Bar, the half-phi grain-size data of Klein are in general agreement with the areal distributions presented in Figure 5.10. At a number of isolated locations, changes in the mean size on the order of 0.1 to 0.4 phi-units are indicated during the period from 1966-1967 to 1973-1974. These changes are not consistent either in terms of the direction of change or in their areal distribution, and as a result, their significance cannot be evaluated.

(iv) Selmah Bar: The areal variations of the grain-size parameters on Selmah Bar have been presented earlier by Dalrymple (1973b) and Dalrymple et al (1975), based on a

portion of the data used in constructing the patterns shown here in Figure 5.11. Any discrepancies between the two sets of contours are due to the addition of more data, and to the substitution of moment measures for the Folk and Ward graphic statistics.

On Selmah Bar (Figure 5.11A), the finest mean sizes (fine sand) are present at the east end of the bar in the region transitional between the bar and the mudflats, and extend westward along the northern edge to a point a short distance beyond the major swatchway. From these areas, there is a regular decrease in the grain size both southward and westward, with the coarsest sizes (coarse sand) occurring along the south-central margin of the bar, adjacent to the gravel lag area on the foreshore (Figure 2.11). There is also a slight coarsening at the western tip of the bar. The northward bend in the 1.5 and 1.75 phi (0.35 and 0.30 mm) contours in Figure 5.11A in the centre of the bar occurs in the major swatchway. The southward bend in the contours just west of the swatchway is defined by samples falling on and just south of the crestline. Other irregularities in the contours in the eastern half of the bar are associated with the minor swatchways (Figure 2.12).

The sorting on Selmah Bar (Figure 5.11B) is the best of all the studied bars, with almost the whole bar having well to very well sorted sand. The best sorting occurs in several separated areas, primarily along the northern side and western

FIGURE 5.11 : Areal variation of grain-size characteristics on Selmah Bar. Divisions same as in Figure 5.8. Contours correspond to verbal class boundaries.

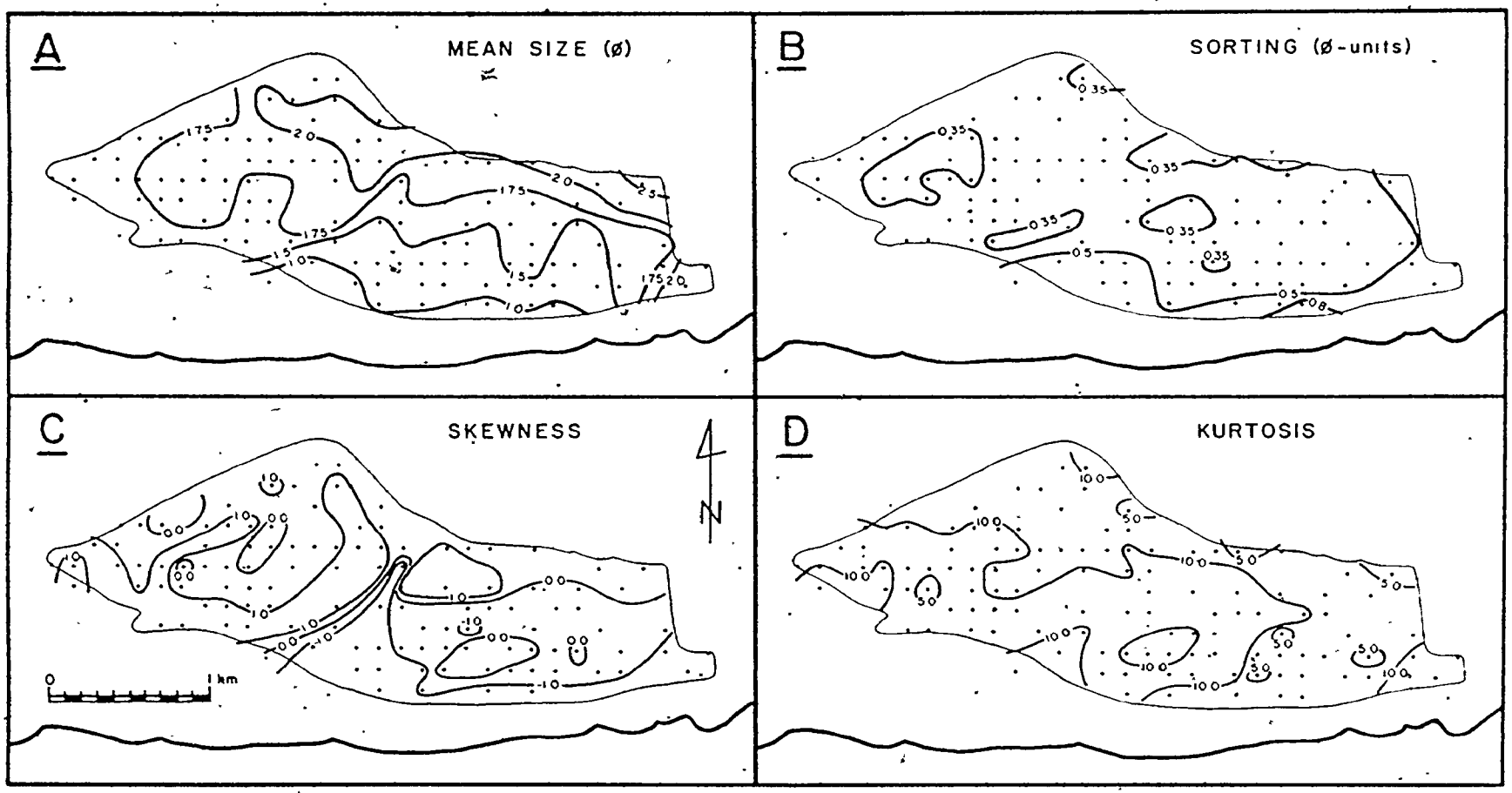
A
MEAN SIZE (ø)
1.75
2.0
1.75
2.0
2.5
1.75
1.5
1.0
1.5
1.75
2.0
1.0
B
SORTING (ø-units)
0.35
0.35
0.35
0.35
0.35
0.5
0.35
0.5
0.8
C
SKEWNESS
N
0
1 km
D
KURTOSIS
100
50
100
50
100
50
100
50
100
50
100
100
100

end of the bar. The poorest sorting is confined to the southern edge and eastern end of the bar in the coarsest and finest sands respectively.

Strong negative skewnesses (Figure 5.11D) are restricted to a narrow band along the southeastern side of the bar, but the -1.0 contour shows a large northward extension in the axis of the major swatchway. Strong positive skewnesses are most common on the western half of the bar, where they occur in a nearly circular band surrounding the topographically highest area (Figure 2.11). Another large area with skewness values greater than 1.0 occurs just to the east of the north end of the major swatchway.

Little topographic control is evident on the distribution of kurtosis values (Figure 5.11D). Kurtosis values in excess of 10.0 occur primarily in the southwest portion of the bar, straddling the major swatchway. A smaller area is also present in the extreme southeastern corner. Values less than 10.0, and occasionally less than 5.0, are located along the entire northern side of the bar, as well as in a broad band at the east end of the bar. Many of the coarsest sands along the southern edge also have low kurtosis values (<10.0).

Based on the areal distributions in the grain-size characteristics just presented for the four major study areas (Figures 5.8 to 5.11), certain generalities can be drawn.

The most obvious similarity between Big Bar, Diamond Bar and Selmah Bar is that the sands become finer (and better sorted in general) as one moves outwards from the shore. The finest sand also occurs on the steeper side of these bars. Economy Point is an exception to the above, having the finest sand closer to the shore; but in all four areas, the coarsest sands lie next to large areas of lag gravel, which, in most cases, occupies the intertidal foreshore. Superimposed on the above dominant pattern is a trend for channel floors to be coarser grained than adjacent higher areas. Furthermore, the western side of a swatchway is generally finer grained than the eastern side.

In all areas, the contours of the various parameters tend to run parallel to the length of the bar, so that the major gradients are transverse to the bar axis. As a result, areas of sediment with similar characteristics occur in bands that lie roughly parallel to the tidal-current flow directions. The reasons for this will be discussed later in Section 5.3, following an investigation of the fundamental size populations present in the data.

### 5.2.5 Hydraulic Control of Mean Size

Many workers who have studied ancient sediments make the simple assumption that coarser grain sizes are associated with stronger currents, based in part on the fact, illustrated in the Hjulström diagram (see Blatt et al, 1972, Figure 4-8),

that coarser sediment ceases movement at higher current speeds than finer material. Because of this, the coarse tail of the size-frequency distribution is progressively truncated, thereby shifting the mean toward finer sizes, as one moves down a flow-strength gradient. The above assumption presupposes, however, that the availability of certain sizes is not limited by the size characteristics of the source area.

In order to determine what control, if any, the areal variations in current strength have on the patterns of mean grain size shown in part A of Figures 5.8 to 5.11, the mean sizes have been regressed linearly against: i) the time-averaged and standardized mean velocity ($\bar{U}$); ii) the time-averaged and standardized shear velocity ($\bar{u}_*$); and iii) the excess shear velocity, defined here as difference between $\bar{u}_*$ and the critical shear velocity ($\bar{u}_{*cr}$) as determined from the Shields relationship for the mean grain size (see Blatt et al, 1972, p.91). The regressions have been performed for each bar independently, and for all of the data combined. Plots of the above relationships are shown in Figure 5.12, and the correlation coefficients are listed in Table 5.3.

Examination of Figure 5.12 and Table 5.3 shows that current strength, regardless of how it is defined, has little or no control over the mean grain size of the sediment on the scale of a single sand bar, because only one of the fifteen relationships tested (mean size versus the shear velocity on Big Bar) gave a correlation coefficient that was significant

FIGURE 5.12 : Relationships between mean grain size and current strength.
A - Time-averaged mean speed (m/s) versus mean grain size.
B - Time-averaged shear velocity (cm/s) versus mean grain size.
C - Excess shear velocity (time-averaged value minus Shields' critical shear velocity) (cm/s) versus mean grain size.
r = correlation coefficient.
Heavy lines are regression lines for all data; broken line for Big Bar data only. Mean size is the dependent variable.

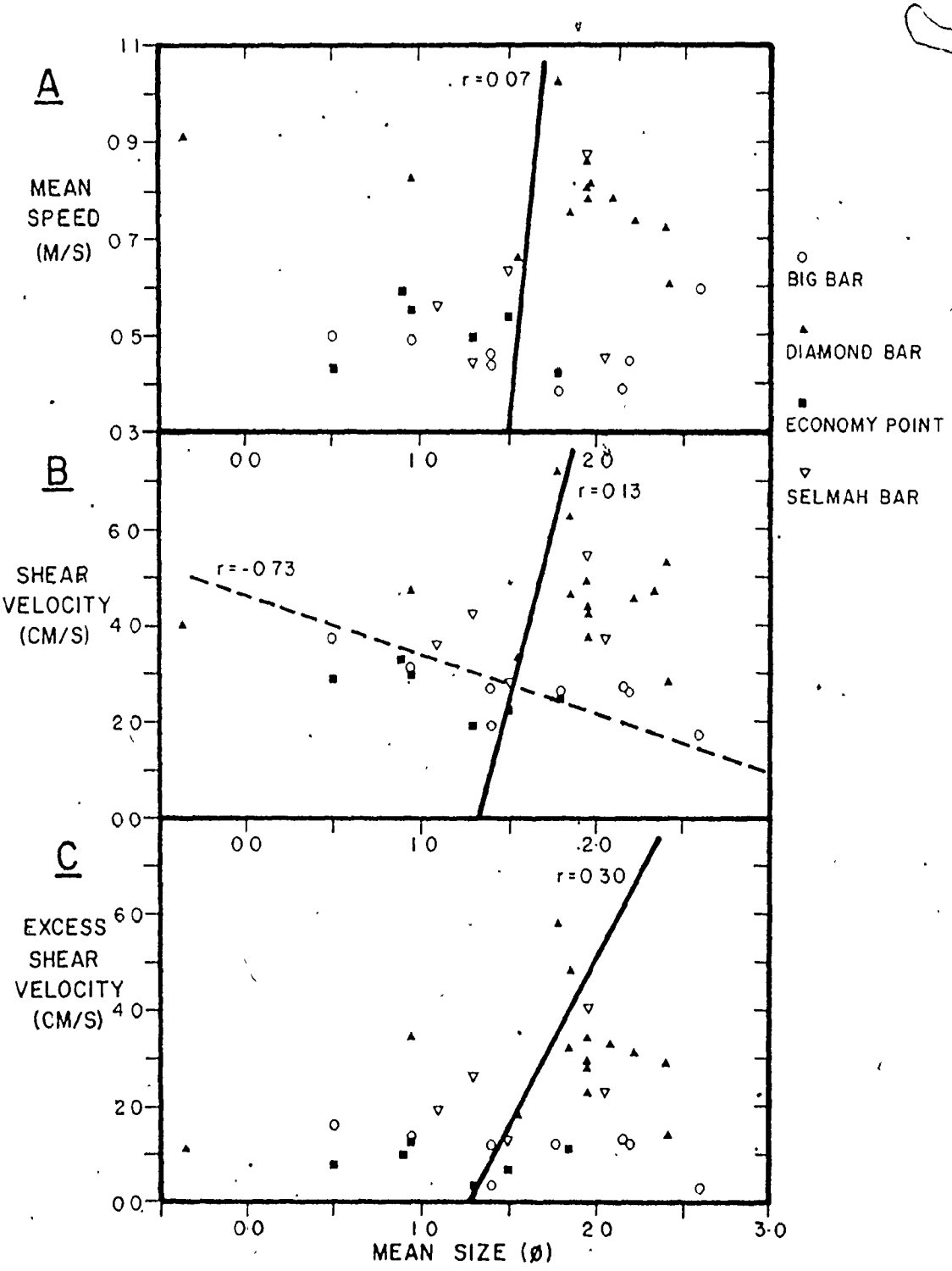
A
B
C
MEAN SPEED (M/S)
SHEAR VELOCITY (CM/S)
EXCESS SHEAR VELOCITY (CM/S)
MEAN SIZE (ø)
r=0 07
r=0 13
r=-0 73
r=0 30
BIG BAR
DIAMOND BAR
ECONOMY POINT
SELMAH BAR

TABLE 5.3 : Relationship between mean grain size and current strength. Correlation coefficients for the regression of mean grain size against the hydraulic parameters listed on the left. * - significant between 95% and 99%.

| Mean Size versus | Big Bar | Diamond Bar | Economy Point | Selmah Bar | Combined Data |
|---|---|---|---|---|---|
| Mean speed | 0.03 | -0.44 | -0.24 | 0.23 | 0.07 |
| Shear velocity | -0.73* | 0.07 | -0.61 | 0.39 | 0.13 |
| Excess shear velocity | -0.51 | 0.36 | -0.17 | 0.49 | 0.30 |

at greater than the 95% level. The negative correlation coefficient signifies that the grain size is generally finer in areas with lower time-averaged and standardized shear velocities. In contrast to this trend, nine of the correlation coefficients, including all of those for Selmah Bar and two of the three for Diamond Bar, are positive, indicating that there is a weak tendency for the finer mean sizes to be associated with stronger currents.

The lack of a strong hydraulic control on the mean grain size should not be unexpected, because several factors mitigate against observing the expected relationships: i) the complex nature of the flow, in terms of the directional reversals and unsteadiness, may not permit the necessary size segregations to take place; ii) the range of mean sizes encountered may be too narrow and the current strengths too high, within the rather small areas studied, to allow the expected relationships to emerge; iii) there may be source-area controls which overshadow the potential hydraulic effects; and iv) the mean size may not be the most appropriate grain-size parameter to use in a study such as this, because it is known that each individual size-frequency distribution is a complex mixture of several size populations, each of which has been suggested as having hydraulic significance. For this last reason, further discussion of the factors controlling the individual size-frequency distributions and their areal variations will be left until the end of the chapter, after the size populations have been studied.

## 5.3 Size Populations

### 5.3.1 Previous Work

The composite nature of many size-frequency distributions was first recognized by Udden (1898, 1914), who noted the presence of two modes in many of his samples. He also believed that each mode represented grains transported by a different mechanism.

> "The principal deposit it (the transporting medium) makes will consist of materials it can momentarily lift. With this it will leave an excess of another considerably coarser ingredient which it can roll, smaller in quantity." (Udden, 1914, p.737).

In the period since this recognition, considerable effort has been directed toward understanding the nature of size-frequency distributions, but many questions remain regarding the exact form and significance of the component populations present in many sands.

One of these questions centres on the mathematical form of the distribution followed by the component populations. Doeglas (1946) proposes that three basic, non-log-normal components exist, which when mixed in varying proportions, produce the observed size distributions. Moss (1962, 1972) also advocates the existence of non-log-normal size populations, but most authors today do not ascribe to this idea, and believe instead, following Krumbein (1938) that the log-normal (or phi normal) distribution (hereafter referred to simply as the

normal distribution) is of fundamental importance in the analysis of grain-size data.

Sindowski (1957), Harris (1958) and Visher (1969), among others, have noted that grain-size data, when plotted on probability paper, can be closely approximated by a small number of connected, straight-line segments, as was done in Figure 5.3. It has been suggested that each of these segments represents a truncated normal distribution. A number of other workers, including Tanner (1959, 1964), Fuller (1961), Spencer (1963), Folk (1971), and Clark and Clark (1976), maintain, however, that the populations are overlapping normal distributions, based on the fact that sand-size distributions can be successfully dissected into a small number of overlapping normals, either by graphical or numerical methods. Clark and Clark (1976) also demonstrate that the size populations determined in this way correspond closely with populations based on grain-shape characteristics. Various other workers dealing primarily with fine-grained sediments (Curray, 1960; Oser, 1972; van Andel, 1973) also employ overlapping normal distributions in their studies. Reed et al (1975) have found, however, that both overlapping and truncated models may be appropriate in different circumstances.

The controversy that exists regarding the nature of the populations may in part stem from differences in the interpretation given the various components; that is, whether they are of source or hydraulic sorting origin.

Shea (1974) has found that an average of more than 11,000 size analyses, collected from many different areas and depositional environments, contained a number of straight-line segments separated by discontinuities, or "breaks", similar to those shown for individual samples in Figure 5.3. He concludes that the size characteristics of the parent material, combined with the nature of the comminution process, are of utmost importance in determining the populations.

The majority of authors who believe that the populations are overlapping normals also believe that the character of the populations is controlled in large measure by the sediment source(s). For example, van Andel (1973) and Oser (1972) indicate that certain components in Pacific Ocean silts and clays are composed almost entirely of the tests of single coccolith species. Furthermore, Curray (1960) and van Andel (1973) suggest that the populations (or modes) can retain their identity over long transport distances and that the dispersal patterns and sources of the sediment may be determined by tracing masses of sediment characterized by the same population. It is important to note that many of these studies deal predominantly with fine-grained sediments.

In contrast to the above, those authors working primarily with coarser, sandy sediments advocate the presence of truncated normal populations, each produced by a different transport mechanism. There is, however, little consistency between the interpretations of the various workers who

postulate hydraulic controls on the size populations. The prime advocate of transport-mechanism populations is Visher (1969), who believes that three basic populations exist, produced by traction (rolling and sliding), saltation, and suspension. Moss (1962, 1972) interpretes his three populations in similar terms, but in addition, suggests that rheological motion may be of importance in the formation of the saltation population, and stresses the influence of shape sorting and packing mechanisms in the determination of the composite size distributions. G. P. Allen et al (1972) distinguish four populations in their data from the Gironde Estuary, using R-mode factor analysis, and propose that they reflect surface creep, saltation, graded suspension, and suspension transport.

In the most recent work on this topic, Middleton (1976) shows that the three basic populations present in fluvial sediments should more rightly be ascribed to traction, intermittent suspension, and wash load (or permanent suspension) transport. The exclusion of saltation as a separate, major transport mechanism is based on the long known fact that saltation is of relatively minor importance in water, because as Kalinske (1943, p.47) has shown, the maximum height that a saltating grain can attain in water is only 1/800 of what is possible in air, due to the density differences between the two media. Francis (1973) has also observed in a flume that true saltation does not attain a height of more than four grain diameters above the bed. This means that saltation

transport should be considered together with rolling and sliding as a traction phenomenon. Sediment transported by the mechanism of intermittent suspension (Blatt et al, 1972, p.91) is periodically suspended in the flow by the upward components of the turbulence, but returns to the bed at intervals due to the random nature of the turbulent fluctuations.

Lane and Kalinske (1939; see also Inman, 1949) suggest that the initiation of suspension should occur at the point when the shear velocity ($u_*$) is approximately equal to the settling velocity (w) of the grains:

$$w/u_* \sim 1 \qquad (5.5)$$

and Francis (1973) has noted in a series of experiments using solitary mobile grains on a fixed bed of similar grains that the transition between saltation and intermittent suspension occurs in accordance with equation (5.5). Using this criterion and assuming truncated-normal size populations, Middleton (1976) proposed that the "break" between the traction and intermittent suspension populations is controlled by some effective shear velocity, and consequently, that the position of the "break" in an ancient sediment can be used to determine the shear velocity of the flow. This idea was tested by Middleton (1976) using size data for rivers with accompanying hydraulic information, and reasonable agreement was obtained between the calculated and observed shear velocities. This

fact provides strong, though indirect, evidence that the two coarsest size populations are hydraulically produced.

From the above review of the previous work, it is clear that the fundamental questions concerning the overlapping- versus truncated-normal models, and source versus hydraulic control of size populations are far from resolved. The investigations that follow consider both of these questions, and while no universal solutions are possible within the limited scope of the present study, the results should be of some general interest. For simplicity in the subsequent discussions, terminology used in referring to the various populations will follow that used by Moss (1962) and Middleton (1976). Therefore, the "C" population is the one which fits the poorly-sorted coarse tail of the cumulative curve; the "A" population(s) fit the steeper, central part of the cumulative curve; and the "B" population fits the flat, fine tail.

### 5.3.2 Graphical Dissection of Size Distributions

As stated above, two different distributions have been suggested for the component size populations: truncated normals, and non-truncated, overlapping normals. At present, there is little theoretical justification for the acceptance of either model. The success of Middleton (1976), assuming truncated normals, might suggest that this model is more appropriate, but Middleton emphasizes (p.406) that the choice of truncated normals was largely for practical reasons, due

to the imprecision of the data used. Other authors (Fuller, 1961; Oser, 1972; Spencer, 1963; Tanner, 1958, 1959, 1964; van Andel, 1973) have been able to closely reproduce the original size distributions by summing non-truncated, overlapping normals, thereby implying that this model is correct. Until further theoretical or experimental evidence is available regarding the nature of the populations, the choice of a model must be largely subjective.

If the truncated-normal model is used, then the dissection of the original size distributions into components amounts to nothing more than fitting straight-line segments to the cumulative curves, as has been done in Figure 5.3. The truncation points of the components then lie approximately at the "breaks" in the cumulative curve; that is, where the straight-line segments intersect. It must be remembered that at least two, and preferrably three, points are needed to draw a straight line. The characteristics of each component (mean and standard deviation) can then be determined, using standard graphical or moment methods, after replotting the data points contained in each segment to one hundred percent. This is done by dividing each observed cumulative percentage ($p_i$) by the proportion of the sample represented by the component in question (P).

As can be seen in Figure 5.3, the size distributions can be represented reasonably well by a small number of truncated normal distributions. However, as was stated in

Section 5.2.1 and shown in Figure 5.3 by the dashed lines, many of the "breaks" are markedly rounded, resulting in rather poor fits in these areas. In addition, many of the nearly straight portions of the distributions are gently curved. Both of these features suggest the presence either of non-normal distributions or of significant overlap and mixing between components. Because of this, considerable attention has been devoted here to the overlapping-normal model. Further comments on the appropriateness and significance of each model will be made at various points during the subsequent discussions.

Mathematicians have devoted considerable effort toward the development of methods for the dissection of multicomponent distributions into the constituent normal populations. M. W. Clark (1976) has summarized many of these. Various numerical methods are available for this purpose, and have the advantage of allowing a large number of samples to be processed quickly. Unfortunately, the program that was to be used (I. Clark, 1976) did not give acceptable results and had to be abandoned. In its place, the graphical technique developed by Cassie (1954, 1963) was substituted. This method is more sophisticated and less subject to error than are other graphical dissection methods, such as those of Harding (1949) and Tanner (1959). In the following paragraphs, the Cassie dissection method will be described in some detail, because few readers will be familiar with it, and because

various features of the method had to be revised in order to achieve best results.

The sample selected as the example for this presentation is CB38-C (for its location, see Figure 5.1C). The cumulative percentages for the sample are listed in Table 5.4 and are plotted in Figure 5.13, where it is evident that the cumulative curve can be represented by five straight-line segments: -3.0 to -1.0 phi (8.0 - 2.0 mm); -1.0 to 1.0 phi (2.0 - 0.5 mm); 1.0 to 2.0 phi (0.5 - 0.25 mm); 2.0 to 3.0 phi (0.25 - 0.125 mm); and finer than 3.0 phi. The junctions between the segments are rounded, however. Experience indicates that three overlapping normal populations are present, excluding the finest (B) population, which constitutes less than 0.2% of the total and is therefore ignored. The three populations are a single C population, plus two A populations. The steps necessary for the determination of the characteristics of these components are outlined below, and cover most eventualities encountered during the dissection of size distributions.

Step 1: Enter the size classes and observed cumulative percentages ($p_i$) in a table (columns 1 and 2 of Table 5.4), and plot the cumulative curve on probability paper (Figure 5.13A) (steps 1, 4 and 5 of Cassie, 1963).

Step 2: Determine the number of populations present and the proportions of each ($P_c$) in the sample (steps 6 to 8 of Cassie, 1963). Harding (1949) and Cassie (1954, 1963) both state that

the proportion of the components can be determined from the positions of the inflections in the cumulative curve; in this case, an inflection is present between the C and coarsest A population ($A_1$), at approximately 25%, but no inflection is evident between the two A populations, due to the closeness of their means. The experience gained from the dissection of over thirty samples, involving an average of two trials each, indicates that the position of the inflection consistently underestimates the proportion of the less abundant population, and that in this case, a better estimate would be approximately 35% population C. Furthermore, in the case where no inflection is evident, the proportion can be estimated approximately from the position of the "break"; that is, the $A_2$ population has a proportion of approximately 5%, leaving the central 60% for the $A_1$ population. Thus: $P_{c1} = 35\%$; $P_{c2} = 60\%$; and $P_{c3} = 5\%$. The selection of appropriate proportions is the key to the success of the Cassie method, because incorrect choice of proportions leads to a poor fit of the summed components, as will become evident.

Step 3: Beginning with the most poorly sorted population (in all cases studied by this author, this is the C population), calculate and replot the cumulative percentages contained within the size range of the population out of 100%:

$$q_{1i} = 100\ p_i/P_{c1} \quad (q_{1i} \leq 100\%) \qquad (5.6)$$

(step 14 of Cassie, 1963; column 3 of Table 5.4).

FIGURE 5.13 : Dissection of sample CB38-C. A - Trial 1; B - Trial 2. Vertical axis is probability scale. Mean and standard deviation given for each dissected population. See text and Table 5.4 for further information.

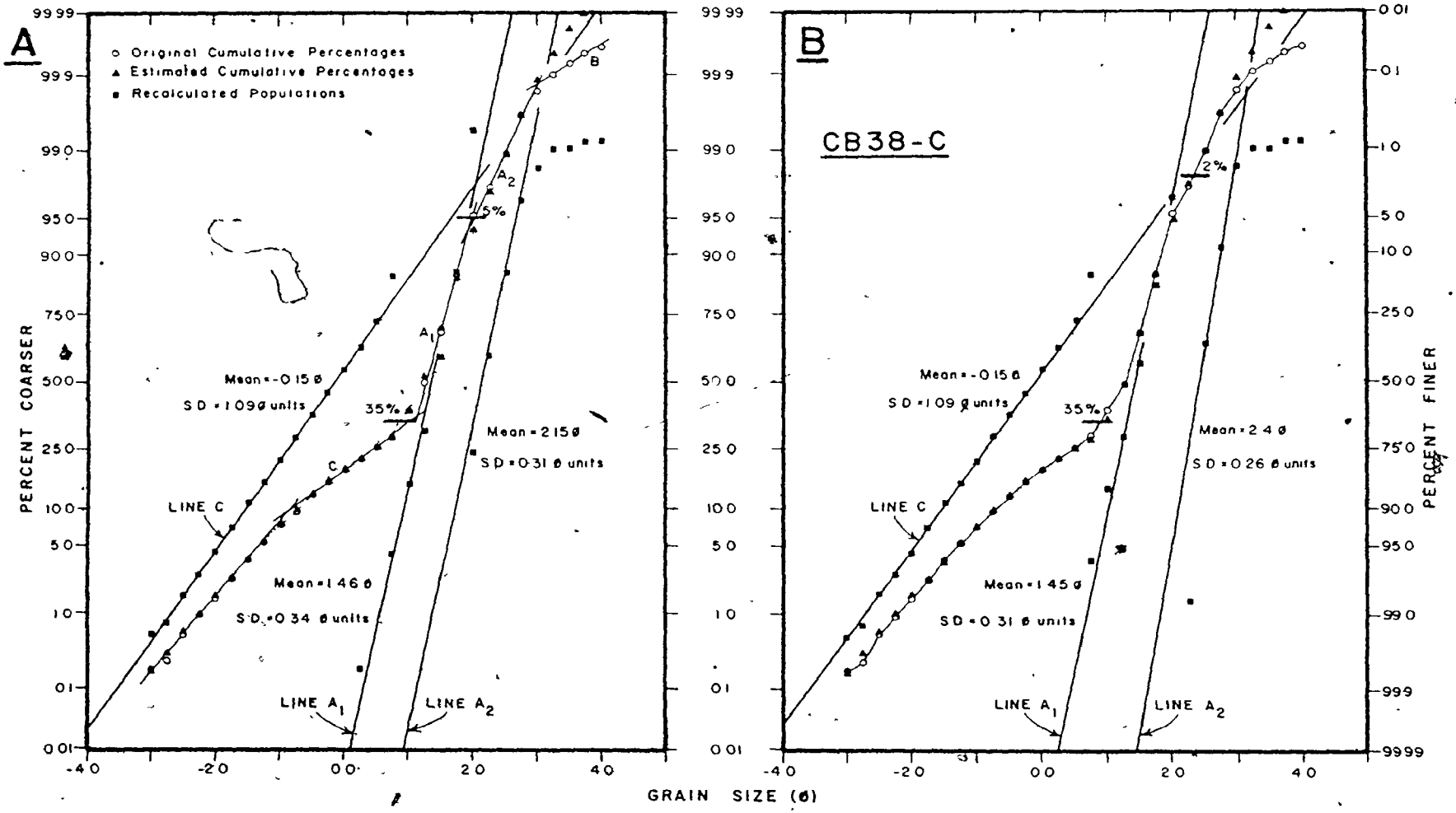
A
Original Cumulative Percentages
Estimated Cumulative Percentages
Recalculated Populations
Mean = -0.15 ø
SD = 1.09 ø units
Mean = 1.46 ø
SD = 0.34 ø units
Mean = 2.15 ø
SD = 0.31 ø units
35%
5%
LINE C
LINE A1
LINE A2
PERCENT COARSER
B
CB38-C
Mean = -0.15 ø
SD = 1.09 ø units
Mean = 1.45 ø
SD = 0.31 ø units
Mean = 2.4 ø
SD = 0.26 ø units
35%
2%
LINE C
LINE A1
LINE A2
PERCENT FINER
GRAIN SIZE (ø)

TABLE 5.4 : Dissection of sample CB38-C. Method after Cassie (1954, 1963). See text for further details.

| Phi (1) | $p_i$ (2) | $q_{1i}$ (3) | $\hat{p}_{1i}$ (4) | $q_{3i}$ (5) | $\hat{p}_{3i}$ (6) | $q_{2i}$ (7) | $\hat{p}_{2i}$ (8) | $\hat{p}_i$ (Trial 1) (9) | $\hat{p}_i$ (Trial 2 (10) |
|---|---|---|---|---|---|---|---|---|---|
| -3.0 | 0.20 | 0.57 | 0.19 | | | | | 0.19 | 0.19 |
| | 0.27 | 0.77 | 0.35 | | | | | 0.35 | 0.35 |
| -2.5 | 0.59 | 1.69 | 0.63 | | | | | 0.63 | 0.63 |
| | 0.98 | 2.80 | 1.03 | | | | | 1.03 | 1.03 |
| -2.0 | 1.51 | 4.31 | 1.72 | | | | | 1.72 | 1.72 |
| | 2.56 | 7.31 | 2.63 | | | | | 2.63 | 2.63 |
| -1.5 | 3.96 | 11.31 | 3.85 | | | | | 3.85 | 3.85 |
| | 5.52 | 15.77 | 5.60 | | | | | 5.60 | 5.60 |
| -1.0 | 7.64 | 21.83 | 7.70 | | | | | 7.70 | 7.70 |
| | 10.03 | 28.66 | 10.29 | | | | | 10.29 | 10.29 |
| -0.5 | 12.95 | 37.00 | 13.02 | | | | | 13.02 | 13.02 |
| | 16.02 | 45.77 | 16.10 | | | | | 16.10 | 16.10 |
| 0.0 | 19.20 | 54.86 | 19.25 | | | | 0.0 | 19.25 | 19.25 |
| | 22.31 | 63.74 | 22.19 | | | 0.20 | 0.05 | 22.24 | 22.20 |
| 0.5 | 25.55 | 73.00 | 25.20 | | | 0.58 | 0.42 | 25.62 | 25.33 |
| | 29.94 | 85.54 | 27.48 | | | 4.10 | 2.40 | 29.88 | 27.98 |
| 1.0 | 38.80 | | 29.61 | | 0.0 | 15.32 | 9.00 | 38.61 | 34.90 |
| | 49.60 | | 31.26 | | 0.02 | 30.53 | 21.60 | 52.88 | 48.90 |
| 1.5 | 68.33 | | 32.48 | | 0.12 | 59.55 | 38.70 | 71.30 | 68.39 |
| | 85.72 | | 33.36 | | 0.55 | 86.35 | 51.78 | 85.69 | 85.91 |
| 2.0 | 95.19 | | 33.99 | 24.00 | 1.55 | 99.42 | 58.02 | 93.56 | 94.67 |
| | 97.44 | | 34.41 | 60.60 | 3.05 | | 59.70 | 97.16 | 97.70 |
| 2.5 | 98.95 | | 34.65 | 86.00 | 4.30 | | 59.98 | 98.93 | 98.93 |
| | 99.63 | | 34.81 | 96.40 | 4.84 | | 60.00 | 99.65 | 99.63 |
| 3.0 | 99.82 | | 34.90 | 98.40 | 4.98 | | 60.00 | 99.88 | 99.88 |
| | 99.90 | | 34.95 | 99.00 | 5.00 | | 60.00 | 99.95 | 99.95 |

TABLE 5.4 (Continued)

| Phi (1) | $p_i$ (2) | $q_{1i}$ (3) | $\hat{p}_{1i}$ (4) | $q_{3i}$ (5) | $\hat{p}_{3i}$ (6) | $q_{2i}$ (7) | $\hat{p}_{2i}$ (8) | $\hat{p}_i$ (Trial 1) (9) | $\hat{p}_i$ (Trial 2) (10) |
|---|---|---|---|---|---|---|---|---|---|
| 3.5 | 99.93 | | 34.98 | 99.00 | 5.00 | | 60.00 | 99.98 | 99.98 |
| | 99.95 | | 34.99 | 99.20 | 5.00 | | 60.00 | 99.99 | 99.99 |
| 4.0 | 99.96 | | 35.00 | 99.20 | 5.00 | | 60.00 | 100.00 | 100.00 |
| | Proportion | | 35% | | 5% | | 60% | | |
| | Mean | | -0.15 ø | | 2.15 ø | | 1.37 ø | | |
| | St. Dev. | | 1.09 ø-units | | 0.31 ø-units | | 0.34 ø-units | | |

Step 4: Fit by eye the best straight line to the replotted $q_{1i}$ values (Line C, Figure 5.13A) (step 15 of Cassie, 1963). In fitting this line, pay particular attention to those points in the central part of the component distribution. Points in the tails must usually be ignored, due to the influence of overlap, or deviations from a true normal distribution resulting from sampling error or real but unknown factors.

Step 5: From the fitted line, read the estimated cumulative percentages for the C population ($\hat{q}_{1i}$) and recalculate them in terms of the total sample, that is out of 35%:

$$\hat{p}_{1i} = \hat{q}_{1i} P_{c1}/100 \quad (\hat{q}_{1i} \leq 100\%) \qquad (5.7)$$

(steps 16 and 17 of Cassie, 1963; column 4 of Table 5.4).

Step 6: Go to the second most poorly sorted component, in this case it is apparently the $A_2$ population, judging from the slope of the straight-line segments, and repeat Step 3, after correcting the original cumulative percentages ($p_i$) for the overlap of the C population ($p_i - (\hat{p}_{1i} + P_{c2})$):

$$q_{3i} = 100\ (p_i - (\hat{p}_{1i} + P_{c2}))/P_{c3} \qquad (5.8a)$$

(after Cassie, 1954, p.515; column 5 of Table 5.4). This step can alternatively be accomplished by inverting the probability paper and using the percent-finer scale in place of the percent-coarser one to plot $q_{3i}$ calculated from:

$$q_{3i} = 100((100 - p_i) - (P_{c1} - \hat{p}_{1i}))/P_{c3} \qquad (5.8b)$$

The correction for the overlap is necessitated by the fact that a part of the frequency in the size classes under consideration has been accounted for by the already estimated C population ($\hat{p}_{1i}$).

The dissection method proposed by Cassie (1954, 1963) advocates progressing sequentially through the cumulative curve, beginning at one tail, and ending at the other. This procedure will only work where the populations all have approximately equal variances, and the amount of overlap is minimal. In most size distributions, where the variances of the populations are markedly unequal, the correction for overlap can only be accomplished by fitting the populations in order from worst to best sorted.

Step 7: Repeating Step 4, fit the best straight line to the replotted $q_{3i}$ values (Line $A_2$, Figure 5.13A). Note that the values derived from points falling on the B population straight-line segment deviate markedly from the fitted $A_2$ line and have been ignored.

Step 8: Repeat Step 5 to obtain the cumulative percentages supplied by the $A_2$ population to the total sample ($\hat{p}_{3i}$):

$$\hat{p}_{3i} = \hat{q}_{3i} P_{c3}/100 \qquad (5.9)$$

(column 6 of Table 5.4).

Step 9: Recalculate and plot the points from the $A_1$ population out of 100% ($q_{2i}$), correcting for the overlap of the C and $A_2$ populations, in a manner similar to that used in Step 6:

$$q_{2i} = 100(p_i - (\hat{p}_{1i} + \hat{p}_{3i}))/P_{c2} \qquad (5.10)$$

(column 7 of Table 5.4).

Step 10: Fit by eye the best straight line to these $q_{2i}$ values (Line $A_1$, Figure 5.13A).

Step 11: Read the estimated percentages off the $A_1$ line ($\hat{q}_{2i}$) and recalculate them out of 60% (as in Steps 5 and 8):

$$\hat{p}_{2i} = \hat{q}_{2i} P_{c2}/100 \qquad (5.11)$$

(column 8 of Table 5.4).

Step 12: Calculate the mean and standard deviation of each estimated population (step 27 of Cassie, 1963; bottom of Table 5.4). The mean value can be read directly from the point where each fitted line crosses the 50% level ($\hat{q}_{50}$). To obtain the standard deviation, first read the phi value at either the 99.99% level ($\hat{q}_{99.99}$ - top of graph paper) or the 84.13% level ($\hat{q}_{84.13}$), and insert in the appropriate formula:

$$\text{St.Dev.} = (\hat{q}_{99.99} - \hat{q}_{50})/3.72 \qquad (5.12a)$$

$$\text{St.Dev.} = (\hat{q}_{84.13} - \hat{q}_{50})/1.00 \qquad (5.12b)$$

Step 13: Sum the estimated cumulative percentages from the three populations to obtain the estimated composite sample ($\hat{p}_i$):

$$\hat{p}_i = \hat{p}_{1i} + \hat{p}_{2i} + \hat{p}_{3i} \qquad (5.13)$$

Step 14: Replot the estimated cumulative curve ($\hat{p}_i$) against the observed one ($p_i$) (Figure 5.13A) and check the fit. It can be seen that the estimated curve is a reasonable approximation to the original one, except at the fine tail, for which no component has been added, and at the junction between the $A_1$ and $A_2$ populations, where the estimated points fall on

the concave side of the original curve. This indicates that the proportion of $A_2$ used is too high, and that a second trial is necessary.

Step 15: Return to Step 2, and repeat Steps 3 to 14 after making a new choice for $P_{c3}$, say 2% instead of the original 5%.

Because the results of the first trial indicate that the $A_1$ population is slightly less well sorted than the $A_2$ population, the order of fitting these populations should, in most circumstances, be reversed during the second trial. The example used here illustrates a situation, however, in which such a reversal is not appropriate, because the small proportion of the $A_2$ population ($P_{c3}$ = 2%) so magnifies any discrepancies between the original and estimated curves remaining after the fitting of the C and $A_1$ populations that the recalculated $A_2$ values ($q_{3i}$) would be unlikely to define the proper normal population. Therefore, such small tail populations should be fitted before estimating the major A population. If the populations are to be fitted from coarsest to finest, however, the equations in Steps 6 and 9 must be modified respectively to:

$$q_{2i} = 100(p_i - \hat{p}_i)/P_{c2} \qquad (5.14)$$

and

$$q_{3i} = 100(p_i - (\hat{p}_{1i} + \hat{p}_{2i}))/P_{c3} . \qquad (5.15)$$

The mechanics of the second trial have not been reproduced here, but the final estimated cumulative percentages are listed in column 10 of Table 5.4, and are shown in Figure 5.13B, together with the original cumulative curve and the estimated populations. It is clear that the composite curve resulting from the second estimate is a better fit than the first, and indeed, is a better fit to the original than is the estimate using five straight-line segments. Unfortunately, no well-established test of the fit exists for use with weight percent data. Cassie (1963) suggests using the $\chi^2$ test to check the goodness of fit, but this is only applicable to number frequency data, and the fit must, therefore, be judged subjectively. For the purposes of this investigation, a fit such as that obtained in Figure 5.13B is acceptable. A slightly better fit might be achieved in the vicinity of the overlap between the C and $A_1$ populations. The slight displacement of the estimated points on the convex side of the "break" indicates that the proportion of the C population ($P_{c1}$) might be marginally higher than the 35% value used. The increase of 2 to 3% necessary to improve the fit would not, however, bring about a significant change in the parameters of the C population, and would not be worth the time required for an additional trial.

With practice, a single trial of a three-component dissection can be completed in approximately three-quarters of an hour to an hour. A two-component dissection requires about

fifteen minutes less. For some of the initial samples dissected by this author, up to six trials were necessary, but with experience, fits as good as that in Figure 5.13B could be obtained on the initial trial. It is obvious, therefore, that the proper estimation of the proportions ($P_C$) is crucial if many samples are to be processed by the graphical method.

A total of 32 samples have been dissected in the course of the present study. The locations of the samples are shown in Figure 5.1, and the results are listed in Table 5.5. Four further examples representing a variety of curve shapes, are shown in Figures 5.14 and 5.15. Certain points relating to the appropriateness of the overlapping-normal model that are illustrated by these examples require further comment.

It is noteworthy that the example used in the above demonstration of the dissection technique (sample CB38-C, Figure 5.13) is a type B curve, as defined in Section 5.2.1. From the dissection, it is evident that the two coarsest straight-line segments present in this curve type are part of the single, normal C population. Indeed, cumulative curves of this type, that is, with two steep portions joined by a flatter segment, can confidently be interpreted as representing the sum of two non-truncated normal distributions with only a small amount of overlap (Harding, 1949; Spencer, 1963), such that a bimodal frequency distribution is produced.

TABLE 5.5 : Summary of size-population characteristics. See text for an explanation of the different "break" determination methods.

| Sample | Population | Proportion (%) | Mean (ø) | St. Dev. (ø-units) | C-A Break Size (ø) | | |
|---|---|---|---|---|---|---|---|
| | | | | | Method 1 | Method 2 | Method 3 |
| BB1 | $A_1$ | 4% | 1.75 | 0.70 | --- | --- | --- |
| | $A_2$ | 96% | 2.60 | 0.31 | | | |
| BB21-C | $A_1$ | 15% | 1.45 | 0.87 | --- | --- | --- |
| | $A_2$ | 85% | 2.30 | 0.39 | | | |
| BB24-C | C | 38% | -0.40 | 1.16 | 2.00 | 1.50 | 1.25 |
| | A | 62% | 2.25 | 0.44 | | | |
| BB26-T | C | 40% | -0.75 | 1.28 | 2.05 | 1.60 | 1.30 |
| | A | 60% | 2.35 | 0.46 | | | |
| BB28 | C | 50% | -1.70 | 1.10 | 2.08 | 0.75 | 0.60 |
| | A | 50% | 2.12 | 0.61 | | | |
| BB40 | C | 25% | 0.15 | 1.08 | 1.69 | 1.49 | 1.05 |
| | A | 75% | 2.02 | 0.51 | | | |
| BB68-C | C | 45% | 0.45 | 1.20 | 1.35 | 1.31 | 0.90 |
| | A | 55% | 1.70 | 0.52 | | | |
| BB69-T | C | 58% | -1.70 | 1.03 | 1.88 | 0.15 | 0.20 |
| | A | 42% | 1.65 | 0.85 | | | |
| BB94 | C | 54% | -0.40 | 0.93 | ? | 0.58 | 0.60 |
| | A | 46% | 1.50 | 0.89 | | | |

TABLE 5.5 (Continued)

| Sample | Population | Proportion (%) | Mean (ø) | St. Dev. (ø-units) | C-A Break Size (ø) Method 1 | Method 2 | Method 3 |
|---|---|---|---|---|---|---|---|
| DB1 | C | 7% | 1.15 | 0.83 | 0.99 | 1.40 | 0.70 |
| | A | 93% | 1.55 | 0.31 | | | |
| DB2 | $A_1$ | 1% | 1.70 | 0.73 | ---- | ---- | ---- |
| | $A_2$ | 99% | 1.97 | 0.32 | | | |
| DB3 | $A_1$ | 1% | 2.35 | 1.30 | ---- | ---- | ---- |
| | $A_2$ | 99% | 2.40 | 0.28 | | | |
| DB26 | $A_1$ | 1% | 0.85 | 0.62 | 0.88 | 1.48 | 0.60 |
| | $A_2$ | 98% | 1.87 | 0.40 | | | |
| | B | 1% | 2.50 | 2.28 | | | |
| DB27 | C | 15% | -0.75 | 0.92 | 0.39 | 0.32 | -0.30 |
| | A | 75% | 1.05 | 0.62 | | | |
| | B | 10% | 2.55 | 0.77 | | | |
| DB39 | A | 98% | 2.09 | 0.30 | ---- | ---- | ---- |
| | B | 2% | 2.67 | 1.09 | | | |
| DB40 | C | 0.3% | 0.80 | 0.97 | 1.31 | 1.70 | 1.10 |
| | A | 93.7% | 1.90 | 0.22 | | | |
| | B | 6% | 2.75 | 0.89 | | | |
| C7 | C | 25% | -2.05 | 1.49 | -0.03 | 0.23 | -1.60 |
| | $A_1$ | 55% | -0.25 | 0.71 | | | |
| | $A_2$ | 19.5% | 0.69 | 0.28 | | | |
| | B | 0.5% | 2.35 | 0.83 | | | |
| C9 | C | 4% | 1.45 | 1.52 | 0.83 | 1.79 | 0.40 |
| | A | 96% | 1.80 | 0.49 | | | |

TABLE 5.5 (Continued)

| Sample | Population | Proportion (%) | Mean (ø) | St. Dev. (ø-units) | C-A Break Size (ø) | | |
|---|---|---|---|---|---|---|---|
| | | | | | Method 1 | Method 2 | Method 3 |
| CB20 | C | 30% | 0.30 | 0.94 | 1.23 | 1.21 | 0.80 |
| | A | 70% | 1.59 | 0.35 | | | |
| CB38-C | C | 35% | -0.15 | 1.14 | 1.12 | 1.09 | 0.80 |
| | $A_1$ | 63% | 1.45 | 0.31 | | | |
| | $A_2$ | 2% | 2.40 | 0.26 | | | |
| CB58-C | C | 5% | 0.72 | 1.26 | 1.00 | 1.54 | 0.50 |
| | $A_1$ | 80% | 1.89 | 0.47 | | | |
| | $A_2$ | 15% | 2.10 | 0.22 | | | |
| EB1 | C | 2% | 0.10 | 1.50 | 1.04 | 1.51 | -0.20 |
| | $A_1$ | 13% | 1.48 | 0.70 | | | |
| | $A_2$ | 85% | 1.83 | 0.33 | | | |
| EB9 | C | 25% | -0.95 | 1.59 | 0.63 | 0.32 | -0.40 |
| | $A_1$ | 55% | 0.80 | 0.56 | | | |
| | $A_2$ | 20% | 1.35 | 0.27 | | | |
| EB18 | C | 5% | -0.15 | 0.89 | 0.30 | 0.70 | -0.40 |
| | $A_1$ | 20% | 0.48 | 0.41 | | | |
| | $A_2$ | 75% | 1.10 | 0.37 | | | |

TABLE 5.5 (Continued)

| Sample | Population | Proportion (%) | Mean (ø) | St. Dev. (ø-units) | C-A Break Size (ø) | | |
|---|---|---|---|---|---|---|---|
| | | | | | Method 1 | Method 2 | Method 3 |
| SB32 | $A_1$ | 2% | 0.45 | 0.34 | ---- | ---- | ---- |
| | $A_2$ | 96% | 1.30 | 0.33 | | | |
| | B | 2% | 2.08 | 0.62 | | | |
| SB35 | C | 2% | 1.30 | 1.20 | 1.90 | 1.61 | 0.75 |
| | $A_1$ | 78% | 1.70 | 0.27 | | | |
| | $A_2$ | 20% | 2.00 | 0.47 | | | |
| SB53 | $A_1$ | 5% | 1.70 | 0.54 | ---- | ---- | ---- |
| | $A_2$ | 80% | 2.00 | 0.22 | | | |
| | $A_3$ | 15% | 2.35 | 0.43 | | | |
| SB66 | $A_1$ | 5% | 1.00 | 0.30 | ---- | ---- | ---- |
| | $A_2$ | 93% | 1.51 | 0.26 | | | |
| | B | 2% | 3.00 | 0.62 | | | |
| SB111 | C | 5% | -0.58 | 1.42 | 0.32 | 0.70 | -0.15 |
| | A | 95% | 1.15 | 0.44 | | | |
| SB142 | $A_1$ | 1% | 1.20 | 0.35 | ---- | ---- | ---- |
| | $A_2$ | 59% | 1.86 | 0.20 | | | |
| | $A_3$ | 38% | 2.27 | 0.25 | | | |
| | B | 2% | 2.95 | 0.30 | | | |

TABLE 5.5 (Continued)

| Sample | Population | Proportion (%) | Mean (ø) | St. Dev. (ø-units) | C-A Break Size (ø) Method 1 | Method 2 | Method 3 |
|---|---|---|---|---|---|---|---|
| SB170 | $A_1$ | 7% | 1.15 | 0.22 | ---- | ---- | ---- |
| | $A_2$ | 85% | 1.75 | 0.23 | | | |
| | $A_3$ | 8% | 2.35 | 0.37 | | | |
| SB179 | C | 0.5% | 0.95 | 1.01 | 0.33 | 1.27 | 0.20 |
| | $A_1$ | 40% | 1.39 | 0.35 | | | |
| | $A_2$ | 57.5% | 1.85 | 0.20 | | | |
| | B | 2% | 2.15 | 0.78 | | | |
| Averages | C | 14.9% (0.0-58%) | -0.18 (-2.05-1.45) | 1.15 (0.83-1.59) | | | |
| | A | 50.2% (1-99%) | 1.70 (-0.25-2.60) | 0.44 (0.20-1.30) | | | |
| | B | 3.2% (0.5-10%) | 2.56 (2.08-3.00) | 0.93 (Q.30-2.28) | | | |

FIGURE 5.14 : Examples of dissected grain-size distributions. A - Sample BB68-C; B - Sample BB24-C. Mean and standard deviation given for each dissected population (heavy inclined lines). Percentages in figures give proportions of each population. "Breaks" indicated by heavy horizontal bars. See text for further discussion.

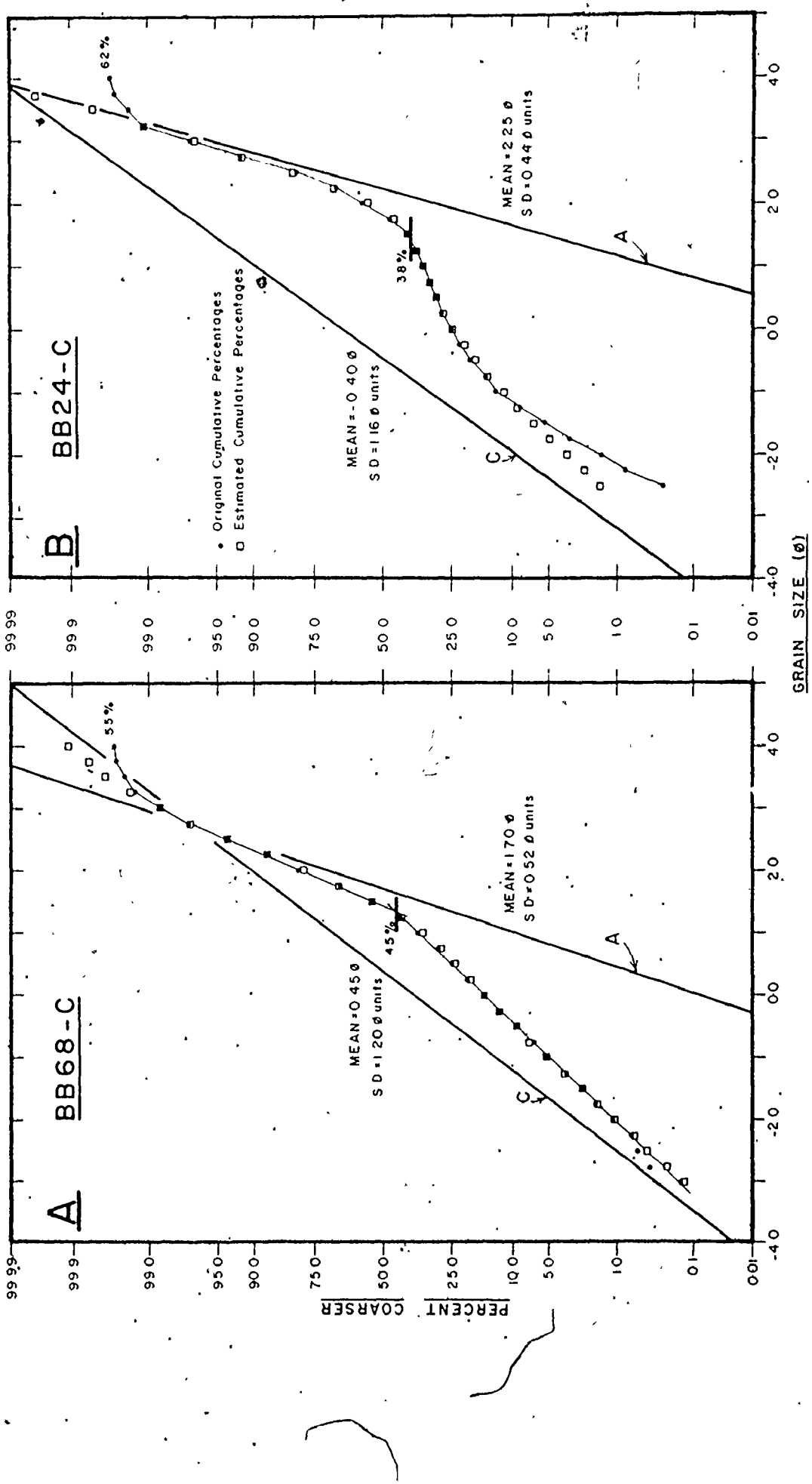
A
BB68-C
MEAN=0 45 ø
S D=1 20 ø units
MEAN=1 70 ø
S D=0 52 ø units
55%
45%
B
BB24-C
MEAN=-0 40 ø
S D=1 16 ø units
MEAN=2 25 ø
S D=0 44 ø units
62%
38%
• Original Cumulative Percentages
□ Estimated Cumulative Percentages
A
C
PERCENT COARSER
GRAIN SIZE (ø)

FIGURE 5.15 : Examples of dissected grain-size distributions. A - Sample EB9; B - Sample SB53. See caption of Figure 5.14 and text for further comments.

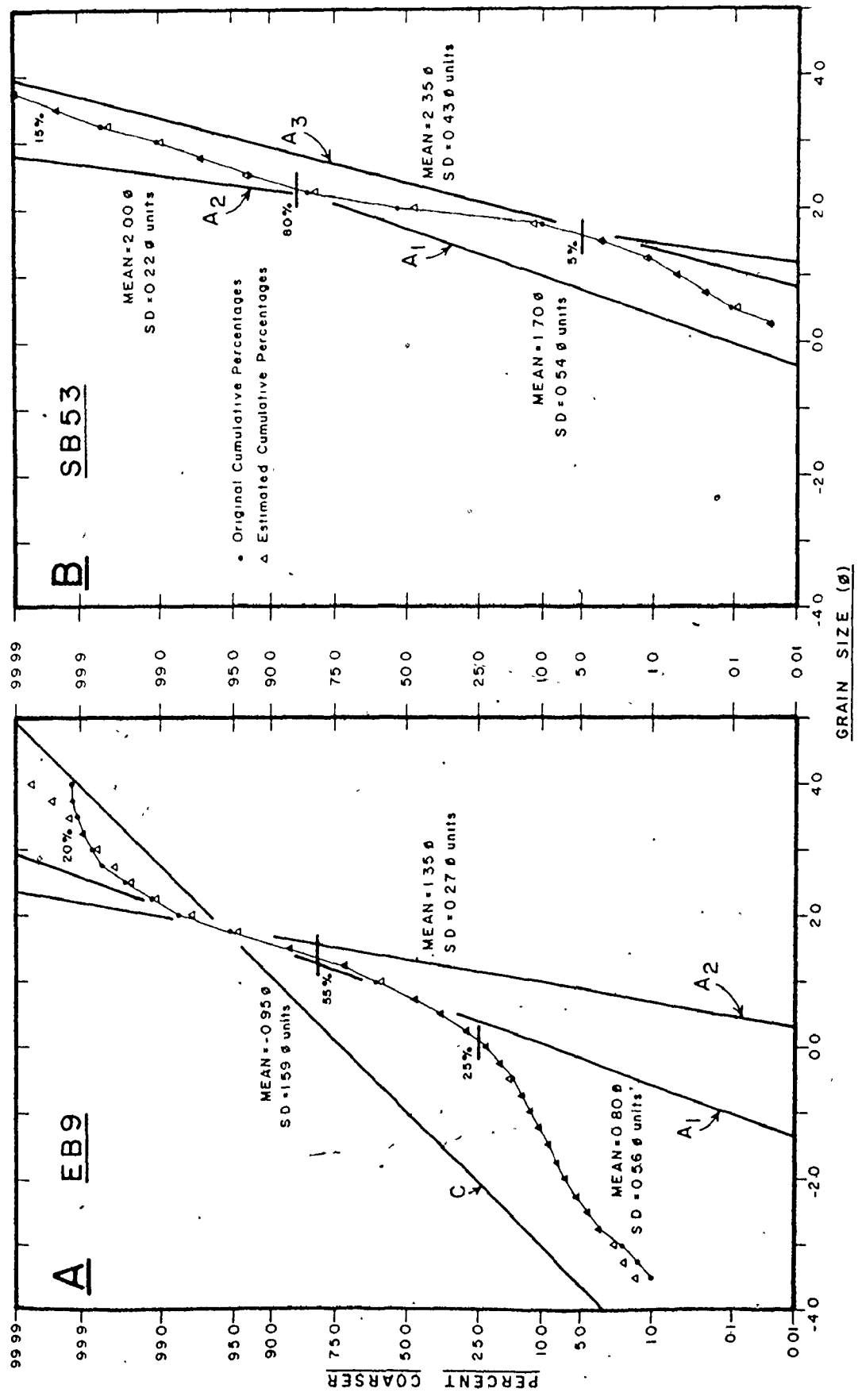
A
EB9
MEAN = -0 95 ø
SD = 1 59 ø units
MEAN = 1 35 ø
SD = 0 27 ø units
MEAN = 0 80 ø
SD = 0 56 ø units
20%
55%
25%
A1
A2
C
B
SB53
MEAN = 2 00 ø
SD = 0 22 ø units
MEAN = 2 35 ø
SD = 0 43 ø units
MEAN = 1 70 ø
SD = 0 54 ø units
15%
80%
5%
A1
A2
A3
• Original Cumulative Percentages
△ Estimated Cumulative Percentages
PERCENT COARSER
GRAIN SIZE (ø)
99 99
99 9
99 0
95 0
90 0
75 0
50 0
25 0
10 0
5 0
1 0
0 1
0 01
40
20
00
-2 0
-4 0

Type A cumulative curves, as illustrated by sample BB68-C (Figure 5.14A), can also be closely approximated by overlapping normals, but represent the situation where the overlap is considerable, such that no minimum exists in the frequency distribution. Sample BB68-C is also of interest because of the sharpness of the "break" between the A and C populations. The good fit achieved shows that such sharp kinks need not signify truncation of the populations at the "break".

One of the few cases in which truncation of any sort appears probable is shown by sample BB24-C (Figure 5.14B). Here, the good fit between the estimated and observed cumulative percentages for sizes finer than -1.0 phi (2.0 mm) strongly suggests that the populations extracted are the correct ones. If this is the case, then the discrepancy in the coarsest sizes indicates that the coarse tail of the original distribution has been truncated. A similar but less severe truncation may be present in sample EB9 (Figure 5.15A). A number of factors may be responsible for this truncation: inadequate sampling of the coarsest sizes; limited abundance in the source; and hydraulic segregation due either to the partial elimination of the coarsest sizes by some critical hydrodynamic barrier, or to the preferential deposition of these sizes in the bedform trough as discussed in Section 5.2.3.

The dissection of sample EB9 (Figure 5.15A) is interesting because of the very poorly-sorted nature of the C population, which results in it containing more fine and very fine sand than either of the two intermittent suspension populations. This means that these fine sizes are more likely to travel as part of the traction load than in intermittent suspension, a result which intuitively seems unreasonable. A similar interpretation is possible for sample BB68-C (Figure 5.14A). If a hydraulic interpretation is accepted for the populations, then a certain amount of overlap can be expected, due to turbulence and other time variations in flow strength. The extreme overlap indicated in sample EB9 (Figure 5.15A) is, however, difficult to understand. It is possible that the fine tail of the C population may, in fact, be truncated, but experimental investigations into the nature of traction transport are necessary before the choice between models can be made with certainty.

The existence of two A populations in sample EB9 (Figure 5.15A) was not expected by the author on the basis of the cumulative curve shape, but the use of only a single A population did not allow a satisfactory fit to be obtained. The extremely rounded nature of the "break" could only be fit with reasonable accuracy by introducing a second A population. As will be discussed more fully in Section 5.3.4, the significance of two and even three A populations (see sample SB53, Figure 5.15B) in some samples is not understood, and the

possibility exists that a number of the populations extracted are spurious and the result of attempting to fit overlapping normal populations to truncated-normal or other non-normal populations.

Finally, sample SB53 (Figure 5.15B) is an example of a curve that lacks a poorly-sorted C population. The relatively steep coarse tail that is present can, instead, be represented by a population with mean size and sorting characteristics that are much more similar to those of A populations. As a result, sample SB53 is interpreted as containing three A populations. As mentioned above, the possible significance of this will be discussed in a later section.

Despite the variety of curve shapes, it is evident from the above examples that an overlapping-normal model can reproduce the original cumulative curves with a high degree of accuracy. This is in agreement with the findings of others who have dissected size distributions into normal components, and suggests that overlapping normals are the appropriate model for grain-size populations. The poor fit achieved by the truncated-normal model at the "breaks", in comparison to the overlapping-normal model, gives further strong support to this conclusion.

### 5.3.3 Population Characteristics and Areal Variations

The proportion, mean size and sorting (standard deviation) of each population extracted from the dissected samples

are listed in Table 5.5, together with the average and range of values for each parameter for the three population types (B, C and A). Each will be discussed in turn.

(i) Type B Populations: Due to the small proportion of the total represented by the B population (average estimate less than 1.5%), only eight attempts have been made to estimate its parameters, and as a result, the averages for the B population are less representative than those for the other populations. The average mean size of 2.56 phi (0.17 mm) is in the fine sand grade, and the average standard deviation (0.93 phi-units) indicates that this population is moderately sorted according to the Friedman (1962) classification. In these eight samples, the B population is generally more abundant (3.2%) than in an average sample, and appears to be somewhat coarser and better sorted than in other samples where the separation of the B population has not been attempted.

(ii) Type C Populations: In the 32 samples studied, the C (coarse tail) population comprises slightly less than 15% of the total, but with considerable variability between samples, ranging from non-existent in eleven samples to a high of 58% in sample BB69-T. The average mean size of the C population, when present, is very coarse sand (-0.18 phi - 1.13 mm), and the average sorting is 1.15 phi-units, which falls in the moderately sorted category of Friedman (1962). Figure 5.16 shows the areal variations in the amount and characteristics of the C population on the four study bars.

FIGURE 5.16 : Areal variations of C population characteristics. A - Big Bar; B - Diamond Bar; C - Economy Point; D - Selmah Bar. Mean sizes (phi) given by heavy contours; standard deviations (phi-units) by broken, light lines. Proportions shown in brackets.

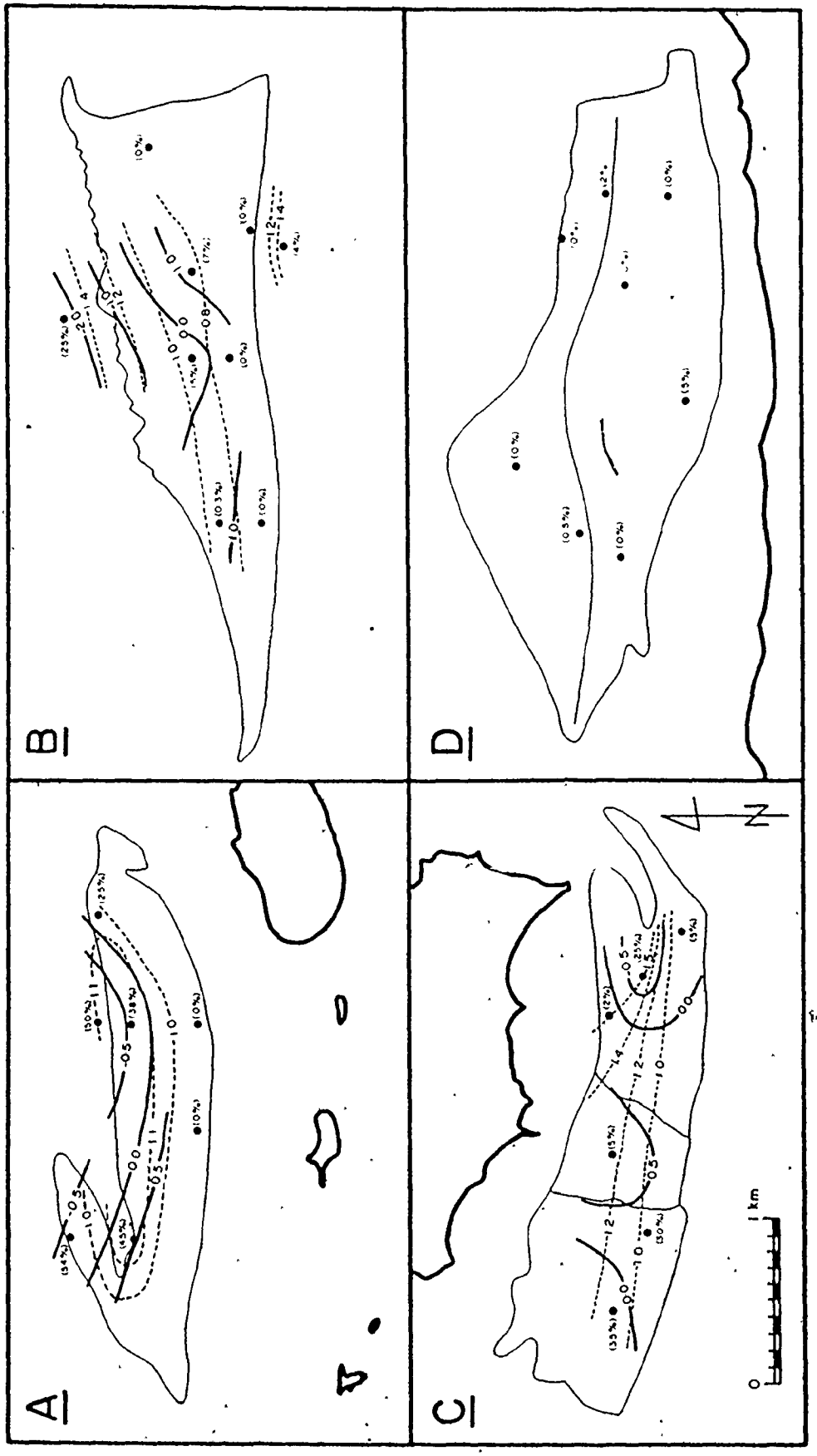
A
B
C
D
N
1 km
0

On Big Bar (Figure 5.16A), the proportion of the C population present is highest along the northern edge of the bar, and decreases in a southerly direction, toward the bar crest. No C population exists in samples lying south of the crest. The mean sizes of the C population also show a southward fining trend, while the sorting is poorest in the central portion of the northern edge of the bar.

The C population is absent in all samples derived from ebb-dominated areas on Diamond Bar (Figure 5.16B; compare Figure 3.15), with the exception of sample C9, which contains an unusually fine-grained but poorly sorted coarse-tail population. On the northern, flood-dominated side of the bar, the abundance, mean size, and standard deviation all decrease in a southerly direction toward the bar crest. The 0.0 phi (1.0 mm) contour of mean size is deflected southward markedly, immediately to the east of the minor swatchway.

At Economy Point (Figure 5.16C), all samples contain a C population, with the proportion being highest on Centre Bar, and in the vicinity of the blind ebb channel on East Bar. The coarsest mean sizes (coarser than 0.0 phi; >1.0 mm) are also found in these areas. In contrast to the contour pattern of mean size, the contours of sorting run nearly parallel to the axis of the complex, the best sorting (moderately sorted) being located along the outer edge of the bars.

Five of the eight dissected samples from Selmah Bar (Figure 5.16D) contain no C population, making the delineation of trends in mean size and sorting of this population impossible. Visual examination of undissected samples shows that the C population is primarily restricted to samples derived from the flood-dominated portion of the bar lying east of the swatchway, with the abundance decreasing northward away from the shore.

The data presented in Figure 5.16 indicates that the amount of the C population present is generally greatest in areas close to extensive gravel lag, and decreases as distance from the gravel lag increases. The highest proportions of the C population, not surprisingly, also occur in areas where the mean size of the entire size-frequency distribution is coarsest (part A of Figures 5.8 to 5.11). The possible factors responsible for the trends observed in Figure 5.16 will be discussed in Section 5.3.4.

(iii) Type A Populations: One, or more A populations combined, constitute the largest component (81.9%) in the samples studied. There is wide variability, however, in the contribution made by individual A populations, ranging from 1% in the case of several small, coarse-tail components (e.g., DB2) up to 99%, with an average proportion of 50.2%. The mean sizes of these populations overlap with those of both C and B populations, and range from -0.25 phi (1.19 mm) to 2.60 phi (0.165 mm). The average value (1.70 phi - 0.31 mm) is in the

medium sand grade. As would be expected from the steepness of the A portion of the cumulative curves, A populations are better sorted on average (moderately well sorted: standard deviation = 0.44 phi-units) than either B or C populations. Standard deviations range from a low of 0.20 phi-units (samples SB142 and SB179) to an anomalously high value of 1.30 phi-units, obtained for the minor "coarse-tail" component of sample DB3.

Inspection of the mean size and sorting values of A populations in Table 5.5 for samples with multiple A populations reveals that a general relationship exists between the mean sizes and sorting within a single sample. In 14 of the 15 samples with two A populations, the finer-grained population is better sorted than the coarser one, regardless of the relative proportions of each component. The most abundant (dominant) A population is, however, the better sorted of the two in 11 of the 15 samples. In 2 of the 3 samples with three A populations, the middle (and dominant) one is the best sorted (see, for example, sample SB53, Figure 5.15B).

When the sorting is plotted against the mean size for all A populations (Figure 5.17A), no pattern is evident, however, either for all the data combined, or for any bar individually, with the exception of Big Bar where there is a well-defined trend for better sorting at finer mean sizes. Some of the scatter is removed by considering only the dominant A populations (Figure 5.17B). Although no overall trend is

FIGURE 5.17 : Plots of sorting versus mean size for A populations.
A - All data;
B - Dominant (most abundant) A population only.
Diagonal lines give the trend of the data points for the indicated bar. No trend is evident for the Economy Point data. Thin vertical and horizontal lines are verbal class boundaries (see Section 5.1.3).

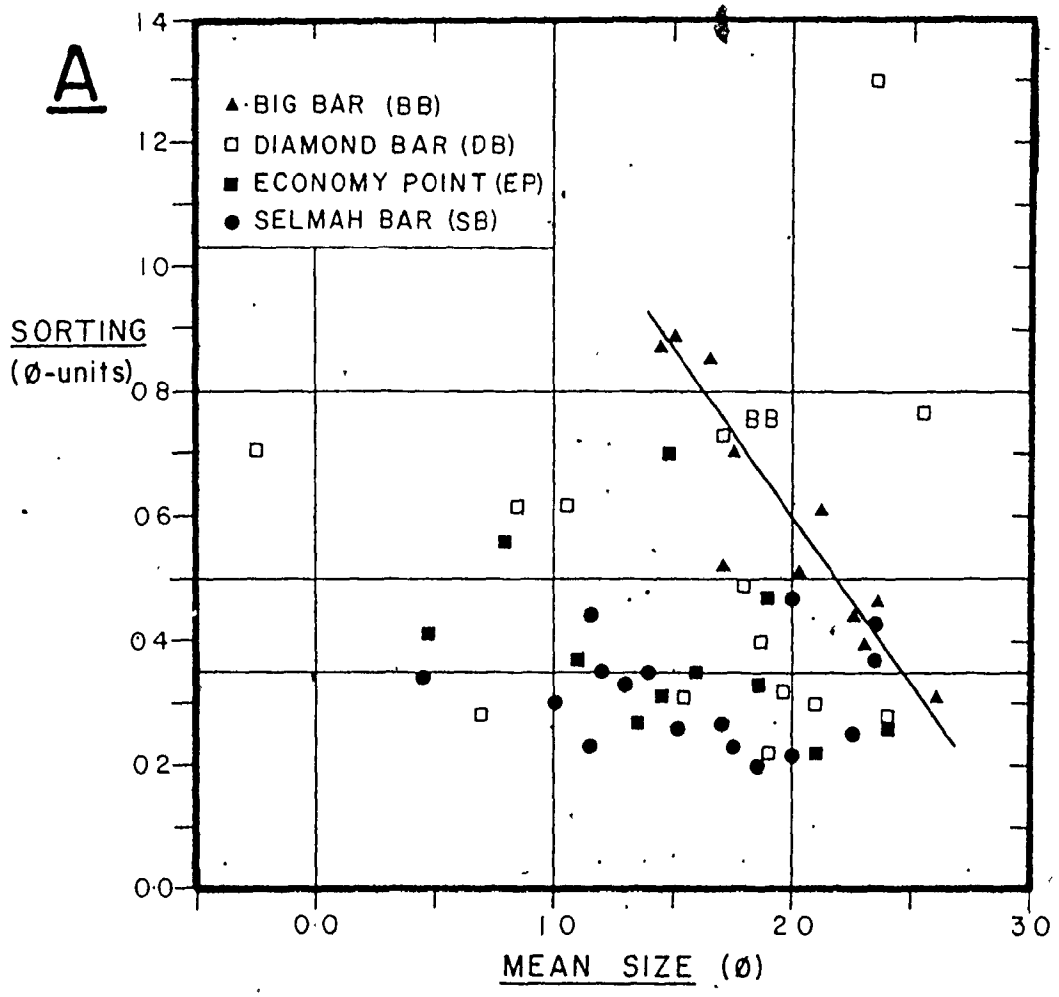
A
▲ BIG BAR (BB)
□ DIAMOND BAR (DB)
■ ECONOMY POINT (EP)
● SELMAH BAR (SB)
SORTING
(ø-units)
1.4
1.2
1.0
0.8
0.6
0.4
0.2
0.0
BB
0.0
1.0
2.0
3.0
MEAN SIZE (ø)

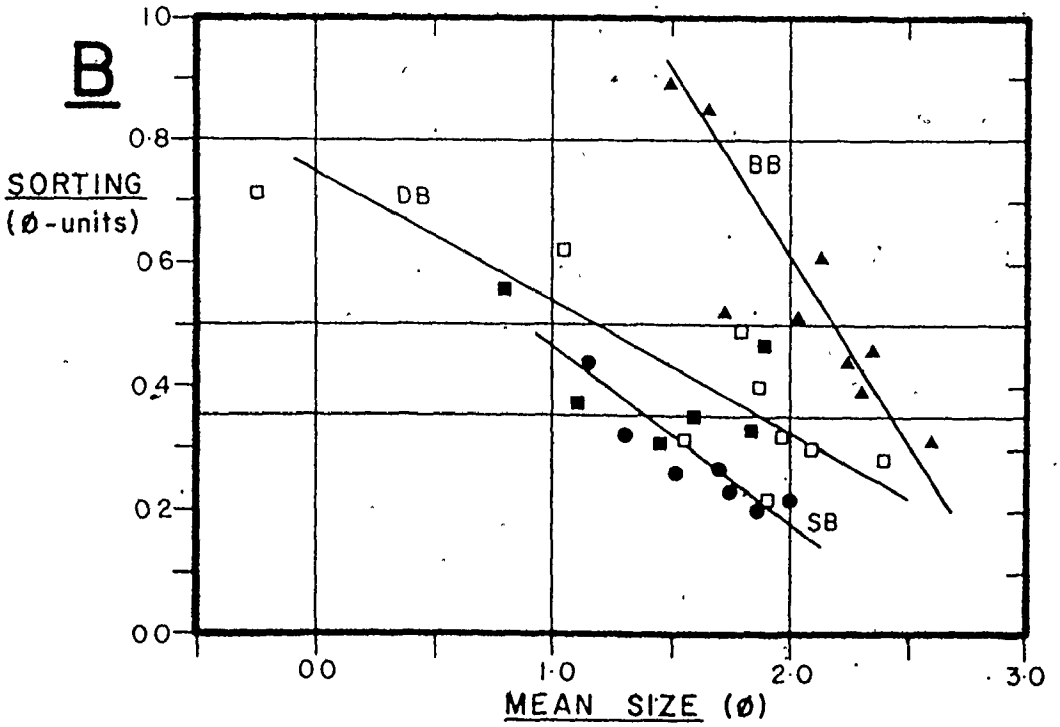
B
SORTING
(ø-units)
1.0
0.8
0.6
0.4
0.2
0.0
BB
DB
SB
0.0
1.0
2.0
3.0
MEAN SIZE (ø)

evident, the data for Diamond and Selmah Bars now indicate trends similar to that seen on Big Bar, but with an obvious displacement of these trends toward coarser mean sizes, relative to Big Bar. Still no pattern can be seen in the Economy Point data.

The areal variations in the amount, mean size, and sorting of the dominant A populations on the four study bars are shown in Figure 5.18.

On Big Bar (Figure 5.18A), the dominant A population is most abundant on the south side of the bar crest, where the C population is absent, and decreases in abundance northward as the contribution from C increases. The A populations are also finest along the south side, and coarsest on the northwestern arm of the bar. Surprisingly, the mean sizes are finer than 2.0 phi (0.25 mm) over the entire eastern end of the bar, so that the contours in Figure 5.18A show a significantly different trend from the contours of mean size for the entire sample in Figure 5.8A. As expected from the pattern revealed by the data for Big Bar in Figure 5.17, the contours of sorting closely parallel those of mean size.

On Diamond Bar (Figure 5.18B), the dominant A population forms over 90% of the samples, except in the one from the northern channel and another from the north-central part of the bar, immediately east of the minor swatchway. In these two samples, the C population is more abundant than elsewhere on the bar. The mean size of the dominant A population is

FIGURE 5.18 : Areal variations of dominant A population characteristics. A - Big Bar; B - Diamond Bar; C - Economy Point; D - Selmah Bar. Mean sizes (phi) given by heavy contours; standard deviations (phi-units) by broken, light lines. Proportions shown in brackets.

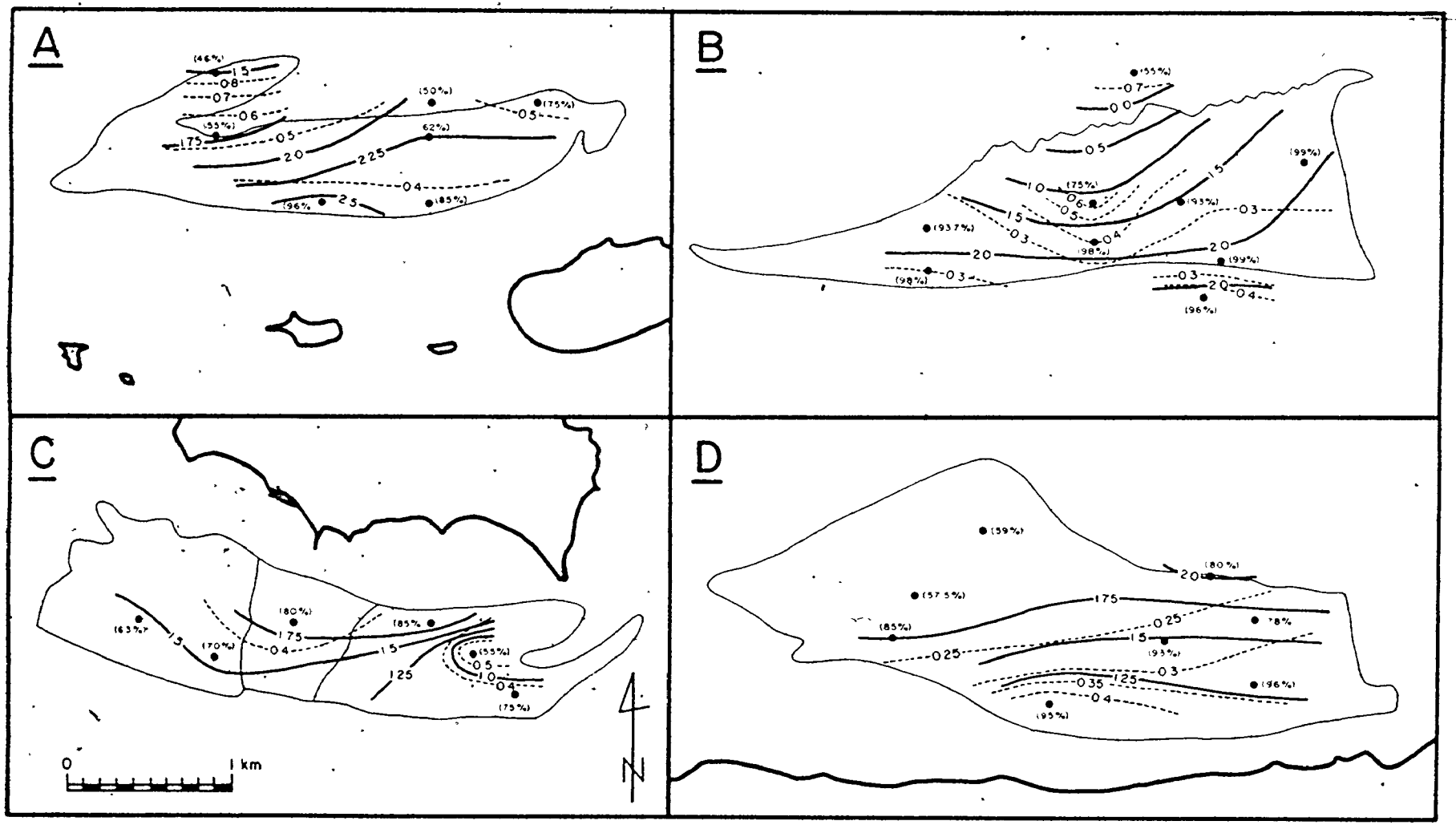
A
B
C
D
0
1 km
N

finest (>2.0 phi; <0.25 mm) in a band running along the southern edge of the bar, in the ebb-dominated area (compare Figure 3.15). The mean size is only slightly coarser in the southern channel, but coarsens significantly on the north side of the bar crest, and in the northern channel. Sorting values show a trend that is similar to that of the mean sizes, with the best sorting occurring in a band south of the bar crest, and poorer sorting on either side, but particularly to the north where the mean sizes are coarsest.

At Economy Point (Figure 5.18C), the proportion of the dominant A population is highest (over 80%) in that area with the finest mean sizes (>1.75 phi; <0.30 mm), which lies in the north-central portion of the area, adjacent to the headland, and in the area of lowest current strength (Figure 3.16). Mean sizes become coarser to the south and east, with the coarsest values present in the blind ebb channel on East Bar. The sorting of the A population is poorest in this location, and also in the low area between East and Centre Bars. The best sorting generally lies along the outer edge of the complex.

The mean sizes of the A populations on Selmah Bar (Figure 5.18D) become finer in a regular manner from south to north, particularly in the eastern half of the bar. At the western end, mean sizes are extremely constant; the two northern-most samples differing by only 0.01 phi-unit. Furthermore, the sorting values for these two A populations are identical (0.20 phi-units), and are the best encountered on

any of the bars. From this area, the sorting becomes poorer both eastward and southward, with the worst values located along the southern edge of the bar. It is of interest to note that all but one of the samples dissected on Selmah Bar (sample SB111 - see Figure 5.1D for locations) contains more than one A population. Subequal amounts of the secondary A populations account for the low percentages of the dominant A population in some of the samples. In the three northernmost samples (SB35, 53 and 142), the secondary A population is finer than the dominant one and has a mean size in the 2.0 to 2.35 phi range (0.25 - 0.20 mm) (Table 5.5). In sample SB179, the secondary population is coarser, having a mean size of 1.39 phi (0.38 mm) (Table 5.5). This point will be discussed further in Section 5.3.4.

Because the dominant A population is by far the most abundant population in the majority of samples (average proportion = 76.5%), it is to be expected that the mean of this population should coincide with the dominant mode of the total sample (as defined in Section 5.2.1 and Figure 5.2E). A comparison of the two for the dissected samples shows that such is indeed the case in all but 6 of the 32 samples. In these six samples, 2 each on Big, Diamond and Selmah Bars, admixture of an abundant C or secondary A population has shifted the sample mode by one modal group (using the Roman numeral designation as in Figure 5.2E) from that indicated by the dominant A population mean. Nevertheless, plots of the

areal distribution of the dominant modal types (Figure 5.19) provide a reasonably accurate representation of the distributions of dominant A population mean sizes, with considerably better areal coverage than is available with the dissection results alone (Figure 5.18).

On Big Bar (Figure 5.19A), mode VIII is dominant in samples from the western end of the bar, and from those lying in a band along its southern edge. Progressively coarser modes dominate the northwestern corner of the bar.

On Diamond Bar (Figure 5.19B), mode VIII is dominant in a strip along the eastern two-thirds of the south side (in the ebb-dominated area), and is surrounded by mode VIIC (1.75 - 2.0 phi; 0.30 - 0.25 mm) on the bar crest to the north, and in the channel to the south. Most of the flood-dominated northern side of the bar possesses sands in which mode VIIA (1.25 - 1.50 phi; 0.42 - 0.35 mm) is dominant; whereas mode VI is present in the northern channel.

At Economy Point (Figure 5.19C), the pattern of modal types is very complex. In general, finer modes (VIIB, VIIC and VIII) are dominant along much of the shoreward side of the bars, while coarser modes (VIIA, VI and even V) are found along the outer edge.

The dominant modal types on Selmah Bar (Figure 5.19D) show a progressive northward and eastward fining, from mode VI through modes VIIA, B and C, and finally to VIII, that is in agreement with the pattern of A-population mean sizes seen

FIGURE 5.19 : Areal variation of dominant sample mode size. A - Big Bar; B - Diamond Bar; C - Economy Point; D - Selmah Bar. See Figure 5.2E for the grain size of each indicated modal type.

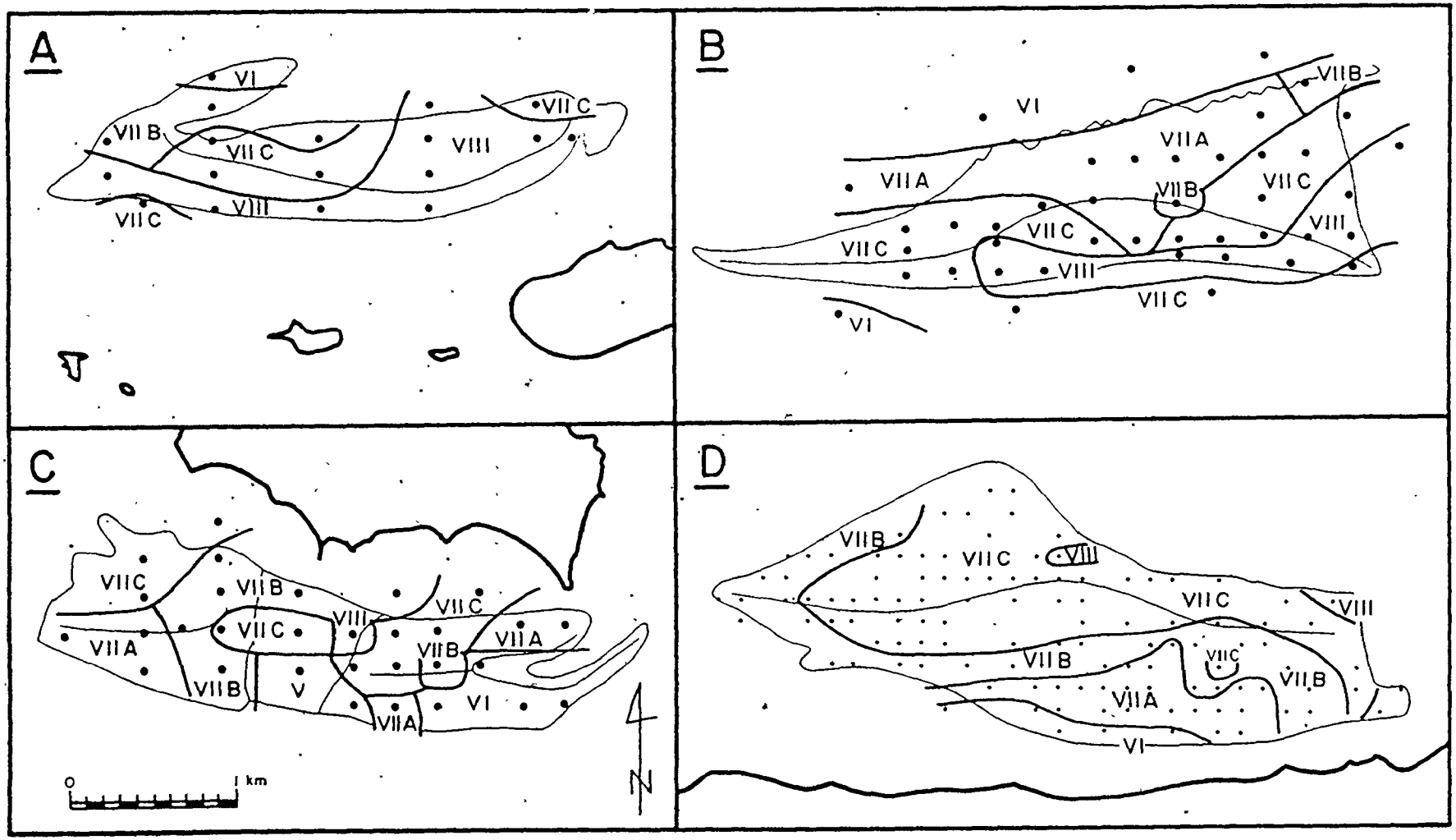
A
VI
VII B
VII C
VIII
VII C
VIII
B
VI
VII B
VII A
VII A
VII B
VII C
VII C
VII C
VIII
VIII
VII C
VI
C
VII C
VII B
VIII
VII C
VII C
VII A
VII B
VII A
VII B
V
VI
VII A
0
1 km
N
D
VII B
VII C
VIII
VII C
VIII
VII B
VII C
VII B
VII A
VI

in Figure 5.18D. At the extreme western end of the Bar, the lobate-shaped area occupied by mode VIIC is surrounded on three sides by the coarser mode VIIB.

To this point, the discussion has involved only the presentation of the general characteristics and areal variations of the populations determined by the graphical dissections. No attempt has yet been made to determine the factors controlling the nature of the populations and the areal variations just described, although certain qualitative correlations with hydraulic variables and transport paths have been mentioned in passing. These points will be investigated in more detail in the next section.

### 5.3.4 Factors Controlling Size Populations

It has long been recognized that two basic factors interact continuously to create the size-frequency distributions, and presumably also the component size populations, that are observed in nature: namely, hydraulic sorting mechanisms, and inheritance from the source. A third possible factor, mixing, is of less fundamental significance in the formation of individual size populations, but can be important in the production of the composite distributions. It is the purpose of this section to investigate the role that each of these factors plays in generating the size-population characteristics and their areal variations that were discussed in the previous section; and thereby to better understand the sediment dynamics of intertidal sand bars.

The hydraulic interpretation of size populations is based on the realization that widely different size fractions can be transported by different mechanisms, simultaneously at a given flow strength. According to Middleton (1976), the two fundamental sediment transport mechanisms operating to produce the C and A populations respectively are: traction or bed-load transport (including sliding, rolling and saltation); and intermittent suspension. The coarsest size that can be moved by traction (traction competence) for a given flow strength, can be determined from the Shields (1936) criterion for the initiation of motion. For specified fluid and sediment properties, this criterion can be given in terms of the sediment size and shear velocity only[1] (Figure 5.20; see also Figure 4.15). No finer limit is known for the sizes transported by traction processes in the bed-load layer, but it may be influenced by the coarsest size that can be transported by intermittent suspension. As discussed in Section 5.3.1, Middleton (1976) has suggested that the competence of intermittent suspension can be determined from equation (5.5); that is, the size whose fall velocity is equal to the shear velocity of the transporting flow. This competence relationship has also been plotted in Figure 5.20, using fall velocity data for natural grains given by Graf and Acaroglu (1966), and separates the field of grain suspension from the field of grain traction (or non-suspension).

FIGURE 5.20 : Competence relationships for traction and intermittent suspension transport. Traction competence given by incipient motion criterion of Shields (1936). Intermittent suspension competence is believed to be given by the grain size whose settling velocity is equal to the shear velocity. The fields of transport behaviour defined by these competence relationships are indicated

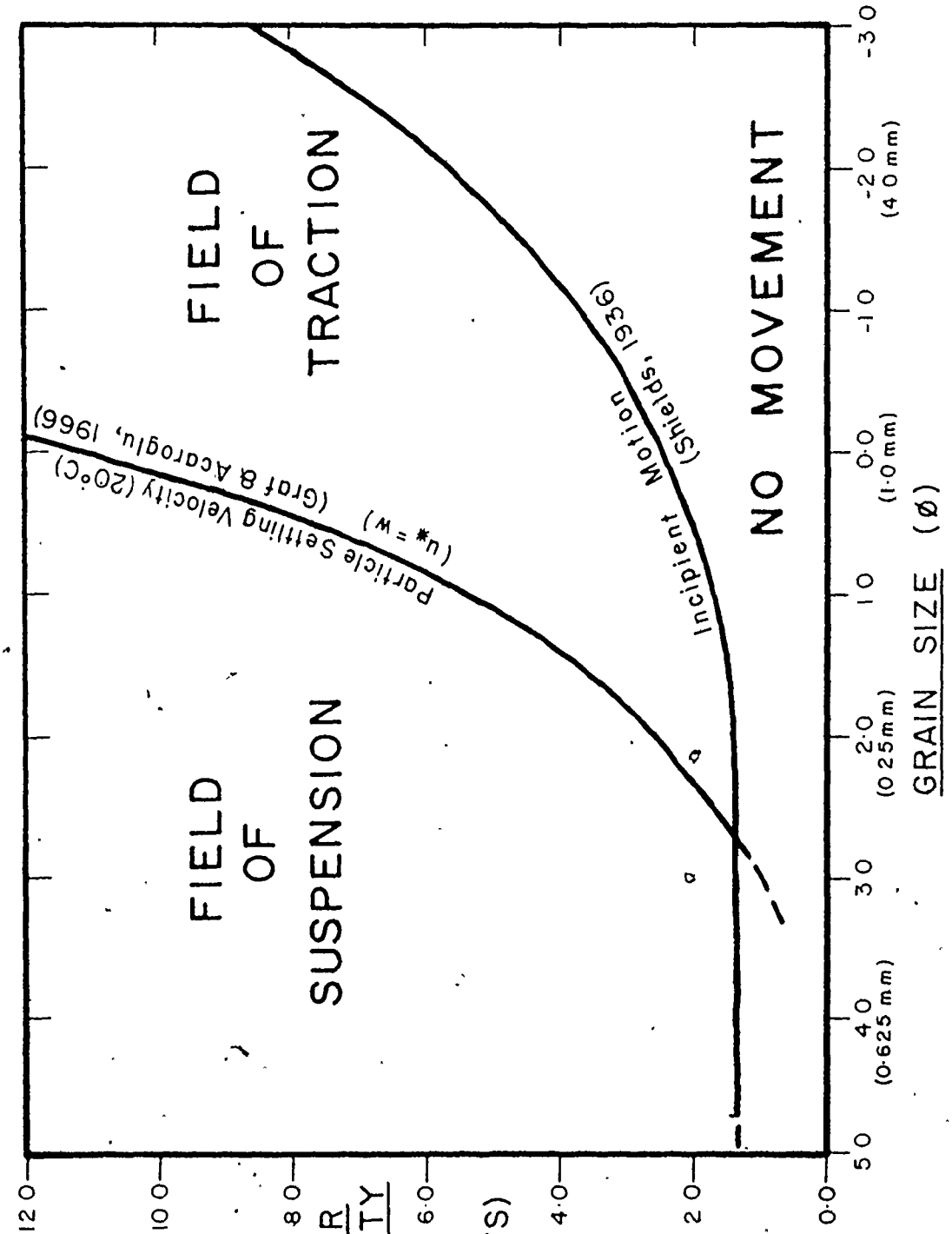
FIELD OF TRACTION
FIELD OF SUSPENSION
NO MOVEMENT
Incipient Motion (Shields, 1936)
Particle Settling Velocity (20°C)
(Graf & Acaroglu, 1966)
(u* = w)
SHEAR VELOCITY (CM/S)
GRAIN SIZE (Ø)
12·0
10·0
8·0
6·0
4·0
2·0
0·0
5·0
4·0 (0·625 mm)
3·0
2·0 (0·25 mm)
1·0
0·0 (1·0 mm)
-1·0
-2·0 (4·0 mm)
-3·0

The extent to which these transport mechanisms and the competence relationships shown in Figure 5.20 will act to modify the size populations present in the sediment at any given point will depend on the nature of the sediment transported to that location, which in turn depends on the hydraulic conditions upstream. Because of this, two different transport situations must be distinguished: the first is transport down a flow-strength gradient, that is, transport from an area of high current speeds to an area of lower speeds; and secondly, transport up a flow-strength gradient, from an area of low flow strength to an area of higher flow strength. The first situation is the one usually encountered in rivers, and is the only one considered by many sedimentologists. The second is not as commonly observed, and may be restricted to tidally-dominated environments.

In the first situation, where the shear velocity decreases downstream, the Shields relationship (Figure 5.20) shows that coarse material will be progressively deposited from the traction population, provided that such coarse material is initially available. In addition, the boundary, or "break" between intermittent suspension and traction should shift to finer sizes as the sediment moves down the transport path. As a result, the mean sizes of both the A and C populations should decrease downstream, and the sorting should improve due to the progressive restriction of the range of sizes transported by both mechanisms.

The second situation, in which the shear velocity increases along the transport path, should cause material which was previously moved by traction to pass into intermittent suspension as the sediment is transported downstream, in turn causing the mean size of the A population to become coarser. Similarly, the traction competence will increase, but because these coarse sizes have been removed previously, none are available for transport. For example, if the shear velocity at the head of the transport path is 1.6 cm/s, then no sediment coarser than 1.30 phi (0.41 mm) (Figure 5.20) will be present at any point along the transport path, unless added by mixing from another source. By the time the shear velocity has reached 4.5 cm/s, all of the previously formed traction population has been taken into intermittent suspension, and any further increase in the shear velocity will not bring about a change in the size distribution of the A population. Therefore, the size characteristics of the sediment will show strong influence of inheritance in the case of transport up a flow-strength gradient.

If traction and intermittent suspension are responsible for the formation and modification of the C and A populations respectively, then the presence of two, and even three, A populations in a number of samples (Table 5.5) requires an explanation. The existence of two intermittent suspension populations might initially be thought to result from the action of the two sets of currents (ebb and flood), in a

manner analogous to that proposed by Visher (1969) for the presence of swash and backwash populations on beaches. If this mechanism were operative, however, it might be expected that most samples would contain two A populations (Type D cumulative curves), but as stated in Section 5.2.1, only 24% of the samples are of this type.

In many of the samples with multiple A populations, the coarsest ($A_1$) population represents the coarse tail of the cumulative curve (see, for example, sample SB53, Figure 5.15B). As will become evident in later discussion, all of these samples come from areas with weak currents, or are part of a transport stream moving up a flow-strength gradient. It is possible, therefore, that these $A_1$ populations are all that remain of C populations that have been severely truncated during (previous) transport down a flow-strength gradient.

The mixing of A populations from two or more sources is another possible explanation. If an A population is added that has a mean size finer than the dominant "equilibrium" A population, then there may be little tendency to modify the finer one, and it might retain its identity during mixing. This may be the situation with those samples on Selmah Bar that were mentioned previously which have a dominant A population with a mean size in the 1.7 to 2.0 phi range (0.31 - 0.25 mm) and a subsidiary A population with a mean size between 2.0 and 2.35 phi (0.25 - 0.20 mm).

One final real possibility that was discussed near the end of Section 5.3.2 is that spurious A populations have been extracted in the process of fitting overlapping normals to non-normal populations.

On the basis of the hydraulic-transport model of size-population modification that was presented above, it is evident that the effects of both hydraulic sorting and inheritance should be visible in the areal distributions of the sediment and size-population characteristics. In order to verify this, it is necessary to review the patterns shown in Figures 5.16, 5.18 and 5.19 in the light of the areal variations in flow strength (Figures 3.13, 3.15, 3.16 and 3.17), and the transport patterns (Figure 3.18) for each bar in turn.

On Big Bar, the southward decrease in the amount and mean size of the C population (Figure 5.16A), away from the gravel lag area, which is presumably the source of this coarse material, closely parallels the pattern of decreasing time-average mean ebb current speeds and shear velocities (Figures 3.13B and 3.13C); implying that the C population characteristics here are hydraulically controlled. At the east end of the bar, the mean sizes of the dominant A populations also show a southward fining (Figures 5.18A and 5.19A), suggesting that a similar hydraulic control is possible. At the west end of the bar, the extensive area of population A mean sizes finer than 2.0 phi (0.25 mm; mode VIII) (Figures 5.18A and 5.19A), —although lying in an area of low current strength (Figure 5.13

and Figure 5.14A), is more extensive than might be expected on the basis of a simple hydraulic model. This pattern is, however, in agreement with the ebb-dominated transport shown for this area in Figure 3.18A, which would move fine sediment across the bar crest at its eastern end. The continuity of the area in which mode VIII is dominant, along the south side of the bar (Figure 5.19A), is not inconsistent with the flood-dominated transport inferred for this part of the bar (Figure 3.18A).

The most important feature of the sediment distribution patterns on Diamond Bar is the extensive area along the south side and at the east end where: the C population is absent (Figure 5.16B); the mean size of the A populations is less than 2.0 phi (0.25mm) (Figure 5.18B); and the dominant mode is either of type VIIC or VIII (Figure 5.19B). The presence of these characteristics in an area with the strongest currents (Figure 3.15) is certainly not consistent with any model based on hydraulic sorting. This area is, however, dominated by ebb tidal currents (Figure 3.15 and 3.18), and as a result the sediment here must be derived from the east, toward the head of Cobequid Bay, where the tidal current strengths are believed to be weaker (Section 2.3.1). This sediment has, therefore, retained the characteristics imposed in the lower energy conditions prevailing at the head of the bay during its westward transport up the flow-strength gradient, as predicted in the above discussion. It may be significant

that the westward termination of the mode VIII area in Figure 5.19B is located in the vicinity of the minor swatchway where mixing with coarser sediment from the north side of the bar is to be expected.

On the north side of Diamond Bar the opposite situation exists, and the residual eastward (flood) transport (Figure 3.18B) occurs in the presence of a decreasing velocity gradient. As a result, some evidence of hydraulic sorting should be seen. The observed decrease in the amount and mean size of the C population (Figure 5.16B), and the fining of the A population (Figures 5.18B and 5.19B) as one moves from the channel toward the bar crest where the flow strength is less (Figure 3.15); is in general agreement with this expectation.

At Economy Point, the scarcity of hydraulic (Figure 3.16) and size-population data (Figures 5.16C and 5.18C), combined with the topographic complexity of the bars and their surroundings (Figures 2.16 and 2.17) makes an interpretation of the sediment patterns difficult. The presence of the finest A and C populations (Figures 5.16C, 5.18C and 5.19C), combined with the small proportion of the C population, in samples from the north-central part of the area (Figure 5.16C), suggests that hydraulic sorting mechanisms are operative. The eastward extension of the mode VIIB area (Figure 5.19C) to the north of modes VIIC and VIII is consistent with the flood-dominated transport indicated for this area (Figure 3.18C)

and might also indicate that current velocities increase shoreward of Buoy EP4, rather than decrease as shown in Figure 3.16. The presence of the coarse mode V (Figure 5.19C) on the south side of the low area between East and Centre Bars can only be explained by noting that the inferred transport paths (Figure 3.18C) are directed away from this area on both the east and west sides, making this the location of a bed-load parting (Kenyon and Stride, 1970). The sediment possessing mode V is, therefore, probably a lag deposit, most of the finer material having been removed to the east and west.

Selmah Bar presents a situation that is very similar to that on Diamond Bar. The ebb-dominated area on the north side of the bar experiences stronger currents (Figure 3.17) than most of the flood-dominated area, but possesses A populations that are finer-grained (Figures 5.18D and 5.19D) than elsewhere. Again, the obvious implication is that these size characteristics are, in part, inherited from lower energy conditions existing eastward of Selmah Bar, and have been retained during transport up a flow-strength gradient. In contrast, the flood-dominated, south side of the bar displays the clearest example of hydraulic sorting seen on any of the study bars. Here, the regular eastward and northward pattern of decreasing dominant A-population mean sizes (Figures 5.18D and 5.19D) occurs in the presence of a similar decrease in flow strength (Figures 3.17B and 3.17C). Furthermore, the residual sediment transport directions are oriented at a high

angle to the contours of mean size (Figure 5.18D) and the modal type boundaries (Figure 5.19D), indicating that the transport is across, rather than parallel to, the bands of similar size composition. Irregularities in the pattern of modal types (Figure 5.19D) are attributable to the presence of the minor swatchways (Figure 2.12) which channel the flow for a part of the tidal cycle.

From the above discussion, it can be seen that the model presented at the beginning of the section, based primarily on a hydraulic interpretation of the size populations, is capable of explaining most of the large-scale areal variations in the characteristics of the size populations. The realization that distinctly different patterns of variation are to be expected, depending on whether the transport path is directed down or up a flow-strength gradient, is of particular significance. In the first situation, the effects of hydraulic sorting are observed; while in the second, a strong "source" control is evident, and the dominant sample mode can even be used to trace the movement of the sediment, in a manner similar to that employed by Curray (1960).

In order to assess the extent of the hydraulic control on the size populations more quantitatively, the mean sizes of the C and dominant A populations have been regressed against various hydraulic parameters. The regression coefficients for the various relationships tested are listed in Table 5.6, and a number of the plots are shown in Figure 5.21.

TABLE 5.6 : Relationships between A and C population mean sizes and flow strength. Correlation coefficients for the regression of population mean sizes against the hydraulic parameters listed.
* - significant between 95% and 99%.
** - significant at greater than 99%.

| | | Time-averaged mean speed | Time-averaged shear velocity | Average maximum shear velocity | Excess shear velocity |
|---|---|---|---|---|---|
| Mean Size of A Populations: | All Data | 0.04 | -0.09 | -0.07 | ---- |
| | Cobequid Bay Flood areas | 0 17 | -0.52 | -0.47 | ---- |
| | Big Bar and Economy Point | -0.51 | -0.57* | -0.70** | ---- |
| Mean Size of C Populations: | | -0.07 | -0.23 | -0.38 | 0.27 |

FIGURE 5.21 : Relationships between population mean size and current strength.
A - Time-averaged mean speed (m/s) versus A population mean size (phi);
B - Time-averaged shear velocity (cm/s) versus A population mean size (phi);
C - Maximum shear velocity (cm/s) versus C population mean size (phi);
D - Excess shear velocity (maximum value minus Shields' critical shear velocity) (cm/s) versus C population mean size (phi).
r = correlation coefficient. Heavy solid lines are regression lines for all data; broken lines are regression lines for Big Bar and Economy Point data combined. Population mean sizes are the dependent variables

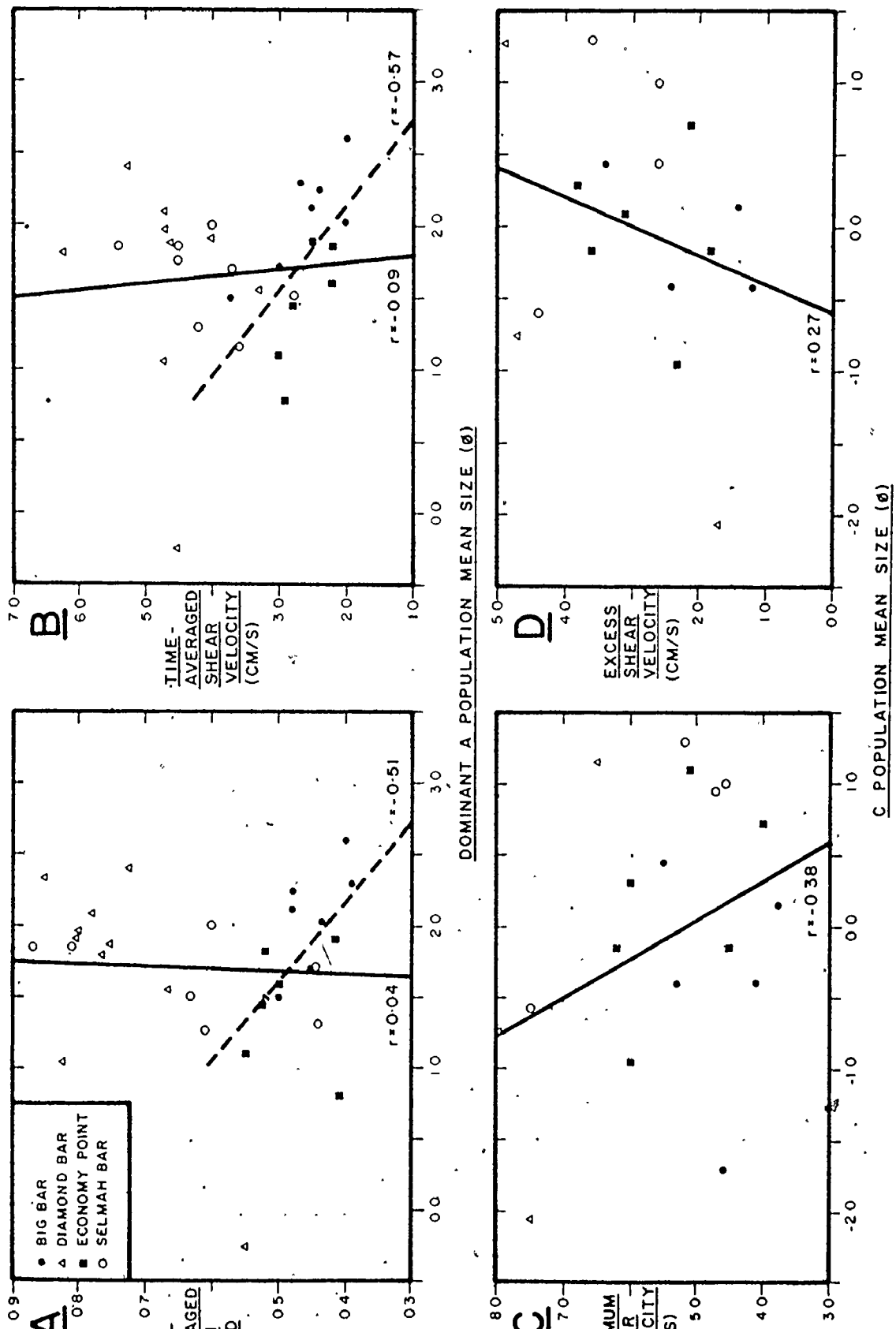
A
B
C
D
BIG BAR
DIAMOND BAR
ECONOMY POINT
SELMAH BAR
TIME-AVERAGED MEAN SPEED (M/S)
TIME-AVERAGED SHEAR VELOCITY (CM/S)
MAXIMUM SHEAR VELOCITY (CM/S)
EXCESS SHEAR VELOCITY (CM/S)
r=-0.51
r=0.04
r=-0.57
r=-0.09
r=-0.38
r=0.27
DOMINANT A POPULATION MEAN SIZE (ø)
C POPULATION MEAN SIZE (ø)

Looking first at the correlation coefficients and plots of relationships involving the mean sizes of the most abundant A populations (Table 5.6; Figures 5.21A and 5.21B), it is clear that when all of the dissected samples are considered together, there is no control exercised by either the time-averaged mean current speed, the time-averaged shear velocity, or the average maximum shear velocity (as defined in Section 4.2.3). This result is expected, because samples associated with both decreasing and increasing flow-strength gradients have been included. When the plots given in Figures 5.21A and 5.21B are viewed in more detail, however, it can be seen that the data points for Big Bar and Economy Point both fall on a single, well-defined trend (broken line), that is statistically significant for relationships involving a shear velocity. Therefore, in these areas finer mean sizes are associated with lower current strengths, which is to be expected if hydraulic sorting mechanisms are operative. By contrast, the data points for Diamond and Selmah Bars are widely scattered. When those values derived from ebb-dominated areas, where inheritance is known to be significant, are eliminated, and the regressions for these bars are recalculated (Table 5.6), the correlation coefficients increase markedly, particularly for relationships involving the shear velocity, although none are statistically significant. The majority of the data points for the flood-dominated parts of Cobequid Bay do, however, fall well above the trend defined by the Big Bar

and Economy Point data (Figures 5.21A and 5.21B). This suggests strongly that there may be some form of source control limiting the availability of coarse material in Cobequid Bay, as was suggested in Section 5.2.1. (The implication of the positive slope for the relationship employing the mean speed - finer mean sizes where the currents are fastest - is not clear at this time.)

Although all the correlations observed are not as well-defined as one might like, there is, nevertheless, an indication that hydraulic sorting mechanisms may operate as predicted earlier in this section to produce finer intermittent suspension populations in areas of weaker currents; provided that only sediment moving down a flow-strength gradient is considered. Failure to consider this last point when studying other modern or ancient deposits may obscure meaningful relationships, and lead to inappropriate conclusions. This factor is, indeed, responsible for a portion of the scatter seen in Figure 5.12, where the hydraulic control on the mean size of the sample was evaluated. There, however, other factors such as the limited availability of coarse material in Cobequid Bay, and the failure to separate the C and A populations, are primarily responsible for the large scatter and the unexpected positive correlation coefficients (Table 5.3).

Examination of the relationships evaluated using the mean size of the C population (Table 5.6; Figure 5.21C) indicates that, for three of the four hydraulic variables used, there is a weak though non-significant trend toward coarser mean sizes in areas where the currents are stronger. This is also in agreement with the hydraulic control anticipated previously. The opposite trend is found, however (Figure 5.21D), when the mean size is regressed against the excess shear velocity, which is defined here as the average maximum shear velocity minus the critical shear velocity for that size as determined from the Shields relation (Figure 5.20). The scatter that is present in the data cannot be explained at this time. Any C populations determined from ebb-dominated areas in Cobequid Bay were excluded from the analysis to avoid the problems associated with increasing flow-strength gradients. In addition, the data points for all bars appear to be equally widely dispersed, so that inter-bar or regional differences are not a major factor as they were for the A populations. It may be that the local hydraulics do not exert a very strong control on the mean size of the traction population, but more data are needed before any firm conclusion is warranted. It is interesting that the relationships involving the shear velocity consistently give correlation coefficients that have higher absolute values (Table 5.6) and are in better agreement with expectation than those using the mean current speed, despite the difficulties of measuring the shear velocity accurately.

The final item to be considered here with regard to the possible hydraulic significance of the size populations involves the hydraulic interpretation of the "break" between the traction and intermittent suspension populations that was suggested by Middleton (1976).

As has been discussed previously, Middleton (1976) believes that the grain size at which intermittent suspension takes over from traction as the predominant transport mechanism is given by the size whose fall velocity is equal to the shear velocity. This relationship has previously been termed the competence of intermittent suspension, and is plotted in Figure 5.20. Using this curve, it is, therefore, possible from a study of the size populations to estimate the shear velocity responsible for the formation of the size distribution. This estimate should be equal to the measured "effective" shear velocity at the sampling point, provided that only samples derived from transport streams moving down a flow-strength gradient are considered.

The first problem encountered in testing this idea is the selection of the size which best separates the range of sizes transported primarily by traction from those sizes moved in intermittent suspension. Three different definitions of this "break" are possible.

Method 1: If one assumes truncated normal populations, as has been done by Middleton (1976), then the required size is given by the intersection between the straight-line segments

which fit the C and predominant A populations (see, for example, Figure 5.3). If, however, the populations are assumed to be overlapping normals, the definition of the "break" becomes arbitrary, because the range of sizes transported by each mechanism also overlap, rather than being mutually exclusive as in the truncated-normal model. Two possible definitions can be given.

Method 2: Middleton (1976) has proposed that the "break" be determined by the "point of equal overlap": that is, the size at which x percent of the traction population is finer, and the same percent of the intermittent suspension population is coarser, with both populations recalculated to 100% ($\hat{q}_i$ values in Table 5.4). An easy graphical method of obtaining this size is to replot one of the populations in an inverted form using the percent-finer scale. The "break" is then given by the point at which the two lines cross. The "point of equal overlap" method of defining the "break" does not consider the relative abundances of the two populations, on the assumption that the amount of the C population is controlled by availability, rather than by the hydraulics.

Method 3: If the relative abundance of the traction and intermittent suspension populations in the sample is considered important, then the "break" can be obtained from the "point of equal contribution": that is, the size to which each population contributes equally. The determination of the "break" by this method is more difficult than

by either of the above methods, and requires the calculation of frequency percentages for each population at closely-spaced intervals, using the $\hat{p}_i$ values of Table 5.4.

The "break" between the C and A populations has been determined for all suitable samples by each of the above methods and the results are listed in Table 5.5. Examination of these sizes shows that there are differences between the methods: the "break" obtained by Method 1 (line intersection) is almost always the finest of the three, whereas that determined by Method 3 (equal contribution) is the coarsest. These differences are consistent, however, as shown by the plots in Figure 5.22, and by the regression parameters in Table 5.7A. All of the correlation coefficients are significant at greater than 99%, and the slopes of the three regression lines are all near one, which suggests that, with an appropriate scaling of the sizes, the values obtained by any of the methods can be used interchangeably. This is particularly significant with regard to the line intersection method, which is based on the assumption of truncated normal populations, as it is by far the easiest to apply because no laborious dissection of the sample is necessary.

Once the size of the "break" has been determined in each sample, the intermittent suspension competence relationship (Figure 5.20) is used to obtain the estimated shear velocity. In testing the accuracy of these estimates, both

FIGURE 5.22 : Relationship between "break" sizes defined in various manners.
A - Line-intersection versus equal-overlap break size;
B - Equal-proportion versus equal-overlap break size.
All units in phi. See text for a discussion of the break-size determination methods. Thin diagonal line is line of one-to-one correspondence. Heavy line is best-fit regression line.
r = correlation coefficient.

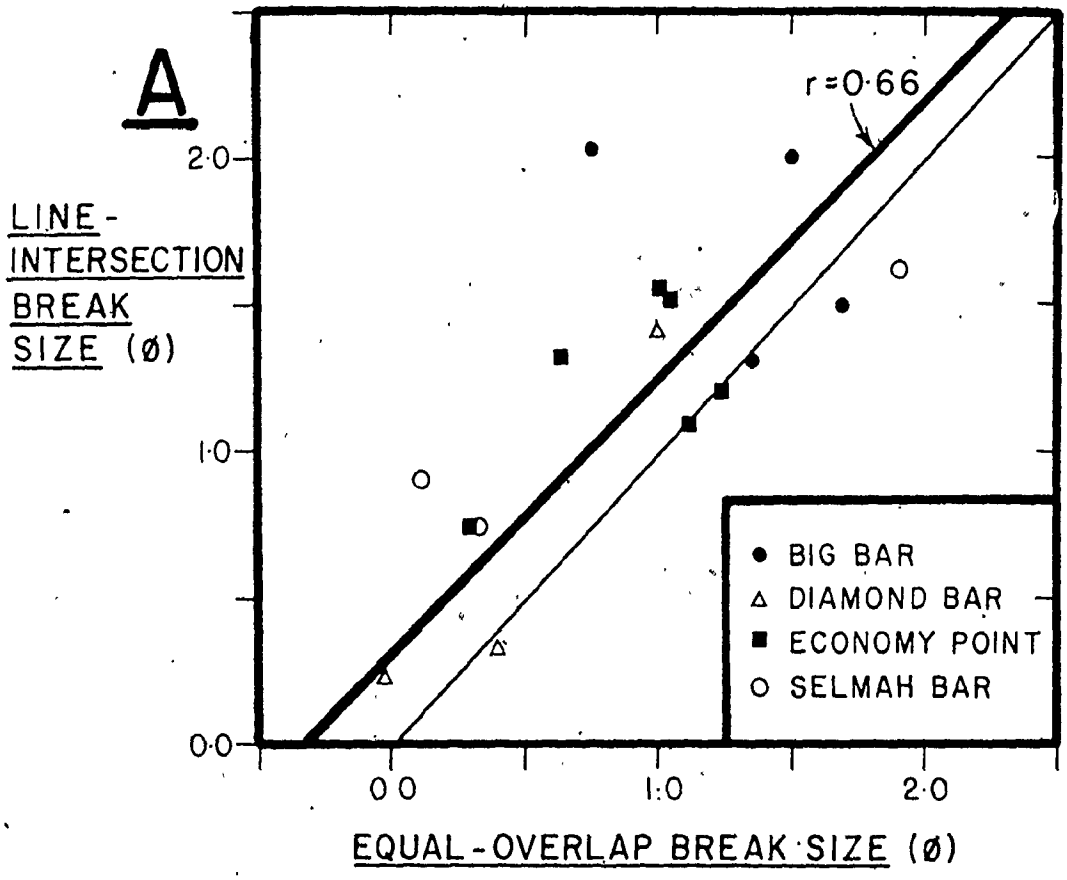
A
r=0·66
2·0
1·0
0·0
LINE-INTERSECTION BREAK SIZE (ø)
BIG BAR
DIAMOND BAR
ECONOMY POINT
SELMAH BAR
0·0
1·0
2·0
EQUAL-OVERLAP BREAK SIZE (ø)

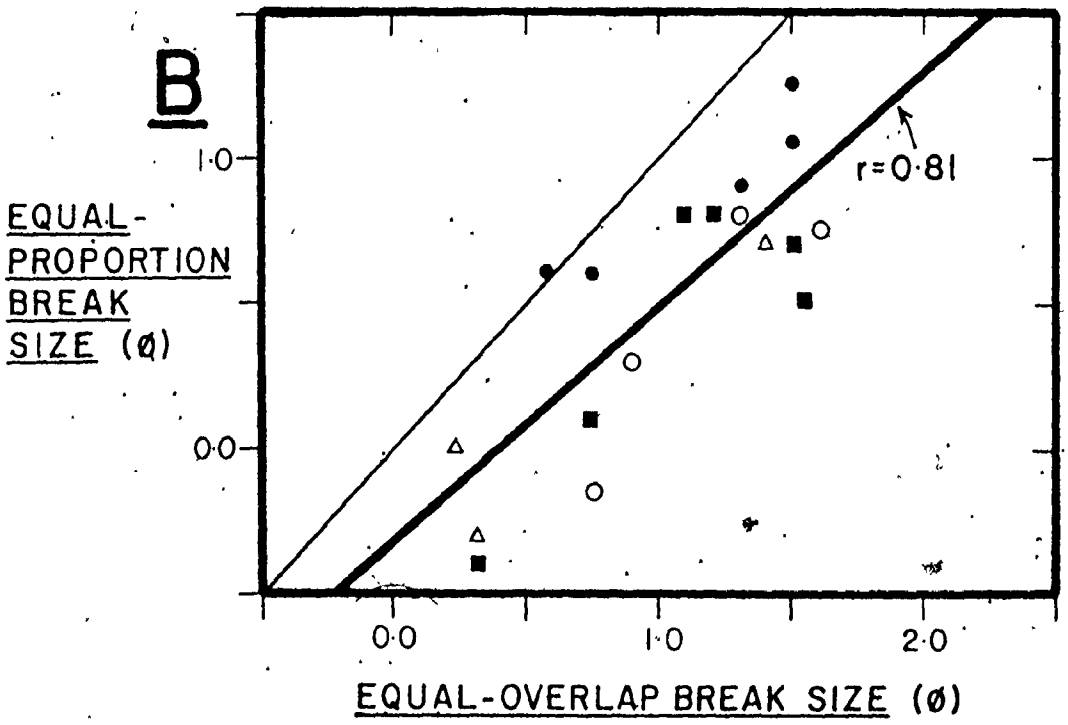
B
r=0·81
1·0
0·0
EQUAL-PROPORTION BREAK SIZE (ø)
0·0
1·0
2·0
EQUAL-OVERLAP BREAK SIZE (ø)

TABLE 5.7 - Regression parameters for relationships involving the C-A population "break" size.
A - Relationships between break sizes determined by the various methods;
B - Relationships between the measured time-averaged and average maximum shear velocities and the shear velocities estimated from the break size.
m = slope of the best-fit line.
b = y-intercept.
r = correlation coefficient.
* - significant between 95% and 99%.
** - significant at greater than 99%.

| Regressed Variables | | | | |
|---|---|---|---|---|
| x | y | m | b | r |
| A | | | | |
| equal overlap | line intersection | 0.94 | 0.30 | 0.66** |
| equal overlap | equal proportion | 0.82 | -0.35 | 0.81** |
| equal proportion | line intersection | 1.08 | 0.50 | 0.78** |
| B | | | | |
| time-averaged $u_*$ | line intersection | 2.39 | -1.41 | 0.71** |
| time-averaged $u_*$ | equal overlap | 1.53 | 0.79 | 0.64** |
| time-averaged $u_*$ | equal proportion | 2.28 | 0.61 | 0.73** |
| maximum average $u_*$ | line intersection | 1.11 | -0.24 | 0.52* |
| maximum average $u_*$ | equal overlap | 0.93 | 0.44 | 0.61** |
| maximum average $u_*$ | equal proportion | 1.34 | 0.43 | 0.67** |

the time-averaged, standardized shear velocities, and the average maximum shear velocities have been plotted against the estimates determined by each of the three methods (Figure 5.23). The regression parameters for all six plots are given in Table 5.7B. If Middleton's (1976) interpretation of the significance of the break is correct, then not only should the correlation coefficient be significant, but the regression line should also have a slope of 1.00 and an intercept of 0:00.

Looking first at the relationships involving the time-averaged shear velocities (Table 5.7B; Figures 5.23A to 5.23C), it can be seen that although the correlation coefficients for all three regression lines are significant at greater than 99%, the values of the slopes and intercepts deviate markedly from the expected values. Virtually all of the data points in Figures 5.23A to 5.23C fall above the line of perfect agreement, indicating that a shear stress in excess of the time-average is the effective value.

Inspection of the remaining regression parameters in Table 5.7B, and of Figures 5.23D to 5.23F shows that the average maximum shear velocity is a good estimate of this effective value. Although the correlation coefficients for the average maximum shear velocities are lower than the respective ones obtained using the time-averaged shear velocities, all of the relationships are significant at over 95%. The regression lines, however, lie much closer to the one-to-one correspondence line; particularly for those for the "break"

determined by methods 1 and 2, while that obtained using the "point of equal contribution" break still falls well above the expected line. From these data, without the application of scaling factors to the break sizes determined by the different methods, it is apparent that the point of equal overlap gives the best agreement between observation and theory. The poorer correlation obtained for the line-intersection data (method 1) indicates that the break determined by this method is not as consistent a representation of the point at which intermittent suspension replaces traction as the dominant transport mechanism as is the point of equal overlap. This lends further support to the argument that the populations are overlapping rather than truncated normals.

From the agreement seen in Figure 5.23, it appears that the hydraulic interpretation of size distributions proposed by Middleton (1976) is supported by these data. The scatter is more than would be liked, because individual estimates of the average maximum shear velocity are in error by up to 2.75 cm/s, and the average error is 1.3 cm/s. The results are nevertheless encouraging, particularly when one considers the inaccuracies inherent in the field determination of shear velocities that were discussed in Chapter 3. It is obvious that further field and experimental studies into this and other aspects of the hydraulic controls on the formation of size populations are warranted.

FIGURE 5.23 : Relationships between shear velocities calculated from the break size and measured values. Time-averaged shear velocity versus settling velocity of:
A - Line-intersection break size;
B - Equal-overlap break size;
C - Equal-proportion break size; and average maximum shear velocity versus settling velocity of:
D - Line-intersection break size;
E - Equal-overlap break size; and
F - Equal-proportion break size.
Light diagonal line is line of one-to-one agreement.
Heavy line is best-fit regression line for all data.
r = correlation coefficient.
All values are cm/s.

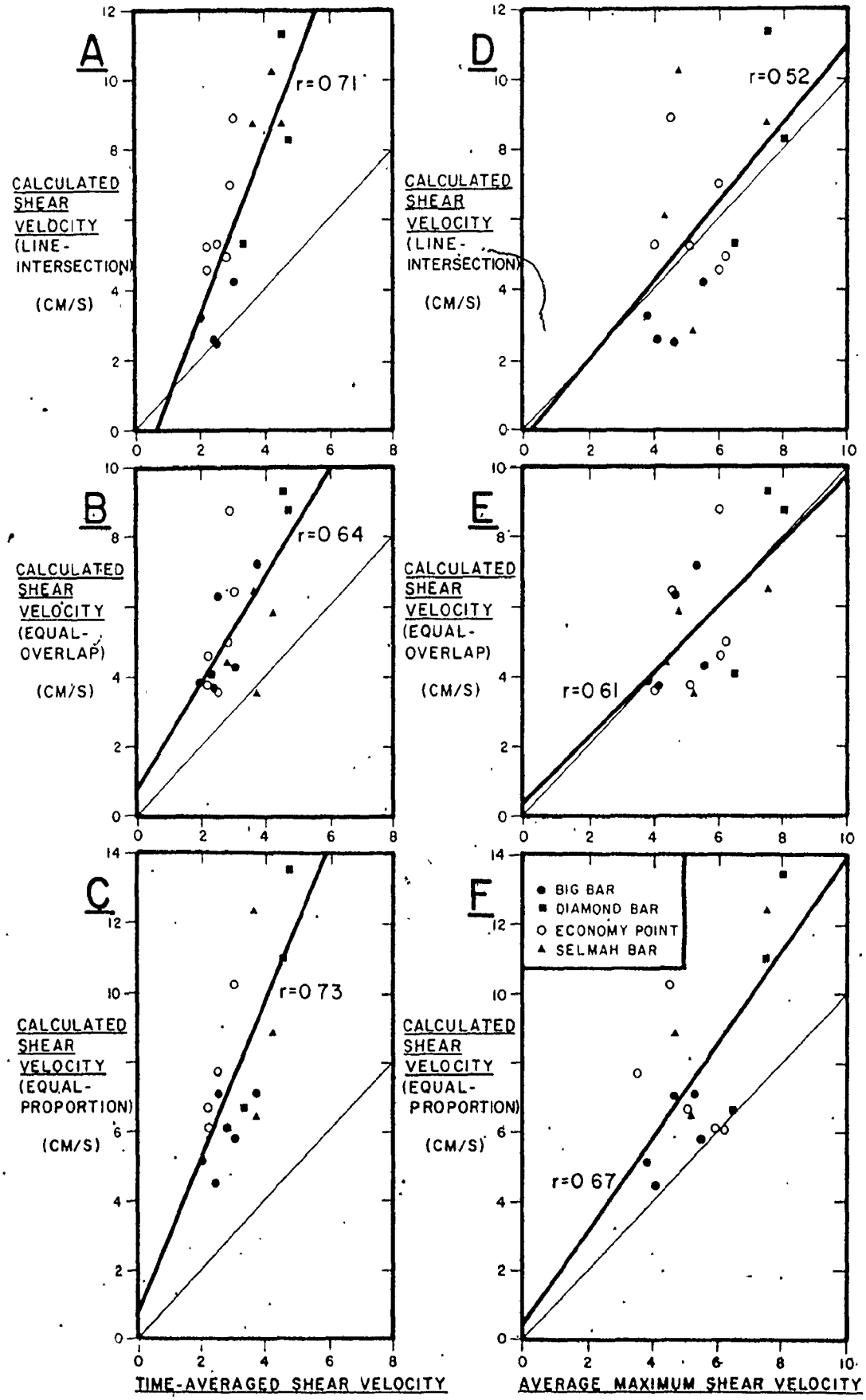
A
r=0 71
CALCULATED SHEAR VELOCITY (LINE-INTERSECTION) (CM/S)
B
r=0 64
CALCULATED SHEAR VELOCITY (EQUAL-OVERLAP) (CM/S)
C
r=0 73
CALCULATED SHEAR VELOCITY (EQUAL-PROPORTION) (CM/S)
TIME-AVERAGED SHEAR VELOCITY
D
r=0 52
CALCULATED SHEAR VELOCITY (LINE-INTERSECTION) (CM/S)
E
r=0 61
CALCULATED SHEAR VELOCITY (EQUAL-OVERLAP) (CM/S)
F
BIG BAR
DIAMOND BAR
ECONOMY POINT
SELMAH BAR
r=0 67
CALCULATED SHEAR VELOCITY (EQUAL-PROPORTION) (CM/S)
AVERAGE MAXIMUM SHEAR VELOCITY

## 5.4 Summary

Based on moment statistics calculated for a total of 296 sieved samples, the average sediment on the intertidal sand bars in this macrotidal environment is medium sand, that is moderately well sorted, very slightly negatively skewed, and leptokurtic. The sand in Cobequid Bay, however, as represented by Diamond and Selmah Bars, has finer mean sizes, better sorting, higher kurtosis values and less negatively skewed size distributions than that present either on Big Bar or at Economy Point. These differences are brought about primarily by the relative scarcity of material coarser than medium sand on the bars in Cobequid Bay, in comparison to Big Bar and the Economy Point complex. In general, these intertidal sediments have size characteristics (sorting, skewness, and percent silt and clay) which are intermediate between those of rivers and beaches as given by Friedman (1967).

Inspection of samples collected from different parts of bedforms indicates that those possessing an avalanche face (megaripples and some rippled sand waves) have the coarser material concentrated in the trough. In contrast, larger rippled and megarippled sand waves which lack a true slip face have coarse material concentrated on the crest, with finer sizes in the trough.

Areal variations of the mean size and sorting over the individual bars, based on bedform-crest samples only, are generally such that the contours tend to parallel the length of the bars. On Big Bar, Diamond Bar and Selmah Bar, the

coarsest mean sizes and poorest sorting are located on the side of the bar closest to the shore where extensive areas of gravel lag are present. A more-or-less regular decrease in the mean size and improvement in the sorting is found in the offshore direction. The trends are reversed at Economy Point, because the shoreline there is composed almost entirely of Triassic sandstone, and lag gravel is only present seaward of the bars. Channel floors are also coarser-grained than adjacent higher areas.

Current strength does not appear to exert any significant control on the areal distributions of the mean size, when all areas are considered. Only on Big Bar is a statistically significant correlation found between the mean size and the time-averaged shear velocity, with finer sizes present where the shear velocity is less.

The areal distributions of skewness and kurtosis are much more complicated than those of mean size and sorting, and plots of these parameters against the mean size reveal non-linear, sinusoidal relationships. Skewness values tend to be most negative for mean sizes between 1 and 2 phi (0.50 - 0.25 mm) and to become less negative and even positive for coarser and finer sizes. Kurtosis values are highest for mean sizes in the range of 1.5 to 2.0 phi (0.35 - 0.25 mm).

These relationships result from the composite nature of the size-frequency distributions, which are formed by the mixing together of three basic populations in various

proportions. In sandy sediments, the material in each population is believed to have been transported by a different mechanism: C population - traction transport; A population(s) - intermittent suspension; and B population - permanent suspension or wash load. Using a graphical population-dissection technique modified slightly after Cassie (1954, 1963), 32 samples have been broken down into their component size populations, which are assumed to have overlapping-normal distributions. This assumption appears justified as the fit between the original and estimated cumulative curves is better than that obtained using truncated normals. The average values of the mean and standard deviation, respectively, for each population type are: C - -0.18 phi (1.13 mm) and 1.15 phi-units; A - 1.70 phi (0.31 mm) and 0.44 phi-units; and B - 2.56 phi (0.17 mm) and 0.93 phi-units.

The areal variations in the characteristics of the C and dominant A populations show trends that are very similar to those of mean size and sorting for the total sample. On Big, Diamond and Selmah Bars, the C population is most abundant, and both the C and dominant A populations are coarsest and commonly most poorly sorted on the part of the bar closest to the shore, where areas of lag gravel are present. The mean sizes of the C and A populations become finer in an offshore direction and sorting generally improves. The C population is absent on the steep, offshore side of these bars. By contrast, at Economy Point, the populations

become coarser grained outward, and the proportion of the C population increases. Sorting, however, is generally poorer close to the shore.

When the C and A population mean sizes of all samples are plotted against various measures of flow strength, no trend is evident, as was the case with the sample mean size. This is due to the failure to separate those areas in which the flow strength increases along the transport path from those where it decreases. In the first case, as seen in the ebb-dominated areas of Diamond and Selmah Bars, weak currents in the head of Cobequid Bay have caused the deposition and removal of all coarse material, leaving only fine sediment, which then retains its fine-grained character even when transported westward into an area where the flow strength is high. In the remaining areas, the transport is generally directed down a flow-strength gradient, and as a result, both C and A population mean sizes tend to be finer where the currents are weaker. This is particularly evident for the A population data from Big Bar and Economy Point, which define a single statistically significant relationship with both the time-averaged and average maximum shear velocities.

The position of the "break" between the traction and intermittent suspension populations is also found to be hydraulically controlled, as suggested by Middleton (1976), who indicated that the settling velocity of the grain size at the break should be equal to the shear velocity of the flow.

In the study, the location of the break was determined in three different ways: the intersection of the straight-line segments; point of equal overlap of normal populations; and the point of equal contribution. All of the estimated shear velocities correlate significantly with both the time-averaged and average maximum shear velocities, but the regression lines determined using the latter measured values fall closest to the line of perfect agreement. The agreement is best using data derived from the point of equal overlap. This gives strong support to the idea that the populations have overlapping-normal distributions that are hydraulically produced.

CHAPTER 6

# SEDIMENT TRANSPORT

## 6.1 Introduction

The transport of sediment by a moving fluid is the single most basic process operating in most sedimentary environments, for most other sedimentary properties, including grain size and bedforms with their associated sedimentary structures are ultimately the result of sediment movement. Despite its obvious fundamental importance, sediment transport in its own right has received little direct attention by sedimentologists in comparison to grain size and bedforms, which are much more visible and easily studied sediment responses. It is the intention in this chapter, however, to investigate the nature of sediment transport on the sand bars in more detail. This is of particular interest in a tidal environment because of the twice-daily transport reversals, and the resulting uncertainty in determining the direction of residual sediment movement.

Previous sections of the thesis have provided a significant amount of background information on the sediment transport that occurs on the bars. In Chapter 3, study of the tidal currents revealed the pervasive existence of

time-velocity asymmetries between the ebb and flood portions of the tidal cycle, with the implication that almost all areas experience a residual or "net" transport of sediment. Examination of the areal distribution of these asymmetries shows that predictable and mutually exclusive areas of ebb- and flood-dominated transport occur, generally on opposite sides of bar crestlines. Bedform asymmetries, net migration directions and the preserved sedimentary structures (Chapter 4) support the observations based on tidal currents, and suggest that residual transport rates in areas of low to moderate current strengths are on the order of 3.0 to 130.0 kg dry weight/tidal cycle/metre width of bed. The patterns of grain-size parameter variation (Chapter 5) are also consistent with the transport paths observed or predicted, and indeed, many of the features of these patterns can only be understood when the transport history of the sediment is considered.

Although the broad pattern of sediment transport is known with reasonable certainty in many areas, numerous points remain to be investigated. In some locations, particularly on Big Bar and at Economy Point, little evidence yet exists to support the directions of residual transport predicted in Section 3.2:5.; and in all areas, a more precise knowledge of the exact direction of sediment motion would be useful. The rates of residual transport are also only poorly known in most areas. On a more detailed level, information on the sediment dispersal characteristics and transport behaviour

of various size fractions is of fundamental interest.

In order to investigate these points, numerous experiments using fluorescent tracer sands have been conducted on the four major study bars. The discussion of these experiments, the procedures used and the results obtained, forms the basis of this chapter. In addition, estimates of the sediment discharge have been obtained using the theoretical transport functions developed by Ackers and White (1973), Einstein (1950), and Engelund and Hansen (1967). The underlying theory, and/or methodology (for both approaches) will be considered first, before the results are presented, compared and discussed. It must be stressed at the outset, however, that the complexity of the sediment transport phenomenon in a tidal environment where large-scale bedforms are present makes the accurate determination of sediment discharges extremely difficult, if not impossible, with the available methods. The results must, therefore, be regarded as only crude, though interesting approximations.

## 6.2 Hydraulic Transport Functions

### 6.2.1 General

For many years, engineers have searched for an easy method of determining the sediment discharge. Of central interest in this search, has been the desire to establish the functional relationship between the flow and sediment properties, and the resulting transport rate. More than [illegible] different formulations have been proposed, but due +

the complexity of the sediment-fluid interactions, none have proven entirely reliable and accurate in all cases. Nevertheless, the better ones can provide a reasonable estimate of the sediment discharge, given only the sediment size, and hydraulic data (see Appendix 2).

Of the many sediment transport theories that are available, three have been chosen for use here; the ones proposed by Einstein (1950), Engelund and Hansen (1967) and Ackers and White (1973). As it is clearly beyond the scope of this work to assess the relative merits of the many transport formulae available, the selection of the above three as the most appropriate has been based largely on the findings of White et al. (1975) who compared observed transport rates from a large body of flume and field data with those calculated by a number of well-regarded methods. The results showed that the Ackers and White, and Engelund and Hansen methods ranked first and second, respectively, and that both gave estimates of the transport rate that fell within a factor of two of the observed rate in more than 60% of the cases. Although the Einstein transport function placed fourth in this test with less than 50% of the predicted values within a factor of two of the observed values, it has been included here because of its wide acceptance among engineers, and because it allows the calculation of the discharge for individual size fractions. In the following pages, the underlying principles and the development of each of the three transport theories will be

considered briefly for those readers not familiar with the procedures.

Despite the different approaches taken by the various authors, all three methods are based on the assumption of steady, uniform flow. It is obvious that this assumption is not valid in the situation under study here, particularly with regard to the significant time variations in flow strength, direction and depth. As a result, it must be assumed that the rate of change of current velocity and flow depth is sufficiently low that the hydraulic data obtained from a single velocity profile can be used to obtain an accurate estimate of the transport rate at that instant in time. The effect of making this assumption of quasi-steady conditions is not known, but it can be expected to increase the inaccuracy of the discharge estimates.

By evaluating the transport rate at a number of points over the tidal cycle in the above manner, the total transport for the ebb and flood portions of the tidal cycle, as well as the residual transport, can be determined by integration. The direction of the resultant transport can also be calculated using vectorial techniques. The results obtained are presented in Section 6.4, where they are considered together with the data derived from the tracer experiments.

### 6.2.2 The Einstein Transport Function

The most widely used set of sediment transport equations are those developed by Einstein (1950), largely because they are considered to be the most detailed and comprehensive in their treatment of the transport process. The total sediment load is divided into the bed and suspended load components which are treated separately, while the wash load, which for the purposes of the calculations is considered to be those sizes finer than 3 phi (0.125 mm), is not included. The transport of individual size fractions (here taken in 0.5 phi-unit intervals) is also treated one at a time, and then summed to obtain the total transport. In the outline below, for simplicity of notation, the subscripts denoting values pertaining to an individual size fraction have been omitted.

The approach adopted by Einstein (1950) for the prediction of bedload transport differs markedly from that of other authors. Rather than use the time averages of the various flow variables, Einstein bases his development on the concept of fluid turbulence. Bed load transport is, therefore, considered as a stochastic process in which any grain has a probability (P) of being moved, equal to the probability that the instantaneous fluid forces will overcome the resistance of the grain. In this way, Einstein avoids the problem of defining a critical flow stage at which

transport begins for a given grain size.

Einstein further considers that during bedload transport, an equilibrium exists between the number of particles eroded and the number deposited in a given area per unit of time. All points on the bed are assumed to be statistically equal (p.34), allowing P to be interpreted as "... the fraction of the bed on which at any time the lift on a particle of a given diameter d is sufficient to cause motion." (p.34). Using this interpretation, the average distance moved by a particle during the given time can be expressed in terms of the probability P and the average step length, which Einstein arbitrarily, and questionably, states to be equal to one hundred times the grain diameter. The determination of the relationship between the flow and P, therefore, forms the core of Einstein's development.

By assuming that all parts of the bed are statistically equal, the presence of bedforms is excluded from consideration. In order to include the influence that bedforms and other channel irregularities may have on the flow, however, Einstein separates the total resistance offered by the bed into two portions by dividing the hydraulic radius (or depth in this case) into a non-effective part (h'') due to form resistance of bed irregularities, and a part (h') that is effective in transporting sediment, due to resistance of the grains on the bed. The value of h' is not easily obtained, and must be

estimated by a trial and error method as described by Yalin (1972, p.268-269).

The height above the bed at which the representative flow velocity is measured is taken to be 0.35 X, where X is a characteristic grain size given by:

$$\begin{aligned} X &= 0.77\Delta \qquad \text{if } \Delta/\delta > 1.80 \\ \text{or } X &= 1.398\delta \qquad \text{if } \Delta/\delta < 1.80 \end{aligned} \qquad \ldots(6.1)$$

$\Delta = d_{65}/x$ is the apparent roughness of the bed; x is a correction factor in the velocity distribution formula; $\delta = 11.6\ \nu/u'_*$ is the thickness of the laminar sublayer for a smooth wall and $u'_*$ is the shear velocity based on the effective depth h'. Two additional correction factors are introduced by Einstein to account for the effect of the flow on non-uniform sediment size distributions: $\xi$ is a hiding factor, needed because small particles "hide" between larger ones; and Y describes the change of the lift coefficient over mixtures with varying roughness conditions. Einstein presents empirical graphical relationships for the evaluation of $\xi$ and Y (Einstein, 1950, Figures 7 and 8, respectively). Using the above concepts, Einstein developes a flow intensity parameter $\Psi$:

$$\Psi = \xi Y \left[ \log 10.6/\log\left(\frac{10.6xX}{d_{65}}\right) \right]^2 \frac{\gamma_s - \gamma}{\gamma} \frac{d}{h'S} \qquad \ldots(6.2)$$

where $\gamma_s$, $\gamma$, and S are consistent with previous usage.

Likewise, the intensity of bedload transport is expressed by a dimensionless quantity $\Phi$:

$$\Phi = \left(\frac{1}{p_i}\right) \frac{q_{sb}}{\gamma_s} \sqrt{\frac{\gamma}{\gamma_s - \gamma} \frac{1}{gd^3}} \qquad \ldots(6.3)$$

where $p_i$ is the fraction of the bed material with the size d; and $q_{sb}$ is the bedload transport rate of the fraction d.

The final step in the determination of the bedload transport function is the establishment of a relationship between $\Psi$ and $\Phi$. Einstein (1950, eq. 57) gives the relation as:

$$1 - \frac{1}{\sqrt{\Pi}} \int_{-B\Psi - 1/\eta_o}^{B\Psi - 1/\eta_o} e^{-t^2} dt = \frac{A\Phi}{1 - A\Phi} \qquad \ldots(6.4)$$

in which A, B, and $\eta_o$ are parameters which Einstein believes are universal constants with the values 43.5, 0.143, and 0.5, respectively. Einstein (1950, Figure 9) gives a graphical representation of equation (6.4) which is used in the calculation procedure.

It should be pointed out that several aspects of Einstein's analysis have been questioned. The reader is referred to Yalin (1972, p.134-141) for a discussion of the problems.

Einstein (1950) considers the suspended discharge

at any height y to be equal to the time-averaged suspended sediment concentration at the level y ($C_y$) multiplied by the average velocity at the same height ($U_y$). The integration of the product from the water surface to the top of the bed layer, which has the dimensionless thickness $A_E = 2d/h$, gives the total suspended load discharge:

$$q_{ss} = \int_{A_E}^{1} C_y \, U_y \, dy. \qquad \ldots(6.5)$$

The required concentrations are determined using the Rouse equation for the concentration distribution

$$\frac{C_y}{C_a} = \left(\frac{h - y}{y} \quad \frac{a}{h - a}\right)^z \qquad \ldots(6.6)$$

where the exponent $z = w / 0.4 \, u_*'$; a is a reference height taken equal to $A_E$; and w is the particle settling velocity. Einstein (1950) assumes that the concentration in the bed layer is uniform and related directly to the transport rate of bed load:

$$C_a = q_{sb} / 11.6 \, u_*' \, a \qquad \ldots(6.7)$$

Using a logarithmic velocity distribution, and substituting equations (6.6) and (6.7) into (6.5), Einstein (1950, eq. 61) evaluates the suspended load as:

$$q_{ss} = q_{sb} \left[2.3 \log \left(\frac{30.2 \, xh}{d_{65}}\right) I_1 + I_2\right] = q_{sb}[P_r I_1 + I_2] \qquad \ldots(6.8)$$

where $I_1$ and $I_2$ are integrals given by:

$$I_1 = 0.216 \frac{A_E^{z-1}}{(1-A_E)^z} \int_{A_E}^{1} \left(\frac{1-y}{y}\right)^z dy \qquad \ldots(6.9)$$

$$I_2 = 0.216 \frac{A_E^{z-1}}{(1-A_E)^z} \int_{AE}^{1} \left(\frac{1-y}{y}\right)^z \ln y \, dy$$

Einstein (1950, Figures 1 and 2) presents graphical solutions for $I_1$ and $I_2$ in terms of z and $A_E$.

The evaluation of equations (6.4) and (6.8) completes the Einstein transport calculations, except for the determination of the total unit load ($q_s$) which is simply the sum of $q_{sb}$ and $q_{ss}$, themselves summed over all size fractions (j):

$$q_s = \sum_j q_{sbi} + \sum_j q_{ssi} \qquad \ldots(6.10)$$

Various tests that have been made, comparing predicted and observed sediment discharges, show that while Einstein's method gives values that agree better than the results of many other formulae, there are consistent discrepancies. Crickmore (1967), Garg, Agrawal and Singh (1971), the Task Committee for Preparation of Sedimentation Manual (1971) (hereafter abbreviated to TCPSM for convenience), and Tywoniuk (1972) have all noted that measured sediment

discharges are usually higher than the predicted values at low water discharges. At high flow rates, however, Tywoniuk (1972) points out that Einstein's predictions are "unreasonably high" (p.536). Despite these findings, the method continues to be widely used. One reason for the discrepancies may be that Einstein used only coarse sand and gravel transport data in the evaluation of the constants in equation (6.4). Yalin (1972) points to findings that indicate that A and B are themselves functions of the sediment and flow properties. Thus, use of values determined for coarse sediment can be expected to result in deviations when applied to finer sand sizes.

### 6.2.3 The Engelund - Hansen Transport Formula

The Engelund and Hansen (1967) transport formula is the only one presented here that was specifically developed for the dune bed phase. The approach adopted is basically similar to that of Bagnold (1956, 1966), in that the available fluid energy is related to the amount of useful work done. In this case, the work done is defined as that amount necessary to lift the transported load up a distance approximating the height of the bedforms. In this development, the bed load and suspended load are not considered separately, but an expression is presented which supposedly predicts the total load.

Following Einstein (1950), the available shear stress

is considered as that portion of the total bed shear ($\tau_o$) that is due to the resistance of the grains ($\tau_o'$). The shear due to form drag is not believed to take part in the movement of sediment. Of the available shear, only that portion in excess of the critical shear ($\tau_{cr}$) necessary to initiate motion is considered as the effective shear. In order to obtain the effective flow energy ($E_f$), the effective available shear must be multiplied by the speed of movement of the transported grains. Engelund and Hansen (1967) assume that this speed is proportional to the friction velocity ($u_*$). Thus, the effective flow energy is given by:

$$E_f = \alpha_1 (\tau_o' - \tau_{cr}) u_* L \qquad \ldots(6.11)$$

where $\alpha_1$ is the proportionality factor between the grain speed and the shear velocity; and L is the length of bed being considered, equal approximately to one dune wavelength.

The rate of work done ($W_f$) on the particles is stated to be equal to the potential energy gained by the transported load as it is lifted up and over the dunes present on the bed. Thus:

$$W_f = (\gamma_s - \gamma) q_s H\alpha_2 \qquad \ldots(6.12)$$

where H is the bedform height, and $\alpha_2$ is another proportionality factor relating the actual distance that the load is raised to the bedform height.

Equating $E_f$ and $W_f$, and rearranging gives:

$$f\Phi = \alpha_3 \left( \frac{fL}{H} \right) (\theta' - \theta_{cr}) \sqrt{\theta_o} \qquad \ldots(6.13)$$

where $\alpha_3$ is a combined proportionality factor, in part expressing the efficiency; f is the Darcy-Weisbach friction factor, defined here as equal to one quarter of the value obtained from equation (3.14) above; $\Phi$ is the dimensionless sediment discharge:

$$\Phi = \frac{q_s}{\sqrt{(\gamma_s/\gamma - 1)\, g\, d_{50}^3}} \qquad \ldots(6.14)$$

and $\theta$ is the dimensionless shear stress, equivalent to Shields $\beta$:

$$\theta = \frac{\tau}{(\gamma_s - \gamma)\, d} \qquad \ldots(6.15)$$

In their analysis, Engelund and Hansen (1967, p.48) assign the critical dimensionless shear stress ($\theta_{cr}$) the value 0.06, which is the value obtained from the Shields curve for large particle Reynolds numbers. They believe that this value is appropriate for all situations with a mobile bed. Furthermore, empirical data presented by them (p.45) shows that for a dune bed, the effective shear ($\theta'$) is related to the total shear by the formula:

$$\theta' = 0.06 + 0.4\, \theta_o^2 . \qquad \ldots(6.16)$$

Additional data indicate that the term (fL / H) in equation (6.13) is a constant for dunes. Therefore, combining this term and $\alpha_3$ into a single constant $A_1$, and introducing equation (6.16), equation (6.13) becomes:

$$f\phi = A_1 \Theta_o^{5/2} \qquad \ldots(6.17)$$

Using U.S.G.S. flume data, Engelund and Hansen (1967, Figure 4.3.1) obtain a good fit for equation (6.17) with $A_1$ equal 0.1. From this relationship, the total sediment discharge ($q_s$) can be calculated.

Although Engelund and Hansen (1967) consider that the load calculated is the total load, the conceptual basis would suggest that it is the bed load transport that is being modelled. With this in mind, the agreement shown in Engelund and Hansen's (1967) Figure 4.3.1 is all the more remarkable when it is realized that the data includes results from upper flow regime conditions as well as for dunes. Engelund and Hansen do state that for fall diameters less than about 2.75 phi (0.15 mm) the large amounts of suspended load make the relationship inapplicable.

Tests of the equation by other workers show satisfactory results. TCPSM (1971) conclude that the Engelund and Hansen formula is one of three relationships out of thirteen tested which gives the best agreement with the river test data used. Cole et al. (1973) also found that the best-fit

line of measured versus calculated discharges for the Engelund and Hansen equation was closest to the line of perfect agreement, and that the deviation about the best-fit line was least for this equation. Cole et al. (1973) did note, however, that the scatter was not normally distributed, suggesting the presence of systematic error in the predictions.

### 6.2.4 The Ackers and White Transport Function

The Ackers and White (1973) transport function is the most recent development presented here. This formula is specifically designed for lower flow regime bedform conditions, and only test data with Froude numbers less than 0.8 were used in the determination of the empirical coefficients present in the general transport function. The relationship is derived using a Bagnold-type analysis, in which the effective energy is related to the particle mobility by an efficiency factor. The general function developed, is intended to give the total sediment discharge, but does not treat the bed load and the suspended load separately.

Ackers and White (1973) recognize that very coarse and very fine sediment behave in different manners. Coarse sediment is considered to be transported close to the bed. Its movement is believed to be governed only by that portion of the total shear not associated with form drag of the bedforms. Fine sediment is transported primarily in suspension, and the motive power for its transport is a function of the

total bed shear. In the consideration of grain size, it was found appropriate to introduce a dimensionless grain size ($D_{gr}$), defined as:

$$D_{gr} = d_{50} \left[ \frac{g(s - 1)}{\nu^2} \right]^{1/3} \qquad ...(6.18)$$

where $s = \gamma_s/\gamma$. $D_{gr}$ can be rationalized as the cube root of the ratio of immersed weight to the viscous forces. Analysis of flume data shows that coarse sediment is that material with $D_{gr} > 60$, and fine sediment has $D_{gr} < 1$. For quartz sand in water at 15°C, these limits are -1.3 phi (2.5 mm) and 4.6 phi (0.04 mm), respectively. Those sizes between these limits exhibit a behaviour intermediate between coarse and fine material, and their movement is governed by some value of shear between that due to grain resistance and the total shear.

For coarse sediment, the applied shear is given as:

$$\sqrt{\frac{\tau_{cg}}{\rho}} = u_{*cg} = \frac{\bar{U}}{\sqrt{32} \log \left(\frac{\alpha h}{d_{50}}\right)} \qquad ...(6.19)$$

where $\alpha$ is a dimensionless numerical constant incorporating the usual constant from the logarithmic velocity distribution, and a constant of proportionality relating $d_{50}$ to $k_s$. $\alpha$ was found to have a value of about 10.0. For fine sediment, the effective shear is defined in the usual fashion:

$$\sqrt{\frac{\tau_o}{\rho}} = u_* = \sqrt{ghS} \qquad ...(6.20)$$

Ackers and White (1973) proceed to define a particle mobility number ($F_{gr}$) which is the ratio of the appropriate applied shear, as defined by either equation (6.19) or (6.20), to the particle resistance. For coarse sediments, the particle resistance is taken as the immersed weight of a layer of grains on the bed; and for fine sediments, it is taken as the settling velocity, defined by Stokes' Law. The two separate relations obtained are quite similar in form. Ackers and White (1973) combine them into a single general form of the particle mobility number, which is applicable to all sizes, by introducing a transition exponent n:

$$F_{gr} = \frac{u_*^n}{\sqrt{gd_{50}(s-1)}} \left[\frac{\bar{U}}{\sqrt{32}\log\left(\frac{10h}{d_{50}}\right)}\right]^{1-n} \qquad \ldots(6.21)$$

in which, n assumes the value 0.0 for coarse sediment, 1.0 for fine sediment, and intermediate values over the transition range.

At this point, Ackers and White (1973) introduce the transport efficiency (E), relating the useful work done to the appropriate effective energy. In the case of coarse sediment, the available power is defined as $\tau_{cg}\bar{U}$, while for fine sediment it is the total stream power ($\tau_o\bar{U}$). Using the derived efficiency factors, a dimensionless transport rate ($G_{gr}$) is defined, as a function of the efficiency, the mobility number, and the dimensionless grain diameter. For

coarse sediments, $G_{cg} = E_{cg} F_{cg}^2$, and for fine sediments, $G_{fg} = E_{fg} F_{fg}^3 D_{fg}^3$. The combined general formula for the transport rate is given as:

$$G_{gr} = \frac{Xh}{sd_{50}} \left( \frac{u_*}{\bar{U}} \right)^n \qquad \ldots(6.22)$$

where n is the transition exponent; and X is the mass flux per unit of flow.

In order to evaluate the value of $G_{gr}$, and arrive at the general transport function, Ackers and White (1973) assume that the appropriate relationship is:

$$G_{gr} = f_1 (F_{gr}; D_{gr}) \qquad \ldots(6.23)$$

where $f_1$ is a function that is to be determined empirically. Both $G_{gr}$ and $F_{gr}$ are dependent on n; which is itself considered to be a function of $D_{gr}$. The efficiency can be eliminated from the analysis by combining it into the mobility number, since the efficiency is believed by Ackers and White (1973) to be a function of the mobility.

Ackers and White (1973) propose that the desired form of the function $f_1$ should be:

$$G_{gr} = C \left( \frac{F_{gr}}{A} - 1 \right)^m \qquad \ldots(6.24)$$

where the parameters C, A, and m are all functions of $D_{gr}$.

In order to evaluate the above parameters, and the transition exponent, data from more than 1,000 flume experiments were analysed, using a regression optimization technique. The best fit relations are given below:

| Parameter | Coarse Sediment ($D_{gr} > 60$) | Transition Range ($1 \leq D_{gr} \leq 60$) |
|---|---|---|
| n | $n = 0.0$ | $n = 1.00 - 0.56 \log D_{gr}$ |
| A | $A = 0.17$ | $A = (0.23/\sqrt{D_{gr}}) + 0.14$ |
| m | $m = 1.5$ | $m = (9.66/D_{gr}) + 1.34$ |
| C | $C = 0.025$ | $\log C = 2.86 \log D_{gr} - (\log D_{gr})^2 - 3.53$ |

The analysis was not extended into the fine sediment region ($D_{gr} < 1.0$) because the effects of cohesion were believed to render the general transport function inapplicable in practice, for these grain sizes.

It must be stressed that the above general transport function (equation 6.24) was developed using flume data exclusively, with flow depths generally less than 0.4 meters. Ackers and White (1973) have, however, tested the relationship in three natural situations, ranging from a small stream, to a tidal estuary. The agreement between observed and predicted values was better for the smaller systems.

## 6.3 Sediment Tracer Techniques

### 6.3.1 General Considerations

Sediment tracers have been used sparingly in sedimentological research because of practical difficulties associated with their application in natural situations, and also possibly because of a lack of quantitative analytical methods. Tracers which model the sediment in motion, or any specific fraction of it, do, however, provide a valuable tool for the investigation of sediment transport mechanisms, rates, and patterns. For this reason, tracers have been used extensively in the present study in order to gain more insight into sediment dynamics on the studied sand bars. Throughout the investigation, every attempt has been made to be as quantitative as possible, both by using pre-existing techniques and by developing new methods for analysing the data. A number of inherent problems preclude a totally rigorous analysis, however, and a subjective element remains.

The fundamental assumption in any tracer study is that the tracer material and natural sediment under consideration behave identically. This implies not only that the tracer must have characteristics (size, shape, density) similar to those of the sediment being modelled, but also that the tracer must experience the same range of conditions as those encountered by the natural sediment. These requirements place strong constraints on the operational procedures adopted:

the type of tracer used, its preparation, placement, and sampling. Unfortunately, practical considerations (time and money) usually impose limitations which do not permit the achievement of the ideal set of procedures.

In this study, the basic objective is to obtain information on the transport behaviour of naturally-occurring (quartz) sediment under the influence of reversing tidal currents, including such specific points as: the direction of net (or residual) transport, the average rate of net particle movement, the net sediment discharge, and the amount of dispersion. Furthermore, these points are to be investigated as a function of grain size (Type 1 experiments), as well as for the bulk sediment (Type 2 experiments).

The first problem to be encountered involves the selection of a suitable tracer material. Three possible options are available: (i) artificial materials; (ii) natural sediment bearing an induced radioactivity; and (iii) natural sediment coated with a visably detectable substance. For the experiments conducted here, the third alternative, in which fluorescent paint was applied to sediment obtained from the study area, was selected for a variety of reasons: (a) low initial cost relative to options (i) or (ii); (b) simplicity of handling procedures and required equipment, combined with an absence of health and environmental hazards, relative to radioactive tracers; (c) absence of unnatural

size, shape, or density characteristics; and (d) versatility with regard to the distinctive labelling of several size fractions for use in a single experiment. The use of fluorescent tracers does necessitate the collection and analysis of large numbers of samples, which places unfavourable practical limits on the sampling efficiency, relative to radioactive tracers, but the considerations listed above outweighed this disadvantage.

The choice of a proper experimental design is also important if the maximum return is to be realized. In unidirectional flows, three different techniques are currently in use (Crickmore, 1967).

(i) Time Integration: In this technique, a known quantity of tracer is instantaneously inserted into the flow, and at some fixed distance downflow, where tracer mixing is complete, the variation of tracer concentration through time is measured. Using continuity considerations that require steady flow conditions, the transport rate and longitudinal dispersion can be determined. Examples of the use of this method can be found in Einstein (1937), Crickmore and Lean (1962b), and Rathbun, Kennedy, and Culbertson (1971).

(ii) Steady Dilution: This technique like the time integration method is Eulerian and requires the measurement of tracer concentration through time at a fixed station. A continuous injection of tracer is used and concentration

measurements are continued until a constant, equilibrium concentration is obtained. Again, steady flow is a requirement and measurements must be made at a sufficient distance from the injection point for complete mixing to take place. Kennedy and Kouba (1970), and Lean and Crickmore (1966) provide examples. Obviously, the transport direction must be known *a priori* in order for the sampling site to be selected when either technique (i) or (ii) is used.

(iii) Spatial Integration: In contrast to the above methods, space coordinates here become the independent variables rather than time. A single injection of tracer is made and the areal variations in concentration are determined at various instants in time. The shape and position of the tracer "cloud" allow the determination of the transport rate, direction and dispersion parameters. Unlike the first two techniques, spatial integration does not require steady, unidirectional flow conditions. Time variations in the transport rate are averaged out and two-dimensional transport can be accommodated by a suitable selection of the sampling area. The most stringent practical limitation usually involves the ability to determine the areal distribution within a period of time that could be considered "instantaneous" relative to the rate of dispersion. This is easily overcome in the intertidal zone where the sampling can be conducted during exposure at low tide, when the tracer cloud is immobile.

Thus, the spatial integration technique is well suited to the conditions of the study area, whereas the others are inappropriate. A few examples of previous applications of the spatial integration method to fluvial, beach and littoral environments can be found in: Rathbun and Nordin (1971), deVries (1966), Ingle (1966), Boon (1968, 1969), Komar and Inman (1970) and Oertel (1972).

In the spatial integration technique, a simple visual examination of the pattern of concentration variation reveals a great deal regarding the transport and dispersal behaviour of the tracer. More quantitative information can be obtained, though, by calculating the centre of gravity (centroid) of the tracer distribution, using the method of moments. From the centroid and higher moments, such quantities as the net transport direction, the average rate of net particle movement, the residual sediment discharge and various dispersion parameters can be determined. The theoretical and practical considerations involved are, however, very complex, particularly with regard to their application in the conditions present on the sand bars under study. Before investigating this situation, let us first review the principles under consideration for the simple case of an equilibrium beach.

On an equilibrium beach, where there is no net deposition or erosion, the theoretical interpretation of the dispersed tracer cloud is straight forward, because the surface

of the beach can be considered to be statistically homogeneous. In practical terms, this results from the presence of a laterally continuous mobile layer with an essentially uniform thickness. This fact also reduces sampling problems to a minimum. In addition, the entire thickness of the mobile layer is completely reworked within a relatively short period of time, so that the tracer distribution in all parts of the layer can be considered to have formed at the same time. The areal variation of tracer material can, therefore, be regarded as a continuous, two-dimensional, statistical distribution, in which the absolute amount of tracer present at any point (x,y), relative to the total amount injected, gives the probability that a particle will travel from the origin (0,0) to the point (x,y) within the time period $\Delta T$. If the amount of tracer is expressed in terms of concentrations, the procedure adopted here, then the areal distribution is instead a measure of the probability of material originally at the origin arriving at the point (x,y) after time T, relative to the probability of material from all other locations arriving at (x,y) at the same instant. The statistical parameters (centroid and dispersion) of the two distributions will of course be identical as long as all concentrations are expressed in a consistent manner.

In most parts of the study area, however, the presence of large-scale bedforms (megaripples and sand waves) complicates

the picture considerably. In this situation, the mobile layer may not be reworked during the time span of a tracer experiment. Furthermore, portions of the surface are sites of net deposition or erosion, thereby reinforcing the non-uniform character of the mobile layer. These features present many practical sampling and interpretive problems.

From Figure 6.1A it is clear that the thickness of the mobile layer varies greatly, from essentially zero in the bedform troughs, to a maximum under the crests, where the thickness is equal to the bedform height. As a result, in the calculation of the centre of gravity of a tracer distribution, each point on the bed should be given a different weighting, dependent on the thickness of the mobile layer at that point. This is impossible in practice, and it is necessary, therefore, to envisage a continuous mobile layer with a uniform thickness, which contains the same volume of sediment per unit area as is present in the existing bedforms. The "effective" thickness of such a mobile layer is usually taken as being one half of the bedform height (Crickmore, 1967; Rathbun and Nordin, 1971; deVries, 1966). The results of Nordin (1971), which show that bed elevations are symmetrically distributed about the mean elevation, support the use of this value. Implicit in this discussion is the assumption that the entire mobile layer is reworked during the period of the experiment. As was seen in Section 4.2.4,

Figure 6.1 Tracer behaviour in the presence of bedforms.

Throughout, stippling density indicates relative tracer concentrations. A - Definition sketch and tracer-injection configuration; B and C - Tracer distribution within bedforms at two subsequent times, in unidirectional flow; D and E - Distribution of tracer in the tidal situation after one and one and a half tidal cycles, respectively. See text for further discussion.

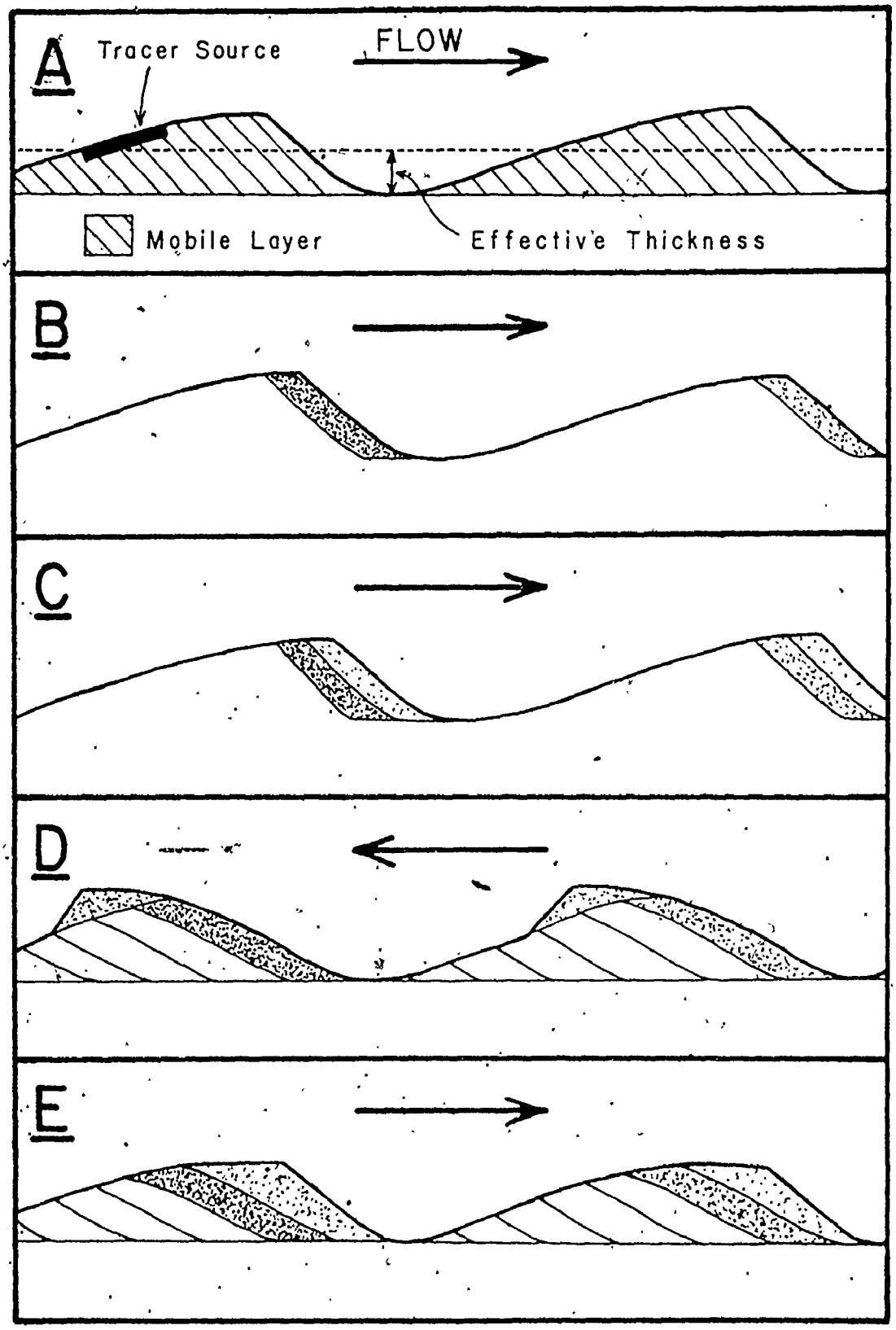
A
Tracer Source
FLOW
Mobile Layer
Effective Thickness
B
C
D
E

however, this may not be the case, particularly with samplings conducted after short elapsed times. Intimately associated with this is the concept of tracer burial within the bedform. Both of these factors create difficult sampling problems.

Suppose, for instance, that an amount of tracer is placed on the eroding stoss side of a dune in a unidirectional flow (Figure 6.1A). This tracer will be carried forward to the brink of the bedform where a portion of it will be deposited on the lee face, over tracer-free sediment. The remainder will continue on, possibly landing for a brief period on the stoss sides of downstream dunes, but all will eventually come to rest on the depositional lee sides of the bedforms (Figure 6.1B). This will continue until the source of tracer has been completely eroded, at which time the newly-deposited tracer-bearing sand will be buried by sediment that is essentially tracer-free (Figure 6.1C). As the bedform migrates forward, tracer-bearing sand will gradually be released again as the previously deposited foreset beds are eroded on the stoss side. Continued burial and erosion will ultimately result in a more uniform distribution of tracer within any single bedform, and concentrations will decrease continuously as dispersion and mixing progress.

The same essential processes are operative in the tidal environment, but are complicated by the reversals in sediment transport direction and bedform morphology

(Figure 4.9). Consider the case of a flood-dominated area such as is shown in Figure 4.9E where bedform reworking during a single tidal cycle is not complete; and suppose also that at the end of the flood tide the tracer distribution is similar to that depicted in Figure 6.1B. During the ebb, erosion of the flood brink will redeposit tracer-rich sand in the ebb cap (Figure 6.1D), as well as further down-flow, thereby bringing about greater longitudinal dispersion and mixing than might be present in the unidirectional flow situation. With the return of flood currents, the ebb cap is eroded and new flood-oriented strata are deposited, burying the remaining portion of the tracer-rich sediment with sand containing less tracer (Figure 6.1E).

In either of the situations discussed above, it is obvious that any set of samples collected solely from the surface, or more specifically, just from the lee faces, will not provide an accurate representation of the tracer distribution, because most of the tracer may be buried in the bedforms. This point is particularly significant for areas where large megarippled sand waves are present, but of minor importance where megaripples are completely reworked each tidal cycle, because mixing will be much more thorough. In many areas, however, where appreciable amounts of tracer are stored for a period that is long relative to the duration of the experiment, only a detailed, three-dimensional sampling plan will be totally adequate. If the three-dimensional variation

in the absolute or relative amount of tracer present can be represented adequately, then that distribution may be interpreted in terms of probabilities, as was proposed in the case of an equilibrium beach. As will be seen in the following sections, such a representation is not practically possible, and consequently, the distributions that are determined cannot be considered in rigorous probabilistic terms. As the recovery efficiency (amount of tracer recovered divided by the amount injected) of the sampled distribution approaches one hundred percent, however, an interpretation in terms of the above probabilities does attain greater validity.

### 6.3.2 Tracer Preparation, Placement and Sampling

As has been mentioned previously, two types of tracer experiments have been conducted: Type 1 experiments investigated the transport behaviour of different size fractions, while Type 2 experiments utilized unsieved, bulk sediment. A total of 29 individual experiments were carried out: 5 on Selmah Bar (1972); 1 on East Noel Bar (1972); 3 on Noel Bay Bar (1972); 6 on Big Bar (1973); 6 on Diamond Bar (1974) and 8 at Economy Point (1974). Of the total, nine are Type 1, three each on Big Bar, Diamond Bar and at Economy Point. The locations of the experimental sites on the four major study bars are shown in Figure 6.2.

The material used in the Type 1 experiments was

Figure 6.2 Location of tracer experiments. A - Big Bar; B - Diamond Bar; C - Economy Point; D - Selmah Bar. Stars are sites of Type 1 experiments; dots of Type 2 experiments.

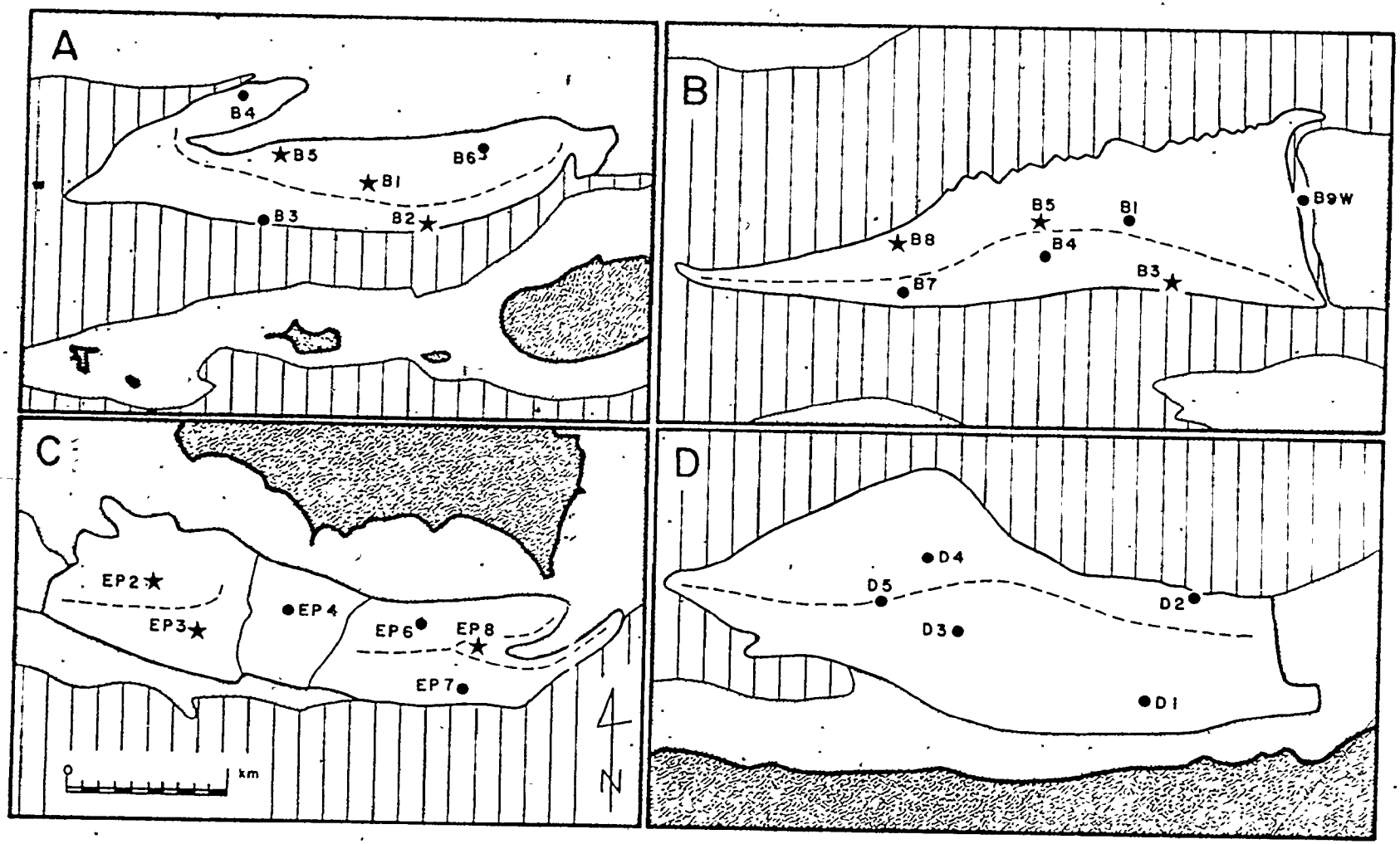
A
B4
B5
B6
B1
B3
B2
B
B9W
B5
B1
B8
B4
B7
B3
C
EP2
EP4
EP3
EP6
EP8
EP7
km
N
D
D4
D5
D2
D3
D1
Land
Water
Studied Bar
(with crestline)
Other Intertidal Areas

obtained from various high tide beach, intertidal foreshore and sand bar locations. This material was first dried, and then sieved for ten minutes in a Soiltest Portable Aggregate Shaker (model CL-400) (Figure 6.4A) using the 14 x 14 inch sieves of their fine series. In order to facilitate the preparation of the fractions, the original unsieved sediments chosen had a modal size as close as possible to the size of the fraction being prepared. The fractions used are given in Figure 6.3, and have been designated by the numerals I through V, from coarsest to finest. The fractions retained were determined by the available mesh sizes and by the pre-requisite that the fractions be discontinuous to allow easy separation during the counting process. The nominal limits and the Wentworth designation of the fractions used are: I: -2.25 to -1.25 phi (pebbles and granules); II: -1.0 to -0.25 phi (very coarse sand); III: 0.25 to 0.75 phi (coarse sand); IV: 1.25 to 2.0 phi (medium sand); and V: 2.0 to 2.75 phi (fine sand).

The sand for the Type 2 experiments was usually obtained from the location where the experiment was to be conducted so that the size distribution of the tracer was as close as possible to that of the sand at the dispersal site. In a few instances, this procedure could not be followed due to time and accessibility restrictions. In these cases, sand from locations with similar size characteristics was

Figure 6.3 Size distributions of tracer fractions used at Buoy 5 on Diamond Bar.

Thick horizontal bars give the nominal size range of each fraction. Thick vertical lines indicate the sieves used in analysing the samples (see also Figure 6.6A).

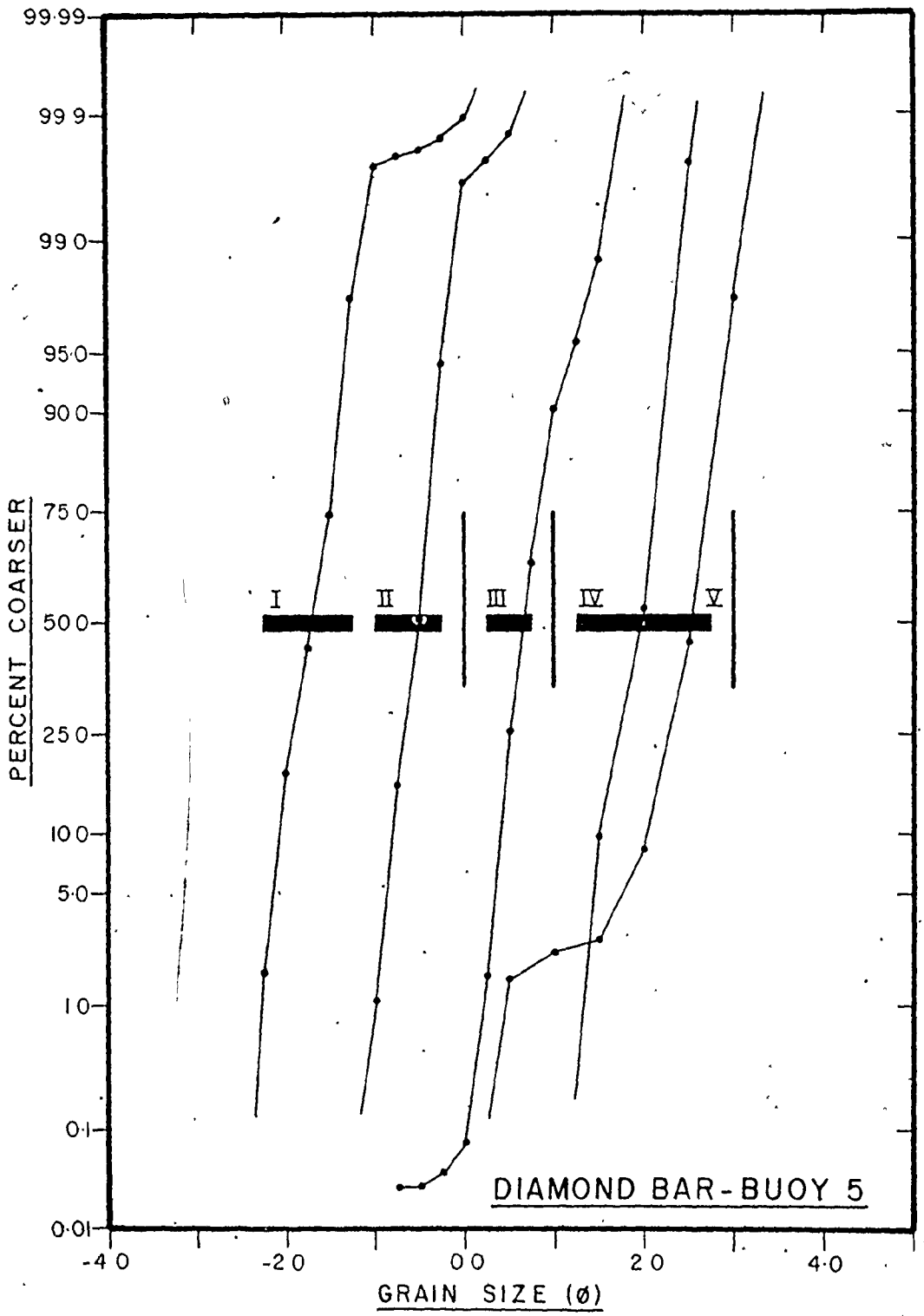
99·99
99 9
99 0
95·0
90 0
75 0
50 0
25 0
10 0
5·0
1 0
0·1
0·01
PERCENT COARSER
I
II
III
IV
V
DIAMOND BAR-BUOY 5
-4 0
-2 0
0 0
2 0
4·0
GRAIN SIZE (ø)

Figure 6.4 Tracer experiment equipment.

A - Soiltest Portable Aggregate Shaker (model CL-400) with sieves;
B - Portable cement mixer for mixing and drying painted sand. Heat lamp speeds drying.
C - Newly injected tracer at Buoy 6, Big Bar. Stake denotes tracer origin.
D - Syntron Volumetric Feeder (model FM-TO-3/4) trough shown at upper left with related sample processing equipment.
E - Syntron Parts Feeder (model EB-00-C; with bowl no. 7A4) shown left of centre. Remaining accessories include feeder control unit (far left), microsplitter, sieves (0.0, 1.0, and 3.0 phi), particle counter, ultraviolet light, and ultraviolet safety glasses.


A
B
C
D
E

used. No preparation other than drying was required prior to painting.

The fluorescent coating was applied to the tracer material with the aid of a portable cement mixer, and the coating mixture used approximated to formulation 6 of Yasso (1966, p.290). The components were: Day-Glo Acrylic Lacquer 202-Line (A.R. Monteith Ltd.), Beetle Resin 227-8 (butylated urea-formaldehyde resin; American Cyanamid Co.), and Toluene (Certified Reagent Grade; Fisher Scientific Co.). The proportions of each component used varied as experience was gained. During the first summer (1972) the amounts were: 3 parts lacquer, 4 parts resin, and 18 to 24 parts toluene (Dalrymple, 1973b). Due to problems of slow drying and aggregation, the proportion of Beetle Resin was cut approximately in half for the experiments in 1973 and 1974. The average mixture used for these experiments was: 5 parts lacquer, 3 parts resin and 26 parts toluene. The resultant coating was easily visible under long wavelength ultra-violet light, was very thin (a surface wash only), and seemed resistant to abrasion. The total amount of coating mixture required varied with the grain size of the tracer sediment. As a rough guide, for 10 kg of sediment with a mean size of -2.0 phi (4.0 mm), 0.5 l of coating is needed; for 0.0 phi (1.0 mm), 0.95 l; and for 2.0 phi (0.25 mm), 1.4 l.

The method used to dry the freshly painted tracer was found to greatly affect the degree of aggregation.

In 1972, the wet tracer was placed on plastic sheets to dry. It was stirred manually to promote drying, but aggregation occurred, necessitating crushing of lumps with a rolling pin and sieving in order to return more closely to the original size distribution. In 1973 and 1974, the coated sediment was retained in the cement mixer and allowed to dry while the cement mixer continued to rotate. A heat lamp was shone into the drum to speed drying (Figure 6.4B). Drying times ranged from 3.5 to 6 hours for 80 kg of material, and aggregation was negligible. Up to 90 kg of tracer could be prepared at one time with this method.

The size characteristics of all tracer materials used are listed in Tables 6.1A and B, and the size distributions for the five fractions used in the Type 1 experiment conducted at Buoy 5, Diamond Bar are shown in Figure 6.3. All results are for samples after painting.

Examination of the data for the Type 1 experiments (Table 6.1A; Figure 6.3) shows that the sieving conducted during the preparation procedure was reasonably effective in removing material outside the desired range of sizes. The positive skewness values obtained for most of the samples of fractions I, II, and III indicates, however, that a slight excess of fine material is still present. The negative skewness values for fractions IV and V, on the other hand, are due to the presence of a small number of aggregates (less than 5%) that formed during the painting. No aggregation is

Table 6.1 Size Characteristics of Tracer Materials

A. Type 1 experiments

B. Type 2 experiments

Equivalent size derived from average grain weight assuming spherical particles. Size analyses for material finer than 1.0 phi (0.5 mm) obtained with a visual accumulation tube.

Table 6.1A Type 1 tracer materials

| Bar and Buoy Location, Tracer Fraction | | Average Grain Weight (gm) | Equivalent Size (phi) | Mean Size (phi) | Sorting (phi-units) | Skewness |
|---|---|---|---|---|---|---|
| BIG BAR | | | | | | |
| Buoy 1: | I | 0.04276108 | -1.63 | | | |
| | II | 0.00466293 | -0.59 | | | |
| | III | 0.00046033 | 0.56 | no samples retained | | |
| | IV | 0.00005668 | 1.56 | | | |
| | V | 0.00000696 | 2.56 | | | |
| Buoy 2: | I | 0.04276108 | -1.63 | | | |
| | II | 0.00466293 | -0.59 | | | |
| | III | 0.00046033 | 0.56 | no samples retained | | |
| | IV | 0.00005668 | 1.56 | | | |
| | V | 0.00000696 | 2.56 | | | |
| Buoy 5: | I | 0.0408143 | -1.62 | -1.62 | 0.30 | 0.58 |
| | II | 0.0043967 | -0.54 | -0.53 | 0.24 | 0.30 |
| | III | 0.0004670 | 0.54 | 0.59 | 0.23 | 0.04 |
| | IV | 0.0000578 | 1.54 | 1.68 | 0.39 | 0.75 |
| | V | 0.00000813 | 2.49 | 2.69 | 0.43 | -0.85 |
| DIAMOND BAR | | | | | | |
| Buoy 3: | I | 0.0429331 | -1.63 | -1.63 | 0.33 | 1.40 |
| | II | 0.005217 | -0.64 | -0.60 | 0.27 | 1.05 |
| | III | 0.0004393 | 0.58 | 0.70 | 0.29 | 1.14 |
| | IV | 0.0000416 | 1.70 | 1.96 | 0.36 | -0.15 |
| | V | 0.0000110 | 2.33 | 2.59 | 0.40 | -0.50 |
| Buoy 5: | I | 0.04550 | -1.67 | -1.67 | 0.36 | 1.72 |
| | II | 0.0041883 | -0.53 | -0.53 | 0.23 | 0.05 |
| | III | 0.0004087 | 0.62 | 0.69 | 0.29 | 0.92 |
| | IV | 0.0000359 | 1.78 | 1.93 | 0.36 | -0.38 |
| | V | 0.0000113 | 2.33 | 2.46 | 0.47 | -1.90 |
| Buoy 8: | I | 0.0535 | -1.74 | -1.71 | 0.35 | 1.81 |
| | II | 0.00554 | -0.68 | -0.65 | 0.25 | 0.28 |
| | III | 0.0003984 | 0.62 | 0.62 | 0.64 | 0.52 |
| | IV | 0.0000295 | 1.73 | 1.91 | 0.35 | -0.25 |
| | V | 0.0000113 | 2.33 | 2.56 | 0.39 | -1.01 |

Table 6.1A / continued

| Bar and Buoy Location, Tracer Fraction | | Average Grain Weight (gm) | Equivalent Size (phi) | Mean Size (phi) | Sorting (phi-units) | Skewness |
|---|---|---|---|---|---|---|
| ECONOMY POINT | | | | | | |
| Buoy EP2: | I | 0.0474805 | -1.69 | -1.70 | 0.33 | 1.39 |
| | II | 0.0041938 | -0.52 | -0.52 | 0.29 | 1.13 |
| | III | 0.0003909 | 0.64 | 0.67 | 0.25 | 0.66 |
| | IV | 0.0000665 | 1.52 | 1.64 | 0.30 | -0.11 |
| | V | 0.00000663 | 2.58 | 2.85 | 0.38 | -0.40 |
| Buoy EP3: | I | 0.04343 | -1.65 | -1.61 | 0.31 | 1.23 |
| | II | 0.00531 | -0.65 | -0.65 | 0.25 | 0.43 |
| | III | 0.0005064 | 0.51 | 0.50 | 0.33 | -0.51 |
| | IV | 0.0000684 | 1.48 | 1.61 | 0.29 | -0.81 |
| | V | 0.0000067 | 2.57 | 2.81 | 0.41 | 0.66 |
| Buoy EP8: | I | 0.0393195 | -1.61 | -1.62 | 0.28 | 0.63 |
| | II | 0.0047512 | -0.60 | -0.60 | 0.26 | 0.36 |
| | III | 0.0004770 | 0.53 | 0.57 | 0.32 | -0.15 |
| | IV | 0.0000340 | 1.81 | 1.95 | 0.41 | -0.43 |
| | V | 0.00000638 | 2.61 | 2.79 | 0.38 | -0.41 |

Table 6.1B Type 2 tracer materials

| Bar and Buoy Location, Tracer Fraction | Average Grain Weight (gm) | Equivalent Size (phi) | Mean Size (phi) | Sorting (phi-units) | Skewness |
|---|---|---|---|---|---|
| SELMAH BAR | | | | | |
| Buoy 1 | 0.0001498 | 1.11 | 0.97 | 0.95 | -1.26 |
| Buoy 2 | 0.0000441 | 1.68 | 1.16 | 0.94 | -0.88 |
| Buoy 3 | 0.0001146 | 1.22 | 1.05 | 1.09 | -1.21 |
| Buoy 4 | 0.0000572 | 1.60 | 1.53 | 0.80 | -1.23 |
| Buoy 5 | 0.0000660 | 1.48 | 0.81 | 1.34 | -0.67 |
| EAST NOEL BAR | | | | | |
| Buoy 6 | 0.0005341 | 0.49 | -0.01 | 0.97 | -0.54 |
| NOEL BAY BAR | | | | | |
| Buoy 7 | 0.0001011 | 1.28 | 0.92 | 0.84 | -0.59 |
| Buoy 8 | 0.0000375 | 1.76 | 1.34 | 0.92 | -0.79 |
| Buoy 9 | 0.0000495 | 1.61 | 1.31 | 0.97 | -1.48 |
| BIG BAR | | | | | |
| Buoy 3 | | | | | |
| int. susp. | 0.00000793 | 2.50 | no sample retained | | |
| traction | - | - | | | |
| Buoy 4 | | | | | |
| int. susp. | 0.0001463 | 1.12 | 0.39 | 0.94 | -0.64 |
| traction | 0.0034372 | -0.45 | | | |
| Buoy 6 | | | | | |
| int. susp. | 0.0000303 | 1.86 | no sample retained | | |
| traction | 0.0036485 | -0.47 | | | |

Table 6.1B/ continued

| Bar and Buoy Location, Tracer Fraction | Average Grain Weight (gm) | Equivalent Size (phi) | Mean Size (phi) | Sorting (phi-units) | Skewness |
|---|---|---|---|---|---|
| DIAMOND BAR | | | | | |
| Buoy 1 | | | | | |
| int. susp. | 0.0000525 | 1.60 | 1.51 | 0.60 | -1.43 |
| traction | 0.0024385 | -0.29 | | | |
| Buoy 4 | | | | | |
| int. susp. | 0.0000750 | 1.43 | 1.09 | 0.86 | -0.71 |
| traction | - | | | | |
| Buoy 7 | | | | | |
| int. susp. | 0.0000173 | 2.12 | no sample retained | | |
| traction | - | - | | | |
| Buoy 9 | | | | | |
| int. susp. | 0.00003198 | 1.83 | 1.82 | 0.40 | -0.42 |
| traction | - | - | | | |
| ECONOMY POINT | | | | | |
| Buoy EP4 | | | | | |
| int. susp. | 0.0000202 | 2.05 | 2.05 | 0.45 | -1.09 |
| traction | - | - | | | |
| Buoy EP6 - Neap | | | | | |
| int. susp. | 0.0000352 | 1.78 | no sample retained | | |
| traction | 0.0023009 | -0.25 | | | |
| Buoy EP6 - Spring | | | | | |
| int. susp. | 0.0000352 | 1.78 | 1.67 | 1.21 | -2.33 |
| traction | 0.0023009 | -0.25 | | | |
| Buoy EP7 - Neap | | | | | |
| int. susp. | 0.0001044 | 1.26 | no sample retained | | |
| traction | 0.0043273 | -0.54 | | | |
| Buoy EP7 - Spring | | | | | |
| int. susp. | 0.0001044 | 1.26 | 0.25 | 1.14 | -0.97 |

present in any of the three coarsest fractions.

Aggregates are also most abundant in the finer-grained sands used in the Type 2 experiments, but never form a significant proportion of the tracer. In general, all Type 2 (bulk) tracer material (Table 6.1B) is coarser-grained and more poorly sorted than the corresponding bedform crest samples (Appendix 3). This results from the fact that most of the experimental sites are located in areas with mega-ripples, and consequently as was seen in Section 5.2.3, the bedform crest samples are impoverished in coarse material.

Ideally the amount of tracer used in an experiment should be as large as possible, so that the tracer cloud can be easily detected, even after long periods. However, the preparation time required, combined with transportation difficulties imposed overriding restrictions. In 1972, the amount of bulk tracer used was 20-25 kg. This quantity was limited by the physical ability to carry the tracer to the desired location. For the experiments conducted in 1973 and 1974, a boat was available for transporting the tracer, and the amount was increased. An average of 68.3 kg of tracer was used in the Type 2 experiments, and in the Type 1 experiments an average of 26.5 kg of each size fraction was used.

The choice of an injection configuration is important in determining the behaviour of the tracer, especially after

short elapsed times. The ideal situation, in which a complete section through a megaripple or sand wave is replaced by tracer, was not practically feasible. As a compromise, the tracer was placed in a shallow trench, averaging 9 cm deep, 80 cm wide and 105 cm long, located in the centre of the stoss side of a megaripple. If sand waves were present as well, the megaripple was itself situated in the middle of the sand wave stoss side. In areas with only ripples or ripples on sand waves, the trench was made shallower so as to place the tracer entirely within the mobile zone. The top of the tracer was flush with the surrounding sediment surface. The centre of the tracer patch (the origin) was marked with a metal rod (Figure 6.4C).

During emplacement, care had to be exercised in order to ensure that the sand was thoroughly wetted. This was necessitated by the aquaphobic nature of the fluorescent coating and the possible tendency to float on the incoming tide. In 1972, an attempt was made to overcome the problem by lightly covering the tracer with a few millimeters of natural sediment. During the subsequent two years, pains were taken to mix water into the tracer until it was completely wet. With both methods, there is the possibility of rapid initial dispersion of a portion of the tracer.

In order to determine the shape of the dispersing tracer cloud, sets of samples were collected from the area

surrounding the origin. Usually, each site was sampled twice, but five of the twenty-nine experiments were sampled only once. The initial sampling was conducted after no more than four tidal cycles had elapsed, and the maximum duration of any experiment was twenty-seven tidal cycles. At most samplings, fifty or more samples were taken.

As was discussed in the previous section, a detailed, three-dimensional sampling scheme is necessary in order to determine the complete tracer distribution. However, the short period of time available during each low tide period, combined with sample processing limitations discussed in the next section, did not allow such a scheme to be implemented. The procedure adopted is, therefore, a compromise.

The samples were collected on a radial pattern which had its centre at the tracer origin. The basic pattern consisted of eight major rays with a 45° spacing. In 1973 and 1974, additional sampling locations were placed between the major rays to give more information in the segments between the rays (Figure 6.5). The grid was oriented by placing one ray perpendicular to the bedform crests, or parallel to the predominant current direction if it was known. This practice was adopted in an attempt to place one row of samples along the net transport direction. The radius of the grid rarely exceeded forty metres. In most cases this size proved satisfactory as tracer concentrations had become

Figure 6.5 Tracer sampling pattern for Buoy 6, Big Bar. Solid circles indicate analysed samples; open circles are unprocessed samples. Residual transport at this site is toward the southwest (see also Figure 6.9).

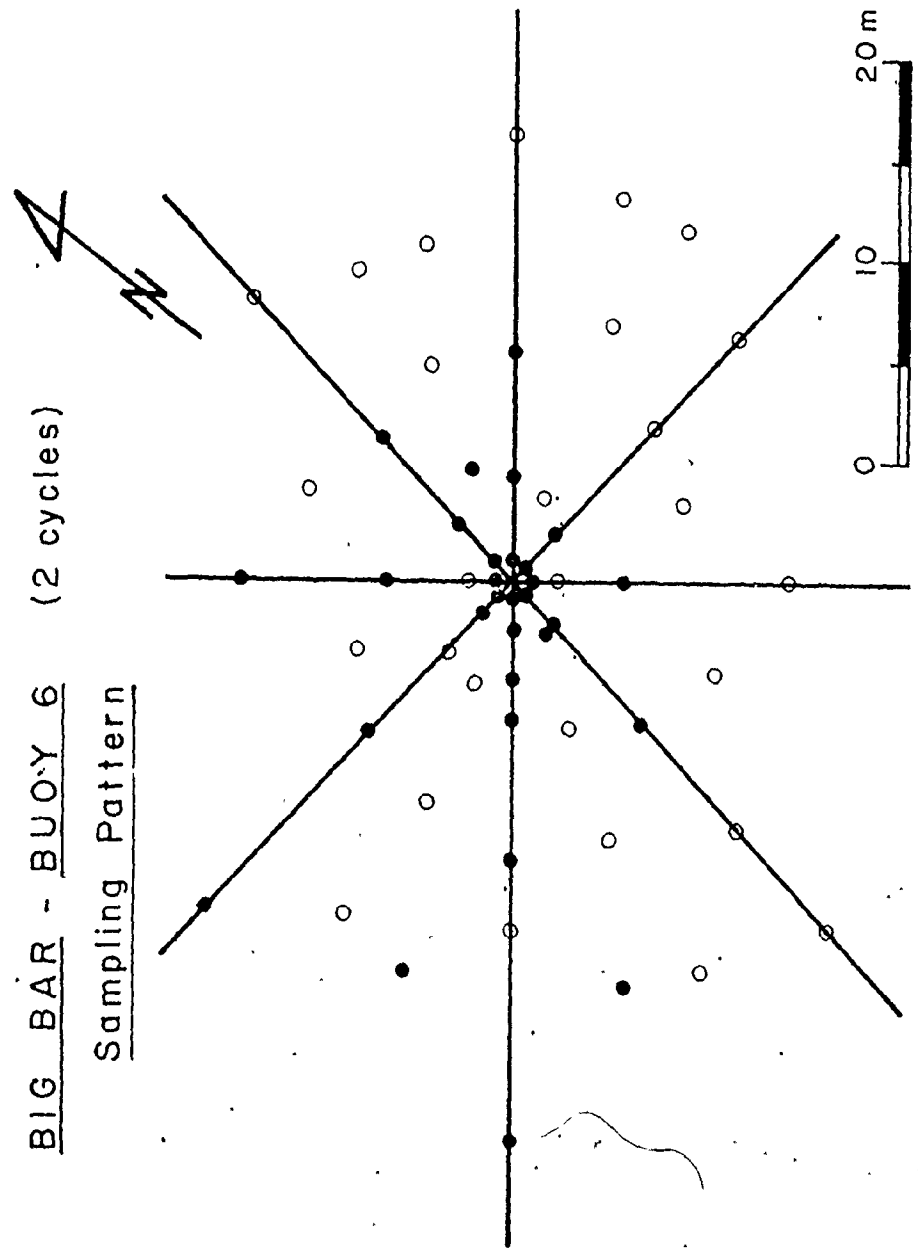
BIG BAR - BUOY 6 (2 cycles)
Sampling Pattern
N
0
10
20 m

diluted to near zero values at this distance. In some instances the results indicated that the sampling area should have been expanded, particularly in the direction of the net transport.

Each individual sample was taken from that portion of the mobile zone deposited or reworked during the previous tidal cycle. In those areas where megaripples, or rippled sand waves with slip faces, were present, most samples were obtained by pushing a 2.5 cm diameter core tube horizontally into the slip face to a depth of 10 to 20 cm. Most of these samples were taken from the half-height level of the bedform to reduce variations in the grain size of the samples. In Type 1 experiments, pairs of samples were sometimes taken from the top and bottom of the lee face. If samples were collected from bedform stosses or troughs, they were scraped from the top centimetre or two. The same strategy was followed in areas where only ripples were present.

The above sampling scheme at best provides a two-dimensional representation of the surface layer of the mobile zone only, because any tracer buried within bedforms is ignored. It is believed, however, that the samples collected can be used as a crude approximation of the tracer content in the entire portion of the mobile layer that has been reworked during the time between injection and sampling. In most cases, the concentrations in the most recently deposited

material should be somewhat less than in earlier deposits, due to the continual dispersion and mixing that takes place (see Figure 6.1). If significantly high concentrations of tracer are buried, then the recovery efficiency will be low, and the results can be treated with scepticism, or ignored.

### 6.3.3 Concentration Determination

In the spatial integration technique, the quantity being measured is the areal variation in the amount of tracer present, often referred to here as the "tracer distribution". For any one given sampling time and location, any consistent measure of tracer concentration can be used. A commonly used quantity is the number of tracer grains present in a standardized sample weight (Boon, 1968, 1969; Kennedy and Kouba, 1970; Komar and Inman, 1970; Murray, 1967), where the concentration units are "number of tracer grains per unit of weight". Although valid centres of gravity can be computed for these tracer distributions, the concentrations themselves are not comparable between tracer fractions and experiments because of grain weight differences. A more fundamental measure of the amount of tracer present is the dimensionless concentration, expressed as a ratio of the weight (or number of grains) of tracer material present to the total weight (or number of grains) of the analysed sample. This measure has been widely used by many authors (Crickmore, 1967; Rathbun, Kennedy, and Culbertson, 1971; deVries, 1966, 1967, 1973)

and is used in this study. Therefore, the tracer concentration of the $i^{th}$ tracer fraction ($C_i$) in a sample is defined here as:

$$C_i = \frac{N_i \, w_i}{W \, p_i} \qquad \ldots(6.25)$$

where: $N_i$ = number of grains of tracer fraction i counted; $w_i$ = average weight of a grain of tracer fraction i; W = total weight of the material scanned; and $p_i$ = proportion of the scanned material composed of sizes within the range of tracer fraction i. In the remainder of this section, the various techniques used in the determination of the above quantities will be presented.

The method used in the determination of the number of tracer grains present ($N_i$) in a sample varied as experience was gained. Three different techniques were used, and each will be described below.

(1) Scanning on Paper: A known weight (W) of sample was placed on a piece of white paper and scanned with an ultraviolet light. A piece of stiff paper was used to spread the sand out into a layer one grain diameter thick, allowing individual fluorescent grains to be counted. This method was fairly rapid, but the chance of missing tracer grains was high if care was not exercised, and fine-grained samples could not be analysed with any accuracy. This method was

used for all of the stations on Noel Bay Bar, East Noel Bar, and Selmah Bar, with the exception of Buoy 2. It was also used for fractions I, II, and III of the Type 1 experiments, and for the traction fraction of the Type 2 experiments.

(2) Volumetric Feeder: The second method utilized a Syntron volumetric feeder machine, model FM-TO-3/4 (supplier: FMC of Canada Ltd.) (Figure 6.4D) which consisted of a large conical hopper, and vibrating feeder trough. Only Type 2 samples from Buoys 4 and 6 on Big Bar, Buoys EP6 and 7 at Economy Point, and Buoy 1 on Diamond Bar were analysed using this machine. The sample to be analysed was placed in the hopper, after first removing the fraction coarser than 0.25 phi (0.84 mm), to ensure a slow, uniform rate of feed. These coarser grains constitute the bulk of the traction population as defined in Chapter 5, and the scanning-on-paper method was used to analyse this fraction separately. The sand in the hopper (the intermittent suspension fraction) was allowed to feed down the trough, and the number of tracer grains present were counted as they fell off the end into a collecting dish. A maximum of twenty minutes of scanning time was allowed for each sample for practical reasons. At the end of this time, or when 400 tracer particles had been counted, whichever came first, scanning was stopped and the weight of the sample scanned (W) was determined. The reasons for the choice of the number 400 as an upper counting limit will be explained

in Section 6.3.5. The use of the Syntron volumetric feeder greatly reduced the chances of missing fluorescent particles as compared to method 1, however, fine-grained samples still could not be processed, as a sufficiently low feed rate could not be obtained.

(3) Vibratory Parts Feeder: The third and most extensively used method employed a Syntron vibratory parts feeder (Model EB-00-C, with bowl number 7A4) (supplier: FMC of Canada Ltd.) (Figure 6.4E). The material to be scanned was placed in the bowl and allowed to migrate up the spiral track. The tracer grains were counted as they fell off the end of the track. Due to strong size segregation within the vibrating bowl, the whole sample could not be placed in the bowl, and only a portion analysed. In order to overcome this problem, the sample was split to a suitable amount using a Sepor microspilitter. This split was placed in the bowl and analysed in its entirety, without regard for the number of grains counted, or the time required. An attempt was made to use a split size that would not greatly exceed the limits set out for the volumetric feeder. A minimum counting time of fifteen minutes was established for samples with low concentrations, and a minimum count of 250 grains was set for samples with high tracer concentrations. If neither of the minimum limits were met, then additional material was split

and analysed. When scanning ceased, the weight of the material used was determined. This method was employed for the finest two fractions in the Type 1 experiments, and for the following Type 2 experiments: Selmah Bar - Buoy 2; Big Bar - Buoy 3; Economy Point - Buoy EP4; and Diamond Bar - Buoys B4, B7, and B9. This method is the most accurate of the three, especially for fine-grained samples.

In order to summarize the counting procedures adopted, flow charts for the analysis of samples from both Type 1 and 2 experiments are given in Figure 6.6, and are outlined below.

The steps followed in the analysis of samples from Type 1 experiments are shown in the flow chart presented in Figure 6.6A. First, the dried sample was sieved into three portions using the 0.0, 1.0, and 3.0 phi sieves (1.0, 0.5, and 0.125 mm). Each of the two coarsest portions of the sample was in turn spread on a sheet of white paper and analysed in the manner described above. The whole of each portion was scanned, unless the tracer concentration was high. In this case, counting continued until either more than 400 grains of each colour of tracer present were obtained, or 600 grains of the more abundant of the two tracer fractions were counted. The 1-3 phi fraction was too fine to be analysed in this way, and the Vibratory Parts Feeder was used. The portion of the sample finer than 3 phi

Figure 6.6 Flow chart for the analysis of tracer samples. A. Type 1 experiments; B. Type 2 experiments. See text for further discussion.

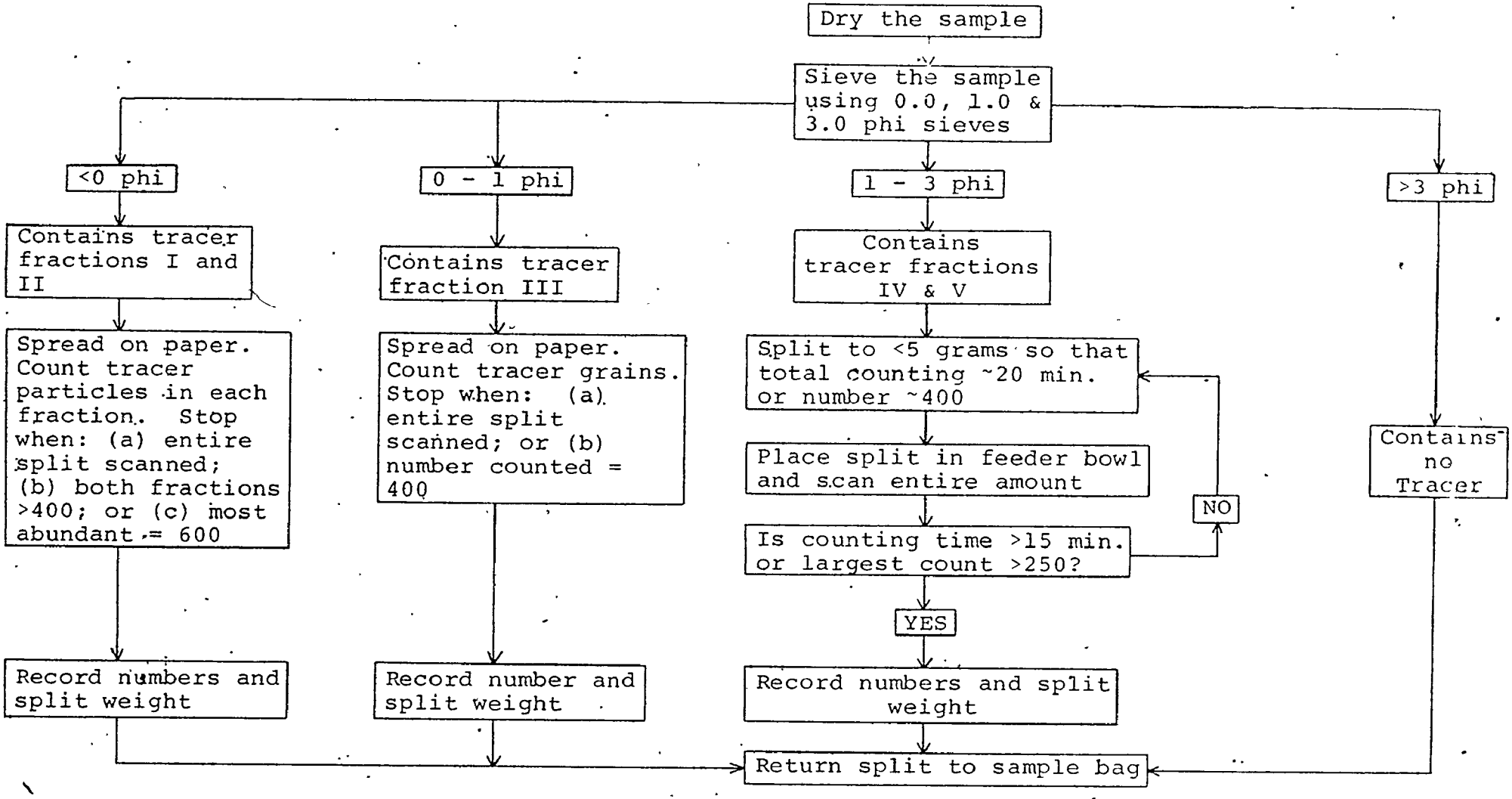
Dry the sample
Sieve the sample using 0.0, 1.0 & 3.0 phi sieves
<0 phi
0 - 1 phi
1 - 3 phi
>3 phi
Contains tracer fractions I and II
Contains tracer fraction III
Contains tracer fractions IV & V
Contains no Tracer
Spread on paper. Count tracer particles in each fraction. Stop when: (a) entire split scanned; (b) both fractions >400; or (c) most abundant = 600
Spread on paper. Count tracer grains. Stop when: (a) entire split scanned; or (b) number counted = 400
Split to <5 grams so that total counting ~20 min. or number ~400
Place split in feeder bowl and scan entire amount
Is counting time >15 min. or largest count >250?
NO
YES
Record numbers and split weight
Record number and split weight
Record numbers and split weight
Return split to sample bag

Figure 6.6A

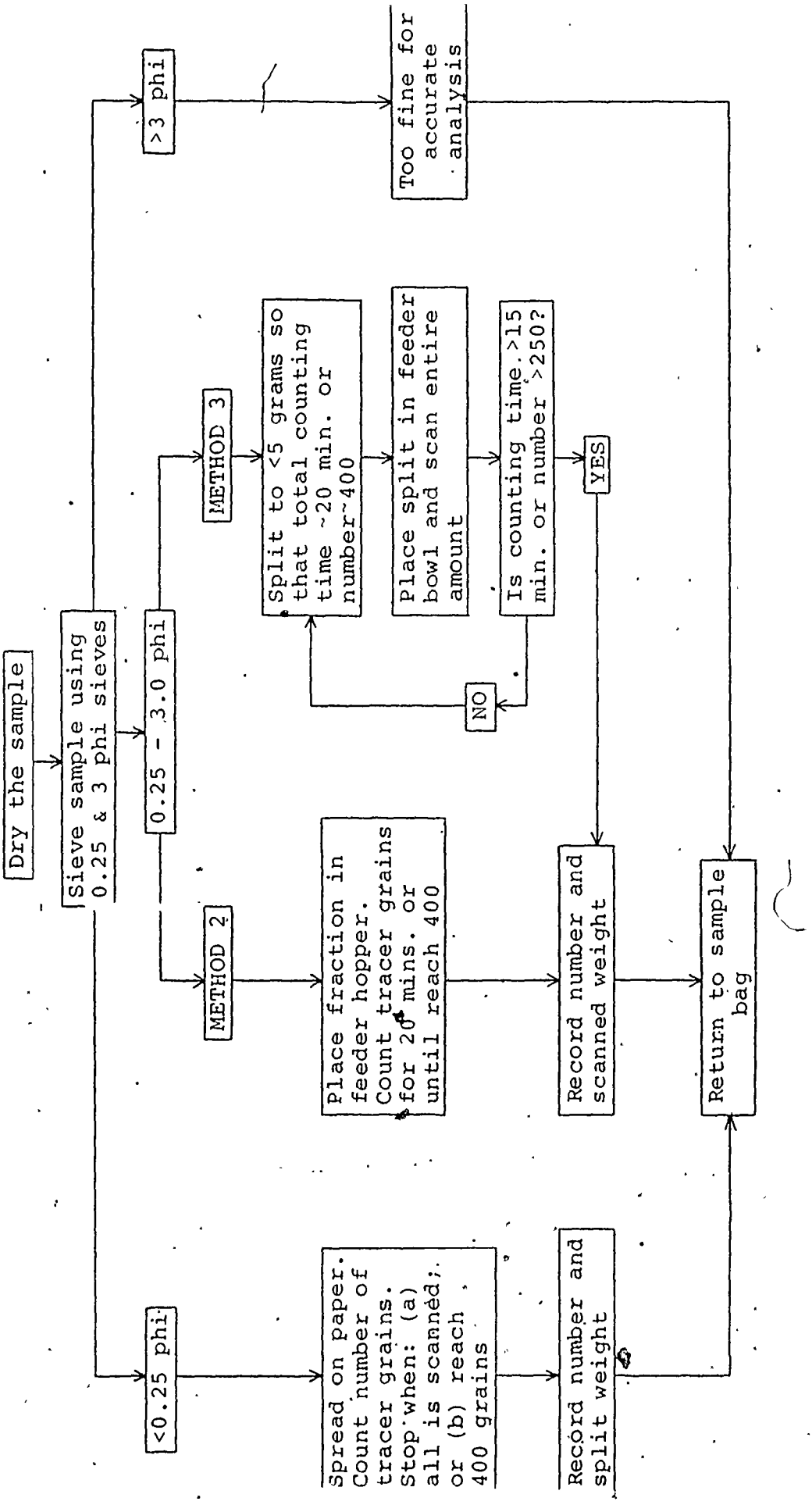
Dry the sample
Sieve sample using 0.25 & 3 phi sieves
>3 phi
Too fine for accurate analysis
0.25 - 3.0 phi
METHOD 3
Split to <5 grams so that total counting time ~20 min. or number~400
Place split in feeder bowl and scan entire amount
Is counting time >15 min. or number >250?
YES
NO
METHOD 2
Place fraction in feeder hopper. Count tracer grains for 20 mins. or until reach 400
Record number and scanned weight
Return to sample bag
<0.25 phi
Spread on paper. Count number of tracer grains. Stop when: (a) all is scanned; or (b) reach 400 grains
Record number and split weight

Figure 6.6B

was removed to simplify the counting. The number of grains of each tracer fraction was recorded separately, as well as the weight of each portion of the sample.

The procedure used in the analysis of Type 2 tracer experiment samples is given in Figure 6.6B. The samples were first sieved through a 0.25 phi (0.84 mm) sieve, approximately separating the traction population from the intermittent suspension population. The coarser fraction was spread on a sheet of paper and the fluorescent grains present were counted by method 1 above. The intermittent suspension fraction was analysed by either method 2 or 3 above. At sites with an appreciable proportion of material finer than 3 phi, this fraction was removed first. For those experiments in which method 1 alone was used to analyse the entire sample, the traction and intermittent suspension populations were not analyzed separately.

The final quantity in equation (6.25) remaining to be determined is the average weight of a tracer grain ($w_i$). Following Rathbun, Kennedy, and Culbertson (1971, p.113), 1000 tracer grains were counted out, and their weight determined. A further 1000 grains were then counted and the cumulative weight obtained. At each step, the overall average grain weight was calculated. This process was continued until the change in the average grain weight by the addition of another 1000 grains was less than 2%. The

average weights so determined are given in Tables 6.1A and B. Included there is the equivalent size which was calculated assuming spherical particles with a density of 2.65.

Due to the considerable time required to analyse one sample (from 25 to 30 minutes), it was not feasible to determine the tracer concentration in all of the 3,424 samples that had been collected. It was therefore necessary to reduce the number of samples despite the resulting loss of information. This was accomplished by selectively eliminating samples from the sample sets. Only at those sites on Selmah, Noel Bay and East Noel Bars where counting method 1 was used, were all of the collected samples analysed.

The guidelines used in the elimination of samples were designed to reduce the sampling density (Figure 6.5) while maintaining an adequate areal coverage. This necessitated a preferential removal of samples from near the origin, and those located between the eight major rays. Along the major rays, alternate samples were eliminated, while retaining those furthest from the origin. In this way, the original number of samples (from 50 to 72) was reduced by half or more, to the range of 25 to 30.

A further reduction was obtained through the introduction and application of the idea of a "statistical zero" tracer grain count, which was defined as less than 5 tracer grains in a sample. This concept was derived from a

statistical analysis of the counting process and will be developed in detail in Section 6.3.5. Samples containing a statistically zero tracer grain count were considered as providing minimal information regarding the tracer distribution and were to be avoided during the counting. This was accomplished by first analysing samples closest to the suspected mode of the distribution and then moving progressively further out each ray. Once a sample containing a count of less than five was encountered, samples located still further from the mode along the same ray were eliminated, as experience showed that tracer concentrations usually decrease monotonically outwards from the mode of the distribution. Tracer material was considered to be totally absent from all areas lying outside of the statistical zero contour (Figure 6.7) in subsequent analysis.

The elimination procedure outlined was followed only for those fractions that were analysed using either of the Syntron feeder devices. Because the coarser fractions required significantly less time to process, all necessary samples were counted. In all, 1,436 samples or 42% of the total, were analysed completely. An additional 351 samples were partially processed, bringing the total number of samples analysed at least in part to 1,787, or 52% of the number collected.

As we shall see in Section 6.3.5, the practical

Figure 6.7 Tracer distribution for Buoy D3, Selmah Bar, with grid used in interpolation procedure.

Both absolute zero and statistical zero contours shown. Note the similarity of centroid locations, and recovery efficiencies ($R_E$) for the two distributions. 4m x 4m grid used for the absolute zero distribution; 2m x 2m grid for the statistical zero distribution. Dots give location of analysed samples.

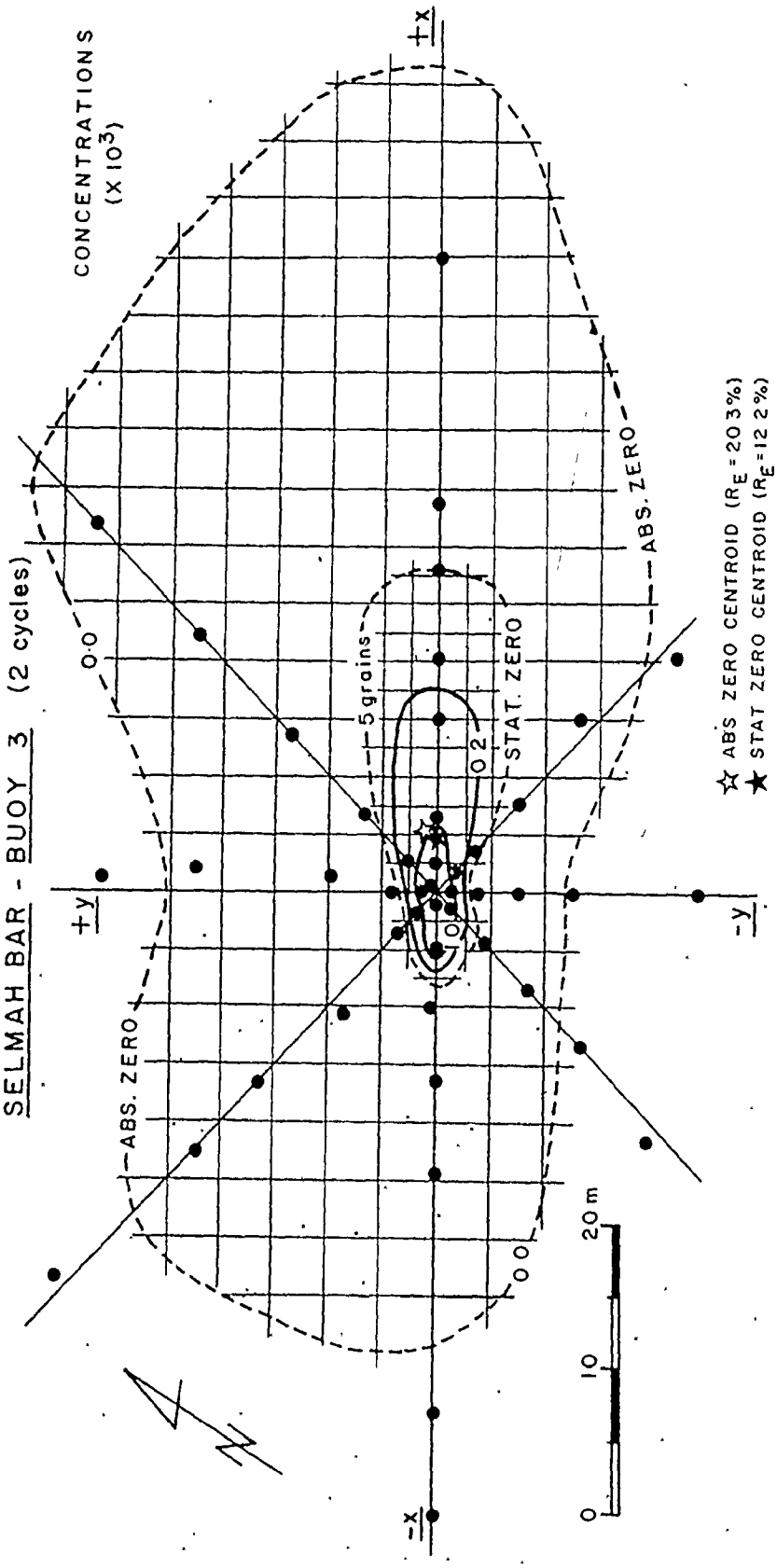
SELMAH BAR - BUOY 3 (2 cycles)
CONCENTRATIONS (X 10³)
+x
-x
+y
-y
ABS. ZERO
STAT. ZERO
5 grains
0·0
0·2
0·4
0·6
☆ ABS ZERO CENTROID ($R_E$ = 20 3%)
★ STAT ZERO CENTROID ($R_E$ = 12 2%)
0
10
20 m

necessity of limiting the size and number of samples analysed has a harmful effect on the reliability of the tracer distributions and the derived quantities. This problem can only be overcome, however, if automated counting machines such as those described by deVries (1967) and Teleki (1967) are available.

### 6.3.4 Data Presentation and Analysis

As one would expect, the almost universally adopted method for the presentation of spatial integration tracer results is the use of maps, contoured in units of concentration. Such a technique is very graphic and allows the easy visualization of the behaviour of the tracer. From such maps, a qualitative estimation can be made of the direction of transport, and the rate of dispersion in various directions; however, by themselves they do not permit a detailed quantitative analysis. Unfortunately, many studies do not go beyond the qualitative level of analysis afforded by maps alone (Blackley et al., 1972; Duane and Judge, 1969; Ingle, 1966; Inman and Chamberlain, 1959; Oertel, 1972). Quantification of the tracer results provides a great deal more information than can be obtained from a simple qualitative investigation.

Moments are statistical quantities that can be used to describe any distribution, and have been used by a growing number of authors in the analysis of tracer data (Courtois and Monaco, 1969; Crickmore, 1967; Inman, Komar and Bowen,

1969; Komar and Inman, 1970; Rathbun and Nordin, 1971; deVries, 1966, 1967). In the present situation, two-dimensional moments are required to characterize the tracer distributions. Written in discrete form, the appropriate formula for moments about the origin (x,y) = (0,0) is (Freund, 1971, p.178):

$$\mu'_{rs} = \Sigma\Sigma x^r y^s C(x,y) \;/\; \Sigma\Sigma C(x,y) \qquad \ldots(6.26)$$

where C is the tracer concentration as defined in equation (6.25) and the summations extend over the entire range of x and y. (In certain cases where the dimensionless concentration C could not be determined because $p_i$ equals zero in equation (6.25), the moments have been calculated using the grain counts (N) themselves in place of the concentrations.) The first moments about the origin in the x and y directions ($\mu'_{10}$ and $\mu'_{01}$, respectively) constitute the centroid of the distribution. Using formulae analogous to equations (5.3) and (5.4), the variance ($\mu_{20}$ and $\mu_{02}$) (second moment about the means) and skewness ($\beta_{10}$ and $\beta_{01}$) parallel to the x and y axes, respectively, can also be calculated for each distribution. For all distributions, the x-axis is chosen as that sampling ray which lies closest to the direction of net motion, with the positive end directed in an easterly direction. The y-axis is at right angles to the x-axis, and has its positive end to the north (Figure 6.7).

It must be realized in the application of equation (6.26) to the observed tracer distributions, that the area represented by each term in the summation must be equal; however, due to the radial sampling pattern, each analysed sample must be considered representative of a different size of area. One possible solution would be to weight each measured concentration according to the area that it represents. Although the idea is simple in theory, it is difficult to apply due to the irregular shapes of the individual areas. As a result, an alternative procedure was adopted (Figure 6.7). First, the concentration distribution was manually contoured and a square grid was superimposed on the contoured distribution, with the grid lines parallel to the x- and y-axes, and one grid point located at the tracer origin. A concentration value was then interpolated at each grid point, and these grid values were used to calculate the moments by equation (6.26).

In addition to providing a concise description of the tracer distributions, these moments allow the derivation of various other quantities of interest. If the centroid location $(\bar{x},\bar{y}) = (\mu'_{10},\mu'_{01})$ is known at two times, $T_1$ and $T_2$, then the change in location ($\Delta x = \bar{x}_2 - \bar{x}_1$; $\Delta y = \bar{y}_2 - \bar{y}_1$) can be used to calculate the average distance of net particle migration (the centroid displacement):

$$D = \sqrt{\Delta x^2 + \Delta y^2} \qquad \ldots(6.27)$$

and the direction of the average net migration:

$$\tan\Omega = \Delta y / \Delta x. \qquad \ldots(6.28)$$

The velocity of centroid migration can be determined from the displacement:

$$V_c = D / \Delta T \qquad \ldots(6.29)$$

where $\Delta T = T_2 - T_1$. Remember that at $t = 0$, the centroid is located at (0,0).

The variance in the x and y directions ($\sigma_x^2 = \mu_{20}$; $\sigma_y^2 = \mu_{02}$) provide a measure of the degree of longitudinal and lateral dispersion respectively (with respect to the transport direction). One method of quantifying the relative degree of dispersion in the x and y directions is to calculate an elongation ratio ($E_\ell$):

$$E_\ell = \frac{\sigma_x}{\sigma_y} \qquad \ldots(6.30)$$

The sediment discharge per unit width of bed ($q_s$) in the direction of centroid migration can be obtained by multiplying the effective thickness of the mobile zone ($\delta_b$) by the speed of centroid movement ($V_c$):

$$q_s = \delta_b V_c (\rho_s \zeta) \qquad \ldots(6.31)$$

where $\zeta$ is one minus the porosity (approximately equal to 0.55;

Pryor, 1971), and $\rho_s$ is the sediment density. $q_s$ is given in kilograms per metre width of bed per tidal cycle. Difficulties arise, however, in accurately defining the quantity $\delta_b$, because not all of the mobile layer may have been reworked since the beginning of the experiment, and because the mobile layer is not generally composed entirely of sizes present in the tracer fraction under consideration.

If it is assumed that the bedforms present have a constant, triangular, cross-sectional shape, then the proportion of the mobile layer that has been reworked after any elapsed time ($\Delta T$) can be calculated from a knowledge of either the distance migrated by the bedform, or its migration rate ($V_b$). The total area of the bedform cross-section is given as one half the length (L) times the height (H) of the bedform. If the bedform migrates a distance ($V_b \Delta T$) that is less than its length (L), then a triangular element remains that has not been reworked. The length of the base of this remaining portion, expressed as a proportion of the total length, is $(1-V_b \Delta T/L)$; and it can be shown geometrically that the height of the non-reworked portion is the same proportion of the total bedform height. Therefore, the fraction of the total area that has not been reworked is the ratio of the remaining area to the total area, which is equal to $(1-V_b \Delta T/L)^2$. The desired value for the proportion reworked ($p_\delta$) is simply one minus this quantity:

$$p_\delta = 1-(1-V_b \Delta T/L)^2 \qquad (p_\delta \leq 1.0) \qquad \ldots(6.32)$$

The second factor affecting the value of $\delta_b$ given above, namely that material with sizes other than those contained in the tracer fraction under consideration are present in the mobile layer, can be incorporated easily. It is only necessary to multiply the mobile layer thickness by the proportion of the mobile layer composed of the proper sizes ($p_T$). This can be obtained from a size analysis of the bed material. The interpretation of $p_T$ does vary, however, depending on the nature of the calculations. For instance, if one desires to calculate the discharge of tracer fraction III alone (Figure 6.3), then $p_T$ would be the proportion of bed material between 0.25 and 0.75 phi (0.84-0.59 mm). If on the other hand the total sediment discharge is being calculated, the value of $p_T$ would be determined for the size range of 0.0 to 1.0 phi (1.0-0.5 mm) (Figure 6.3). This is necessitated by the discontinuities between the tracer fractions used in the Type 1 experiments. The material falling in these gaps is thereby assumed to travel at the same rate as the adjacent tracer sizes.

From the above considerations, it is now possible to calculate the effective thickness of the mobile layer ($\delta_b$):

$$\delta_b = 0.5\ H\ p_T\ p_\delta \qquad \ldots(6.33)$$

This value can be interpreted as the thickness of the layer that would be formed by spreading all of the reworked sediment of the proper size uniformly over the area. It can be seen that $\delta_b$ reduces to the value (0.5 H) if $p_T$ equals 1.0, and if the bedforms have migrated a distance equal to or greater than their own length ($p_\delta = 1.0$).

At this point, all necessary quantities have been calculated for the quantitative description of the tracer distributions, and the sediment transport processes. These values have been listed in Table 6.2 for all experiments and fractions, and will be discussed in Section 6.4. Before proceeding with this, however, it is appropriate to consider specifically some of the factors affecting the reliability of these data.

### 6.3.5. Tracer Data Reliability

Many possible sources of error are present in the experimental design and procedures outlined above. A number of these are specific to this study, but several of the more potentially significant ones affect almost all tracer studies conducted in natural environments. Surprisingly little concern has been devoted to these problems in the past, and their importance is generally unknown. For this reason, considerable attention has been given to the reliability of the tracer results.

The potential sources of error to be considered here

Table 6.2 Tracer Experiment Results. Tracer dispersion characteristics and transport parameters for all tracer experiments. Elapsed times expressed in tidal cycles. I.S. = intermittent suspension fraction; absol. = absolute zero limit used; stat. = statistical zero limit used.

| Data Set and Elapsed Time | Fraction | Axis | Distribution Characteristics Mean (m) | St.Dev. (m) | Skewness | Centroid St. Dev. (m) | Elongation Ratio | Displacement (m) (w.r.t. origin) | Direction | Migration Speed (m/cycle) | Unit Sediment Discharge (kg/cycle) | Recovery Efficiency % |
|---|---|---|---|---|---|---|---|---|---|---|---|---|
| BIG BAR - BUOY 1 | I | x | -0.65 | 0.48 | -0.29 | 0.10 | 1.50 | 0.66 | 248° | 0.33 | 0.05 | 0.4 |
| | | y | 0.15 | 0.32 | 0.45 | 0.32 | | | | | | |
| 2 cycles | II | x | -1.08 | 0.54 | 0.16 | 0.03 | 1.59 | 1.11 | 249° | 0.56 | 0.49 | 1.6 |
| | | y | 0.26 | 0.34 | -0.40 | 0.01 | | | | | | |
| | III | x | -1.08 | 1.04 | -5.46 | 0.04 | 3.85 | 1.08 | 235° | 0.54 | 0.67 | 1.6 |
| | | y | -0.01 | 0.27 | -2.17 | 0.00 | | | | | | |
| | IV | x | -1.67 | 0.91 | -0.57 | 0.13 | 2.17 | 1.67 | 232° | 0.84 | 2.00 | 0.6 |
| | | y | -0.08 | 0.42 | -3.01 | 0.02 | | | | | | |
| | V | x | -3.75 | 3.17 | -2.18 | 0.11 | 7.20 | 3.75 | 234° | 1.88 | 5.50 | 2.6 |
| | | y | -0.08 | 0.44 | -3.34 | 0.01 | | | | | | |
| 27 cycles | I | x | -5.20 | 1.53 | -0.23 | 0.71 | 3.48 | 5.20 | 233° | 0.19 | 0.40 | 6.5 |
| | | y | -0.18 | 0.44 | -0.30 | 0.03 | | | | | | |
| | II | x | -5.75 | 1.37 | 0.05 | 0.36 | 2.58 | 5.75 | 233° | 0.21 | 2.53 | 7.7 |
| | | y | -0.18 | 0.53 | -1.56 | 0.04 | | | | | | |
| | III | x | -6.46 | 2.21 | -1.33 | 0.21 | 1.97 | 6.47 | 232° | 0.24 | 4.12 | 18.8 |
| | | y | -0.32 | 1.12 | -3.57 | 0.04 | | | | | | |
| | IV | x | -8.52 | 3.26 | -2.02 | 0.60 | 2.99 | 8.54 | 231° | 0.32 | 10.55 | 19.4 |
| | | y | -0.58 | 1.09 | -2.08 | 0.06 | | | | | | |
| | V | x | -10.04 | 6.18 | -1.23 | 0.71 | 7.02 | 10.04 | 235° | 0.37 | 14.98 | 7.8 |
| | | y | -0.04 | 0.88 | 0.04 | 0.01 | | | | | | |
| BIG BAR - BUOY 2 | I | x | -0.11 | 0.67 | 0.22 | ? | 0.88 | 0.18 | 186° | 0.09 | 0.00 | ? |
| | | y | -0.15 | 0.76 | 0.29 | ? | | | | | | |
| 2 cycles | II | x | 0.00 | 0.90 | 0.03 | ? | 1.61 | 0.25 | 150° | 0.13 | 0.04 | 1.9 |
| | | y | -0.25 | 0.56 | 0.17 | 0.06 | | | | | | |
| | III | x | 1.10 | 1.90 | 0.89 | 0.13 | 2.11 | 1.11 | 57° | 0.56 | 0.80 | 8.2 |
| | | y | 0.05 | 0.90 | 0.61 | 0.09 | | | | | | |
| | IV | x | 2.09 | 4.08 | 1.54 | 0.43 | 5.16 | 2.09 | 66° | 1.05 | 11.44 | 13.7 |
| | | y | -0.20 | 0.79 | -1.04 | 0.05 | | | | | | |
| | V | x | 0.98 | 10.75 | 0.25 | 0.67 | 5.35 | 1.04 | 80° | 0.52 | 12.39 | 230 |
| | | y | -0.35 | 2.01 | -1.69 | 0.07 | | | | | | |

| Data Set and Elapsed Time | Fraction | Axis | Distribution Characteristics Mean (m) | St.Dev. (m) | Skewness | Centroid St. Dev. (m) | Elongation Ratio | Displacement (m) (w.r.t. origin) | Direction | Migration Speed (m/cycle) | Unit Sediment Discharge (kg/cycle) | Recovery Efficiency % |
|---|---|---|---|---|---|---|---|---|---|---|---|---|
| BIG BAR - BUOY 2 | I | x | -1.17 | 0.81 | 0.45 | ? | 0.76 | 1.33 | 89° | 0.05 | 0.00 | ? |
| | | y | -0.65 | 1.07 | -1.59 | ? | | | | | | |
| 27 cycles | II | x | 3.55 | 4.62 | 2.42 | ? | 3.88 | 3.65 | 73° | 0.14 | 0.04 | ? |
| | | y | -0.82 | 1.19 | -1.27 | ? | | | | | | |
| | III | x | 9.96 | 7.40 | 0.34 | 0.73 | 4.48 | 10.05 | 68° | 0.39 | 0.55 | 64.7 |
| | | y | -1.34 | 1.65 | -0.68 | 0.11 | | | | | | |
| | IV | x | 2.92 | 3.10 | 0.94 | 0.27 | 2.87 | 3.01 | 74° | 0.11 | 1.20 | 21.2 |
| | | y | -0.73 | 1.08 | -1.76 | 0.09 | | | | | | |
| | V | x | 6.24 | 11.98 | 0.80 | 0.54 | 3.86 | 6.44 | 75° | 0.24 | 5.72 | 11.8 |
| | | y | -1.63 | 3.10 | -1.76 | 0.23 | | | | | | |
| BIG BAR - BUOY 3 | I.S. | x | 5.03 | 9.18 | 2.78 | 0.27 | 8.12 | 5.04 | 92° | 2.52 | 73.39 | 19.9 |
| 2 cycles | | y | -0.21 | 1.13 | -5.71 | 0.03 | | | | | | |
| 27 cycles | I.S. | x | 18.59 | 15.88 | 0.86 | 1.08 | 3.61 | 18.88 | 100° | 0.70 | 20.39 | 8.4 |
| | | y | -3.33 | 4.40 | -1.35 | 0.23 | | | | | | |
| BIG BAR - BUOY 4 | Traction | x | -1.48 | 0.58 | 0.66 | 0.07 | 1.81 | 1.48 | 268° | 0.74 | 43.20 | 185 |
| | | y | -0.06 | 0.32 | -3.91 | 0.01 | | | | | | |
| 2 cycles | I.S. - absol. | x | -1.01 | 8.64 | -0.75 | 2.56 | 1.29 | 4.08 | 194° | 2.04 | 145.50 | 137 |
| | | y | -3.93 | 6.70 | -1.58 | 0.47 | | | | | | |
| | I.S. - stat. | x | -0.87 | 4.60 | 0.03 | 0.16 | 0.94 | 3.10 | 196° | 1.55 | 110.60 | 117 |
| | | y | -2.97 | 4.89 | -1.58 | 0.49 | | | | | | |
| 27 cycles | Traction | x | -9.26 | 3.37 | 0.25 | 0.82 | 1.46 | 9.87 | 250° | 0.37 | 21.60 | 39.1 |
| | | y | -3.41 | 2.31 | -0.09 | 0.33 | | | | | | |
| | I.S. - absol. | x | -3.25 | 13.87 | 0.30 | 1.90 | 1.72 | 9.57 | 200° | 0.35 | 24.97 | 124 |
| | | y | -9.00 | 8.07 | -0.72 | 0.95 | | | | | | |
| | I.S. - stat. | x | -3.25 | 11.18 | 0.46 | 0.63 | 1.71 | 8.98 | 201° | 0.33 | 23.54 | 104 |
| | | y | -8.37 | 6.55 | -0.63 | 0.73 | | | | | | |

| Data Set and Elapsed Time | Fraction | Axis | Distribution Characteristics Mean (m) | St.Dev. (m) | Skewness | Centroid St. Dev. (m) | Elongation Ratio | Displacement (m) (w.r.t. origin) | Direction | Migration Speed (m/cycle) | Unit Sediment Discharge (kg/cycle) | Recovery Efficiency % |
|---|---|---|---|---|---|---|---|---|---|---|---|---|
| BIG BAR - BUOY 5 | I | x | -1.32 | 0.54 | 0.25 | 0.16 | 1.20 | 1.33 | 243° | 0.67 | 1.13 | 1.2 |
| | | y | -0.17 | 0.45 | -1.13 | 0.45 | | | | | | |
| 2 cycles | II | x | -1.50 | 0.52 | -0.18 | 0.15 | 1.33 | 1.50 | 249° | 0.75 | 4.30 | 1.3 |
| | | y | -0.04 | 0.39 | -0.96 | 0.04 | | | | | | |
| | III | x | -1.82 | 0.96 | -1.98 | 0.08 | 2.59 | 1.82 | 251° | 0.91 | 9.42 | 4.9 |
| | | y | 0.03 | 0.37 | 2.83 | 0.01 | | | | | | |
| | IV | x | -2.64 | 2.45 | -2.51 | 0.21 | 6.45 | 2.64 | 250° | 1.32 | 19.55 | 7.3 |
| | | y | 0.00 | 0.38 | -0.17 | 0.00 | | | | | | |
| | V | x | -4.84 | 5.75 | -2.71 | 0.26 | 5.99 | 4.84 | 252° | 2.42 | 11.89 | 8.4 |
| | | y | 0.17 | 0.96 | 3.86 | 0.02 | | | | | | |
| 27 cycles | I | x | -3.25 | 1.15 | -0.53 | 0.28 | 3.29 | 3.25 | 250° | 0.21 | 1.59 | 28.9 |
| | | y | 0.00 | 0.35 | 0.00 | 0.00 | | | | | | |
| | II | x | -3.16 | 1.21 | -0.58 | 0.10 | 3.03 | 3.17 | 247° | 0.12 | 3.08 | 42.3 |
| | | y | -0.15 | 0.40 | -0.70 | 0.01 | | | | | | |
| | III | x | -2.55 | 1.29 | 1.62 | 0.09 | 1.70 | 2.55 | 248° | 0.09 | 4.17 | 142 |
| | | y | -0.07 | 0.76 | -10.96 | 0.01 | | | | | | |
| | IV | x | -5.67 | 3.73 | -2.54 | 0.35 | 5.57 | 5.67 | 249° | 0.21 | 13.92 | 52.5 |
| | | y | -0.12 | 0.67 | -0.61 | 0.01 | | | | | | |
| | V | x | -7.78 | 8.02 | -2.16 | 0.46 | 6.91 | 7.78 | 250° | 0.29 | 6.38 | 25.5 |
| | | y | 0.01 | 1.16 | 1.77 | 0.01 | | | | | | |
| BIG BAR - BUOY 6 | Traction | x | -1.18 | 0.48 | -0.05 | 0.04 | 2.67 | 1.18 | 237° | 0.59 | 2.34 | 5.0 |
| | | y | 0.03 | 0.18 | 0.60 | 0.00 | | | | | | |
| 2 cycles | I.S. | x | -2.92 | 5.94 | -3.35 | 0.24 | 3.18 | 2.93 | 240° | 1.47 | 22.36 | 431 |
| | | y | 0.25 | 1.87 | 4.85 | 0.07 | | | | | | |
| 27 cycles | Traction | x | -4.31 | 1.53 | -0.76 | 0.31 | 4.25 | 4.31 | 234° | 0.16 | 4.27 | 40.5 |
| | | y | -0.07 | 0.36 | -0.97 | 0.01 | | | | | | |
| | I.S. | x | -16.18 | 12.47 | -1.24 | 0.82 | 5.31 | 16.19 | 236° | 0.60 | 61.28 | 1506 |
| | | y | 0.30 | 2.35 | 0.82 | 0.03 | | | | | | |

| Data Set and Elapsed Time | Fraction | Axis | Distribution Characteristics Mean (m) | St.Dev. (m) | Skewness | Centroid St. Dev. (m) | Elongation Ratio | Displacement (m) (w.r.t. origin) | Direction | Migration Speed (m/cycle) | Unit Sediment Discharge (kg/cycle) | Recovery Efficiency |
|---|---|---|---|---|---|---|---|---|---|---|---|---|
| DIAMOND BAR-BUOY 1 | I.S. | x | 14.58 | 13.89 | 0.59 | 0.68 | 7.86 | 14.59 | 102° | 3.65 | 632.70 | 52.1 |
| 4 cycles | | y | -0.58 | 1.76 | -2.04 | 0.04 | | | | | | |
| | I.S. - | x | 56.52 | 30.30 | 0.22 | 6.92 | 3.17 | 56.56 | 102° | 3.54 | 613.70 | 25.5 |
| 16 cycles | absol. | y | -1.95 | 9.56 | -0.30 | 1.25 | | | | | | |
| | I.S. - | x | 52.76 | 24.30 | -0.01 | 5.62 | 3.64 | 52.78 | 101° | 3.30 | 572.00 | 21.3 |
| | stat. | y | -1.17 | 6.67 | 0.03 | 0.31 | | | | | | |
| DIAMOND BAR-BUOY 3 | I | x | -9.11 | 2.25 | -0.98 | ? | 1.09 | 9.26 | 295° | 2.32 | 0.00 | ? |
| | | y | -1.67 | 2.07 | -1.04 | ? | | | | | | |
| 4 cycles | II | x | -7.76 | 3.57 | 0.63 | 1.37 | 1.66 | 7.83 | 297° | 1.96 | 0.63 | 49.7 |
| | | y | -1.11 | 2.15 | -0.19 | 0.91 | | | | | | |
| | III | x | -11.58 | 6.19 | -0.52 | 1.37 | 2.67 | 11.64 | 299° | 2.91 | 21.36 | 113 |
| | | y | -1.13 | 2.32 | -1.14 | 0.28 | | | | | | |
| | IV | x | -20.57 | 12.84 | -0.45 | 2.42 | 1.32 | 22.05 | 326° | 5.50 | 783.00 | 451 |
| | | y | 7.95 | 9.74 | 0.97 | 1.45 | | | | | | |
| | V | x | -22.09 | 20.67 | -0.48 | 1.54 | 1.85 | 22.12 | 308° | 5.52 | 988.50 | 274 |
| | | y | 1.17 | 11.17 | 0.11 | 0.46 | | | | | | |
| 21 cycles | III | x | -24.60 | 11.29 | -0.30 | 10.17 | 3.41 | 27.39 | 274° | 1.31 | 9.62 | 40.3 |
| | | y | -12.04 | 3.31 | -0.57 | 4.41 | | | | | | |
| DIAMOND BAR-BUOY 5 | I | x | 8.42 | 1.88 | 0.09 | 3.76 | 2.46 | 8.42 | 111° | 1.69 | 14.73 | 6.7 |
| | | y | -0.07 | 0.76 | 0.11 | 0.04 | | | | | | |
| 5 cycles | II | x | 10.81 | 3.94 | 0.61 | 1.12 | 5.97 | 10.81 | 110° | 2.16 | 39.08 | 4.6 |
| | | y | -0.02 | 0.66 | 0.02 | 0.01 | | | | | | |
| | III | x | 9.96 | 3.28 | 1.05 | 0.39 | 3.90 | 9.96 | 111° | 1.99 | 103.40 | 18.9 |
| | | y | -0.21 | 0.84 | -1.36 | 0.02 | | | | | | |
| | IV | x | 17.59 | 7.90 | 0.34 | 2.17 | 4.67 | 17.60 | 112° | 3.52 | 248.40 | 10.8 |
| | | y | -0.51 | 1.69 | -0.34 | 0.06 | | | | | | |
| | V | x | 27.93 | 15.37 | 0.22 | 6.34 | 6.60 | 27.94 | 112° | 5.58 | 85.35 | 10.7 |
| | | y | -0.78 | 2.33 | -0.28 | 0.16 | | | | | | |

| Data Set and Elapsed Time | Fraction | Axis | Distribution Characteristics Mean (m) | St.Dev. (m) | Skewness | Centroid St. Dev. (m) | Elongation Ratio | Displacement (m) (w.r.t. origin) | Direction | Migration Speed (m/cycle) | Unit Sediment Discharge (kg/cycle) | Recovery Efficiency |
|---|---|---|---|---|---|---|---|---|---|---|---|---|
| DIAMOND BAR-BUOY 5 | II | x | 14.41 | 6.69 | 0.14 | 7.84 | 5.27 | 14.41 | 110° | 0.96 | 19.09 | 0.9 |
| | | y | -0.04 | 1.27 | 0.02 | 0.02 | | | | | | |
| 15 cycles | III | x | 16.60 | 6.12 | -0.10 | 2.12 | 4.05 | 16.61 | 113° | 1.11 | 63.39 | 2.9 |
| | | y | -0.72 | 1.51 | -0.30 | 0.09 | | | | | | |
| DIAMOND BAR-BUOY 7 | I.S. | x | 6.01 | 10.82 | 0.46 | 1.26 | 2.69 | 6.64 | 130° | 1.66 | 598.20 | 15.6 |
| 4 cycles | | y | -2.83 | 4.02 | -0.37 | 0.31 | | | | | | |
| 20 cycles | I.S. | x | 2.16 | 2.61 | -0.01 | 0.56 | 0.87 | 5.12 | 180° | 0.26 | 93.70 | 5.6 |
| | | y | -4.64 | 2.99 | -0.03 | 1.04 | | | | | | |
| DIAMOND BAR-BUOY 8 | I | x | 7.33 | 2.36 | -0.40 | ? | 0.96 | 7.48 | 114° | 1.87 | 0.00 | ? |
| | | y | 1.46 | 2.47 | 0.85 | ? | | | | | | |
| 4 cycles | II | x | 7.05 | 2.20 | 0.07 | ? | 1.00 | 7.57 | 104° | 1.89 | 0.00 | ? |
| | | y | 2.77 | 2.20 | -0.06 | ? | | | | | | |
| | III | x | 6.03 | 2.52 | 0.39 | 0.31 | 1.12 | 6.40 | 105° | 1.60 | 0.21 | 1.7 |
| | | y | 2.15 | 2.26 | 0.43 | 0.16 | | | | | | |
| | IV | x | 6.76 | 3.30 | -0.09 | 0.61 | 2.26 | 6.80 | 119° | 1.70 | 72.69 | 8.0 |
| | | y | 0.76 | 1.46 | 0.31 | 0.18 | | | | | | |
| | V | x | 9.71 | 5.93 | 0.21 | 1.13 | 1.74 | 9.96 | 112° | 2.49 | 59.64 | 2.9 |
| | | y | 2.21 | 3.41 | 0.46 | 0.41 | | | | | | |
| 20 cycles | II | x | 28.38 | 5.72 | 0.48 | ? | 3.86 | 28.38 | 115° | 1.42 | 0.00 | ? |
| | | y | 0.00 | 1.48 | 0.00 | ? | | | | | | |
| | III | x | 19.55 | 8.11 | -0.92 | 3.34 | 5.30 | 19.57 | 113° | 0.98 | 0.45 | 9.7 |
| | | y | 0.70 | 1.53 | 0.34 | 0.14 | | | | | | |

FIGURE 5.3 : Characteristic cumulative curve shapes. Vertical axis is probability scale. Solid lines are best-fit line segments; broken lines indicate rounded nature of "breaks". See text for further discussion of curve types.

| Data Set and Elapsed Time | Fraction | Axis | Distribution Characteristics Mean (m) | St.Dev. (m) | Skewness | Centroid St. Dev. (m) | Elongation Ratio | Displacement (m) (w.r.t. origin) | Direction | Migration Speed (m/cycle) | Unit Sediment Discharge (kg/cycle) | Recovery Efficiency |
|---|---|---|---|---|---|---|---|---|---|---|---|---|
| DIAMOND BAR-BUOY 9 | I.S. | x | -5.52 | 3.35 | -0.04 | 0.96 | 1.12 | 6.53 | 347° | 1.63 | 629.60 | 6.2 |
| 4 cycles | | y | 3.48 | 2.98 | 0.25 | 0.67 | | | | | | |
| ECONOMY PT.- BUOY EP2 | I | x | 1.10 | 0.91 | -0.14 | 0.14 | 1.37 | 1.26 | 96° | 0.32 | 1.69 | 23.5 |
| | | y | 0.61 | 0.67 | 0.08 | 0.07 | | | | | | |
| 4 cycles | II | x | 0.76 | 1.10 | -0.15 | 0.03 | 1.55 | 0.84 | 101° | 0.21 | 1.01 | 18.6 |
| | | y | 0.34 | 0.71 | -0.17 | 0.02 | | | | | | |
| | III | x | 1.00 | 1.51 | 0.46 | 0.04 | 2.01 | 1.04 | 108° | 0.26 | 2.93 | 22.4 |
| | | y | 0.30 | 0.75 | -1.14 | 0.01 | | | | | | |
| | IV | x | -0.50 | 4.25 | -1.49 | 0.68 | 4.57 | 0.60 | 339° | 0.15 | 22.55 | 128 |
| | | y | 0.34 | 0.93 | 0.77 | 0.04 | | | | | | |
| | V | x | 3.17 | 10.74 | 0.66 | 1.18 | 7.11 | 3.23 | 114° | 0.81 | 54.87 | 19.7 |
| | | y | 0.62 | 1.51 | 0.62 | 0.08 | | | | | | |
| 19 cycles | II | x | 7.50 | 1.98 | -0.50 | 1.02 | 3.41 | 7.50 | 125° | 0.39 | 2.03 | 2.1 |
| | | y | -0.04 | 0.58 | 0.00 | 0.02 | | | | | | |
| | III | x | 8.07 | 3.05 | -0.10 | 0.15 | 1.96 | 8.13 | 118° | 0.43 | 5.26 | 0.3 |
| | | y | 1.02 | 1.56 | 1.23 | 0.04 | | | | | | |
| ECONOMY PT.- BUOY EP3 | I | x | -2.04 | 1.21 | -0.06 | 0.27 | 1.32 | 2.07 | 289° | 0.52 | 1.13 | 20.6 |
| | | y | -0.38 | 0.92 | -0.49 | 0.09 | | | | | | |
| 4 cycles | II | x | -3.23 | 2.06 | -0.75 | 0.27 | 1.76 | 3.25 | 294° | 0.81 | 6.20 | 37.0 |
| | | y | -0.33 | 1.17 | -0.53 | 0.05 | | | | | | |
| | III | x | -3.35 | 2.54 | -1.21 | 0.10 | 2.29 | 3.55 | 298° | 0.84 | 14.43 | 74.1 |
| | | y | -0.13 | 1.11 | 0.16 | 0.02 | | | | | | |
| | IV | x | -8.45 | 9.01 | -1.87 | 0.76 | 5.97 | 8.45 | 301° | 2.12 | 185.70 | 185 |
| | | y | 0.15 | 1.51 | 0.56 | 0.24 | | | | | | |
| | V | x | -11.28 | 12.89 | -2.06 | 0.99 | 8.32 | 11.28 | 301° | 2.82 | 85.47 | 127 |
| | | y | 0.24 | 1.55 | 1.37 | 0.05 | | | | | | |

| Data Set and Elapsed Time | Fraction | Axis | Distribution Characteristics Mean (m) | St. Dev. (m) | Skewness | Centroid St. Dev. (m) | Elongation Ratio | Displacement (m) (w.r.t. origin) | Direction | Migration Speed (m/cycle) | Unit Sediment Discharge (kg/cycle) | Recovery Efficiency |
|---|---|---|---|---|---|---|---|---|---|---|---|---|
| ECONOMY PT.- BUOY EP3 | I | x | -3.84 | 1.06 | 0.22 | 0.91 | 0.86 | 3.88 | 292° | 0.20 | 0.51 | 15.8 |
| | | y | -0.55 | 1.23 | 0.05 | 0.20 | | | | | | |
| 19 cycles | II | x | -5.66 | 2.46 | -0.50 | 0.72 | 1.37 | 5.66 | 301° | 0.30 | 2.70 | 40.0 |
| | | y | 0.11 | 1.80 | 1.58 | 0.06 | | | | | | |
| | III | x | -4.87 | 3.27 | 0.55 | 0.22 | 1.57 | 4.88 | 305° | 0.26 | 5.25 | 57.0 |
| | | y | 0.41 | 2.08 | 1.33 | 0.07 | | | | | | |
| | IV | x | -10.16 | 6.45 | -0.53 | 1.96 | 2.54 | 10.22 | 306° | 0.54 | 55.66 | 458 |
| | | y | 1.07 | 2.54 | 0.26 | 0.20 | | | | | | |
| | V | x | -11.74 | 7.98 | -0.22 | 2.65 | 2.91 | 11.79 | 305° | 0.62 | 22.11 | 6.0 |
| | | y | 1.05 | 2.74 | 0.09 | 0.26 | | | | | | |
| ECONOMY PT.- BUOY EP4 | I.S. | x | 0.06 | 1.40 | -1.37 | 0.00 | 1.35 | 0.12 | 76° | 0.02 | 0.38 | 11.2 |
| 4 cycles | | y | 0.10 | 1.04 | 2.59 | 0.01 | | | | | | |
| 19 cycles | I.S. | x | 17.68 | 9.97 | -0.21 | 2.95 | 1.38 | 19.54 | 110° | 1.03 | 147.30 | 11.6 |
| | | y | 8.31 | 7.22 | 0.45 | 1.69 | | | | | | |
| ECONOMY PT.- BUOY EP6 | Traction | x | 2.16 | 1.32 | 0.13 | 0.42 | 2.36 | 2.19 | 51° | 0.53 | 0.17 | 8.4 |
| | | y | 0.34 | 0.56 | 0.42 | 0.07 | | | | | | |
| Neap - 4 cycles | I.S. | x | 4.32 | 7.63 | -0.21 | 0.16 | 1.97 | 6.69 | 55° | 1.67 | 16.54 | 4.0 |
| | | y | 5.11 | 3.88 | 2.23 | 0.19 | | | | | | |
| Neap - 19 cycles | I.S. | x | 19.03 | 18.58 | -0.83 | 1.77 | 2.24 | 25.61 | 63° | 1.35 | 74.28 | 4.2 |
| | | y | 17.14 | 8.29 | 0.41 | 1.46 | | | | | | |
| Spring - 4 cycles | I.S. | x | -4.41 | 9.49 | 0.37 | 0.15 | 1.99 | 5.50 | 322° | 1.38 | 73.99 | 29.5 |
| | | y | 3.30 | 4.76 | 2.39 | 0.17 | | | | | | |

| Data Set and Elapsed Time | Fraction | Axis | Distribution Characteristics Mean (m) | St. Dev. (m) | Skewness | Centroid St. Dev. (m) | Elongation Ratio | Displacement (m) (w.r.t. origin) | Direction | Migration Speed (m/cycle) | Unit Sediment Discharge (kg/cycle) | Recovery Efficiency |
|---|---|---|---|---|---|---|---|---|---|---|---|---|
| ECONOMY PT.- BUOY EP7 | Traction | x | -1.89 | 1.44 | 0.18 | 0.18 | 1.18 | 1.97 | 282° | 0.49 | 17.31 | 55.6 |
| | | y | 0.57 | 1.22 | 0.92 | 0.11 | | | | | | |
| Neap - 4 cycles | I.S. | x | 0.61 | 13.85 | 1.08 | 0.26 | 5.35 | 0.61 | 83° | 0.15 | 13.83 | 43.6 |
| | | y | 0.02 | 2.59 | -0.69 | 0.15 | | | | | | |
| Neap - 19 cycles | Traction | x | -1.77 | 6.90 | -1.17 | 0.79 | 4.73 | 1.79 | 256° | 0.09 | 3.18 | 11.3 |
| | | y | -0.29 | 1.46 | -0.84 | 0.14 | | | | | | |
| | I.S. | x | 2.35 | 20.71 | -0.48 | 1.38 | 2.18 | 3.70 | 136° | 0.19 | 17.52 | 17.3 |
| | | y | -2.86 | 9.48 | -0.34 | 0.56 | | | | | | |
| Spring - 4 cycles | Traction | x | -0.48 | 6.91 | -1.04 | 0.47 | 4.97 | 0.76 | 214° | 0.19 | 6.71 | 95.8 |
| | | y | -0.59 | 1.39 | -0.51 | 0.10 | | | | | | |
| | I.S. - absol. | x | 7.60 | 19.99 | 0.29 | 0.87 | 2.93 | 7.63 | 90° | 1.91 | 176.10 | 38.5 |
| | | y | -0.70 | 6.83 | -0.76 | 0.43 | | | | | | |
| | I.S. - stat. | x | 7.47 | 16.88 | 0.35 | 0.83 | 4.89 | 7.47 | 86° | 1.87 | 172.40 | 27.6 |
| | | y | -0.11 | 3.45 | -0.10 | 0.05 | | | | | | |
| ECONOMY PT.- BUOY EP8 | I | x | -4.03 | 2.26 | 0.51 | 0.47 | 6.65 | 4.03 | 285° | 1.01 | 10.88 | 21.4 |
| | | y | 0.01 | 0.34 | 0.06 | 0.04 | | | | | | |
| 4 cycles | II | x | -4.45 | 1.99 | 1.00 | 0.16 | 5.85 | 4.45 | 286° | 1.11 | 11.95 | 22.0 |
| | | y | 0.08 | 0.34 | 0.40 | 0.01 | | | | | | |
| | III | x | -3.42 | 3.15 | -0.28 | 0.14 | 7.89 | 3.42 | 285° | 0.85 | 30.75 | 97.9 |
| | | y | -0.01 | 0.40 | -0.21 | 0.00 | | | | | | |
| | IV | x | -7.38 | 3.73 | -1.99 | 0.34 | 7.77 | 7.38 | 286° | 1.85 | 65.17 | 41.7 |
| | | y | 0.07 | 0.48 | 3.20 | 0.01 | | | | | | |
| | V | x | -9.65 | 7.24 | -0.74 | 1.14 | 6.19 | 9.65 | 286° | 2.42 | 3.66 | 3.2 |
| | | y | 0.22 | 1.17 | 0.43 | 0.03 | | | | | | |
| 19 cycles | III | x | -16.65 | 15.40 | 1.33 | 2.57 | 3.39 | 17.96 | 263° | 0.94 | 35.42 | 11.1 |
| | | y | -6.73 | 4.59 | -0.15 | 0.91 | | | | | | |

| Data Set and Elapsed Time | Fraction | Axis | Distribution Characteristics Mean (m) | St. Dev. (m) | Skewness | Centroid St. Dev. (m) | Elongation Ratio | Displacement (m) (w.r.t. origin) | Direction | Migration Speed (m/cycle) | Unit Sediment Discharge (kg/cycle) | Recovery Efficiency |
|---|---|---|---|---|---|---|---|---|---|---|---|---|
| SELMAH BAR-BUOY 1 | Total - | x | 0.10 | 0.97 | 5.39 | 0.01 | 1.52 | 0.10 | 90° | 0.05 | 2.94 | 24.6 |
| 2 cycles | absol. | y | 0.00 | 0.64 | -5.23 | 0.01 | | | | | | |
| | Total - | x | 0.90 | 2.42 | 3.17 | 0.10 | 3.97 | 0.91 | 98° | 0.46 | 24.14 | 8.7 |
| | stat. | y | -0.12 | 0.61 | -1.58 | 0.01 | | | | | | |
| 16 cycles | Total - | x | 6.22 | 7.73 | 0.51 | 1.10 | 1.29 | 6.25 | 96° | 0.39 | 22.74 | 1.0 |
| | absol. | y | -0.66 | 5.99 | -1.38 | 0.44 | | | | | | |
| | Total - | x | 5.08 | 0.35 | 0.51 | 0.36 | 0.15 | 5.12 | 83° | 0.32 | 18.66 | 2.0 |
| | stat. | y | 0.66 | 2.36 | 1.36 | 0.09 | | | | | | |
| SELMAH BAR-BUOY 2 | Total | x | 6.55 | 37.16 | -0.03 | 0.36 | 3.02 | 6.77 | 115° | 3.39 | 123.5 | 8446 |
| 2 cycles | | y | -1.67 | 12.32 | -0.39 | 0.08 | | | | | | |
| 16 cycles | Total | x | -6.57 | 31.63 | 0.05 | 0.30 | 2.36 | 8.26 | 243° | 0.52 | 18.95 | 2873 |
| | | y | -5.01 | 13.28 | -0.74 | 0.19 | | | | | | |
| SELMAH BAR-BUOY 3 | Total - | x | 4.49 | 11.22 | 1.57 | 1.76 | 2.37 | 4.58 | 48° | 2.29 | 600.80 | 20.3 |
| 2 cycles | absol. | y | 0.93 | 4.78 | 2.51 | 0.80 | | | | | | |
| | Total - | x | 3.89 | 5.75 | 1.03 | 0.41 | 3.86 | 3.89 | 59° | 1.45 | 380.40 | 12.2 |
| | stat. | y | 0.05 | 1.49 | -0.04 | 0.02 | | | | | | |
| 16 cycles | Total - | x | 20.02 | 12.66 | 0.54 | 6.26 | 2.67 | 20.04 | 63° | 1.25 | 327.90 | 1.8 |
| | absol. | y | -0.92 | 4.75 | -0.19 | 0.33 | | | | | | |
| | Total - | x | 17.90 | 8.96 | 0.10 | 3.35 | 3.56 | 17.91 | 62° | 1.12 | 293.80 | 5.0 |
| | stat. | y | -0.73 | 2.52 | -0.07 | 0.13 | | | | | | |

| Data Set and Elapsed Time | Fraction | Axis | Distribution Characteristics Mean (m) | St. Dev. (m) | Skewness | Centroid St. Dev. (m) | Elongation Ratio | Displacement (m) (w.r.t. origin) | Direction | Migration Speed (m/cycle) | Unit Sediment Discharge (kg/cycle) | Recovery Efficiency |
|---|---|---|---|---|---|---|---|---|---|---|---|---|
| SELMAH BAR-BUOY 4 | Total - | x | -12.81 | 46.98 | 0.20 | 4.52 | 2.74 | 12.91 | 248° | 6.46 | 1647.7 | 11.6 |
| 2 cycles | absol. | y | -1.59 | 17.17 | -0.08 | 0.85 | | | | | | |
| | Total - | x | -5.76 | 37.06 | 0.58 | 2.98 | 5.61 | 6.07 | 237° | 3.04 | 775.4 | 6.0 |
| | stat. | y | -1.91 | 6.61 | -1.35 | 0.40 | | | | | | |
| 16 cycles | Total - | x | -6.59 | 37.79 | 0.33 | 4.76 | 3.47 | 14.87 | 319° | 0.93 | 237.2 | 1.9 |
| | absol. | y | 13.33 | 10.90 | 0.73 | 5.52 | | | | | | |
| | Total - | x | 10.50 | 5.68 | -1.02 | 3.23 | 1.28 | 15.16 | 29° | 0.95 | 242.3 | 0.3 |
| | stat. | y | 10.94 | 4.44 | -0.30 | 3.28 | | | | | | |
| SELMAH BAR-BUOY 5 | Total - | x | 3.52 | 6.90 | 2.07 | 0.50 | 2.51 | 3.53 | 94° | 1.77 | 102.2 | 6.1 |
| 2 cycles | absol. | y | -0.22 | 2.75 | -3.29 | 0.19 | | | | | | |
| | Total - | x | 5.15 | 6.56 | 2.03 | 0.39 | 6.76 | 5.15 | 91° | 2.58 | 148.9 | 2.8 |
| | stat. | y | -0.05 | 0.97 | -0.44 | 0.01 | | | | | | |
| 15 cycles | Total - | x | 35.14 | 22.46 | 0.44 | 6.24 | 5.08 | 35.15 | 91° | 2.34 | 307.0 | 4.7 |
| | absol. | y | -0.79 | 4.42 | -0.10 | 0.29 | | | | | | |
| | Total - | x | 29.19 | 17.07 | 0.37 | 4.80 | 5.60 | 29.20 | 92° | 1.95 | 255.8 | 3.5 |
| | stat. | y | -0.88 | 3.05 | -0.49 | 0.29 | | | | | | |
| EAST NOEL BAR - BUOY 6 | Total - | x | -0.81 | 2.05 | -0.18 | 0.22 | 1.10 | 0.84 | 70° | 0.42 | 7.65 | 0.4 |
| 2 cycles | absol. | y | -0.22 | 1.86 | -3.58 | 0.28 | | | | | | |
| | Total - | x | -1.03 | 1.24 | -0.27 | 0.07 | 1.94 | 1.15 | 292° | 0.58 | 10.67 | 0.4 |
| | stat. | y | 0.52 | 0.64 | -0.52 | 0.04 | | | | | | |
| 17 cycles | Total - | x | -3.87 | 4.82 | -0.31 | 1.26 | 1.46 | 3.89 | 270° | 0.23 | 28.08 | 2.5 |
| | absol. | y | 0.35 | 3.31 | 0.65 | 0.31 | | | | | | |
| | Total - | x | -2.93 | 3.48 | -0.26 | 0.55 | 3.91 | 2.93 | 264° | 0.17 | 20.75 | 1.1 |
| | stat. | y | -0.04 | 0.89 | 0.08 | 0.01 | | | | | | |

| Data Set and Elapsed Time | Fraction | Axis | Distribution Characteristics Mean (m) | St. Dev. (m) | Skewness | Centroid St. Dev. (m) | Elongation Ratio | Displacement (m) (w.r.t. origin) | Direction | Migration Speed (m/cycle) | Unit Sediment Discharge (kg/cycle) | Recovery Efficiency |
|---|---|---|---|---|---|---|---|---|---|---|---|---|
| NOEL BAY BAR → BUOY 7 | Total - absol. | x | 7.00 | 11.15 | 1.49 | 2.22 | 4.39 | 7.16 | 97° | 1.76 | 51.30 | 0.7 |
| | | y | -1.51 | 2.54 | -1.48 | 0.40 | | | | | | |
| 4 cycles | Total - stat. | x | 3.32 | 6.36 | 1.73 | 0.63 | 4.10 | 3.45 | 101° | 0.86 | 25.07 | 0.6 |
| | | y | -0.93 | 1.55 | -1.50 | 0.13 | | | | | | |
| NOEL BAY BAR - BUOY 8 | Total - absol. | x | -0.66 | 10.44 | -0.66 | 1.37 | 1.29 | 5.83 | 212° | 1.46 | 174.5 | 1.1 |
| | | y | -5.79 | 8.08 | -1.57 | 2.29 | | | | | | |
| 4 cycles | Total - stat. | x | 2.39 | 4.45 | 0.29 | 0.21 | 1.89 | 3.60 | 164° | 0.90 | 107.6 | 0.6 |
| | | y | -2.70 | 2.35 | -0.58 | 0.27 | | | | | | |
| NOEL BAY BAR - BUOY 9 | Total - absol. | x | -1.97 | 3.51 | -0.95 | 0.68 | 0.92 | 2.05 | 251° | 0.51 | 47.39 | 0.1 |
| | | y | 0.58 | 3.83 | 1.29 | 0.47 | | | | | | |
| 4 cycles | Total - stat. | x | -0.64 | 1.61 | -1.47 | 0.13 | 1.99 | 0.66 | 225° | 0.17 | 15.80 | 0.3 |
| | | y | -0.17 | 0.81 | -0.44 | 0.03 | | | | | | |

are:

(1) measurement errors in determining the sample locations and weights, and average grain weights;

(2) counting errors resulting from: the failure to count fluorescent grains that are present, the misidentification of natural material as tracer, or sample contamination;

(3) miscalculation of the effective thickness of the mobile layer;

(4) extrapolation and interpolation error or bias during the contouring and gridding process;

(5) failure to sample all of the actual tracer distribution, due either to tracer burial, or to an inadequate sampling grid in terms of extent or density;

(6) local, random concentration variations due to the random arrangement of tracer particles amongst natural sediment grains.

Wherever possible, an attempt has been made to quantify the importance of the factor under consideration. In many cases, however, practical limitations do not allow a quantitative assessment of the error introduced by each of these factors; nevertheless, some qualitative discussion is believed to be warranted.

Measurement errors, including both inaccuracy and imprecision, can never be totally eliminated, but care has been taken at every step to minimize such errors. Sample

locations have been measured to within at most ±0.25 m, which is 0.3% or less of the overall dimensions of the sampled area. All weights were obtained with an analytical balance and are, therefore, highly precise. The determination of the average grain weight is, however, subject to greater error, particularly for fine grain sizes. Errors arising from this source affect all concentrations determined from a single site equally, so that none of the quantities derived from the moments of the contoured tracer distributions (centroid, sediment discharge, etc.) will be affected.

Counting errors are likewise considered to be unimportant. Informal replication studies show that the chances of missing tracer grains during the counting are generally low, but do vary with the procedure used. Of the three methods, the vibratory parts feeder was the most accurate, the volumetric feeder second, and the paper-scanning technique least accurate, particularly when used with grain sizes finer than 2.0 phi (0.25 mm). For sizes coarser than 1.0 phi (0.5 mm), there is almost no chance of missing tracer grains with this last method, particularly as great care was taken during the counting. The misidentification of particles is also unlikely, due to the absence of naturally fluorescent material, with the exception of shell debris which was clearly distinguishable from the tracer with a minimum of experience. Contamination problems have hopefully been virtually eliminated

also, through careful cleaning of all equipment between every sample.

The possibility of miscalculating the effective thickness of the mobile layer is of importance with regard to the reliability of the calculated sediment discharges, and also the recovery efficiencies as will be seen below. One potential source of error here involves the estimation of the bedform height, particularly in megarippled areas, where the bedform height is extremely variable. The values used are the averages of several measurements within or near the sampled area, and should, therefore, be a reasonable estimate. The determination of the average migration rate ($V_b$) of the bedforms is also difficult, and the use of an inaccurate value would affect the determination of $\delta_b$, particularly at short elpased times when $p_\delta$ is less than 1.0. All available stake data and peels have been used, however, to arrive at the values of $V_b$, and there is no way of estimating the actual effect of this factor. Further, potentially significant error can be introduced by the use of non-representative values of $p_T$ in equation (6.33). It is very likely that the small, bedform crest samples (Appendix 3) which were used to obtain the estimates of $p_T$ do not accurately represent the size composition of the entire mobile layer. In particular, for areas with megaripples, it has been seen in Section 5.2.3 that the bedform crests possess less coarse material than is

present elsewhere. As a result, the discharge (and recovery efficiency) of the coarser fractions may be underestimated, whereas the values for the finer sizes are overestimates. The importance of this factor cannot, unfortunately, be evaluated with the available data.

The remaining three sources of possible error are also not easy to overcome. To some extent, they all could be reduced by the collection and analysis of many more, larger samples. A much more comprehensive set of analyses, both areally and vertically in the bed would ensure that no portion of the true tracer distribution was left unsampled, and the more extensive, and denser array of data points would remove much of the "subjectivity" that is presently necessary in the contouring and interpolation procedures. The analysis of larger samples would reduce the random factor as well. The proposed solution is not feasible with the available equipment and time.

The last two potential sources of error listed above, namely inadequate sampling and random concentration variations, unlike the other errors, are open to some degree of quantification, however. As a result, these two factors will be considered in greater depth.

As outlined in previous discussion, severe problems can arise from failure to sample significant portions of the existing tracer distribution. This can occur for several

reasons: (i) burial of high concentrations of tracer in bedforms; (ii) sample density is too low; (iii) sampling area is not sufficiently extensive; and (iv) elimination of the tails of the tracer distribution because of the use of the "statistical zero" contour as the limit of the distribution (Figure 6.7). All of these factors will generally result in the exclusion of some portion of the true distribution, and the amount of tracer considered in calculating the moments will be less than the amount injected. Problems related to this cannot be completely overcome, but can be largely avoided through the use of the recovery efficiency ($R_E$), which has been defined previously as the ratio of the amount of tracer recovered to the amount injected. The procedure involved in its calculation is outlined below.

The amount of tracer used in each experiment (M) (in kilograms) was measured prior to injection. For the Type 2 experiments, the values obtained were the total of the amounts in the traction (<0.25 phi) and intermittent suspension (>0.25 phi) fractions combined. Because these fractions were analysed separately, the appropriate amount injected for each fraction is the total amount (M) times the proportion in the proper size range ($p_c$), which can be obtained from a size analysis of the tracer material. For Type 1 experiments, $p_c$ is 1.0 for all fractions.

The amount of tracer recovered is here considered to be the total amount of tracer present under the interpolated

grid distribution used to calculate the moments. The weight of tracer present in each grid square is given by $(A_s \delta_b \zeta \rho_s C)$, where $A_s$ is the area of the square, C is the tracer concentration, $\delta_b$ is the effective thickness of the mobile layer as determined by equation (6.33), and the other quantities are as defined above. The total recovered is, therefore, $[(A_s \delta_b \zeta \rho_s) \Sigma C]$, where the summation is over all grid squares with a non-zero tracer concentration. Thus, the recovery efficiency ($R_E$) is:

$$R_E = \frac{A_s \delta_b \zeta \rho_s \ (\Sigma C)}{Mp_c} \qquad \ldots(6.34)$$

Recovery efficiencies have been calculated for each tracer fraction in every experiment. The values are listed in Table 6.2 and range from less than 1% in 11 distributions out of 125, to over 100% in 18 other cases, with three being in excess of 1000%. Of the 49 distributions that have been sampled twice, 23 show an increase in the recovery efficiency from the first to the second sampling, due probably to the release of buried tracer. The recovery efficiencies for the remaining 26 distributions decrease with time, most likely due to increased dispersion out of the sampling area. If the three anomalously high values are excluded, the average recovery efficiency is 40.8%; however, over 45% are less than 10%. The number of low values is somewhat discouraging, but

it is not known whether they are the result of the specific procedures used in this study, or if they are representative of all tracer studies conducted in natural environments where large-scale bedforms are present.

In order to assess the significance of using the statistical zero contour, and thereby excluding all areas outside of it from consideration, 17 distributions have been analysed using both statistical and absolute zero concentration limits (Table 6.2). (The absolute zero contour is placed at the inner limit of analysed samples which contain no tracer [Figure 6.7].) As would be expected, the recovery efficiency for most (13 of 17) of the distributions based on the statistical zero is lower than the value obtained using the absolute zero limit. In three cases, however, the recovery efficiency for the statistical zero distribution is higher, because of differences in the interpolated values. The average recovery efficiency for the absolute zero distributions is only 23.6%; while it is 18.4% for the statistical zero case, a drop of just 5.2%. These figures indicate that while the use of the statistical zero contributes to the low recovery efficiencies, it is not the major factor.

Whatever the reason for the low recovery efficiences, these data indicate that the sediment transport information derived from many of the experiments will have to be treated with some caution. In particular, the sediment discharges, and to a lesser extent the centroid movement speeds as well,

that are calculated could be different from the actual values, unless the tracer loss is proportioned uniformly over the sampled area and surroundings. Analysis of the data in Section 6.4 indicates, however, that the results are of reasonable accuracy, despite the low recovery efficiencies.

The last source of error listed above that remains to be considered is the random error associated with each concentration determined. Although this factor is potentially significant, little attention has been given to it in previous studies. For the above reason, and because new techniques have been developed in the course of the present study for dealing quantitatively with this source of error, a detailed discussion is presented below.

If one considers a thoroughly mixed volume of sand containing a known concentration of tracer ($\xi$), then any sample taken from that volume will not necessarily give a concentration equal to $\xi$. This is due to the fact that the tracer grains are arranged randomly in three dimensions amongst the non-painted grains. Therefore, every individual sample must be considered as only an estimate of the true tracer concentration existing in the vicinity of the sample point.

During the counting process, every grain scanned can be classified as either fluorescent (a success) or as non-fluorescent (a failure). In probability theory, this

characteristic leads to the definition of the Binomial distribution for the probability of obtaining m tracer grains out of a total of n grains, given that the true dimensionless concentration is $\xi$ (Freund, 1971. p.74-75):

$$b(m;n,\xi) = \binom{n}{m} \xi^m (1 - \xi)^{n-m} \text{ for } m = 0,1,2..,n \quad ...(6.35)$$

Due to the large values of n ($\sim 10^6$-$10^7$) and the small values of $\xi$ encountered (less than $10^{-3}$ in most instances), the Binomial distribution can, as a first approximation, be replaced by the Poisson distribution (Freund, 1971, p.83.85; Zehna, 1970,p.135):

$$p(m;\lambda) = \frac{\lambda^m e^{-\lambda}}{m!} \quad ...(6.36)$$

where $\lambda = n\xi$. The Poisson distribution has its mean = variance $=\lambda$; and each determined grain count can be considered as an estimate of $\lambda$.

The coefficient of variation (V) (Neville and Kennedy, 1964.p.33) is a measure of the relative error associated with every tracer grain count:

V = standard deviation of count/mean count ...(6.37a)

In terms of the Poisson distribution this becomes:

$$V = 1 / \sqrt{\lambda} \qquad \ldots(6.37b)$$

The relative variability of any concentration is inversely proportional to the square root of the number of grains counted, and it is obvious that the analysis of larger samples containing more fluorescent grains would reduce this variability. Equation (6.37b) has been presented previously by Hubbell and Sayre (1964), deVries (1966, 1967, 1973), and Rathbun, Kennedy and Culbertson (1971).

In Section 6.3.3 during the description of the counting process, 400 tracer grains was set as the upper counting limit. This number was derived from equation (6.37b) by setting the coefficient of variation equal to the acceptably low value of 0.05 and solving for $\lambda$. The concept of a "statistical zero" tracer count was also obtained using equation (6.37b). If any grain count ($\lambda$) with a value of four or less is substituted into (6.37b) then the coefficient of variation is equal to or greater than 0.5, implying that the two standard deviation confidence limits for these grain counts include the value zero. This is equivalent to saying that they are statistically indistinguishable from zero. It must be stated, however, that this derivation of the "statistical zero" count is not strictly correct, because the Normal approximation that is used to interpret equation (6.37b)

is not valid for small $\lambda$. The true two standard deviation confidence limits for a Poisson variable with a value of four are 11.14 and 0.48. The statistical zero concept as defined above has nevertheless proven valuable.

Of the more than 4000 individual concentrations determined, over 90% are based on counts of 100 or fewer grains. This means, using equation (6.37b), that the majority of concentrations have a coefficient of variation at two standard deviations of 20% or more. This fact must have an influence on the reliability of the quantities derived from the tracer distributions. At the invitation of the author, Dr. P.D.M. Macdonald (personal communication, July 7, 1975) of the Applied Mathematics Department, McMaster University, has investigated this problem and has proposed a formula which provides an approximation for the confidence intervals of the centroid co-ordinates. The only source of error considered is the random variation in concentration at a point due to the random placement of tracer grains amongst natural sediment particles. All other quantities are assumed to be free of error. The development is as follows.

Let the true dimensionless tracer concentration at a point $(x,y)$ be given by $\xi(x,y)$, where $\xi(x,y)$ is given by equation (6.25). Suppose that the X-Y plane has been divided into a regular grid, each square having an area A, and suppose that samples have been taken in n of these squares. Let $\hat{C}_k$ denote the concentration measurement in the $k^{th}$ square

and $\sigma_k^2 = \text{Var}(\hat{C}_k)$, where $\hat{C}_k$ is an estimate of $\xi_k$. $\sigma_k^2$ can be estimated from $\hat{C}_k$ using the fact presented above that the fluorescent grain count (N) is a Poisson variable: $\text{Var}(N_k) = N_k$. Also, since $\text{Var}(Kx) = K^2\,\text{Var}(x)$, and since only N is considered variable in equation (6.25) it follows that the estimate of the variance of the measured concentration is:

$$\delta_k^2 = \left(\frac{w}{W_k p}\right)^2 N_k = \hat{C}_k \left(\frac{w}{W_k p}\right). \qquad \ldots(6.38)$$

Concentration values must be assigned to each of the grid squares in which measurements were not made. If the interpolated values that were used in the initial determination of the moments are used in the calculation of the confidence interval, the problem becomes extremely complicated due to the dependence of any value on many surrounding values. Therefore, the interpolation required here is accomplished by selecting, for each of the k squares in which a determination was made, a set of additional squares in which the concentration assumed to be equal to that measured. Suppose that a total of $m_k$ squares is thereby associated with the $k^{th}$ measurement, and denote their co-ordinates by $(x_{kj}, y_{kj})$, $j = 1,2,\ldots,m_k$. In this manner, all squares with $\hat{C} > 0$ are assigned. The moments of the tracer distribution can now be estimated using a variation of equation (6.26):

$$\hat{\mu}'_{rs} = \frac{\sum_{k=1}^{n} \left( \sum_{j=1}^{m_k} x_{kj}^{r} \; y_{kj}^{s} \right) \hat{C}_k}{\sum_{k=1}^{n} m_k \; \hat{C}_k} \qquad \ldots(6.39)$$

Note that now $\hat{\mu}'_{rs}$ equals the ratio of two random variables R and S:

$$\hat{\mu}'_{rs} = R / S$$

where:

$$R = \sum_{k=1}^{n} a_k \, C_k$$

$$S = \sum_{k=1}^{n} m_k \, C_k \qquad \ldots(6.40)$$

and $$a_k = \sum_{j=1}^{m_k} x_{kj}^{r} \; y_{kj}^{s}.$$

Also, letting E denote expectation, $\mu'_{rs} = E(R) / E(S)$.

Since the n determinations of concentration $(\hat{C}_1, \hat{C}_2, \ldots, \hat{C}_n)$ are independent:

$$v_{11} \equiv \text{Var}\,(R) = \sum_{k=1}^{n} a_k^2 \, \sigma_k^2$$

$$v_{22} \equiv \text{Var}\,(S) = \sum_{k=1}^{n} m_k^2 \, \sigma_k^2 \qquad \ldots(6.41)$$

and $$v_{12} \equiv \text{Cov}\,(R,S) = \sum_{k=1}^{n} a_k \, m_k \, \sigma_k^2.$$

By the central limit theorem, R and S will follow a bivariate normal distribution when n is large. Furthermore, by the use of Fieller's (1954) method, it can be shown that

$$\frac{R - \mu'_{rs} S}{\sqrt{v_{11} - 2\mu'_{rs} v_{12} + \mu'^{2}_{rs} v_{22}}}$$

follows a standard normal distribution. Thus,

$$\text{Prob}\left[\frac{|\ R - \mu'_{rs}\ S\ |}{\sqrt{v_{11} - 2\mu'_{rs} v_{12} + \mu'^{2}_{rs} v_{22}}} < z_{\alpha/2}\right] = 1 - \alpha \qquad \ldots(6.42)$$

where $z_{\alpha/2}$ is the abscissa of the standard normal curve with an area $(\alpha/2)$ to the right. Solving inequality (6.42) for $\mu'_{rs}$ gives the confidence limits for any specified probability $(1 - \alpha)$:

$$\mu'_{rs}\left\{\left[\frac{1 - z^2_{\alpha/2}\frac{v_{12}}{RS}}{1 - z^2_{\alpha/2}\frac{v_{22}}{S^2}}\right] \pm \left[\frac{z_{\alpha/2}\sqrt{\left(\frac{v_{11}}{R^2} - 2\frac{v_{12}}{RS} + \frac{v_{22}}{S^2}\right) + z^2_{\alpha/2}\left(\left(\frac{v_{12}}{RS}\right)^2 - \frac{v_{11}v_{22}}{R^2S^2}\right)}}{1 - z^2_{\alpha/2}\frac{v_{22}}{S^2}}\right]\right\} \qquad \ldots(6.4$$

The required confidence interval will be the interval between these bounds provided that

$$z^2_{\alpha/2} \frac{v_{22}}{s^2} < 1.$$

Otherwise, the bounds may be imaginary, or the confidence region will be the pair of half-lines outside these bounds. Therefore, if the variance of the sum of the concentrations ($v_{22}$) is large (that is, the recovery is low), we may be restricted to low levels of confidence (large values of $\alpha$).

It must be remembered that the confidence intervals were not calculated from the smooth, interpolated tracer distribution from which the original moments were obtained (denoted $\xi(x,y)$). Rather, they were calculated from a more discrete approximation in which larger areas were considered to have uniform concentrations (denoted $\hat{C}(x,y)$). Therefore, the confidence intervals of $\hat{C}(x,y)$ will only be valid for $\xi(x,y)$ as $\hat{C}(x,y)$ approaches $\xi(x,y)$. In order that $\hat{C}(x,y)$ be as accurate a model as possible, the following procedure was used:

(1) each interpolated grid concentration of $\xi(x,y)$ was compared with the measured concentrations, and the grid square was assigned on the basis of concentration similarity, rather than spatial proximity;

(2) the centroid and confidence intervals of $\hat{C}(x,y)$ were calculated;

(3) if the centroid of $\xi(x,y)$ lay within the 95% confidence interval of $\hat{C}(x,y)$, then it was inferred that the two distributions were sufficiently similar to allow the transference of the confidence intervals of $\hat{C}(x,y)$ to $\xi(x,y)$, without undue error, but if the centroid of $\xi(x,y)$ fell outside the 95% confidence interval of $\hat{C}(x,y)$, then squares were reassigned, and the process was repeated until the two centroids were not significantly different.

In the majority of cases, the initial trial produced centroids that were not significantly different at a confidence level of 68% or less. As well, the reassignment was largely academic as the confidence intervals did not seem to be very sensitive to the minor changes that were required to bring the centroids close together.

In practice, $v_{11}$, $v_{12}$, and $v_{22}$ are not known and must be computed from the estimates $\sigma_1^2$, $\sigma_2^2$, ..., $\sigma_n^2$. In this case, for the computed confidence intervals, the true confidence level will be somewhat less than $(1 - \alpha)$; in other words, the confidence interval is underestimated. As a result, the probability content of the rectangle about the centroid formed by the two confidence intervals, at a given probability, is greater by an unknown amount than the confidence level of the intervals used. This means that the centroids cannot be rigorously tested against each other, or against the origin, for statistical similarity or difference.

An approximate test can be devised, however, by assuming that the half-width of the 68% confidence interval is equivalent to the standard deviation of the centroid co-ordinate. Using these values, each co-ordinate of the two centroids $(x_1,y_1)$ and $(x_2,y_2)$, or the origin, can be compared in turn using the formula:

$$|x_1 - x_2| - z_{\alpha/2}\sqrt{\sigma^2_{x_1} + \sigma^2_{x_2}} = 0.0 \qquad \ldots(6.44)$$

and solving for $z_{\alpha/2}$. The value of $\alpha$ can be obtained from tabulated values for the area under the normal curve, and gives the probability of observing a difference this great or greater if there is, in fact, no difference between the co-ordinates tested. Although this technique lacks rigor, it is believed that it is a valuable advance in the quantitative analysis of tracer results.

The standard deviation has been calculated for all possible centroid co-ordinates, using the half-width of the 68% confidence interval. The results are listed in Table 6.2. The only co-ordinates for which confidence intervals could not be calculated are those that are based on grain counts rather than on concentrations. The calculated standard deviations range from zero, to a maximum of 10.17 m for x co-ordinates, and 5.52 m for y co-ordinates. The average values are 1.24 m and 0.32 m in the x- and y-directions, respectively.

Values of $\alpha$ (the probability of observing a difference this great or greater, when there is, in fact, no

difference) have also been calculated using equation (6.44) for all centroid pairs of interest. The 95% probability level has been chosen to distinguish between significant and non-significant differences. If both co-ordinates of a centroid pair are not significantly different, then the two centroids can be considered as having the same location, and consequently, the centroid displacement and direction of movement, relative to the origin, are also likely to be identical, although such a test is not strictly valid. If, however, one of the co-ordinates is significantly different, the interpretation becomes more complex, and depends on the relative magnitudes of the x and y co-ordinates. If the co-ordinates which are statistically similar are considerably larger than the other ones, then the displacement and transport direction may also be statistically similar, because the larger values contribute most to the determination of these quantities - see equations (6.27) and (6.28). When the absolute values of both co-ordinates are approximately equal, however, no conclusion is possible.

It is of interest to use the above concepts to investigate further the effects of using the statistical zero contour as the limit of the distributions instead of the absolute zero contour. It has been seen that the use of the former limit results in a reduction of the recovery efficiency in most cases. Testing of the centroids determined for the

two distributions shows, however, that both of the co-ordinates for eleven of the seventeen pairs are not significantly different at 95% (see for example Figure 6.7); and that only one of the remaining six pairs shows a significant difference for both co-ordinates. This indicates clearly that the exclusion of the tails of the distribution does not harm the estimate of the centroid. Furthermore, the elimination of the low concentration in the tails decreases the average standard deviation of the centroid co-ordinates, from 2.54 m and 0.90 m in the x- and y-directions for distributions using the absolute zero limit, to 1.44 m and 0.37 m, respectively, using the statistical zero limit.

From the discussion of the potential errors presented in this section, it is evident that the use of tracers in a natural setting is subject to many problems, and that the results may be of low accuracy and reliability. The attempts that have been made to quantify the various factors are only partially successful, because many of the sources of error or imprecision cannot be included in the analysis at present. The calculated recovery efficiencies and centroid standard deviations do, however, provide valuable rough guidelines in determining the reliance that can be placed on any specific piece of data. In the end, the validity of the results, which are to be presented in the next section, can only be judged using sedimentological insight.

## 6.4 Sediment Transport Description

### 6.4.1 General Results

The results of all tracer experiments in which there is sufficient recovery to allow the calculation of moments are listed in Table 6.2, and several representative tracer distributions are shown in Figures 6.7 to 6.14. In this section, the general features of these data will be discussed, and unless otherwise stated, all distributions with a recovery efficiency greater than 10%, regardless of the fraction involved, have been included in the analysis. The effects of grain size are to be considered separately in Section 6.4.2, and the patterns and rates of sediment transport on the various bars are discussed in detail in Section 6.4.3.

Examination of the data in Table 6.2 and Figures 6.7 to 6.14 reveals that all stations and tracer fractions experience some amount of residual transport, such that the centroid of the tracer distributions, and very often the mode as well, become displaced from the origin, regardless of the recovery efficiency. Indeed, no case exists in which the centroid and the origin are statistically indistinguishable (both co-ordinates statistically similar) at the 95% probability level. The speed of centroid migration does show wide variation from location to location, however. The average migration speed for all data sets with a recovery

Figure 6.8 Distribution of tracer at Buoy 1, Diamond Bar.

Distribution after four tidal cycles shown by diagonal ruling and open star. Distribution obtained at sixteen tidal cycles contoured (heavy lines - solid star). Characteristics of both distributions given; all units in metres. X-direction parallel to long axis of distributions.

## DIAMOND BAR - Buoy I

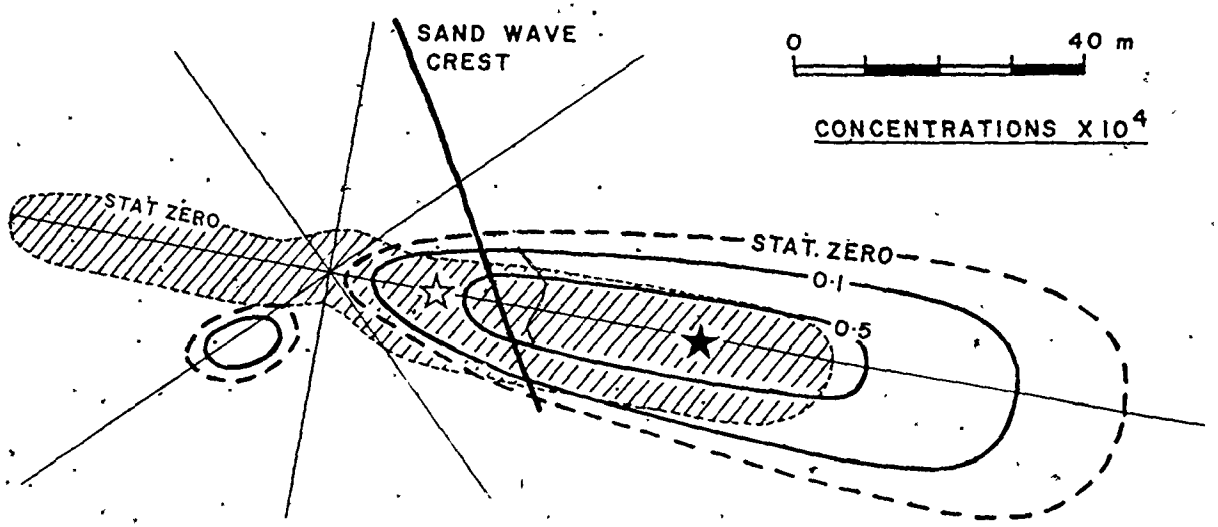


☆ T = 4 Cycles ($R_E$ = 52·1%)

| | Mean | St. Dev. | Skew. |
|---|---|---|---|
| X | 14·58 | 13·89 | 0·59 |
| Y | -0·58 | 1·76 | -2·04 |

★ T = 16 Cycles ($R_E$ = 21·3%)

| | Mean | St. Dev. | Skew. |
|---|---|---|---|
| X | 52·76 | 24·30 | -0·01 |
| Y | -1·17 | 6·67 | 0·03 |

Figure 6.9 Distribution of tracer at Buoy 6, Big Bar, after 27 tidal cycles.

Traction fraction distribution shown by diagonal ruling and open star. Intermittent suspension distribution contoured; samples used to define this distribution are shown by dots. Statistical zero limit used for both fractions.

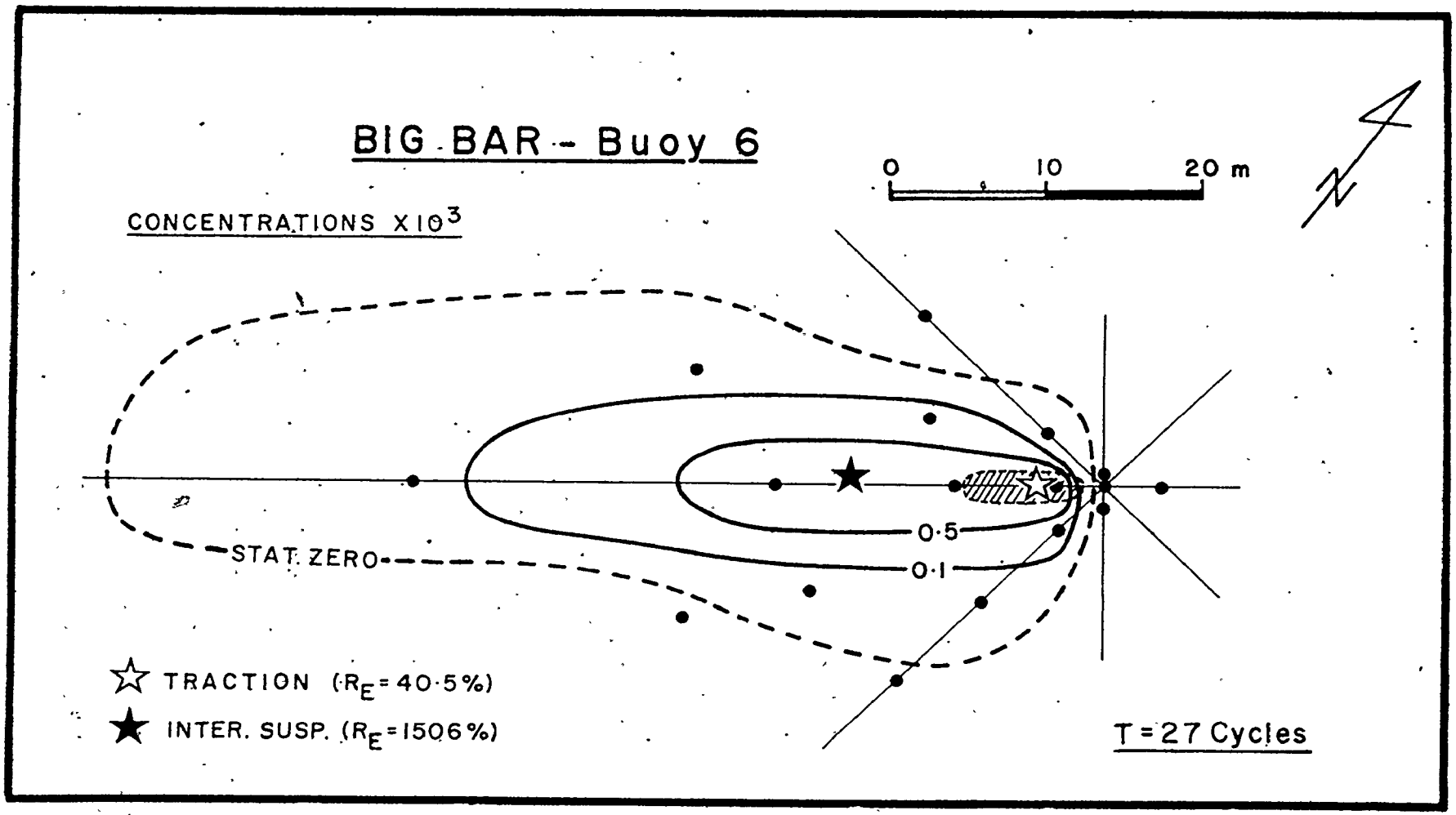
BIG BAR - Buoy 6
0
10
20 m
N
CONCENTRATIONS X10³
0·5
0·1
STAT. ZERO
TRACTION (R_E = 40·5%)
INTER. SUSP. (R_E = 1506%)
T = 27 Cycles

Figure 6.10 Tracer distributions at Buoy 4, Big Bar, after 27 tidal cycles.

See Figure 6.9 for further comments.

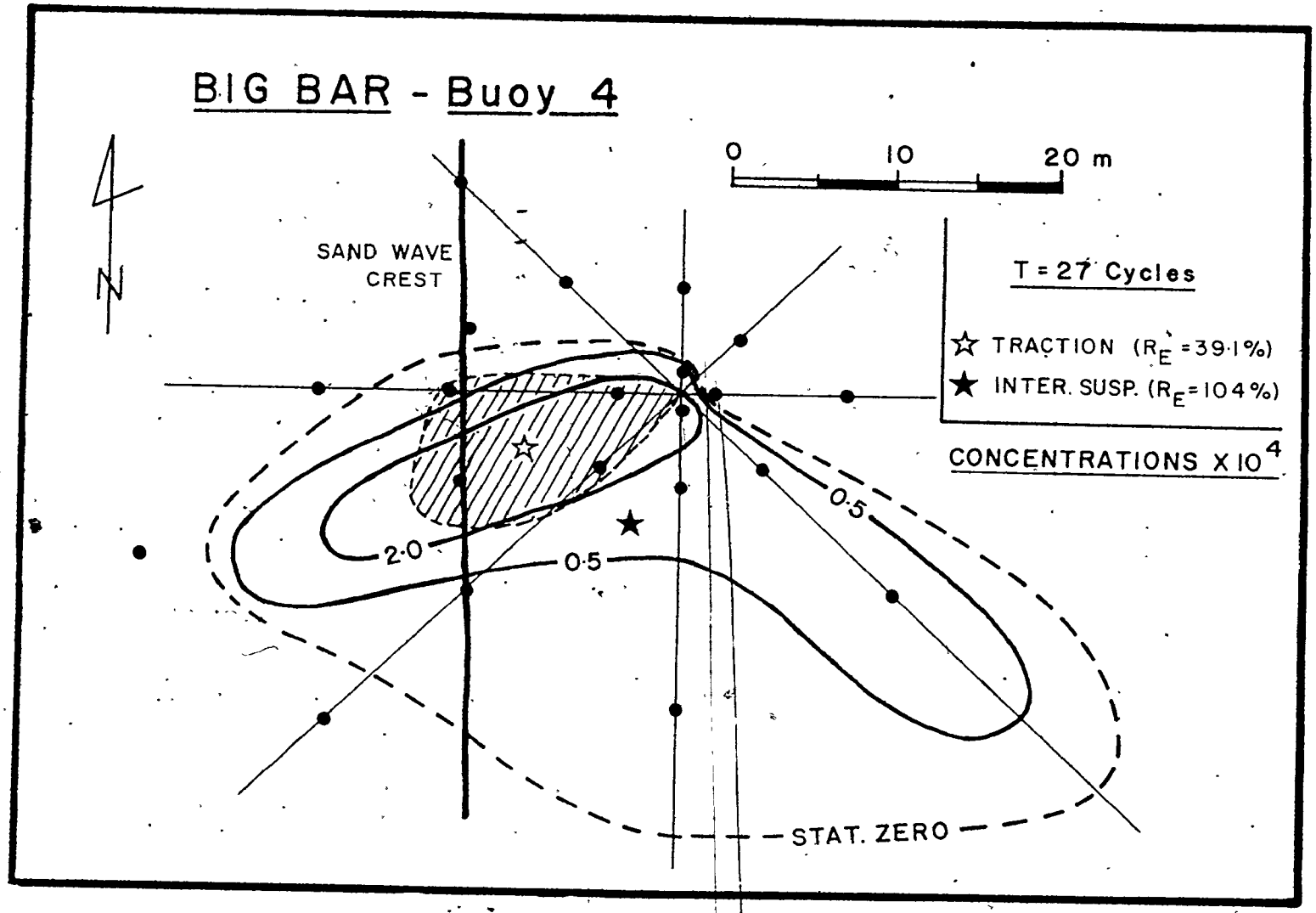
BIG BAR - Buoy 4
0
10
20 m
N
SAND WAVE CREST
T = 27 Cycles
TRACTION ($R_E$ = 39·1%)
INTER. SUSP. ($R_E$ = 10·4%)
CONCENTRATIONS X $10^4$
2·0
0·5
0·5
STAT. ZERO

Figure 6.11 Tracer distributions for the intermittent suspension fraction at Buoy EP4, Economy Point.

Contoured tracer distributions and their characteristics are shown for elapsed times of 4 tidal cycles (light contours with diagonal ruling and solid star) and 19 tidal cycles (heavy contours and open star). Means and standard deviations have units of metres.

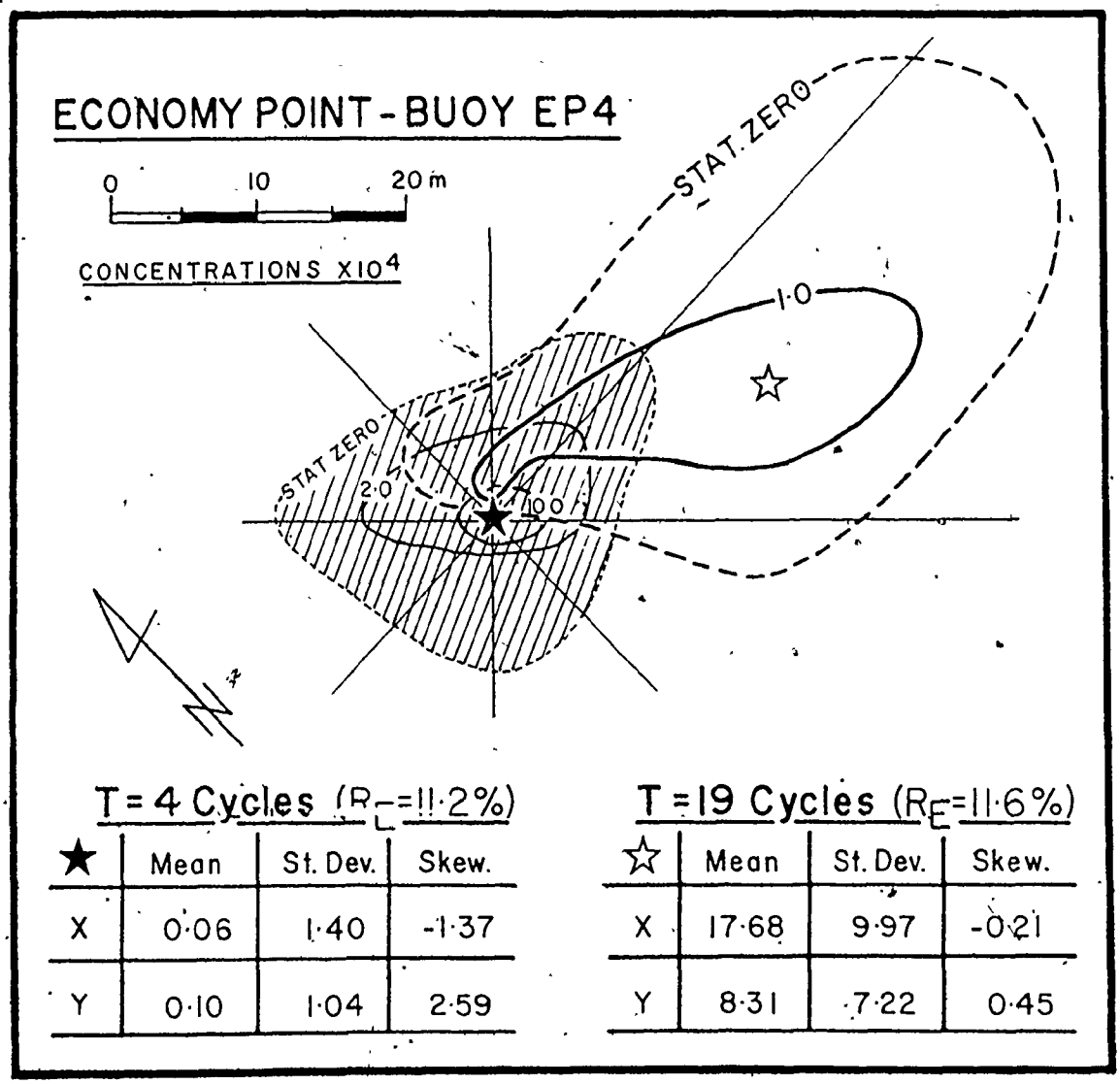


T = 4 Cycles ($R_E$ = 11·2%)

| ★ | Mean | St. Dev. | Skew. |
|---|---|---|---|
| X | 0·06 | 1·40 | -1·37 |
| Y | 0·10 | 1·04 | 2·59 |

T = 19 Cycles ($R_E$ = 11·6%)

| ☆ | Mean | St. Dev. | Skew. |
|---|---|---|---|
| X | 17·68 | 9·97 | -0·21 |
| Y | 8·31 | 7·22 | 0·45 |

Figure 6.12 Tracer distribution for the intermittent suspension fraction, at Buoy EP7, Economy Point.

Elapsed time = 19 tidal cycles. Dots give locations of analysed samples. Heavy diagonal lines are the brinks of flood-asymmetric sand waves. Means and standard deviations in metres.

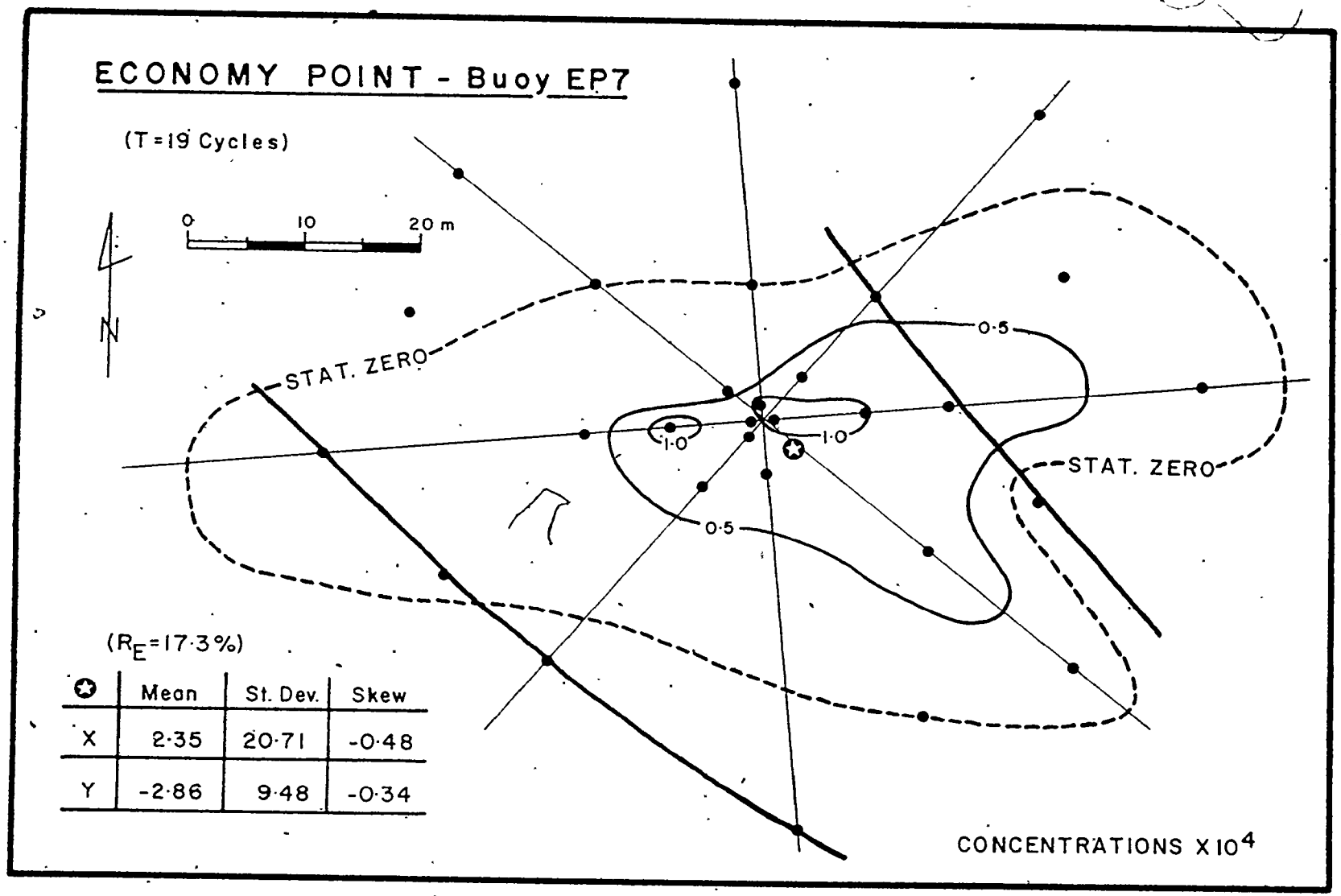


| ✪ | Mean | St. Dev. | Skew |
|---|---|---|---|
| X | 2·35 | 20·71 | -0·48 |
| Y | -2·86 | 9·48 | -0·34 |

Figure 6.13 Distribution of tracer fractions at Buoy 3, Diamond Bar.

Elapsed time = 4 tidal cycles. Legend of symbols given at right. Disp. = centroid displacement from the origin, in metres. Statistical zero limit shown for all fractions. The distribution for fraction V has not been included because of its large size.

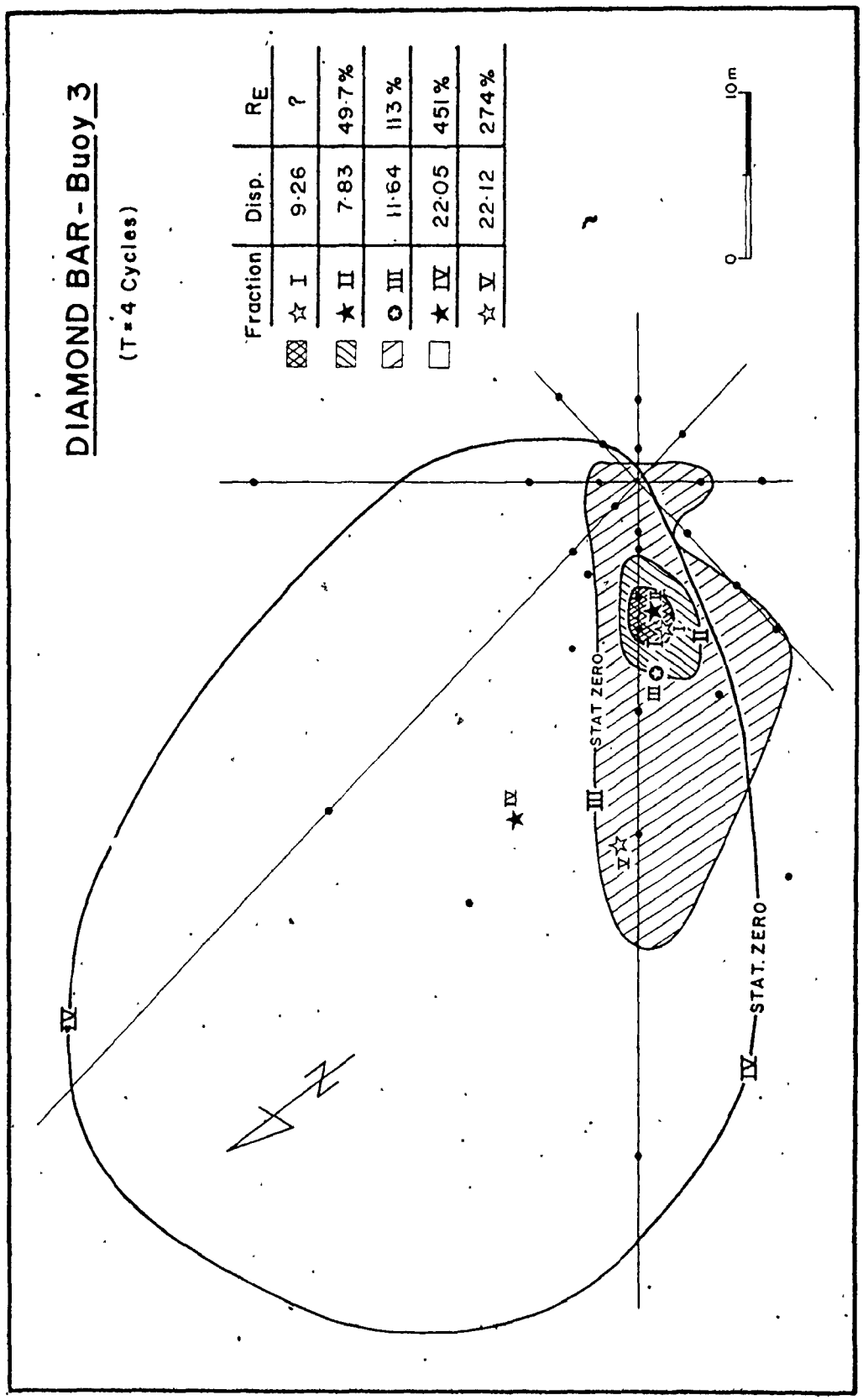
DIAMOND BAR - Buoy 3
(T = 4 Cycles)
Fraction | Disp. | RE
☆ I | 9·26 | ?
★ II | 7·83 | 49·7%
○ III | 11·64 | 113%
★ IV | 22·05 | 451%
☆ V | 22·12 | 274%
10m
0
STAT ZERO
STAT. ZERO
N

Figure 6.14 Distribution of tracer fractions at Buoy EP3, Economy Point.

Elapsed time = 4 tidal cycles. Legend of symbols given at upper right. Disp. = centroid displacement from the origin in metres. Statistical zero limit shown for all fractions.

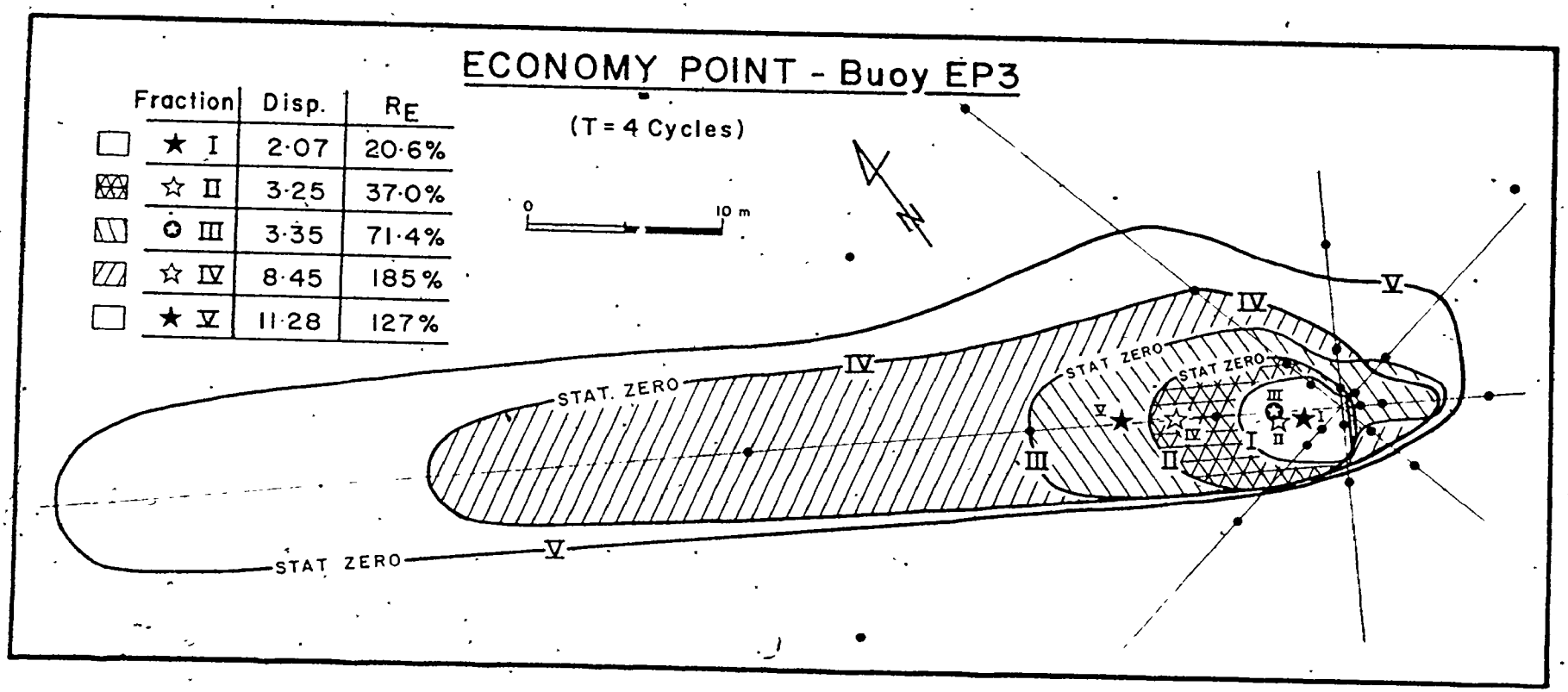
ECONOMY POINT - Buoy EP3
(T = 4 Cycles)
Fraction | Disp. | RE
★ I | 2·07 | 20·6%
☆ II | 3·25 | 37·0%
✪ III | 3·35 | 71·4%
☆ IV | 8·45 | 185%
★ V | 11·28 | 127%
0
10 m
N
STAT. ZERO
STAT ZERO
STAT ZERO
STAT ZERO
I
II
III
IV
V

efficiency greater than 10% is 1.33 m/tidal cycle, but values range from 0.05 m/cycle (Selmah Bar, Buoy 1, first sampling with the absolute zero limit) to 6.46 m/cycle (Selmah Bar, Buoy 4, first sampling, absolute zero limit). It is significant that these values are nearly two orders of magnitude less than the average migration speed of 100 metres per tidal cycle quoted by Balazs and Klein (1972) for Big Bar. By contrast, the present data (Table 6.2) indicate that the average value for that area is 0.63 m/cycle.

As might be expected, the migration rate of the centroid is generally faster where the current strength and the time-velocity asymmetry is greatest. Compare for instance the results for the neap- and spring-tide experiments (tidal coefficients 0.65 and 0.90, respectively) conducted at Economy Point, Buoy EP7 (Table 6.2). These values show that the migration speed of the intermittent suspension fraction is more than 10 times greater during the spring tides. Buoy EP4 at Economy Point (Figure 6.11) also displays a similar behaviour: the first sampling ($V_c$ = 0.02 m/cycle) was conducted at neap tide (Tr = 0.62), whereas the second set of samples ($V_c$ = 1.03 m/cycle) was collected following a period of large tides (Tr = 0.90). The influence of current strength on the migration speed will be considered in more detail in the next section when the effect of grain size is discussed.

The direction of centroid movement (Table 6.2) is in most cases consistent for both samplings of a tracer distribution. At a few locations, such as Diamond Bar, Buoy 7, and Selmah Bar, Buoy 4, a considerable difference exists between the flow direction and the migration directions determined for the first and second samplings. In these cases, however, the recovery efficiencies are very low, suggesting that the tracer results are spurious. For most of the distributions, the transport direction is generally in close agreement with the flow direction of the dominant currents (part A of Figures 3.13, 3.15, 3.16, and 3.17). It is notable that in 78.9% of the cases, the centroid shows movement in an upslope direction. It is also interesting to note that in all cases where tracer experiments have been conducted on large, megarippled sand waves (Diamond Bar, Buoy 1 - Figure 6.8; Big Bar, Buoy 4 - Figure 6.10; Economy Point, Buoy EP7 - Figure 6.12; and Selmah Bar, Buoy 1), the transport direction and the greatest elongation of the tracer distribution is at an angle of approximately 45° to the sand wave strike. This skewed orientation was mentioned as a characteristic of large sand waves in Section 4.2.1. The orientations of the megaripples superimposed on the sand waves are in much better agreement with the tracer transport results. Further comments on the patterns and rates of sediment transport on each of the bars are reserved for

Section 6.4.3.

The pattern of tracer dispersion at each site, as indicated by the shape of the tracer distributions, varies greatly between sites (Figures 6.7 to 6.14). For example, the distribution shown in Figure 6.11 for Economy Point, Buoy EP4 after two tidal cycles (diagonal shading) displays nearly equal dispersion in all directions (elongation ratio ($E_\ell$) = 1.35), with the mode and centroid remaining approximately at the origin. On the other hand, the distribution obtained after four tidal cycles at Buoy 1 on Diamond Bar (Figure 6.8, diagonal shading) ($E_\ell$ = 7.86) is an example from the other extreme, in which the longitudinal dispersion is much greater than the lateral dispersion. This example shows two lobes of tracer, one on either side of the origin, 180° apart, produced by ebb and flood transport of tracer. The mode is, however, displaced eastward from the origin. This flood-current dominance is even more clearly displayed in the distribution present after fifteen tidal cycles (Figure 6.8 - heavy lines) because the ebb-produced lobe has dissipated, leaving only the flood lobe.

Most of the distributions display simple forms that are similar to those just described for Buoy 1 on Diamond Bar (Figure 6.8), with either a single lobe, or at most two that are 180° apart. A number of the distributions do, however, show more complicated patterns of transport and

dispersion, having two lobes separated by an angle other than 180° (for example the intermittent suspension fraction at Buoy 4, Big Bar - Figure 6.10), or even three lobes (intermittent suspension fraction at Buoy EP7, Economy Point - Figure 6.12). In the latter case, the lobe extending to the southeast may be due to the presence of a secondary, spiral flow that is produced as the flood currents interact with the large megarippled sand waves that lie at an oblique angle to the flow. No satisfactory explanation can be given for the pattern obtained at Buoy 4 on Big Bar (Figure 6.10) in which the southeastern lobe lies at almost 90° to the principal current direction (Figure 3.13A).

The size of the tracer distributions also varies greatly from place to place, with standard deviations, ranging from 0.58 to 46.98 m in the x-direction, and from 0.32 to 17.17 m in the y-direction. As indicated in the above descriptions, the tracer distributions are generally elongated parallel to the transport direction and to the predominant flow direction, which is approximately equivalent to the x-axis of the chosen grid in most cases. Elongation ratios range from 0.76 to 8.32, with an average value of 3.57, which implies that longitudinal dispersion is more than three and a half times greater than the lateral dispersion. The distribution defined by the statistical zero contour at Buoy 3 on Selmah Bar (Figure 6.7) has an elongation that is close to the average value. This

inequality in the longitudinal and lateral dispersion appears (qualitatively) to be much greater than that produced by waves alone. Compare, for example, the above mentioned distribution with those shown by Murray (1967, Figure 2) from a wave-dominated environment.

The results also show that the rate of dispersion, as measured by the standard deviation divided by the elapsed time, tends to increase as the migration rate and flow strength increases. A regression of the longitudinal dispersion rate against the migration speed for the intermittent suspension fraction of Type 2 experiments gives a correlation coefficient of 0.92 (number of points = 14), which is significant at greater than 99%. In addition, positive but non-significant correlations are obtained for the regression of the longitudinal dispersion rate on both the maximum mean current speed ($r = 0.41$) and the average maximum shear velocity ($r = 0.27$). In the analysis, only distributions derived from the first samplings were used, in order to eliminate the effect of elapsed time that is discussed below.

The skewness of the distributions varies considerably as well, with absolute values ranging up to 5.39 in the x-direction and 10.96 parallel to the y-axis. Although the direction of the skewness is somewhat erratic, there is a tendency for the distributions to be skewed in the direction of residual transport. If the end of the x-axis lying

closest to the transport direction is considered positive, then the average skewness is +0.60. This behaviour is identical to that observed in unidirectional flows (Crickmore, 1967; Crickmore and Lean, 1962a; Hubbell and Sayre, 1964), although the degree of asymmetry appears to be less in the tidal case, presumably because of the reversing currents. As might be expected, skewness transverse to the transport direction (along the y-axis) shows no preferred orientation. If skewnesses to the left of the line of transport are considered positive, the average value is only -0.14, which implies that the dispersion is laterally symmetrical and that the transport process is essentially isotropic, unless prominent bedforms are present as in the case of Buoy EP7, Economy Point (Figure 6.12). The gravitational component resulting from the slope of the bed also appears to have little general influence on the dispersion (average value = -0.06; up-slope being positive), although in some cases down-slope extensions are seen which may result from lateral flow off the bar during emergence.

It is also of interest to examine the nature of the tracer transport and dispersion as a function of time. Examination of data in Table 6.2 and the examples shown in Figures 6.8 and 6.11 reveals as expected that the transport distance and the amount of dispersion increases with the elapsed time. A comparison of the migration speeds calculated for the first and second samplings shows, however, that

the migration speed generally decreases as time increases: the average migration speeds for the first and second samplings of all distributions, for which results are available at two times, are 1.34 and 0.63 m/cycle, respectively. Similarly, the rate of dispersion for these same distributions decreases as time increases. For the first samplings, at elapsed times of two to five tidal cycles, the average rates of dispersion in the x- and y-directions are 2.34 and 0.81 m/cycle; whereas for the subsequent sampling (elapsed times of 16 to 27 tidal cycles), the values have dropped to 0.43 and 0.15 m/cycle, respectively.

The rapid initial transport and dispersion observed at the first sampling is the result of the exposed position of the tracer on the bedform stoss sides when first injected, and the incomplete mixing of the tracer and natural sediment (Crickmore, 1967). Because of the above, the values obtained during this "accommodation" period (deVries, 1966) are not representative of the average behaviour of all sediment particles in the mobile layer. As the mixing becomes more thorough, however, the rates should gradually stabilize at near constant values (Yang and Sayre, 1971), with of course periodic variations due to the influence of tidal range. Therefore, the absolute values of the transport velocities, dispersion rates, and sediment discharges calculated from the second samplings can be expected to be more representative

than those from the first samplings. The inclusion of $p_\delta$ (the proportion of the mobile layer reworked) in the definition of the effective thickness of the mobile layer (equation 6.33) does, however, provide a partial solution to this problem with regard to the calculated sediment discharges (equation 6.31). All distributions are also likely to be affected in a similar manner, so that any relationships present should not be altered. As a result, values from the first samplings are often used exclusively as mentioned above, because a larger number of values are available and recovery efficiencies are higher. In addition, the range of elapsed times for the first samplings (2 to 5 tidal cycles) is less than for the subsequent samplings (16 to 27 tidal cycles).

Further examination of the data shows that the tracer distributions also tend to become more symmetrical with time, as shown specifically by Figures 6.8 and 6.11. In the x-direction, the average absolute values of the skewness for the first and second samplings of all distributions are 1.21 and 1.04; in the y-direction the respective values are 1.51 and 0.91. (All possible distributions for which two samplings are available have been used, regardless of the recovery efficiency.) It is significant that an identical behaviour is also observed for tracer distributions in unidirectional flows (Hubbell and Sayre, 1964; Yang and Sayre, 1971).

The fact that the third moment of the tracer distributions, which is the most sensitive to error of the parameters calculated, can provide useful information is encouraging in itself. It appears, therefore, that the effects of truncating the distributions at the statistical zero contour, and of other sources of error, although potentially important, are not as severe as they could be.

It is notable that there are basic similarities in the transport and dispersion of sediment between the tidal and fluvial or flume situations. The reversing flow and resulting bidirectional transport does have some influence, though, on the longitudinal skewness as noted above, and on the longitudinal dispersion, which should be greater than in unidirectional flow. Despite the greater dispersion, it is probable that the accommodation time in the tidal environment is greater than in unidirectional flow, because of the substantially lower net transport rate, as indicated by the bedform migration studies reported in Section 4.2.2. These differences are relatively minor, however, and do not negate the basic similarities that exist between the residual transport in this tidal environment and the transport occurring in unidirectional flow. It appears, therefore, that the findings of the present study may be more universally applicable than would initially be suspected.

### 6.4.2 Transport of Size Fractions

The transport behaviour of different grain sizes has long been of interest to both sedimentologists and engineers, but little quantitative work has been devoted to the subject. It is for this reason that the Type 1 tracer experiments were conducted. Further general information is also available from the coarse (traction) and fine (intermittent suspension) fractions separated during the processing of the Type 2 experiments. Unless otherwise stated, only values derived from the first samplings will be used regardless of the recovery efficiency for the reasons outlined above, and because these data sets are more complete than those from the subsequent sampling. In addition, all values obtained from the first samplings on Selmah Bar, with the exception of Buoy 2, have been included with the intermittent suspension values.

As was mentioned above, the areal distributions of tracer concentration for all five of the size fractions in the Type 1 experiments (Figures 6.13 and 6.14) generally have a simple form, most commonly with only one lobe. There are systematic differences in the size and shape of these distributions, however, that are a function of the grain size (Figure 6.15).

In Fig. 6.15A it can be seen that both the longitudinal and lateral dispersions (standard deviations in the x- and y-directions) increase as the grain size decreases.

In both directions, the rate of increase is low and fairly uniform for the coarsest three sizes, but increases much more rapidly for fractions IV and V (medium and fine sand, respectively). Furthermore, because the elapsed time is the same for all sizes in a single experiment, these differences in the standard deviations between sizes also imply that the rates of dispersion increase in both directions as the size decreases. Despite the similarities in the patterns, it is evident that the longitudinal dispersion increases at a faster rate than the lateral dispersion. As a result, the elongation ratio also becomes larger for the finer grain sizes, but at an almost constant rate (Figure 6.15A).

The features just described can also be seen in the data for individual sites (Table 6.2; see also Figures 6.13 and 6.14), indicating that the inclusion of distributions with low recovery efficiences has not influenced the trends significantly. The average values calculated for the traction and intermittent suspension fractions also conform with the trends shown in Figure 6.15A. For these two fractions, the longitudinal standard deviations are 1.79 m and 11.19 m, respectively, and the lateral dispersions are 0.61 m and 3.77m, giving elongation ratios of 2.60 and 3.46 for the traction and intermittent suspension fractions.

The trend noted in Figure 6.15A for the rate of lateral dispersion to be inversely related to the grain

Figure 6.15 Variation of dispersion characteristics with grain size.

A - Average longitudinal and lateral dispersion as a function of elapsed time, and elongation ratio versus grain size;
B - Longitudinal and lateral dispersion as a function of centroid migration distance versus grain size;
C - Longitudinal and lateral skewness versus grain size;
D - Transport direction versus grain size.
Points plotted at the middle of the nominal size range of each tracer fraction (see Figure 6.3). See text for further comments.

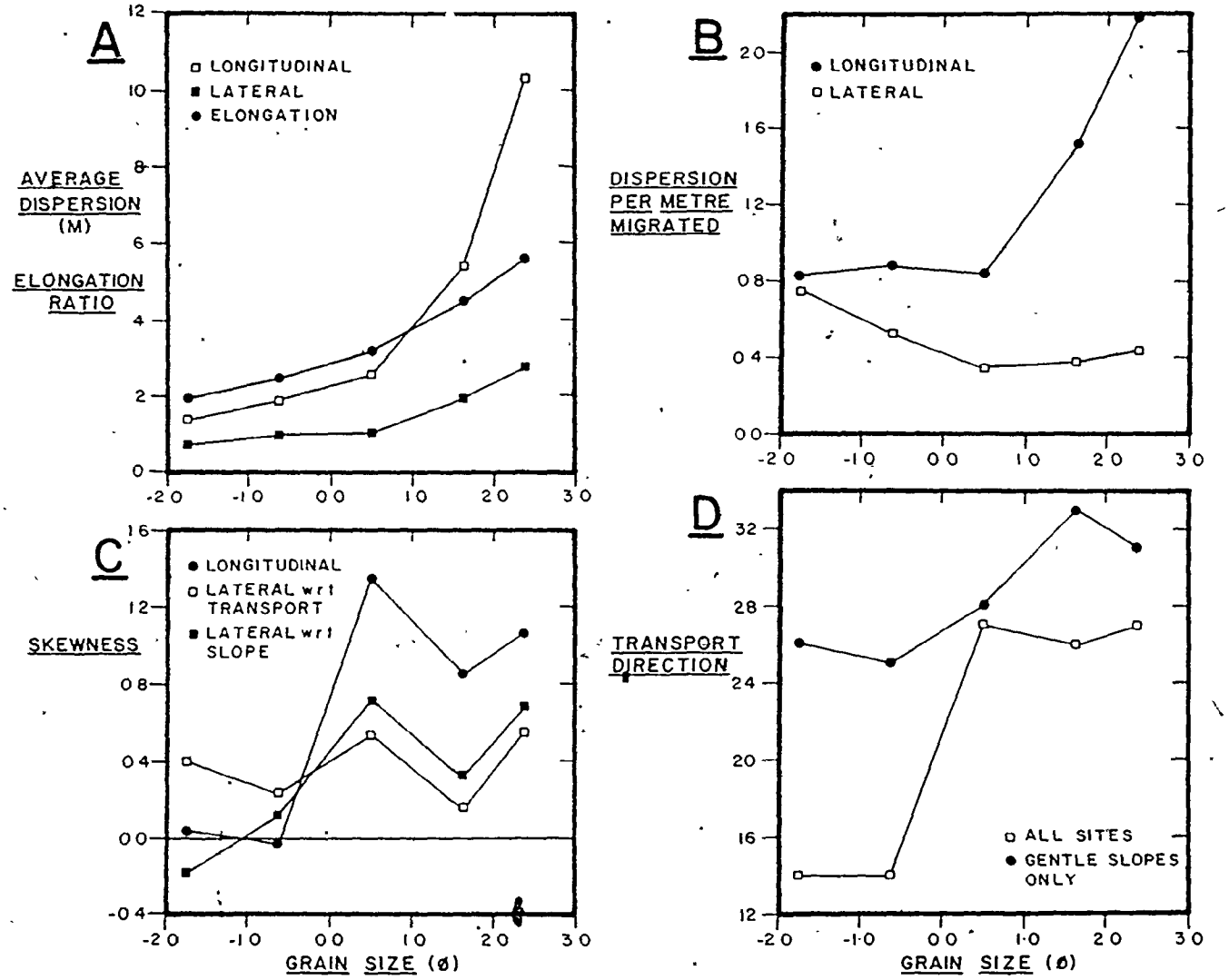
A
LONGITUDINAL
LATERAL
ELONGATION
AVERAGE DISPERSION (M)
ELONGATION RATIO
B
LONGITUDINAL
LATERAL
DISPERSION PER METRE MIGRATED
C
LONGITUDINAL
LATERAL wrt TRANSPORT
LATERAL wrt SLOPE
SKEWNESS
GRAIN SIZE (ø)
D
ALL SITES
GENTLE SLOPES ONLY
TRANSPORT DIRECTION
GRAIN SIZE (ø)

size would appear at first glance to be the opposite of that observed by authors who have used either the time-integration or the steady dilution tracer technique in unidirectional flow (Crickmore and Lean, 1962b; Kennedy and Kouba, 1970). The apparent discrepancy is, however, a function of the methods used: in this study, the dispersion rates have been standardized with respect to the elapsed time, and not to the migration distance; whereas in time-based methods, the migration distance is a constant and the time is variable. If the various standard deviations are divided by the centroid migration distance, quite different patterns result (Figure 6.15B). The amount of longitudinal dispersion per metre of migration remains virtually constant for the coarsest three fractions, and then increases steeply for the finer grain sizes. The rate of lateral dispersion by comparison exhibits the opposite trend, with the dispersion rate per metre decreasing as the grain size decreases for fractions I to III, and then remaining nearly constant, or increasing slightly for fractions IV and V. This variation in the rate of lateral dispersion is not inconsistent with the observations of either Crickmore and Lean (1962b) or Kennedy and Kouba (1970). The reasons for the different behaviour of the various sizes will be discussed at the end of this section.

The variation of average skewness with grain size

(Figure 6.15C) does not show consistent patterns as was the case with the standard deviations.

The longitudinal skewness (parallel to the x-axis), calculated with the direction of transport as positive, is strongly positive for the finest three fractions, whereas the distributions for fractions I and II are very nearly symmetrical. The average value shown for fraction III is believed to be somewhat high, however, due to the inclusion of one unusually large positive skewness. If this one value is omitted, the result reduces to 0.85, suggesting that the longitudinal skewness might become increasingly positive as the grain size decreases.

The skewness parallel to the y-axis (skewnesses to the left facing down-movement considered as positive) is positive for all size fractions, but shows no trend with respect to grain size. No sedimentological reason can be given for this behaviour, specifically as it was noted in Section 6.4.1 that the overall average skewness defined in this manner is negligible. It is possible that a consistent error was made in selecting the orientation of the sampling grid, so that the centre of gravity does not lie on the x-axis, thereby introducing an apparent lateral skewness. Lateral skewness defined in terms of the slope of the bar surface (up-slope being positive) shows a trend similar to that of the longitudinal skewness, with negative or near

zero values for the coarsest two fractions, and positive skewnesses for the finest three fractions. This suggests that the finer grain sizes might have a greater tendency to move up-slope than coarser material.

Examination of the direction of movement for each fraction (Table 6.2) with respect to the strike of the bar surface supports with contention (Figure 6.15D). (In calculating the averages shown in Figure 6.15D, the angle between the transport direction and the bed strike is considered to be positive if the transport is directed up-slope, and negative if down-slope.) When the values from all nine sites are considered, a clean break is evident between fractions II and III, with the transport of the finer three size fractions directed more than ten degrees further up-slope than the coarser fractions. It is notable that all five fractions experience an up-slope movement; indeed, only fractions I and II at Buoy 2, Big Bar have down-slope centroid displacements. As might be expected, the influence of gravity on the transport direction is greatest at those places where the slope is steepest (Table 6.2), namely Big Bar, Buoy 2, and Diamond Bar, Buoy 3 (Figure 6.13) (see Figure 6.2 for locations). When the values from these two sites are excluded from the averages (Figure 6.15D), the difference in transport direction between the sizes is much less, but a tendency nevertheless remains for the finer

sizes to be transported in a more up-slope direction than coarser material.

The most significant finding of the Type 1 tracer experiments is the variation of transport speed (migration speed of the centroid) with grain size. Figure 6.16A shows the average value for each fraction and an overall trend toward increased speed for finer grain sizes is evident as expected intuitively; the rate of increase, however, is not regular. The transport speed for the coarsest three fractions remains almost constant and increases only slightly as the grain size decreases. A sharp change in behaviour then occurs, and fractions IV and V show a marked increase in transport speed as the grain size continues to decrease in the medium and fine sand grades. The plots of centroid migration speed for each site individually (Figure 6.16B) contain greater scatter, but the same general trend is evident in every one (see also Figures 6.13 and 6.14) despite significant variations in the recovery-efficiencies and in the speed of movement between sites.

The difference in behaviour shown by the material coarser and finer than approximately 1.0 phi (0.5 mm) is further emphasized by the data in Table 6.3 which shows the number of sites at which the indicated pairs of centroids are not significantly different. In constructing this table, centroid pairs have been designated as not significantly

Figure 6.16 Transport speed versus grain size.

A - Average values;
B - Results for each experimental site.
Points plotted at the middle of the nominal size range of each tracer fraction (see Figure 6.3).

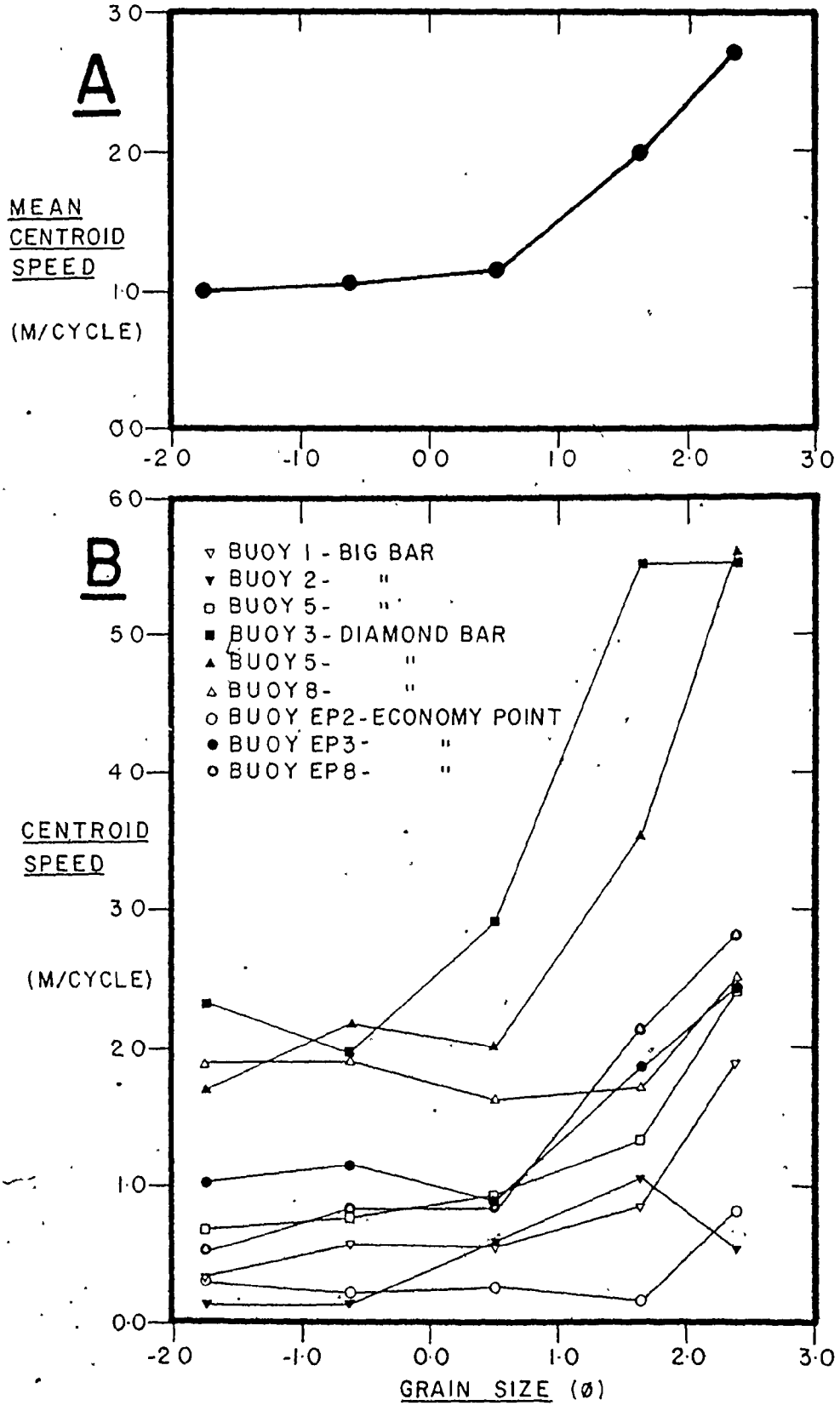
A
MEAN CENTROID SPEED
(M/CYCLE)
3·0
2·0
1·0
0·0
-2·0
-1·0
0·0
1·0
2·0
3·0
B
BUOY 1 - BIG BAR
BUOY 2- "
BUOY 5- "
BUOY 3 - DIAMOND BAR
BUOY 5- "
BUOY 8- "
BUOY EP2 - ECONOMY POINT
BUOY EP3- "
BUOY EP8- "
CENTROID SPEED
(M/CYCLE)
6·0
5·0
4·0
3·0
2·0
1·0
0·0
-2·0
-1·0
0·0
1·0
2·0
3·0
GRAIN SIZE (ø)

Table 6.3 Comparison of Centroid Locations for Different Size Fractions. Tabulated values give number of centroid pairs whose positions are not significantly different at the 95% level, according to equation (6.44)

| Fraction | II | III | IV | V |
|---|---|---|---|---|
| I | 3 | 4 | 0 | 1 |
| II | - | 4 | 1 | 0 |
| III | - | - | 1 | 2 |
| IV | - | - | - | 4 |

different if the value of $\alpha$ obtained from equation (6.44) for the larger of the two co-ordinates is greater than 5%. Based on this definition, one third to one half of the sites show no significant difference between any of the coarsest three fractions. On the other hand, the centroids of these three fractions are generally significantly different from those obtained for fractions IV and V. These two fractions in turn are often not different from each other. This last point is not believed to be significant, however, but rather to reflect only the greater dispersion of these finest sizes.

Average centroid migration speeds calculated for the traction and intermittent suspension fractions (0.40 and 1.64 m/tidal cycle, respectively) also indicate a marked increase in the transport speed as the grain size decreases. The reasons for these differences will be discussed below.

An examination of the differences in transport speeds between buoy locations (Figure 6.16B) suggests that current strength has a strong influence on the speed of movement of all grain sizes. In order to test this, the migration speeds determined for each fraction have been regressed against four measures of current strength: (i) the maximum mean speed; and (ii) the average maximum shear velocity, both evaluated for the dominant half of the tidal cycle; (iii) the difference between the cube of the maximum mean speeds for the ebb and flood, which is a measure of the potential transport asymmetry

as described in Section 4.2.2 and equation (4.3); and (iv) the total combined stream power ($\omega$) as given in Figure 3.14, which is the sum of the stream power integrated over both the ebb and flood portions of the tidal cycle. For each buoy location, the values used for the first three parameters listed above have been evaluated for the tidal cycle with the tidal coefficient closest to that occurring at the time when the tracer samples were collected. If, however, the time-velocity asymmetry is not in agreement with the tracer transport direction, the site was excluded from the regression.

The correlation coefficients of the four relationships evaluated are given in Table 6.4 for all five size fractions. Of the twenty listed, 12 are significant at more than the 99% level, despite the fact that only 7 to 9 points are available to define each relationship. Only 3 of them are significant at less than 95%. This indicates that the transport speed of all sizes, regardless of their individual behaviour, is strongly controlled by the hydraulics. Of the four hydraulic variables used, the total combined stream power gives the best overall correlations. It is also notable that the shear velocities produce better results than the mean current speeds.

The correlation coefficients listed in Table 6.4 give little indication that the degree of hydraulic control varies with grain size. It is possibly of importance,

Table 6.4 Hydraulic Control on the Speed of Size-Fraction Movement. Correlation coefficients for the linear regression of centroid migration speed for each size fraction in the Type 1 experiments on the various measures of current strength listed on the left

| Migration Speed Versus | Fraction I | II | III | IV | V |
|---|---|---|---|---|---|
| Max. Mean Speed | 0.76* | 0.88** | 0.68 | 0.64 | 0.79* |
| Average Max. Shear Velocity | 0.82* | 0.76* | 0.89** | 0.86** | 0.96** |
| Transport Potential Asymmetry $\lvert U_E^3 - \bar{U}_F^3 \rvert$ | 0.82* | 0.92** | 0.38 | 0.95** | 0.95** |
| Total Stream Power | 0.96** | 0.89** | 0.91** | 0.89** | 0.84** |

* significant between 95% and 99%

** significant at greater than 99%

however, that the three lowest correlation coefficients occur for fractions III and IV which lie on either side of the break in slope that is present in the plots of dispersion (Figure 6.15A and B) and migration speed (Figure 6.16A) versus grain size. A closer examination of the individual trends in Figure 6.16B reveals that there is a weak tendency for the position of the break in slope to be displaced toward coarser grain sizes as both the overall speed of movement and the current strength increase. For example, at Buoy 1 on Big Bar, the transport speed remains essentially constant for fractions I through IV, and increases only for the finest fraction. On the other hand, the values for Buoy 3 on Diamond Bar, where all fractions move more rapidly, suggest that the change in behaviour occurs between fractions II and III. Thus, at low current strengths, fractions III and IV behave similarly to coarser material, whereas at greater strengths, they both may act more like fraction V.

The results reported here regarding the relationship of centroid migration speed and grain size are at variance with those obtained in a number of other studies, particularly those in which bedforms are absent. Meland and Norrman (1966) measured the velocity of single particles over a fixed bed of similar grains, and found that the speed of movement increased continuously as the particle size increased, for particles coarser than medium sand. In a later set of flume

experiments using a fully mobile bed, but without well developed bedforms, Meland and Norrman (1969) observed that in the size range from 0.25 to -3.0 phi (0.84-8.00 mm) the most rapid movement occurred at approximately -1.0 phi (2.0 mm). Rathbun et al. (1971) have also found that the particle speed increases as the grain size increases for sizes between 0.7 and 0.2 mm (0.5-2.3 phi) for the upper flow regime condition in a natural environment. They did, however, observe a sharp increase in the speed of still finer particles and ascribed it to the onset of suspension. The reason for the direct relationship between transport speed and particle diameter over a wide range of sizes on a plane bed is presumably the result of the decreasing influence of bed roughness on particle motion as the size increases (Meland and Norrman, 1969; Rathbun et al., 1971). When bedforms are present, however, a direct relationship between speed and size is not observed when the transport is averaged over a long time period. Rather, the rate of movement is found to increase continuously as the size decreases between 0.1 and 0.6 mm (3.3-0.75 phi) (Crickmore and Lean, 1962b; Yang and Sayre, 1971). It is obvious, therefore, that the bedforms exert a strong influence on the transport behaviour.

Based on a consideration of the transport processes involved, it is believed that many of the points noted in this study are the result of the different manner in which

the various grain sizes move with respect to the bedforms that are present. Specifically, the contrasting behaviour of the coarse and fine material is believed to reflect the difference in the nature of traction and intermittent suspension transport over bedforms.

Coarse grain sizes that move as a part of the traction or contact load never rise far above the bed, and as a result, when the brink of a bedform is encountered, most of the material moving in this fashion is deposited on the lee face, where it is buried by the advancing bedform (J.R.L. Allen, 1965, 1968b; Jopling, 1965). This material then remains stationary for a period that is determined by the size and migration speed of the bedforms. When it is eventually exposed, the material is transported to the next bedform downstream and buried once again. The traction load will, therefore, move in a series of steps with a length that is somewhat less than the bedform length, separated by long rest periods. Because the length of time spent buried is long relative to the time in motion, and because these rest periods will be of approximately equal duration regardless of the grain size, all traction material should have an average migration speed that reflects primarily the bedform movement rate. Any differences in transport speed that exist between size fractions while they are actually in motion will only be of minor importance. This explains

why the transport speed is virtually constant, and independent of the grain size for the coarsest fractions (Figure 6.16).

As the grain size becomes smaller, and the particles begin to spend a part of their time in intermittent suspension, their chance of bypassing any given lee face increases (J.R.L. Allen, 1968b; Jopling, 1965). As a result, these particles can move several bedform lengths before being buried in a bedform. It might be expected, therefore, that the transport speed will increase continuously as the grain size decreases, because lighter particles are more easily supported by the turbulence, and will remain in suspension longer. This behaviour is in excellent agreement with that observed for the finest fractions (Figure 6.16).

Unfortunately, little experimental evidence is available to support the above models of transport behaviour for the traction and intermittent suspension fractions. Grigg (1970) has found that the mean step length of particles with sizes of 1.15 and 1.6 phi (0.45 and 0.33 mm) is directly related to the bedform length, and that the effect of grain size is of secondary importance, as predicted for traction transport. Insufficient data are presented, however, to allow any differences in behaviour to be observed that might reflect a change from traction to intermittent suspension transport, although the flow conditions used in the experiments indicate, according to Figure 5.20, that each mechanism should

have been dominant in one or more runs for each grain size. It is probable that the shallow flow depths used (less than 0.18 m) greatly inhibited the development of intermittent suspension, so that the results reflect predominantly the traction mode of transport.

It is clear that the contrasting behaviour of the coarse and fine fractions can be well explained by their supposed methods of transport in the presence of bedforms. From this it follows that the break in slope in the trends shown in Figure 6.16 should indicate the size at which intermittent suspension takes over from traction as the predominant transport mechanism. If this is the case, then it also follows from the discussion in Sections 5.3.1 and 5.3.4 that the position of this break should be controlled by the shear velocity of the flow, according to equation (5.5). The tendency noted in Figure 6.16 for the break in slope to move to coarser sizes as the flow strength increases is in good agreement with this. More specifically, the plotted values for Buoy 1 on Big Bar suggest that the break occurs close to fraction IV, say between 1.5 and 1.75 phi (0.35-0.30 mm). In Figure 5.20, this size indicates a shear velocity in the range of 3.7 to 3.2 cm/s. The average maximum shear velocity measured for this site is 3.5 cm/s. For Buoy 3 on Diamond Bar, the break in slope appears to occur between fractions II and III, at approximately 0.0 phi

(1.0 mm). This size yields a shear velocity of 11.1 cm/s (Figure 5.20) which again is in excellent agreement with the measured average maximum value of 11.5 cm/s. These results provide convincing support for the concepts presented here and in Section 5.3 regarding the nature and significance of the break between the traction and intermittent suspension transport mechanisms. (It should be noted that the equal-overlap "break" in the size distributions for these two stations (Table 5.6) is not in agreement with the size at which the transition in behaviour occurs. This is due to the fact that the C population is almost absent in both samples, and at Buoy 3 on Diamond Bar in particular, these size characteristics are inherited from the low-energy conditions at the head of the bay.)

A number of features presented above with respect to the transport and dispersion of the various size fractions remain to be explained. Many of these are a direct consequence of the transport differences outlined above.

In the plots of the dispersion versus grain size (Figures 6.15A and B), the sharp breaks that occur between fractions III and IV are another reflection of the change from traction to intermittent suspension as the size decreases. For material transported by traction, the longitudinal dispersion, measured with respect to both time and distance, is low and essentially invariant for all sizes

because the step length of these particles is small and almost constant. The longitudinal dispersion increases rapidly for particles moving in intermittent suspension, however, because the step length is larger and more strongly influenced by turbulence.

The explanation just given also appears to be applicable to the variation in lateral dispersion at a given time (Figure 6.15A). The opposite trend noted for lateral dispersion with respect to the migration distance (Figure 6.15B) can also be explained in terms of the different transport mechanisms. It is suggested (Kennedy and Kouba, 1970, p.8) that the coarse material moving close to the bed experiences a high degree of flow-direction variability due to the presence of secondary flows induced by the bed irregularities. Finer sizes moving higher in the flow are not so strongly influenced by the secondary flows, and are dispersed only by the fluid turbulence. As a result, their lateral dispersion is less.

The extent to which the skewness variations (Figure 6.15C) are significant is not clear at this time. Obviously, the detection of skewness is much more dependent on the number of control points available to define the tracer distribution than are the transport distance and dispersion. The lower dispersion of the coarser sizes does reduce the number of samples falling within the distribution, and

consequently, the more nearly symmetrical shape of these distributions may be an artifact of the sampling density. Alternatively, it may reflect the uniformity of the step lengths experienced by these particles. The large skewness values for fraction III are not compatible with such an explanation, however, because this size generally behaves in a similar manner to the coarser fractions.

With regard to the influence of bed slope on the transport direction (Figure 6.15D), fraction III also shows a behaviour that differs from that of fractions I and II when the data from all sites are considered. It is expected that all traction material should have a smaller up-slope component than material moving by intermittent suspension because of the greater weight of the particles, and because they are preferentially deposited in megaripple troughs (see Section 5.2.3, Table 5.3) where late-stage ebb runoff can transport them down-slope. It is conceivable that fraction III might display a tendency intermediate between that of traction and intermittent suspension, but the observed behaviour cannot be explained, unless it is due to erroneous values for this fraction. The reason for the strong up-slope component exhibited by the intermittent suspension sizes (fractions IV and V) cannot be fully explained at this time. Comparison of the transport directions for these fractions with the vector mean of bottom

currents measured 0.75 metres above the bed (weighted by the measured velocity), reveals that these sizes move in a direction that is oriented 18° further up-slope on average than the bottom currents. The reason for the discrepancy is not known.

The observations presented here regarding the transport and dispersion characteristics as a function of grain size have many implications in both sedimentology and engineering, provided that they are not merely a result of the reversing tidal flow. As was mentioned at the conclusion of Section 6.4.1, it is believed, however, that these observations have a more universal significance, if for no other reason that it is believed that the relative behaviour of the size fractions is not altered by the reversing currents. The many similarities noted in the transport and dispersal processes between the tidal and unidirectional flow situations, plus the presence of strong residual transport in virtually all areas studied lends support to this. Furthermore, the generality of the explanations provided for the behaviour of the size fractions suggests that the observations should also have general significance.

### 6.4.3 Sediment Transport Patterns

In addition to the interesting information that the tracer experiments have provided with regard to the details

of sediment transport and dispersion (Sections 6.4.1 and 6.4.2), much useful data have been obtained about the patterns and rates of residual transport on the studied sand bars as shown in Figure 6.17. The values shown for each buoy are the sum of all tracer fractions listed in Table 6.2 and are also the average of the results for the two samplings. If, however, the recovery efficiency of one sampling is significantly worse than the other, only the discharge obtained from the sampling with the best recovery has been used.

An examination of the magnitude of the sediment discharge vectors obtained from the tracer experiments (Figure 6.17 - numbers in brackets) reveals that the transport rates vary widely from place to place, with a range of nearly four orders of magnitude, from 0.38 kg/cycle during neap tides at Buoy EP4 at Economy Point, to 1793 kg/cycle at Buoy 3 on Diamond Bar. Further inspection shows, however, that a strong correlation exists between the transport rates for the individual buoys and the flow strength at the site as indicated by any of the hydraulic variables discussed in Section 3.2.4. The average sediment discharges calculated for the bars (Figure 6.17) also show this relationship. Big Bar and Economy Point, with averages of 49.4 and 87.3 kg/cycle, respectively, have transport rates that are approximately an order of magnitude less than those on Diamond and Selmah Bars where the averages are 709.0 and 619.0 kg/cycle,

Figure 6.17 Sediment transport directions and rates from tracer experiments.

A - Big Bar; B - Diamond Bar; C - Economy Point; D - Selmah Bar. Vector length is proportional to the log of the unit sediment discharge (see scale at bottom left of section B). The absolute values are given in brackets, in kilograms per metre width per tidal cycle. Unless otherwise stated, all values refer to the entire size distribution. T. = traction fraction; I.S. = intermittent suspension fraction; N. = neap tide; S. = spring tide.

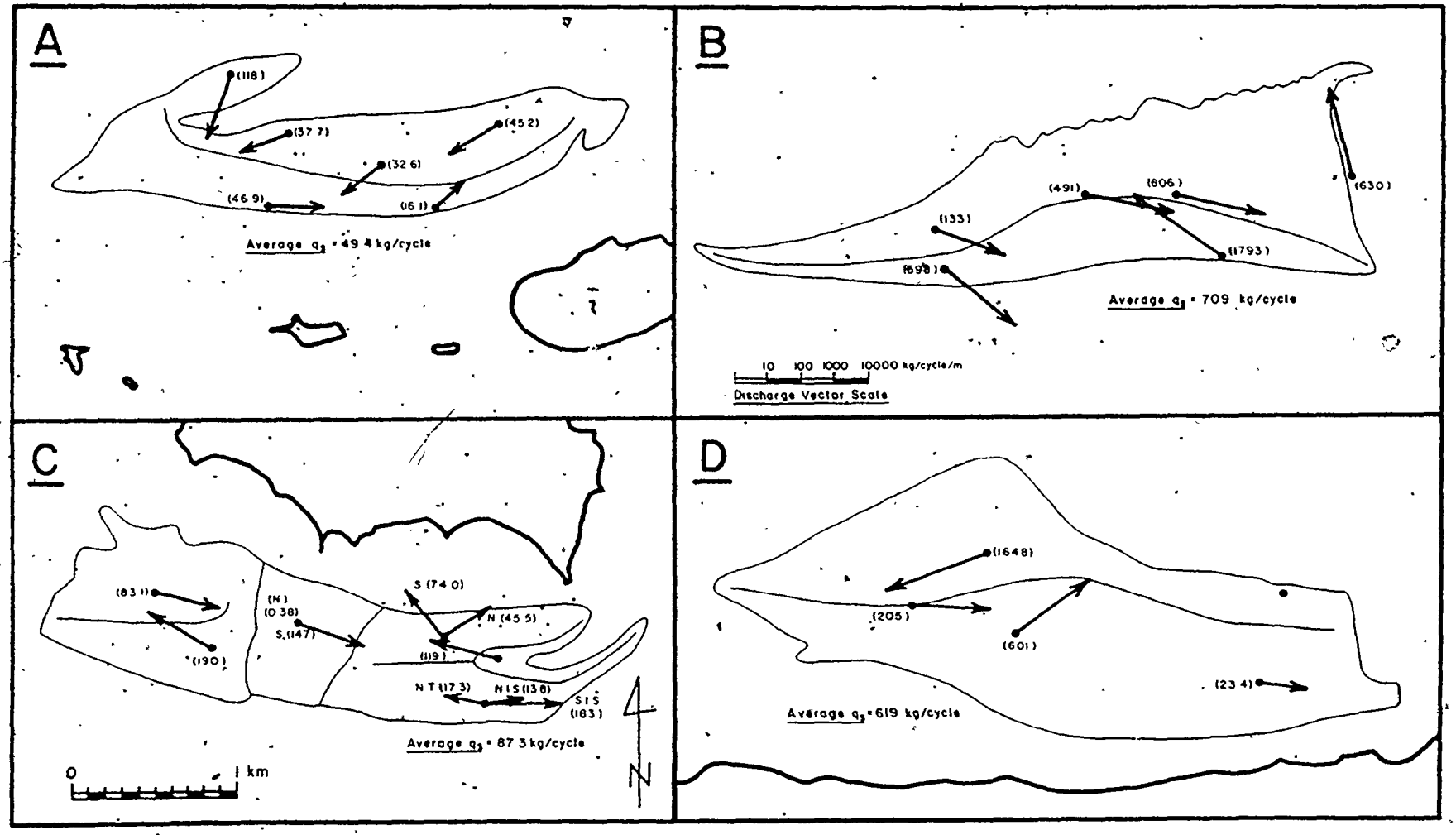
A
(118)
(37 7)
(45 2)
(32 6)
(46 9)
(06 1)
Average $q_s$ = 49 4 kg/cycle
B
(491)
(606)
(630)
(133)
(1793)
(698)
Average $q_s$ = 709 kg/cycle
10 100 1000 10000 kg/cycle/m
Discharge Vector Scale
C
(83 1)
(N)
(0 38)
S (74 0)
N (45 5)
S (147)
(119)
(190)
N T (17 3)
N I S (13 8)
S I S
(183)
Average $q_s$ = 87 3 kg/cycle
0
1 km
N
D
(1648)
(205)
(601)
(23 4)
Average $q_s$ = 619 kg/cycle

respectively. Examination of Figure 3.14 reveals that the differences in total combined stream power between the bars are not only consistent with these variations in the transport rates, but are also of exactly the same order of magnitude.

The determination of the sediment discharge with any reasonable accuracy is difficult in even the most simple situations with unidirectional flow. It might, therefore, be expected that the much more complicated situation existing in the study area, due to the presence of unsteady and reversing tidal currents, would make the accurate estimation of the sediment discharge many times more difficult. The problems associated with these points are likely to be most strongly felt when attempting to estimate the discharge using the theoretical transport functions (Section 6.2), but the more direct methods based on bedform migration and tracer movement may be more reliable because of the time-averaging nature of the calculations.

When the transport rates obtained from bedform migration in Section 4.2.2 are compared with those derived from the tracers (Figure 6.18A) an excellent agreement is found for areas with low transport rates. For example, on the north side of Big Bar, the bedform migration rates indicate an average discharge of 26.5 kg/cycle and a maximum of 55.9 kg/cycle. The tracer discharges obtained

Figure 6.18 Calculated sediment discharges versus measured tracer discharges.

A - Discharge obtained from bedform migration rates versus tracer discharge;
B - Einstein (1950) transport formula versus tracer;
C - Engelund and Hansen (1967) formula versus tracer;
D - Ackers and White (1973) transport theory versus tracer results.
Heavy lines are best-fit regression lines, with the correlation coefficient (r) indicated. * = significant between 95% and 99%; ** = significant at greater than 99%. All units are the logarithm of the discharge in kilograms per metre width per tidal cycle.

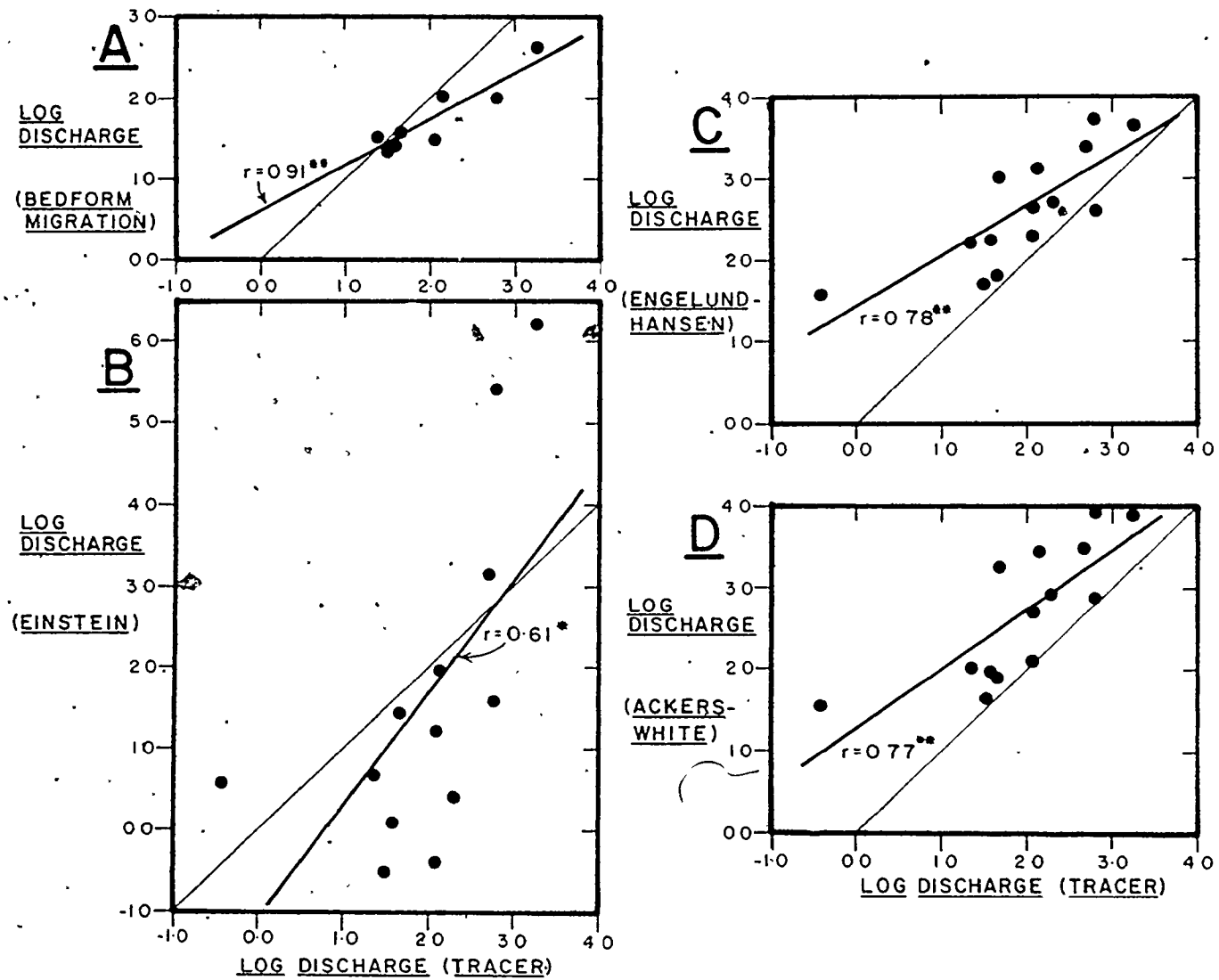
A
LOG DISCHARGE (BEDFORM MIGRATION)
r=0.91**
B
LOG DISCHARGE (EINSTEIN)
r=0.61*
C
LOG DISCHARGE (ENGELUND-HANSEN)
r=0.78**
D
LOG DISCHARGE (ACKERS-WHITE)
r=0.77**
LOG DISCHARGE (TRACER)

at Buoys 1, 5, and 6, are 32.6, 37.7, and 45.2 kg/cycle, respectively. A similar close correspondence is seen at Buoy 1 on Selmah Bar: the bedform discharge is approximately 35 kg/cycle whereas the tracer discharge is 23.4 kg/cycle. In areas where the transport rates are higher, however, the agreement becomes poorer (Figure 6.18A), with the results of the tracer studies giving higher discharges than the bedform migration rates. For example, the calculated discharges at Buoy 4 on Big Bar are 31.0 and 118 kg/cycle, by the bedform and tracer methods, respectively; at Buoy 1 on Diamond Bar: 102 and 606 kg/cycle; and at Buoy 3 on Diamond Bar: 292 to 583 kg/cycle and 1793 kg/cycle. Such results are, of course, to be expected because the amount of material in intermittent suspension becomes greater as the transport rate increases, with the result that an increasing portion of the total discharge does not contribute to the bedform migration ($C_1 > 0.0$ in equation 4.2). It would appear, therefore, that the values calculated from the tracer experiments are a good estimate of the net sediment discharges that occur on the sand bars.

As described in Section 6.2, the residual transport has also been calculated for all possible sites using the hydraulic transport functions of Einstein (1950), Engelund and Hansen (1967), and Ackers and White (1973). In applying these transport functions, the discharge is evaluated for

every measured velocity profile using the data listed in Appendix 2, and the net discharge vector is then determined by integrating the discharge over the tidal cycle. If more than one discharge can be calculated for a given site, a representative value is obtained by averaging the individual net discharges. The values calculated by each of the three transport functions are shown in Figure 6.18, plotted against the discharges derived from the tracer experiments. Note that all axes are logarithmic.

Of the three transport functions used, the Einstein (1950) method gives the least satisfactory results (Figure 6.18B). The data points show that this function tends to greatly overestimate the discharge when the tracer discharge is high, and to underestimate it for low tracer discharges. This behaviour has been noted previously by Crickmore (1967), Garg et al. (1971), TCPSM (1971), and Tywoniuk (1972). The correlation coefficient for the regression line is only barely significant at the 95% level. Furthermore, the Einstein equations indicate that no transport is possible in over half of the velocity profiles measured, and in 12 instances, no transport is indicated for an entire tidal cycle, despite observations to the contrary. The reason for this is discussed below.

By comparison, the Engelund-Hansen (1967) and Ackers-White (1973) transport theories (Figures 6.18C and D,

respectively) provide remarkably good estimates of the tracer discharge, all factors considered. Both methods give values which are consistently higher than the tracer results, but the correlation coefficients for both relationships are significant at greater than 99%. The Engelund-Hansen formula overestimates the tracer values somewhat less than the Ackers-White function: the two methods overestimate the tracer discharge by factors of 5.5 times and 8.1 times, respectively. The reason(s) for the consistent differences are not known at this time.

The markedly different behaviour of the Einstein transport function relative to the other two methods can be directly attributed to the use of the energy slope (S) in equation (6.2) as the primary variable expressing the intensity of the flow in the Einstein function. In the Engelund-Hansen formula, the shear stress ($\tau_o$) is the parameter indicating the flow strength (equations 6.13 and 6.15), and in the Ackers-White function, the mean current speed and the shear velocity are used (equations 6.19 and 6.20). Examination of the hydraulic values for the study areas tabulated in Appendix 2 reveals that the energy slope varies several orders of magnitude more than the mean speed, shear velocity, or the shear stress. As a result, the Einstein discharge estimates vary much more erratically than those of the other two methods. The use of the energy slope in

equation (6.2) is also responsible for the large number of profiles in which no transport can be calculated. For low values of S, the calculated flow intensity parameter ($\Psi$) becomes so large that it plots off the graph of Einstein's bedload function (Einstein, 1950, Figure 9). Based on the above results, it is clear that the Einstein transport function is not appropriate in the present situation, largely because of the uncertainty of the calculated energy slopes. On the other hand, the Engelund-Hansen and Ackers-White formulae can be used with reasonable confidence.

A comparison of the transport directions given by the tracers (Figure 6.17) with those deduced or predicted from the hydraulic data (Figure 3.18) shows that a remarkable agreement exists in most areas. In particular, all of the predictions made in Section 3.2.5 are supported by the tracer results.

On Big Bar (Figure 6.17A), the ebb-dominated transport on the north side of the crest is confirmed, and the up-slope component is clearly visible. The southerly transport shown for Buoy 4 on the northwest arm (see Figure 6.2 for the location of all buoy sites) is unexpected, and cannot be explained in terms of the observed surface flow directions (Figure 3.13A), although it is possible that these surface measurements do not reflect the conditions existing near the bed. The most notable feature of the

transport pattern on Big Bar, however, is the flood-dominated transport along the entire steep southern side, as suggested by Klein (1970) and predicted in Section 3.2.5 (Figure 3.18A). It may be that longshore transport by waves from the west is of some importance in promoting the eastward transport on the south side.

On Diamond Bar (Figure 6.17B), the flood-dominance on the northern side of the bar crest can be plainly seen, and ebb directed transport is evident at the eastern end and along the eastern half of the south side, as indicated by the current data (Figure 3.15). Up-slope components are evident in both flood and ebb areas, showing that the residual transport does converge toward the bar crest as suggested in Section 3.2.5. The southeasterly residual for Buoy 7 at the southwest end of the bar is not in agreement with the consistent ebb dominance shown for this station by all of the hydraulic variables studied in Section 3.2.4 (see Figure 3.15). No explanation can be given for this, unless it is possible that the tracer result is spurious, despite the recovery efficiency of 15.6%.

At this point it is of interest to digress briefly to consider the variation in sediment discharge along the length of the large sand waves on the north side of Diamond Bar. For this purpose it is necessary to use the values obtained by the Engelund-Hansen transport formula. At

Buoy 1, where the sand wave height is 0.4 metres, the calculated residual transport rate averages 384 kg/cycle. Proceeding northward to the station in the north channel, where the sand wave height is approximately 3 metres, the residual discharge increases to 1185 kg/cycle. If these values are now substituted into equation (4.2), with $C_1$ assumed to be equivalent at the two stations (and arbitrarily set equal to zero) a theoretical bedform migration rate ($V_b$) can be calculated for each station. When this is done, the result for Buoy 1 is 1.32 m/cycle, whereas in the north channel the value is only 0.54 m/cycle, despite the higher transport rate there. Obviously, the greater bedform height more than offsets the higher discharge. This differential in the migration speed across the sand wave field is believed to be wholly responsible for the skewed orientation of the large sand waves relative to the transport direction (Figure 6.8). In other areas, such as on Saints' Rest Bar and Spencer Point Bar, the skewed orientation is apparently the result of differing directions of residual transport on either side of the bars (flood on the north side and ebb on the south side). This behaviour is a direct result of the large size and continuity of the sand waves (Section 4.2.1), for it allows a single sand wave to span a greater range of flow conditions than is possible for the smaller and less continuous megaripples.

At Economy Point (Figure 6.17C) most of the predicted

features of the sediment transport pattern are born out by the tracer results. Ebb-directed transport is present on the southern part of Centre Bar (Buoy EP3) and in the blind channel on East Bar (Buoy EP8). The remaining areas appear to be flood-dominated: the north side of Centre Bar (Buoy EP2); the area between Centre and East Bars (Buoy EP4); and the area surrounding the blind channel on East Bar (Buoys EP6 and EP7), although some unusual features are evident in the latter areas.

At Buoy EP6, the results for the tracer injected at neap tide show an easterly residual transport (Figure 6.17C) in agreement with the hydraulics (Figure 3.16) and the bedform migration (Section 4.2.2). For the spring-tide injection, however, the net transport is to the northwest, suggesting an ebb dominance.

At Buoy EP7, the results for both neap and spring samplings (Table 6.2) reveal that the traction and intermittent suspension fractions are transported in opposite directions (Figure 6.17C); the coarse material moving westward, and the finer sediment moving eastward. This is the only location studied where this phenomenon is observed. J.J. Lambiase (1976, personal communication) has evidence to indicate, however, that a similar behaviour exists in one area at the mouth of the Avon River estuary (Figure 1.2).

It is also interesting to note the differences in

the transport rates for the neap and spring samplings at Buoy EP7. For the neap sampling, the vectorial addition of the traction and intermittent suspension transport yields a weak ebb residual, whereas for the spring sampling, the transport of the intermittent suspension fraction has increased by an order of magnitude while the traction transport has remained essentially constant, thereby producing a strong flood residual. This may explain the reversal in bedform migration direction noted for this site in Section 4.2.2 (Figure 4.12).

A strong dependence between the sediment discharge and the tidal range is also evident at Buoy EP4, where the transport increased from 0.38 kg/cycle to 147 kg/cycle as the tidal coefficient rose from 0.62 at the first sampling to over 0.90 just before the second sampling. These areas at Economy Point are the only ones where this dependence is so strikingly evident.

The tracer discharge results for Selmah Bar (Figure 6.17D) are in agreement with the flood dominance suggested for the entire south side of the bar in Section 3.2.5. Buoy 3 located in the major swatchway displays a strong northward transport of sediment. Ebb transport is shown for Buoy 4 on the north side of the crest. Unfortunately, the transport directions calculated for Buoy 2 (Table 6.2) are not sufficiently consistent or reliable to allow any

conclusions to be drawn regarding the validity of the ebb-dominance indicated for the eastern end of the north side (Figures 3.17 and 3.17D). (The spurious high recovery efficiencies achieved at this site (Table 6.2) are a consequence of the very fine grain size present there (Figure 5.11A), and the resulting difficulty encountered during the processing of the samples and the determination of the average grain weight.)

Despite the shortcomings of the tracer data, several conclusions are clear regarding the general nature of residual sediment transport patterns in this tidally dominated environment. It is apparent that almost all areas experience opposite directions of sediment transport on either side of the bar crest regardless of the crestline configuration. In addition, there is a convergence of sediment toward the crest of the bar, most commonly at a low angle as on Diamond Bar (Figure 6.17B), but in some instances at nearly 90° as at Economy Point (Figure 6.17C). Wave activity is an important factor in limiting the height to which the bar crests can build, as evidenced by the westward decrease in bar height shown by the bars in Cobequid Bay (Figures 2.12 and 2.15). The angle at which the transport streams converge toward the bar crests also appears to have some influence, however, because the two places at Economy Point where the sediment converges directly toward the crest from both sides (the

east end of Centre Bar, and the nose of the blind channel on East Bar - Figure 6.17C) are the locations where the highest elevations are encountered on any of the bars (Figure 2.17), despite the fact that Economy Point is the site of the strongest wave activity (Section 2.2.2).

It has been suggested (Houbolt, 1968; Klein, 1970) that some form of equilibrium "race-track" circulation of sediment characterizes all tidal sand bodies. Such a model in which sediment follows a closed path around a single bar requires that the sediment "turn the corner" at the end of the bar. The transport pattern indicated for Big Bar (Figures 3.18A and 6.17A), the simplest of the bars studied, comes the closest to agreeing with this model. An examination of the data for the remaining bars, and particularly Diamond and Selmah Bars in Cobequid Bay, shows that the transport patterns are more complex. For example, on Diamond Bar (Figure 6.17B), the sediment at the east end of the bar is moving in the opposite direction to that required of a simple clockwise circulation pattern for the bar as a whole.

It is evident that some exchange does occur between oppositely directed transport streams on either side of the bar crests. The strong cross-bar component to the residual sediment discharge in the swatchways on Diamond and Selmah Bars (Figures 6.17B and D) shows that the swatchways are important sites where material is transferred from one transport stream to the other. Further interchange of sediment

is believed to take place along the remaining portions of the crestlines as well. An examination of the transport vectors for the west half of Big Bar (Figure 6.17A) indicates that material might be moving diagonally across the crest from northeast to southwest in that area. This situation may indeed be the cause of the asymmetry of the bar, in the manner suggested by Houbolt (1968). A similar situation might also exist at the west end of Diamond Bar (Figure 6.17B), for the results at Buoy 7 (Table 6.2) on the south side are at least consistent in showing the lack of an up-slope component, whereas such a component is present on the north side of the crest.

From the above, it appears that, strictly speaking, elliptical sediment transport cells such as those envisaged by Houbolt (1968) and Klein (1970) do not exist in Cobequid Bay, on the scale of an individual bar. Instead, the swatchways define smaller units as can be seen on Diamond Bar (Figures 3.18B and 6.17B). Here, sediment that is moving westward on the south side of the bar is deflected northwestward along the west side of both swatchways. From here it returns eastward on the flood-dominated northern side of the bar. The closure of this clockwise sediment circulation cell does not occur at any specific point, but may take the form of north to south sediment transport across the bar crest along its entire length.

A consideration of the hydraulic data and sediment transport results for Diamond and Selmah Bars in the context of the entire Cobequid Bay sand body (Figure 1.3), together with airphoto interpretation and additional observations of R.J. Knight (1975, personal communication), permits a larger-scale flow and sediment transport pattern to be suggested for the Cobequid Bay complex (Figure 6.19), the basic features of which are very reminiscent of the ebb-tidal delta model of Hayes et al. (1973). The deep, major channels present along the north and south shores are both flood dominated as shown by the data for the north side of Diamond Bar, and the south side of Selmah Bar. Both of these channels shallow toward the head of the bay, and eventually terminate in dead ends. The system of shallower channels present in the centre of the bay are ebb dominated by contrast (Figure 6.19), as indicated by the south side of Diamond Bar and the north side of Selmah Bar. These channels are connected directly with the Salmon and Schubenacadie Rivers, and much of the ebb-tide discharge from the head of Cobequid Bay is, therefore, channelized down the axis of the bay.

As a result of this generalized flow and sediment transport pattern two large-scale elliptical cells of sediment transport are believed to exist within Cobequid Bay, the northern one with a clockwise sediment circulation encompassing Diamond and Great Village Bars, and the southern

Figure 6.19 Sediment transport pattern in Cobequid Bay.

Directions of residual transport based on direct observations, airphoto interpretation, and personal communication from R.J. Knight (1975). Arrow length is not significant.

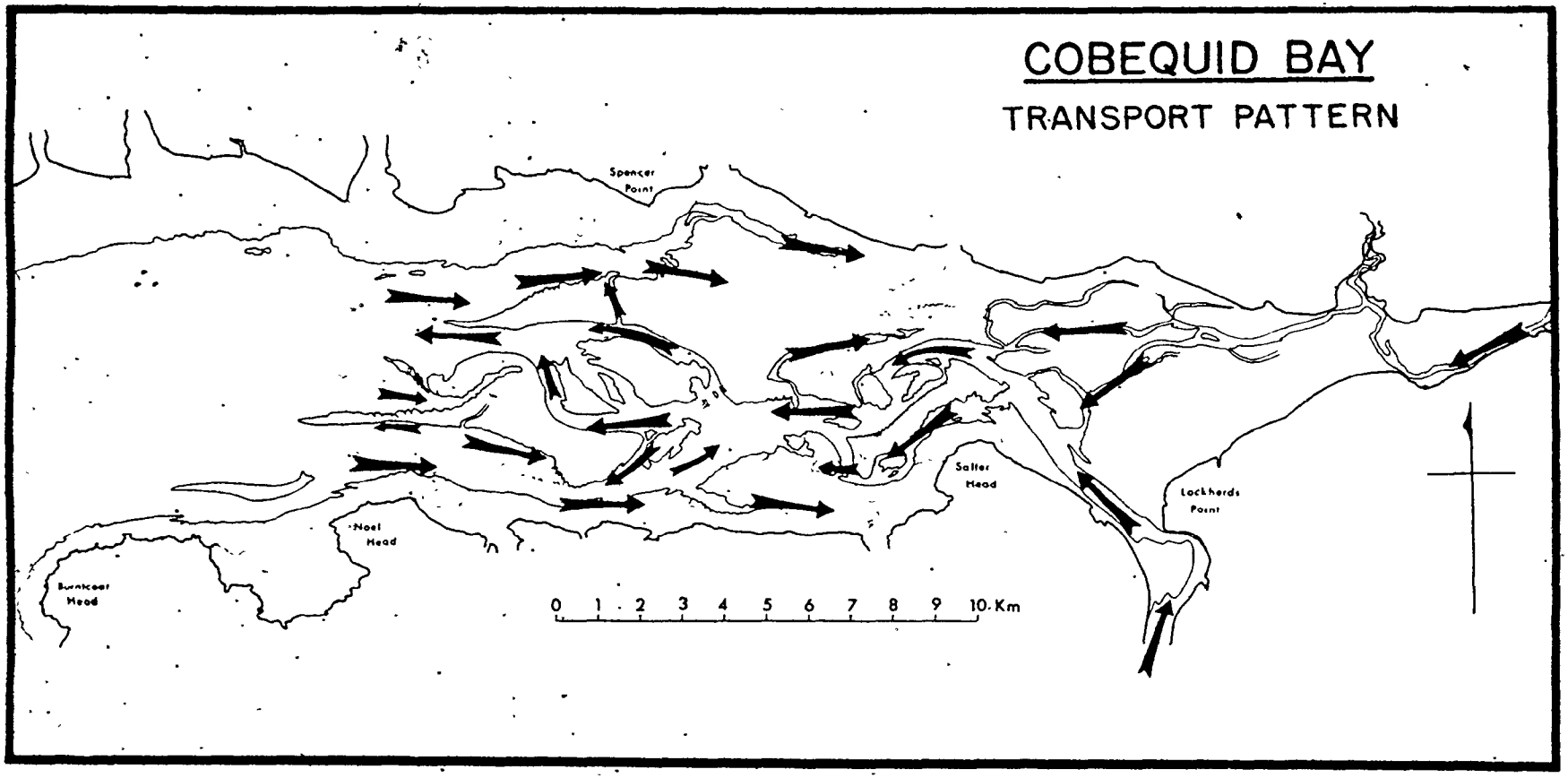
COBEQUID BAY
TRANSPORT PATTERN
Spencer Point
Noel Head
Burntcoat Head
Salter Head
Lockhards Point
0 1 2 3 4 5 6 7 8 9 10 Km

one with a counterclockwise transport direction including Noel Shore and Selmah Bars (Figure 6.19). Many irregularities exist, however, to disrupt the basic pattern just outlined. The swatchways act as short-cuts and allow mixing between incoming and outgoing sediment producing the smaller sediment circulation cells described above in the process. As evidenced by Diamond Bar, the direction of transport in each smaller cell is the same as the sense of movement in the larger one of which it is a part. Minor channels and re-entrants such as the flood-dominated one at the west end of Noel Shore Bar (Figure 6.19) also complicate the picture.

The basic sediment circulation pattern must, however, remain essentially intact, because fine-grained sands with characteristics that are indicative of formation in low energy conditions are present in areas of high energy on the south side of Diamond Bar and the northern part of Selmah Bar (Section 5.3.4). It has already been suggested that these characteristics have been transported up a flow strength gradient from some location near the head of Cobequid Bay. Indeed, the position of the "break" in the size distribution on the south side of Diamond Bar (ranging between 1.9 and 2.5 phi), as determined by the point of equal overlap (see Section 5.3.4), indicates that these sands may have originated in an area with an average maximum shear velocity of approximately two to three centimetres per second (Figure 5.20). These values are so low, that only

ripples can be formed (Figure 4.15). It would appear possible, therefore, that the sand which is now present on the south side of Diamond Bar has been transported there from the very head of Cobequid Bay. The transport must have been rapid and the amount of mixing low in order for the character of the sands to have remained so unaltered. Some idea of the speeds at which the sediment moves in various parts of the system can be gained from the tracer experiments on Diamond and Selmah Bars.

From the results at Buoy 3 on Diamond Bar and Buoy 4 on Selmah Bar, it appears that the speed of net movement does not decrease markedly toward the head of the bay in the ebb-dominated portion of the system. Therefore, using a conservative average transport speed of 4.5 metres per tidal cycle, as determined from the data for Buoy 3 on Diamond Bar (weighted by grain-size abundances), it can be calculated that it requires only 1.25 years (890 tidal cycles) for the sediment to move the length of Diamond Bar, and approximately 6.25 years for it to be transported from the head of the bay to the western tip of Diamond Bar. This rapid movement is presumably due to the channelized nature of the ebb flow. This also explains why the sediments on the south side of Diamond Bar are so little modified texturally despite the long distance of transport.

For the flood-dominated parts of the system, an

average transport speed of only 1.8 m/cycle is obtained from the tracer discharge values for Diamond and Selmah Bars. At this rate, more than 15.5 years are required for sediment to move directly from the western end of the sand body to the head of the bay. The slower transport speed in flood-dominated areas allows the sediment characteristics greater time to respond to the changing flow conditions.

It should be emphasized that the times given above are crude estimates at best. All available data does, however, support the transport speed differential between the flood and ebb portions of the system. This difference may also explain why a larger proportion of the surface of the sand body is dominated by flood currents than by ebb flow, as can be seen on both Diamond and Selmah Bars (Figures 3.15 and 3.17). If indeed some form of equilibrium exists in which there is a transport balance between the incoming and outgoing portions of the system, then the greater extent of flood dominance is a direct consequence of the lower transport speed.

The reason for the existence of this general transport system is not clear at this time. By analogy with the tidal-delta model of Hayes et al. (1973), it may be that the inertia of the channelized ebb currents issuing from the Salmon and Schubenacadie Rivers is in some way responsible for the deflection of the newly turned flood tide up the

lateral channels along either shore, thereby initiating preferred and mutually exclusive flow paths for the ebb and flood currents which are reinforced with each tide. Additional, comprehensive studies of the hydraulics in the channels are required to test this idea and determine the cause of the overall flow and sediment transport system in Cobequid Bay.

## 6.5 Summary

Movement of the constituent particles is a necessary process in the formation of virtually all attributes of clastic sediments, including bedforms and grain size characteristics. In order to study the transport of sediment on the sand bars fluorescent tracer experiments were conducted at 29 sites, 25 of them on the four major study bars. The areal distributions of tracer concentration determined at various elapsed times were analysed using two-dimensional moments to characterize the size and shape of the distributions. The movement of the centroid allowed the average net transport speed, transport direction, and sediment discharge to be calculated. The recovery efficiencies of these distributions range from less than 1% to over 1000%; however, more than 45% of them are less than 10%.

The shape of the dispersing tracer cloud is generally simple with only one mode. Most commonly the distributions exhibit a single, elliptical lobe extending in the direction

of the residual transport. Less commonly, two lobes 180° apart are present on either side of the origin, and rarely, three lobes are observed. The tracer distributions are almost invariably elongate parallel to the currents. The distributions tend to be skewed in the direction of the residual transport (average longitudinal skewness = +0.60; defined with the transport direction as positive), but the degree of asymmetry appears to be less than in unidirectional flow, presumably due to the reversing currents. Lateral skewness, measured either with respect to the transport direction or the bar slope, is erratic and the average values are near zero. The absolute values of both the longitudinal and lateral skewness decreases as the dispersion time increases; a characteristic also noted in unidirectional flows.

As indicated by the elongation of the tracer distributions, the longitudinal dispersion is greater than the lateral dispersion by an average of approximately three and a half times. The rate of longitudinal dispersion is found to be significantly and positively correlated with the migration speed of the centroid; however, positive but non-significant correlations are obtained with various measures of current strength. A comparison of the dispersion for the first and second samplings shows that both the longitudinal and lateral dispersion decrease as the elapsed time

increases. The rapid initial dispersion is also accompanied by faster than average centroid movement. Despite potentially greater longitudinal dispersion due to the reversing currents, the accommodation time is believed to be longer in the tidal environment than in unidirectional flow because of the lower residual sediment discharges in the tidal situation.

All sites show significant displacements of the centroid from the origin. The speed of movement varies greatly from place to place, but averages between one and two metres per tidal cycle; nearly two orders of magnitude less than the value suggested by Balazs and Klein (1972) for Big Bar. The residual unit sediment discharges calculated from these values range from 0.38 to 1793 kg/cycle. The average unit discharge is lowest for Big Bar (49.4 kg/cycle) and highest for Diamond Bar (709 kg/cycle). Differences in discharge across a field of sand waves, combined with variations in their height produce migration rate variations that account for the skewed orientation of the sand waves.

A comparison of the sediment discharges obtained from the tracers with those derived from bedform migration rates shows an excellent agreement between the two for low transport rates. For higher transport rates, the discharges calculated from the bedforms are invariably lower, due to the presence of intermittent suspension transport. Residual sediment discharges obtained from the Engelund-Hansen (1967)

and Ackers-White (1973) transport theories both are in remarkable agreement with the tracer results (correlation coefficients are greater than 0.75 and significant at greater than 99%), although both overestimate the tracer discharge: the Engelund-Hansen method by an average of 5.5 times and the Ackers-White formula by 8.1 times. The Einstein (1950) total load function produces much less favourable results, underestimating the tracer discharge at low transport rates, and overestimating it markedly at high discharges.

The tracer experiments show that grain size has a strong influence on the transport behaviour. Coarse grain sizes that move as part of the traction load have longitudinal and lateral dispersion rates (as a function of time), and transport speeds that are nearly constant for all sizes, or that increase only slowly as the grain size decreases. This lack of differentiation results from the fact that all portions of the traction load have little chance of bypassing a bedform lee, because they move in contact with the bed. The step lengths and transport speeds are, therefore, controlled by the bedform size and migration rate rather than by the grain size. For material coarser than about 1.0 phi (0.5 mm) the dispersion rates and transport speed increase continuously as the grain size decreases. This contrasting behaviour occurs because these sizes travel primarily by intermittent suspension, and are able to travel several

bedform lengths before being deposited. The distance travelled in each step should, therefore, be an inverse function of the grain size for material moving in intermittent suspension, because the smaller sizes are more easily supported by turbulence. The point at which the change in behaviour between traction and intermittent suspension occurs is generally abrupt. Significantly, the fall velocity of the grain size at which the transition occurs is almost identical to the average maximum shear velocity of the flow in agreement with the prediction of Middleton (1976). The transport speed of each tracer fraction is also positively and significantly correlated with at least some measure of flow strength.

The patterns of residual sediment transport on the major bars as determined by the tracers are in perfect agreement with the predictions made in Chapter 3. Virtually all areas display opposite directions of sediment transport on either side of the bar crest, regardless of the crestline configuration. This transport is directed up-slope at nearly 80% of the sites occupied, but the component is greatest for the finer sizes. It appears that the height of the bar is partially controlled by the angle at which the sediment converges toward the crest, and some evidence indicates that the asymmetry of the bar might be due to a stronger up-slope component on the gentle side.

In Cobequid Bay a sediment circulation pattern appears to exist that is broadly analogous to the ebb-tidal delta model of Hayes et al. (1973). The shallow channels in the centre of the bay are ebb dominated, while those along either shore are generally flood dominated, producing two major sediment transport cells, the northern one having clockwise sediment transport, and the southern one counter-clockwise transport. The swatchways allow mixing between the outgoing and incoming sediment streams, and disrupt the major cells into smaller units. Transport speeds in the ebb portion of the system are high, and sediment requires only 6.25 years to move the length of the sand body. Flood-dominated transport is considerably slower, requiring more than 15.5 years for the return trip, These transport speed differences may explain why the areal extent of flood dominance is greater than that of the ebb in Cobequid Bay.

# CHAPTER 7

## SUMMARY AND CONCLUSIONS

### 7.1 Setting and Processes

The research reported in this thesis is a study of the sedimentation dynamics of intertidal sand bars in a macrotidal environment. Tidal current velocities, bedform types, grain-size characteristics, and sediment transport patterns and rates have been investigated in some detail in order to describe the environment and to understand as completely as possible the nature of the sedimentological response accompanying the action of the tidal currents. Every attempt has been made to evaluate the fundamental process-response relationships in the most quantitative manner possible.

The study area is located in the eastern arm at the head of the Bay of Fundy (Figure 1.1); specifically in the Minas Basin and Cobequid Bay, Nova Scotia, Canada. This area reputedly possesses the largest tides in the world, having a maximum measured tidal range of 16.3 metres, which is believed to be due to near-resonant amplification of the lunar semidiurnal ($M_2$) tidal wave in the Bay of Fundy-Gulf of Maine system. Because of the large tidal range, and extensive intertidal zone with an estimated area of

between 200 and 300 $km^2$ is exposed in the Minas Basin and Cobequid Bay (Figure 1.2) at low tide.

The most distinctive features of this intertidal zone are the large sand bars that occupy much of Cobequid Bay and are present in places on the lower intertidal foreshore surrounding the Minas Basin. In Cobequid Bay, the bars are the exposed upper portion of a large sand body with a length of over 25 km, a width of 10 km, and a maximum thickness of nearly 20 m. All major bars are elongated in an east-west direction, approximately parallel to the tidal currents. Their lengths range from 1 to 10 km, and widths from 0.2 to 4.25 km. The bar crests commonly rise 10 to 15 m above the channel bottoms, but only the upper 6 to 7 metres is exposed at low tide. Water depths over the crests at high tide average about 6 metres. Within Cobequid Bay, the relief decreases markedly in an eastward direction, at the same time as the absolute elevation of the crests increases. Bars at the outer (western) end of Cobequid Bay are more elongate than those in the inner part.

All bar surfaces are covered by a variety of current-produced bedforms: ripples, sand waves, and megaripples. In Cobequid Bay, megaripples predominate on the outer third of the sand body, and sand waves are best developed on the middle third. The sediment in these areas is almost exclusively medium sand. Ripples only are present at the

head of the bay, in the mouths of the Salmon and Schubenacadie Rivers, where the sediment is fine sand.

Five major sand bars from a variety of locations have been investigated in detail (Figures 1.2 and 1.3).

Big Bar (Klein, 1970) is situated on the intertidal foreshore north of the islands at Five Islands (Figure 2.10), where it is sheltered from the brunt of wave and tidal current action. Big Bar is asymmetric in cross-section with a gentle northern side and a steep southern side, but is the simplest of the bars studied, because the crestline is unbroken.

Centre and East Bars (Klein, 1970) are located at the tip of Economy Point (Figure 2.16) and are exposed to the strongest wave action of any of the bars studied. Topographically, these bars are complex: a portion of the crestline of Centre Bar is oriented north-south, normal to the current flow direction; and, at the east end of East Bar, the crestline bifurcates to enclose a blind ebb channel. Prominent bedrock ledges around Economy Point further complicate the setting of these bars.

Diamond Bar (Figure 2.14) lies in the outer portion of Cobequid Bay and is separated from the influences of shore irregularities to the north by a channel that is more than one kilometre wide at low tide. The crest of the bar is displaced toward the south side, and its continuity is

broken by a swatchway which cuts the bar in two. Diamond Bar is separated from Great Village Bar to the east by another major swatchway which is never completely emergent.

Selmah Bar (Figure 2.11) is situated along the south shore in the central portion of Cobequid Bay, but is separated from the shore by a channel that becomes shallower to the east. This bar is also broken into two parts by a swatchway. The western half if nearly symmetrical, but the crest swings to the north side of the bar east of the swatchway. Mudflats lie immediately to the east of the bar in the lee of Salter Head.

Two intertidal facies assemblages exist in association with the sand bars: the exposed foreshores; and sheltered embayments.

The intertidal foreshores (Figure 2.7) that are exposed to wave attack, are covered with a zero to two metre thick mantle of sediment resting on a wave-cut platform that may be up to 2 km wide. Near-vertical cliffs, that are cut primarily into friable Triassic sandstones or Pleistocene material, border most foreshores and have predominantly gravel beaches at their base. Immediately seaward of the beach, there is an abrupt transition to mud which forms a thin veneer over lag gravel or bedrock. The gravel lag and bedrock reappear from beneath the mud in the lower part of the foreshore. Locally, accumulations of sand form small,

isolated bars that rest on the gravel lag. The intertidal foreshores generally become narrower and muddier toward the head of Cobequid Bay due to decreased wave and tidal current action.

Mudflats and salt marshes, drained by steep-sided tidal gullies, are developed in all sheltered areas (Figure 2.8). The extent of these facies is generally limited by an increase in the exposure to waves and tidal currents, such that mudflats can be bordered laterally or seaward by gravel lag. Salt marsh progradation is rare, and restricted to the area at the mouths of the Salmon and Schubenacadie Rivers. This is also the only extensive area where the classic intertidal zone sequence (Reineck, 1972) from sand flats through mixed flats and mud flats to salt marsh is seen.

The Minas Basin and Cobequid Bay can be considered as a single large estuary, because the discharge of the rivers, although negligible when compared to the volume of the tidal prism, is sufficient to lower the salinity to between 26 and 31°/$_{oo}$, with the lower values present toward the head of Cobequid Bay. The water at the head of Cobequid Bay is also warmer and more turbid than water in the Minas Basin. Despite the longitudinal gradients, no vertical stratification is found at any time during the tidal cycle. As a result, density-driven circulation is of no importance in this macrotidal environment.

Four dynamic processes are active however: winter ice; channelized, late-stage, ebb runoff; waves; and tidal currents. Of these, tidal currents are by far the dominant process operating on the sand bars.

During the months of December through March, when air temperatures are below freezing and the water temperature is near 0°C, large quantities of ice are present in the intertidal zone (Figure 2.6). A shorefast ice foot forms at the high tide mark and protects the shoreline from erosion by waves. Cakes and blocks of drift ice of various sizes move back and forth with the tides and wind, often becoming grounded in the intertidal zone at low tide. An ice crust also forms over much of the intertidal zone and immobilizes the surface sediment. Most evidence of the action of winter ice is, however, quickly obliterated by tidal currents in the spring.

During the last stages of emergence, the remaining water on the bar is confined to the bedform troughs and flows laterally away from the bar crest. This ebb runoff produces a number of modifications to the bedforms produced earlier, but is of little general significance.

Unlike many shallow marine environments, waves are only of secondary importance in the study area. The Minas Basin and Cobequid Bay are effectively isolated from the Bay of Fundy by Capes Blomidon and Split (Figure 1.2), so that the effective fetch is severely limited. Observations and

predictions indicate that wave heights are rarely in excess of one metre, although waves up to three and even four metres can be expected in exposed locations during exceptional storms. In addition, the rapid rate of water level change disperses the action of the waves over a large area and does not allow the wave energy to be concentrated at any level for very long. Wave action is, therefore, dominant only near the high tide level.

The tidal currents attaim maximum, near-bottom speeds of 0.5 to 1.5 m/s over the studied sand bars, and are, therefore, the dominant process operating in the environment. These tidal currents are characterized by a high degree of variability in both time and space, and nearly 1300 velocity profiles have been measured in order to describe them (Appendix 1). Analysis of the profiles shows that more than 67% have statistically significant logarithmic velocity distributions, which allows the hydraulic theory for open channel, turbulent boundary layer flows to be used to characterize the tidal currents (Appendix 2).

High tide is nearly synchronous throughout the study area and corresponds with the time of zero current flow, indicating that the tides are the result of a standing wave. After high water, mean current speeds and shear velocities increase rapidly for the first two hours of the ebb (Figures 3.5 to 3.9). Peak values are attained progressively

later, however, as one moves eastward into Cobequid Bay. During the middle portion of the ebb, the current speed and shear velocity may either remain essentially constant, or decrease slightly. In the latter case, a second period of higher values is commonly observed subsequent to the emergence of the bar crest which causes a channeling of the flow. At Economy Point, a sudden drop in flow strength occurs in the middle of the ebb, presumably because bedrock ledges east of the headland deflect the currents out around the sand bars.

In all areas, the ebb is of longer duration than the flood, because the turn of the tide at low water is delayed by bottom friction and by the ebb hydraulic gradient which must be overcome by the flood tide in Cobequid Bay. This delay increases in an eastward direction, ranging from between 15 and 30 minutes in the Minas Basin, up to 1.5 hours or more at Selmah Bar. Within Cobequid Bay, the flow in the channels at low tide is independent of the tide for up to 1.5 hours. During the flood, current speed and shear velocity generally attain their maximum values shortly after the turn of the tide, or submergence, while the flow is channelized, and then remain constant or decrease gradually to zero at high tide. The hypsometry of the area being flooded or drained is believed to play an important role in determining local differences in the time-variation of flow

strength.

The time-averaged values of both the mean current speed and shear velocity increase as the tidal range increase (Figures 3.11 and 3.12). The rate of increase is higher for Diamond Bar than it is for Big Bar, but in both areas the trends are less steep than that required to give zero flow when the tidal range is zero.

Considerable areal variations in flow strength occur within and between the five bars studied. Diamond Bar and the western half of Selmah Bar experience the highest mean current speeds (0.5 to 0.9 m/s) and shear velocities (3.0 to 5.0 cm/s) of the four areas, while Big Bar has the lowest values, with mean current speeds of 0.2 to 0.5 m/s and shear velocities of 1.0 to 3.0 cm/s. Within any area, the strongest currents are found in the channels and swatchways where the flow duration is also greatest. On Big Bar (Figure 3.13), the weakest currents are located in a band stretching from northeast to southwest diagonally across the bar crest. On Diamond Bar (Figure 3.15), the lowest flow strengths occur in two separate locations immediately north of the crestline, on either side of the minor swatchway. At Economy Point (Figure 3.16), the current speeds and shear velocities decrease inward toward the tip of the headland, and are lowest between Centre and East Bars. On Selmah Bar (Figure 3.17), the currents become progressively weaker in an easterly direction

on the south side of the bar crest, as the head of the channel and the mudflats east of the bar are approached.

Current speeds and shear velocities for the ebb and flood are unequal in virtually all areas, creating time-velocity asymmetries, such that residual water discharges, and by inference sediment discharges as well, are produced (Figure 3.18). It also appears to be an almost universal feature of the tidal hydraulics that opposite sides of a bar are dominated by different halves of the tidal cycle. The north side of Big Bar is ebb dominated, while the south side may be flood dominated. On Diamond Bar, ebb currents dominate along the entire southern side and at the eastern end of the bar in the major swatchway, whereas flood currents are stronger than the ebb on the north side of the crestline. At Economy Point, a flood dominance is observed between East and Centre Bars, and on all parts of East Bar except for the blind, ebb channel. An ebb dominance is also predicted for the southeastern part of Centre Bar to complement the flood dominance shown by Klein (1970) for the area north of the crest. On Selmah Bar, the limited current data indicate that all of the bar is flood dominated with the exception of a band along the northern side that extends only a short distance west of the major swatchway.

These time-velocity asymmetries and their areal distributions are believed to result primarily from the influence

of the bar topography on the flow. When the bar crests are submerged, the tidal currents flow obliquely up one side of the bar and down the other, because the crestlines are oriented at a slight angle to both the ebb and flood currents. The inertia of the currents as they encounter the bar produces high current speeds and shear velocities on the exposed up-stream side and low values on the sheltered down-stream side. When the tidal currents reverse, the areas of strong and weak flow are interchanged, thereby producing opposite directions of dominance on either side of the bar. Because the strongest currents are directed up-slope during both the flood and ebb, a convergence of sediment toward the bar crest can occur without the necessity of invoking helical flow. Indeed, examination of flow-direction changes between the top and bottom of profiles, combined with the existence of a down-slope flow on one side of the bar during both halves of the tidal cycle, clearly indicate that helical flow is not present in this macrotidal environment.

## 7.2 Sedimentological Responses

### 7.2.1 Sediment Transport

The tidal currents and the sediment transport produced by them are responsible for most of the sedimentological characteristics of the sand bars that were studied, including specifically the bedforms and sediment grain size. In order to study the sediment transport directly, fluorescent tracer

experiments were conducted at 29 sites, using a two-dimensional spatial-integration technique. During the course of the analysis, a method was devised, with the aid of Dr. P.D.M. Macdonald of the Applied Mathematics Department, McMaster University, for the estimation of the confidence intervals of the tracer distribution centroid. The efficiency of tracer recovery has also been calculated for each distribution, with results that range from less than 1% to more than 1000%. The average recovery is 40.8%, but more than 45% of them are less than 10%. Despite this, the internal consistency of the data, combined with favourable comparisons with additional data obtained in this and other studies suggests that tracer results (Table 6.2) are reasonably accurate, and provide valuable information regarding the sediment transport on the sand bars.

As suggested by the existence of time-velocity assymmetries, all sites show a residual discharge of sediment. The average speed of particle movement (centroid migration speed) ranges from 0.05 to 6.46 metre per tidal cycle, but averages between one and two m/cycle for all sites; nearly two orders of magnitude less than the 100 m/cycle value given by Balazs and Klein (1972). The residual unit sediment discharges calculated from the tracers vary greatly from place to place and range from 0.38 to 1793 kg/cycle, with an average of approximately 350 kg/cycle. The residual

discharges are generally higher in the channels than on the bar crests, because the flow is stronger and of longer duration in the channels. The average discharge also varies between bars in accordance with flow strength differences: Big Bar with the weakest currents, has an average unit discharge of 49.4 kg/cycle; whereas Diamond Bar with the strongest currents has an average unit discharge of 709 kg/cycle.

The residual sediment discharges calculated from the hydraulic data using the transport theories of Engelund and Hansen (1967) and Ackers and White (1973) are in good agreement with the tracer results (Figure 6.18), considering the high degree of flow unsteadiness. The correlation coefficients for both relationships are more than 0.75 and are significant at greater than 99%; however, the tracer discharges are overestimated by a factor of 5.5 times by the Engelund-Hansen method, and 8.1 times by the Ackers-White formula. The Einstein (1950) transport function produces less consistent results, underestimating the tracer discharge at low transport rates, and overestimating it at high discharges; a characteristic noted in other studies. The tracer results are believed to be reasonably accurate, as they are in nearly perfect agreement with the discharges derived from net bedform migration rates at low transport rates. As expected, the bedform migration rates underestimate the tracer discharges at higher transport rates,

because the increased amount of material moving in intermittent suspension does not all contribute to the bedform movement. It is notable that the residual discharges in the tidal environment are 10 to 100 times less than those measured in unidirectional flows with comparable bedforms.

The directions of residual sediment transport as determined by the tracers (Figure 6.17) are in excellent agreement with those deduced from the time-velocity assymmetries of the tidal currents. On Big Bar, sediment moves westward on the north side of the crest, and eastward on the south side. At Economy Point, the transport is to the east in most of the area studied, except in the blind ebb channel on East Bar and on the southeast portion of Centre Bar where it is ebb-dominated. A transport parting is suggested for the southern half of the low area between Centre and East Bars. In Cobequid Bay, flood-dominated transport occurs on the gentle north side of Diamond Bar, and on the south side and much of the west end of Selmah Bar. A westward ebb transport is present on the opposite steep side of both bars.

Sediment is, therefore, moving in opposite directions on either side of sand bar crestlines in almost all areas studied. The sediment converges toward the bar crest in most places, and there is a suggestion that the up-slope component is strongest on the gentle side of the bars. It also appears that the bar crests stand higher in those areas where the

angles between the transport directions and the crestline are greatest. Wave activity also influences the height to which the bars build.

The results from Diamond and Selmah Bars, combined with other observations, indicate that Cobequid Bay has an overall pattern of sediment circulation (Figure 6.19) which is broadly similar to the ebb-tidal delta model of Hayes et al. (1973). Sediment moves westward down the axis of the bay at a high rate, requiring only an estimated 6.25 years to move directly down the length of the sand body. Sediment moves back eastward toward the head of the bay in the channels bordering both the north and south shores, but at a slower rate, so that more than 15.5 years are needed for the return trip. The pattern of sediment transport produces two large-scale sediment circulation cells, one located in the northern half of Cobequid Bay with a clockwise direction of transport, and the other in the southern half of the bay with counter-clockwise sediment movement. Transport transverse to the axis of the bay occurs in the swatchways, as shown particularly by the ebb dominance in the major swatchway at the east end of Diamond Bar. This brings about mixing between the outgoing and incoming sediment streams, and disrupts the two major sediment circulation cells into smaller units which have the same direction of transport as the major cell of which they are a part.

The tracer experiments also provide considerable information on the characteristics of sediment dispersion from a point source under the influence of tidal currents. The tracer distributions (see Figures 6.7 to 6.14) generally exhibit a simple elliptical shape, with a single mode, displaced from the origin in the direction of the residual transport. Occasionally, tracer is found dispersed in both the ebb and flood directions producing bilobate but unimodal distributions. More complicated distributions are rare, and most result from the secondary flow associated with large bedforms. Virtually all distributions are elongated parallel to the tidal currents; the longitudinal dispersion averaging approximately 3.5 times the lateral dispersion. The tracer distributions tend to be skewed in the direction of transport, as is also the case in unidirectional flow, but the longitudinal asymmetry appears smaller in the tidal situation. Transverse to the flow, the distributions are nearly symmetrical on average, with respect to both the direction of transport and the slope of the bar surface.

A comparison of distributions obtained from the same sites at different elapsed times reveals that the tracer distributions become more symmetrical as the dispersion time increases, both parallel and transverse to the flow. This behaviour is noted in unidirectional flow as well. In addition, the centroid migration rate, and the rates of longitudinal and lateral dispersion, are highest at short elapsed

times and decrease as the time increases. Insufficient data are available to allow determination of the time required for the rates to stabilize as expected. The accommodation time is believed, however, to be generally longer in the tidal environment than in unidirectional flow, despite the increased longitudinal dispersion caused by the reversing currents, because the residual discharges are lower in the tidal case. The experiments show that the initial rate of longitudinal dispersion is positively correlated with the migration speed of the centroid, and with the maximum mean current speed and average maximum shear velocity. Only the first relationship is statistically significant, however.

The many similarities in transport behaviour noted between tidal and unidirectional flows indicate that the residual transport produced by the asymmetrical, reversing tidal currents is not fundamentally different from that in fluvial or flume conditions. This implies that many of the features noted in this study regarding bedform and grain size characteristics may have a more universal significance.

### 7.2.2 Bedforms

The variety of bedforms developed on the sand bars are an obvious expression of the sediment transport just described. Two large-scale types with apparent unidirectional flow analogues are recognized: megaripples (dunes) and sand

waves.

Megaripples (Figure 4.1) have a three-dimensional appearance and crestal continuity is generally poor, although many examples are more continuous than their unidirectional flow counterparts. The troughs of all megaripples possess scour pits which produce the trough and crestline elevation irregularities that are characteristic of the megaripples. Heights range widely from 0.1 to 1.2 metres, but average 0.26 metres. Lengths average 4.2 metres, and are rarely greater than 8 metres. Unless modified during emergence, megaripples invariably possess an angle of repose slip face which produces a single set of cross-bedding (Figure 4.7). Reactivation surfaces break the continuity of the cross-stratification in areas where the megaripples are not completely reworked during each half of the tidal cycle. The horizontal spacing between successive reactivation surfaces gives the residual migration of the bedform in one tidal cycle. This could be used in an ancient deposit to obtain a minimum estimate of the paleotransport rates. Grain size segregation occurs over megaripples, with the coarse material being concentrated in the trough and lower part of the slip face (Table 5.2).

In contrast to megaripples, sand waves (Figure 4.2) lack scour pits, so that trough and crestline elevations are uniform. Sand waves are more continuous than megaripples

although the difference is in part an illusion produced by the larger size of sand waves, which have a mean height of 0.44 metres and a mean length of 12.8 metres. The largest sand wave observed has a height and length of 3.5 and 350 metres, respectively. The above average values indicate that sand waves are distinctly flatter than megaripples which have length to height ratios generally less than 20 to 1. An almost perfect discrimination between megaripples and sand waves is obtained (Figure 4.6) with the equation (all values in metres):

$$\text{Height} = 0.072 \quad \text{Length} - 0.21$$

Furthermore, sand wave crestline orientations are generally skewed at approximately 45° to the flow and sediment (tracer) transport directions (Figures 6.8 and 6.12), whereas megaripples are generally oriented normal to the flow. The oblique orientation of the sand waves occurs because of migration rate differences along the length of their crestlines, brought about by lateral variations in sand wave height and sediment discharge.

Two varieties of sand wave can be distinguished, on the basis of the predominant superimposed bedform type: rippled, and megarippled sand waves. Rippled sand waves generally have smaller heights than the megarippled type, but lengths overlap considerably.

Most sand waves do not possess an angle of repose slip face, and lee-side inclinations of about 20° are common. Even the very large subtidal extensions of the sand waves on the north side of Diamond Bar lack avalanche faces and have lee-side dips of approximately 12°. The internal stratification of most sand waves is, therefore, composite and produced by the superimposed bedforms. This would make the identification of the sand wave form difficult in an ancient deposit. Unlike megaripples, the crestal area of sand waves that lack a slip face is coarser grained than the trough. Some small rippled sand waves do have slip faces, however, and in these the size segregation is the same as that found over megaripples. Internally these sand waves contain many closely-spaced reactivation surfaces.

Flow strength and mean grain size exercise a strong controlling influence on the type of bedform developed (Figure 4.13). Water depth is of secondary importance. Ripples and rippled sand waves form at lower current speeds and shear velocities than do megarippled sand waves and megaripples. On the basis of the available data, however, the stability fields of the latter two bedforms overlap markedly in terms of flow strength, but are clearly separated by a mean grain size of 1.7 phi (0.31 mm), with no megarippled sand waves present in finer sands. In addition, rippled sand waves are not known from sands coarser than approximately

1.0 phi (0.50 mm). The time-velocity asymmetry may also be greater in areas where sand waves are present than it is over megaripples. The existence of well defined stability fields for the different bedform types suggests that the morphological distinctions used here are valid and of potential usefulness.

The stratigraphic sequence expected to result from progradation in the study area is given by Knight and Dalrymple (1975). A thick cross-bedded unit of medium sand that represents the elongate tidal sand bars, which form in the subtidal zone and lower half of the intertidal zone, is present at the base. This is overlain by fine, rippled sand similar to that present at the head of Cobequid Bay. Mudflat and salt marsh deposits cap the sequence. Within the medium sand unit, cross-bedding directions will tend to be unidirectional in a restricted area, due to the dominance of one half of the tidal cycle. Laterally or vertically adjacent beds could show transport in the opposite direction, however, because the zones of ebb and flood dominance are mutually exclusive. In Cobequid Bay, the areal extent of flood dominance is greater than that of the ebb, possibly because of the residual transport rate differences noted above. As a result, flood-oriented cross-strata may be more abundant than ebb-oriented sets. Herringbone cross-bedding is likely to be rare, except in areas with little residual transport,

such as on bar crests.

In addition to reactivation surfaces, various other minor features should be preserved that are indicative of the unsteady flow and/or emergence (Figure 4.16). Upper flow regime parallel bedding, produced by locally steepened water surface slopes at low tide, may be present near the base of some ebb channels. Ripples that are produced by the low velocity flows near high and low tide, or during emergence, mantle all previously formed bedforms in the intertidal zone, and presumably in the subtidal zone as well. On the exposed parts of the bars, however, these ripples, and small deltas that have been built laterally into scour pits by the ebb runoff, indicate flow at a high angle to that of the larger bedforms. This may not be the case in the subtidal zone. Wave ripples, and beach-like parallel lamination that forms on the steeper exposed portions of some bars, may also be preserved. Convolute bedding (Figure 4.17), produced by the wave-shock liquefaction of fine sands in shallow water (and not by earthquakes) might also be present. Water-level marks on bedform lee faces are the best indicators of emergence.

Little visible evidence of winter conditions (Figure 4.18) is likely to exist in the sand bar deposits. The ice crust immobilizes most of the sediment in the intertidal zone, but sediment movement continues in the channels at this

time, and should even be increased by the 1.75-fold viscosity increase resulting from the lower water temperatures. Drift ice deposits exotic coarse material, including pieces of salt marsh and bedrock, that cannot normally be moved by the tidal currents. Large-scale ebb cross-bedding that fills deep scours formed where the ice crust is breached, may be preserved even in flood-dominated areas. Lateral runoff channels are more erosive during the winter because the ice crust concentrates the ebb drainage.

Winter and low-tide modification features are not expected to be commonly preserved in the stratigraphic record because of thorough tidal-current reworking. They do, however, provide extremely valuable information regarding the conditions of sedimentation and should not be ignored. The bulk of the preserved sediments will be characterized by cross-bedding produced by the tidal megaripples.

### 7.2.3 Grain Size

Analysis of nearly 300 samples (Appendix 3) from various sand bars shows that the average size characteristics of the sediment in this macrotidal environment are: mean size - 1.50 phi (medium sand); sorting - 0.63 phi-units (moderately well sorted); skewness - -0.19 (nearly symmetrical); and kurtosis - 8.92 (leptokurtic). A distinct difference exists, however, between the sands in Cobequid Bay and those

forming the isolated bars on the Minas Basin foreshore (Big Bar and Economy Point). The latter areas possess considerably greater quantities of pebbles and granules, which makes the sediments there coarser grained, more poorly sorted and more negatively skewed. Taken as a whole, the tidal sand bar sediments have size characteristics that are intermediate between those of rivers and beaches (Friedman, 1967).

On all of the bars studied, the grain size is coarsest and the sorting poorest in those areas lying closest to extensive areas of gravel lag (Figures 5.8 to 5.11). This lag gravel generally occupies the intertidal foreshore on the shoreward side of the bars, except at Economy Point where it is found on the outer edge of the sand bar complex. In addition, there is a tendency for the sand in the channels to be coarser grained and more poorly sorted than sediment on the bar crests. This should be reflected in the preserved stratigraphic sequence. In Cobequid Bay, the sediment circulation pattern, combined with the headward decrease in grain size mentioned earlier has a strong influence on the distribution of grain size. The ebb-dominated channels along the axis of the bay contain fine, well-sorted sands that have been transported westward from the area of rippled, fine sand at the head of the bay. In contrast, the flood-dominated channels along either shore contain coarser and more poorly sorted sediment. Big Bar is the only area where

there is a statistically significant correlation between mean grain size and flow strength; finer sizes occurring where the shear velocity is lower.

Examination of individual samples reveals that they are formed by the mixing of three size populations in various proportions. This is reflected in the interrelationships that exist between the mean size and both the skewness and kurtosis: skewness values are most negative for mean sizes between 1 and 2 phi (0.50-0.25 mm), becoming less negative in both finer and coarser sands (Figure 5.6); and kurtosis is highest for sizes between 1.5 and 2 phi (0.35-0.25 mm) (Figure 5.7).

In this study the three basic size populations are considered to be composed of material that has been transported by different mechanisms: the coarse C population is moved by traction, that is by rolling, sliding and saltation in the bedload layer; the intermediate A population is bed material that is transported in intermittent suspension, the particle weight supported temporarily by fluid turbulence; and the fine B population is the wash load that moves in continuous suspension. The sharp kinks or "breaks" in the cumulative curves correspond to the grain sizes at which one transport mechanism is replaced by another. In previous studies, both truncated-normal (straight-line segments) and overlapping-normal models have been proposed for the size

distribution of the populations. In this study, the latter model has been adopted, and the graphical dissection technique of Cassie (1954, 1963) has been used to extract the component populations in 32 samples (Table 5.5). In nearly all cases, the fit obtained with overlapping-normal populations is better than that using truncated-normals (see Figures 5.13 to 5.15).

The average mean size and standard deviation of each population type are: C populations - -0.18 phi (very coarse sand) and 1.15 phi-units (moderately sorted); A populations - 1.70 phi (medium sand) and 0.44 phi-units (moderately well sorted); and B populations - 2.56 phi (fine sand) and 0.93 phi-units (moderately sorted). The "break" between the C and A populations has also been determined, using three different methods: (i) the point of intersection of straight-line segments; (ii) point of equal overlap of normal populations; and (iii) the point of equal contribution of overlapping normal populations. The break sizes obtained from the point of equal overlap (Table 5.5) range from 0.15 to 1.79 phi (0.90-0.29 mm). The sizes derived from method (i) are consistently finer than these values, whereas those obtained by method (iii) are generally coarser; however, statistically significant relationships exist between the three sets of results (Figure 5.22).

The areal variations of C and A population

characteristics (Figures 5.16 and 5.18) conform closely, as expected, to the variations of sample mean size and sorting. The coarse C population is more abundant, and the mean sizes of both the C and A populations are coarser in those areas where the entire sample is coarser and more poorly sorted; namely adjacent to areas of gravel lag and in the channels. The sorting of both C and A populations improves, and the mean sizes become finer away from these areas. Within Cobequid Bay, the finest and best sorted A populations are present in the ebb-dominated portion of the system.

Hydraulic sorting mechanisms, particularly the competence relationships of traction and intermittent suspension transport (Figure 5.20), are believed to be important in determining the characteristics of the populations, provided that there are no source limitations. For traction transport, the competence can be derived from the Shields curve. The competence of intermittent suspension should be given by the grain size whose fall velocity is equal to the shear velocity of the flow (Middleton, 1976). A comparison of the fall velocity determined for the "break" between the C and A populations by each of the three methods listed above with both the time-averaged and average maximum shear velocities (Figure 5.23) yields statistically significant correlation coefficients. The time-averaged shear velocity underestimates the fall velocity of the "break" considerably; however, the

average maximum shear velocity provides almost perfect agreement. The point of equal overlap appears to be the best estimate of the size at which intermittent suspension transport becomes important. These results provide strong evidence that the size populations are hydraulically produced, and that they have overlapping-normal distributions.

In order to explain the areal variations of the C and A population mean sizes, it is necessary to consider two situations: transport down a flow-strength gradient, and transport up a flow-strength gradient.

In the first case, the gradual decrease in flow strength leads to the progressive truncation of both the A and C populations through the action of the competence relationships given above (Figure 5.20). As a result, the mean sizes of the C and A populations should be finer where the flow is weaker. This relationship is clearly evident on Big Bar and at Economy Point, where the dominant A population mean sizes are significantly correlated with both the time-averaged and average maximum shear velocities (Figures 5.21A and B). Similar, though non-significant relationships are obtained for the flood-dominated portions of Diamond and Selmah Bars.

In contrast, the ebb-dominated areas of these bars represent the second case in which sediment is transported from lower to higher energy conditions. In this situation,

the sediments inherit the fine-grained characteristics that they acquired at the head of the bay. This takes place because the coarser material that could be transported in the stronger flows is not available, having been hydraulically removed by the low-energy conditions at the source.

The tracer experiments utilizing five different coloured size fractions show that the transport speed of all sizes is significantly and positively correlated with some measure of flow strength (Table 6.4). There are, however, important differences in the transport behaviour as a function of size (Figures 6.15 and 6.16) between the traction and intermittent suspension fractions. For those coarse sizes that are part of the traction (C) population, the transport speeds, and the longitudinal and lateral dispersion rates as a function of time are virtually independent of grain size, increasing only slightly as the grain size decreases. For finer material moving in intermittent suspension, the transport speed and dispersion rates are strongly dependent on the grain size and increase continuously as the size decreases. The differing dependence on grain size exhibited by the two transport mechanisms may explain why C populations are more poorly sorted than A populations.

These contrasting behaviours are a direct result of the mode of transport of the various grain sizes. All sizes moving by traction remain in close contact with the bed and,

therefore, have little chance of bypassing a bedform lee where deposition occurs. As a result, the step lengths and transport speeds of the different sizes are controlled by bedform migration rather than by grain size. In intermittent suspension, however, the grains rise above the bed and can bypass one or more bedforms before being deposited. The ability of the flow to maintain a grain in suspension must increase as the grain size and settling velocity decrease, so that the step lengths and transport speeds are inversely related to the grain size.

Further examination of the results reveals that the fall velocity of the size at which the transition occurs between traction and intermittent suspension behaviour is almost identical to the average maximum shear velocity of the flow, as it should be according to the intermittent suspension competence criterion (Figure 5.20). This provides strong independent evidence that the hydraulic interpretation of the size populations adopted here is correct.

## REFERENCES


ACKERS, P. and WHITE, W.R., 1973. Sediment transport: new approach and analysis. Proc. Amer. Soc. Civil Eng., 99, no. HY11, 2041-2060.

ALLEN, G.P., 1972. Étude des processus sédimentaires dans l'estuaire de la Gironde. Unpubl. Thèse de Doctorat d'Etat es sciences naturelles, L'Université de Bordeaux, 314p.

ALLEN, G., DERESSEGUIER, A. and KLINGEBIEL, A., 1969. Évolution des structures sédimentaires sur un banc sableux d'estuaire en fonction de l'amplitude des marées. C. R. Acad. Sci., 269D, no. 22, 2167-2169.

ALLEN, G.P., CASTAING, P. and KLINGEBIEL, A., 1972. Distinction of elementary sand populations in the Gironde Estuary (France) by R-mode factor analysis of grain-size data. Sedimentology, 19, 21-35.

ALLEN, J.R.L., 1965. Sedimentation in the lee of small underwater sand waves: an experimental study. Jour. Geol., 73, 95-116.

ALLEN, J.R.L., 1968a. Current Ripples: Their Relation to Patterns of Water and Sediment Motion. North-Holland Pub. Co., Amsterdam, 433p.

ALLEN, J.R.L., 1968b. The diffusion of grains in the lee of ripples, dunes, and sand deltas. Jour. Sed. Petrol., 38, 621-633.

ALLEN, J.R.L., 1973. Features of cross-stratified units due to random and other changes in bed forms. Sedimentology, 20, 189-202.

ALLEN, J.R.L. and BANKS, N.L., 1972. An interpretation and analysis of recumbent-folded deformed cross-bedding. Sedimentology, 19, 257-284.

ALLEN, J.R.L. and COLLINSON, J.D., 1974. The superimposition and classification of dunes formed by unidirectional aqueous flows. Sedimentary Geology, 12, 169-178.

AMOS, C., 1975. The sediment budget of the Minas Basin, Nova Scotia. Rept. of the Workshop on the Mathematical Aspects of Fundy Tidal Power, Canadian Math. Congress Summer Research Inst., Halifax, N.S., p.3.

ATLANTIC TIDAL POWER ENGINEERING AND MANAGEMENT COMMITTEE (ATPEMC), 1969. Report to Atlantic Tidal Power Programming Board on Feasibility of Tidal Power Development in the Bay of Fundy, Halifax, Nova Scotia.

BAGNOLD, R.A., 1954. Experiments on a gravity-free dispersion of large solid spheres in a Newtonian fluid under shear. Roy. Soc. London Proc., Ser. A, 225, 49-63.

BAGNOLD, R.A., 1956. The flow of cohesionless grains in fluids. Phil. Trans. Roy. Soc. London, Ser. A, 249, 235-297.

BAGNOLD, R.A., 1966. An approach to the sediment transport problem from general physics. U.S.G.S. Prof. Paper 422-I, 37p.

BAJARD, J., 1966. Figures et structures sédimentaires dans la partie orientale de la baie du Mont Saint-Michel. Rev. Geog. Phys. Geol. Dym., VIII, 39-112.

BALAZS, R.J. and KLEIN, G. de V., 1972. Roundness-mineralogical relations of some intertidal sands. Jour. Sed. Petrol., 42, 425-433.

BANKS, N.L., 1973. The origin and significance of some downcurrent-dipping cross-stratified sets. Jour. Sed. Petrol., 43, 423-427.

BARR, J.L., DINKELMAN, M.G. and SANDUSKY, C.L., 1970. Large epoxy peels. Jour. Sed. Petrol., 40, 445-449.

BASUMALLICK, S., 1966. Size differentiation in a cross-stratified unit. Sedimentology, 6, 35-88.

BLACKLEY, M.W.L., CARR, A.P. and GLEASON, R., 1972. Tracer experiments in the Taw-Torridge estuary with particular reference to Braunton Burrows NNR. Rept. no. USC 1972/22, Unit of Coastal Sedimentation, 19p.

BLATT, H., MIDDLETON, G.V. and MURRAY, R., 1972. Origin of Sedimentary Rocks. Prentice-Hall, Inc., Englewood Cliffs, N.J., 634p.

BOERSMA, J.R., 1969. Internal structure of some tidal mega-ripples on a shoal in Westerchelde Estuary, The Netherlands. Geol. en Mijnbouw, 48, 409-414.

BOON, J.D., III, 1968. Trend surface analysis of sand tracer distributions on a carbonate beach, Bimini, B.W.I. Jour. Geol., 76, 71-87.

BOON, J.D., III, 1969. Quantitative analysis of beach sand movement, Virginia Beach, Virginia. Sedimentology, 13, 85-103.

BOOTHROYD, J.C., 1969. Hydraulic conditions controlling the formation of estuarine bedforms. In Coastal Environments: N.E. Massachusetts and New Hampshire. Contr. no. 1-CRG, Univ. Mass. Dept. Geology Pub. Series, 417-427.

BOOTHROYD, J.C. and HUBBARD, D.K., 1972. Bedform development and distribution pattern, Parker and Essex River estuaries, Massachusetts. U.S. Army Corps of Engineers, Coastal Engineering Research Centre, Misc. Paper 1-74, 79p.

BOOTHROYD, J.C. and HUBBARD, D.K., 1975. Genesis of bedforms in mesotidal estuaries. In Estuarine Research (ed. L.E. Cronin), Vol. 2, 217-234. Academic Press, Inc., N.Y.

BOUYSSE, P., HORN, R., LAPIERRE, F. and LE LANN, F., 1976. Etude des grands bancs de sable du sud-est de la mer Celtique. Marine Geol., 20, 251-275.

BOWDEN, K.F. and HOWE, M.R., 1963. Observations of turbulence in a tidal current. Jour. Fluid Mech., 17, pt. 2, 271-284.

BRIGGS, L.I. and MIDDLETON, G.V., 1965. Hydromechanical principles of sediment structure formation. In Primary Sedimentary Structures and their Hydrodynamic Interpretation (ed. G.V. Middleton). Soc. Econ. Paleont. and Mineral., Spec. Pub. No. 12, Tulsa, 5-16.

CAMERON, H.C., 1961. Interpretation of high-altitude small-scale photography. The Canadian Surveyor, XV, no. 110, 567-573.

CAMERON, W.M. and PRITCHARD, D.W., 1963. Estuaries. In The Sea (ed. M.N. Hill), Vol. 2, John Wiley and Sons, N.Y., 306-324.

CANADIAN HYDROGRAPHIC SERVICE, 1971-1975. Canadian Tide and Current Tables. Atlantic Coast and Bay of Fundy, Dept. of the Environment, Ottawa, Vol. 1.

CASSIE, R.M., 1954. Some uses of probability paper in the analysis of size frequency distributions. Australian Jour. Marine and Freshwater Res., 5, 513-522.

CASSIE, R.M., 1963. Tests of significance for probability paper analysis. New Zealand Jour. Sci., 6, 474-482.

CASTON, V.N.D., 1972. Linear sand banks in the southern North Sea. Sedimentology, 18, 63-78.

CASTON, V.N.D. and STRIDE, A.H., 1970. Tidal sand movement between some linear sand banks in the North Sea off northeast Norfolk. Marine Geol., 9, M38-M42.

CHARNOCK, H., 1959. Tidal friction from currents near the seabed. Geophys. Jour. Roy. Astron. Soc., 2, 215-221.

CHURCHILL, F.J., 1924. Recent changes in the coast line in the county of Kings, Nova Scotia. Proc. and Trans., Nova Scotia Inst. Sci., 1b, 84-86.

CLARK, I., 1976. ROKE: A program for non-linear least squares decomposition of mixtures of distributions. Geocom Bull., in press.

CLARK, M.W., 1976. A discussion of some methods for the statistical analysis of multimodal distributions, and their application to grain size data. Internat. Assoc. Math. Geol., in press.

CLARK, M.W. and CLARK, I., 1976. A sedimentological pattern recognition problem. In Quantitative Techniques for the Analysis of Sediments (ed. D.F. Merriam), Pergamon Press, Toronto, 121-141.

CLIFTON, H.E., 1969. Beach lamination: nature and origin. Marine Geol., 7, 553-559.

COASTAL ENGINEERING RESEARCH CENTRE, 1973. Shore Protection Manual. Corps of Engineers, U.S. Dept. of the Army, Fort Belvoir, Virginia, 3 vols.

COLBY, B.R., 1964. Discharge of sands and mean-velocity relationships in sand-bed streams. U.S.G.S. Prof. Paper 462-A, 47p.

COLE, C.U., TARAPORE, Z.S., KANHERE, V.N. and DIXIT, J.G., 1973. Sediment discharge formulae - a comparative analysis. Internat. Assoc. for Hydraulic Res., Proc. Internat. Symp. on River Mech., Bangkok, 547-560.

COLLINSON, J.D., 1970. Bedforms of the Tana River, Norway. Geog. Annaler, 52, 31-56.

COSTELLO, W.R., 1974. Development of bed configurations in coarse sands. Rept. 74-1, Mass. Inst. Technology, Cambridge, Mass., 120p.

COURTOIS, G. and MONACO, A., 1969. Radioactive methods for the quantitative determination of coastal drift rates. Marine Geol., 7, 183-206.

CRAIG, H.D., 1976. Biofacies and biogenic structures of Cobequid Bay. M.Sc. Thesis, McMaster University, in preparation.

CRAIG, H.D. and RISK, M.J., 1975. Biofacies of Cobequid Bay, Bay of Fundy. Geol. Soc. Amer. Abstr. with Programs, 7, no. 6, 741-742.

CRICKMORE, M.J., 1967. Measurement of sand transport in rivers with special reference to tracer methods. Sedimentology, 8, 175-228.

CRICKMORE, M.J. and LEAN, G.H., 1962a. The measurement of sand transport by means of radioactive tracers. Proc. Roy. Soc. London, Ser. A, 266, 402-421.

CRICKMORE, M.J. and LEAN, G.H., 1962b. The measurement of sand transport by the time-integration method with radioactive tracers. Proc. Roy. Soc. London, Ser. A, 270, 27-47.

CURRAY, J.R., 1960. Sediments and history of Holocene transgression, continental shelf, northwest Gulf of Mexico. In Recent Sediments, Northwest Gulf of Mexico (eds. F.P. Shepard, F.B. Phlegar and T.H. Van Andel). Amer. Assoc. Petroleum Geologists, Tulsa, 221-266.

DABOLL, J.M., 1969. Holocene sediments of the Parker River estuary. In Coastal Environments, N.E. Massachusetts and New Hampshire (ed. M.O. Hayes). Contr. No. 1-CRG, Univ. Mass. Dept. Geology Pub. Series, 337-355.

DALRYMPLE, R.W., 1973a. Preliminary study of an intertidal sand body, Cobequid Bay, Bay of Fundy, Nova Scotia. Maritime Sediments, 9, 21-28.

DALRYMPLE, R.W., 1973b. Sediment texture and transport studies in an intertidal environment: a progress report. Maritime Sediments, 9, 45-58.

DALRYMPLE, R.W., 1974. Factor analysis of grain-size data from Cobequid Bay, Bay of Fundy, Nova Scotia. Geol. Soc. Amer. Abstr. with Programs, 5, no. 1, 17.

DALRYMPLE, R.W., 1976. Sediment transport in a macrotidal environment (Bay of Fundy). Trans. Amer. Geophys. Union (EOS), 57, 268.

DALRYMPLE, R.W., KNIGHT, R.J. and MIDDLETON, G.V., 1975. Intertidal sand bars in Cobequid Bay (Bay of Fundy). In Estuarine Research (ed. L.E. Cronin), Vol. II, 293-307. Academic Press, Inc., N.Y.

DAVIES, J.L., 1964. A morphogenic approach to world shorelines. Zeits. fur Geomorph., 8, 127-142.

DAWSON, W., 1917. Tides at the head of the Bay of Fundy. Dept. of Naval Service, Ottawa, 34p.

DOEGLAS, D.J., 1946. Interpretation of the results of mechanical analyses. Jour. Sed. Petrol., 16, 19-40.

DUANE, D.B. and JUDGE, C.W., 1969. Radioisotopic sand tracer study, Point Conception, California. Coastal Engineering Research Centre, Misc. Paper 2-69.

DUFF, G.F.D., 1970. Tidal resonance and tidal barriers in the Bay of Fundy system. Jour. Fish. Res. Bd. Canada, 27, 1701-1728.

DYER, K.R., 1970. Current velocity profiles in a tidal channel. Geophys. Jour. Roy. Astron. Soc., 22, 153-161.

DYER, K.R., 1972. Bed shear stresses and the sedimentation of sandy gravels. Marine Geol., 13, M31-M36.

EINSTEIN, H.A., 1937. Bed load transport as a probability problem. Translation in Shen, H.W. (ed.), 1972, Sedimentation. Symp. to Honour Prof. H.A. Einstein, Fort Collins, C1-C105.

EINSTEIN, H.A., 1950. The bed-load function for sediment transportation in open channel flows. U.S. Dept. Agriculture, Soil Conservation Service, Tech. Bulletin No. 1026, 78p.

EMERY, K.O., 1945. Entrapment of air in beach sand. Jour. Sed. Petrol., 15, 39-49.

ENGELUND, F. and HANSEN, E., 1967. A monograph on sediment transport in alluvial streams. Teknisk Forlag, Copenhagen, 62p.

EVANS, G., 1965. Intertidal flat sediments and their environments of deposition in the Wash. Geol. Soc. London, Quart. Jour., 121, 209-245.

FIELLER, E.C., 1954. Some problems in interval estimation. Jour. Roy. Stat. Soc., Ser. B., 16, 175-185.

FOLK, R.L., 1955. Student operator error in determination of roundness, sphericity, and grain size. Jour. Sed. Petrol., 25, 297-301.

FOLK, R.L., 1971. Longitudinal dunes of the northwestern edge of the Simpson Desert, Northern Territory, Australia. 1. Geomorphology and grain size relationships. Sedimentology, 16, 5-54.

FOLK, R.L. and WARD, W.C., 1957. Brazos River bar, a study in the significance of grain-size parameters. Jour. Sed. Petrol., 27, 3-27.

FRANCIS, J.R.D., 1973. Experiments on the motion of solitary grains along the bed of a water stream. Proc. Roy. Soc. London, Ser. A, 332, 443-471.

FREUND, J.E., 1971. Mathematical Statistics, second edition. Prentice-Hall, Inc., Englewood Cliffs, N.J., 463p.

FRIEDMAN, G.M., 1962. On sorting, sorting coefficients and the lognormality of the grain-size distribution of sandstones. Jour. Geol., 70, 737-753.

FRIEDMAN, G.M., 1967. Dynamic processes and statistical parameters compared for size frequency distribution of beach and river sands. Jour. Sed. Petrol., 37, 327-354.

FRIEDMAN, G.M., 1971. Staining. In Procedures in Sedimentary Petrology (ed. R.E. Carver), Chapter 22, 511-530. John Wiley and Sons, Inc., Toronto, 653p.

FULLER, A.O., 1961. Size distribution characteristics of shallow marine sands from the Cape of Good Hope, South Africa. Jour. Sed. Petrol., 31, 256-261.

GARG, S.P., AGRAWAL, A.K. and SINGH, P.R., 1971. Bed load transportation in alluvial channels. Proc. Amer. Soc. Civil Eng., 97, no. HY5, 653-664.

GARRETT, C., 1972. Tidal resonance in the Bay of Fundy and Gulf of Maine. Nature, 238, 441-443.

GARRETT, C., 1974. Normal modes of the Bay of Fundy and Gulf of Maine. Can. Jour. Earth Sci., 11, 549-556.

GODIN, G., 1968. The 1965 current survey of the Bay of Fundy - A new analysis of the data and an interpretation of the results. Bedford Inst. Oceanography, Marine Sci. Branch, Rept. Ser. No. 8, 97p.

GOLDTHWAIT, J.W., 1924. Physiography of Nova Scotia. Geol. Survey Canada, Mem. 140, 179p.

GRAF, W.H. and ACAROGLU, E.R., 1966. Settling velocities of natural grains. Internat. Assoc. Sci. Hydrology Bull., 11, no. 4, 27-43.

GRANT, D.R., 1970. Recent coastal submergence of the Maritime Provinces, Canada. Can. Jour. Earth Sci., 7, 676-689.

GRANT, D.R., 1971. Glacial deposits, sea-level changes and Pre-Wisconsin deposits in southwest Nova Scotia. Geol. Survey Canada, Paper 71-1, part B, 110-113.

GREEN, C.D., 1975. A study of hydraulics and bedforms at the mouth of the Tay Estuary, Scotland. In Estuarine Research (ed. L.E. Cronin), Vol. II, 323-344. Academic Press, Inc., N.Y.

GRIGG, N.S., 1970. Motion of single particles in alluvial channels. Proc. Amer. Soc. Civil Engineers, 96, no. HY12, 2501-2518.

HÄNTZSCHEL, W., 1938. Bau und Bildung von Gros-Rippeln im Wattenmeer. Senckenbergiana, 20, 1-42.

HARDING, J.P., 1949. The use of probability paper for graphical analysis of polymodal frequency distributions. Jour. Marine Biological Assoc., 28, 141-153.

HARLEMAN, D.R.L., 1966. Real estuaries. In Estuary and Coastline Hydrodynamics (ed. A.T. Ippen. McGraw-Hill Book Co., Inc., N.Y., 522-545.

HARRIS, I. McK. and SCHENK, P.E., 1975. The Meguma Group. Maritime Sediments, 11, 25-46.

HARRIS, S.A., 1958. Probability curves and the recognition of adjustment to depositional environment. Jour. Sed. Petrol., 28, 151-163.

HAYES, M.O., 1975. Morphology of sand accumulations in estuaries: an introduction to the symposium. In Estuarine Research (ed. L.E. Cronin), Vol. II, 3-22. Academic Press, Inc., N.Y.

HAYES, M.O., OWENS, E.H., HUBBARD, D.K. and ABELE, R.W., 1973. The investigation of form and processes in the coastal zone. In Coastal Geomorphology (ed. D.R. Coates), Publ. in Geomorphology, S.U.N.Y., Binghamton, 11-41.

HIND, H.Y., 1875. The ice phenomena and the tides of the Bay of Fundy. Can. Monthly and National Review, 8, no. 3, 189-203.

HOUBOLT, J.J.H.C., 1968. Recent sediments in the southern bight of the North Sea. Geol. en Mijnbouw, 47, 245-273.

HUBBELL, D.W. and SAYRE, W.W., 1964. Sand transport studies with radioactive tracers. Proc. Amer. Soc. Civil Engineers, 90, no. HY3, 39-68.

INGLE, J.C., Jr., 1966. The movement of beach sand: an analysis using fluorescent tracers. Developments in Sedimentology, No. 5, Elsevier, Amsterdam.

INMAN, D.L., 1949. Sorting of sediments in the light of fluid mechanics. Jour. Sed. Petrol., 19, 51-70.

INMAN, D.L. and CHAMBERLAIN, T.K., 1959. Tracing beach sand movement with irradiated quartz. Jour. Geophys. Res., 64, 41-47.

INMAN, D.L., KOMAR, P.D. and BOWEN, A.J., 1969. Longshore transport of sand. Chapter 18, Coastal Eng. 1, Proc. 11th Conf. Coastal Eng., 298-309.

JENSEN, L.R., 1975. Late Triassic redbeds, Kingsport area. Maritime Sediments, 11, 77-81.

JONES, T.A., 1970. Comparison of the descriptors of sediment grain-size distributions. Jour. Sed. Petrol., 40, 1204-1215.

JOPLING, A.V., 1965. Laboratory study of the distribution of grain sizes in cross-bedded deposits. In Primary Sedimentary Structures and their Hydrodynamic Interpretation (ed. G.V. Middleton). Soc. Econ. Paleont. and Mineral., Spec. Pub. No. 12, Tulsa, 53-65.

JORDON, G.F., 1962. Large submarine sand waves. Science, 136, 839-848.

KALINSKE, A.A., 1943. Turbulence and the transport of sand and silt by wind. N.Y. Acad. Sci. Annals, 44, 41-54.

KENNEDY, J.F., 1963. The mechanics of dunes and antidunes in erodible-bed channels. Jour. Fluid Mechanics, 16, 521-544.

KENNEDY, V.C. and KOUBA, D.L., 1970. Fluorescent sand as a tracer of fluvial sediment. U.S.G.S. Prof. Paper 562-E, 13p.

KENYON, N.H. and STRIDE, A.H., 1970. The tide-swept continental shelf sediments between the Shetland Isles and France. Sedimentology, 14, 159-173.

KEULEGAN, G.H., 1938. Laws of turbulent flows in open channels. U.S. Nat. Bureau Standards, Jour. Res., 21, Paper no.1151, 707-741.

KLEIN, G. de V., 1962. Triassic sedimentation, Maritime Provinces, Canada. Geol. Soc. Amer. Bull., 73, 1127-1146.

KLEIN, G. de V., 1963. Bay of Fundy intertidal zone sediments. Jour. Sed. Petrol., 33, 844-854.

KLEIN, G. de V., 1967. Comparison of Recent and ancient tidal flat and estuarine sediments. In Estuaries (ed. G.H. Lauff), Amer. Assoc. Adv. Sci., Spec. Pub. 83, 207-218.

KLEIN, G. de V., 1968. Intertidal zone sedimentation, Minas Basin north shore, Bay of Fundy, Nova Scotia. In National Symposium on Ocean Sciences and Engineering of the Atlantic Shelf (eds. A.E. Margulies and R.C. Steere), Marine Tech. Soc. Trans., 91-107.

KLEIN, G. de V., 1970. Depositional and dispersal dynamics of intertidal sand bars. Jour. Sed. Petrol., 40, 1095-1127.

KLEIN, G. de V., 1971. An environmental model for some sedimentary quartzites. Program with Abstracts, VIII Internat. Sedimentological Congress, Heidelberg, p.51.

KLEIN, G. de V. and WHALEY, M.L., 1972. Hydraulic parameters controlling bedform migration on an intertidal sand body. Geol. Soc. Amer. Bull., 83, 3465-3470.

KNIGHT, R.J., 1971. Cobequid Bay sedimentology project - a progress report. Maritime Sediments, 7, 33-37.

KNIGHT, R.J., 1972. Cobequid Bay sedimentology project - a progress report. Maritime Sediments, 8, 45-60.

KNIGHT, R.J., 1973. Intertidal sedimentation in Cobequid Bay, Nova Scotia. In Fluvial Processes and Sedimentation, Proc. Hydrology Symp., Edmonton, Dept. of the Environment, Ottawa, 639-650.

KNIGHT, R.J. and DALRYMPLE, R.W., 1975. Intertidal sediments from the south shore of Cobequid Bay, Bay of Fundy, Nova Scotia, Canada. In Tidal Deposits (ed. R.N. Ginsburg), Springer-Verlag, N.Y., 47-55.

KNIGHT, R.J. and DALRYMPLE, R.W., 1976. Winter conditions in a macrotidal environment, Cobequid Bay, Nova Scotia. Rev. Géogr. Montr., XXX, nos.1-2, 65-85.

KOMAR, P.D. and INMAN, D.L., 1970. Longshore sand transport on beaches. Jour. Geophys. Res., 75, 5914-5927.

KRUMBEIN, W.C., 1934. Size frequency distributions of sediments. Jour. Sed. Petrol., 4, 65-77.

KRUMBEIN, W.C., 1938. Size frequency distributions of sediment and the normal phi curve. Jour. Sed. Petrol., 8, 84-90.

LAMBIASE, J.J., 1976. Sediment distribution and transport in the macrotidal Avon River estuary, Nova Scotia. Geol. Soc. Amer., Abstracts with Programs, 8, no. 2, 214.

LANE, E.W. and KALINSKE, A.A., 1939. The relation of suspended to bed material in rivers. Amer. Geophys. Union Trans., 20, 637-641.

LEAN, G.H. and CRICKMORE, M.J., 1966. Dilution methods of measuring transport of sand from a point source. Jour. Geophys. Res., 71, 5843-5855.

LUDWICK, J.C., 1972. Migration of tidal sand waves in Chesapeake Bay entrance. In Shelf Sediment Transport (eds. D.J.P. Swift, D.B. Duane and O.H. Pilkey), Dowden, Hutchinson and Ross, Stroudsburg, Pa., 377-410.

LUDWICK, J.C., 1974. Tidal currents and zig-zag sand shoals in a wide estuary. Geol. Soc. Amer. Bull., 85, 717-726.

LUDWICK, J.C., 1975a. Variations in the boundary-drag coefficient in the tidal entrance to Chesapeake Bay, Virginia. Marine Geol., 19, 19-28.

LUDWICK, J.C., 1975b. Tidal currents, sediment transport, and sand banks in Chesapeake Bay entrance, Virginia. In Estuarine Research (ed. L.E. Cronin), Vol. II, 365-380. Academic Press Inc., N.Y.

MAXWELL, D.H., 1966. Tides. Amer. Elsevier Pub. Co., Inc., N.Y., 240p.

McCAVE, I.N., 1971. Sand waves in the North Sea off the coast of Holland. Marine Geol., 10, 199-225.

McMANUS, D.A., 1963. A criticism of certain usage of the phi notation. Jour. Sed. Petrol., 33, 670-674.

McMANUS, J., 1973. Graded beach gravels as palaeowind indicators. Jour. Sed. Petrol., 43, 844-847.

McQUIVEY, R.S. and RICHARDSON, E.V., 1969. Some turbulence measurements in open-channel flow. Amer. Soc. Civil Eng. Proc., 95, no. HY1, 209-223.

McWHIRTER, N. and McWHIRTER, R. (eds.), 1972. Guinness Book of Records. Nineteenth Edition, Redwood Press Ltd., Enfield, G.B., 317p.

MELAND, N. and NORRMAN, J.O., 1966. Transport velocities of single particles in bed-load motion. Geographiska Annaler, 48, Ser. A, 165-182.

MELAND, N. and NORRMAN, J.O., 1969. Transport velocities of individual size fractions in heterogeneous bed load. Geographiska Annaler, 51, Ser. A, 127-144.

MIDDLETON, G.V., 1976. Hydraulic interpretation of sand size distributions. Jour. Geol., 84, 405-426.

MIDDLETON, G.V., KNIGHT, R.J. and DALRYMPLE, R.W., 1976. Abstracts, Amer. Assoc. Petroleum Geologists Annual Meeting, New Orleans, 90-91.

MIDDLETON, G.V., KNIGHT, R.J., DALRYMPLE, R.W. and LAMBIASE, J.J., 1975. Intertidal sand bodies in the Minas Basin, Bay of Fundy. Geol. Soc. Amer., Abstracts with Programs, 7, no. 2, 822.

MOFFAT, J.S., 1975. Fecal pellet production by Macoma balthica and pellet transport in Cobequid Bay, Nova Scotia. Unpub. B.Sc. Thesis, Dept. Geology, McMaster Univ., Hamilton, Ont.

MOSS, A.J., 1962. The physical nature of common sandy and pebbly deposits. Part 1. Amer. Jour. Sci., 260, 337-373.

MOSS, A.J., 1972. Bed-load sediments. Sedimentology, 18, 159-219.

MURRAY, S.P., 1967.. Control of grain dispersion by particle size and wave state. Jour. Geol., 75, 612-634.

NECE, R.E. and SMITH, J.D., 1970. Boundary shear stress in rivers and estuaries. Amer. Soc. Civil Eng. Proc., 96, no. WW2, 335-358.

NEVILLE, A.M. and KENNEDY, J.B., 1964. Basic Statistical Methods for Engineers and Scientists. International Textbook Co., Scranton, Pa., 325p.

NORDIN, C.F., Jr., 1971. Statistical properties of dune profiles. U.S.G.S. Prof. Paper 562-F, 41p.

OERTEL, G.F., 1972. Sediment transport of estuary entrance shoals and the formation of swash platforms. Jour. Sed. Petrol., 42, 857-863.

OFF, T., 1963. Rhythmic linear sand bodies caused by tidal currents. Bull. Amer. Assoc. Petrol. Geol., 47, 324-341.

OSER, R.K., 1972. Sedimentary components of northwest Pacific pelagic sediments. Jour. Sed. Petrol., 42, 461-467.

PELLETIER, B.R. and McMULLEN, R.M., 1972. Sedimentary patterns in the Bay of Fundy and Minas Basin. In Tidal Power (eds. T.J. Grey and O.K. Gashus), Plenum Press, N.Y., 153-187.

PETTIJOHN, F.J., POTTER, P.E. and SIEVER, R., 1972. Sand and Sandstone. Springer-Verlag, N.Y., 618p.

PHLIPPONNEAU, M., 1956. La baie du Mont Saint-Michel. Mem. Soc. Geol. Min. Bretagne, XI, 7-65.

POSTMA, H., 1967. Sediment transport and sedimentation in the estuarine environment. In Estuaries (ed. G.H. Lauff), Amer. Assoc. Adv. Sci., Spec. Pub. 83, 158-179.

POWERS, M.C., 1953. A new roundness scale for sedimentary particles. Jour. Sed. Petrol., 23, 117-119.

PREST, V.K., 1970. Quaternary geology in Canada. In Geology and Economic Minerals of Canada (ed. R.J.W. Douglas), Chapter XII, 676-764. Geol. Survey of Canada, Ottawa.

PRITCHARD, D.W. and BURT, W.V., 1951. An inexpensive and rapid technique for obtaining current profiles in estuarine waters. Jour. Marine Res., 10, 180-189.

PRYOR, W.A., 1971. Reservoir inhomogeneities of some Recent sand bodies. Final Rept. Amer. Petroleum Inst. Res. Project 91-B, 1 July, 1966 - 30 June 1968. Dallas, Amer. Petroleum Inst.

RAICKLEN, F., 1967. Some turbulence measurements in water. Amer. Soc. Civil Eng. Proc., 93, no. EM2, 73-97.

RAO, D.B., 1968. Natural oscillations of the Bay of Fundy. Jour. Fish. Res. Bd. Canada, 25, 1097-1114.

RATHBUN, R.E., KENNEDY, V.C. and CULBERTSON, J.K., 1971. Transport and dispersion of fluorescent tracer particles for the flat-bed condition, Rio-Grande conveyance channel, near Bernardo, New Mexico. U.S.G.S. Prof. Paper 562-I, 56p.

RATHBUN, R.E. and NORDIN, C.F., 1971. Tracer studies of sediment transport processes. Proc. Amer. Soc. Civil Eng., 97, no. HY9, 1305-1316.

RAUDKIVI, A.J., 1967. Loose Boundary Hydraulics. Pergamon Press, N.Y., 331p.

REDFIELD, A.C., 1950. The analysis of tidal phenomena in narrow embayments. Papers Phys. Oceanog. Meteorol., M.I.T., and Woods Hole Oceanog. Inst., 11, no. 4, 36p.

REED, W.E., LE FEVER, R. and MOIR, G.J., 1975. Depositional environment interpretation from settling-velocity (Psi) distributions. Geol. Soc. Amer. Bull., 86, 1321-1328.

REINECK, H.E., 1963. Sedimentgefüge im Bereich der Südlichen Nordsee. Abhandl. Senckenberg. Naturforsch. Ges., 505, 1-136.

REINECK, H.E., 1967. Layered sediments of tidal flats, beaches and shelf bottoms of the North Sea. In Estuaries (ed. G.H. Lauff), Amer. Assoc. Adv. Sci., Spec. Pub. 83, 191-206.

REINECK, H.E., 1972. Tidal flats. In Recognition of Ancient Sedimentary Environments (eds. J.K. Rigby and W.K. Hamblin), Soc. Economic Paleont. and Mineral., Spec. Pub. No. 16, 146-159.

REINECK, H.E. and SINGH, I.B., 1967. Primary sedimentary structures in the recent sediments of the Jade, North Sea. Marine Geol., 5, 227-235.

REINECK, H.E. and SINGH, I.B., 1975. Depositional Sedimentary Environments. Springer-Verlag, N.Y., 439p.

REINECK, H.E. and WUNDERLICH, F., 1968. Classification and origin of flaser and lenticular bedding. Sedimentology, 11, 99-104.

RISK, M.J., MOFFAT, J.S., YEO, R.K., CRAIG, H.D. and TUNNICLIFF, V.J., 1976. Animal-sediment relationships in the Minas Basin, Bay of Fundy. Geol. Assoc. Canada, Abstracts with Programs, 1, 84.

ROBINSON, A.H.W., 1960. Ebb-flood channel systems in sandy bays and estuaries. Geography, 45, 183-199.

ROGERS, J.J.W., 1965. Reproducibility and significance of measurements of sedimentary-size distributions. Jour. Sed. Petrol., 35, 722-732.

SCHENK, P.F., 1969. Carbonate-sulfate-redbed facies and cyclic sedimentation of the Windsorian Stage (Middle Carboniferous), Maritime Provinces. Can. Jour. Earth Sci., 6, 1037-1066.

SCHENK, P.E., 1975. A regional synthesis. Maritime Sediments, 11, 17-24.

SCHLICHTING, H., 1968. Boundary-Layer Theory. McGraw-Hill Book Co., Toronto, 748p.

SCHWARZ, H.-U., 1975. Sedimentary structures and facies analysis of shallow marine carbonates. Contributions to Sedimentology, no. 3, E. Schweigerbart'sche Verlangsbuchhandlung, Stuttgart, 100p.

SEWARD-THOMPON, B.L. and HAILS, J.R., 1973. An appraisal of the computation of statistical parameters in grain size analysis. Sedimentology, 20, 161-170.

SHEA, J.H., 1974. Deficiencies of clastic particles of certain sizes. Jour. Sed. Petrol., 44, 985-1003.

SHIELDS, A., 1936. Application of similarity principles and turbulence research to bed-load movement. Translated by W.P. Ott and J.C. Van Uchelen, U.S. Dept. Agriculture, Soil Conservation Service, Coop. Lab., Calif. Inst. Tech., 42p.

SIMONS, D.B. and RICHARDSON, E.V., 1961. Forms of bed roughness in alluvial channels. Amer. Soc. Civil Eng. Proc., 87, no. HY3, 87-105.

SIMONS, D.B., RICHARDSON, E.V. and NORDIN, C.F. Jr., 1965a. Sedimentary structures generated by flow in alluvial channels. In Primary Sedimentary Structures and their Hydrodynamic Interpretation (ed. G.V. Middleton). Soc. Economic Paleont. and Mineral., Spec. Pub. No. 12, 34-52, Tulsa.

SIMONS, D.B., RICHARDSON, E.V. and NORDIN, C.J., Jr., 1965b. Bedload equation for ripples and dunes. U.S.G.S. Prof. Paper 462-H, 9p.

SINDOWSKI, K.H., 1957. Die synoptische Methode des Kornkurven-Vergleiches zur Ausdeutung fossiler Sedimentations räume. Geol. Jahrb., 73, 235-275.

SMITH, J.D., 1969. Geomorphology of a sand ridge. Jour. Geol., 77, 39-55.

SOUTHARD, J.B., 1971. Representation of bed configurations in depth-velocity-size diagrams. Jour. Sed. Petrol., 41, 903-915.

SOUTHARD, J.B., 1975. Bed Configurations. In Depositional Environments as Interpreted from Primary Sedimentary Structures and Stratification Sequences. Chapter 2, Short Course no. 2, Soc. Econom. Paleont. and Mineral., Dallas, Texas.

SPENCER, D.W., 1963. The interpretation of grain size distribution curves of clastic sediments. Jour. Sed. Petrol., 33, 180-190.

STERNBERG, R.W., 1968. Friction factors in tidal channels with differing bed roughness. Marine Geol., 6, 243-260.

STERNBERG, R.W., 1970. Field measurements of the hydrodynamic roughness of the deep-sea boundary. Deep-Sea Res., 17, 415-442.

STEVENSON, I.M., 1958. Truro map-area, Colchester and Hants counties, Nova Scotia. Geol. Survey Canada, Mem. 297, 124p.

STEWART, H.B. and JORDON, G.F., 1965. Underwater sand ridges on Georges Shoal. In Papers in Marine Geology (ed. R.D. Miller). MacMillan, N.Y., 102-116.

STREETER, V.L., 1971. Fluid Mechanics. McGraw-Hill Book Co., Toronto, 751p.

SWIFT, D.J.P. and BORNS, W.W., Jr., 1967. A raised fluvio-marine outwash terrace, north shore of the Minas Basin, Nova Scotia. Jour. Geol., 75, 673-711.

SWIFT, D.J.P. and McMULLEN, R.M., 1968. Preliminary studies of intertidal sand bodies in the Minas Basin, Bay of Fundy, Nova Scotia. Can. Jour. Earth Sci., 5, 175-183.

SZCZUCZKO, R.B., 1975. Transport and destruction of pelecypod valves in the Minas Basin, Bay of Fundy. Unpub. B.Sc. Thesis, Dept. Geology, McMaster Univ., Hamilton, Ont.

TANNER, W.F., 1958. The zig-zag nature of type I and type IV curves. Jour. Sed. Petrol., 28, 372-375.

TANNER, W.F., 1959. Sample components obtained by the method of differences. Jour. Sed. Petrol., 29, 408-411.

TANNER, W.F., 1964. Modification of sediment size distributions. Jour. Sed. Petrol., 34, 156-164.

TASK COMMITTEE FOR PREPARATION OF SEDIMENTATION MANUAL (TCPSM), 1971. Sediment transportation mechanics: H. Sediment discharge formulas. Proc. Amer. Soc. Civil Eng., 97, no. HY4, 523-567.

TEE, K.T., 1974. Tide-induced residual current - a 2-D non-linear numerical tidal model. Unpub. Mansc., Dalhousie Univ., Halifax, 46p.

TELEKI, P.G., 1967. Automatic analysis of tracer sand. Jour. Sed. Petrol., 37, 749-759.

THOMPSON, R.W., 1968. Tidal flat sedimentation on the Colorado River delta, northwestern Gulf of California. Geol. Soc. Amer. Mem. 107.

THOMAS, R.L., KEMP, A.L.W. and LEWIS, G.F.M., 1972. Distribution, composition and characteristics of the surficial sediments of Lake Ontario. Jour. Sed. Petrol., 42, 66-84.

THOMAS, R.L., KEMP, A.L.W. and LEWIS, G.F.M., 1973. The surficial sediments of Lake Huron. Can. Jour. Earth Sci., 10, 226-265.

TUNNICLIFF, V.J., 1975. Factors influencing the distribution of the bivalve Macoma balthica on the intertidal mudflats of Cobequid Bay, Nova Scotia. Unpub. B.Sc. Thesis, Dept. Geology, McMaster Univ., Hamilton, Ont.

TYWONIUK, N., 1972. Sediment discharge computation procedures. Proc. Amer. Soc. Civil Eng., 98, no. HY3, 521-540.

UDDEN, J.A., 1898. Mechanical composition of wind deposits. Augustana Library Pub. No. 1, 69p.

UDDEN, J.A., 1914. Mechanical composition of clastic sediments. Geol. Soc. Amer. Bull., 25, 655-744.

VAN ANDEL, T.H., 1973. Texture and dispersal of sediments in the Panama Basin. Jour. Geol., 81, 434-457.

VAN STRAATEN, L.M.J.U., 1953. Megaripples in the Dutch Wadden Sea and in the Basin of Arcachon (France). Geol. en Mijnbouw, No. 1, 1-12.

VANONI, V.A., 1953. Some effects of suspended sediment on flow characteristics. Proc. 5th Hydraulics Conf., State Univ. Iowa Studies in Engineering, Bull. 34, 137-158.

VANONI, V.A., 1974. Factors determining bed forms of alluvial streams. Proc. Amer. Soc. Civil Eng., 100, no. HY3, 363-377.

VISHER, G.S., 1969. Grain-size distributions and depositional processes. Jour. Sed. Petrol., 39, 1074-1106.

VISHER, G.S., 1972. Genesis of grain size distributions. Geol. Soc. Amer., Abstracts with Programs, 5, no. 7, 849.

de VRIES, M., 1966. Applications of luminophores in sand transport studies. Delft Hydraulics Lab. Pub. No. 39, 86p.

de VRIES, M., 1967. Photometric counter for fluorescent tracers. Houille Blance, 22, 717-722.

de VRIES, M., 1973. Applicability of fluorescent tracers. In Tracer Techniques in Sediment Transport, Internat. Atomic Energy Agency, Vienna. Tech. Rept. Series No. 145, 105-123.

WEEKS, L.J., 1948. Londonderry and Bass River map-areas, Colchester and Hants Counties, Nova Scotia. Geol. Survey Canada, Mem. 245, 86p.

WELLS, J.T. and LUDWICK, J.C., 1974. Application of multiple comparisons to grain size on sand waves. Jour. Sed. Petrol., 44, 1029-1036.

WENTWORTH, C.K., 1922. A scale of grade and class terms for clastic sediments. Jour. Geol., 30, 377-392.

WHITE, W.R., MILLI, H. and CRABBE, A.D., 1975. Sediment transport theories: a review. Proc. Instn. Civil Eng., Part 2, 59, 256-292.

WIGHTMAN, D.M., 1975. Paleotidal range and Pleistocene sea-level changes at Cape d'Or, Bay of Fundy, Nova Scotia. Geol. Soc. Amer., Abstracts with Programs, 7, no. 6, 880-881.

WIGHTMAN, D., 1976. The sedimentology and paleotidal significance of a late Pleistocene raised beach, Advocate Harbour, Nova Scotia. Unpub. M.Sc. Thesis, Dept. Geology, Dalhousie Univ., Halifax, 156p.

WRIGHT, L.D., COLEMAN, J.M. and THOM, B.G., 1973. Processes of channel development in a high-tide range environment: Cambridge Gulf-Ord River delta, Western Australia. Jour. Geol., 87, 15-41.

WRIGHT, L.D., COLEMAN, J.M. and THOM, B.G., 1975. Sediment transport and dispersion in a macrotidal river channel - Ord River, Western Australia. In Estuarine Research (ed. L.E. Cronin), Vol. II, 309-321. Academic Press, Inc., N.Y.

WUNDERLICH, F., 1967. Die Entstehung von "convolute bedding" an Platenrändern. Senckenbergiana Lethaea, 48, 337-343.

WUNDERLICH, F., 1970. Genesis and environment of the "Nellenköpfehenschichten" - in comparison with modern coastal environment of the German Bay. Jour. Sed. Petrol., 40, 102-130.

YALIN, M.S., 1972. Mechanics of Sediment Transport. Pergamon Press Ltd., Toronto, 290p.

YANG, C.T. and SAYRE, W.W., 1971. Stochastic model for sand dispersion. Proc. Amer. Soc. Civil Eng., 97, no. HY2, 265-288.

YASSO, W.E., 1966. Formulation and use of fluorescent tracer coatings in the sediment transport studies. Sedimentology, 6, 287-301.

YUEN, K.B., 1969. Effect of tidal barriers upon the $M_2$ tide in the Bay of Fundy. Jour. Fish. Res. Bd. Canada, 26, 2477-2492.

YULE, G.U. and KENDALL, M.G., 1950. An Introduction to the Theory of Statistics. 14th edition, Chas. Griffin and Co. Ltd., London, 702p.

ZEHNA, P.W., 1970. Probability Distributions and Statistics. Boston, Allyn and Bacon, Inc., 622p.

# APPENDIX 1

## VELOCITY PROFILE DATA

This appendix contains all of the primary velocity profile data obtained in the four major study areas during the course of the thesis research. The data presented consist of current speed (SPEED - metres per second) and flow direction (DIR) values measured at various heights above the bed (DEPTH - metres). The time at which each profile was obtained (TIME - hours and fractions after the morning high tide; times before high water are negative) is also given. The locations of all current metering stations are shown in Figure 3.1, and the equipment used and its calibration are described in Section 3.1.2.

Also included for each tidal cycle are: the heights of the morning and evening high tides, and the intervening low tide in metres, based on Marine Environmental Data Service tidal height predictions for Burntcoat Head (D.G. Mitchell, personal communication, Nov. 1, 1974); the predicted time of the morning high tide (Atlantic Daylight Saving Time) from the same source; and the tidal coefficients of the ebb and flood, based on the large tidal range of 16.1 metres given for Burntcoat Head by the Canadian Hydrographic Service (1975).

BIG BAR - BUOY 1 ..... DATE - 26/ 7/73

TIDAL HEIGHTS
HIGH : 12.9
LOW : 1.2
HIGH : 13.8

TIME - 7165

TIDAL COEFFICIENTS
EBB : .87
FLOOD : .86

| TIME | DEPTH | SPEED | DIR |
|---|---|---|---|
| .50 | | | |
| | | | 199. |
| 5.08 | | | |
| | | | 254. |
| 5.50 | | | |
| | | | 230. |
| 9.00 | | | |
| | | | 150. |
| 9.25 | | | |
| | | | 156. |
| 9.58 | | | |
| | | | 114. |
| 10.58 | | | |
| | | | 98. |
| 11.92 | | | |
| | | | 110. |
| 11.25 | | | |
| | | | 107. |

| TIME | DEPTH | SPEED | DIR |
|---|---|---|---|
| 1.11 | .75 | .516 | 232. |
| 9.02 | | | |
| | | | 105. |
| 11.49 | | | |
| | | | 130. |
| 3.19 | .50 | .369 | 239. |
| 10.25 | | | |
| | | | 190. |

BIG BAR - BUOY 1 ..... DATE - 18/ 8/73

TIDAL HEIGHTS
HIGH : 11.5
LOW : 1.2
HIGH : 12.8

TIME - 11015

TIDAL COEFFICIENTS
EBB : .91
FLOOD : .90

| TIME | DEPTH | SPEED | DIR |
|---|---|---|---|
| .62 | | | |
| | | | 265. |
| .63 | | | |
| | | | 277. |
| .75 | | | |
| | | | 265. |
| 1.52 | | | |
| | | | 230. |
| 1.75 | | | |
| | | | 244. |
| 2.00 | | | |
| | | | 215. |
| 2.79 | | | |
| | | | 262. |
| 9.08 | | | |
| | | | 249. |
| 9.19 | | | |
| | | | 237. |
| 9.05 | | | |
| | | | 77. |
| 9.27 | | | |
| | | | 92. |
| 9.50 | | | |
| | | | 61. |

| TIME | DEPTH | SPEED | DIR |
|---|---|---|---|
| 1.07 | | | |
| | | | 290. |
| 2.25 | | | |
| | | | 248. |
| 9.01 | .50 | .210 | 92. |
| 9.75 | | | |
| | | | 61. |
| 1.25 | | | |
| | | | 247. |
| 2.43 | | | |
| | | | 248. |
| 8.83 | | | |
| | | | 96. |

BIG BAR - BUOY 1 ..... DATE - 21/ 8/73

TIDAL HEIGHTS
HIGH : 12.9
LOW : 1.8
HIGH : 13.1

TIME - 6129

TIDAL COEFFICIENTS
EBB : .93
FLOOD : .93

| TIME | DEPTH | SPEED | DIR |
|---|---|---|---|
| .38 | | | |
| | | | 268. |
| .33 | | | |
| | | | 263. |
| .68 | | | |
| | | | 271. |
| 1.11 | | | |
| | | | 296. |
| 1.31 | | | |
| | | | 296. |

| TIME | DEPTH | SPEED | DIR |
|---|---|---|---|
| 1:02 | | | |
| | | | |
| 1:12 | | | |
| | | | |
| 1:22 | | | |
| | | | |
| 1:32 | | | |
| | | | |
| 1:42 | | | |
| | .98 | .442 | 251. |

| TIME | DEPTH | SPEED | DIR |
|---|---|---|---|
| 2:12 | | | |
| | | | |
| 2:22 | | | |
| | | | |
| 2:32 | | | |
| | | | |
| 2:42 | | | |
| | | | |
| 2:52 | | | |
| | | | |

| TIME | DEPTH | SPEED | DIR |
|---|---|---|---|
| 3:17 | | | |
| | | | |
| 3:27 | | | |
| | | | |
| 3:37 | | | |
| | | | |
| 3:47 | | | |
| | | | |
| 3:57 | | | |
| | | | |

| TIME | DEPTH | SPEED | DIR |
|---|---|---|---|
| 4:22 | | | |
| | | | |
| 4:32 | | | |
| | | | |
| 4:42 | | | |
| | | | |
| 4:52 | | | |
| | | | |
| 5:02 | | | |
| | | | |

| TIME | DEPTH | SPEED | DIR |
|---|---|---|---|
| 5:05 | | | |
| | | | |
| 5:15 | | | |
| | | | |
| 5:25 | | | |
| | | | |
| 5:35 | | | |
| | | | |
| 5:45 | | | |
| | | | |

| TIME | DEPTH | SPEED | DIR |
|---|---|---|---|
| 10:37 | | | |
| | | | |
| 10:47 | | | |
| | | | |
| 10:57 | | | |
| | | | |
| 11:07 | | | |
| | | | |
| 11:17 | | | |
| | | | |

| TIME | DEPTH | SPEED | DIR |
|---|---|---|---|
| 10:58 | | | |
| | | | |
| 11:08 | | | |
| | | | |
| 11:18 | | | |
| | | | |
| 11:28 | | | |
| | | | |
| 11:38 | | | |
| | | | |

| TIME | DEPTH | SPEED | DIR |
|---|---|---|---|
| 10:47 | | | |
| | | | |
| 10:57 | | | |
| | | | |
| 11:07 | | | |
| | | | |
| 11:17 | | | |
| | | | |
| 11:27 | | | |
| | | | |

| TIME | DEPTH | SPEED | DIR |
|---|---|---|---|
| 11:09 | | | |
| | | | |
| 11:19 | | | |
| | | | |
| 11:29 | | | |
| | | | |
| 11:39 | | | |
| | | | |
| 11:49 | | | |
| | | | |

| TIME | DEPTH | SPEED | DIR |
|---|---|---|---|
| 11:47 | | | |
| | | | |
| 11:57 | | | |
| | | | |
| 12:07 | | | |
| | | | |
| 12:17 | | | |
| | | | |
| 12:27 | | | |
| | | | |

| TIME | DEPTH | SPEED | DIR |
|---|---|---|---|
| 11:49 | | | |
| | | | |
| 11:59 | | | |
| | | | |
| 12:09 | | | |
| | | | |
| 12:19 | | | |
| | | | |
| 12:29 | | | |
| | | | |

| TIME | DEPTH | SPEED | DIR |
|---|---|---|---|
| 11:55 | | | |
| | | | |
| 12:05 | | | |
| | | | |
| 12:15 | | | |
| | | | |
| 12:25 | | | |
| | | | |
| 12:35 | | | |
| | | | |

DIG.DAT:.DUST.S.... : DATE = 25/ 7/73

TIDAL HEIGHTS

HIGH = 12.9
LOW = 3.3
HIGH = 12.8

TIME = 0150

TIDAL COEFFICIENTS

EBB = .92
FLOOD = .98

| TIME | DEPTH | SPEED | DIR |
|---|---|---|---|
| 1:20 | | | |
| | | | |
| 1:30 | | | |
| | | | |
| 1:40 | | | |
| | | | |
| 1:50 | | | |
| | | | |
| 2:00 | | | |
| | | | |

| TIME | DEPTH | SPEED | DIR |
|---|---|---|---|
| 2:30 | | | |
| | | | |
| 2:40 | | | |
| | | | |
| 2:50 | | | |
| | | | |
| 3:00 | | | |
| | | | |
| 3:10 | | | |
| | | | |

| TIME | DEPTH | SPEED | DIR |
|---|---|---|---|
| 3:43 | | | |
| | | | |
| 3:53 | | | |
| | | | |
| 4:03 | | | |
| | | | |
| 4:13 | | | |
| | | | |
| 4:23 | | | |
| | | | |

| TIME | DEPTH | SPEED | DIR |
|---|---|---|---|
| 4:53 | | | |
| | | | |
| 5:03 | | | |
| | | | |
| 5:13 | | | |
| | | | |
| 5:23 | | | |
| | | | |
| 5:33 | | | |
| | | | |

| TIME | DEPTH | SPEED | DIR |
|---|---|---|---|
| 5:55 | | | |
| | | | |
| 6:05 | | | |
| | | | |
| 6:15 | | | |
| | | | |
| 6:25 | | | |
| | | | |
| 6:35 | | | |
| | | | |

| TIME | DEPTH | SPEED | DIR |
|---|---|---|---|
| 6:58 | | | |
| | | | |
| 7:08 | | | |
| | | | |
| 7:18 | | | |
| | | | |
| 7:28 | | | |
| | | | |
| 7:38 | | | |
| | | | |

| TIME | DEPTH | SPEED | DIR |
|---|---|---|---|
| 8:00 | | | |
| | | | |
| 8:10 | | | |
| | | | |
| 8:20 | | | |
| | | | |
| 8:30 | | | |
| | | | |
| 8:40 | | | |
| | | | |

| TIME | DEPTH | SPEED | DIR |
|---|---|---|---|
| 9:05 | | | |
| | | | |
| 9:15 | | | |
| | | | |
| 9:25 | | | |
| | | | |
| 9:35 | | | |
| | | | |
| 9:45 | | | |
| | | | |

| TIME | DEPTH | SPEED | DIR |
|---|---|---|---|
| 10:17 | | | |
| | | | |
| 10:27 | | | |
| | | | |
| 10:37 | | | |
| | | | |
| 10:47 | | | |
| | | | |
| 10:57 | | | |
| | | | |

| TIME | DEPTH | SPEED | DIR |
|---|---|---|---|
| 11:43 | | | |
| | | | |
| 11:53 | | | |
| | | | |
| 12:03 | | | |
| | | | |
| 12:13 | | | |
| | | | |
| 12:23 | | | |
| | | | |

| TIME | DEPTH | SPEED | DIR |
|---|---|---|---|
| 12:05 | | | |
| | | | |
| 12:15 | | | |
| | | | |
| 12:25 | | | |
| | | | |
| 12:35 | | | |
| | | | |
| 12:45 | | | |
| | | | |

| TIME | DEPTH | SPEED | DIR |
|---|---|---|---|
| 11:10 | | | 48. |
| 11:52 | | | 45. |

SIG.BAR.-BUOY 2 DATE - 7/ 6/73

TIDAL HEIGHTS
HIGH = 11:5
LOW = 5:10
HIGH = 11:4
TIME - 4110

TIDAL COEFFICIENTS
FOR
FLOOD = .92
.96

| TIME | DEPTH | SPEED | DIR |
|---|---|---|---|
| :47 | | | 299. |
| :47 | | | 292. |
| :48 | | | 299. |
| 1:12 | | | 291. |
| 1:31 | | | 291. |
| 1:50 | | | 234. |
| 1:51 | | | 216. |
| 2:08 | | | 229. |
| 2:29 | | | 230. |
| 2:49 | | | 232. |
| 2:03 | | | 210. |
| 3:00 | | | 218. |
| 3:39 | | | 217. |
| 3:49 | | | 207. |
| 3:05 | | | 214. |
| 9:38 | | | 92. |
| 9:58 | | | 96. |
| 9:03 | | | 94. |
| 9:13 | | | 91. |
| 9:37 | | | 92. |
| 9:54 | | | 78. |
| 9:53 | | | 99. |
| 10:13 | | | 88. |
| 11:31 | | | 79. |
| 10:59 | | | 88. |
| 10:02 | | | 98. |
| 10:12 | | | 86. |
| 10:35 | | | 78. |

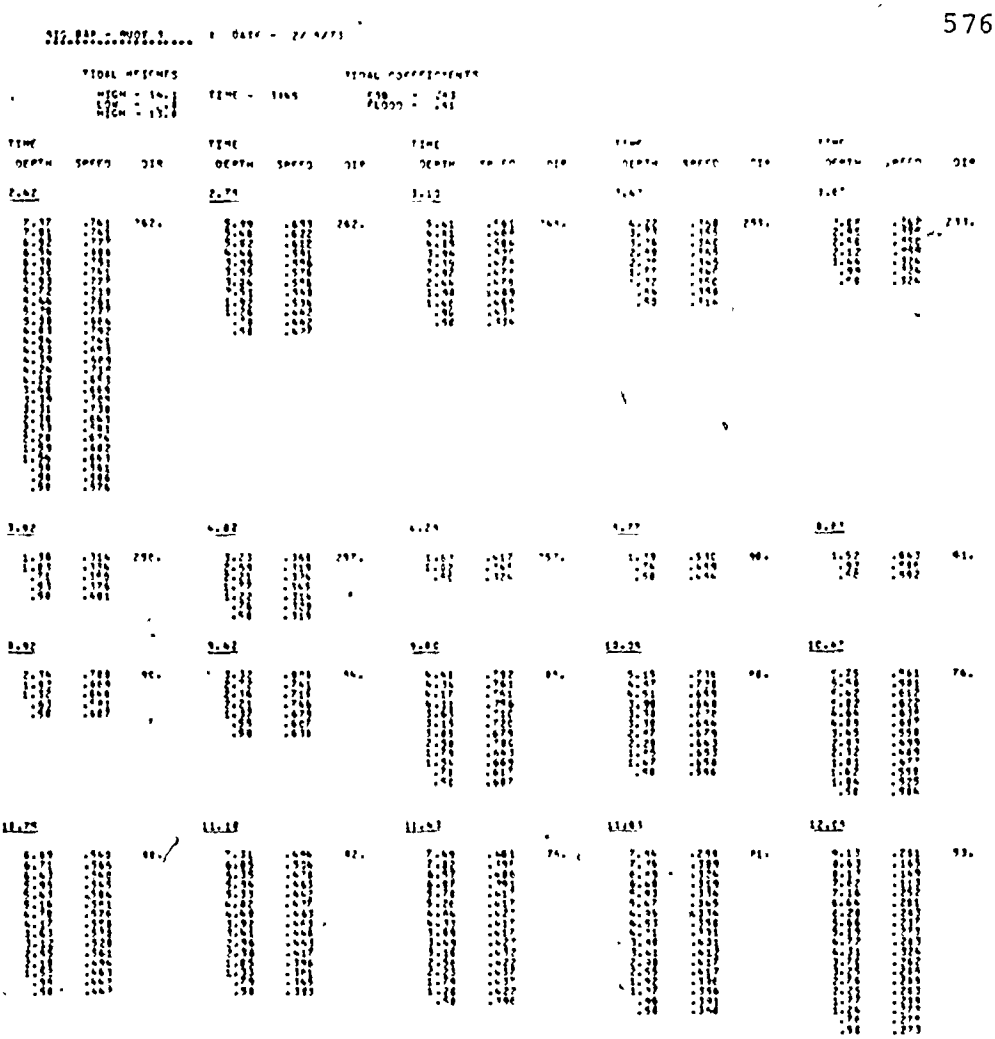

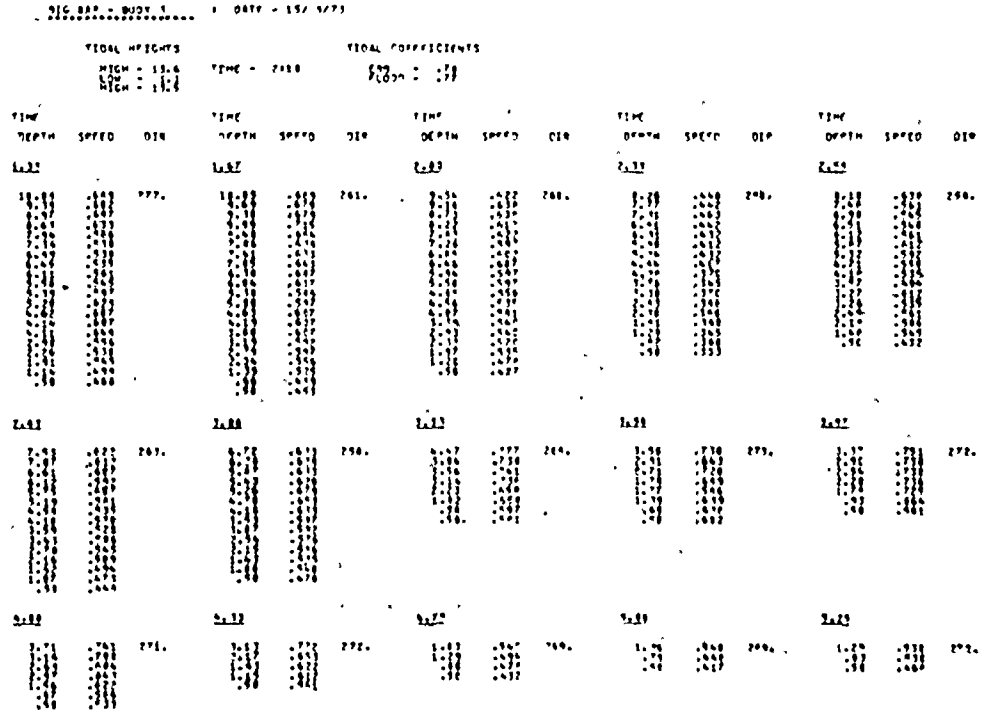

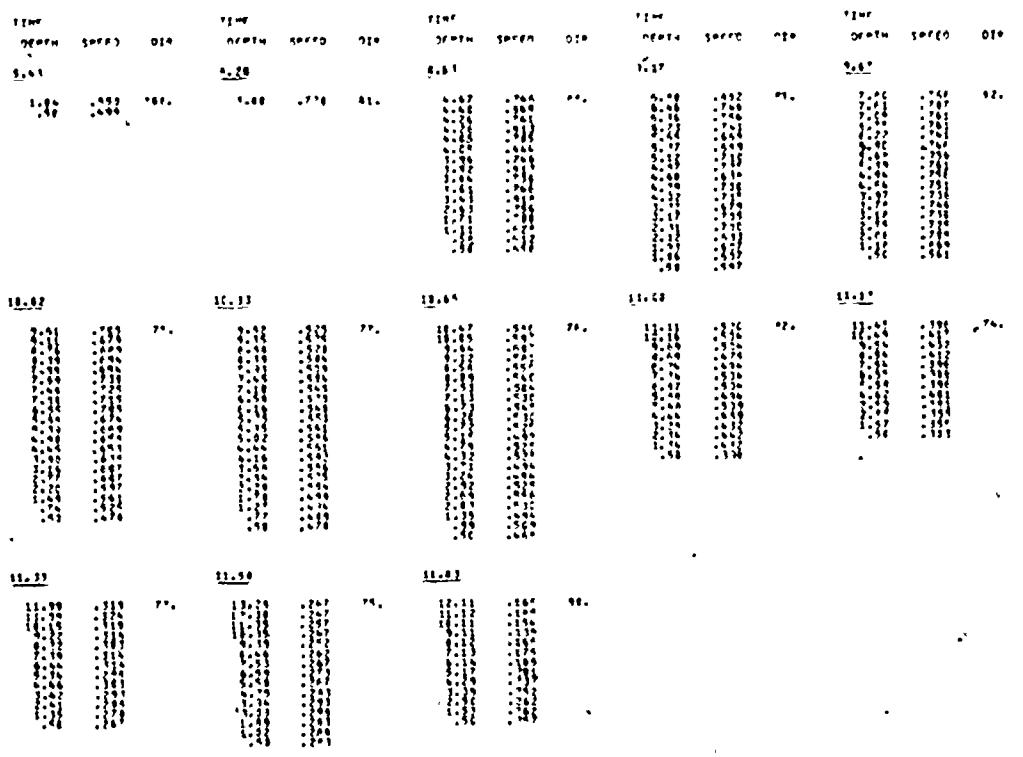

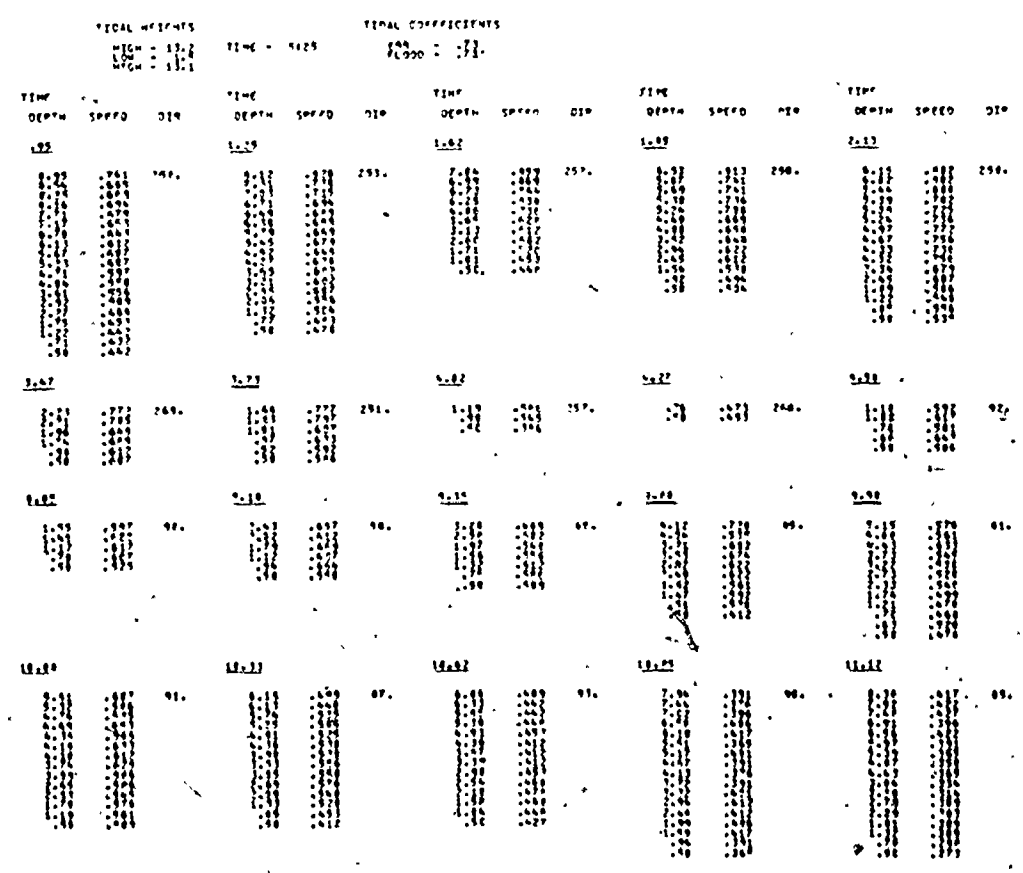

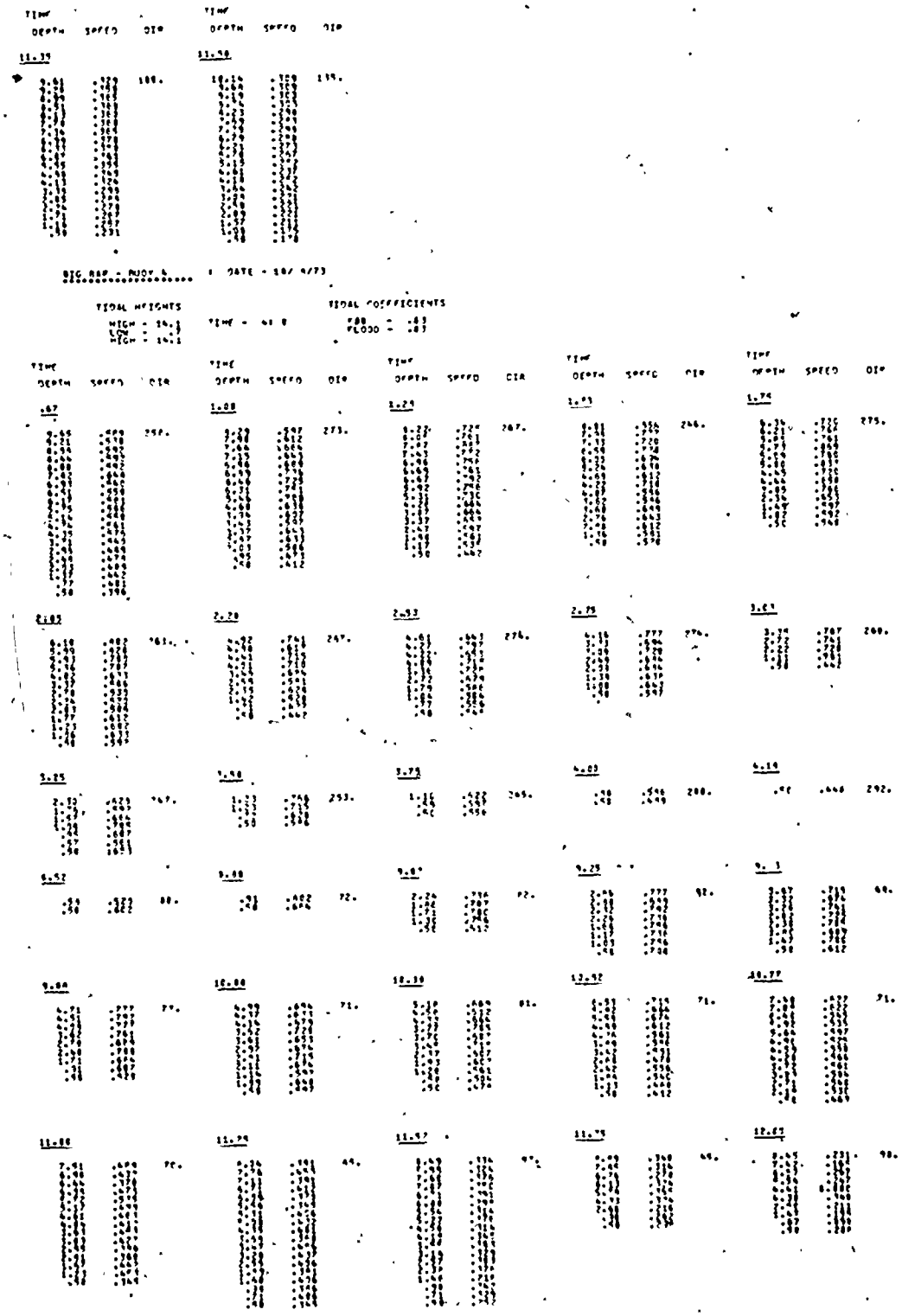

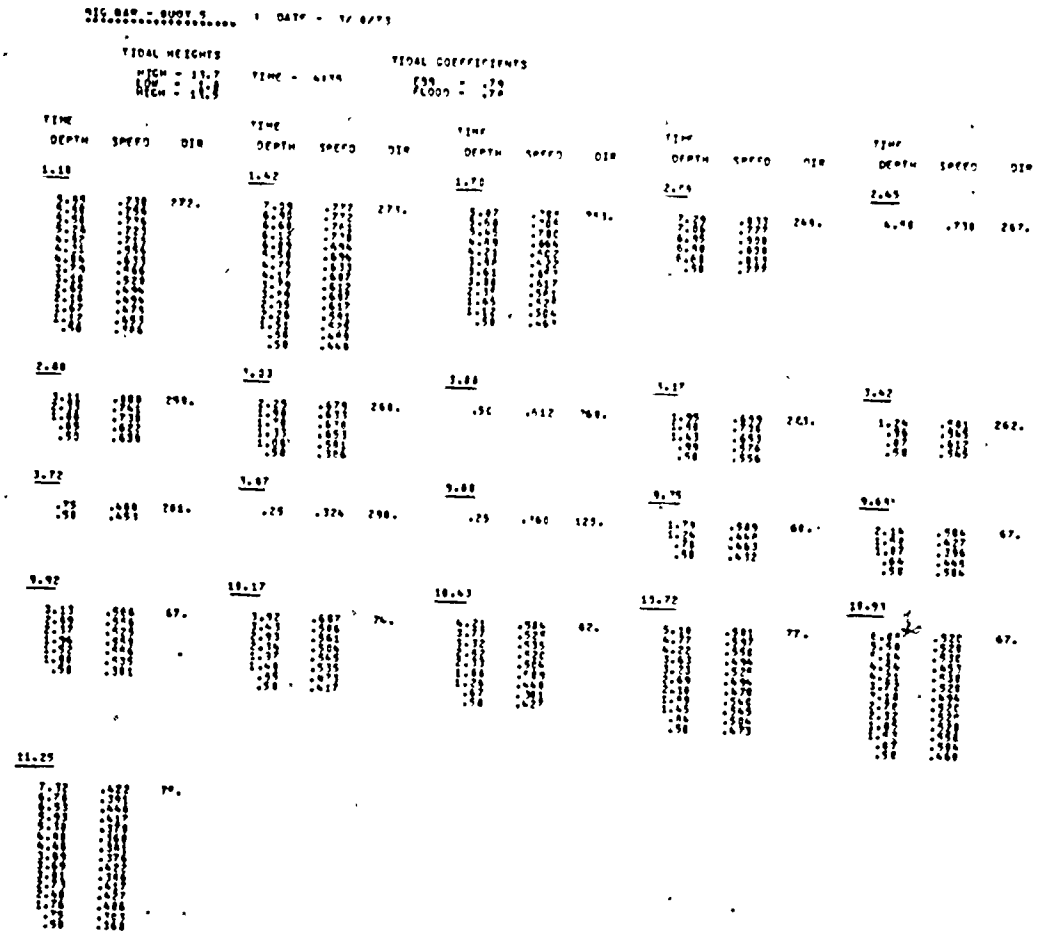
TIDAL HEIGHTS
TIDAL COEFFICIENTS
TIME
DEPTH
SPEED
DIR

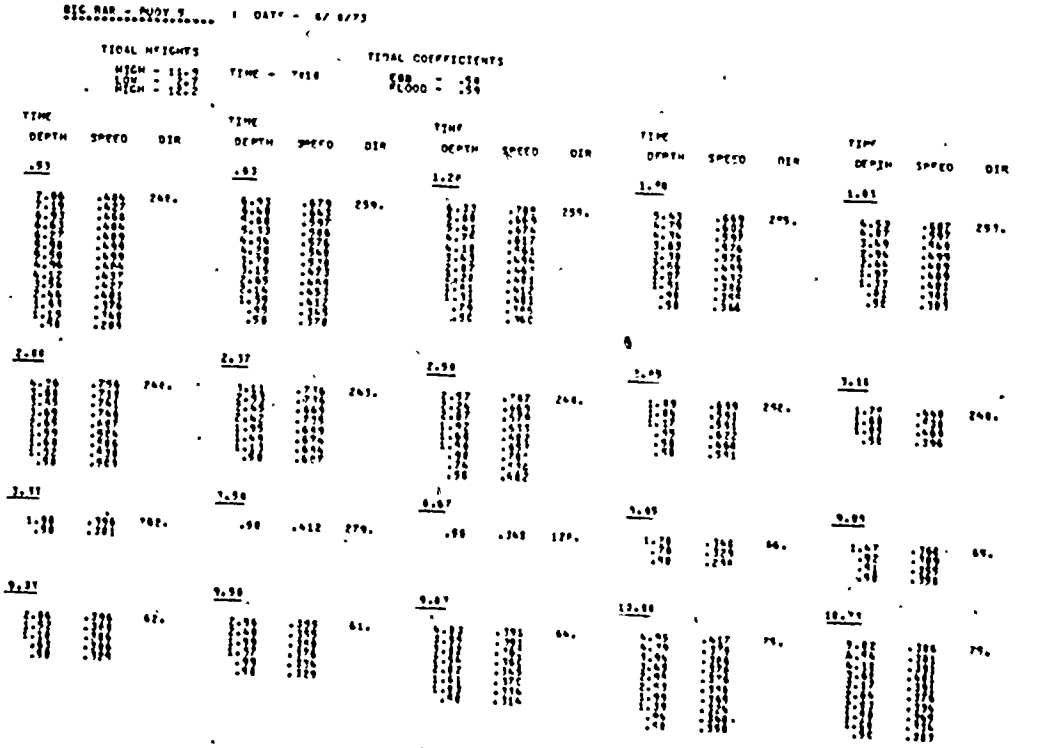
TIDAL HEIGHTS
TIDAL COEFFICIENTS
TIME
DEPTH
SPEED
DIR

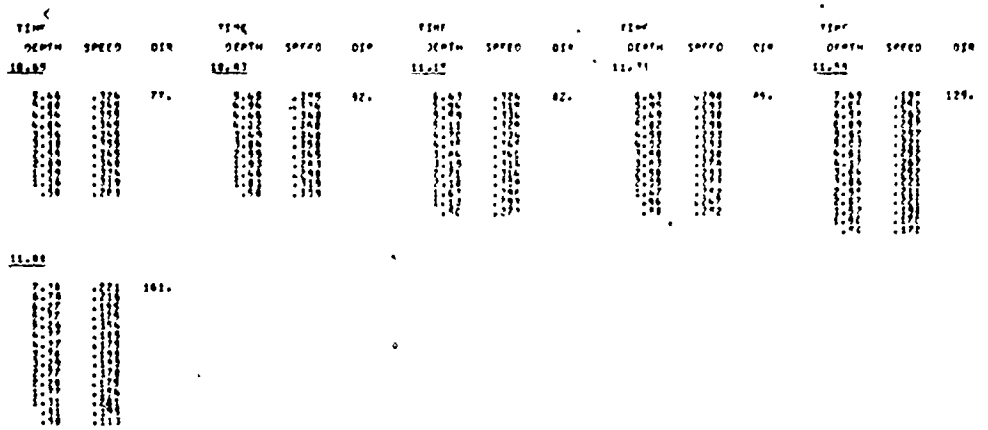

SEC.SEP..2007.3..... * DATE - SAT 9/73

TIDAL HEIGHTS
HIGH = 15.6
LOW = 1.2
HIGH = 13.7

TIME = 2149

TIDAL COEFFICIENTS
EBB = .81
FLOOD = .81

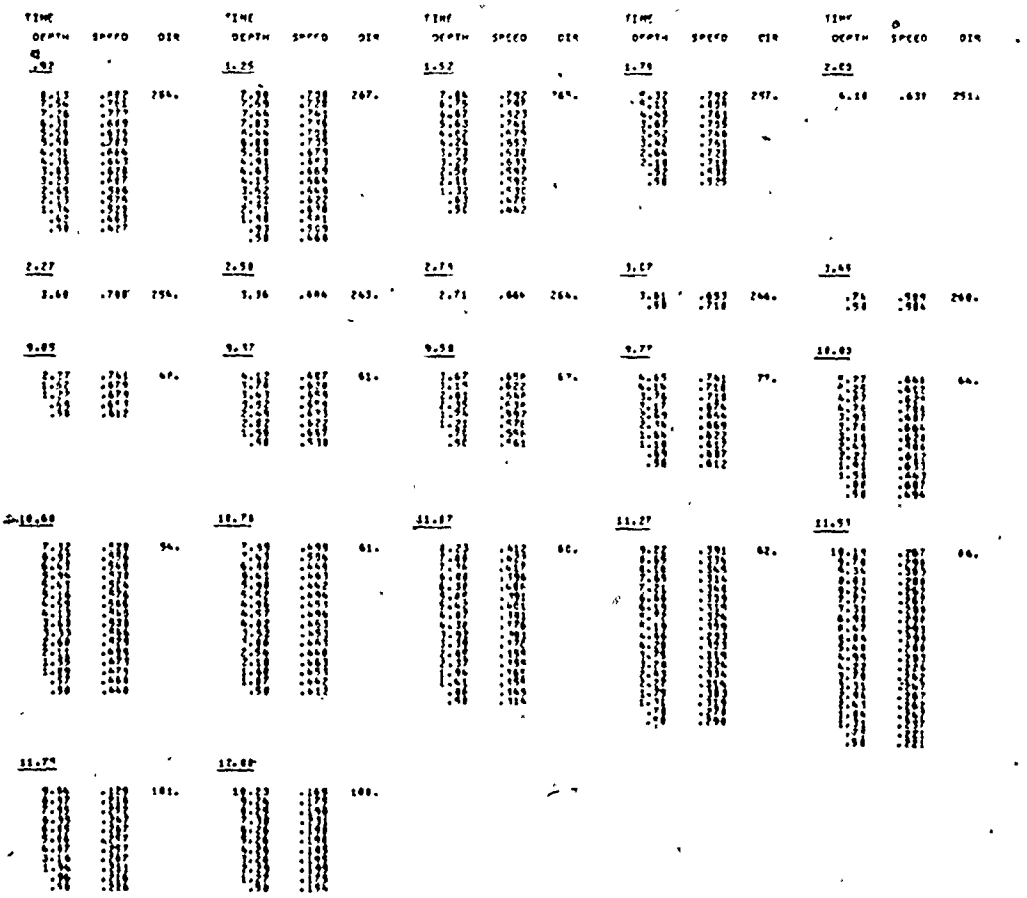

[illegible] DATE - 6/ 6/73

TIDAL HEIGHTS
HIGH : [illegible]
LOW : [illegible]

TIME - [illegible]

TIDAL COEFFICIENTS
FOR FLOOD : .32

| TIME | DEPTH | SPEED | DIR |
|---|---|---|---|
| .32 | | | 264. |
| .58 | | | 261. |
| .75 | | | 274. |
| 1.33 | | | 268. |
| 1.35 | | | 276. |
| 1.68 | | | 291. |
| 1.77 | | | 291. |
| 2.03 | | | 268. |
| 2.32 | | | 237. |
| 2.72 | | | 268. |
| 2.78 | | | 268. |
| 3.02 | | | 264. |
| 3.27 | | | 297. |
| 3.43 | .50 | .262 | 213. |
| 6.73 | | | 94. |
| 8.58 | | | 79. |
| 9.03 | | | 108. |
| 9.83 | | | 81. |
| 9.25 | | | 82. |
| 9.55 | | | 69. |
| 9.75 | | | 99. |
| 10.30 | | | 69. |
| 10.25 | | | 98. |
| 10.58 | | | 170. |
| 10.75 | | | 194. |
| 11.08 | | | 198. |
| 11.25 | | | 82. |

[illegible] DATE - 28/ 6/73

TIDAL HEIGHTS
HIGH : [illegible]
LOW : [illegible]

TIME - [illegible]

TIDAL COEFFICIENTS
FOR FLOOD : .32

| TIME | DEPTH | SPEED | DIR |
|---|---|---|---|
| .32 | | | 262. |
| .93 | | | 259. |
| .75 | | | 297. |
| 1.02 | | | 299. |
| 1.29 | | | 230. |
| 1.98 | 9.29 | .664 | 230. |
| 1.99 | | | 297. |
| 2.27 | | | 268. |
| 2.52 | | | 262. |
| 2.98 | | | 263. |

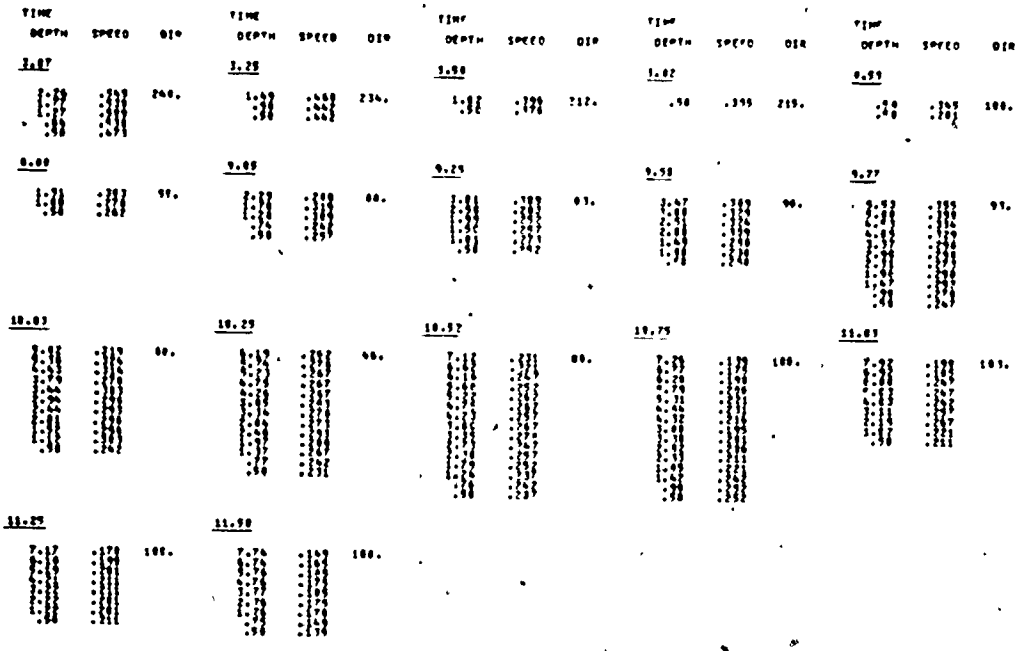


BIG.BEN...PORT.2.... ( DATE - 9/ 8/73

TIDAL HEIGHTS

HIGH : 11.3
LOW : 1.1
HIGH : 11.0

TIME - LOCLS

TIDAL COEFFICIENTS

FOR
FLOOD : .33

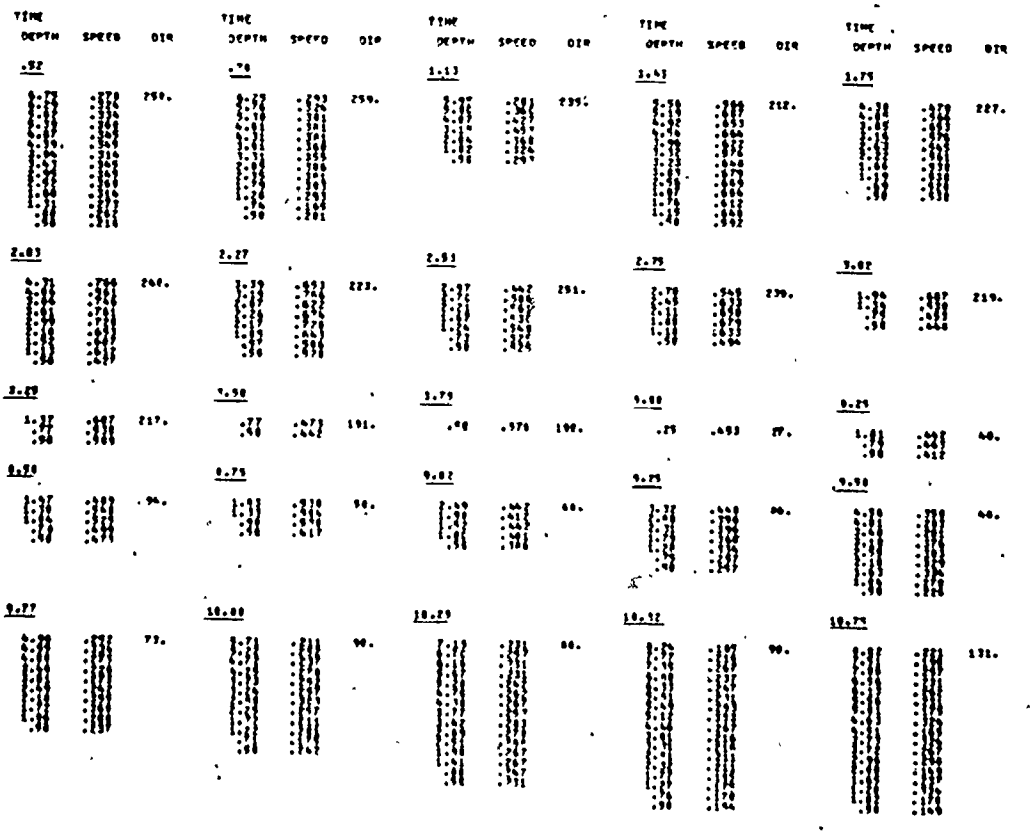

[illegible] DATE = 22/ 6/73

TIDAL HEIGHTS
HIGH = [illegible]
LOW = [illegible]

TIME = 7125

TIDAL COEFFICIENTS
FOR FLOOD = .83

| TIME | DEPTH | SPEED | DIR |
|---|---|---|---|
| .07 | | | 291. |
| .37 | | | 254. |
| .53 | | | 263. |
| 1.00 | | | 267. |
| 1.33 | | | 265. |
| 1.60 | | | 230. |
| 2.00 | | | 240. |
| 2.35 | | | 262. |
| 2.53 | | | 236. |
| 2.83 | | | 236. |
| 3.00 | | | 227. |
| 3.33 | | | 212. |
| 3.58 | .58 | .674 | 79. |
| 9.52 | | | 64. |
| 9.73 | | | 59. |
| 9.87 | | | 64. |
| 9.10 | | | 75. |
| 9.33 | | | 78. |
| 9.62 | | | 68. |
| 9.98 | | | 68. |
| 11.00 | | | 85. |
| 10.43 | | | 76. |
| 10.56 | | | 118. |
| 13.05 | | | 88. |
| 11.18 | | | 87. |
| 11.33 | | | 87. |

[illegible] DATE = 17/ 6/73

TIDAL HEIGHTS
HIGH = 14.1
LOW = .1
HIGH = 14.1

TIME = 3128

TIDAL COEFFICIENTS
FOR FLOOD = .83

| TIME | DEPTH | SPEED | DIR |
|---|---|---|---|
| 1.00 | | | 284. |
| 1.17 | | | 261. |
| 1.50 | | | 251. |
| 1.73 | | | 266. |
| 1.97 | | | 266. |
| 2.17 | | | 240. |
| 2.43 | | | 247. |
| 2.67 | | | 236. |
| 2.95 | | | 246. |
| 3.15 | | | 238. |
| 9.17 | | | 89. |
| 9.48 | | | 66. |
| 9.67 | | | 76. |
| 9.92 | | | 78. |
| 10.17 | | | 66. |

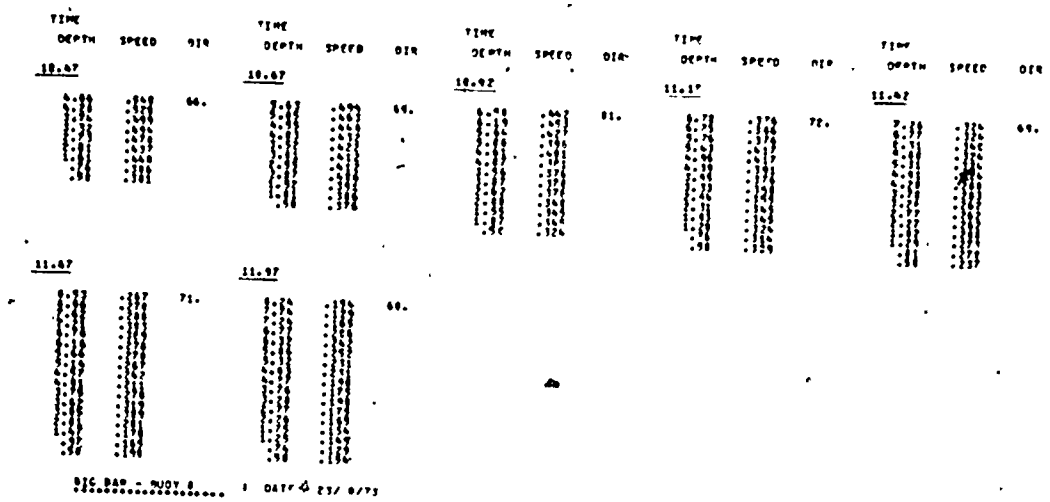


[illegible] DATE - [illegible]

TIDAL HEIGHTS
HIGH : [illegible]
LOW : [illegible]
TIME - 0130

TIDAL COEFFICIENTS
FLOOD : [illegible]

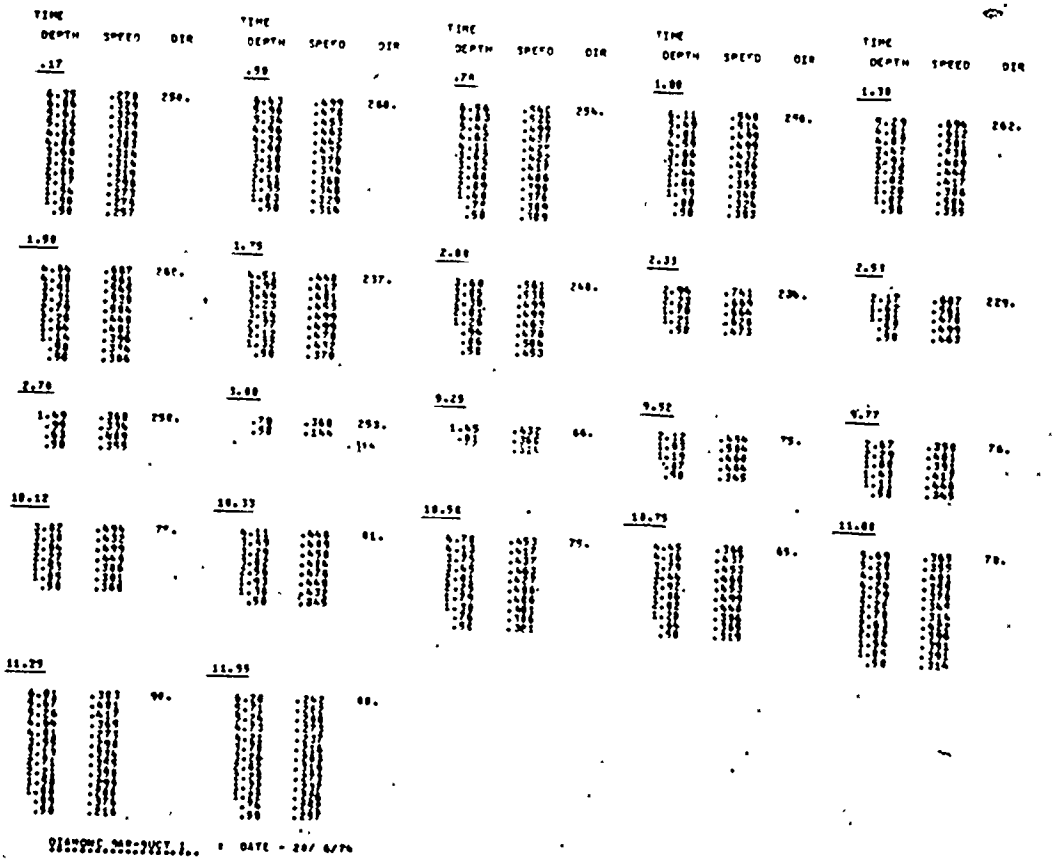


[illegible] DATE - [illegible]

TIDAL HEIGHTS
HIGH : [illegible]
LOW : [illegible]
TIME - 0120

TIDAL COEFFICIENTS
FLOOD : [illegible]

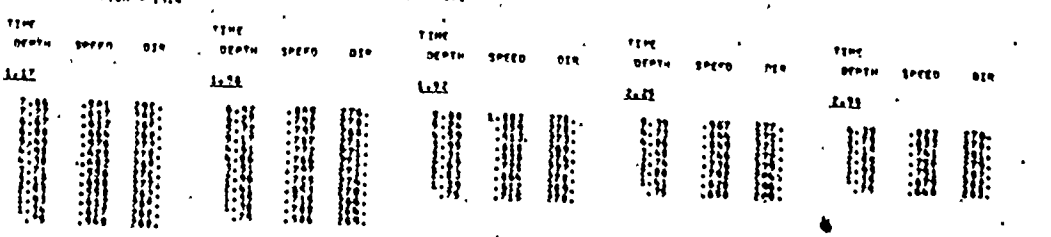

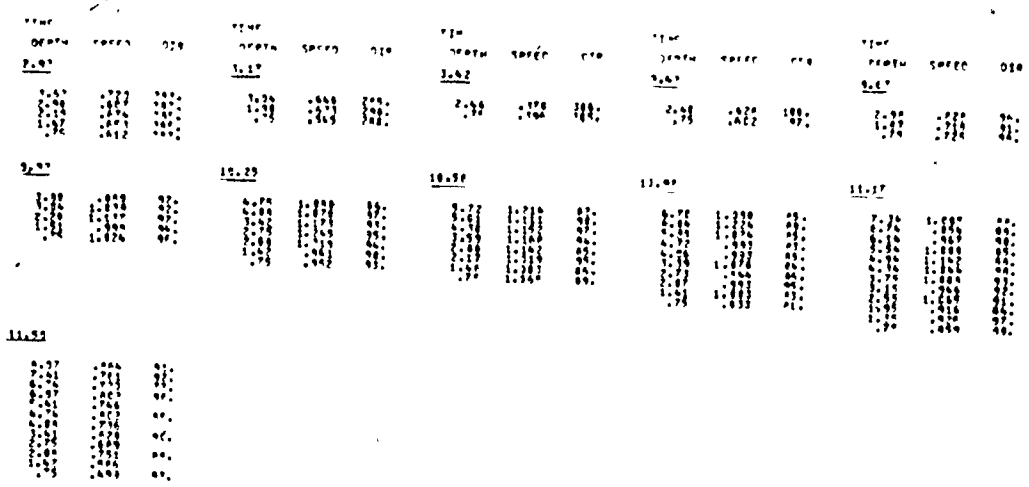

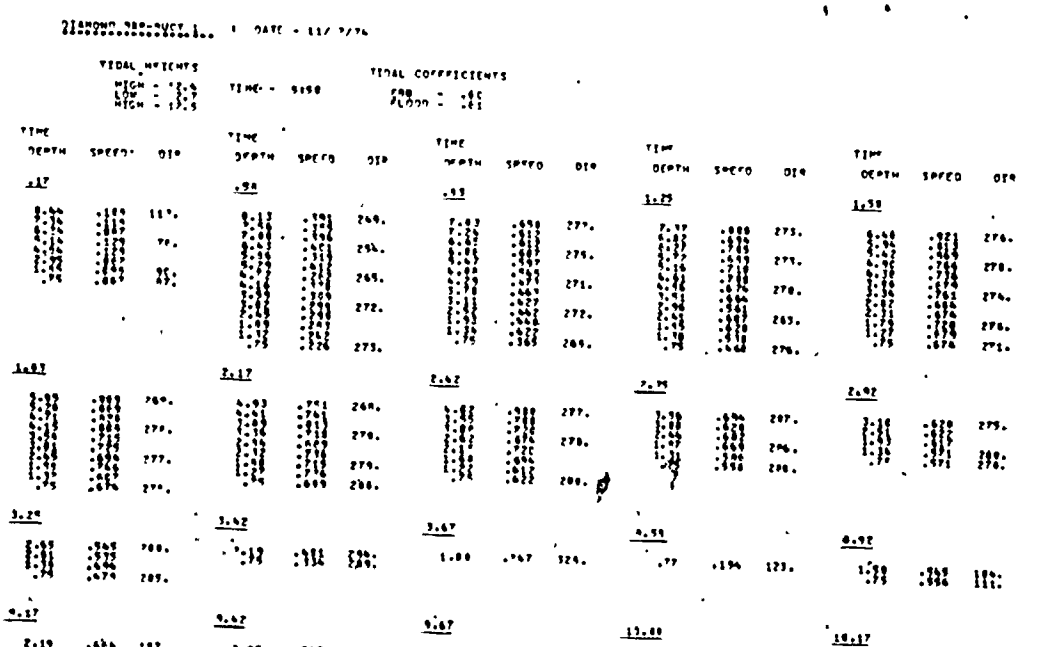

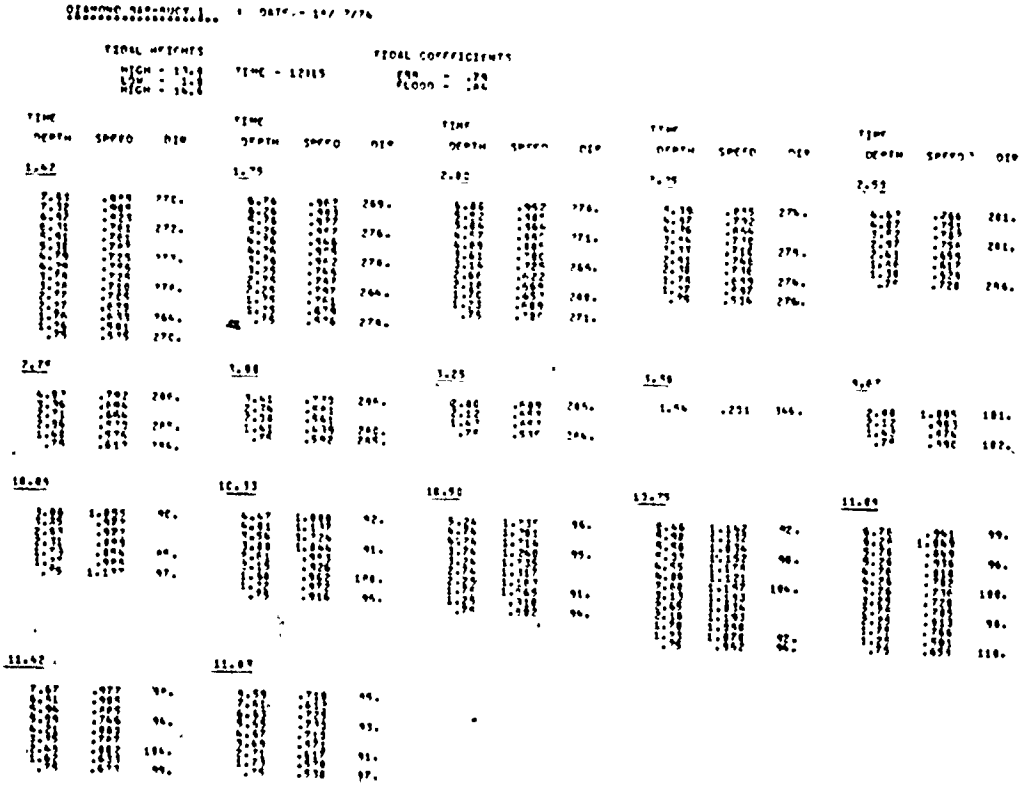

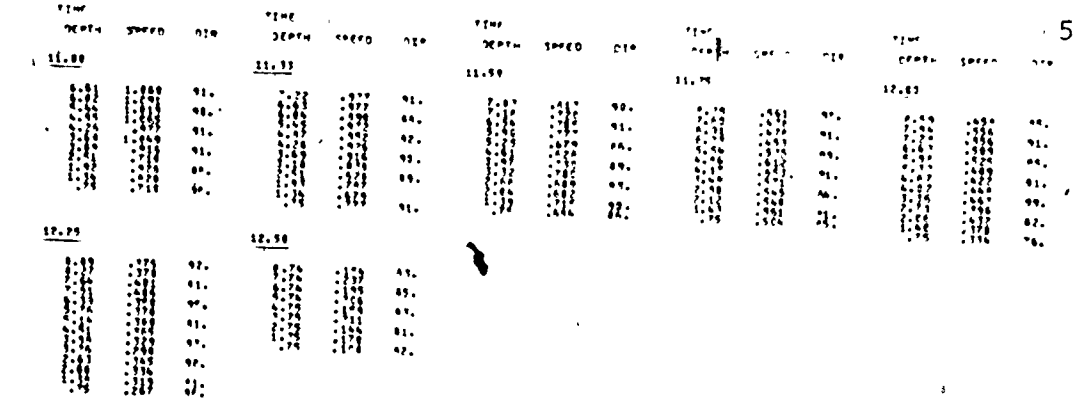

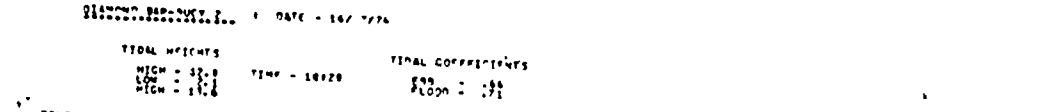

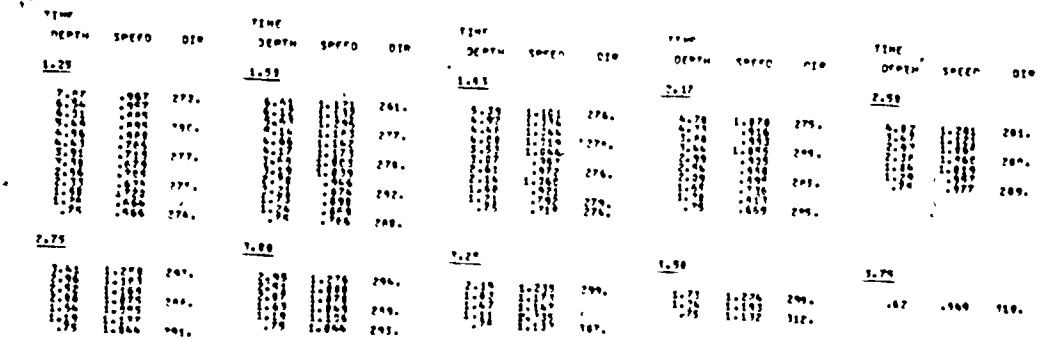

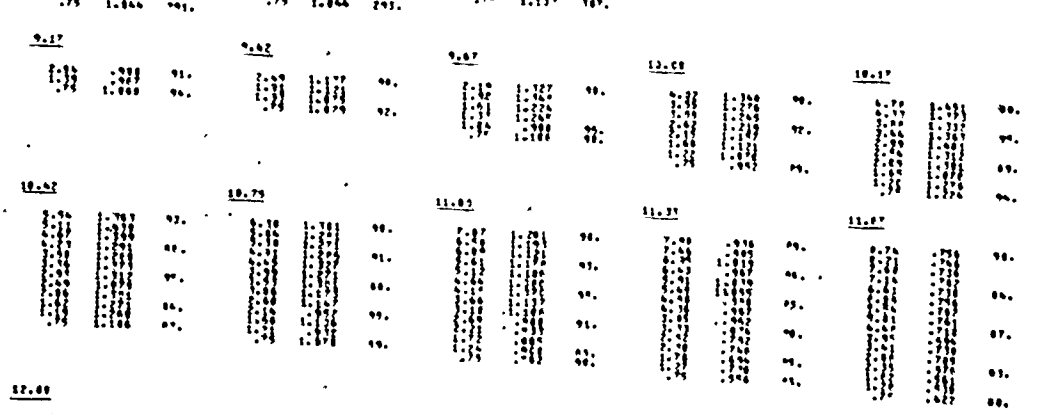

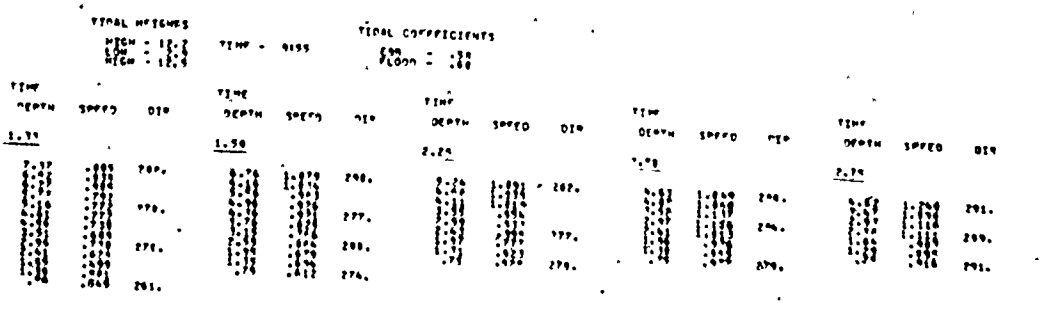

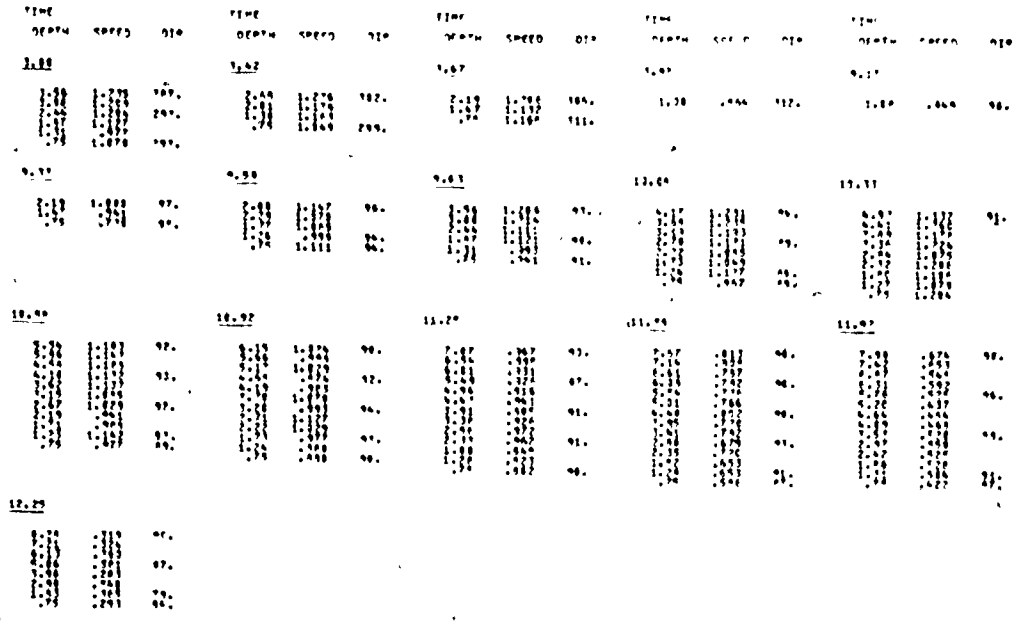

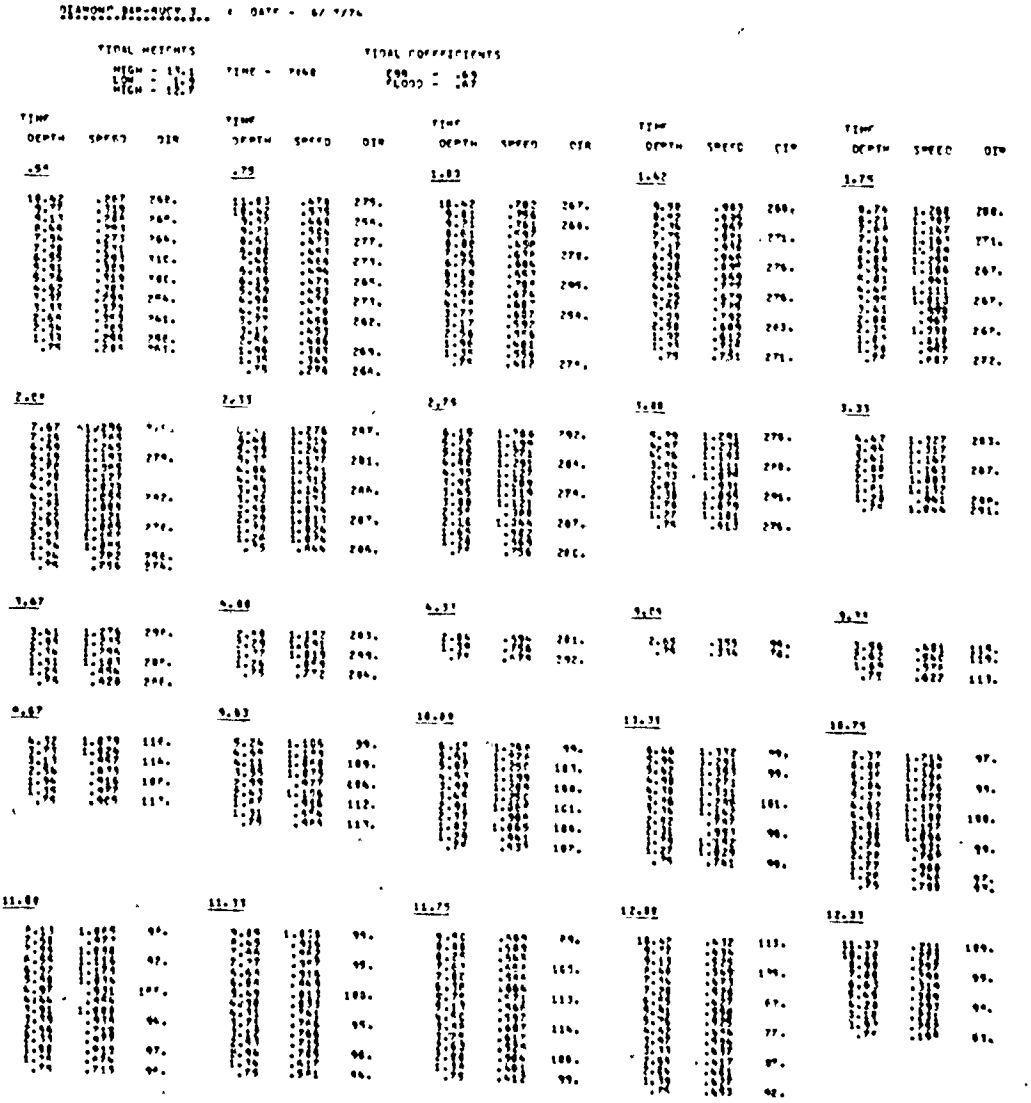

[illegible] DATE = [illegible]

TIDAL HEIGHTS
HIGH = 13.1
LOW = 12.6
MEAN = 12.9

TIME = 11:59

TIDAL COEFFICIENTS
EBB = .97
FLOOD = .91

| TIME | DEPTH | SPEED | DIR |
|---|---|---|---|
| 1:25 | | | |
| | | | 284. |
| | | | 282. |
| | | | 279. |
| | | | 276. |
| | | | 273. |
| 1:50 | | | |
| | | | 284. |
| | | | 281. |
| | | | 278. |
| | | | 276. |
| | | | 276. |
| 2:17 | | | |
| | | | 287. |
| | | | 284. |
| | | | 281. |
| | | | 279. |
| | | | 282. |
| 2:42 | | | |
| | | | 286. |
| | | | 283. |
| | | | 280. |
| | | | 277. |
| 3:07 | | | |
| | | | 297. |
| | | | 294. |
| 3:33 | | | |
| | | | 278. |
| 3:58 | | | |
| | | | 276. |
| | | | 276. |
| | | | 276. |
| | | | 276. |
| | | | 276. |
| 4:23 | | | |
| | | | 276. |
| | | | 276. |
| | | | 276. |
| | | | 276. |
| | | | 276. |
| 4:48 | | | |
| | | | 276. |
| | | | 276. |
| | | | 276. |
| | | | 276. |
| | | | 276. |
| 5:13 | | | |
| | | | 276. |
| | | | 276. |
| | | | 276. |
| | | | 276. |
| | | | 276. |
| 5:38 | | | |
| | | | 276. |
| | | | 276. |
| | | | 276. |
| | | | 276. |
| | | | 276. |
| 6:03 | | | |
| | | | 276. |
| | | | 276. |
| | | | 276. |
| | | | 276. |
| | | | 276. |
| 6:28 | | | |
| | | | 276. |
| | | | 276. |
| | | | 276. |
| | | | 276. |
| | | | 276. |
| 6:53 | | | |
| | | | 276. |
| | | | 276. |
| | | | 276. |
| | | | 276. |
| | | | 276. |
| 7:18 | | | |
| | | | 276. |
| | | | 276. |
| | | | 276. |
| | | | 276. |
| | | | 276. |
| 7:43 | | | |
| | | | 276. |
| | | | 276. |
| | | | 276. |
| | | | 276. |
| | | | 276. |
| 8:08 | | | |
| | | | 276. |
| | | | 276. |
| | | | 276. |
| | | | 276. |
| | | | 276. |
| 8:33 | | | |
| | | | 276. |
| | | | 276. |
| | | | 276. |
| | | | 276. |
| | | | 276. |
| 8:58 | | | |
| | | | 276. |
| | | | 276. |
| | | | 276. |
| | | | 276. |
| | | | 276. |
| 9:23 | | | |
| | | | 276. |
| | | | 276. |
| | | | 276. |
| | | | 276. |
| | | | 276. |
| 9:48 | | | |
| | | | 276. |
| | | | 276. |
| | | | 276. |
| | | | 276. |
| | | | 276. |
| 10:13 | | | |
| | | | 276. |
| | | | 276. |
| | | | 276. |
| | | | 276. |
| | | | 276. |
| 10:38 | | | |
| | | | 276. |
| | | | 276. |
| | | | 276. |
| | | | 276. |
| | | | 276. |
| 11:03 | | | |
| | | | 276. |
| | | | 276. |
| | | | 276. |
| | | | 276. |
| | | | 276. |
| 11:28 | | | |
| | | | 276. |
| | | | 276. |
| | | | 276. |
| | | | 276. |
| | | | 276. |
| 11:53 | | | |
| | | | 276. |
| | | | 276. |
| | | | 276. |
| | | | 276. |
| | | | 276. |

[illegible] DATE = [illegible] (SC E.)

TIDAL HEIGHTS
HIGH = 14.3
LOW = 13.8
MEAN = 14.1

TIME = 12:50

TIDAL COEFFICIENTS
EBB = .92
FLOOD = .94

| TIME | DEPTH | SPEED | DIR |
|---|---|---|---|
| 1:52 | | | |
| | | | 279. |
| | | | 277. |
| | | | 275. |
| | | | 272. |
| | | | 269. |
| | | | 269. |
| | | | 272. |
| | | | 269. |
| 2:17 | | | |
| | | | 279. |
| | | | 279. |
| | | | 279. |
| | | | 279. |
| | | | 277. |
| | | | 277. |
| 2:42 | | | |
| | | | 279. |
| | | | 279. |
| | | | 279. |
| | | | 279. |
| | | | 277. |
| | | | 277. |
| 3:07 | | | |
| | | | 279. |
| | | | 279. |
| | | | 279. |
| | | | 279. |
| | | | 279. |
| | | | 279. |
| 3:32 | | | |
| | | | 282. |
| | | | 281. |
| | | | 281. |
| | | | 282. |
| | | | 282. |
| 3:57 | | | |
| | | | 279. |
| | | | 279. |
| | | | 279. |
| | | | 279. |
| | | | 279. |
| 4:22 | | | |
| | | | 279. |
| | | | 279. |
| | | | 279. |
| | | | 279. |
| | | | 279. |
| 4:47 | | | |
| | | | 279. |
| | | | 279. |
| | | | 279. |
| | | | 279. |
| | | | 279. |
| 5:12 | | | |
| | | | 279. |
| | | | 279. |
| | | | 279. |
| | | | 279. |
| | | | 279. |
| 5:37 | | | |
| | | | 279. |
| | | | 279. |
| | | | 279. |
| | | | 279. |
| | | | 279. |
| 6:02 | | | |
| | | | 279. |
| | | | 279. |
| | | | 279. |
| | | | 279. |
| | | | 279. |
| 6:27 | | | |
| | | | 279. |
| | | | 279. |
| | | | 279. |
| | | | 279. |
| | | | 279. |
| 6:52 | | | |
| | | | 279. |
| | | | 279. |
| | | | 279. |
| | | | 279. |
| | | | 279. |
| 7:17 | | | |
| | | | 279. |
| | | | 279. |
| | | | 279. |
| | | | 279. |
| | | | 279. |
| 7:42 | | | |
| | | | 279. |
| | | | 279. |
| | | | 279. |
| | | | 279. |
| | | | 279. |
| 8:07 | | | |
| | | | 279. |
| | | | 279. |
| | | | 279. |
| | | | 279. |
| | | | 279. |
| 8:32 | | | |
| | | | 279. |
| | | | 279. |
| | | | 279. |
| | | | 279. |
| | | | 279. |
| 8:57 | | | |
| | | | 279. |
| | | | 279. |
| | | | 279. |
| | | | 279. |
| | | | 279. |
| 9:22 | | | |
| | | | 279. |
| | | | 279. |
| | | | 279. |
| | | | 279. |
| | | | 279. |
| 9:47 | | | |
| | | | 279. |
| | | | 279. |
| | | | 279. |
| | | | 279. |
| | | | 279. |
| 10:12 | | | |
| | | | 279. |
| | | | 279. |
| | | | 279. |
| | | | 279. |
| | | | 279. |
| 10:37 | | | |
| | | | 279. |
| | | | 279. |
| | | | 279. |
| | | | 279. |
| | | | 279. |
| 11:02 | | | |
| | | | 279. |
| | | | 279. |
| | | | 279. |
| | | | 279. |
| | | | 279. |
| 11:27 | | | |
| | | | 279. |
| | | | 279. |
| | | | 279. |
| | | | 279. |
| | | | 279. |
| 11:52 | | | |
| | | | 279. |
| | | | 279. |
| | | | 279. |
| | | | 279. |
| | | | 279. |

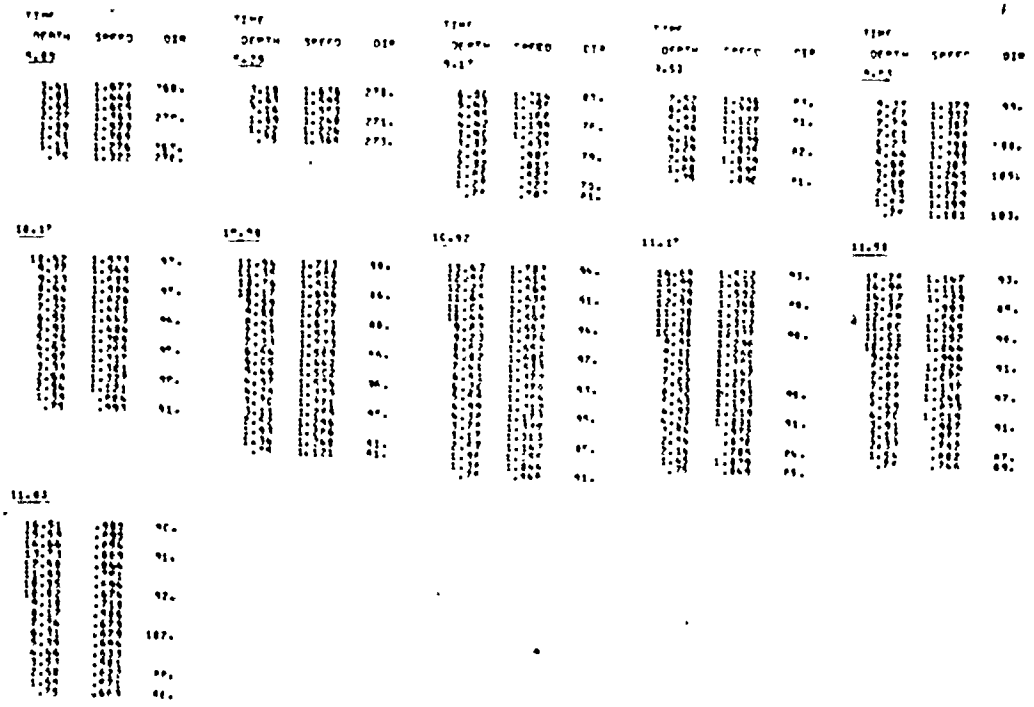

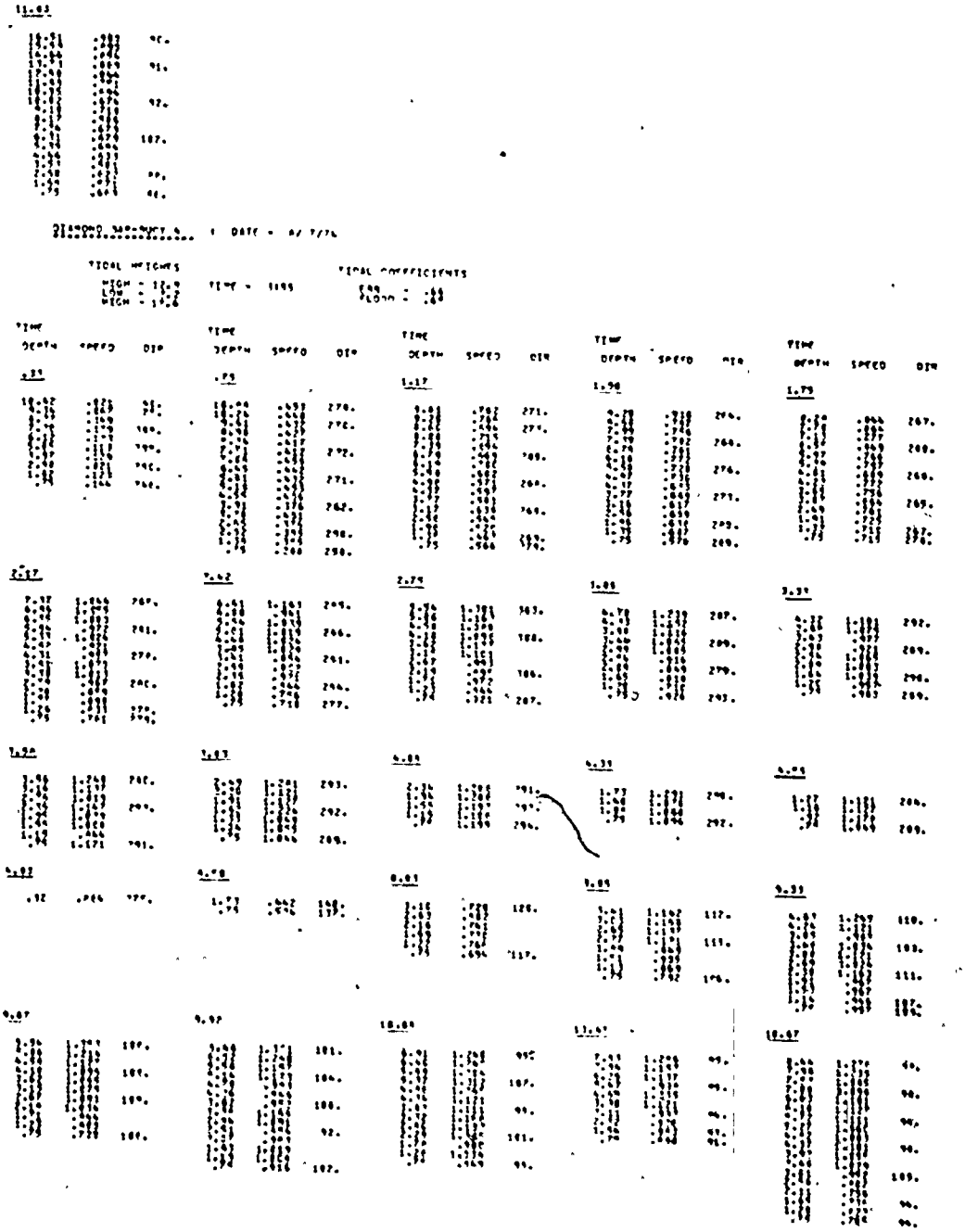

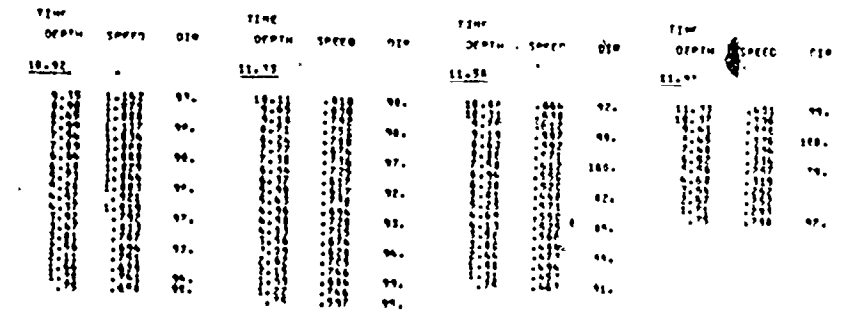

TIDAL HEIGHTS

HIGH : 13.3
LOW : 2.6
HIGH : 14.1

TIME - 11420 '

TIDAL COEFFICIENTS

FOR
FLOOD : 73

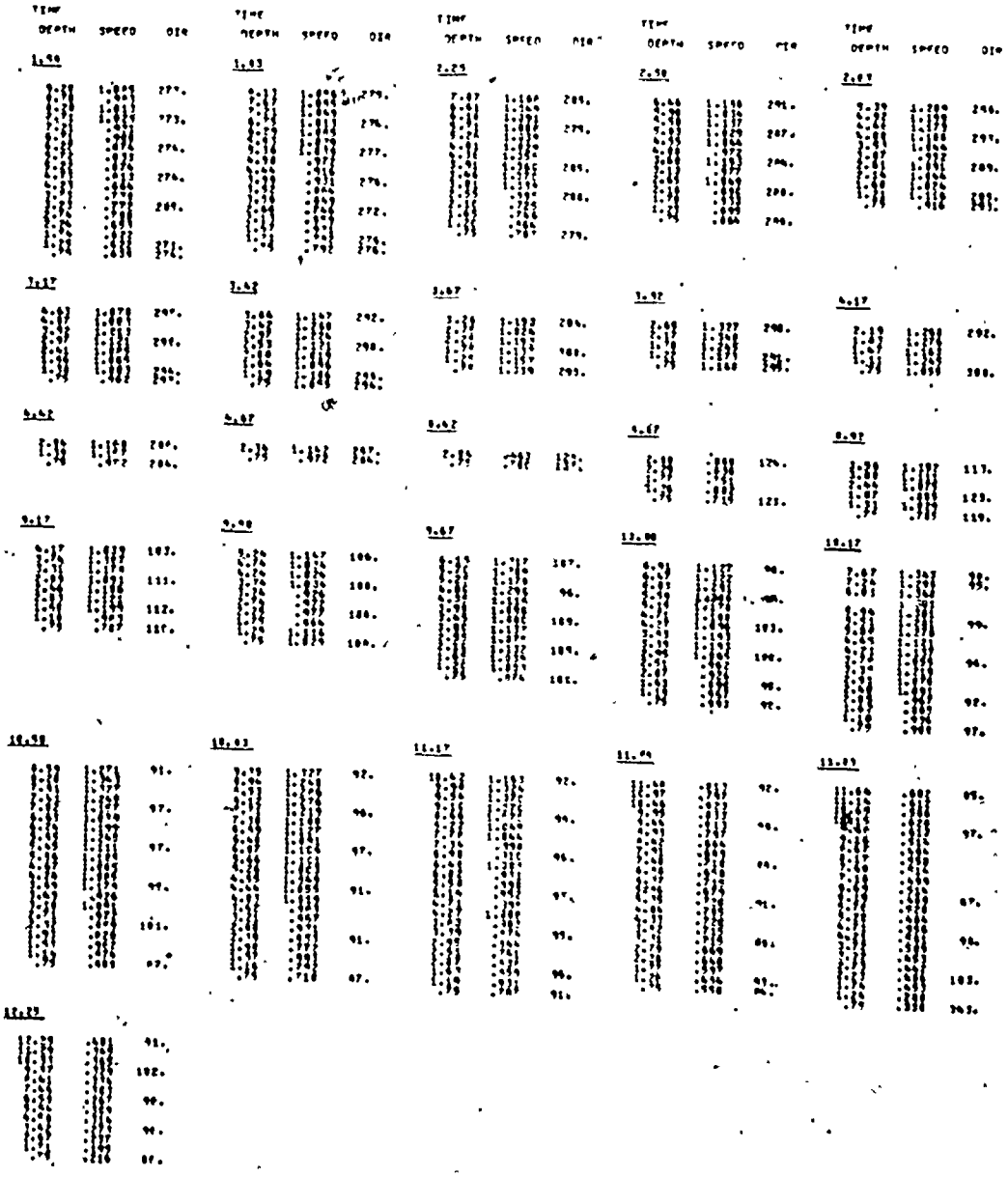

DIAMOND.BAR:DUCT.3... DATE = 07 7/74

TIDAL HEIGHTS
HIGH = 13.7
LOW = 13.2
TIME = 0130

TIDAL COEFFICIENTS
SPD
FLOOD = .65

| TIME | DEPTH | SPEED | DIR |
|---|---|---|---|
| .42 | | | |
| | | | 290. |
| | | | 290. |
| | | | 270. |
| | | | 267. |
| .93 | | | |
| | | | 293. |
| | | | 296. |
| | | | 281. |
| | | | 287. |
| | | | 273. |
| | | | 277. |
| | | | 269. |
| 1.17 | | | |
| | | | 270. |
| | | | 267. |
| | | | 269. |
| | | | 270. |
| | | | 269. |
| | | | 269. |
| 1.79 | | | |
| | | | 273. |
| | | | 275. |
| | | | 287. |
| | | | 271. |
| | | | 275. |
| | | | 272. |
| 1.81 | | | |
| | | | 272. |
| | | | 285. |
| | | | 281. |
| | | | 293. |
| | | | 273. |
| 2.17 | | | |
| | | | 277. |
| | | | 287. |
| | | | 290. |
| | | | 290. |
| | | | 270. |
| 2.58 | | | |
| | | | 298. |
| | | | 278. |
| | | | 297. |
| | | | 299. |
| 2.79 | | | |
| | | | 284. |
| | | | 295. |
| | | | 289. |
| | | | 290. |
| 3.09 | | | |
| | | | 295. |
| | | | 291. |
| | | | 291. |
| 3.25 | | | |
| | | | 294. |
| | | | 290. |
| | | | 289. |
| 3.25 | | | |
| | | | 298. |
| | | | 304. |
| 4.08 | | | |
| | | | 309. |
| | | | 317. |
| 4.25 | | | |
| | | | 307. |
| | | | 301. |
| 4.58 | | | |
| .77 | .369 | 344. | |
| 9.67 | | | |
| .62 | .989 | 124. | |
| 9.92 | | | |
| | | | 121. |
| | | | 121. |
| 9.83 | | | |
| | | | 109. |
| | | | 113. |
| 9.29 | | | |
| | | | 105. |
| | | | 110. |
| | | | 107. |
| 9.58 | | | |
| | | | 100. |
| | | | 99. |
| | | | 100. |
| 9.75 | | | |
| | | | 97. |
| | | | 104. |
| | | | 97. |
| | | | 97. |
| 10.04 | | | |
| | | | 99. |
| | | | 98. |
| | | | 96. |
| | | | 95. |
| 10.25 | | | |
| | | | 91. |
| | | | 98. |
| | | | 103. |
| | | | 99. |
| | | | 98. |
| 10.58 | | | |
| | | | 96. |
| | | | 92. |
| | | | 102. |
| | | | 98. |
| | | | 92. |
| 10.83 | | | |
| | | | 98. |
| | | | 91. |
| | | | 99. |
| | | | 96. |
| | | | 94. |
| | | | 96. |
| 11.17 | | | |
| | | | 89. |
| | | | 95. |
| | | | 97. |
| | | | 103. |
| | | | 99. |
| | | | 91. |
| 11.58 | | | |
| | | | 98. |
| | | | 92. |
| | | | 96. |
| | | | 91. |
| | | | 97. |
| | | | 95. |
| 11.87 | | | |
| | | | 89. |
| | | | 93. |
| | | | 98. |
| | | | 106. |
| | | | 98. |
| | | | 94. |
| 12.17 | | | |
| | | | 92. |
| | | | 97. |
| | | | 92. |
| | | | 98. |
| | | | 96. |

DIAMOND.BAR:DUCT.3... DATE = 08/ 7/74

TIDAL HEIGHTS
HIGH = 15.8
LOW = 14.9
TIME = 1430

TIDAL COEFFICIENTS
SPD
FLOOD = .97

| TIME | DEPTH | SPEED | DIR |
|---|---|---|---|
| .79 | | | |
| | | | 267. |
| | | | 264. |
| | | | 269. |
| | | | 269. |
| | | | 262. |
| | | | 282. |
| 1.17 | | | |
| | | | 270. |
| | | | 270. |
| | | | 283. |
| | | | 286. |
| | | | 256. |
| | | | 264. |
| 1.58 | | | |
| | | | 267. |
| | | | 271. |
| | | | 269. |
| | | | 276. |
| | | | 273. |
| | | | 269. |
| 1.92 | | | |
| | | | 269. |
| | | | 270. |
| | | | 272. |
| | | | 269. |
| | | | 281. |
| 2.02 | | | |
| | | | 279. |
| | | | 277. |
| | | | 281. |
| | | | 271. |
| | | | 270. |

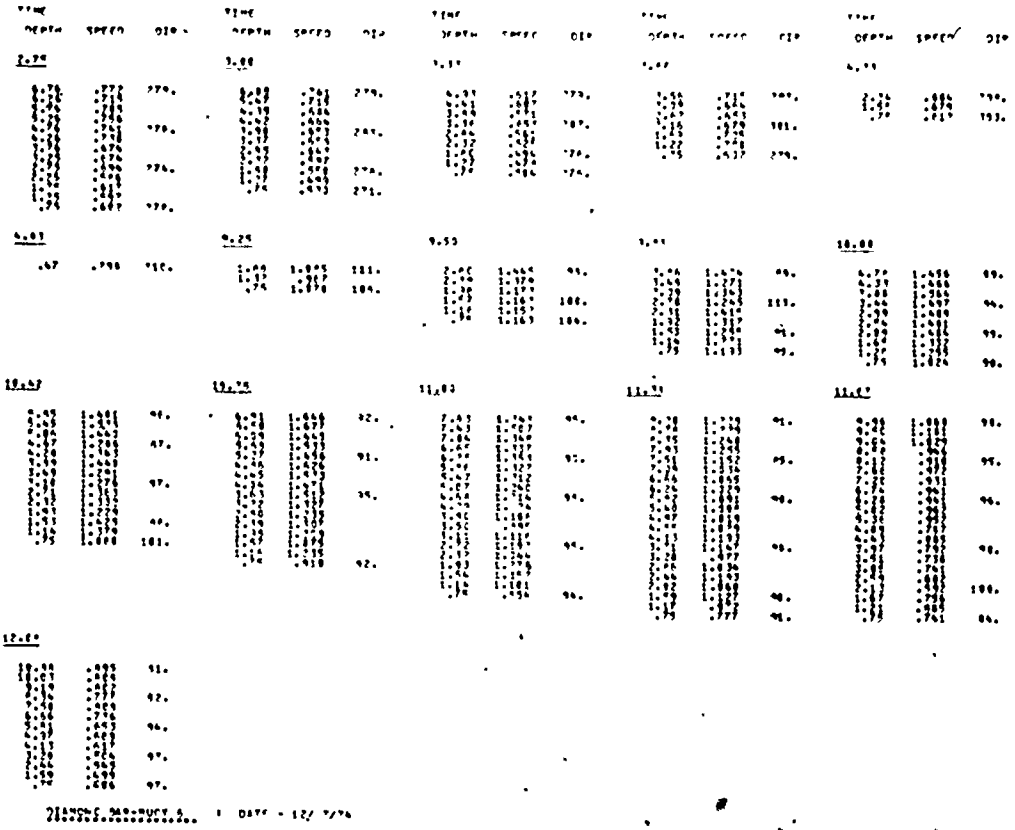

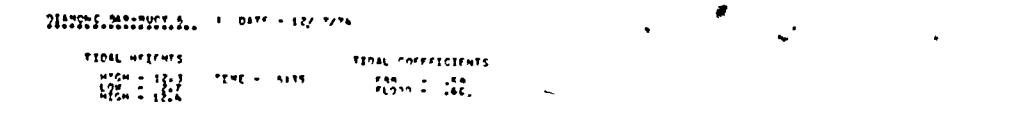

TIDAL HEIGHTS

TIDAL COEFFICIENTS

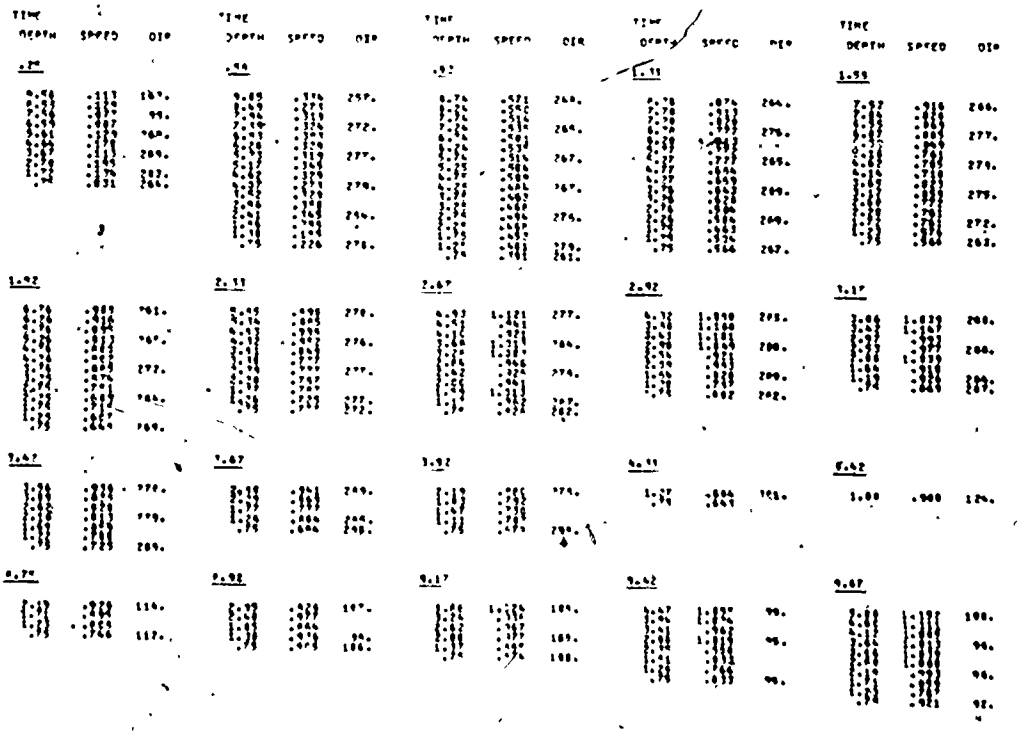

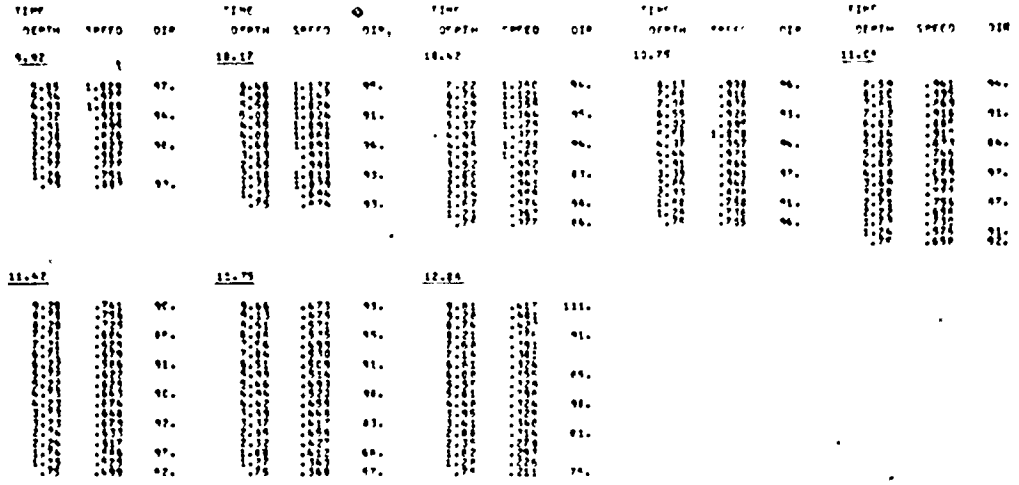

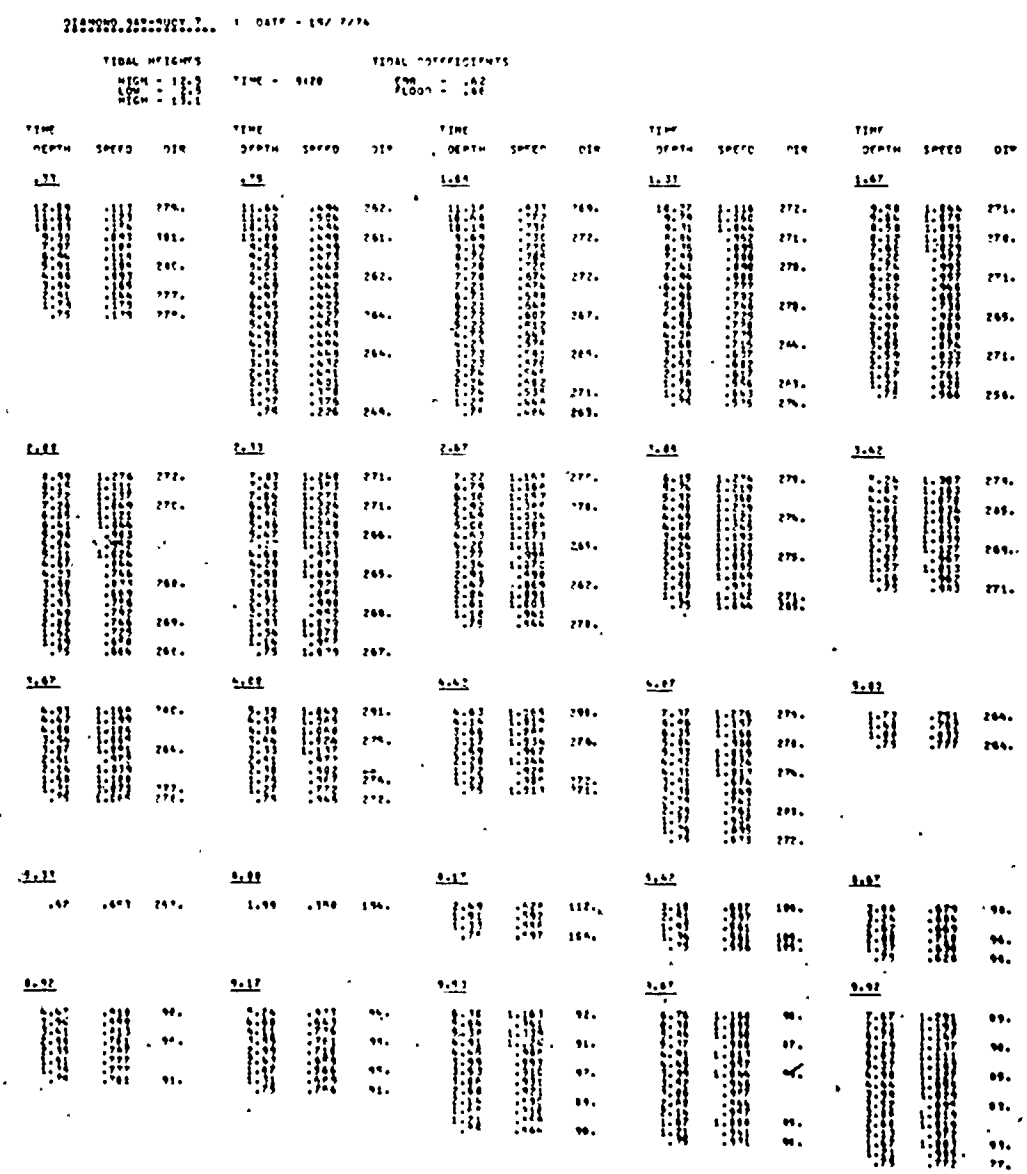

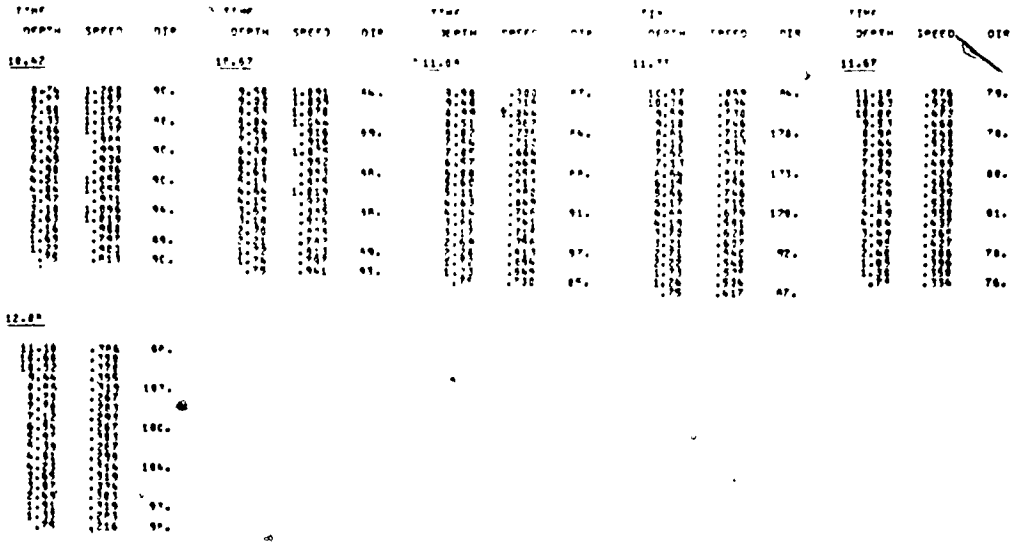

DIAMOND SHOAL LIGHT, 2... DATE - 5/ 8/74

TIDAL HEIGHTS

HIGH = 1.1
LOW = 1.1
HIGH = 1.1

TIME - 2458

TIDAL COEFFICIENTS

EBB = .69
FLOOD = .69

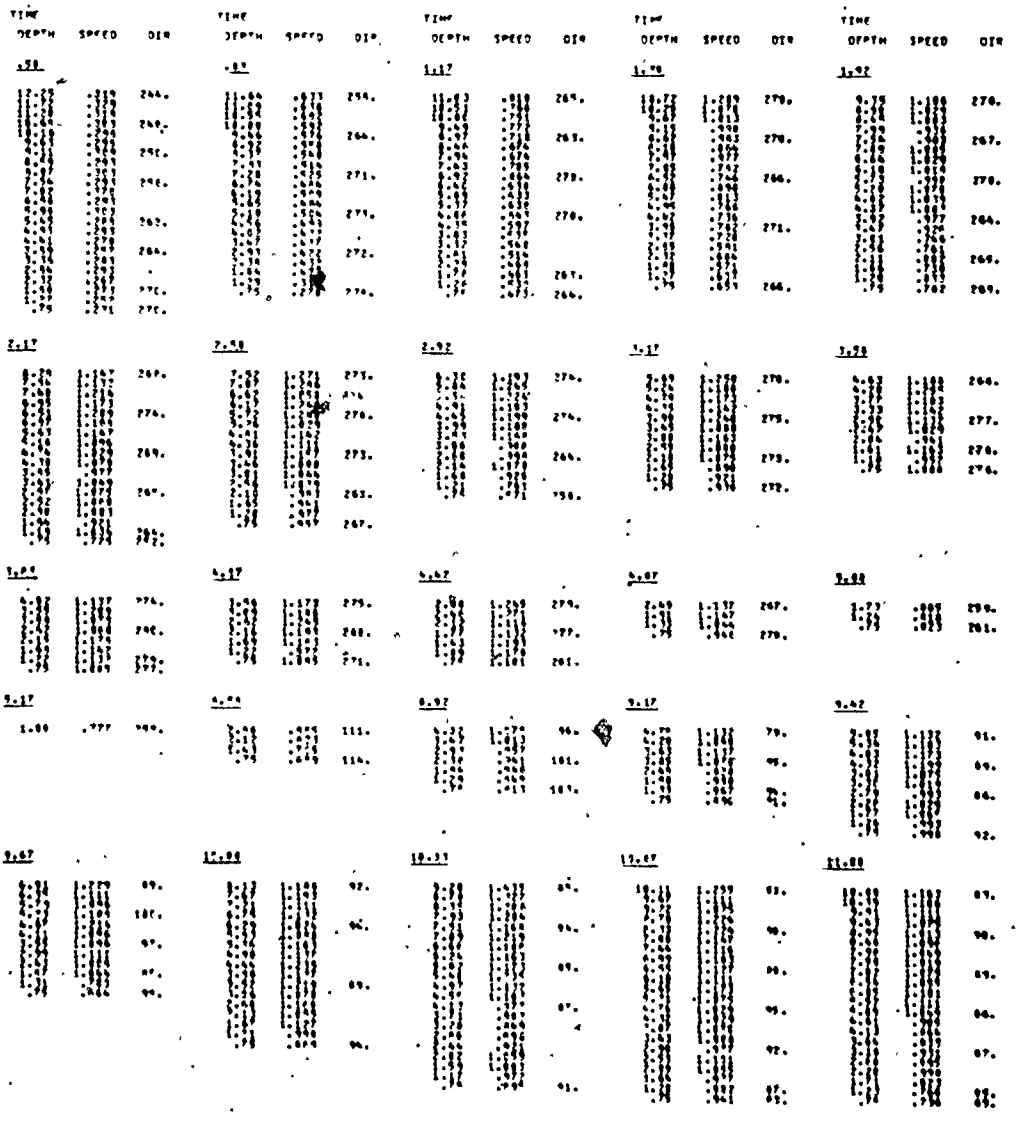

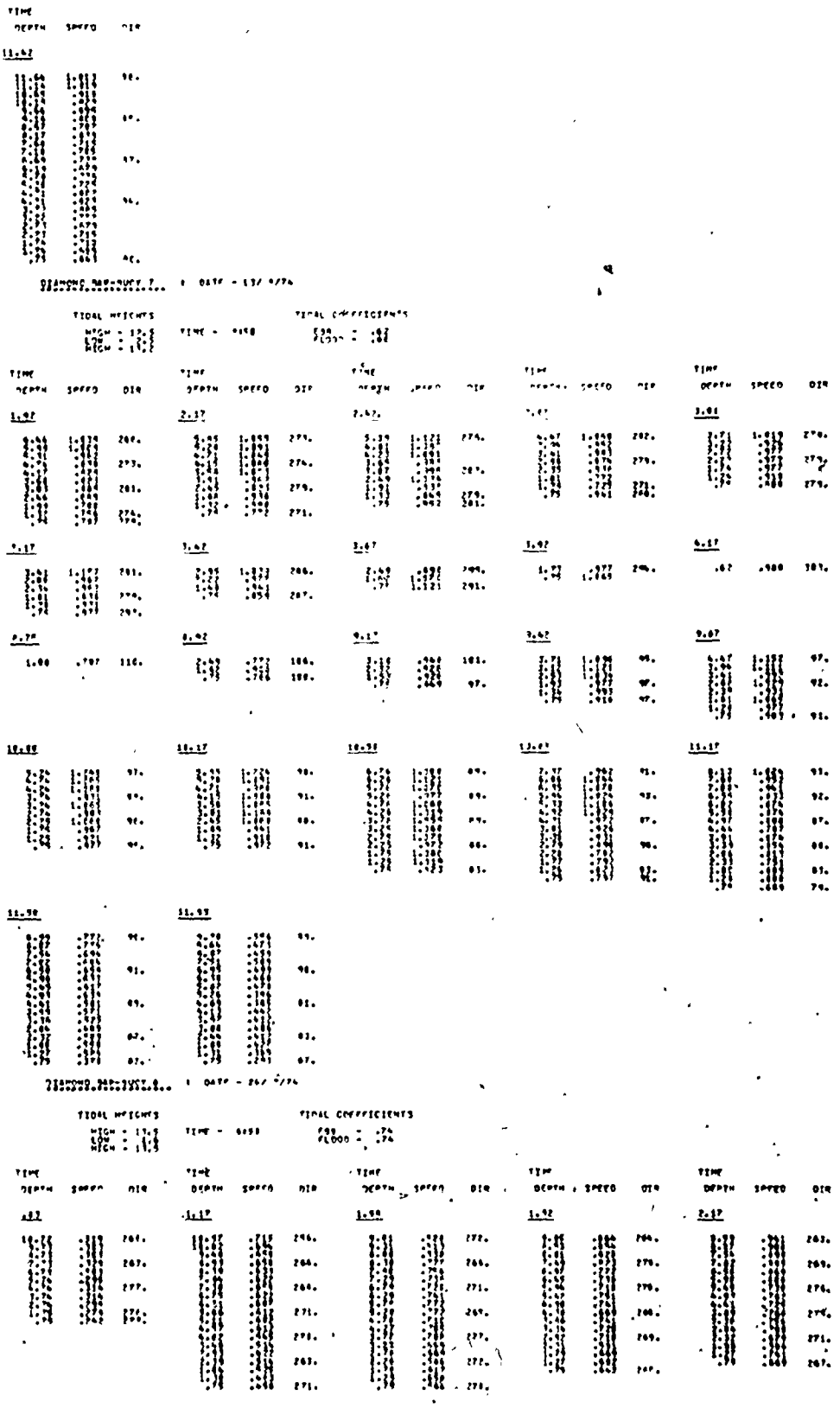

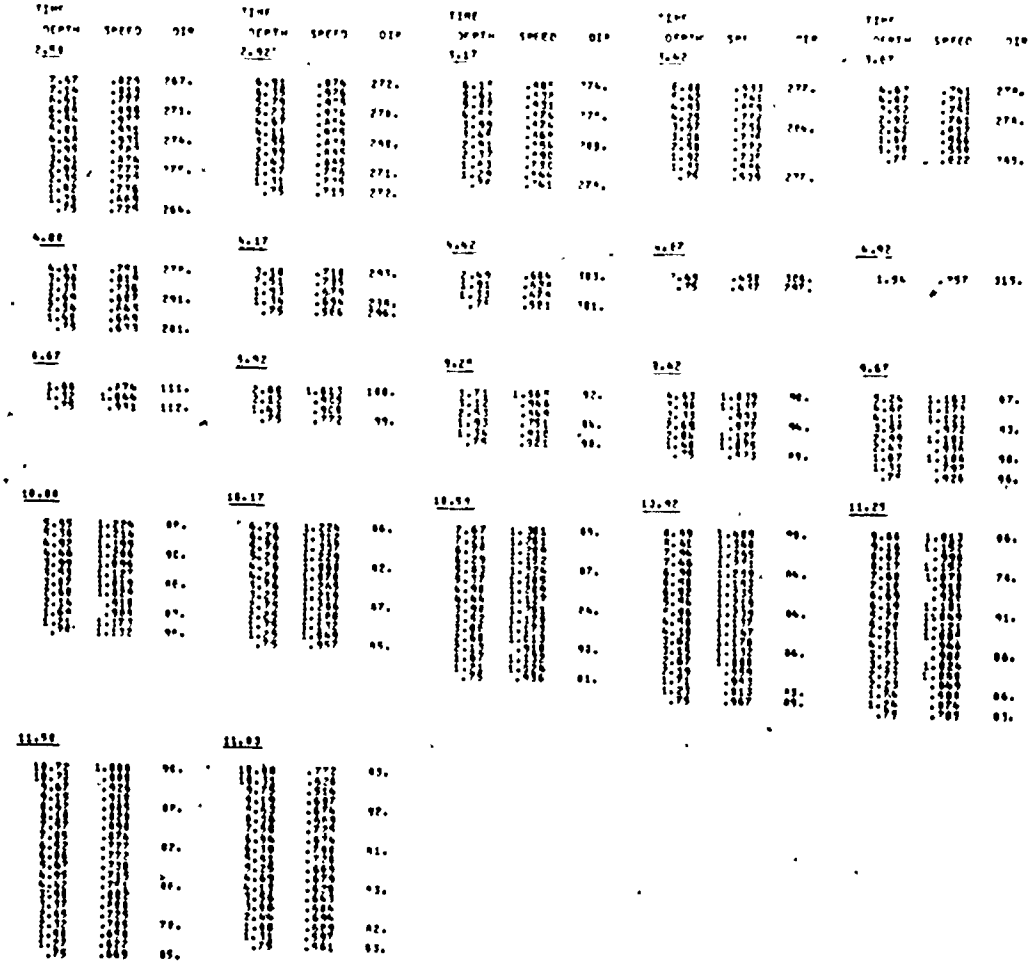

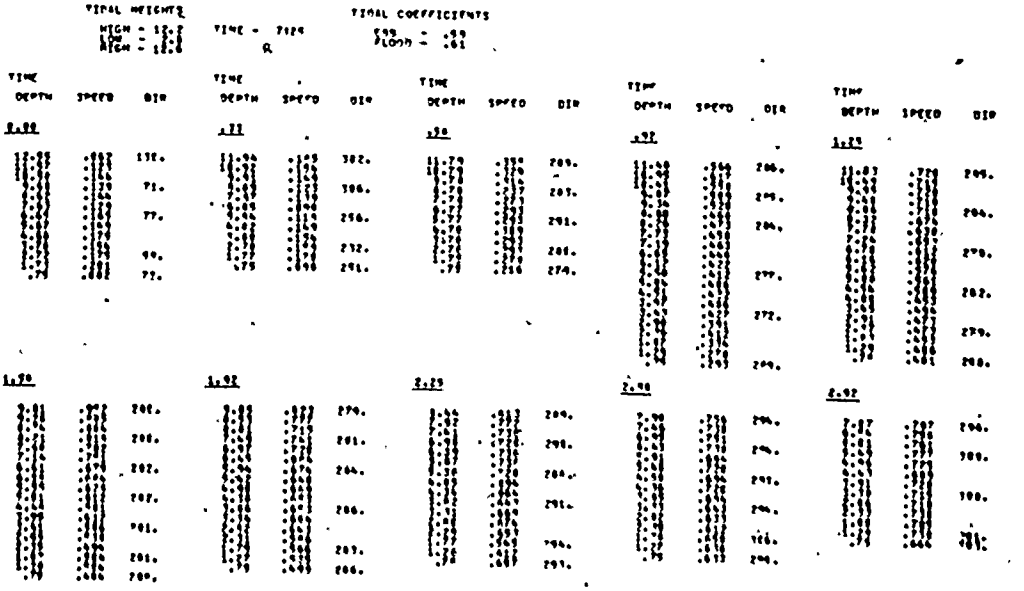

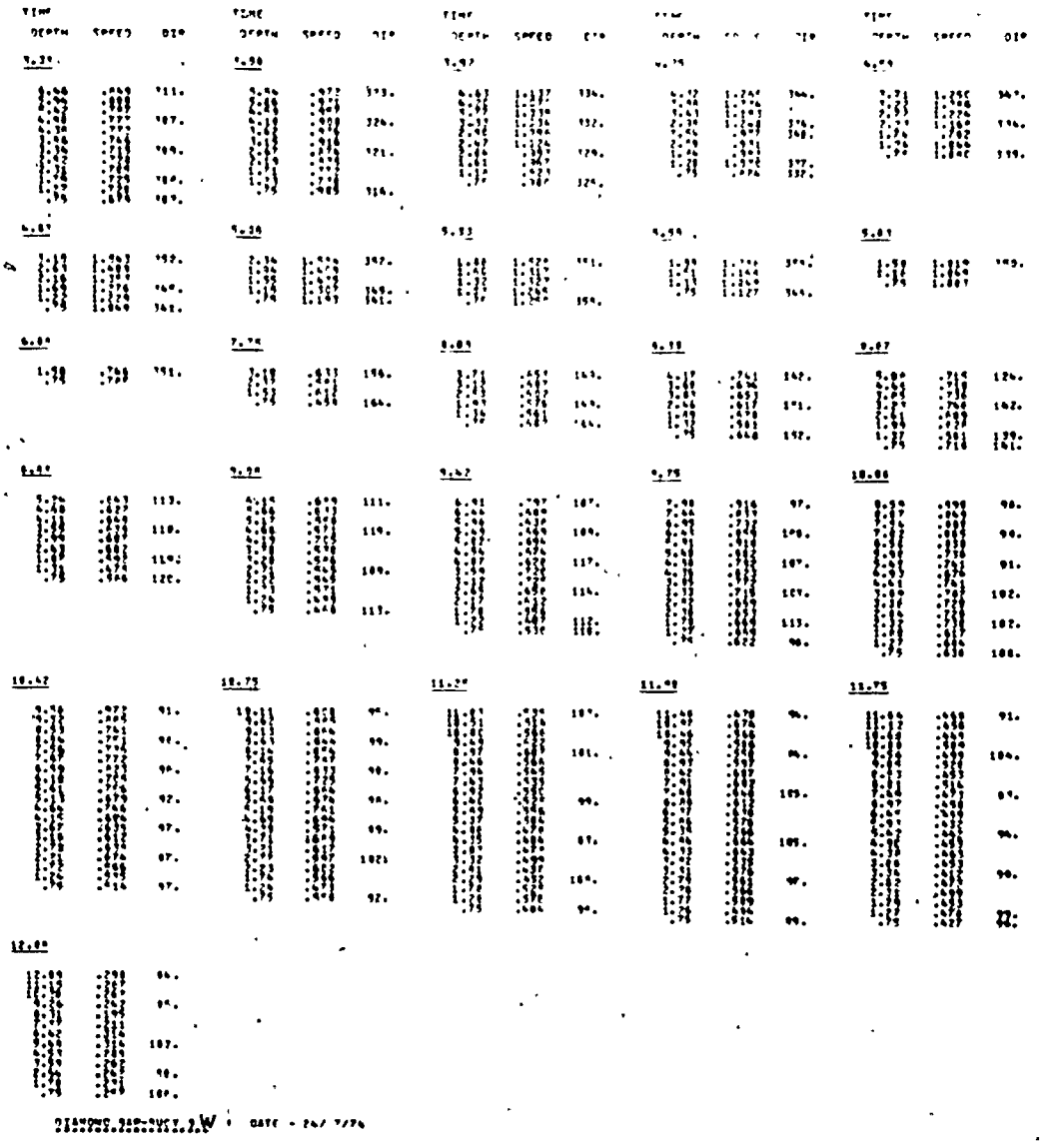

TIDAL HEIGHTS

HIGH : 10.7
LOW : 1.5
HIGH : 10.6

TIME - 21 0

TIDAL COEFFICIENTS

SAN
FLOOD : 88

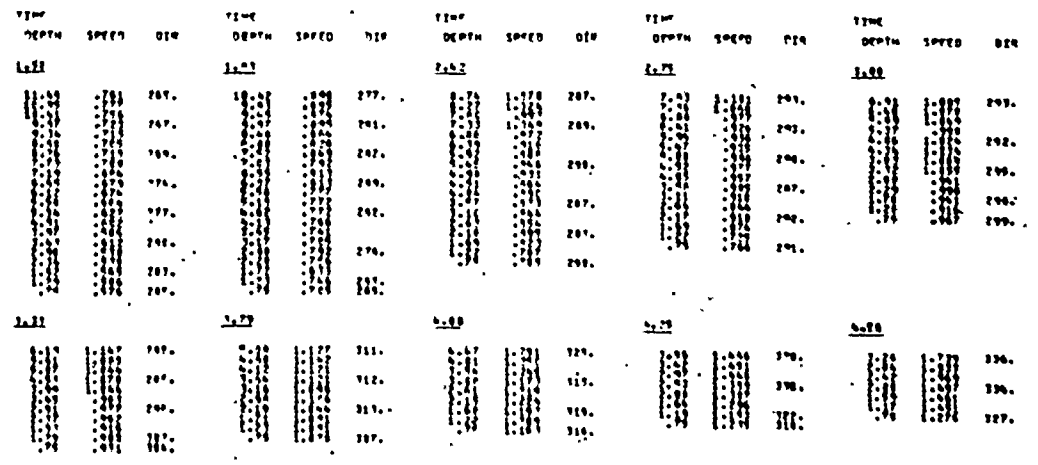

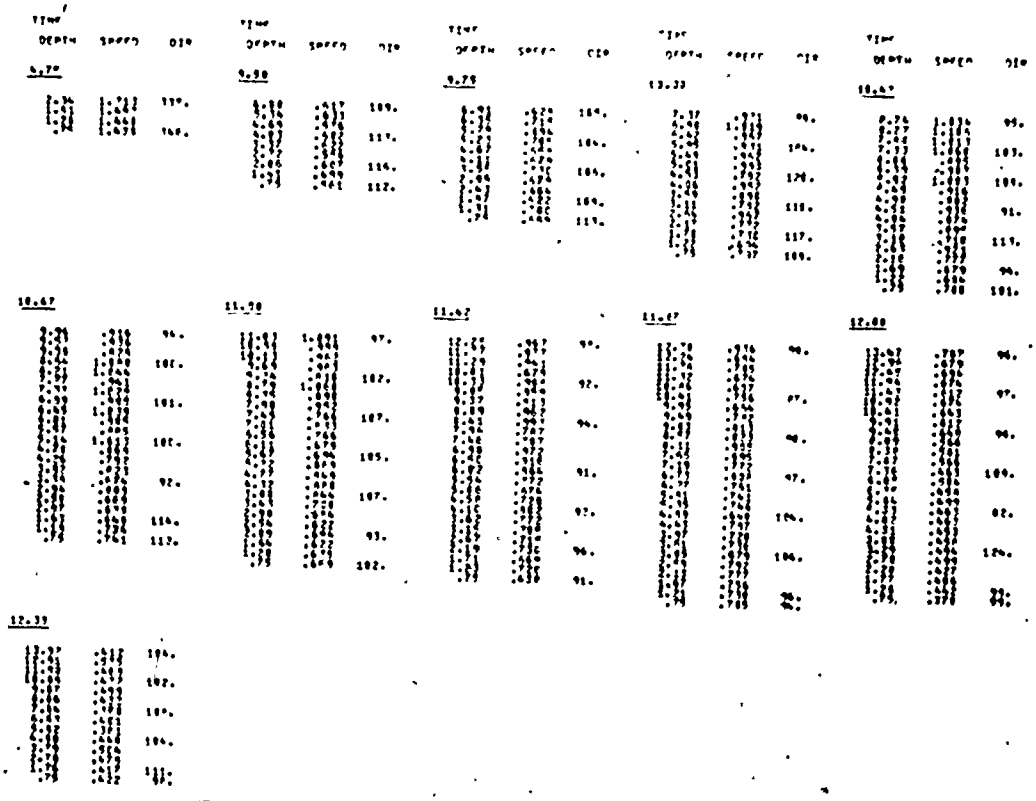

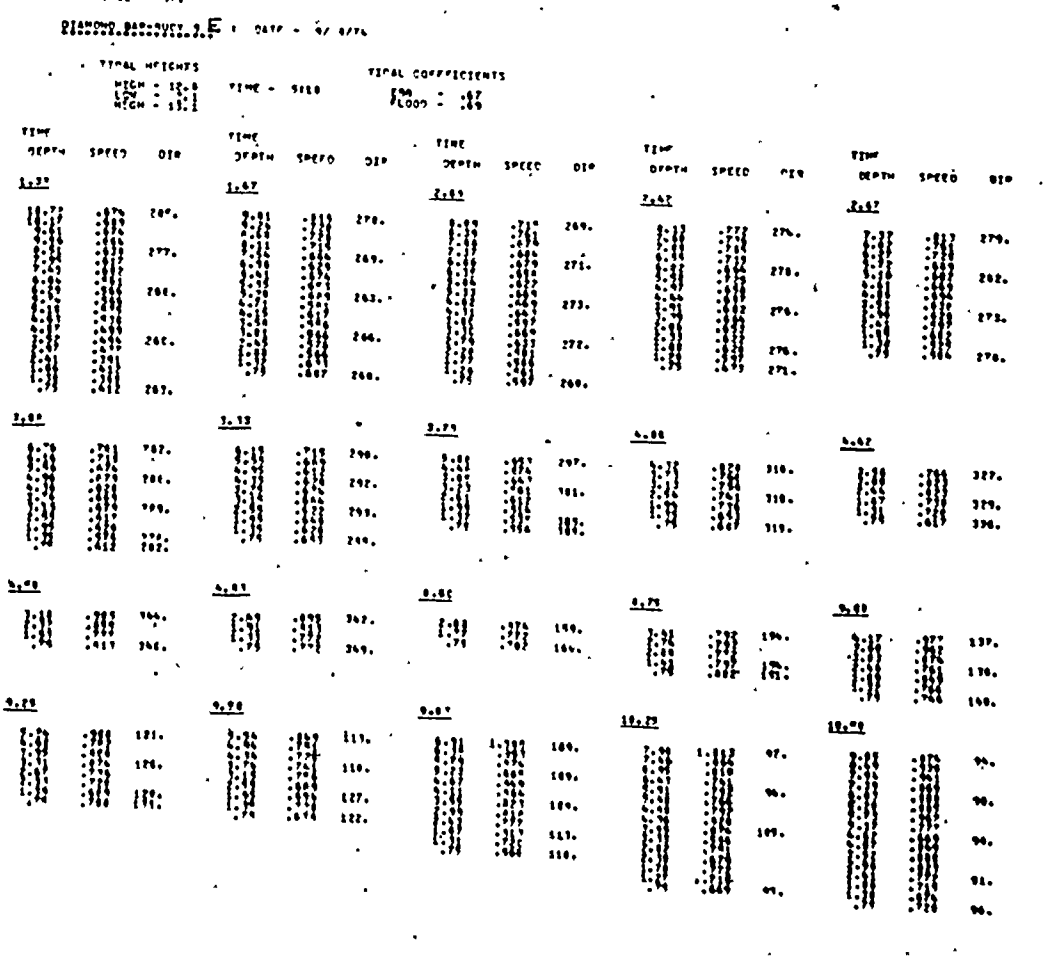

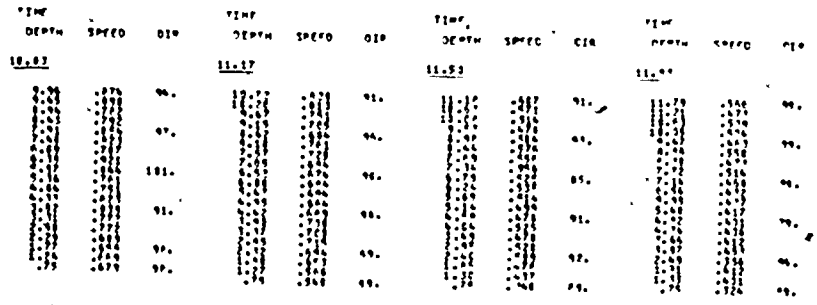

DIAMOND.BAR:SUCV.BE. ! DATE - 25/ 7/74

TIDAL HEIGHTS

HIGH : 14.1
LOW : 1.6
HIGH : 13.9

TIME - 5155

TIDAL COEFFICIENTS

SOB
FLOOD : .82

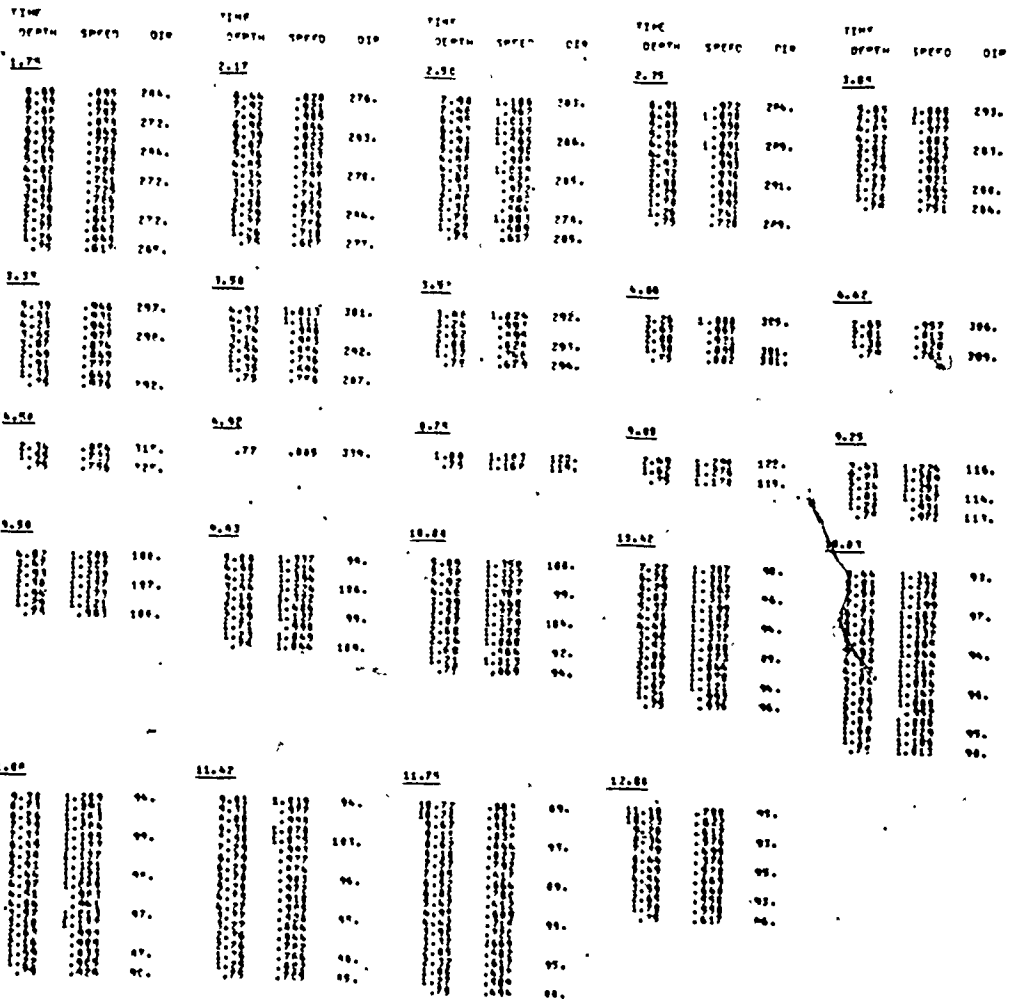

DIAMOND SHOAL CHANNEL - DATE - 22/ 7/74

TIDAL HEIGHTS

HIGH - 15.1
LOW -
HIGH - 15.1

TIME - 1115

TIDAL COEFFICIENTS

EBB
FLOOD.C .97

| TIME | DEPTH | SPEED | DIR |
|---|---|---|---|
| .25 | | | |
| | | | 90. |
| | | | 70. |
| | | | 0. |
| | | | 339. |
| | | | 331. |
| | | | 290. |
| | | | 283. |
| .92 | | | |
| | | | 291. |
| | | | 274. |
| | | | 266. |
| | | | 276. |
| | | | 283. |
| | | | 256. |
| | | | 264. |
| | | | 260. |
| 1.59 | | | |
| | | | 257. |
| | | | 278. |
| | | | 262. |
| | | | 263. |
| | | | 259. |
| | | | 269. |
| | | | 268. |
| | | | 266. |
| | | | 267. |
| 1.92 | | | |
| | | | 295. |
| | | | 276. |
| | | | 255. |
| | | | 273. |
| | | | 279. |
| | | | 279. |
| | | | 273. |
| | | | 276. |
| 2.24 | | | |
| | | | 264. |
| | | | 257. |
| | | | 251. |
| | | | 248. |
| | | | 263. |
| | | | 268. |
| | | | 272. |
| | | | 272. |
| 2.59 | | | |
| | | | 267. |
| | | | 268. |
| | | | 269. |
| | | | 256. |
| | | | 263. |
| | | | 199. |
| | | | 269. |
| | | | 267. |
| | | | 261. |
| 2.92 | | | |
| | | | 255. |
| | | | 268. |
| | | | 259. |
| | | | 269. |
| | | | 269. |
| | | | 268. |
| | | | 257. |
| | | | 268. |
| 3.33 | | | |
| | | | 256. |
| | | | 268. |
| | | | 267. |
| | | | 256. |
| | | | 261. |
| | | | 256. |
| | | | 255. |
| 3.67 | | | |
| | | | 271. |
| | | | 266. |
| | | | 264. |
| | | | 253. |
| | | | 251. |
| | | | 256. |
| | | | 268. |
| 3.92 | | | |
| | | | 258. |
| | | | 259. |
| | | | 266. |
| | | | 267. |
| | | | 263. |
| | | | 256. |
| 4.29 | | | |
| | | | 262. |
| | | | 259. |
| | | | 253. |
| | | | 257. |
| | | | 262. |
| | | | 252. |
| 4.58 | | | |
| | | | 268. |
| | | | 261. |
| | | | 260. |
| | | | 268. |
| | | | 257. |
| | | | 260. |
| 5.00 | | | |
| | | | 269. |
| | | | 268. |
| | | | 268. |
| | | | 259. |
| | | | 268. |
| 5.29 | | | |
| | | | 270. |
| | | | 266. |
| | | | 261. |
| | | | 262. |
| 5.58 | | | |
| | | | 256. |
| | | | 267. |
| | | | 251. |
| | | | 252. |
| 5.79 | | | |
| | | | 237. |
| | | | 259. |
| | | | 256. |
| | | | 252. |
| 6.08 | | | |
| | | | 239. |
| | | | 251. |
| | | | 252. |
| 6.33 | | | |
| | | | 258. |
| | | | 268. |
| | | | 267. |
| 6.54 | | | |
| | | | 270. |
| | | | 267. |
| | | | 270. |
| 6.79 | | | |
| | | | 233. |
| | | | 252. |
| | | | 252. |
| 7.08 | | | |
| | | | 285. |
| | | | 287. |
| | | | 291. |
| 7.29 | | | |
| | | | 269. |
| | | | 270. |
| | | | 270. |
| 7.58 | | | |
| | | | 69. |
| | | | 66. |
| | | | 68. |
| 7.79 | | | |
| | | | 83. |
| | | | 73. |
| | | | 72. |
| 8.08 | | | |
| | | | 73. |
| | | | 66. |
| | | | 72. |
| | | | 66. |
| 8.29 | | | |
| | | | 76. |
| | | | 67. |
| | | | 69. |
| | | | 75. |
| | | | 69. |
| 8.62 | | | |
| | | | 67. |
| | | | 64. |
| | | | 68. |
| | | | 62. |
| | | | 69. |
| | | | 67. |
| 8.92 | | | |
| | | | 71. |
| | | | 68. |
| | | | 65. |
| | | | 67. |
| | | | 69. |
| | | | 69. |
| | | | 73. |
| | | | 72. |
| 9.33 | | | |
| | | | 78. |
| | | | 67. |
| | | | 64. |
| | | | 75. |
| | | | 68. |
| | | | 70. |
| | | | 83. |
| | | | 69. |
| | | | 76. |
| | | | 72. |
| 9.79 | | | |
| | | | 77. |
| | | | 67. |
| | | | 68. |
| | | | 77. |
| | | | 67. |
| | | | 70. |
| | | | 72. |

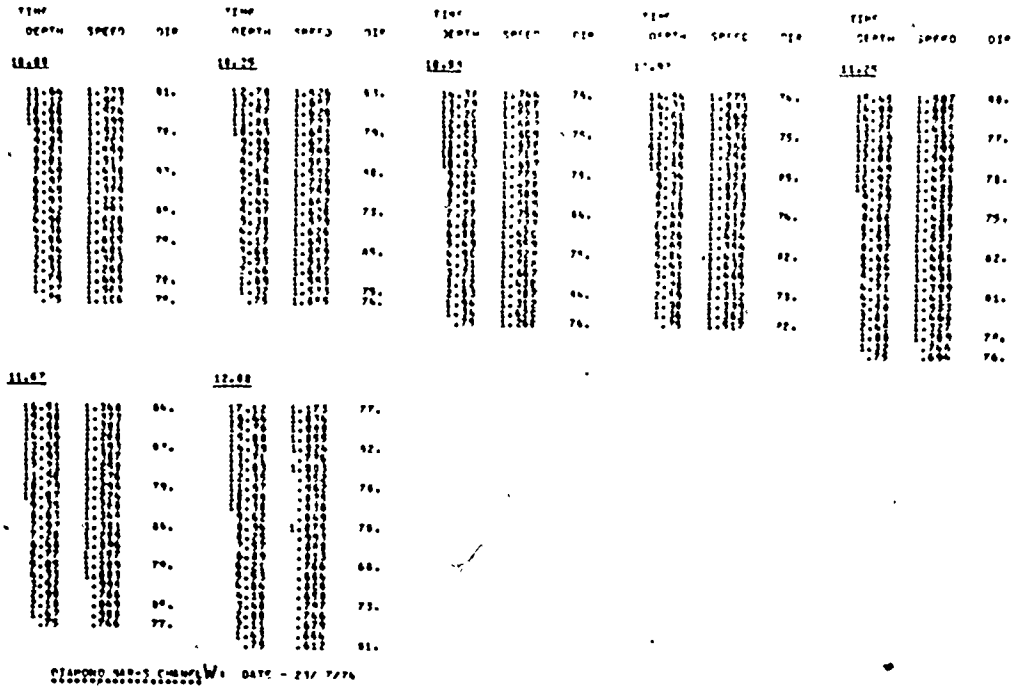


DIAMOND HEAD, CHANNEL W. DATE - 21/ 7/74

TIDAL HEIGHTS
HIGH = 19.0
LOW = .0
HIGH = 16.0
TIME - 01 0

TIDAL COEFFICIENTS
100
1000 : 87

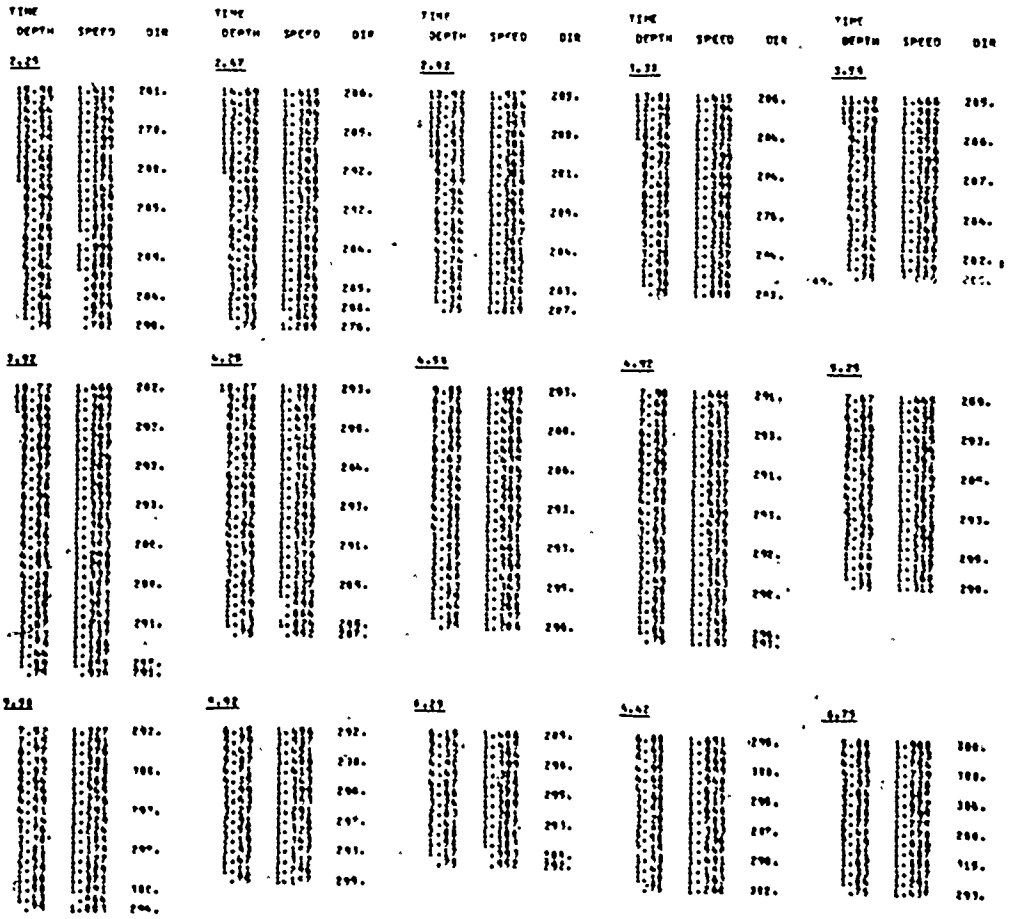

[illegible] DATE - 27 8/74

TIDAL HEIGHTS

HIGH : 12.0
LOW : 12.1
HIGH : 12.6

TIME - 1030

TIDAL COEFFICIENTS

$\frac{HW}{LW_{000}}$ : .87
.84

| TIME DEPTH | SPEED | DIR | TIME DEPTH | SPEED | DIR | TIME DEPTH | SPEED | DIR | TIME DEPTH | SPEED | DIR | TIME DEPTH | SPEED | DIR |
|---|---|---|---|---|---|---|---|---|---|---|---|---|---|---|
| .83 | | | 1.33 | | | 1.84 | | | 1.87 | | | 2.31 | | |
| | | 280. | | | 269. | | | 271. | | | 277. | | | 273. |
| | | 276. | | | 264. | | | 267. | | | 270. | | | 267. |
| | | 274. | | | 269. | | | 269. | | | 269. | | | 267. |
| | | 279. | | | | | | 271. | | | 258. | | | 262. |
| | | 291. | | | 269. | | | | | | 274. | | | 269. |
| | | 299. | | | 271. | | | 274. | | | 266. | | | |
| 2.87 | | | 2.92 | | | 3.25 | | | 3.55 | | | 3.92 | | |
| | | 278. | | | 278. | | | 279. | | | 279. | | | 268. |
| | | 278. | | | 276. | | | 262. | | | 276. | | | 276. |
| | | 272. | | | 272. | | | 267. | | | 258. | | | 270. |
| | | 272. | | | 276. | | | 263. | | | 275. | | | 269. |
| | | | | | 270. | | | 272. | | | 266. | | | |
| 4.33 | | | 4.58 | | | 4.87 | | | 5.25 | | | 5.67 | | |
| | | 277. | | | 279. | | | 279. | | | 273. | | | 276. |
| | | 276. | | | 275. | | | 271. | | | | | | 271. |
| | | 261. | | | 276. | | | | | | | | | 267. |
| | | 272. | | | 268. | | | | | | | | | |
| 5.92 | | | 6.25 | | | 6.58 | | | 6.83 | | | 7.08 | | |
| | | 268. | | | 276. | | | 269. | | | 278. | | | 268. |
| | | 276. | | | 276. | | | 268. | | | 278. | | | 264. |
| | | 277. | | | 276. | | | 271. | | | 278. | | | 261. |
| | | 269. | | | 279. | | | | | | | | | |
| | | 270. | | | | | | | | | | | | |
| 7.33 | | | 8.58 | | | 8.83 | | | 9.08 | | | 9.42 | | |
| | | 237. | | | 92. | | | 96. | | | 96. | | | 93. |
| | | 190. | | | 97. | | | 99. | | | 96. | | | 96. |
| | | 163. | | | 99. | | | | | | 98. | | | 99. |
| | | | | | 96. | | | | | | 100. | | | 96. |
| | | | | | 91. | | | | | | | | | |
| 9.83 | | | 10.17 | | | 10.54 | | | 10.79 | | | 11.17 | | |
| | | 96. | | | 93. | | | 89. | | | 92. | | | 89. |
| | | 96. | | | 86. | | | 91. | | | 98. | | | 94. |
| | | 99. | | | 102. | | | 87. | | | 92. | | | 91. |
| | | 101. | | | 97. | | | 95. | | | 93. | | | 92. |
| | | | | | | | | | | | | | | |
| 11.58 | | | 11.92 | | | 12.17 | | | | | | | | |
| | | 89. | | | 93. | | | 78. | | | | | | |
| | | 88. | | | 94. | | | 113. | | | | | | |
| | | 92. | | | 98. | | | 92. | | | | | | |
| | | 92. | | | 91. | | | 100. | | | | | | |
| | | 95. | | | 89. | | | | | | | | | |

ECONOMY POINT-EP 1 ... DATE - 27/ 7/74

TIDAL HEIGHTS
HIGH = 15.0
LOW = 1.0

TIME - 7:58

TIDAL COEFFICIENTS
EBB = .87
FLOOD = .80

| TIME | DEPTH | SPEED | DIR |
|---|---|---|---|
| | .67 | | |
| | | | 303. |
| | | | 297. |
| | | | 290. |
| | | | 287. |
| | | | 294. |
| | 2.17 | | |
| | | | 189. |
| | | | 184. |
| | | | 194. |
| | 5.67 | | |
| | | | 142. |
| | | | 134. |
| | 10.92 | | |
| | | | 123. |
| | | | 127. |
| | | | 139. |
| | | | 132. |
| | 1.88 | | |
| | | | 304. |
| | | | 308. |
| | | | 301. |
| | | | 304. |
| | | | 307. |
| | 4.58 | | |
| | | | 199. |
| | | | 197. |
| | 9.92 | | |
| | | | 139. |
| | | | 143. |
| | 11.17 | | |
| | | | 121. |
| | | | 120. |
| | | | 129. |
| | | | 131. |
| | 1.33 | | |
| | | | 314. |
| | | | 311. |
| | | | 305. |
| | | | 302. |
| | | | 301. |
| | 4.75 | | |
| | | | 189. |
| | | | 197. |
| | 10.17 | | |
| | | | 124. |
| | | | 127. |
| | 11.58 | | |
| | | | 130. |
| | | | 131. |
| | | | 126. |
| | 1.67 | | |
| | | | 309. |
| | | | 310. |
| | | | 306. |
| | | | 306. |
| | 4.92 | | |
| | | | 199. |
| | | | 197. |
| | 13.42 | | |
| | | | 129. |
| | | | 135. |
| | | | 139. |
| | 11.83 | | |
| | | | 130. |
| | | | 132. |
| | | | 129. |
| | | | 130. |
| | 1.92 | | |
| | | | 306. |
| | | | 301. |
| | | | 307. |
| | 4.67 | | |
| | | | 188. |
| | | | .666 |
| | 10.79 | | |
| | | | 125. |
| | | | 126. |
| | | | 132. |

ECONOMY POINT-EP 2 ... DATE - 21/ 8/74

TIDAL HEIGHTS
HIGH = 15.1
LOW = 1.7

TIME - 3:55

TIDAL COEFFICIENTS
EBB = .92
FLOOD = .91

| TIME | DEPTH | SPEED | DIR |
|---|---|---|---|
| | .67 | | |
| | | | 296. |
| | | | 289. |
| | | | 284. |
| | | | 289. |
| | | | 279. |
| | | | 286. |
| | 2.22 | | |
| | | | 291. |
| | | | 299. |
| | | | 299. |
| | | | 296. |
| | | | 302. |
| | 5.25 | | |
| | | | 77. |
| | | | |
| | | | |
| | | | |
| | | | |
| | | | |
| | 11.83 | | |
| | | | 101. |
| | | | 110. |
| | | | 109. |
| | | | 106. |
| | | | 99. |
| | 1.88 | | |
| | | | 293. |
| | | | 292. |
| | | | 291. |
| | | | 290. |
| | | | 290. |
| | | | 291. |
| | | | 295. |
| | 4.67 | | |
| | | | 279. |
| | | | 287. |
| | | | 293. |
| | | | 298. |
| | | | |
| | | | |
| | | | |
| | | | |
| | | | |
| | | | |
| | 9.96 | | |
| | | | 93. |
| | | | 98. |
| | | | |
| | | | |
| | | | |
| | | | |
| | | | |
| | | | |
| | 11.58 | | |
| | | | 110. |
| | | | 103. |
| | | | 106. |
| | | | 107. |
| | | | 109. |
| | | | |
| | | | |
| | | | |
| | | | |
| | | | |
| | | | |
| | 1.33 | | |
| | | | 303. |
| | | | 306. |
| | | | 300. |
| | | | 299. |
| | | | 302. |
| | | | 301. |
| | | | |
| | | | |
| | | | |
| | | | |
| | | | |
| | | | |
| | 4.92 | | |
| | | | 272. |
| | | | 268. |
| | | | |
| | | | |
| | | | |
| | | | |
| | | | |
| | | | |
| | | | |
| | | | |
| | 9.79 | | |
| | | | 96. |
| | | | 102. |
| | | | |
| | | | |
| | | | |
| | | | |
| | | | |
| | | | |
| | | | |
| | | | |
| | 11.79 | | |
| | | | 111. |
| | | | 109. |
| | | | 105. |
| | | | 108. |
| | | | 105. |
| | | | |
| | | | |
| | | | |
| | | | |
| | | | |
| | | | |
| | 1.67 | | |
| | | | 300. |
| | | | 299. |
| | | | 298. |
| | | | 296. |
| | | | 295. |
| | | | |
| | | | |
| | | | |
| | | | |
| | | | |
| | | | |
| | 4.75 | | |
| | | | 235. |
| | | | 236. |
| | | | |
| | | | |
| | | | |
| | | | |
| | | | |
| | | | |
| | | | |
| | | | |
| | 10.17 | | |
| | | | 107. |
| | | | 104. |
| | | | 104. |
| | | | 104. |
| | | | |
| | | | |
| | | | |
| | | | |
| | | | |
| | | | |
| | | | |
| | 13.25 | | |
| | | | 107. |
| | | | 104. |
| | | | 104. |
| | | | 104. |
| | | | |
| | | | |
| | | | |
| | | | |
| | | | |
| | | | |
| | | | |
| | 1.92 | | |
| | | | 294. |
| | | | 297. |
| | | | 295. |
| | | | 301. |
| | | | |
| | | | |
| | | | |
| | | | |
| | | | |
| | | | |
| | | | |
| | 4.58 | | |
| | | | 261. |
| | | | |
| | | | |
| | | | |
| | | | |
| | | | |
| | | | |
| | | | |
| | | | |
| | | | |
| | 10.67 | | |
| | | | 106. |
| | | | 107. |
| | | | 107. |
| | | | 109. |
| | | | 108. |
| | | | |
| | | | |
| | | | |
| | | | |
| | | | |
| | | | |
| | | | |

ECONOMY POINT-SD 6 DATE - 6/ 6/74

TIDAL HEIGHTS
HIGH : 13.
LOW : 1.
HIGH : 1.

TIME - 3128

TIDAL COEFFICIENTS
EBB :
FLOOD : .71

| TIME | DEPTH | SPEED | DIR |
|---|---|---|---|
| .92 | | | |
| | | | 270. |
| | | | 290. |
| | | | 287. |
| | | | 290. |
| | | | 307. |
| | | | 293. |
| 5.25 | | | |
| | | | 291. |
| | | | 293. |
| | | | 296. |
| | | | 297. |
| | | | 299. |
| 1.58 | | | |
| | | | 303. |
| | | | 293. |
| | | | 294. |
| | | | 297. |
| 1.92 | | | |
| | | | 239. |
| | | | 308. |
| | | | 287. |
| | | | 296. |
| 2.17 | | | |
| | | | 294. |
| | | | 302. |
| 2.58 | | | |
| | | | 110. |
| | | | 117. |
| | | | 77. |
| 2.83 | | | |
| | | | 16. |
| | | | 92. |
| | | | 136. |
| 3.17 | | | |
| | | | 177. |
| | | | 182. |
| 3.58 | | | |
| | | | 201. |
| | | | 205. |
| 3.67 | | | |
| | | | 202. |
| 3.92 | | | |
| 1.88 | .247 | 189. | |
| 5.58 | | | |
| 1.88 | .247 | 6. | |
| 6.92 | | | |
| | | | 82. |
| 9.17 | | | |
| | | | 95. |
| | | | 93. |
| 9.42 | | | |
| | | | 87. |
| | | | 95. |
| | | | 96. |
| 9.67 | | | |
| | | | 51. |
| | | | 48. |
| | | | 67. |
| 10.08 | | | |
| | | | 182. |
| | | | 187. |
| | | | 188. |
| | | | 182. |
| 10.33 | | | |
| | | | 58. |
| | | | 61. |
| | | | 68. |
| | | | 75. |
| 10.83 | | | |
| | | | 126. |
| | | | 113. |
| | | | 108. |
| | | | 106. |
| | | | 109. |
| 11.08 | | | |
| | | | 105. |
| | | | 106. |
| | | | 109. |
| | | | 110. |
| 11.33 | | | |
| | | | 108. |
| | | | 111. |
| | | | 111. |
| | | | 107. |
| | | | 103. |
| 11.67 | | | |
| | | | 108. |
| | | | 107. |
| | | | 110. |
| | | | 111. |
| | | | 111. |
| 12.33 | | | |
| | | | 191. |
| | | | 139. |
| | | | 99. |
| | | | 108. |
| | | | 171. |

ECONOMY POINT-SD 6 DATE - 7/ 6/74

TIDAL HEIGHTS
HIGH : 13.
LOW : 1.
HIGH : 1.

TIME - 3055.

TIDAL COEFFICIENTS
EBB :
FLOOD : .69

| TIME | DEPTH | SPEED | DIR |
|---|---|---|---|
| 1.67 | | | |
| | | | 282. |
| | | | 277. |
| | | | 270. |
| | | | 267. |
| | | | 284. |
| 2.42 | | | |
| | | | 281. |
| | | | 296. |
| | | | 294. |
| | | | 299. |
| 1.79 | | | |
| | | | 268. |
| | | | 262. |
| | | | 261. |
| 2.08 | | | |
| | | | 240. |
| | | | 238. |
| 2.33 | | | |
| | | | 227. |
| 2.50 | | | |
| 1.34 | .179 | 187. | |
| 2.83 | | | |
| 1.94 | .098 | 286. | |
| 9.58 | | | |
| | | | 71. |
| 9.92 | | | |
| | | | 98. |
| | | | 98. |
| 10.09 | | | |
| | | | 70. |
| | | | 72. |
| 10.33 | | | |
| | | | 81. |
| | | | 78. |
| | | | 99. |
| 10.58 | | | |
| | | | 98. |
| | | | 84. |
| | | | 102. |
| 11.08 | | | |
| | | | 83. |
| | | | 79. |
| | | | 85. |
| | | | 77. |
| 11.33 | | | |
| | | | 77. |
| | | | 99. |
| | | | 92. |
| | | | 98. |
| 11.58 | | | |
| | | | 81. |
| | | | 104. |
| | | | 88. |
| | | | 88. |
| 12.08 | | | |
| | | | 122. |
| | | | 21. |
| | | | 84. |
| | | | 99. |

ECONOMY POINT-FO 1 ... DATE - 28/ 8/74

TIDAL HEIGHTS
HIGH : 15.2
LOW : 1.2
HIGH : 16.2

TIME - 2155

TIDAL COEFFICIENTS
EBB :
FLOOD : :

| TIME | DEPTH | SPEED | DIR |
|---|---|---|---|
| .92 | | | |
| | | | 284. |
| | | | 310. |
| | | | 281. |
| | | | 284. |
| | | | 290. |
| | | | 301. |
| | | | 290. |
| | | | 292. |
| 2.58 | | | |
| | | | 119. |
| | | | 112. |
| 5.03 | | | |
| | | | 76. |
| | | | 74. |
| 11.50 | | | |
| | | | 89. |
| | | | 88. |
| | | | 86. |
| | | | 87. |
| | | | 88. |

| TIME | DEPTH | SPEED | DIR |
|---|---|---|---|
| 1.29 | | | |
| | | | 256. |
| | | | 263. |
| | | | 264. |
| | | | 268. |
| | | | 269. |
| | | | 258. |
| 2.83 | | | |
| | | | 114. |
| | | | 112. |
| 10.33 | | | |
| | | | 79. |
| | | | 79. |
| | | | 78. |
| | | | 76. |

| TIME | DEPTH | SPEED | DIR |
|---|---|---|---|
| 1.58 | | | |
| | | | 254. |
| | | | 266. |
| | | | 259. |
| | | | 253. |
| 3.88 | | | |
| | | | 109. |
| 10.67 | | | |
| | | | 83. |
| | | | 84. |
| | | | 89. |
| | | | 86. |
| | | | 87. |

| TIME | DEPTH | SPEED | DIR |
|---|---|---|---|
| 1.92 | | | |
| | | | 256. |
| | | | 218. |
| | | | 276. |
| | | | 287. |
| 5.33 | | | |
| | .42 | .103 | 258. |
| 10.92 | | | |
| | | | 89. |
| | | | 82. |
| | | | 83. |
| | | | 93. |
| | | | 88. |
| | | | 81. |

| TIME | DEPTH | SPEED | DIR |
|---|---|---|---|
| 2.25 | | | |
| | | | 249. |
| | | | 241. |
| | | | 243. |
| 8.54 | | | |
| | | | 97. |
| | | | 81. |
| 11.25 | | | |
| | | | 98. |
| | | | 89. |
| | | | 83. |
| | | | 98. |
| | | | 85. |
| | | | 79. |

ECONOMY POINT-FO 2 ... DATE - 28/ 8/74

TIDAL HEIGHTS
HIGH : 15.6
LOW : 1.2
HIGH : 15.8

TIME - 0155

TIDAL COEFFICIENTS
EBB :
FLOOD : :

| TIME | DEPTH | SPEED | DIR |
|---|---|---|---|
| .79 | | | |
| | | | 255. |
| | | | 268. |
| | | | 273. |
| | | | 264. |
| | | | 269. |
| 2.21 | | | |
| | | | 209. |
| | | | 207. |
| | | | 213. |
| 5.88 | | | |
| 1.29 | .011 | | 79. |
| 10.33 | | | |
| | | | 88. |
| | | | 83. |
| | | | 73. |
| | | | 79. |

| TIME | DEPTH | SPEED | DIR |
|---|---|---|---|
| 1.38 | | | |
| | | | 253. |
| | | | 267. |
| | | | 261. |
| | | | 267. |
| | | | 264. |
| 2.96 | | | |
| | | | 213 |
| | | | 228. |
| | | | 229. |
| 9.25 | | | |
| | | | 94. |
| | | | 96. |
| 10.58 | | | |
| | | | 79. |
| | | | 84. |
| | | | 77. |
| | | | 78. |

| TIME | DEPTH | SPEED | DIR |
|---|---|---|---|
| 1.62 | | | |
| | | | 256. |
| | | | 263. |
| | | | 266. |
| | | | 253. |
| 2.87 | | | |
| | | | 239. |
| 9.58 | | | |
| | | | 84. |
| | | | 81. |
| 10.97 | | | |
| | | | 82. |
| | | | 76. |
| | | | 83. |
| | | | 82. |

| TIME | DEPTH | SPEED | DIR |
|---|---|---|---|
| 1.79 | | | |
| | | | 248. |
| | | | 249. |
| | | | 258. |
| | | | 262. |
| 5.25 | | | |
| | | | 289. |
| | | | 192. |
| 9.79 | | | |
| | | | 82. |
| | | | 81. |
| | | | 77. |
| 11.29 | | | |
| | | | 93. |
| | | | 78. |
| | | | 77. |
| | | | 87. |

| TIME | DEPTH | SPEED | DIR |
|---|---|---|---|
| 2.08 | | | |
| | | | 299. |
| | | | 232. |
| | | | 277. |
| 5.33 | | | |
| 1.38 | .110 | | 97. |
| 10.04 | | | |
| | | | 81. |
| | | | 78. |
| | | | 82. |
| 11.54 | | | |
| | | | 99. |
| | | | 88. |
| | | | 88. |
| | | | 79. |

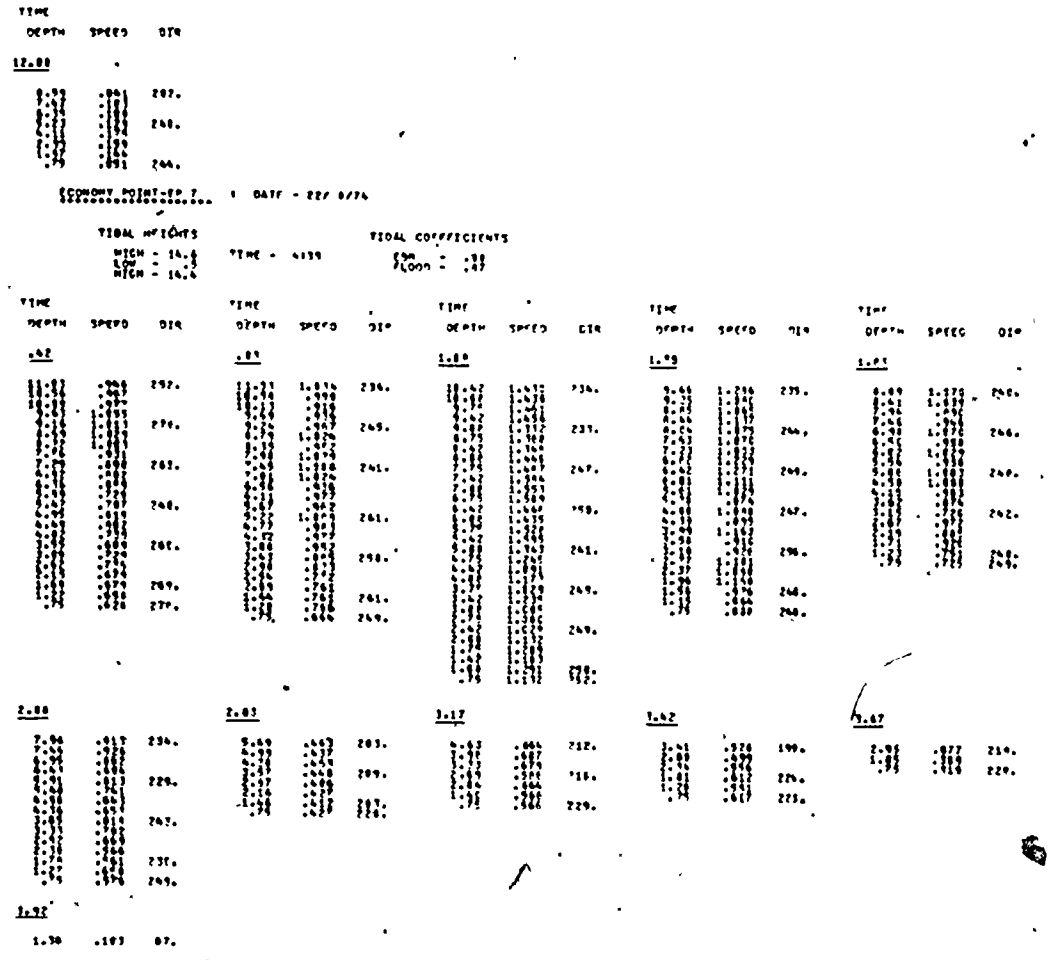
TIME
DEPTH SPEED DIR
12.00
287.
268.
244.
ECONOMY POINT-EP 2 DATE - 22/ 8/74
TIDAL HEIGHTS
HIGH = 14.6
LOW = 1.4
HIGH = 16.4
TIME - 4139
TIDAL COEFFICIENTS
EBB
FLOOD = .33
.42
.83
1.08
1.58
2.08
2.83
3.17
3.42
3.67
3.92
1.38 .103 87.
ECONOMY POINT-EP 2 DATE - 22/ 8/74
TIDAL HEIGHTS
HIGH = 13.6
LOW = 1.7
HIGH = 15.9
TIME - 7169
TIDAL COEFFICIENTS
EBB
FLOOD = .82
.83
1.08
1.29
1.58
1.79
2.08
2.29
2.83
3.38
3.58
10.29
10.79
11.03
11.29
11.42
11.79
287.
289.
289.
272.
272.
276.
277.
275.
274.
276.
278.
276.
262.
1.18 .859 261.
1.23 ..269 256.
1.39 .221 198.
103.
264.
98.
91.
91.
98.
98.
98.
131.
87.
91.

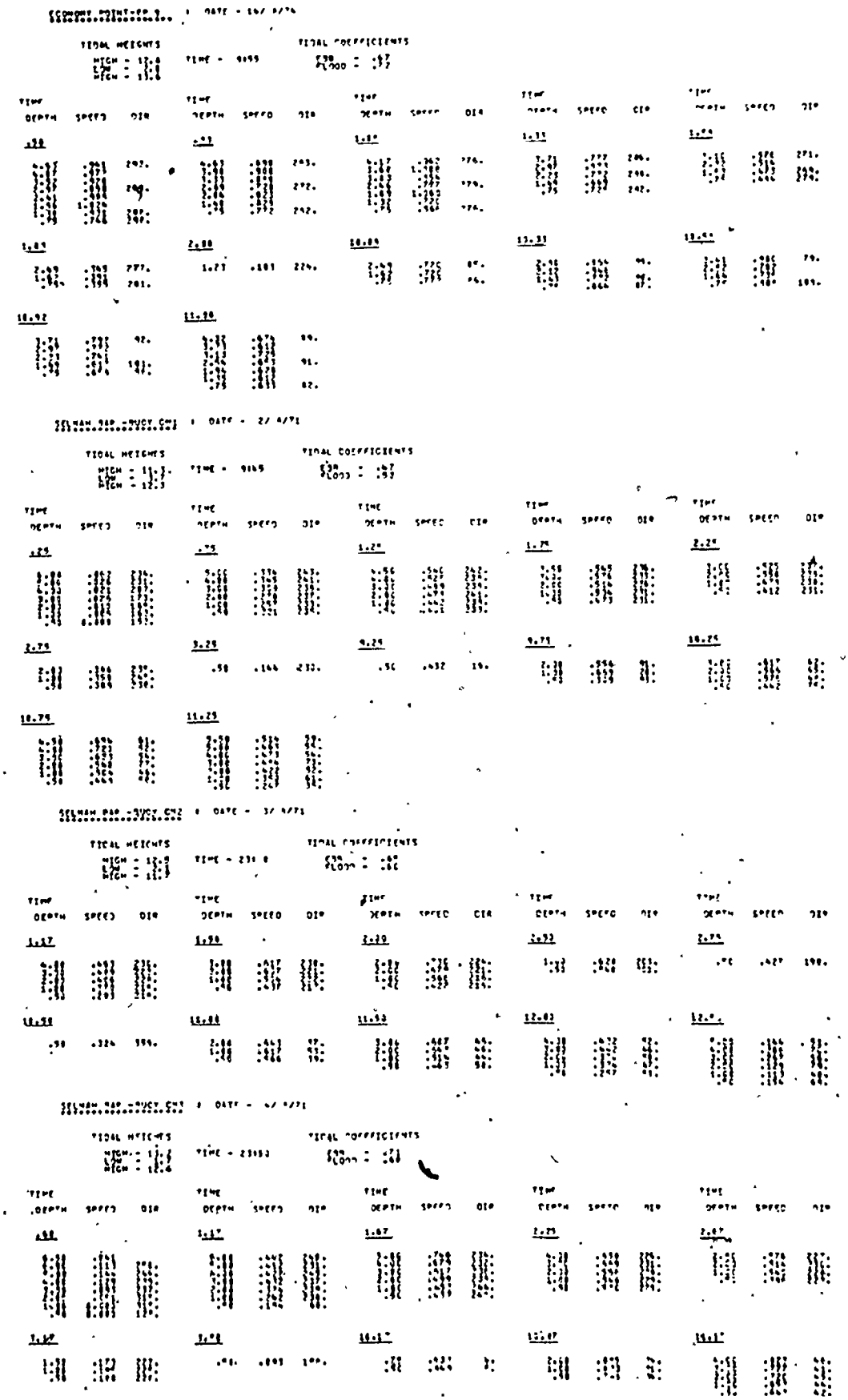

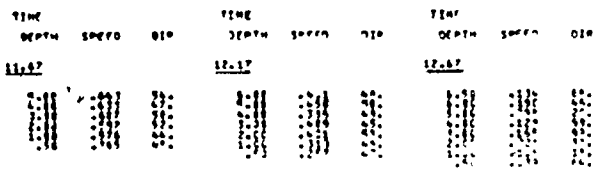
TIME
DEPTH
SPEED
DIR
11:47
12:17
12:47

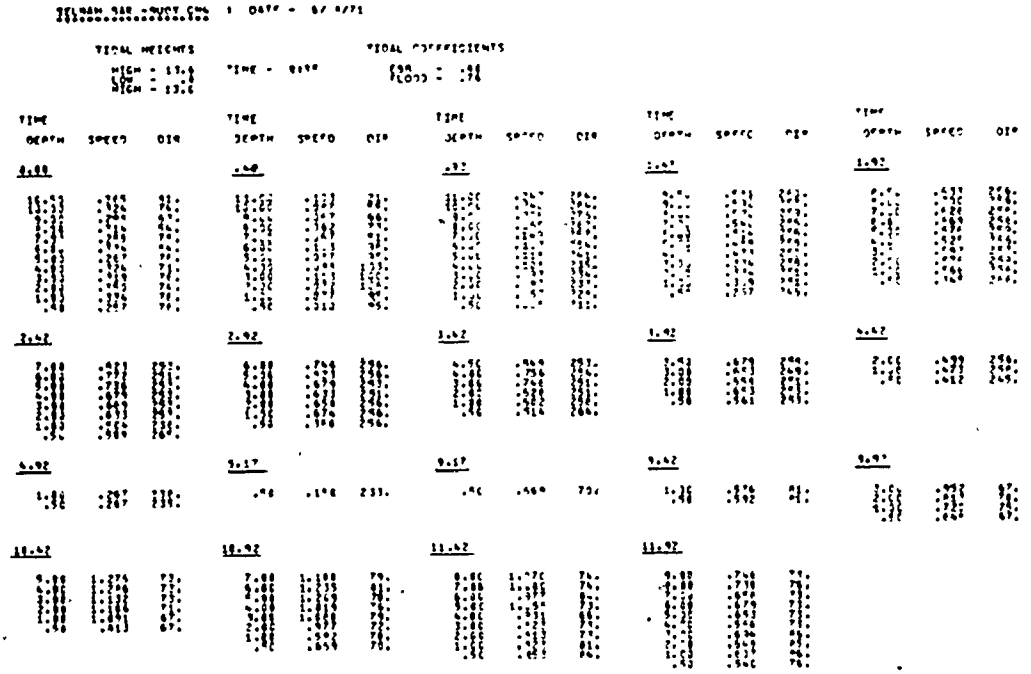
TIDAL HEIGHTS
TIDAL COEFFICIENTS
TIME
DEPTH
SPEED
DIR
8:08
:40
:32
1:07
1:32
2:02
2:32
3:02
3:32
4:02
4:32
5:02
5:17
9:17
9:47
10:02
10:32
11:02
11:32

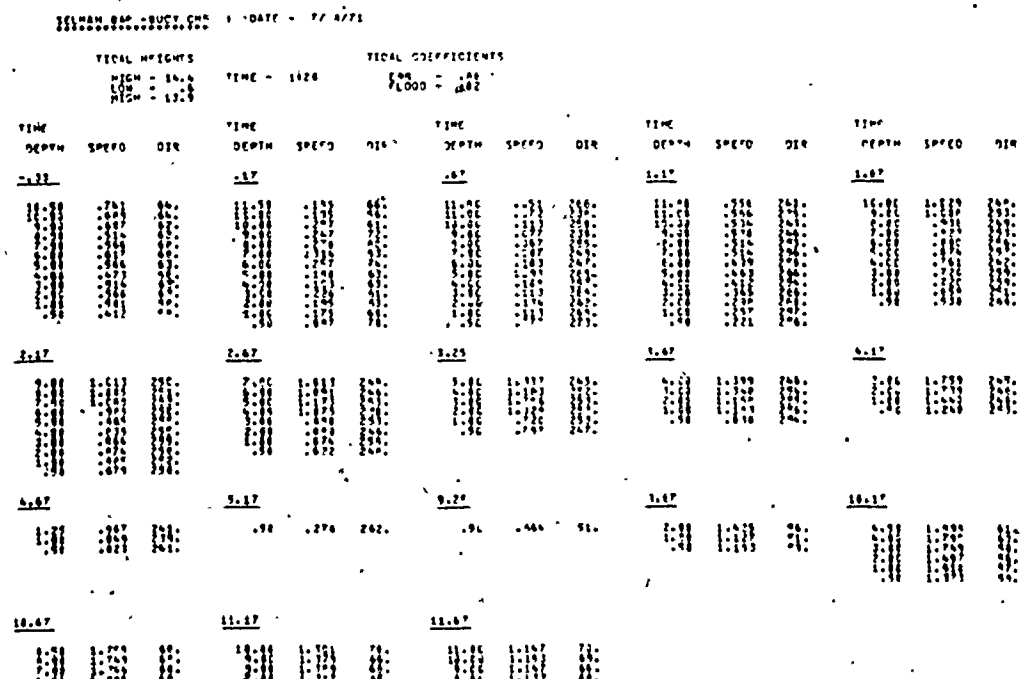
TIDAL HEIGHTS
TIDAL COEFFICIENTS
TIME
DEPTH
SPEED
DIR
-:32
:17
:47
1:17
1:47
2:17
2:47
3:25
3:47
4:17
4:47
5:17
9:29
9:47
10:17
10:47
11:17
11:47

APPENDIX 2

## COMPUTED HYDRAULIC PARAMETERS

The data presented in this appendix are the various hydraulic parameters that have been calculated to characterize the tidal currents. The computations involved are described in Section 3.1.3, and are based on the least-squares regression of the current speed on the logarithm of the height above the bed, using the data listed in Appendix 1. If less than three measurements are available to define a profile, or the slope of the computed regression line is negative, certain of the parameters cannot be evaluated, and are left blank in the listing. Profiles for which the correlation coefficient is non-significant are indicated by dots, positioned to the left of the profile time: one dot if the level of significance is between 0.75 and 0.95; and two dots if it is less than 0.75.

The locations of all current metering stations are shown in Figure 3.1. Tidal height and tidal coefficient data preceding the computed parameters for each tidal cycle are identical to those appearing in Appendix 1. A brief description of each of the computed parameters, together

with their units and the number of the equations (Section 3.1.3) used to obtain them, are listed below.

| Column Heading | Meaning | Units | Equation Number |
|---|---|---|---|
| TIME | time of profile after morning high tide (E = ebb; F = flood) | hours | - |
| TOTAL DEPTH | total water depth (h) | m | - |
| BOTTOM DIR. | flow direction measured nearest to the bed (for Big Bar stations it is a surface direction) | degrees | |
| MEAN SPEED | mean current speed ($\bar{U}$); average of current speeds (u) evaluated at 0.2 h and 0.8 h using the regression line | m/s | - |
| DISCHARGE | volume flow rate of water per metre width ( $q = \bar{U}h$). | $m^2/s$ | - |
| U100 | current speed evaluated one metre above the bed using the regression line | m/s | - |
| TURB | standard deviation of data points about the regression line | m/s | - |
| U STAR | shear velocity ($u_*$) | m/s | (3.11) |
| TAU | shear stress at the bed ($\tau_o$) | $kg/ms^2$ | (3.9) |
| STREAM POWER | rate at which flow performs work on a unit area of the bed ($\omega$) | $kg/s^3$ | (3.13) |
| ENERGY SLOPE | slope of the energy grade line (S) | - | (3.7b) |
| F | Darcy-Weisbach friction factor (f) | - | (3.14) |
| KS | equivalent sand roughness ($k_s$) | m | (3.10) and (3.12) |

| Column Heading | Meaning | Units | Equation Number |
|---|---|---|---|
| ZO | height above bed ($z_o$) where flow velocity goes to zero as estimated from the regression line. | m | - |
| FROUDE NUMBER | dimensionless number proportional to the ratio of inertial to gravitational forces | - | (3.16) |
| REYNOLDS NUMBER | dimensionless number proportional to the ratio of inertial to viscous forces | - | (3.5) |

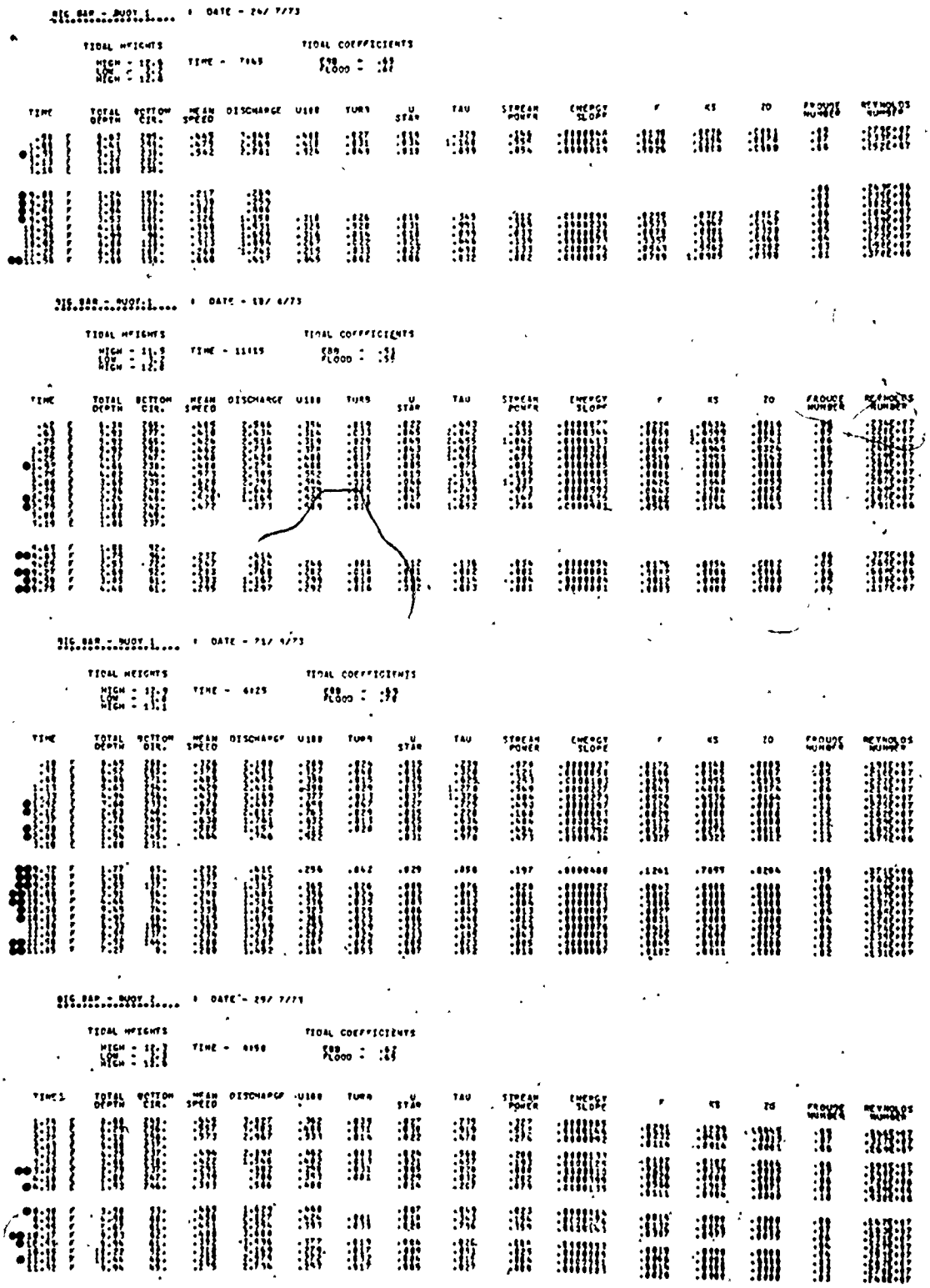

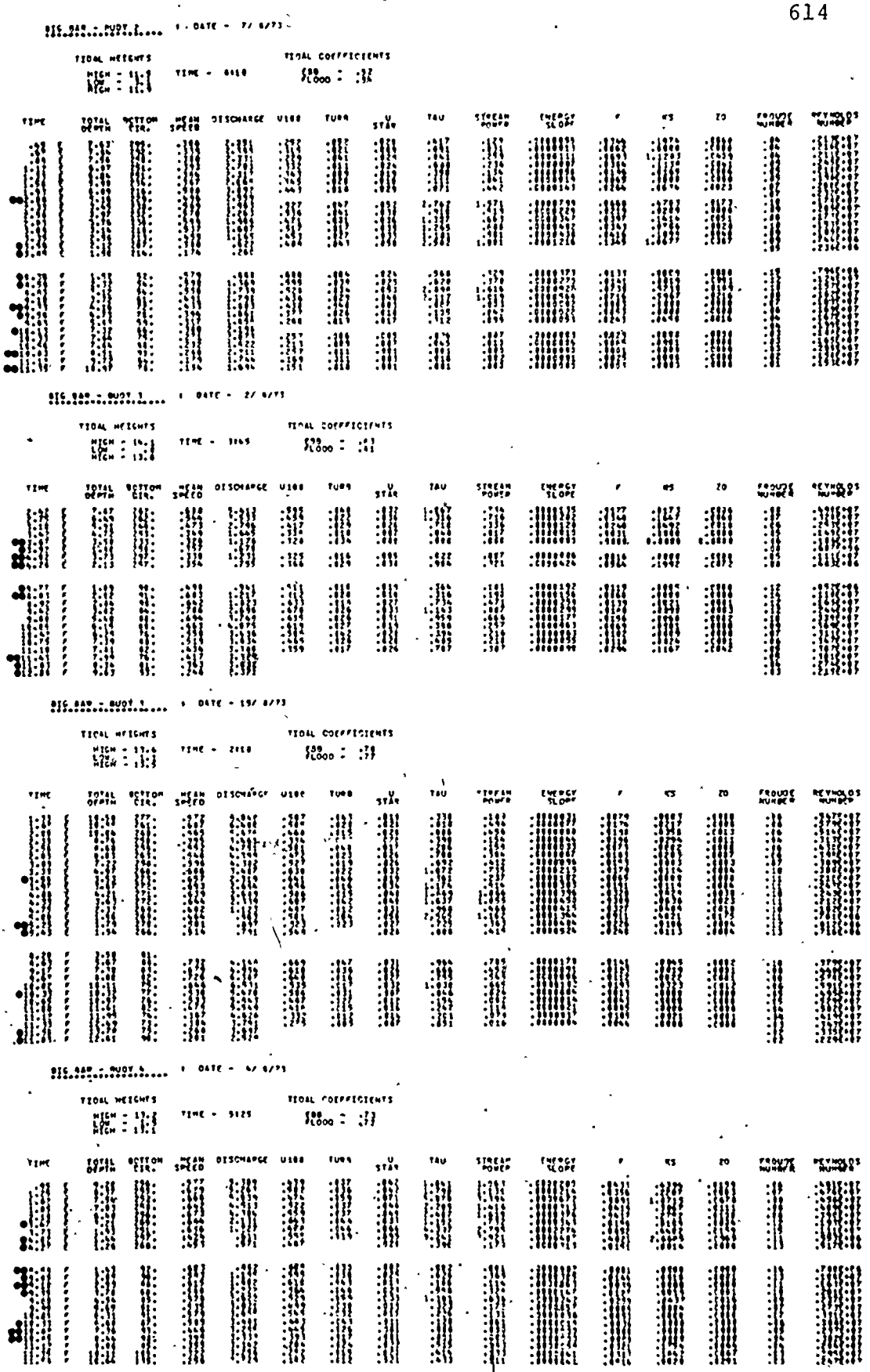

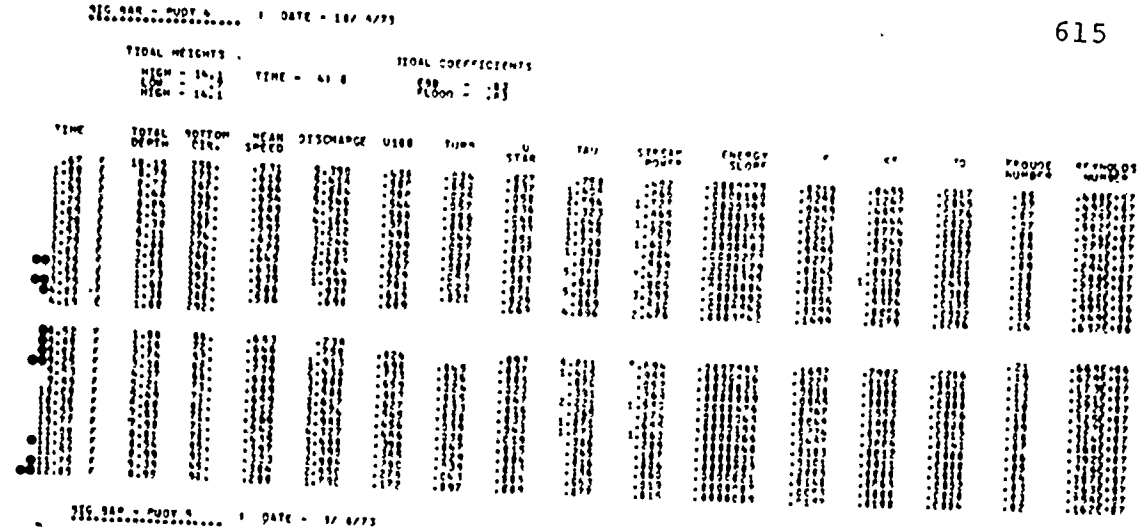
TIDAL HEIGHTS
TIME =
TIDAL COEFFICIENTS
TIME
TOTAL DEPTH
BOTTOM CIRC.
MEAN SPEED
DISCHARGE
U100
TURB
U STAR
TAU
STREAM POWER
ENERGY SLOPE
F
KS
ZO
FROUDE NUMBER
REYNOLDS NUMBER

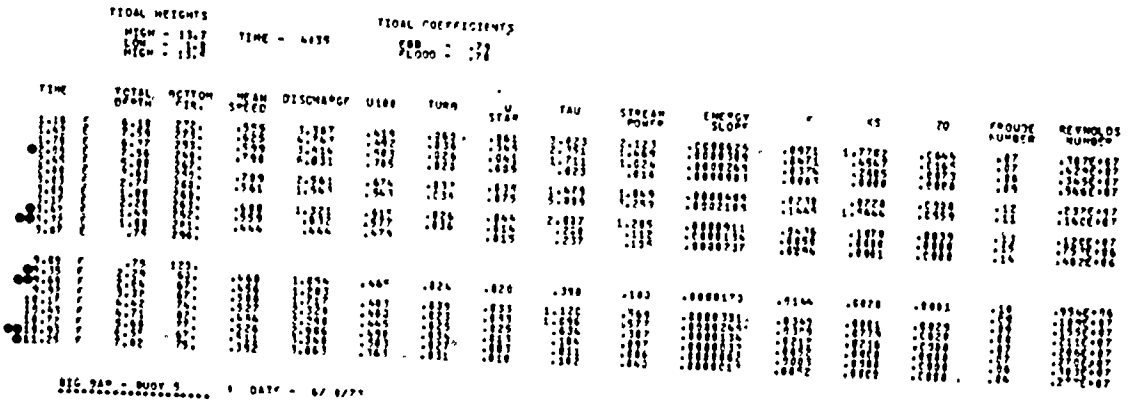
TIDAL HEIGHTS
TIME =
TIDAL COEFFICIENTS
TIME
TOTAL DEPTH
BOTTOM CIRC.
MEAN SPEED
DISCHARGE
U100
TURB
U STAR
TAU
STREAM POWER
ENERGY SLOPE
F
KS
ZO
FROUDE NUMBER
REYNOLDS NUMBER

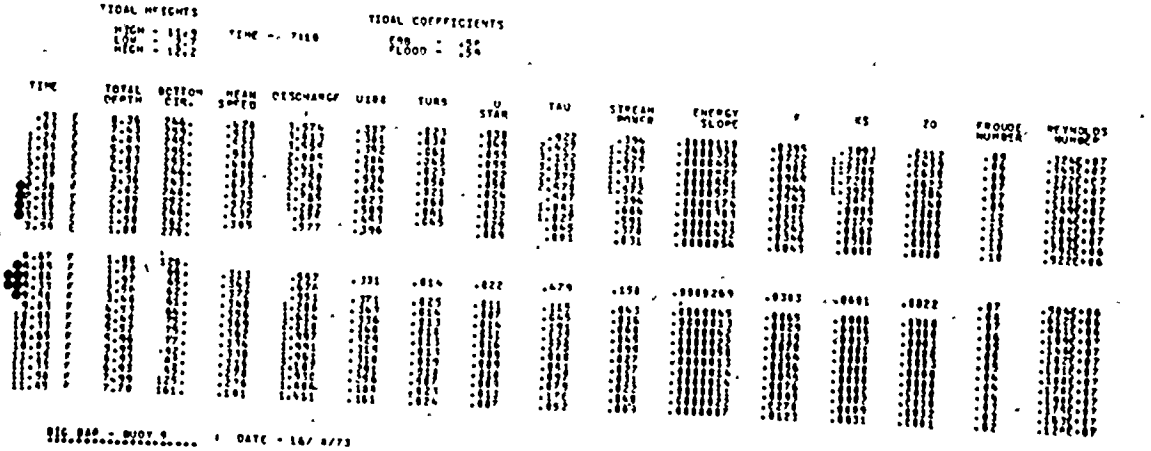
TIDAL HEIGHTS
TIME =
TIDAL COEFFICIENTS
TIME
TOTAL DEPTH
BOTTOM CIRC.
MEAN SPEED
DISCHARGE
U100
TURB
U STAR
TAU
STREAM POWER
ENERGY SLOPE
F
KS
ZO
FROUDE NUMBER
REYNOLDS NUMBER

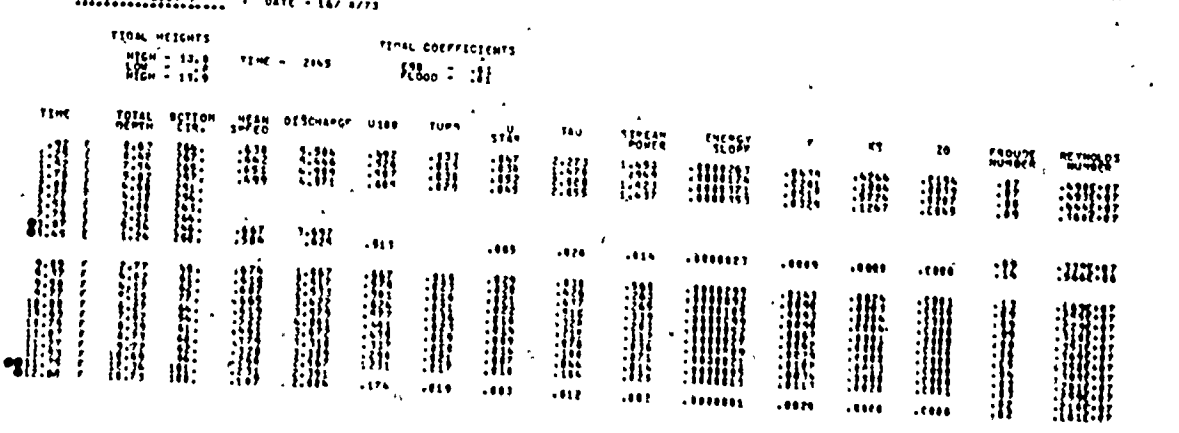
TIDAL HEIGHTS
TIME =
TIDAL COEFFICIENTS
TIME
TOTAL DEPTH
BOTTOM CIRC.
MEAN SPEED
DISCHARGE
U100
TURB
U STAR
TAU
STREAM POWER
ENERGY SLOPE
F
KS
ZO
FROUDE NUMBER
REYNOLDS NUMBER

316.040...BUOY 8..... DATE = 8/ 8/73

TIDAL HEIGHTS

HIGH = 11.3
LOW = 11.5
HIGH = 11.8

TIME = 0115

TIDAL COEFFICIENTS

EBB = .00
FLOOD = .92

| TIME | TOTAL DEPTH | BOTTOM CIRC. | MEAN SPEED | DISCHARGE | U100 | TURB | U STAR | TAU | STREAM POWER | ENERGY SLOPE | F | KS | ZO | FROUDE NUMBER | REYNOLDS NUMBER |
|---|---|---|---|---|---|---|---|---|---|---|---|---|---|---|---|
| | | | | | | | | | | | | | | | |
| | | | | | | | | | | | | | | | |
| | | | | | | | | | | | | | | | |
| | | | | | | | | | | | | | | | |
| | | | | | | | | | | | | | | | |
| | | | | | | | | | | | | | | | |
| | | | | | | | | | | | | | | | |
| | | | | | | | | | | | | | | | |
| | | | | | .252 | | .015 | .228 | .051 | .0009151 | .0725 | .0309 | .0311 | | |
| | | | | | .239 | .017 | .021 | .449 | .115 | .0000107 | .0019 | .3149 | .0314 | | |
| | | | | | | | | | | | | | | | |
| | | | | | | | | | | | | | | | |
| | | | | | | | | | | | | | | | |
| | | | | | | | | | | | | | | | |
| | | | | | | | | | | | | | | | |

316.040...BUOY 8..... DATE =[illegible] 8/73

TIDAL HEIGHTS

HIGH = 13.6
LOW = 13.7
HIGH = 13.9

TIME = 0130

TIDAL COEFFICIENTS

EBB = .77
FLOOD = .77

| TIME | TOTAL DEPTH | BOTTOM CIRC. | MEAN SPEED | DISCHARGE | U100 | TURB | U STAR | TAU | STREAM POWER | ENERGY SLOPE | F | KS | ZO | FROUDE NUMBER | REYNOLDS NUMBER |
|---|---|---|---|---|---|---|---|---|---|---|---|---|---|---|---|
| | | | | | | | | | | | | | | | |
| | | | | | | | | | | | | | | | |
| | | | | | | | | | | | | | | | |
| | | | | | | | | | | | | | | | |
| | | | | | | | | | | | | | | | |
| | | | | | | | | | | | | | | | |
| | | | | | | | | | | | | | | | |
| | | | | | | | | | | | | | | | |
| | | | | | .156 | .015 | .004 | .025 | .003 | .0000092 | .0042 | .0000 | .C000 | | |
| | | | | | | | | | | | | | | | |
| | | | | | | | | | | | | | | | |
| | | | | | | | | | | | | | | | |
| | | | | | | | | | | | | | | | |
| | | | | | | | | | | | | | | | |
| | | | | | | | | | | | | | | | |

316.040...BUOY 7..... DATE = 9/ 8/73

TIDAL HEIGHTS

HIGH = 11.3
LOW = 11.5
HIGH = 11.8

TIME = 10015

TIDAL COEFFICIENTS

EBB = .00
FLOOD = .92

| TIME | TOTAL DEPTH | BOTTOM CIRC. | MEAN SPEED | DISCHARGE | U100 | TURB | U STAR | TAU | STREAM POWER | ENERGY SLOPE | F | KS | ZO | FROUDE NUMBER | REYNOLDS NUMBER |
|---|---|---|---|---|---|---|---|---|---|---|---|---|---|---|---|
| | | | | | | | | | | | | | | | |
| | | | | | | | | | | | | | | | |
| | | | | | | | | | | | | | | | |
| | | | | | | | | | | | | | | | |
| | | | | | | | | | | | | | | | |
| | | | | | | | | | | | | | | | |
| | | | | | | | | | | | | | | | |
| | | | | | | | | | | | | | | | |
| | | | | | | | | | | | | | | | |
| | | | | | | | | | | | | | | | |
| | | | | | | | | | | | | | | | |
| | | | | | | | | | | | | | | | |
| | | | | | | | | | | | | | | | |
| | | | | | | | | | | | | | | | |

316.040...BUOY 7..... DATE = 22/ 8/73

TIDAL HEIGHTS

HIGH = 13.6
LOW = 13.7
HIGH = 13.9

TIME = 7025

TIDAL COEFFICIENTS

EBB = .83
FLOOD = .83

| TIME | TOTAL DEPTH | BOTTOM CIRC. | MEAN SPEED | DISCHARGE | U100 | TURB | U STAR | TAU | STREAM POWER | ENERGY SLOPE | F | KS | ZO | FROUDE NUMBER | REYNOLDS NUMBER |
|---|---|---|---|---|---|---|---|---|---|---|---|---|---|---|---|
| | | | | | | | | | | | | | | | |
| | | | | | | | | | | | | | | | |
| | | | | | | | | | | | | | | | |
| | | | | | | | | | | | | | | | |
| | | | | | | | | | | | | | | | |
| | | | | | | | | | | | | | | | |
| | | | | | | | | | | | | | | | |
| | | | | | | | | | | | | | | | |
| | | | | | | | | | | | | | | | |
| | | | | | | | | | | | | | | | |
| | | | | | | | | | | | | | | | |
| | | | | | | | | | | | | | | | |
| | | | | | | | | | | | | | | | |
| | | | | | | | | | | | | | | | |

[illegible] DATE - 17/ 8/73

TIDAL HEIGHTS
HIGH : [illegible]
LOW : [illegible]
HIGH : [illegible]

TIME - 3120

TIDAL COEFFICIENTS
FOR FLOOD : .83

| TIME | TOTAL DEPTH | BOTTOM STR. | MEAN SPEED | DISCHARGE | U100 | TURB | U STAR | TAU | STREAM POWER | ENERGY SLOPE | F | KS | ZO | FROUDE NUMBER | REYNOLDS NUMBER |
|---|---|---|---|---|---|---|---|---|---|---|---|---|---|---|---|
| [illegible] | | | | | | | | | | | | | | | |

[illegible] DATE - 23/ 8/73

TIDAL HEIGHTS
HIGH : [illegible]
LOW : [illegible]
HIGH : [illegible]

TIME - 0130

TIDAL COEFFICIENTS
FOR FLOOD : .83

| TIME | TOTAL DEPTH | BOTTOM STR. | MEAN SPEED | DISCHARGE | U100 | TURB | U STAR | TAU | STREAM POWER | ENERGY SLOPE | F | KS | ZO | FROUDE NUMBER | REYNOLDS NUMBER |
|---|---|---|---|---|---|---|---|---|---|---|---|---|---|---|---|
| | | | | | .401 | | .193 | *0.666 | 6.814 | .0030186 | 12.9169 | 10.2623 | .3717 | | |

[illegible] DATE - 28/ 8/73

TIDAL HEIGHTS
HIGH : [illegible]
LOW : [illegible]
HIGH : [illegible]

TIME -- 0120

TIDAL COEFFICIENTS
FOR FLOOD : .71

| TIME | TOTAL DEPTH | BOTTOM STR. | MEAN SPEED | DISCHARGE | U100 | TURB | U STAR | TAU | STREAM POWER | ENERGY SLOPE | F | KS | ZO | FROUDE NUMBER | REYNOLDS NUMBER |
|---|---|---|---|---|---|---|---|---|---|---|---|---|---|---|---|
| | | | | | .087 | | | | | | | | | | |

[illegible] DATE - 11/ 9/73

TIDAL HEIGHTS
HIGH : [illegible]
LOW : [illegible]
HIGH : [illegible]

TIME - 5100

TIDAL COEFFICIENTS
FOR FLOOD : .81

| TIME | TOTAL DEPTH | BOTTOM STR. | MEAN SPEED | DISCHARGE | U100 | TURB | U STAR | TAU | STREAM POWER | ENERGY SLOPE | F | KS | ZO | FROUDE NUMBER | REYNOLDS NUMBER |
|---|---|---|---|---|---|---|---|---|---|---|---|---|---|---|---|
| | | | | | | | | | | | | | | | |

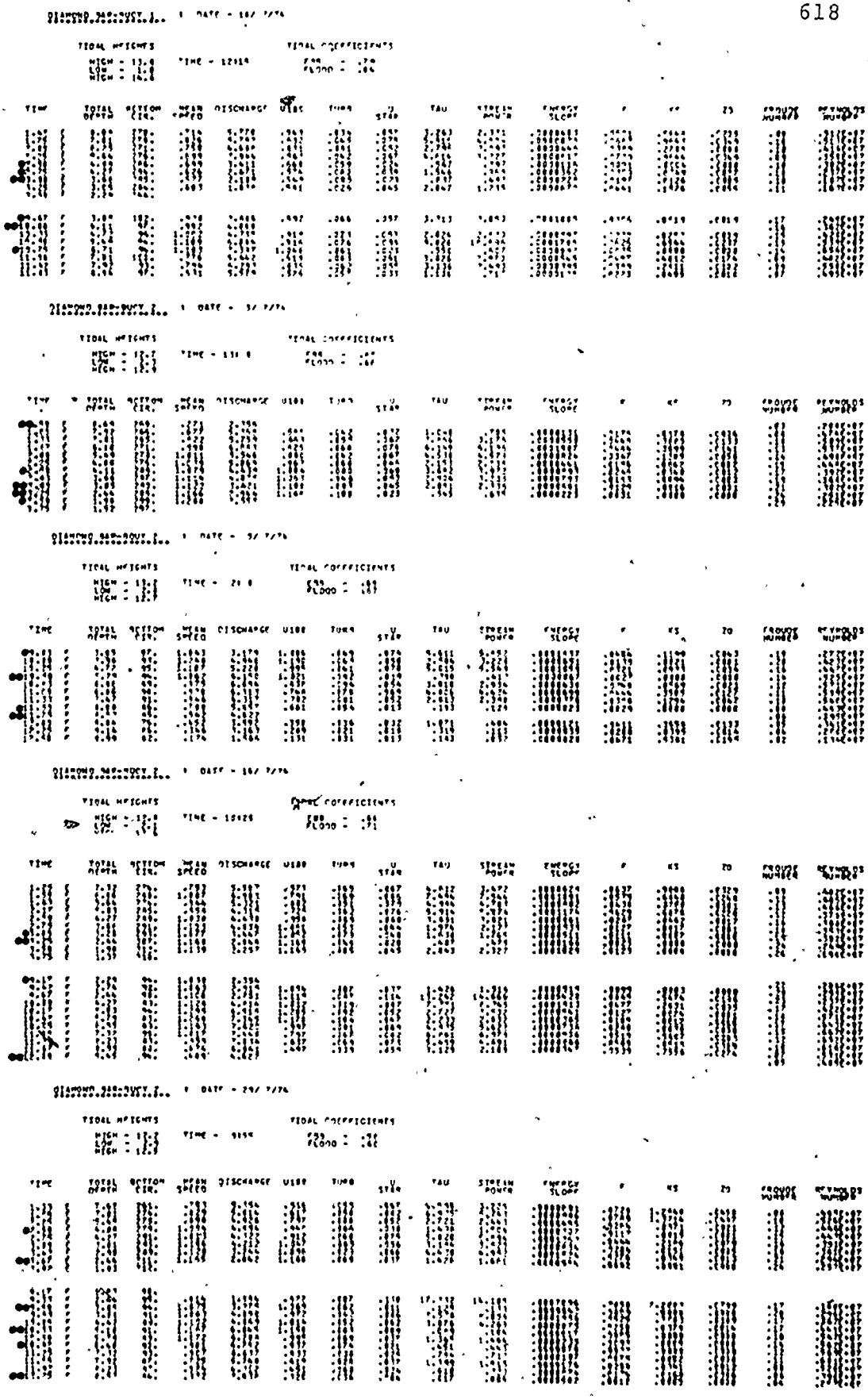

DIAMOND.SUS:RUCT.1.. * DATE = 6/ 7/74

TIDAL HEIGHTS
HIGH = 13.1
LOW = 1.9

TIME = 2148

TIDAL COEFFICIENTS
$C_{D100}$ = .07

| TIME | TOTAL DEPTH | BOTTOM STRESS | MEAN SPEED | DISCHARGE | U100 | TURB | U STAR | TAU | STREAM POWER | ENERGY SLOPE | F | RS | ZO | ROUGHNESS NUMBER | REYNOLDS NUMBER |
|---|---|---|---|---|---|---|---|---|---|---|---|---|---|---|---|
| 2148 | 13.1 | .119 | | | | | .087 | .044 | .319 | .0000015 | .0079 | .0000 | .0088 | | |
| 2148 | 1.9 | | | | | | | | | | | | | | |

DIAMOND.SUS:RUCT.1.. * DATE = 31/ 7/74

TIDAL HEIGHTS
HIGH = 13.1
LOW = 1.4

TIME = 22155

TIDAL COEFFICIENTS
$C_{D100}$ = .07

| TIME | TOTAL DEPTH | BOTTOM STRESS | MEAN SPEED | DISCHARGE | U100 | TURB | U STAR | TAU | STREAM POWER | ENERGY SLOPE | F | RS | ZO | ROUGHNESS NUMBER | REYNOLDS NUMBER |
|---|---|---|---|---|---|---|---|---|---|---|---|---|---|---|---|
| 2215 | 13.1 | | | | | | | | | | | | | | |
| 2215 | 1.4 | | | | | | | | | | | | | | |

DIAMOND.SUS:RUCT.1.. * DATE = 17/ 8/74 (SC.E.)

TIDAL HEIGHTS
HIGH = 14.5
LOW = 1.4

TIME = 22158

TIDAL COEFFICIENTS
$C_{D100}$ = .07

| TIME | TOTAL DEPTH | BOTTOM STRESS | MEAN SPEED | DISCHARGE | U100 | TURB | U STAR | TAU | STREAM POWER | ENERGY SLOPE | F | RS | ZO | ROUGHNESS NUMBER | REYNOLDS NUMBER |
|---|---|---|---|---|---|---|---|---|---|---|---|---|---|---|---|
| 2158 | 14.5 | | | | | | | | | | | | | | |
| 2158 | 1.4 | | | | | | | | | | | | | | |

DIAMOND.SUS:RUCT.1.. * DATE = 24/ 7/74

TIDAL HEIGHTS
HIGH = 13.2
LOW = 1.6

TIME = 2159

TIDAL COEFFICIENTS
$C_{D100}$ = .08

| TIME | TOTAL DEPTH | BOTTOM STRESS | MEAN SPEED | DISCHARGE | U100 | TURB | U STAR | TAU | STREAM POWER | ENERGY SLOPE | F | RS | ZO | ROUGHNESS NUMBER | REYNOLDS NUMBER |
|---|---|---|---|---|---|---|---|---|---|---|---|---|---|---|---|
| 2159 | 13.2 | | | | | | | | | | | | | | |
| 2159 | 1.6 | | | | | | | | | | | | | | |

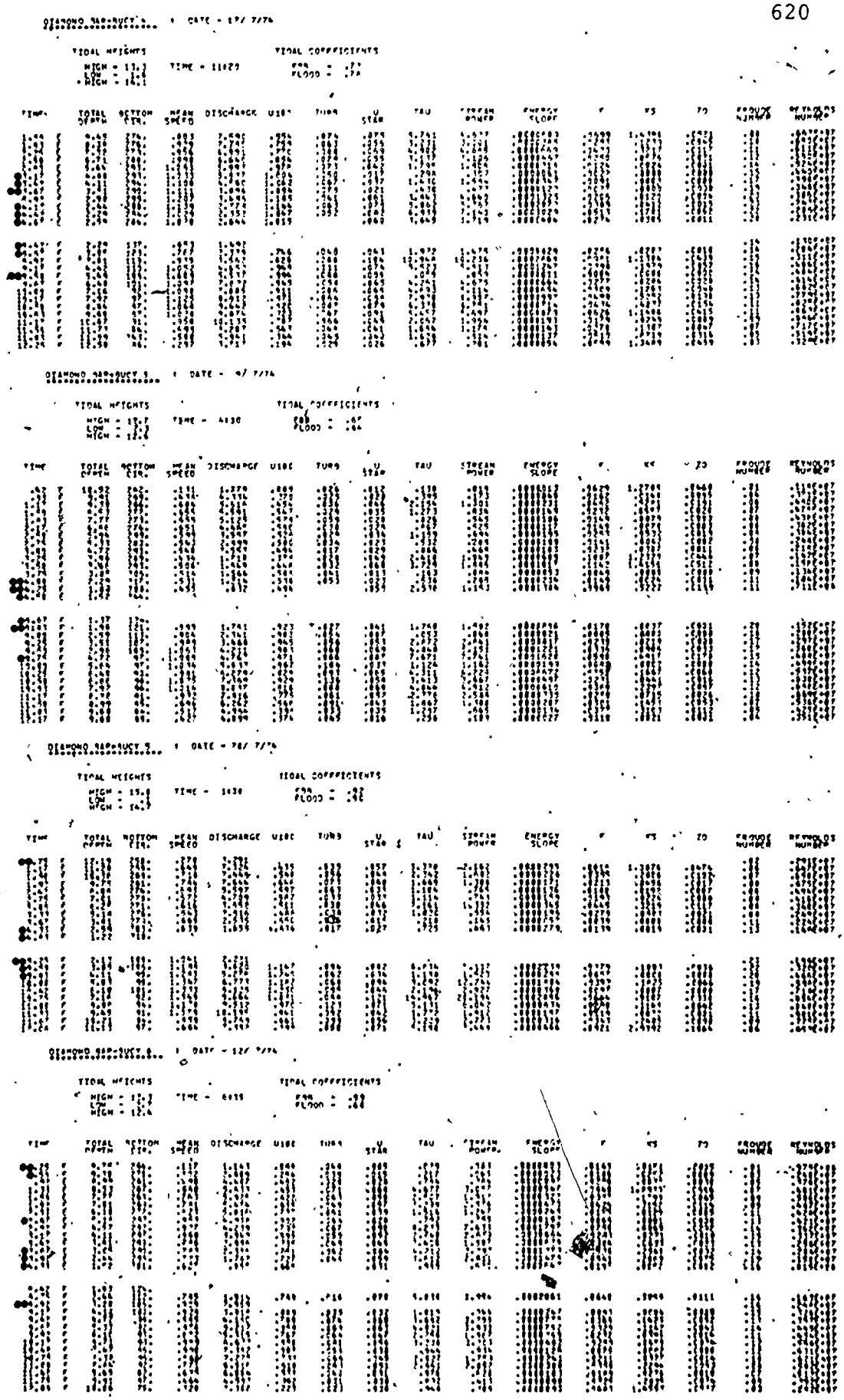

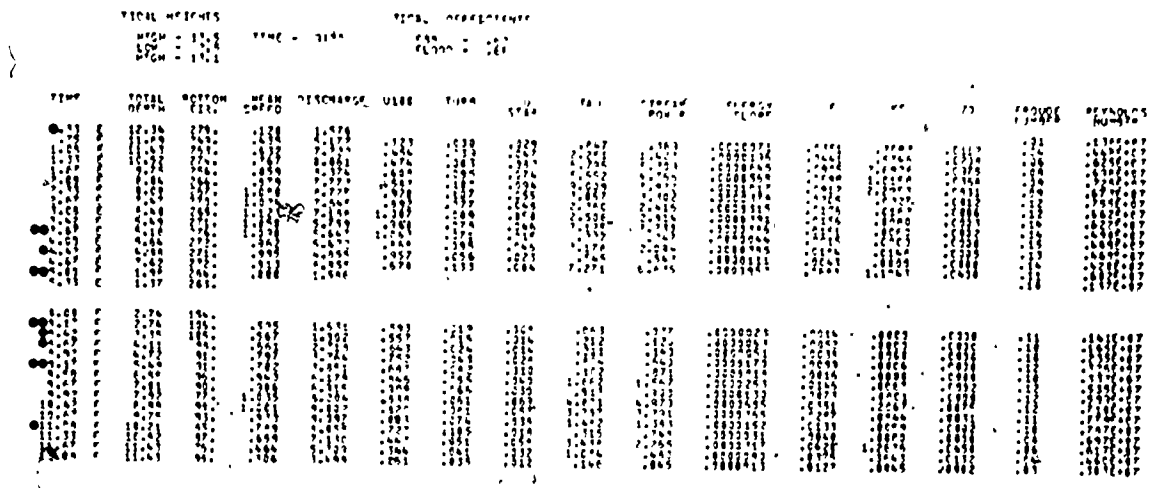

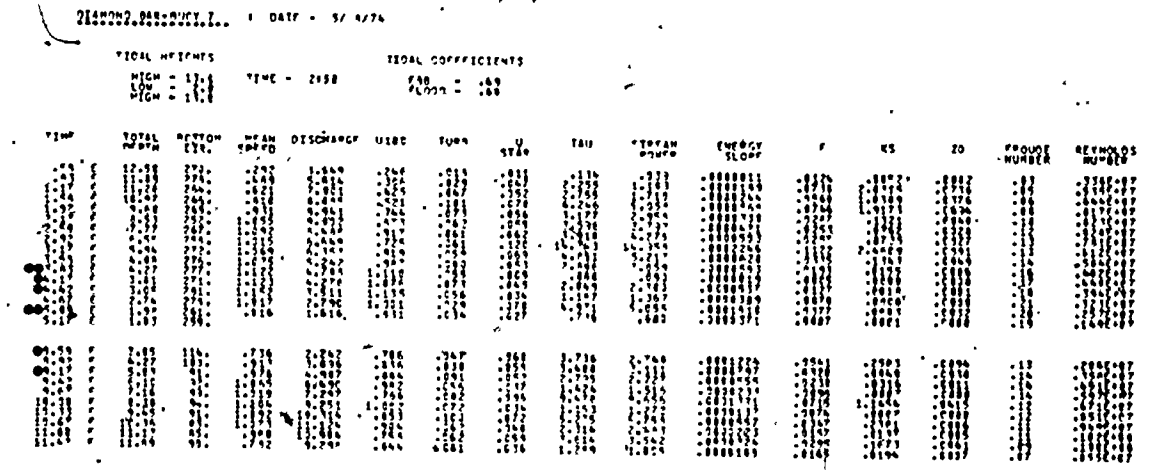

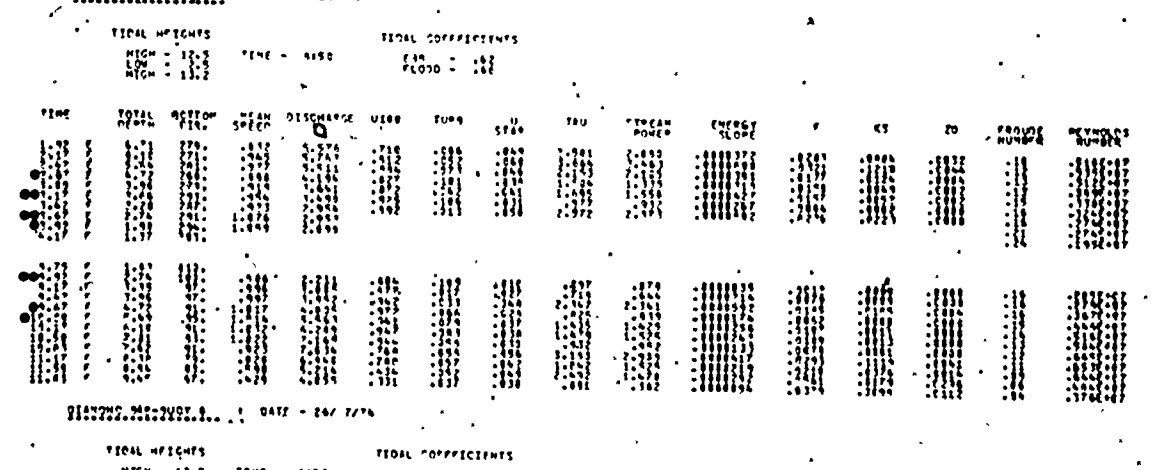

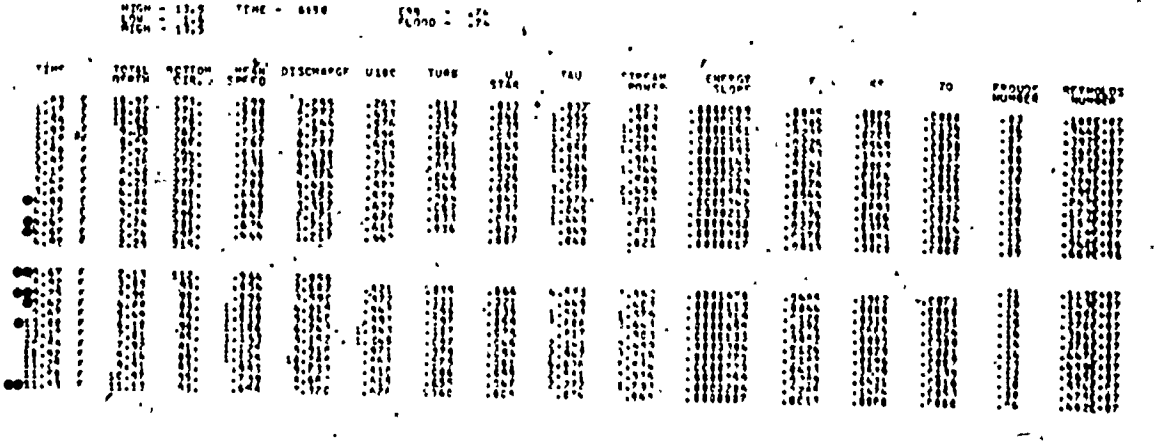

DIAMOND PRODUCT S.W. DATE = 1/ /74

TIDAL HEIGHTS

HIGH = 12.7
LOW = 2.6
HIGH = 12.6

TIME = 7:24

TIDAL COEFFICIENTS

EBB = .74
FLOOD = .71

| TIME | TOTAL DEPTH | BOTTOM SEC. | MEAN SPEED | DISCHARGE | U SEC | TURB | U STAR | TAU | STREAM POWER | ENERGY SLOPE | F | RS | ZO | FROUDE NUMBER | REYNOLDS NUMBER |
|---|---|---|---|---|---|---|---|---|---|---|---|---|---|---|---|
| | | | | | | | | | | | | | | | |
| | | | | | | | | | | | | | | | |

DIAMOND PRODUCT S.W. DATE = 24/ /74

TIDAL HEIGHTS

HIGH = 14.7
LOW = 2.2
HIGH = 14.2

TIME = 11:8

TIDAL COEFFICIENTS

EBB = .88
FLOOD = .87

| TIME | TOTAL DEPTH | BOTTOM SEC. | MEAN SPEED | DISCHARGE | U SEC | TURB | U STAR | TAU | STREAM POWER | ENERGY SLOPE | F | RS | ZO | FROUDE NUMBER | REYNOLDS NUMBER |
|---|---|---|---|---|---|---|---|---|---|---|---|---|---|---|---|
| | | | | | | | | | | | | | | | |
| | | | | | | | | | | | | | | | |

DIAMOND PRODUCT S.E. DATE = 9/ /74

TIDAL HEIGHTS

HIGH = 13.8
LOW = 2.1
HIGH = 13.1

TIME = 5:19

TIDAL COEFFICIENTS

EBB = .87
FLOOD = .84

| TIME | TOTAL DEPTH | BOTTOM SEC. | MEAN SPEED | DISCHARGE | U SEC | TURB | U STAR | TAU | STREAM POWER | ENERGY SLOPE | F | RS | ZO | FROUDE NUMBER | REYNOLDS NUMBER |
|---|---|---|---|---|---|---|---|---|---|---|---|---|---|---|---|
| | | | | | | | | | | | | | | | |
| | | | | | | | | | | | | | | | |

DIAMOND PRODUCT S.E. DATE = 24/ /74

TIDAL HEIGHTS

HIGH = 14.1
LOW = 1.9
HIGH = 13.4

TIME = 11:54

TIDAL COEFFICIENTS

EBB = .82
FLOOD = .82

| TIME | TOTAL DEPTH | BOTTOM SEC. | MEAN SPEED | DISCHARGE | U SEC | TURB | U STAR | TAU | STREAM POWER | ENERGY SLOPE | F | RS | ZO | FROUDE NUMBER | REYNOLDS NUMBER |
|---|---|---|---|---|---|---|---|---|---|---|---|---|---|---|---|
| | | | | | | | | | | | | | | | |
| | | | | | | | | | | | | | | | |

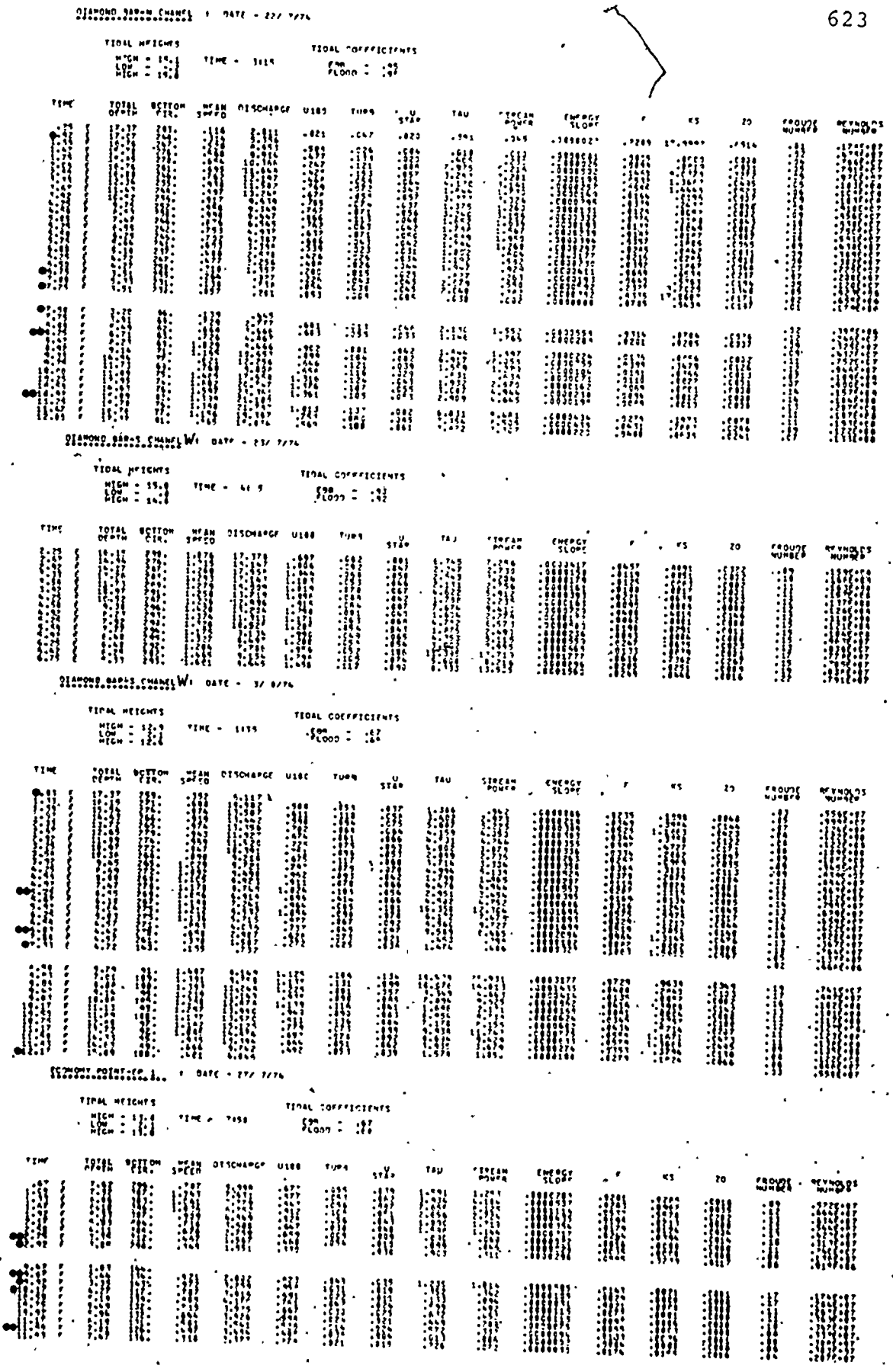

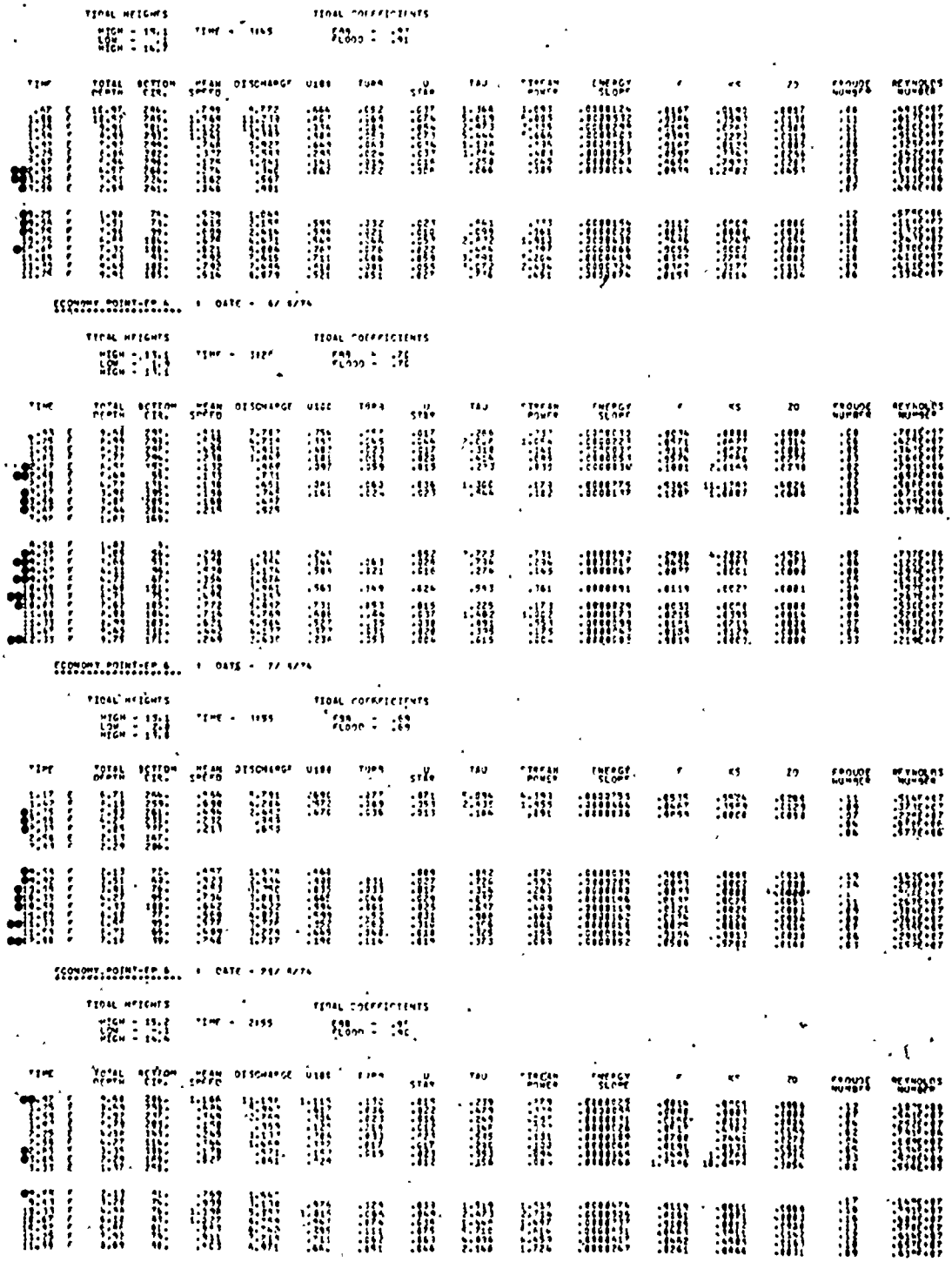

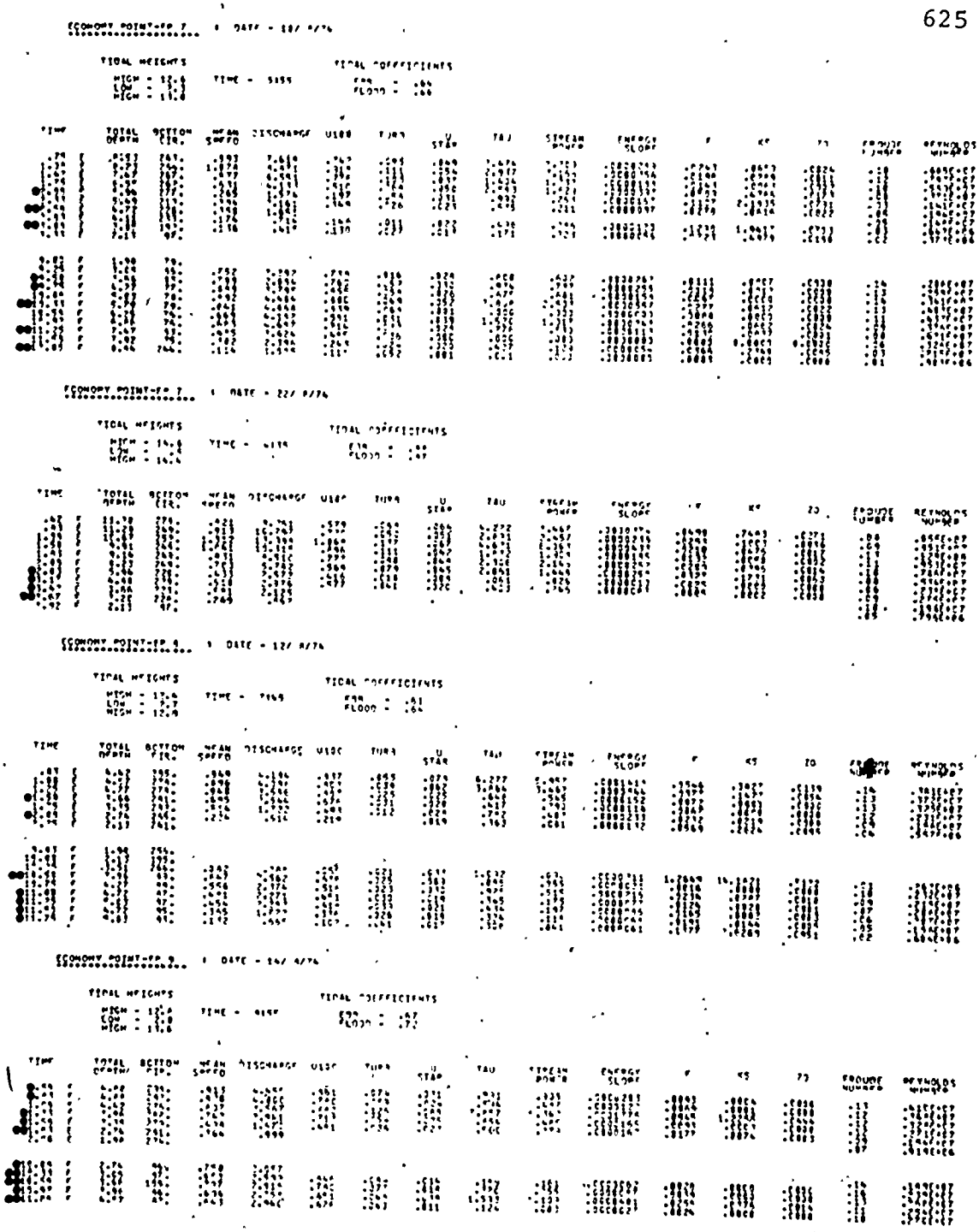

SELMAN.PAR_CRUCY.CM1 * DATE = 2/ 8/71

TIDAL HEIGHTS
HIGH = 11.3
LOW =
HIGH = 12.3

TIME = 0145

TIDAL COEFFICIENTS
FOR FLOOD = .87

| TIME | TOTAL DEPTH | BOTTOM CIR. | MEAN SPEED | DISCHARGE | U180 | TURB | U STAR | TAU | STREAM POWER | ENERGY SLOPE | F | KS | Z0 | FROUDE NUMBER | REYNOLDS NUMBER |
|---|---|---|---|---|---|---|---|---|---|---|---|---|---|---|---|
| 00 | | | | | | | | | | | | | | | |
| 06 | | | | | | | | | | | | | | | |

SELMAN.PAR_CRUCY.CM2 * DATE = 2/ 8/71

TIDAL HEIGHTS
HIGH = 12.0
LOW =
HIGH = 13.0

TIME = 2313

TIDAL COEFFICIENTS
FOR FLOOD = .87

| TIME | TOTAL DEPTH | BOTTOM CIR. | MEAN SPEED | DISCHARGE | U180 | TURB | U STAR | TAU | STREAM POWER | ENERGY SLOPE | F | KS | Z0 | FROUDE NUMBER | REYNOLDS NUMBER |
|---|---|---|---|---|---|---|---|---|---|---|---|---|---|---|---|
| 00 | | | | | | | | | | | | | | | |
| 06 | | | | | | | | | | | | | | | |

SELMAN.PAR_CRUCY.CM3 * DATE = 2/ 8/71

TIDAL HEIGHTS
HIGH = 12.8
LOW =
HIGH = 13.8

TIME = 2359

TIDAL COEFFICIENTS
FOR FLOOD = .88

| TIME | TOTAL DEPTH | BOTTOM CIR. | MEAN SPEED | DISCHARGE | U180 | TURB | U STAR | TAU | STREAM POWER | ENERGY SLOPE | F | KS | Z0 | FROUDE NUMBER | REYNOLDS NUMBER |
|---|---|---|---|---|---|---|---|---|---|---|---|---|---|---|---|
| 00 | | | | | | | | | | | | | | | |
| 06 | | | | | | | | | | | | | | | |

SELMAN.PAR_CRUCY.CM4 * DATE = 2/ 8/71

TIDAL HEIGHTS
HIGH = 13.6
LOW =
HIGH = 14.6

TIME = 0048

TIDAL COEFFICIENTS
FOR FLOOD = .96

| TIME | TOTAL DEPTH | BOTTOM CIR. | MEAN SPEED | DISCHARGE | U180 | TURB | U STAR | TAU | STREAM POWER | ENERGY SLOPE | F | KS | Z0 | FROUDE NUMBER | REYNOLDS NUMBER |
|---|---|---|---|---|---|---|---|---|---|---|---|---|---|---|---|
| 00 | | | | | | | | | | | | | | | |
| 06 | | | | | | | | | | | | | | | |

SELMAN.PAR_CRUCY.CM5 * DATE = 2/ 8/71

TIDAL HEIGHTS
HIGH = 14.4
LOW =
HIGH = 15.4

TIME = 0128

TIDAL COEFFICIENTS
FOR FLOOD = .98

| TIME | TOTAL DEPTH | BOTTOM CIR. | MEAN SPEED | DISCHARGE | U180 | TURB | U STAR | TAU | STREAM POWER | ENERGY SLOPE | F | KS | Z0 | FROUDE NUMBER | REYNOLDS NUMBER |
|---|---|---|---|---|---|---|---|---|---|---|---|---|---|---|---|
| 00 | | | | | | | | | | | | | | | |
| 06 | | | | | | | | | | | | | | | |

# APPENDIX 3

## GRAIN-SIZE DATA

The basic grain-size data for all 296 analysed sediment samples are listed below in the form of cumulative weight percentages at quarter-phi intervals as obtained by sieving. The phi size scale is shown at the left of the page. Also included are the mean size (phi), standard deviation (sorting) (phi-units), skewness, and kurtosis for each sample, calculated by the method of moments. The analytical techniques and computational procedures are described in Section 5.1.3.

The locations of all samples collected in the four major study areas are shown in Figure 5.1. The locations of the remaining samples obtained from the minor study bars are available from the author on request. The letter prefixes attached to each sample number indicate the bar from which each samples comes: BB - Big Bar; DB - Diamond Bar; C - channels surrounding Diamond Bar; CB - Centre Bar; EB - East Bar; SB - Selmah Bar; ENB - East Noel Bar; NBB - Noel Bay Bar; SR - Saints' Rest Bar; SPB - Spencer Point Bar; HVB - Highland Village Bar; and PF - Pinnacle Falts. As

described in Section 5.1.2, the letter designations following certain sample numbers indicate the position on the bedform where the sample was collected: C - bedform crest; L - base of bedform lee side; T - bedform trough; S - stoss side, where only one stoss side is present; ES - ebb stoss side; FS - remnant flood stoss side; and F - flat or rippled surface. All samples lacking a letter designation come from bedform crests.